AD-A256 200

WL-TR-91-3119

ELECTRONICS RELIABILITY FRACTURE MECHANICS

VOLUME 2. FRACTURE MECHANICS

J. Kallis, L. Duncan, D. Buechler,
P. Backes, D. Sandkulla, I. Chen
Hughes Aircraft Company
P. O. Box 902
El Segundo, California 90245

C. Popelar, D. Davidson, D. Pomerening,
M. Kanninen, J. Spencer, J. Campbell
Southwest Research Institute
P.O. Drawer 28510
San Antonio, Texas 78228-0510

D. Harris, R. Sire, D. Dedhia
Failure Analysis Associates, Inc.
149 Commonwealth Drive
Menlo Park, California 94025

May 1992

Final Report for Period May 1987 - September 1991

**DTIC
ELECTE
OCT 13 1992
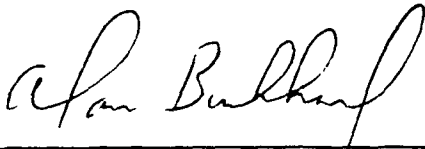S A D**

92-26856

FLIGHT DYNAMICS DIRECTORATE
WRIGHT LABORATORY
AIR FORCE SYSTEMS COMMAND
WRIGHT-PATTERSON AIR FORCE BASE, OHIO 45433-6553

NOTICE

When Government drawings, specifications, or other data are used for any purpose other than in connection with a definitely Government-related procurement, the United States Government incurs no responsibility or any obligation whatsoever. The fact that the government may have formulated or in any way supplied the said drawings, specifications, or other data, is not to be regarded by implication, or otherwise in any manner construed, as licensing the holder, or any other person or corporation; or as conveying any rights or permission to manufacture, use, or sell any patented invention that may in any way be related thereto.

This report is releasable to the National Technical Information Service (NTIS). At NTIS, it will be available to the general public, including foreign nations.

This technical report has been reviewed and is approved for publication.

ALAN H. BURKHARD
Project Engineer
Environmental Control Branch

ALBERT R. BASSO, II, CM
Chief, Environmental Control Branch
Vehicle Subsystems Division

RICHARD E. COLCLOUGH, JR.
Chief
Vehicle Subsystems Division

If your address has changed, if you wish to be removed from our mailing list, or if the addressee is no longer employed by your organization please notify WL/FIVE, WPAFB, OH 45433-6553 to help us maintain a current mailing list.

Copies of this report should not be returned unless return is required by security considerations, contractual obligations, or notice on a specific document.

REPORT DOCUMENTATION PAGE	Form Approved OMB No. 0704-0188

1a. REPORT SECURITY CLASSIFICATION UNCLASSIFIED	1b. RESTRICTIVE MARKINGS

2a. SECURITY CLASSIFICATION AUTHORITY	3. DISTRIBUTION/AVAILABILITY OF REPORT
2b. DECLASSIFICATION/DOWNGRADING SCHEDULE	Approved for public release; distribution is unlimited

4. PERFORMING ORGANIZATION REPORT NUMBER(S) EDSG Report R160309	5. MONITORING ORGANIZATION REPORT NUMBER(S) WL-TR-91-3119

6a. NAME OF PERFORMING ORGANIZATION Hughes Aircraft Company	6b. OFFICE SYMBOL (If applicable)	7a. NAME OF MONITORING ORGANIZATION Flight Dynamics Directorate (WL/FIVE) Wright Laboratory

6c. ADDRESS (City, State, and ZIP Code) P.O. Box 902 El Segundo, CA 90245	7b. ADDRESS (City, State, and ZIP Code) Wright-Patterson AFB, OH 45433-6553

8a. NAME OF FUNDING/SPONSORING ORGANIZATION Flight Dynamics Directorate	8b. OFFICE SYMBOL (If applicable) WL/FIVE	9. PROCUREMENT INSTRUMENT IDENTIFICATION NUMBER Contract No. F33615-87-C-3403

8c. ADDRESS (City, State, and ZIP Code) Wright-Patterson AFB, OH 45433-6553	10. SOURCE OF FUNDING NUMBERS			

PROGRAM ELEMENT NO.	PROJECT NO.	TASK NO.	WORK UNIT ACCESSION NO.
63205F	2978	03	01

11. TITLE (Include Security Classification)
Electronics Reliability Fracture Mechanics,
Volume 2. Fracture Mechanics

12. PERSONAL AUTHOR(S)
(On reverse)

13a. TYPE OF REPORT Final	13b. TIME COVERED FROM May 87 TO Sep 91	14. DATE OF REPORT (Year, Month, Day) May 1992	15. PAGE COUNT 351

16. SUPPLEMENTARY NOTATION

17. COSATI CODES			18. SUBJECT TERMS (Continue on reverse if necessary and identify by block number)
FIELD	GROUP	SUB-GROUP	Reliability (Electronics) Fracture (Mechanics)
20	03		
20	11		Fatigue (Mechanics) Finite Element Analysis

19. ABSTRACT (Continue on reverse if necessary and identify by block number)

This is the second of two volumes. The other volume (WL-TR-92-3015) is "Causes of Failures of Shop Replaceable Units and Hybrid Microcircuits."

The objective of the Electronics Reliability Fracture Mechanics (ERFM) program was to develop and demonstrate a life prediction technique for electronic assemblies, when subjected to environmental stresses of vibration and thermal cycling, based upon the mechanical properties of the materials and packaging configurations which make up an electronic system.

The application of fracture mechanics to microscale phenomena in electronic assemblies was a pioneering research effort. The small scale made the experiments very difficult; for example, the 1-mil-diameter bond wires in microelectronic devices are 1/3 the diameter of a human hair. A number of issues had to be resolved

(CONTINUES ON BACK)

20. DISTRIBUTION/AVAILABILITY OF ABSTRACT [X] UNCLASSIFIED/UNLIMITED ☐ SAME AS RPT. ☐ DTIC USERS	21. ABSTRACT SECURITY CLASSIFICATION Unclassified

22a. NAME OF RESPONSIBLE INDIVIDUAL Alan H. Burkhard	22b. TELEPHONE (Include Area Code) (513) 255-5752	22c. OFFICE SYMBOL WL/FIVE

DD Form 1473, JUN 86   Previous editions are obsolete.   SECURITY CLASSIFICATION OF THIS PAGE

BLOCK19. ABSTRACT *(Continued)*

to determine whether a fracture mechanics modelling approach is correct for the selected failures; specifically, the following two issues had to be resolved:

* What fraction of the lifetime is spent in crack initiation?
* Are macro fracture mechanics techniques, used in large structures such as bridges, applicable to the tiny structures in electronic equipment?

The following structural failure mechanisms were selected for modelling:

* bondwire fracture from mechanical cycling
* bondwire fracture from thermal (power) cycling
* plated through hole (PTH) fracture from thermal cycling.

The bondwire fracture test specimens were Al-1% Si wires, representative of wires used in the parts in the modules selected for detailed investigation in this program (see Vol. 1 of this report); 1-mil-diameter wires were tested in this program. The PTH test specimens were sections of 14-layer printed wiring boards of the type used in the modules; copper foil, as used in PTHs, also was tested.

The key conclusions of this research are:

Fracture mechanics is valid for damage tolerance analysis on the microscale.

With these extremely encouraging beginnings, a vigorous follow-up to realize the full potential of fracture mechanics for microscale structural elements is recommended.

BLOCK 12. PERSONAL AUTHORS

J. Kallis, L. Duncan, D. Buechler, P. Backes, D. Sandkulla, I. Chen
Hughes Aircraft Company
El Segundo, California

C. Popelar, D. Davidson, D. Pomerening, M. Kanninen, J. Spencer, J. Campbell
Southwest Research Institute
San Antonio, Texas

D. Harris, R. Sire, D. Dedhia
Failure Analysis Associates, Inc.
Menlo Park, California

ACKNOWLEDGMENTS

TABLE OF CONTENTS

TABLE OF CONTENTS (Continued)

TABLE OF CONTENTS (Continued)

LIST OF ILLUSTRATIONS

LIST OF ILLUSTRATIONS (Continued)

LIST OF ILLUSTRATIONS (Continued)

LIST OF ILLUSTRATIONS (Continued)

LIST OF ILLUSTRATIONS (Continued)

LIST OF TABLES

ABBREVIATIONS, ACRONYMS, AND SYMBOLS

AFWAL	Air Force Wright Aeronautical Laboratories (now WL)
AIAA	American Institute of Aeronautics & Astronautics
ANSI	American National Standard Institute
ASD	Aeronautical Systems Division
AVIP	Avionics/Electronics Integrity Program
CERT	Combined Environments Reliability Test
CTE	Coefficient of Thermal Expansion
CTOD	Crack Tip Opening Displacement
DIP	Dual Inline Package
DUT	Device Under Test
EPFM	Elasto-Plastic Fracture Mechanics
ERFM	Electronics Reliability Fracture Mechanics
ESD	Electrostatic Discharge
ESS	Environmental Stress Screening
FaAA	Failure Analysis Associates
FCG	Fatigue Crack Growth
FE	Finite Element
FEA	Finite Element Analysis
FEM	Finite Element Model
FFOP	Failure Free Operating Period
FIEE	Symbol for AFWAL Environmental Control Branch (now WL/FIVE)
FIVE	Symbol for WL (formerly WRDC) Environmental Control Branch (formerly FIEE)
HAC	Hughes Aircraft Company
IC	Integrated Circuit
ID	Inner Diameter
IEEE	Institute of Electrical & Electronics Engineers
IF	Influence Function
IPC	Institute for Interconnecting & Packaging Electronic Circuits (formerly Institute of Printed Circuits)
ISTFA	International Symposium for Testing & Failure Analysis
JIM	J-Integral Module
JPL	Jet Propulsion Laboratory
LEFM	Linear Elastic Fracture Mechanics
LRU	Line Replaceable Unit

LSIF	Linearized Stress with Influence Function
LVDT	Linear Variable Differential Transformer
MIT	Massachusetts Institute of Technology
NASA	National Aeronautics & Space Administration
NDE	Nondestructive Examination
NDI	Nondestructive Inspection
OD	Outer Diameter
PTH	Plated Through Hole
PWB	Printed Wiring Board
S-N	Stress or Strain (S) vs. Number (N) of Cycles to Failure
S/N	Serial Number
SEM	Scanning Electron Microscope
SRU	Shop Replaceable Unit
STP	Special Technical Publication
SwRI	Southwest Research Institute
TEM	Transmission Electron Microscopy
TSD	Technology Support Division
TTL	Transistor-Transistor Logic
U/S	Ultrasonic
WL	Wright Laboratory (formerly WRDC; formerly AFWAL)
WPAFB	Wright-Patterson Air Force Base
WRDC	Wright Research & Development Center (formerly AFWAL; now WL)

1.0 INTRODUCTION

The program overview is summarized in Refs. 1-1, 1-2.

1.1 BACKGROUND

Electronic assemblies at all levels of assembly, component, printed wiring board (PWB) and Line Replaceable Unit (LRUs) employ many combinations of equipment. The reliability (performance over time) of these assemblies is dependent upon the degeneration processes initiated by the interaction of the design and manufactured (package) configuration with the operational and environmental stresses imposed during its period of usage. In general, life limiting failure mechanisms generally arise from the configuration and use of materials which interact with one or more environmental parameters such as temperature, relative humidity, nuclear radiation, electrical potential gradients, mechanical fatigue cycling and corrosive chemicals. The manifested failures in electronic assemblies have been found to most often originate at the interface between different materials, at high stress sites and/or at sites where latent defects preexisted within the electronics.

Studies by many investigators have identified that the environmental stresses of vibration and thermal cycling significantly contribute to the failure rate of modern electronics (Ref. 1-3). Vibration and thermal cycling induce mechanical stress and strain in the materials and interfaces. The effects of cyclic stress and strain loading on materials have been extensively studied and modelled under the technical disciplines of fatigue analysis, linear elastic fracture mechanics and nonlinear fracture mechanics. In general, this work has been for structural materials used as load carrying members of large structures such as airframes or space structures as opposed to microscale structural configurations typical to an electronic assembly.

Over the past 15 years technical work to understand and in some cases model the reliability of specific failure prone sites within an electronic assembly has been accomplished. Generally this work has been done for a specific problem using techniques such as linear fracture mechanics, curve fitting of experimental data, fatigue analysis, and chemical reaction rate relationships. The focus of the Electronics Reliability Fracture Mechanics (ERFM) program was to bring this work together in a coherent manner so that Failure Free Operating Period (FFOP) predictions can be made based upon material properties and/or defect characteristics for the environmental effects of vibration and thermal cycling.

ERFM is a follow-on of a program called "Latent Defect Life Model & Data," which Hughes Aircraft Company performed under contract to the Air Force during the period 1984-1986 (Ref.

1-3). The conclusions and recommendations of that investigation led to the ERFM program, which Hughes performed under contract to the Air Force during the period 1987 - 1991 and which is documented here.

The life prediction technique demonstrated in the ERFM program will be used in future equipment acquisitions under the Avionics/Electronics Integrity Program (AVIP) by the Air Force (Ref. 1-4). Additionally it will permit an equipment manufacturer to translate reliability requirements to levels of quality, and appropriate manufacturing methods. These shall be expressed in terms of needed material properties and defect characteristics in the shipped product.

1.2 OBJECTIVE

The objective of the Electronics Reliability Fracture Mechanics (ERFM) program was to develop and demonstrate a life prediction technique for electronic assemblies, when subjected to environmental stresses of vibration and thermal cycling, based upon the mechanical properties of the materials and packaging configurations which make up an electronic system.

1.3 ORGANIZATION OF THIS REPORT

The ERFM program is documented in a two-volume report:

Volume 1, Causes of Failures of Shop Replaceable Units and Hybrid Microcircuits (WL-TR-92-3015), covers a detailed study of field failures in two APG-63 Shop Replaceable Units (SRU), evaluation of the latent defects hidden in these SRUs fresh off the production line, development of analytical models for hybrid microcircuit contamination failure mechanisms and special combined environment reliability test on the selected SRUs.

Volume 2, Fracture Mechanics (WL-TR-91-3119), covers the technical efforts to investigate the feasibility of using existing fracture mechanics technology to analyze the durability of microscale elements typically used in modern electronics.

Papers summarizing several aspects of the program have been presented at symposia. They are cited in the respective sections of this report.

2.0 APPROACH

The application of existing fracture mechanics technology to very small structural elements typical of modern electronics would extensively expand at relatively low development cost the analytical tools available to evaluate the durability of modern electronics. This research effort was focused at addressing the feasibility of this approach.

2.1 TEAM

A contractor team of experts in electronics reliability and fracture mechanics was assembled for this research. The team was led by the prime contractor, Hughes Aircraft. The major subcontractors, who contributed fracture mechanics expertise, were:

> Southwest Research Institute (SwRI), San Antonio, TX
> Failure Analysis Associates (FaAA), Menlo Park, CA

A second-tier subcontractor to SwRI for transmission electron microscopy (TEM) was the University of North Texas, Denton, TX.

The contractor team had frequent technical interchange with the Air Force Aeronautical Systems Division (ASD) structural engineers.

2.2 THE TECHNICAL CHALLENGE AND ISSUES TO BE RESOLVED

The results of the previous program (Ref. 1-3) and the early part of the ERFM program indicated that the application of fracture mechanics to microscale phenomena in electronic assemblies would be a pioneering research effort. The expected technical barriers were as follows:

- The simplest and most highly developed analytical tool, linear elastic fracture mechanics (LEFM), was not expected to be applicable to most materials and configurations of interest for avionics. The models were expected to require technologies at the cutting edge of current research, such as elasto-plastic fracture mechanics (EPFM) for cyclic loading.

- The small scale was expected to make the experiments very difficult. For example, the 1-mil-diameter bond wires in microelectronic devices are 1/3 the diameter of a human hair.

In view of the success achieved in the damage tolerance approach to aircraft structures and other components, a fracture mechanics based life modelling approach was undertaken. However, because of the small size of electronic components, it first had to be determined that such an approach is appropriate. A number of issues had to be resolved to determine whether a fracture mechanics modelling approach is correct for the selected failures. Specifically, the following two issues are to be resolved:

1. What fraction of the lifetime is spent in crack growth and

2. are macro fracture mechanics techniques used in large structures, such as bridges, applicable to the tiny structures in electronic equipment?

2.3 APPROACH TO RESOLVING THESE ISSUES

The approach to answering these questions was as follows:

1. Focus on one component.
2. Formulate a simple problem.
3. Perform a "proof of principle" experiment and analysis.
4. Proceed, based on the results of the initial test/analysis.

The component for which a data base and lifetime model was developed was selected on the basis of several different factors. First, the specific choice should be reasonably representative of the complexities that are involved in the various elements. Second, the geometry and loading conditions should allow an amenable analysis problem to be solved, e.g., via a plane stress solution procedure. Third, it should be possible to perform simulation testing to obtain realistic material properties and "proof of principle" test results.

The particular choice best satisfying these requirements appeared to be a wire attached to a rigid support that is subjected to inertial loading arising from high frequency vibratory loading of the base. The failure mechanism to be considered is progressive crack growth in planes transverse to the wire length.

In developing a lifetime prediction model, we choose to begin with a LEFM model using bulk material properties. Even though the suitability of bulk material properties for a structural element of this size has not been demonstrated, this model would help to scope the problem and identify weaknesses where further work is needed. At the same time, closely controlled, well-instrumented experiments were initiated to check the accuracy of the model (and later improved versions) and to provide a quantitative assessment of the key issue: the correspondence (or lack of correspondence) between bulk and small-scale mechanical and crack growth material properties. This type of coupled model development and experimentation was intended to pave the way for consideration of the elastic-plastic creep-fatigue lifetime prediction that was expected to have to be developed.

A flow chart of the overall test and analysis activities is shown in Figure 2-1. The flow chart indicates the directions taken depending upon the results of each task. As seen in the figure, the key issues are crack initiation/crack growth and the applicability of LEFM. Specific criteria for the resolution of these issues are discussed next.

With respect to crack initiation/crack growth, the test results, for example, on wires were expected to be extremely variable. This is due both to variable properties and to the difficulties in controlling the test conditions precisely. It follows that the test results were expected to contain a great deal of scatter. As reflected in Figure 2-2, a large number of test results, therefore, were expected to be needed.

```
                    ┌──────────────────────┐
                    │  FATIGUE LIFE TESTS  │
                    └──────────────────────┘
```

```
┌──────────────┐    ┌──────────────┐    ┌────────────────────┐
│    CRACK     │    │    CRACK     │    │  CRACK INITIATION  │
│  INITIATION  │    │ PROPAGATION  │    │        AND         │
│  DOMINATES   │    │  DOMINATES   │    │ CRACK PROPAGATION  │
│              │    │              │    │    SIGNIFICANT     │
└──────────────┘    └──────────────┘    └────────────────────┘
```

```
┌──────────────┐    ┌──────────────┐    ┌────────────────────┐
│   DEVELOP    │    │  FRACTURE    │    │  DEVELOP COMBINED  │
│   FATIGUE    │    │  MECHANICS   │    │ FATIGUE AND FRACTURE│
│   MODELS     │    │  APPROACH    │    │  MECHANICS MODELS  │
└──────────────┘    └──────────────┘    └────────────────────┘
```

```
                    ┌──────────────┐
                    │ TO WHAT EXTENT│
                    │      IS       │
                    │LEFM APPLICABLE?│
                    └──────────────┘
```

```
            ┌─────────┐              ┌─────────┐
            │  LARGE  │              │  SMALL  │
            └─────────┘              └─────────┘
```

```
            ┌─────────┐              ┌─────────┐
            │ DEVELOP │              │ DEVELOP │
            │  LEFM   │              │  EPFM   │
            │  MODEL  │              │  MODEL  │
            └─────────┘              └─────────┘
```
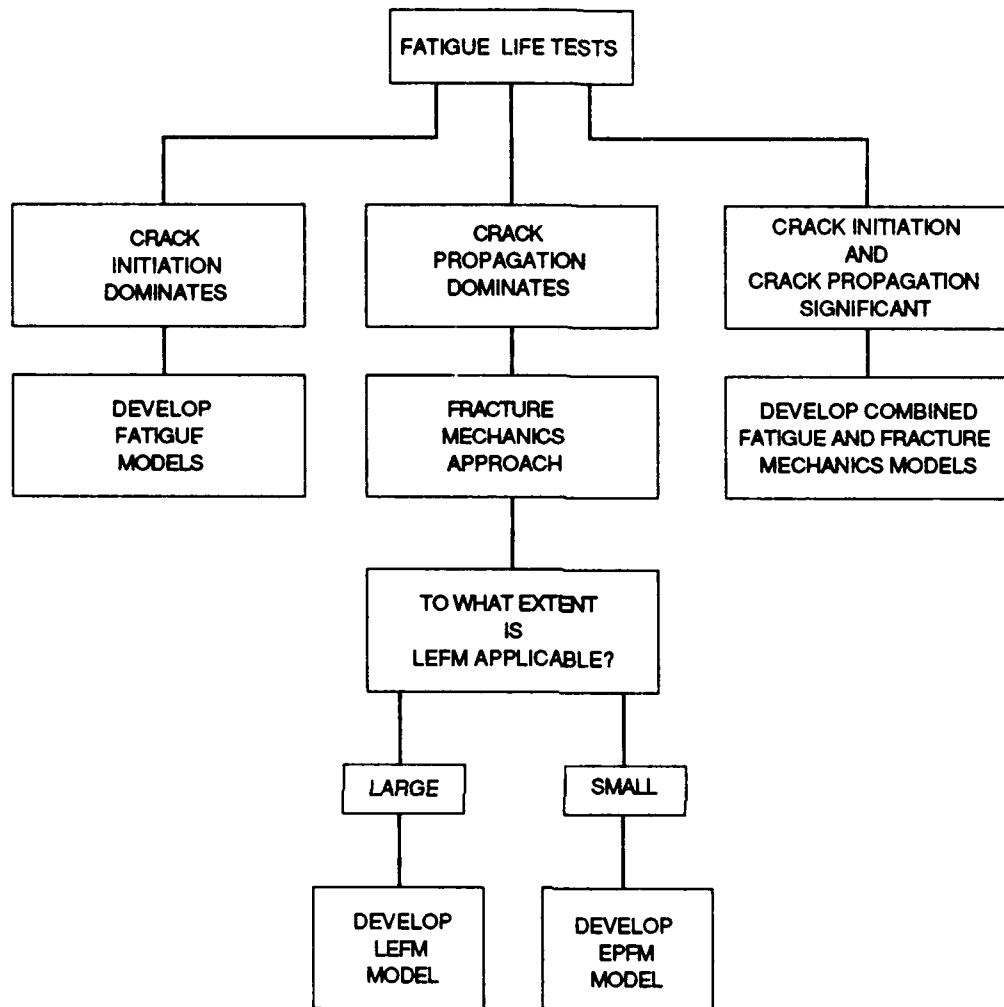
Figure 2-1. Flow Chart for Tests and Analyses

TEST RESULT WILL BE CURVE A OR CURVE B OR CURVE C

(y-axis: FREQUENCY OF TEST RESULTS)

A: CRACK GROWTH CAN BE NEGLECTED

C: INITIATION CAN BE NEGLECTED

B: BOTH ARE IMPORTANT

(x-axis: 0 ... 0.5 ... 1.00)

FRACTION OF LIFE SPENT IN CRACK GROWTH
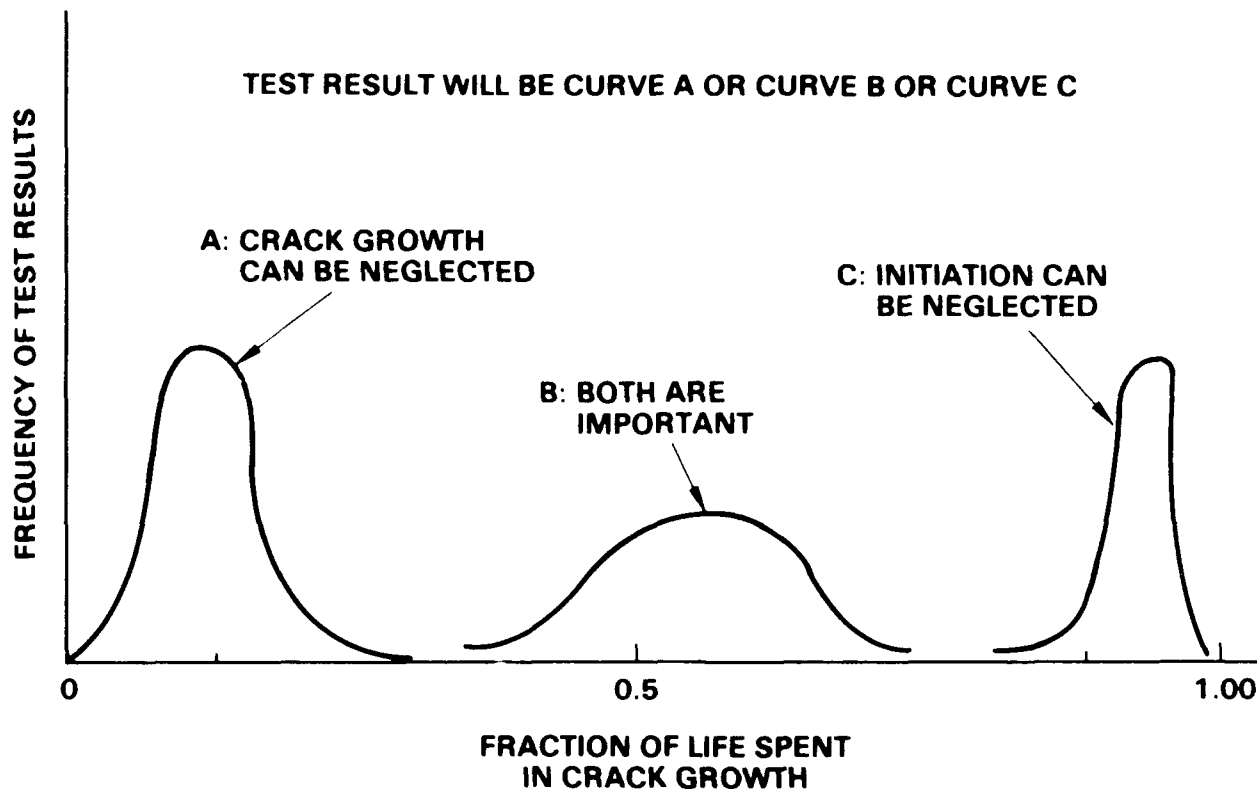
Figure 2-2. Empirical Basis for S-N Versus Fracture Mechanics for Fatigue Analyses

In any one test it is necessary either to observe or to infer (e.g., by a change in compliance) that a crack exists. However, the time after which a crack is growing is important only relative to the overall lifetime. The lifetime is defined here as the total loss of load carrying capability. This usually occurs quickly once the crack has propagated over halfway through the loaded member.

Fatigue lifetime is usually dominated by the time period in which the crack is relatively small. Hence, it is difficult to accurately determine the fraction of the life spent in crack growth. This is a further reason to expect scatter in these results. Assuming nevertheless that the testing is reasonably reproducible, the fatigue results can be expected to group in one of three different ways, as indicated in Figure 2-2.

If the predominance of the results indicated that a relatively small amount of time is spent in crack growth (e.g., less than 10% of the total life), then crack growth can be neglected. A conventional S-N approach is, therefore, appropriate. On the other hand, if the data are clustered around 90% of life consumed in crack growth, then the exclusive use of a fracture mechanics approach is appropriate. Finally, if the data are in the intermediate range, the situation is much more complex. Then a fracture mechanics approach must be coupled with an initiation model. Regardless, in all three instances, an analysis procedure can be formulated.

The analyses to develop and verify the life models begin with linear elastic fracture mechanics. Comparisons of results and predictions to the test data establish whether there is a need to move into more complex inelastic formulations. In either case, existing handbook solutions for the appropriate fracture mechanics parameters are a starting point. If these methods are shown to be inadequate, solutions can be obtained by means of finite element analysis.

For example, if the results of wire fatigue tests indicate that the predominance of the lifetime is consumed in growing a crack, then a fracture mechanics approach is, by definition, appropriate. The simplest such approach assumes that small-scale yielding conditions are met whereupon linear elastic fracture mechanics (LEFM) is valid. The crack driving force parameter in LEFM is the stress intensity factor, conventionally denoted by K. In fatigue, it follows that the key parameter is the change in K from the maximum to the minimum load. This is commonly denoted as ΔK. If the crack growth per loading cycle is expressed as da/dN, fatigue results might then be as shown in Figure 2-3.

RESULTS FOR RANGE OF INITIAL FLAWS

IF SPREAD IN da/dN RESULTS IS ACCEPTABLY SMALL (e.g., FACTOR OF 2), THEN LEFM IS APPROPRIATE. IF NOT, THEN EPFM WOULD BE DEVELOPED FOR SAME TYPE OF COMPARISON

$\frac{da}{dN}$

ΔK
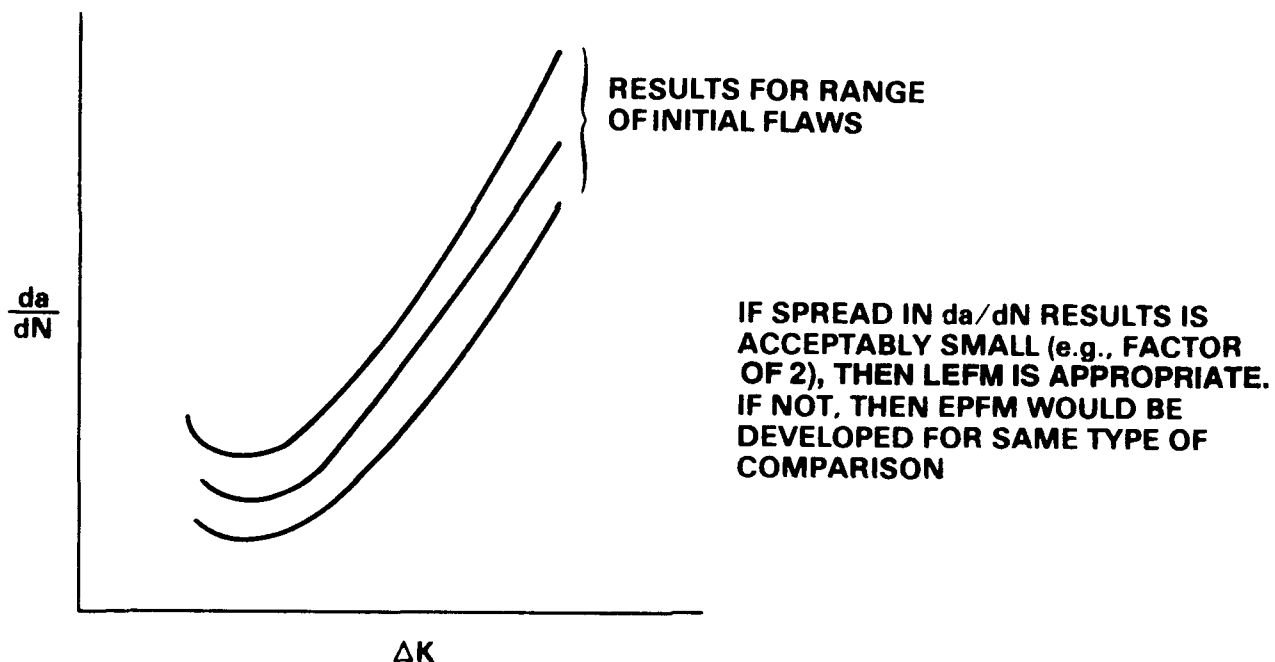
Figure 2-3. Basis for a Decision on Fracture Mechanics Approach

Owing to the scatter that will surely occur from material and test procedure variations, it may be that no discernible trend in the da/dN versus ΔK data is evident. If so, this may mean that LEFM is invalid whereupon an elastic-plastic fracture mechanics (EPFM) approach is required. The most commonly used EPFM parameter is J, a generalized energy release rate that also characterizes the near-tip stress and deformation field for power-law hardening elastic-plastic materials.

Beyond J are a host of parameters that take time and rate effects into account; e.g., the C* parameter for situations in which creep is important. Regardless, by redefining K such that, for example:

$$K = (EJ)^{1/2}$$

then the representation shown on Figure 2-3 is representative of any and all fracture mechanics approaches. However, it should be recognized that K is not necessarily the LEFM stress intensity factor. If it is not, it may not be readily obtainable from handbooks, but can be determined through EPFM finite element computations.

To continue, assume that (1) an appropriate fracture mechanics analysis procedure can be identified, and (2) that da/dN data can be reasonably well consolidated by it. Then, for fracture mechanics to be valid, the results for different wire sizes, initial flaw depths, and possibly other perturbations must give rise to exactly the same da/dN vs ΔK behavior.

It should be recognized that in metals, even under well controlled conditions, variations in da/dN of about 2 can be expected. Thus, if the spread of da/dN for a given ΔK, over the entire range of ΔK, is not much more than this, then it can be concluded that the fracture mechanics approach is valid.

In this spirit, even if there is a large difference between da/dN results for different testing conditions in the wire tests, it might be possible to represent the data by allowing wire sizes, initial flaw sizes, etc. to be parameters in the law the 's evolved. This will be acceptable so long as the results are reasonably reproducible.

2.4 FAILURE LOCATIONS INVESTIGATED

The following structural failure mechanisms were selected for modelling:

• bondwire fracture from mechanical cycling

• bondwire fracture from thermal (power) cycling

• plated through hole (PTH) fracture from thermal cycling.

Per the approach discussed in Section 2.3, they were investigated in the order listed above.

The bondwire fracture test specimens were Al-1% Si wires described in Hughes Standard HMS-20-1603, Rev. H, "Wire, Aluminum for Microelectronic Circuits." They are representative of wires used in the parts in the APG-63 2102 and 9800 modules selected for detailed investigation in this program (see Vol. 1 of this report). The modules use 1-mil and 5-mil diameter wires. Only 1-mil-diameter wires were tested in this program.

The PTH test specimens were sections of 14-layer printed wiring boards of the type used in the APG-63 2102 modules. Copper foil, as used in PTHs, also was tested.

The investigations of these failure mechanisms are described in Sections 3.0, 4.0, and 5.0, respectively.

3.0 WIRE MECHANICAL CYCLING

3.1 PRELIMINARY TESTS AND ANALYSIS

To investigate the application of classical fracture mechanics to microscale structures of modern electronics, the logical flow outlined in Figure 2-1 was followed. A detailed literature search was conducted to review techniques and approaches used by other investigators (see Appendix A pages A-16–A-18). To reduce analysis complexity, a simple structural configuration was chosen for the initial fatigue studies. It was determined that the thin bond wire used inside the microcircuit electronic packages would be appropriate for these studies. This wire is used to electrically join various circuits inside the electronic packages as shown in Figure 4-1. Three configurations for this test were investigated; a simple pull tension cycling test, cantilever vibration fatigue testing, and loop vibration fatigue testing. Each of these approaches will be discussed separately below.

Tension Cycling Tests

A pull tension cycling test consisted of pulling a wire specimen under cyclic tension loading. Because of the size of the wire, 1-mil-diameter Al-1 percent Si Hughes Standard H:MS-20-1603, Rev. H, "Wire, Aluminum for Microelectronics Circuits," this testing would have to be accomplished within a Scanning Electronic Microscope (SEM) in order to view cracks in the wire. The SEM provides the high resolution and high depth of field capability required to accurately determine crack growth increments and to adequately image crack surfaces.

To reduce cost, fatigue testing of wire specimens outside of an SEM were initiated to develop confidence in the test setup and procedures. These tests (described in Appendix A, Section V.C) were conducted in an Instron at Hughes Aircraft. It took millions of cycles, at loads 50 percent and 75 percent of the strength of bulk aluminum, for a wire to break. Examination of the failure surface in a SEM indicated that the failure occurred by necking down and eventual overload of the reduced cross-section, rather than by the growth of a crack. Cycling at a lower stress would avoid the undesired failure mode of necking/overload failure. Based upon these results, it was decided that tensile cycling would require excessive test time to fatigue a reasonable number of samples to fatigue failure so that the resultant fracture surface could be examined.

Cantilever Vibration Fatigue Testing

This test consisted of using some bond wire in a cantilever configuration, one end of the wire was clamped to a rigid base and the other end was left free. Sinusoidal vibration was applied through the base. This type of setup was attractive since several wire specimens could be tested simultaneously (see Appendix A, Section VI for more details). No testing was accomplished using this approach since the wire loop configuration was more attractive for several reasons. An

aerodynamic calculation indicated that the drag on the vibrating cantilever cylindrical wire test specimen can be of the same order of magnitude as the inertial load. Thus, aerodynamic loading would have to be taken into account to determine the correct stress distribution within the wire, greatly complicating any analysis.

Loop Vibration Fatigue Testing

This configuration consisted of taking a loop of the bond wire as shown in Figure 3-1 and 3-2. At the top of the loop, the wire is in pure bending. Testing in this mode was more attractive for the following reasons: (1) An initiated crack under direct tension will become unstable very quickly in a fine wire leaving little time to measure a stable crack growth rate. The tendency for necking to occur is thereby eliminated. (2) It is thought that bending stresses at the locations where the bond wires are attached in actual application produce fatigue failures. A crack initiated in bending will be restricted to a localized area for observation and will have a more stable growth rate because of the local gradient. Initial calculations using the geometry of a cracked circular bar in bending was accomplished to help structure this series of experiments (see Appendix B).

3.2 LOOP VIBRATION FATIGUE TESTS

Section 3.2 and Appendix G are summarized in Ref. 3-1.

To obtain an initial assessment of the viability of fracture mechanics for microscale structural elements, a series of experiments was performed on a simple system. These consisted of high cycle fatigue testing on looped 0.001-inch-diameter aluminum 1% silicon wires. The wires were tested in the undefected condition, and with two types of artificially induced damage. The tests on undefected wires and on wires with crater-like defects produced no failures after a large number of load cycles even though the stress levels were above the yield stress. This result was found to be consistent with the very fine grain sizes that exist in these wires. In contrast, the tests on wires with sharp razor-induced notches produced crack growth initiation, fatigue crack propagation and fracture. An analysis of these results showed that a relation of the Paris Law type can be made to correlate the fatigue crack propagation observed in the wires. In addition, this relation is roughly comparable to preexisting results for bulk aluminum. Consistent with these test results, a model of high cycle fatigue in bond wires was developed; it is described in Appendix G. Taken together, these findings support the further development and use of fracture mechanics for microscale structural elements.

There are two essential requirements for established fracture mechanics techniques to be applied (Ref. 3-2). First, there must at some stage be an identifiable, crack-like defect in the component. Second, the rate of growth of this defect must be uniquely related to a parameter associated with the crack tip deformation state.

Accordingly, to determine the feasibility of applying fracture mechanics on the size scale typical of avionics elements, a relatively simple element was selected for a trial examination. This was a small-diameter aluminum 1% silicon wire (dia = 0.001 inch), typical of those used in avionics components, that was to be cycled in tension-tension fatigue to failure. The specific objectives were to determine as a function of stress level (1) the number of cycles required to initiate an identifiable crack-like defect in the wires, and (2) the rate of progression of such a crack to the complete fracture of the wires.

Clearly, repeatable and observable initiation and propagation events are required if any currently established fracture mechanics techniques, linear elastic or inelastic, are to be applied. If such observations are not possible, then the more traditional S-N curve approach is the only alternative. Regardless of the outcome, it was anticipated that the test results would be significant in helping to determine the feasibility of fracture mechanics for microscale structural elements.

In order to perform the fatigue testing, 0.001-inch diameter aluminum wires were installed in a loading device specially designed and constructed at SwRI. A key feature of the testing procedure was to install the wires in the form of loops; the smaller loops giving rise to higher stress values. The tests were performed on wires in a pristine condition and on wires with artificial defects. The defects were of two types: crater-like defects introduced by electrical discharge and sharp cracks introduced with razor blades.

3.2.1 Test Specimen and Configuration

The objectives of the fatigue testing on the 0.001-inch diameter aluminum wires were to determine if crack growth initiation and propagation could be observed and characterized. Because of the very small sizes that are involved, this demanded a procedure that would induce failures in a predetermined location in the wire. As appropriate for an initial assessment, it was neither the intent of the testing to look at the full complexity of actual avionics components, nor to account for stress concentrations due to attachments. Accordingly, a test procedure was adopted that could address the basic issues while accommodating the problems arising from the small scale and high ductility of 0.001-inch-diameter wires.

All testing described here was conducted on 0.001-inch diameter, aluminum 1% silicon wire (Bar 702550, P.O. No. X4-444182-UGB, Spec. HMS 20-1603 CL2 Ty2, 4 April 1985) supplied by Hughes Aircraft Company. The specimen, fixturing and test equipment used in this research are described below.

3.2.1.1 Looped Wire Specimens

The approach selected was to perform fatigue testing on looped wire specimens. This configuration was selected because it would produce the maximum stress at a location on the wire

remote from the support points and in a location which facilitated inspection for cracking. In addition, because the curvature is fairly uniform over a length of the wire, it is possible to relate the stress simply to the curvature of the wire. The initial diameter of the loop controls the mean stress at the apex of the wire loop. The cyclic portion of the stress is controlled by the relative end displacement of the wire. The test configuration is depicted in Figure 3-1.

For a wire in the configuration shown in Figure 3-1, the bending stress in any element can be related to the curvature. It is, therefore, necessary to determine the curvature of the loop as a function of the relative end-displacements of the wire during a cycle. While a closed-form solution to such a problem, known as the elastica, exists (Ref. 3-3), reliance was placed on finite element results of a commercially available code capable of analyzing such highly nonlinear problems. The elastica was used only to check the large deformation capability of the finite element solution. To to this properly, the correct boundary conditions (pinned ends) had to be used. The good agreement that was achieved validated the finite element model for use in the analysis of the problem of interest – the wire loop – for which fixed end conditions were used as the best approximation to the test conditions. The stress analysis of the looped wire specimen is discussed in detail in Section 3.2.2.

A cyclic bending load is produced in the specimen by applying a translational displacement to the ends of the wire. The stress near the apex of the loop is primarily the result of bending and, therefore, is related to the instantaneous curvature of the loop. Because it was not possible to
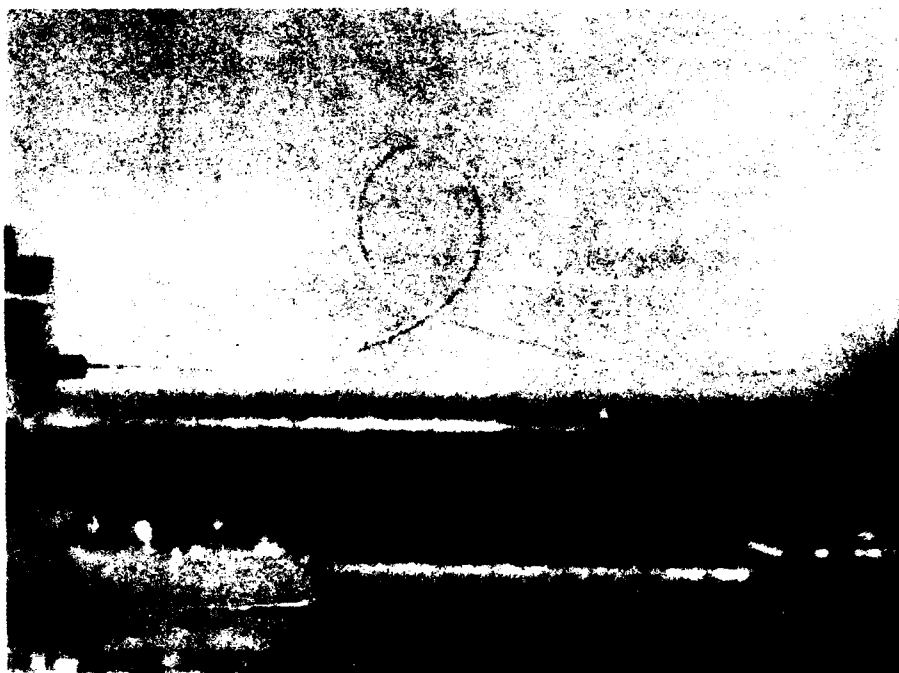
Figure 3-1. The Looped Wire Fatigue Test Specimen

3-4

measure the curvature dynamically, some preliminary static tests were used to determine the curvature as a function of the applied displacement. It was assumed that the relation between the displacement and the loop curvature did not change under the dynamic loading.

3.2.1.2 Fixture Design and Fabrication

To have the wire tests meet the objectives of the ERFM program, it was important to design a test fixture with some flexibility. The overall design of the test fixture that was developed is shown schematically in Figure 3-2, and in the photographs provided as Figure 3-3. As can be seen, the looped specimens were mounted in a fixture consisting of two parallel aluminum bars. Grooves were milled in the bars so that short sections of a hypodermic needle could be clamped to the lower bar. The clamping devices were attached independently with small Allen head screws for each of five specimen locations. In this way the shape, and thus the stress level, of individual loops could be adjusted separately. Locking bars were designed so that the specimens could be held in place at the minimum and maximum deflection positions during assembly and subsequent inspections.

The wires were mounted in the hypodermic needles using super glue. The outer diameter (OD) of the hypodermic needles was 0.028 inch. The inner diameter (ID) was not measured. Due to the method of placing both the glue and the wire into a hypodermic needle at the same time, it was impossible to consistently cover the wire with glue out to the end of the needle. Therefore, there was some variability in the end conditions of the wires. This variability was not believed to have seriously affected the test results, however.

After the hypodermic needles were attached to the wires, a loop was formed and the wire clamped onto one of the support bars. Each wire loop was formed in turn. The initial radius of each loop could be set to a different value in order to give a variation in the mean stress for the group of wires to be tested. While the fixture was designed to accommodate five wires, no more than three wires were tested in any group in order to avoid any possibility of wire-to-wire interaction.

After all the wires were installed, the entire fixture was attached to the fixed base and shaker via two 1-inch-thick aluminum interface plates. The locking bars were removed after installation. The looped wires were then cycled at a constant rate with periodic pauses for inspection at the potential site of damage. As noted earlier, the testing rig was designed to allow for the removal of the specimens for examination of fatigue damage. The specimen removal was done simply by installing the locking bars and removing the attachment screws of the interface plate. Individual specimens could then be readily removed from the test fixture by removing the clamps of the support bars. The test fixture was designed and fabricated at SwRI.
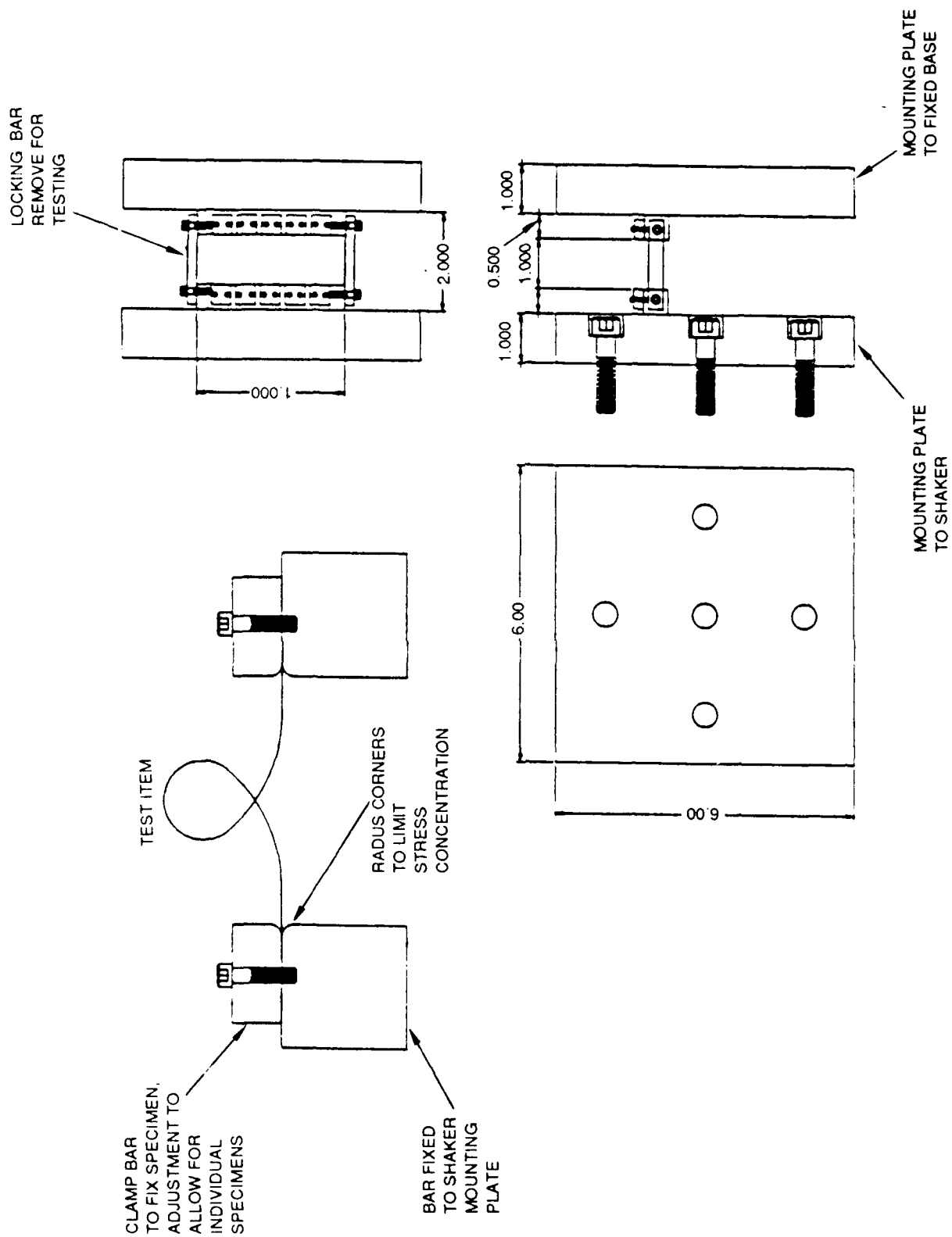
Figure 3-2. SwRI Design of the Test Fixture
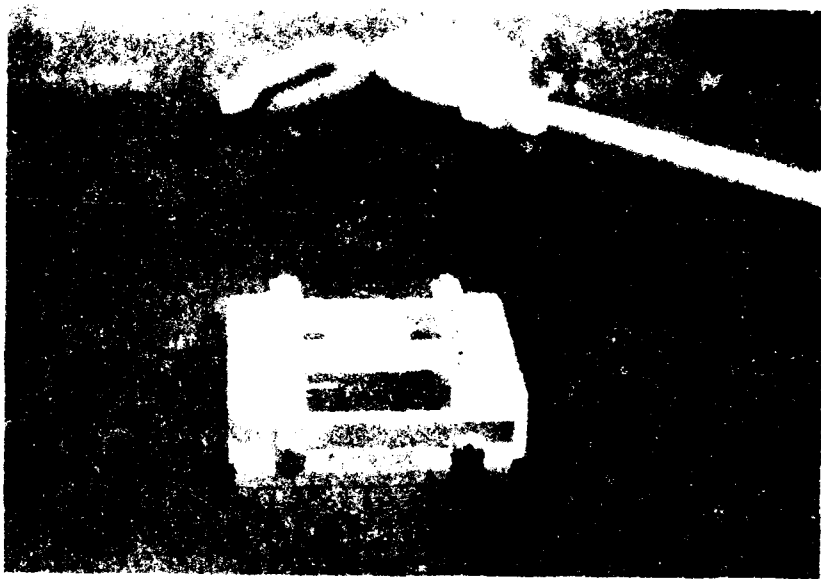
Figure 3-3. Photographs of the Test Fixture and Looped Wires

3.2.1.3 Test Equipment

The equipment utilized to perform the cyclic fatigue testing for this program was fairly simple. A 1600-pound Unholtz-Dickie electrodynamic shaker was utilized to provide excitation to the test fixture. This shaker was driven by a function generator set at a specified frequency. A sinusoidal wave form was used. The level of excitation was measured utilizing a linear variable differential transformer (LVDT) to measure the relative position between the stationary support and the moving head of the shaker. The time history of the LVDT was displayed on a oscilloscope. In this way it was possible to set the required displacement by monitoring the dynamic output of the LVDT.

In addition to the output of the LVDT, the frequency generator was monitored by a frequency counter to determine accurately the number of cycles per second. This could be varied from 5 to 20 cycles per second, depending on the specific test objectives. The total number of cycles to which the wires were subjected were calculated from the frequency and the duration of the testing.

The motion of the wires was observed by utilizing a strobe light during the testing. Care was taken to ensure that the strobe captured the opening and closing of the loop. In some cases there was limited out-of-plane motion of the loops due to the test setup. When out-of-plane motion was detected, it was corrected by making slight adjustments to the ends of the wire. Thus, neglecting the wire thickness, the data that were obtained correspond exclusively to in-plane deformation.

3.2.1.4 Preliminary Test Analysis

The first set of data was obtained in a series of static tests to measure the curvature of the wire for incremental motion of the ends of the wire loop. Photographs of the wire were made for displacements up to 20 mm with an initial loop radius of approximately 3.8 mm. The measured curvature was plotted as a function of the end-displacement of the wire. These data are shown in Figure 3-4.

A linear relation between the curvature and the displacement is evident in Figure 3-4. Hence, a fit to these data is given as:

$$R = R_0 - 0.0775 \, \delta \tag{3-1}$$

where R is the radius of curvature, R_0 is the radius of curvature of the loop at the zero-displacement position, and δ is the relative displacement of the ends of the wire.

It was found that, as the wire was removed from the spool, the wire had a residual radius of curvature such that $R_0 = 15$ mm. The stress σ in the wire, based on elemental beam theory (Ref. 3-4) relating the stress to thexous curvature and residual curvature of the wire, is given by:

$$\sigma = \frac{Ed}{2} \left[\frac{1}{R} - \frac{1}{R_0} \right] \tag{3-2}$$
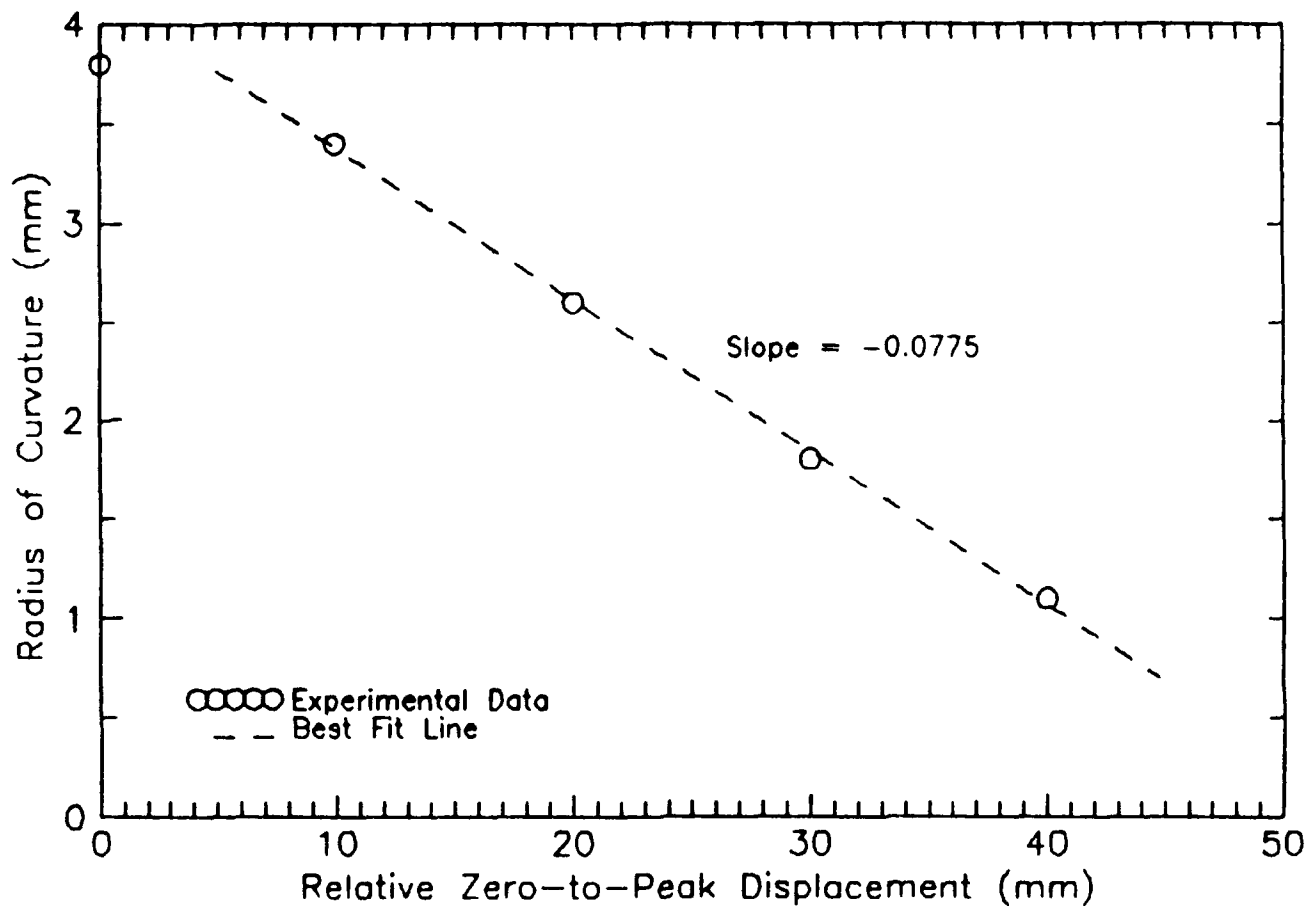
Figure 3-4. Experimental Relationship Between the Radius of Curvature
and the End Displacement

where E is the modulus of elasticity, d is the wire diameter, and, as above, R is the radius of curvature of the loop and R_0 is the initial (residual) radius of curvature.

Along with measurements of the initial and final radii, Equation (3-2) was used to estimate the yield stress of the wire. Specifically, it was noted that, as the end-displacement was greatly increased, the wire formed a kink at the apex of the loop. Thus, to estimate the yield stress, for a given initial loop diameter, the displacement was slowly increased until the wire kinked. By inserting the loop diameter just prior to the point when the wire was observed to kink into Equation (3-2), the yield stress could be estimated. The resulting estimate of the yield stress was 55 ksi. This agrees reasonably well with tensile test data (Ref. 3-5) that indicate that values in the range of 40 to 50 ksi are appropriate for 0.001-inch diameter aluminum wires.

3.2.2 Looped Wire Fatigue Testing Analysis

The forming process of the wire into a loop and the actual fatigue cycling result in large displacements not accounted for in the elemental beam theory utilized in the proceeding section. To examine this issue, a more rigorous analysis of the wires was performed using a large displacement finite element analysis. The following describes the finite element model (FEM), its verification, and the results.

3.2.2.1 Large Rotation Finite Element Modelling Procedure

Because the wire undergoes gross displacements as it is formed into a loop, modelling of the looped wire requires an analytical procedure involving large displacements and rotations. Thus, a finite element code with elements capable of large deflections is required in order to properly model the looped wire. Because ABAQUS, a commercially available code, has elements capable of large displacements and demonstrates good agreement with known solutions to classical large displacement problems (Ref. 3-6), it was chosen for the FEM effort.

Specimen yielding not only makes testing difficult as the result of a kink in the wire, but further complicates the stress analysis. Hence, both testing and the subsequent analyses assume linear elastic response. The wire was modelled using three-node quadratic beam elements. These elements use Timoshenko beam theory which includes transverse shear. For ease of analysis 10 such elements were used to model half the wire by taking a plane of symmetry at the midspan. The boundary conditions at the symmetry plane prohibit horizontal displacement and rotation. Further, no vertical displacement was allowed at the end of the wire.

Because the looped wire is assumed to be in a postbuckled condition, the applied loading is required to be such that the wire buckles and the end of the wire are pushed back beyond the plane of symmetry. This was achieved by prescribing the horizontal displacement of the end of the wire in a series of finite steps to ensure a convergent solution.

3.2.2.2 Validation of the Model: The Elastica

Prior to analyzing the actual problem, it was desirable to verify the model with a known solution to a similar problem which would demonstrate the large displacement capabilities. The elastica, an extension of column buckling far into the postbuckling range, has a known solution which is described in Ref. 3-3. The postbuckling load is described by a complete elliptic integral of the first kind. The position of any point is described by complete elliptic integrals of the second kind. This known solution provides a basis to validate the large rotation formulation of the finite element model.

To perform this postbuckling analysis, however, bifurcation of the solution into the post-buckling mode must be forced. This was done by perturbing the column geometry into a slightly buckled configuration. Therefore, one-half of a column length was generated using 10 quadratic beam elements such that the maximum perturbation, at the end of the column, was only a few column widths. Then, the horizontal displacement of the end of the column was prescribed so that the end was pushed back beyond the midplane by 0.9 times the column length. Figure 3-5 shows, from top to bottom, a progression of the column buckling far into the postbuckling regime. Although it may not be readily apparent, the initial geometry, indicated by the dashed lines in Figure 3-5, is in the slightly buckled configuration previously described.

In order to assess the accuracy of the model, the reaction force resulting from the prescribed displacement was compared to the postbuckling load given in Ref. 3-3 at various stages of the total displacement. These results are presented in Figure 3-6. The difference in reaction forces between theoretical and FEM results was found to be less than 1 percent. This excellent agreement between the model and the known solution of the elastica strongly indicates that the large displacement formulation of the FEM code is accurate.

3.2.2.3 Unnotched Looped Wire Analysis

Because the wires have a pronounced initial curvature, the bifurcation to the postbuckling solution is automatically forced. Thus, the exact initial wire geometry can be used for analysis. An analysis was performed to complement testing of the looped unnotched wire experiments previously described. The horizontal displacement of the wire model was prescribed such that the relative displacement of the ends would coincide with the test configurations. Figure 3-7 shows the wire in the mean displacement configuration (solid line) and the initial geometry (dashed line).
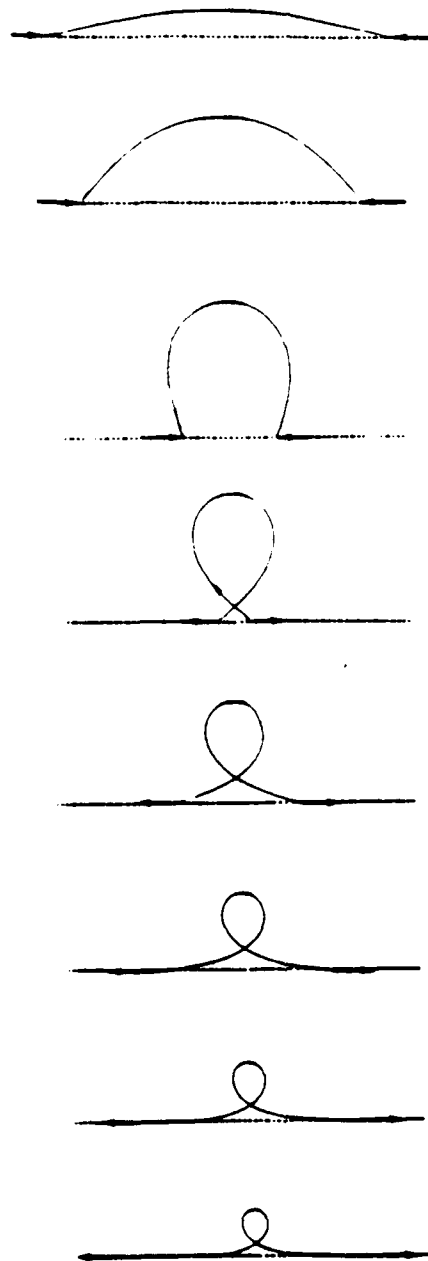
Figure 3-5. Progression (top and bottom)
of a Column Forming into the Elastica
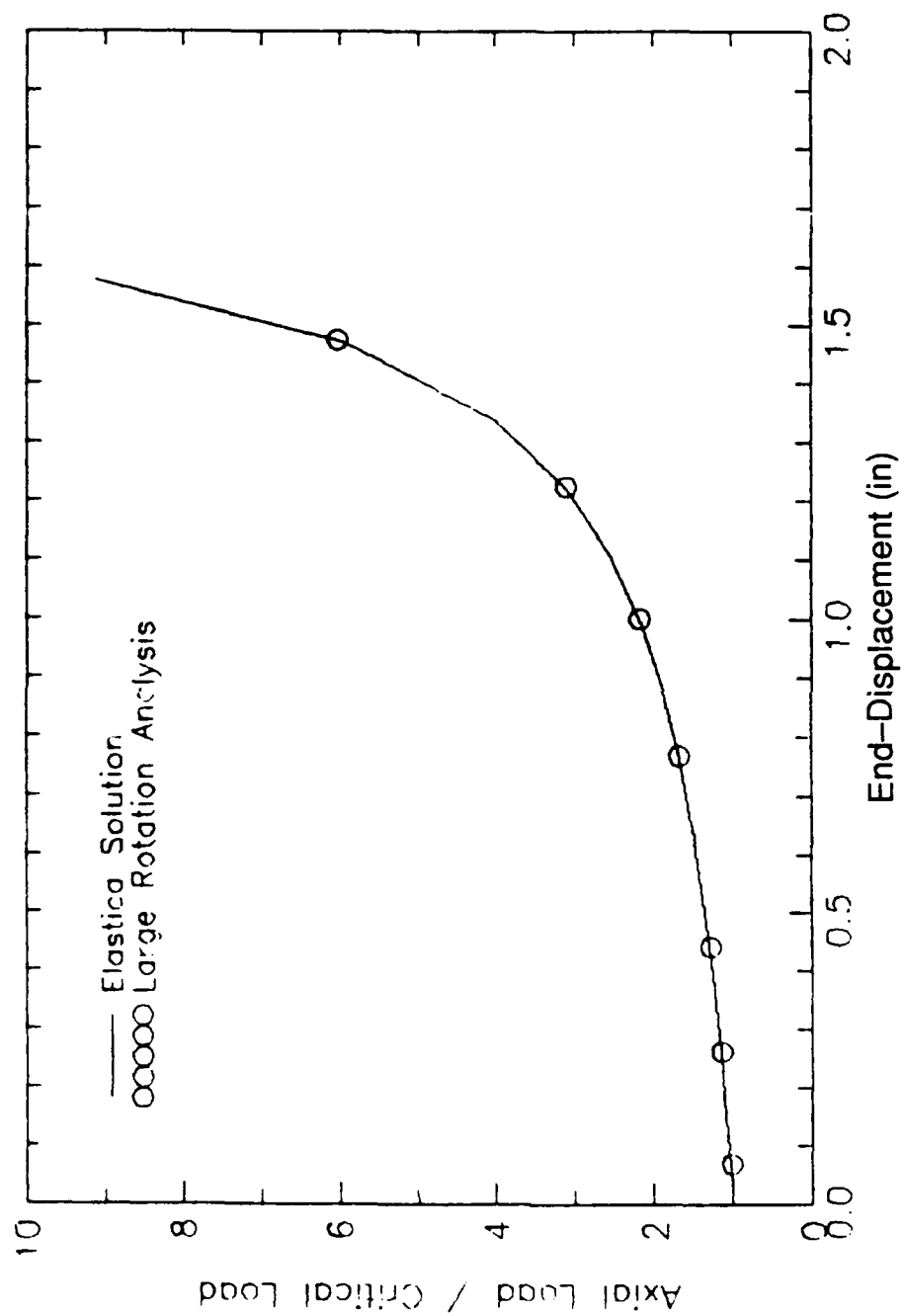
Figure 3-6. Comparison of the FEM Analysis to the Elastica Solution

3-13
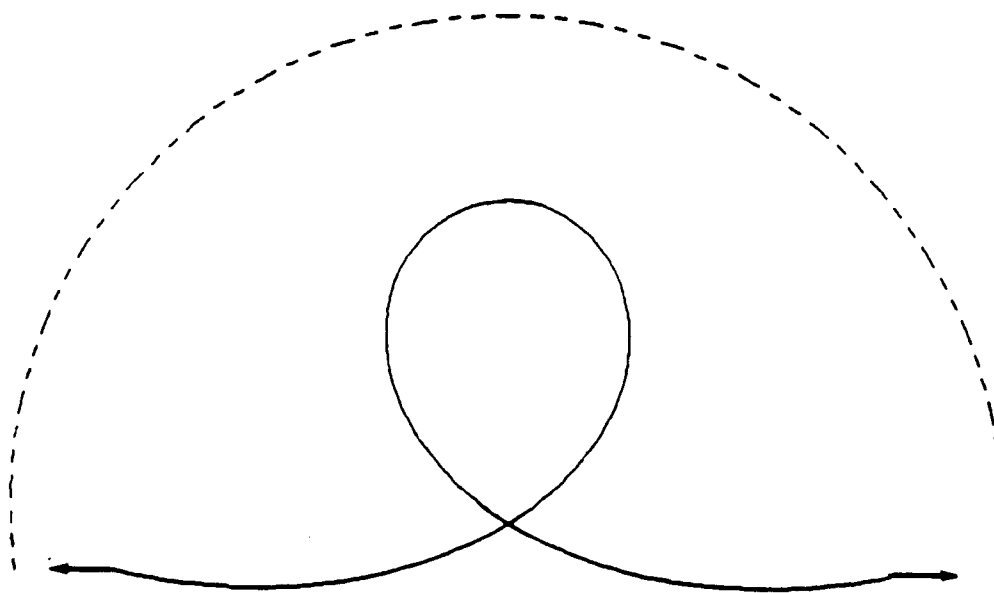
Figure 3-7. Deformed Shape (solid) and Initial Geometry (dashed)
of the Looped Wire

The elemental beam theory was compared to the finite element results. The maximum stress found from the analysis and the corresponding radius of curvature calculated from the nodal displacement at the apex were compared to the beam theory predictions given by Equation (3-2). Although there is a slight variation at lower loop radii, there is good agreement between beam theory and the FEM in the test range regime, as indicated in Figure 3-8.

As previously described, for convenience, the radius of curvature was related to the relative end-displacement by Equation (3-1). In order to evaluate the accuracy of this relationship, Equations (3-1) and (3-2) were used to relate the relative end-displacement to the stress. This relationship is compared to FEM results in Figure 3-9.

While the relationship shown in Figure 3-9 seems to deteriorate at high displacements, it appears to be entirely adequate in the test range regime. In this range, indicated in Figure 3-9, only a small overestimate of the stresses at the high end of the test range occurs. This is consistent with the yield stress value reported in Section 3.2.1.4, i.e., about 20% above the reported tensile strength values.

The excellent agreement between the finite element computations and simple beam theory is due in part to the large curvature-to-wire-diameter ratio, and to the fact that near the apex of the loop the wire is subjected to almost pure bending. The latter will be of significant importance for the determination of an appropriate crack driving force for the notched wire, described next.

3.2.2.4 Notched Looped Wire Analysis

A portion of the looped wire fatigue testing was performed on wires with artificially-induced notches. To analyze these, it was necessary to determine the effect of the resulting increase in the compliance of the finite element computations were required. However, the beam elements used in the unnotched wire analysis (albeit demonstrating excellent agreement with known solutions to large displacement problems) do not permit modelling discontinuities such as cracks.

To avoid the complications of incorporating crack tip elements into the modelling effort, it was deemed sufficient to replace the beam element where the crack would ordinarily be (i.e., the element at the top of the loop) with a beam element whose compliance was modified to account for an increase in compliance as if a crack were present. The results of such a computation provide a relation between the end displacements and the curvature of the wire.
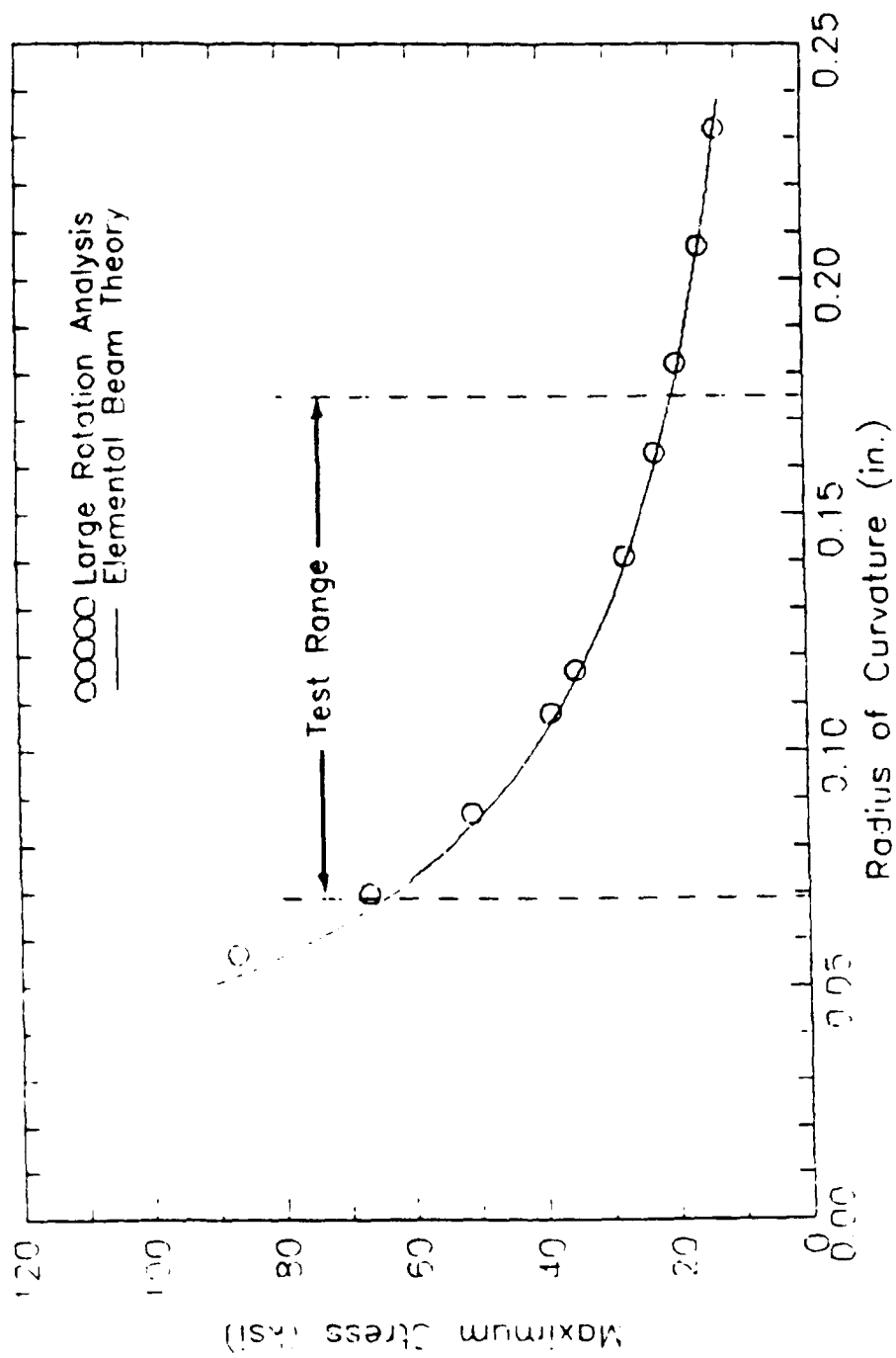
Figure 3-8. Comparison of the FEM Analysis and Beam Theory
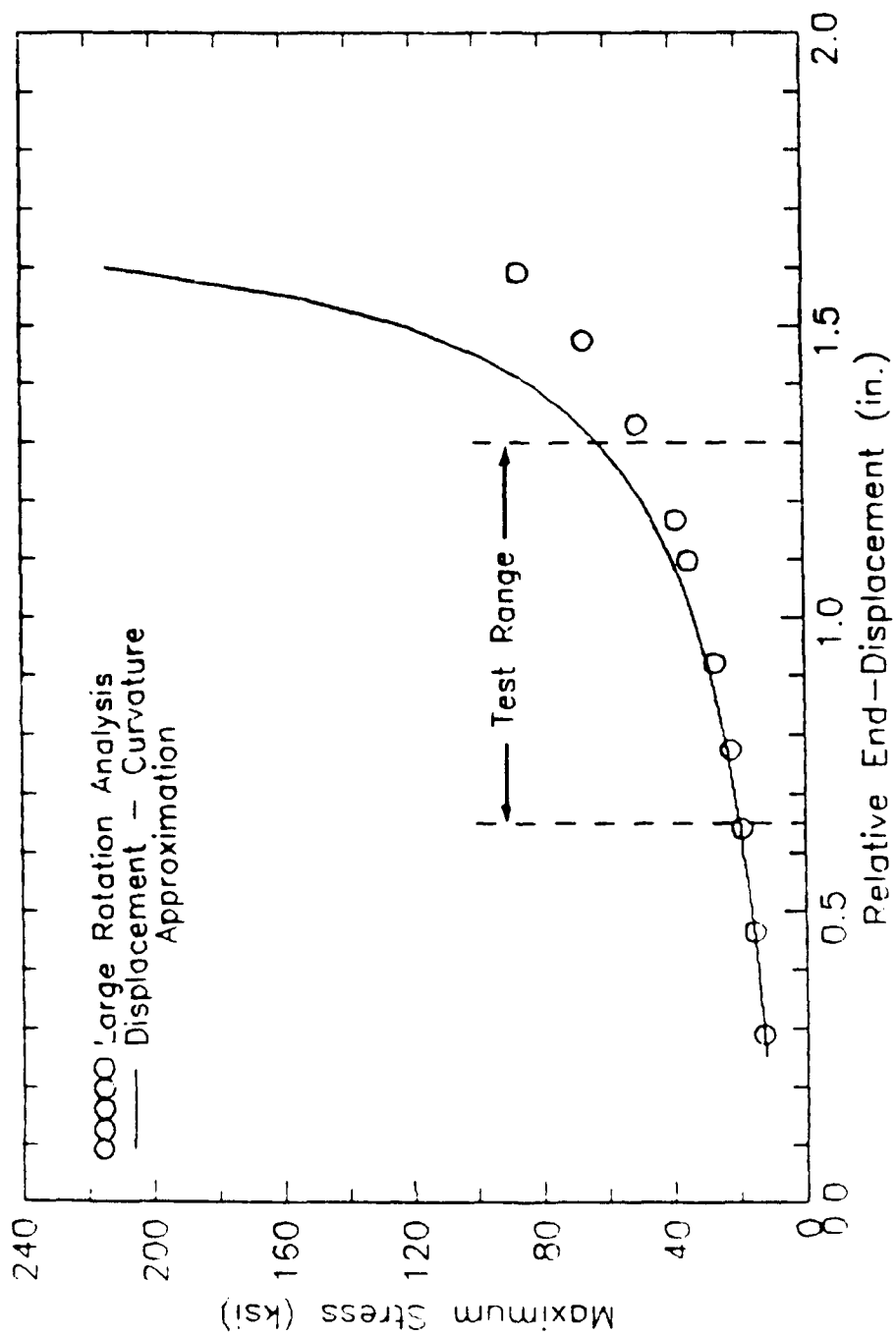
Figure 3-9. Comparison of the FEM Analysis and the Displacement-Curvature Relationship

For a crack in a linear elastic material, the overall compliance is the sum of the compliance of the uncracked configuration and the increase in compliance resulting from the presence of the crack. An analytical expression for the equivalent compliance of an element at the top of the loop containing a crack was developed by Harris (Ref. 3-7; an updated version is Appendix B) using classical energy methods. The change in compliance as a function of crack depth for various element lengths is shown in Figure 3-10.

As shown in Figure 3-10, with an element length-to-diameter ratio of 10, the change in compliance is minimal for crack depths of 0.0003 inch or less. Thus, for the notch depths used in this study, only slight differences occur between the notched and unnotched wire loop curvature-end displacement relations. Thus, the relation for the unnotched loop suffices in describing the curvature-end displacement relationship for crack growth initiation and for the initial stages of propagation that were observed in the experiments.

Because the wire near the apex of the loop is in (nearly) pure bending, an expression for the stress intensity factor which closely approximates the region of the wire near the top of the loop can be developed in a simple way. The result is given as (Ref. 3-8):

$$K = \sigma_b \sqrt{\pi a} \; F_B \tag{3-3}$$

where a is the crack depth, σ_b is the "outer-fiber" bending stress, and F_B is a dimensionless geometric parameter given by:

$$F_B = 0.59 \sec \beta \sqrt{\frac{\tan \beta}{\beta}} \left[0.923 + 0.199(1 - \sin \beta)^4 \right] \tag{3-4}$$

where:

$$\beta = \frac{\pi a}{2d} \tag{3-5}$$

and, as shown in Figure 3-11, d is the wire diameter. The expression for the stress intensity factor is reported in Ref. 3-8 to have reasonable accuracy for a < d/2.

While the initial artificially-induced razor notch will likely have a straight crack front, the crack is likely to grow with a curved crack front such as that shown in Figure 3-11. However, because the crack front curvature effects would greatly complicate the analysis, they were ignored. Note that, for ease of estimation, Equation (3-4) can be simplified by assuming $\beta \ll 1$. This procedure gives:

$$F_B = 0.66[1 - 0.177\beta + 1.73\beta^2] \tag{3-6}$$

in which β is given by Equation (3-5).
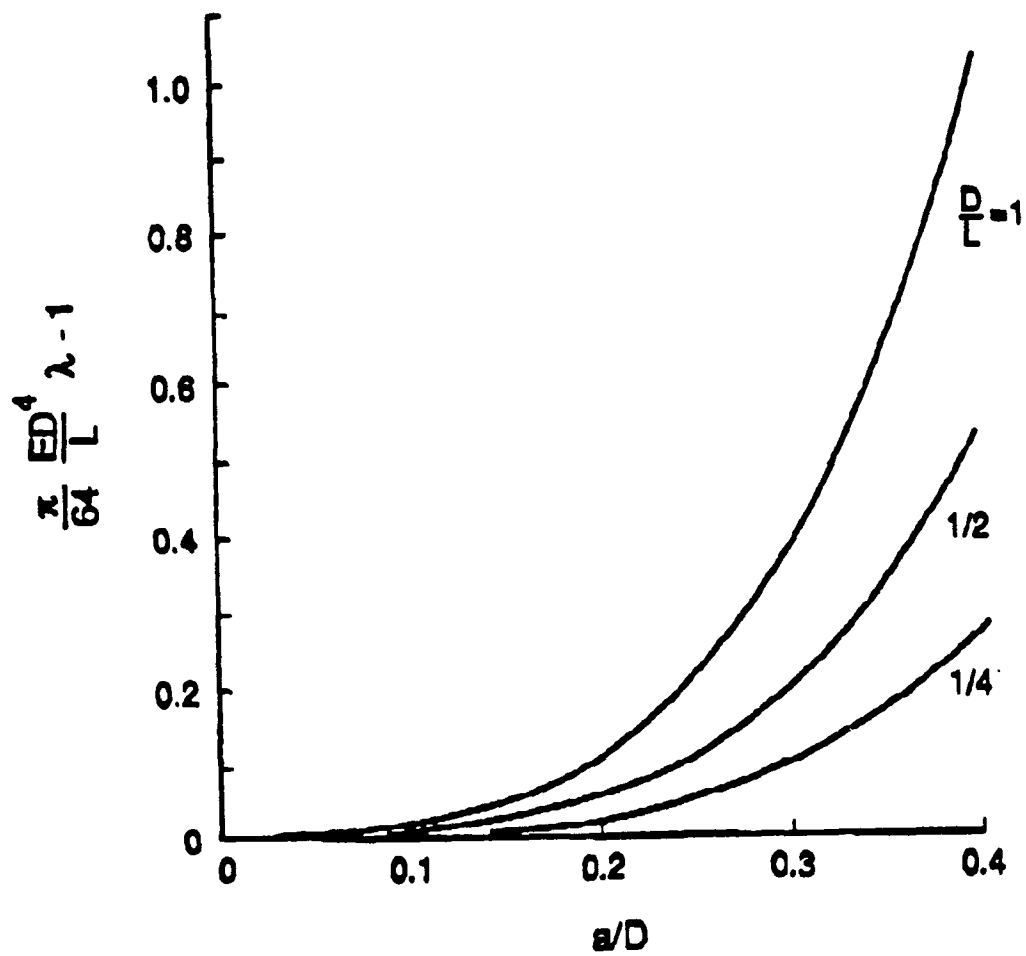
Figure 3-10. Change in Compliance as a Function of Crack Depth
for Various Element Lengths
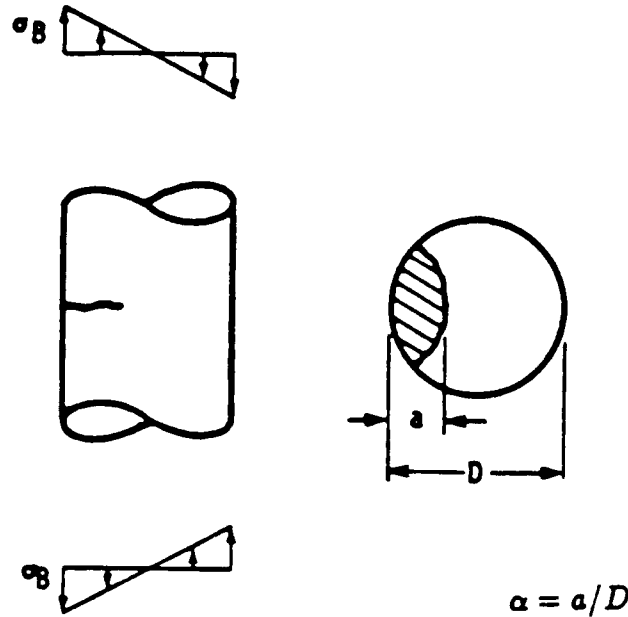
Figure 3-11. Geometry Used for the Stress Intensity Factor Approximating the Apex of the Looped Wire

3.2.3 Unnotched and Blunt Notched Looped Wire Fatigue Testing

Fatigue testing was first performed on unnotched wires to determine if naturally-occurring crack-like defects would develop and propagate in the highly stressed region of the pristine wire. This type of testing was followed by tests on wires with crater-like defects. The following discussion describes the details of the experiments and results of these two sets of wire vibration fatigue tests. Included in this section is a description of a detailed metallographic examination of the aluminum 1% silicon wires that help to understand these results.

3.2.3.1 Unnotched Looped Wires

Four different groups of pristine wires were subject to tension-tension fatigue testing using the looped configuration described in Section 3.2.3. Each group of unnotched looped wire tests is described in this subsection and summarized in Table 3-1.

Group One Tests. In the first test group a total of three loops were made, but one was damaged during installation. The two remaining loops had mean radii of 3.0 mm and 2.4 mm. The cycling began with a peak-to-peak displacement of 6.4 mm at a rate of 20 cycles per second. For this condition the stress was estimated to range from 31 to 38 ksi and from 39 to 50 ksi in the 3.0 mm and 2.4-mm loops, respectively. The two wires underwent a total of 10,000,000 cycles under these conditions with no sign of damage. Because no damage was observed, the amplitude of the relative end displacement was increased.

3-20

TABLE 3-1. SUMMARY OF UNNOTCHED WIRE FATIGUE TESTING

Group	Wire	Initial Radius (mm)	Peak-to-peak Displacement (mm)	Stress (ksi)		Cycles (x10^6)	Comments
				Minimum	Maximum		
1	2	3.0	6.35	31	38	10	No notable damage
	3	2.4		39	50		
	2	3.0	11.89	28	42	10.3	No notable damage
	3	2.4		35	56		Wire 2 slightly out-ot-plane
	3	1.1	6.35	86	140	1.3	No notable damage
2	2	1.8	6.35	53	73	3.3	No notable damage
	3	1.3		73	110		Yielding in wire 3
3	1	3.0		28	42		
	2	3.7	12.70	22	31	1.7	No notable damage
	3	4.1		20	27		
	1	3.0		26	46		
	2	3.7	16.76	21	33	9.1	No notable damage
	3	4.1		18	28		
4	1	3.5	8.66	21	37	8.4	No notable damage
	1	3.1	10.59	23	49	10.1	No notable damage

The continuation of the test was performed at a level of 11.9 mm peak-to-peak displacement. A total of 10,300,000 cycles were run under these conditions, also at a rate of 20 cycles per second. The stress variations in the loops after the increase in the end-displacement were estimated to range from 28 to 42 ksi for the larger loop and 35 to 56 ksi for the smaller loop. No sign of damage was observed, even though the estimated levels of stress in the wires should have produced yielding. It should be noted that, while a close inspection was not made to detect kinking in the wires, no gross indication of yielding was evident.

A final stage of testing was performed on the first group of wires in which the loop radii of the specimens were tightened prior to testing. Only the smaller loop survived the installation process. The radius of this loop was adjusted from 2.4 mm to 1.1 mm. Testing was resumed with a 6.4-mm peak-to-peak displacement, corresponding to an estimated stress range of 86 to 140 ksi assuming elastic behavior. The wire was subjected to a total of 1,300,000 cycles at a rate of 20 cycles per second under these conditions. Although the stress levels exceeded the yield strength of the wire, no sign of kinking or damage was noted.

Group Two Tests. The second group of wires had very tight loops. The loop radii for the two specimens that survived the installation process were 1.8 mm and 1.3 mm. Tests were performed at a peak-to-peak displacement of 6.4 mm at a rate of 20 cycles of second. For this series of tests, the estimated stress ranged from 53 to 73 ksi and 73 to 110 ksi, respectively.

Note that these calculations are based on the assumption that yielding of the wire does not occur. In actuality, it appeared that the wires yielded and a hinge formed at the apex of the smaller loop. This hinge drastically altered the loop geometry. The wires were subjected to a total of 3,300,000 cycles under these conditions. Nevertheless, no sign of crack-like damage in the wires was noted.

Group Three Tests. The tests on the third group of wires were designed to cycle wires below the yield point with the maximum possible excursion on the cyclic portion of the stress. The three specimens surviving the installation process had loop radii of 3.0 mm, 3.7 mm and 4.1 mm. The testing was started with a peak-to-peak displacement of 12.7 mm at a rate of 20 cycles per second. The stress ranges for the three samples were 28 to 42 ksi, 22 to 31 ksi and 19 to 27 ksi, respectively. The wires were subjected to a total of 1,700,000 cycles under these conditions. At the end of this testing, no sign of physical damage was noted.

The level of excitation was increased to 16.8 mm peak-to-peak at a rate of 15 cycles per second. At this displacement level the stress ranges for the three samples were estimated at 26 to 46 ksi, 21 to 33 ksi and 18 to 28 ksi. A total of 9,100,000 cycles were accumulated under these conditions. Once again, upon examination of the maximum stress region of the wires in the SEM, no evidence of fatigue damage was found.

Group Four Tests. The final group of unnotched wire tests was designed to cycle below yield, but over an extended period of time. The test consisted of a single wire with a loop radius of 3.5 mm and a peak-to-peak displacement of 8.66 mm. This corresponds to a stress ranging from 21 to 37 ksi. These stress estimates were based on a high speed video of the wire. After cycling the wire to 8,400,000 cycles under these conditions, the wires were examined. No fatigue damage was observed.

The loop was tightened to a radius of 3.1 mm. The wires were cycled with a peak-to-peak displacement of 10.59 mm, corresponding to a stress ranging from 23 to 49 ksi. Under these conditions an additional 10,100,000 cycles were accumulated, but again, without any sign of fatigue damage.

Comments on Unnotched Wire Tests. As evident from the results in Table 3-1, fatigue testing of the wires in a pristine condition did not produce any signs of fatigue damage, even at stresses very near the yield strength. One reason for this was thought to be due to a high concentration of compressive residual stresses on the surface of the wire resulting from the

3-22

fabrication process. Consequently, it was proposed to test wires with artificially-induced defects designed to provide a stress concentration and locally remove any residual stresses. These tests are described next.

3.2.3.2 Electrical Discharge Notched Wires

Due to the extreme fragility of the wires, a delicate notching procedure is needed to allow defects to be introduced into the wires while in the looped condition to assure that the location of the defect would be in the maximum stress region at the apex of the loop. The first technique attempted was to defect the wire by inducing a small crater through electrical discharge. In order to notch the loop, one end of a tungsten wire was honed to a fine point. It was then attached to the positive end of a 10-μF, 25-V capacitor. With the capacitor charged to 20 V, the point of the tungsten wire was touched to the apex of the looped wire. The resulting electrical discharge induced a crater-like notch in the wire as shown in Figure 3-12.
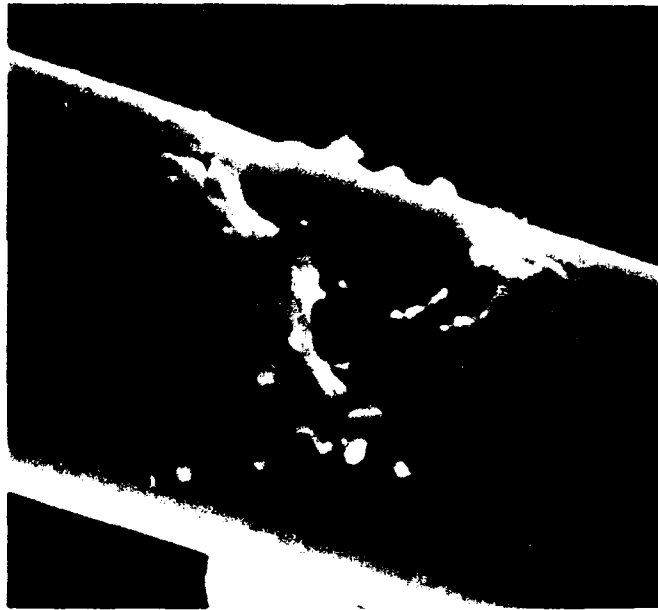
Figure 3-12. Photograph of an Electrical Discharge Notch
(Specimen not tested)

While these notches are far from crack-like defects, it is clear that a stress concentration is achieved over that of the pristine wire. They also may serve to simulate installation damage. However, because the notching procedure results in a localized melting of the wire, the melting and subsequent solidification may locally alter the metallurgy of the wire. In general, any resulting metallurgical changes can change the mechanical performance of the wires. It was not possible to examine the microstructure of the wire near the notch.

3-23

Two different groups of notched wires were subjected to fatigue testing in the same manner as previously described. These groups of tests have been designated as Group 5 and Group 6 to maintain continuity with the unnotched wire testing. These tests are described below. A summary of the notched wire testing is given in Table 3-2.

TABLE 3-2. SUMMARY OF ELECTRICAL DISCHARGE NOTCHED FATIGUE TESTING

Group	Wire	Initial Radius (mm)	Peak-to-peak Displacement (mm)	Stress (ksi)		Cycles (x10^6)	Notch Depth Estimate (%dia.)	Comments
				Minimum	Maximum			
5	1	2.0	6.22	48	64	2.6	10-20	No notable damage
6	1	2.0	5.97	48	64	23.6	Negligible	No notable damage
	2	2.3		38	55			
	3	2.3		38	55			

Group Five Tests. The first group of artificially notched wire tests was designed to test wires with a stress concentration at the maximum stress region at the apex of the loop. Only one wire survived the installation and notching procedure. This wire had a loop radius of 2.0 mm and was cycled at a peak-to-peak displacement of 6.22 mm. The corresponding nominal stress ranged from 48 to 64 ksi. The wire underwent 2,650,000 cycles without signs of fatigue damage.

Because the wires are so delicate, it is not possible to examine the notch prior to testing. While every attempt was made to keep the notching procedure the same, there may be large variations in all notches. Figure 3-13 shows a SEM photograph of the notch cycled in Group 5. It can be seen that the notch, or defect, is by no means a crack-like flaw. However, in loss of cross section alone, the defect certainly acts as a stress riser, roughly on the order of 3 times the nominal stress.

Group Six Tests. The final group of tests was designed to fatigue notched wires for an inordinately large number of cycles. Three wires were notched using the procedure described above. The wires of radii 2.0, 2.3 and 2.3 mm were cycled at a peak-to-peak displacement of 5.97 mm. The corresponding maximum stress ranged from 48 to 64 ksi, 38 to 55 ksi and 38 to 55 ksi, respectively. Once again, no sign of fatigue damage was observed even after 23,600,000 cycles.

Upon SEM examination of the notches, the notching procedure was found to have produced a very small pit in each of the wires. Due to the diminutive size of the defect, the resulting stress concentration was likely to be minimal. Consequently, these tests should correspond more nearly to the pristine wire, which they evidently do.

Figure 3-13. Photograph of a Notch in a
Fatigue Tested Wire (Group 5)

Comments on Notched Wire Tests. As shown in Table 3-2, no damage was found after cycling pristine and bluntly notched wires, even after large numbers of cycles at stress levels approaching the yield strength. As the fatigue resistance of a material is often influenced by its microstructure, an evaluation was initiated to investigate the microstructure of the wires. This investigation is described next.

3.2.4 Microstructural Evaluation of Wires

During tests of the smooth wires, crack initiation resistance was found to be very different than that of wrought aluminum alloys, and this caused speculation about the microstructure of these wires. As there is a relationship between microstructure and fatigue crack initiation, an evaluation of the microstructure of the wires was initiated. Professor R. F. Pinizzotto at the Center for Materials Characterization at the University of North Texas, because of his familiarity with applicable specimen preparation techniques, was contracted to investigate the microstructure of these wires using transmission electron microscopy (TEM) (Ref. 3-9).

Due to the small size of the wires, it is very difficult to prepare specimens so thin that they are electron transparent. It is desirable to examine specimens by TEM having structures as close as possible to that of the bulk material. For metals, this means introducing as little deformation as possible during specimen thinning. For most metal specimens, cutting and grinding methods are used to prepare a blank specimen, with final thinning by chemical polishing. But these methods

3-25

are only effective for large pieces of material (several mm in diameter). Another method was clearly necessary for the 25-μm-diameter bond wires.

The method used for thinning the bond wires was to slice off thin sections with an ultramicrotome using a diamond blade. Microtomes are routinely used to cut electron transparent specimens from biological materials. For the bond wires, specimens were cut at both ambient and liquid nitrogen temperatures. Since the bond wires are made of a very soft and ductile alloy, the low temperature was used to minimize deformation of the wire during cutting. As expected, it was not possible to entirely eliminate deformation during specimen preparation. However, the deformation resulting from cutting was sufficiently small so that the conclusions drawn from the investigation were not affected.

Two results, directly related to fatigue properties, were obtained from the microstructural analysis:

1. The grain size of the bond wire was approximately 0.5 ± 0.23 μm, and

2. silicon in the alloy was present in the wire as particles of silicon smaller than the resolution of the microscopy techniques used and well dispersed.

The first result, obtained by statistical analysis of bright field microscopy photographs, means that a typical bond wire contained 30 to 100 grains within the cross section. These grains generally were separated by relatively high angle grain boundaries, as determined by dark field TEM. No foreign matter (ceramic particles, dirt, intermetallic particles, etc.) was observed in the wires by either TEM or SEM examination. The second result, derived from electron diffraction, indicates that the silicon particles are evenly dispersed throughout the material and are very small. The particles may impart some strength to the alloy and may aid in resisting dynamic recrystallization of the wires as they are being drawn. They assist in maintaining a small grain size as the wire is reduced to its final 25-μm dimension. However, they do not adversely affect the fatigue resistance of the material. An example of the small grain structure found for this material is shown in Figure 3-14. The cross section appears elongated in this photograph because cutting was not perpendicular to the wire axis. The lines seen were caused by cutting during specimen preparation. Note that there are also a few large grains in the wire, but most are found in the interior. A higher magnification photograph with a few large grains is shown in Figure 3-15.

Materials lacking inclusions and having a small grain structure are as resistant to fatigue crack initiation as is possible to make. If fatigue cracks do not initiate at inclusions in single phase alloys, they do so at grain boundaries or within single grains. Grain boundary initiation is usually caused by some sort of environmental attack. Initiation within grains results from deformation, a process enhanced by a material having single slip such as the superalloys. While this aluminum alloy has many active slip systems, it is very difficult to initiate cracks due to slip. The small

Figure 3-14. Transmission Electron Micrograph of an Entire Section Through
a Bond Wire Showing the Grain Structure

Figure 3-15. Transmission Electron Micrograph of the Outer
Portion of a Section Through a Bond Wire
Showing the Variation in Grain Size

diameter of the grains does not allow for the generation of substructures within the grain which become unstable and lead to crack formation. Thus, the microstructural investigation by TEM provided a clear indication of the high fatigue resistance of the bond wires. This conclusion is consistent with the inability to generate a fatigue crack in pristine wires.

3.2.5 Sharply Notched Looped Wire Fatigue Testing

In an effort to provide the maximum opportunity for crack growth initiation, a technique was developed to place a sharp notch into the wires. The fatigue crack initiation prediction, described in Appendix G, gave guidance regarding the notch depth and sharpness needed to initiate a crack. The results obtained with this procedure are described in this section.

3.2.5.1 Experimental Procedure

A very fine razor blade of the type found in commercially available single- and double-bladed razors was used to delicately place a sharp notch into the wire. As with the previous notching technique, all notching was performed on a previously formed loop to ensure the notch to be in the highly stressed apex of the wire loop. Once a loop was formed and placed in the specimen test fixture, a piece of heat-shrink tubing was held under the apex of the loop for support. A razor blade was lowered onto the wire and removed. No additional force other than the weight of the blade was applied.

This notching procedure has three major advantages over the electrical discharge method. First, notches can consistently be induced to a desired depth relative to the wire diameter. Second, because of the very sharp razor blade, the razor blade notch produces a crack-like defect, not a stress concentration resulting from a loss in cross section as was observed from the electrical discharge notching method described in Section 3.2.3. Third, local melting of the wire does not occur which may otherwise generate unknown changes in fatigue resistance resulting from microstructural changes.

3.2.5.2 Experimental Results

Two different groups of notched wires were subjected to fatigue testing in the same manner as previously described. Each group of tests (designated as Group 7 and Group 8) is described below. A summary of the razor blade notched wire testing is included in Table 3-3.

Group Seven Tests. Three wires were successfully formed and notched to a depth of approximately 40 percent of the wire diameter. A typical notch is shown in Figure 3-16. Note the increased sharpness over the electrical discharge defects shown in Figures 3-12 and 3-13. The radius of curvature at the root of these razor blade notches is estimated at 1/15 of the wire diameter.

TABLE 3-3. SUMMARY OF RAZOR BLADE NOTCHED FATIGUE TESTS

Group	Wire	Initial Radius (mm)	Peak-to-peak Displacement (mm)	Stress (ksi)		Cycles (x10³)	Notch Depth Estimate (%dia.)	Comments
				Minimum	Maximum			
7	1	3.4	12.7	20	40	55	≈40	Wires 1 and 2 failed after 55K cycles. No damage to Wire 3.
	2	3.4		20	40			
	3	3.4		20	40			
8	1	3.2	7.62	26	39	3,165	≈20	Wire 2 failed. Crack from Wire 1 notch. Wire 3 undamaged.
	2	3.2		26	39			
	3	3.2		26	39			
	1	3.2	7.62	26	39	63	≈30	Crack grew to ≈50%

Load cycling that was conducted at 15 cycles per second produced a bending stress ranging from 20 to 40 ksi at the extremes of the fatigue cycle. From Section 3.2.2.4, the resulting stress intensity factor ranged from 0.5 to 1.0 ksi in$^{1/2}$ with a R-ratio (defined as the ratio of the minimum stress to the maximum stress) of 0.5.

After 55,000 cycles two of the three wires had broken. At this point the third wire loop was opening out-of-plane during cycling. Testing was stopped and the two failed wires were examined under a scanning electron microscope (SEM). Photographs showing the overall fracture surfaces of these two wires are shown in Figure 3-17. In both cases the fracture appears to be intergranular. This finding is supported by the reasonable comparison of the grain size (0.32 μm) and the particle size of the fracture surface (0.4μm).

A more detailed examination of one wire is shown in Figures 3-18 and 3-19. In Figure 3-18 the initial notch is in the lower portion of the photograph. Near the top of the photograph a ridge, or overload lip, is clearly visible. The location of the lip is located approximately two-thirds of the way through the initial remaining unnotched section of the wire. A possible explanation for the occurrence of such a lip is the following. A fatigue crack initiated and propagated from the razor notch. Some time later, another crack initiated on the under side of the wire in a region undergoing fully reversed plastic deformation. The two cracks grew toward each other, meeting at a line indicated by the overload lip.

A close examination of a region near the overload lip shows the presence of fatigue striations. These striations are visible in the upper right portion of Figure 3-19. The overload lip runs across the top of the photograph.
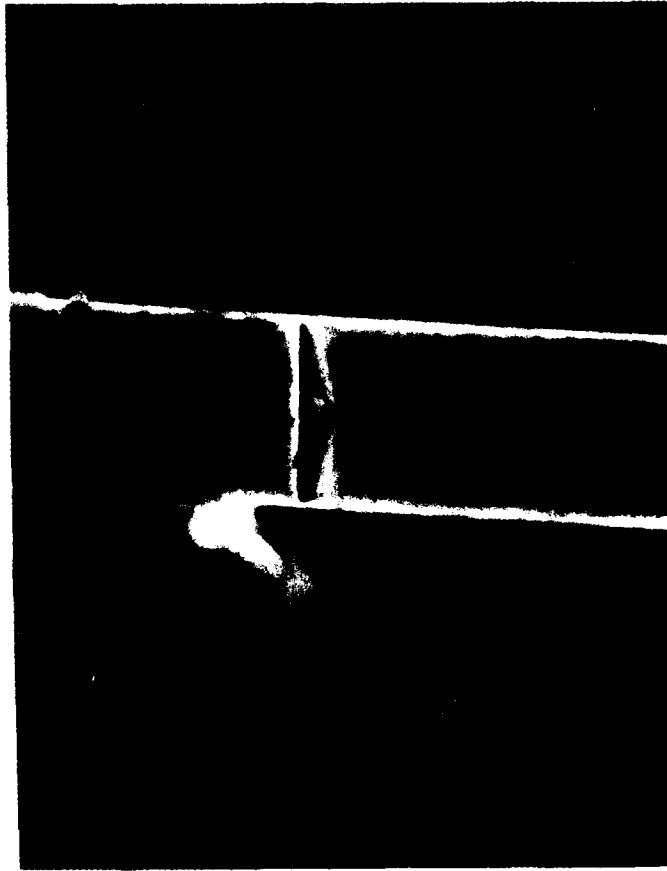
Figure 3-16. Photograph of a Typical Razor Blade Notch
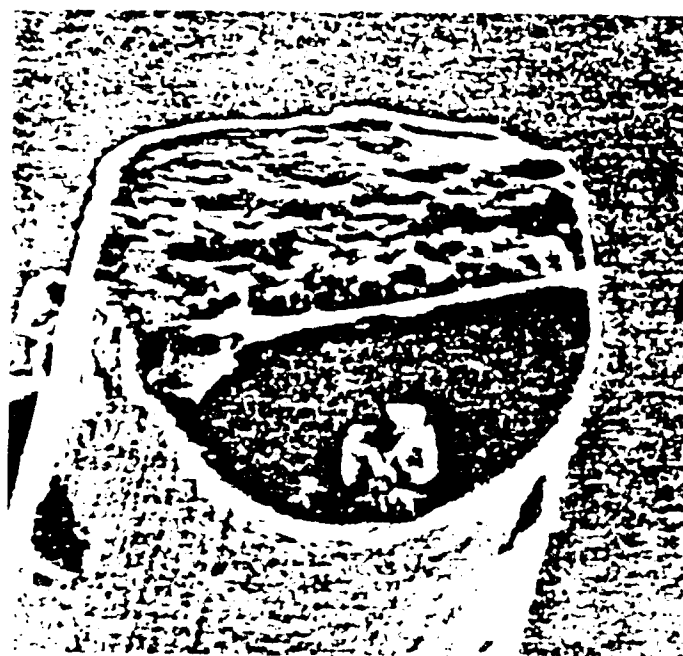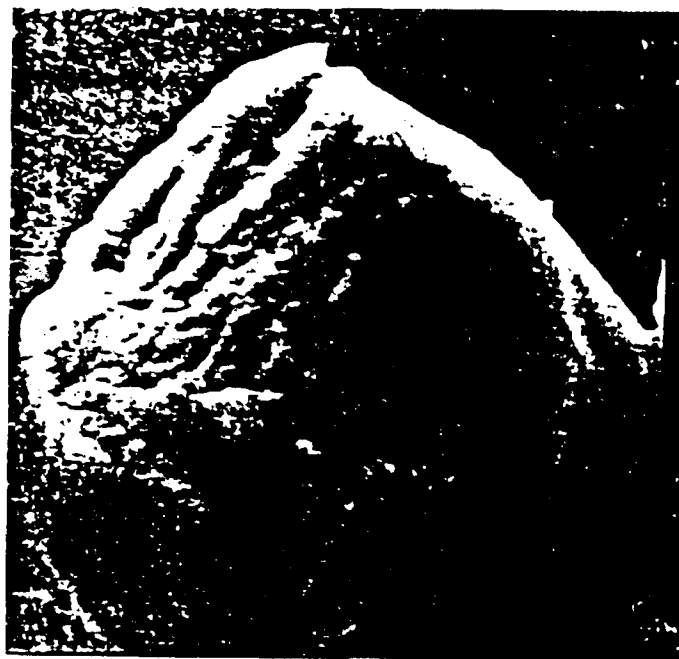
Figure 3-17. Fracture Surface of Two Group 7 Wires

Figure 3-18. Detailed View of the Fracture Surface
of a Group 7 Wire

Figure 3-19. Photograph Near the Overload Lip

Group Eight Tests. Three more wire loops were formed and notched according to the previously described procedure. These notches extended to a point approximately half as deep (0.0002 inch) as the Group 7 notches. The wires were cycled to produce a bending stress ranging from 26 to 39 ksi at the respective extremes of the fatigue cycle. The corresponding stress intensity factor ranged from 0.4 to 0.6 ksi in$^{1/2}$ giving an R-ratio of 0.67.

Testing was interrupted after 3,156,300 cycles when one of the three wires was found broken. As was observed in the fractographic examinations of the Group 7 wires, the broken Group 8 wire reveals a predominantly intergranular fracture surface, as shown in overall fracture surface of Figure 3-20. Also noticeable is an overload lip. Figure 3-21 shows a region of the fracture surface near the lip. Clearly visible are fatigue striations on either side of the lip.

A crack was found to extend from the initial notch of one of the two remaining wires. The crack appeared to extend approximately 0.0001 inch (2.5 μm) beyond the razor notch. This is shown in Figure 3-22. After the SEM examinations the wire was returned to the test fixture for further cycling under the same conditions. The other wire showed no signs of cracking and was not cycled further.

After an additional 63,000 cycles the test was interrupted to examine the wire for further signs of crack growth. Figures 3-23 and 3-24 show the wire after the additional cycling. While it is difficult to ascertain the exact depth of the crack, it appears as if the crack (including razor notch) extends one half of the wire diameter at its deepest point. Also clearly visible in Figure 3-24 is the extreme amount of damage accumulating opposite the crack. This experimental observation provides support to the previous conjecture of a second crack initiating on the back side of the wire and growing toward the initial crack.

The average fatigue crack growth rate, assuming the crack grew from 0.0003 to 0.0005 inch (7.6 μm to 12.7 μm) over the additional 63,000 cycles, is 3.2 x 10^{-9} in/cycle (8.1 x 10^{-11} m/cycle). Assuming the initial loading conditions, the corresponding cyclic stress intensity factor, ΔK, is approximately 0.3 ksi in$^{1/2}$. Employing a fatigue crack growth rate relation for bulk aluminum assuming no threshold, Harris et al. (Ref. 3-10) would predict the crack growth rate to be on the order of 10^{-12} m/cycle. The latter prediction was made from bulk aluminum fatigue properties which, given the microstructure of the wire, may differ significantly from those of the wire. What is important is the fact that fatigue crack growth rates can be observed and correlated with fracture mechanics parameters. Nonetheless, that these results are similar to those obtained in much larger size aluminum test specimens, therefore, offers strong additional support for the feasibility of fracture mechanics for microscale structural elements.

Figure 3-20. Overall Fracture Surface of a Group 8 Wire

/ μm
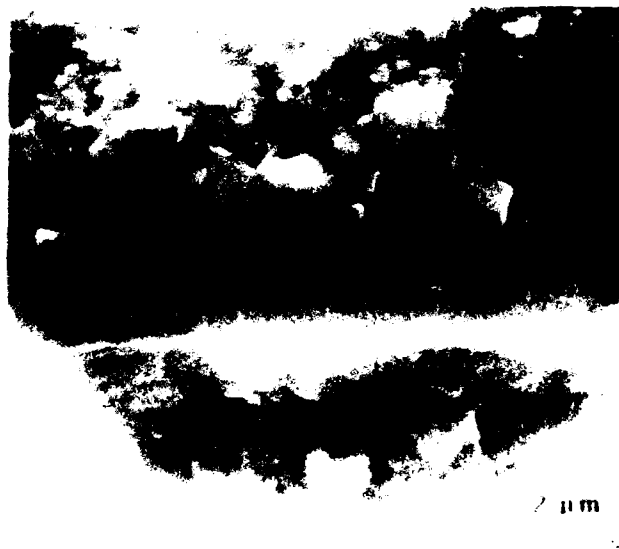
Figure 3-21. Fatigue Striations in the Group 8 Wire

3-35

Figure 3-22. Fatigue Crack Extending from
the Razor Notch of a Group 8 Wire after
3.156×10^6 cycles
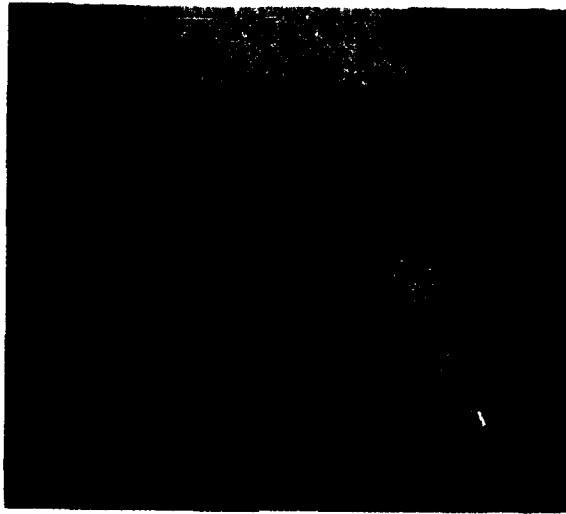
Figure 3-23. Fatigue Crack of Figure 3-22
After an Additional 63,000 cycles

Figure 3-24. Fatigue Crack of Figure 3-23
Showing Accumulation of Damage Opposite the Crack

3-37

After the additional 63,000 cycles were applied to the cracked specimen, a stereoimaging technique was used to measure the displacements resulting from the cyclic loading. The wire loop test fixture was designed to allow for removal of the entire fixture from the loading facility and insertion within the specimen chamber of an SEM.

Accordingly, the test fixture with the cracked wire specimen was photographed with the SEM at each extreme of the cyclic displacement. Displacements resulting from this loading were measured by stereoimaging. The crack tip opening displacement (COD) and strains in the wire were determined from the measured displacements. These quantities are shown in Figure 3-25. Fatigue cracks in many other materials have been found to exhibit CODs proportional to the square root of the distance from the crack tip. This relationship is confirmed by Figure 3-25(a). Mohrs circles of strain in the wire, shown in Figure 3-25(b), indicate the large magnitude of strain throughout the wire, especially at the crack tip and near the opposite surface, as shown by the surface deformation. The crack tip effective strain was found to be 0.145 (maximum shear strain 0.186) and the largest effective strain on the opposite side of the wire was 0.087 (maximum shear strain 0.151).

3.2.5.3 Estimation of Crack Driving Force

The concept of the J-integral may be used to estimate the crack driving force from the micromechanics parameters measured for the partly failed wire. For power law hardening materials, the J-integral can be estimated by:

$$J = \sigma_y \delta \tag{3-7}$$

where δ = crack tip opening displacement (CTOD) and σ_y is the yield strength.

For convenience, the crack driving force ΔK can be shown to be related to the J-integral and the CTOD through (Ref. 3-2):

$$\Delta K = \left[\left(\frac{1-r}{1+r}\right)E\Delta J\right]^{1/2} = \left[\left(\frac{1-r}{1+r}\right)E\sigma_y\Delta\delta\right]^{1/2} \tag{3-8}$$

where E is the modulus of the material. A value of CTOD must be chosen from the graph of Figure 3-25(a) and σ_y can be estimated either from the strain at the crack tip, or as twice the yield stress. Taking CTOD at a distance of 0.5 μm and the cyclic yield strength as $2\sigma_y = 75$ksi Equation (3-8) yields $\Delta K = 3.8$ksi in$^{1/2}$. The average crack growth rate is estimated to be approximately 10×10^{-11} m/cyc for this crack length.

(a)

2 microns   20 % strain
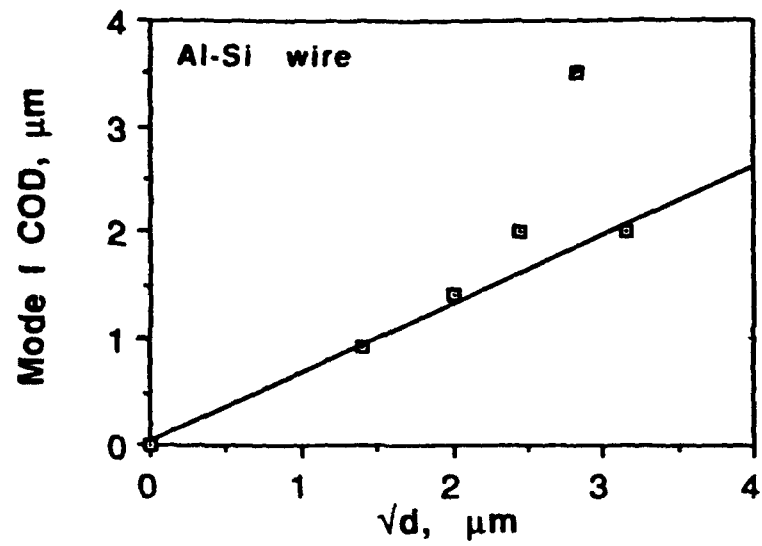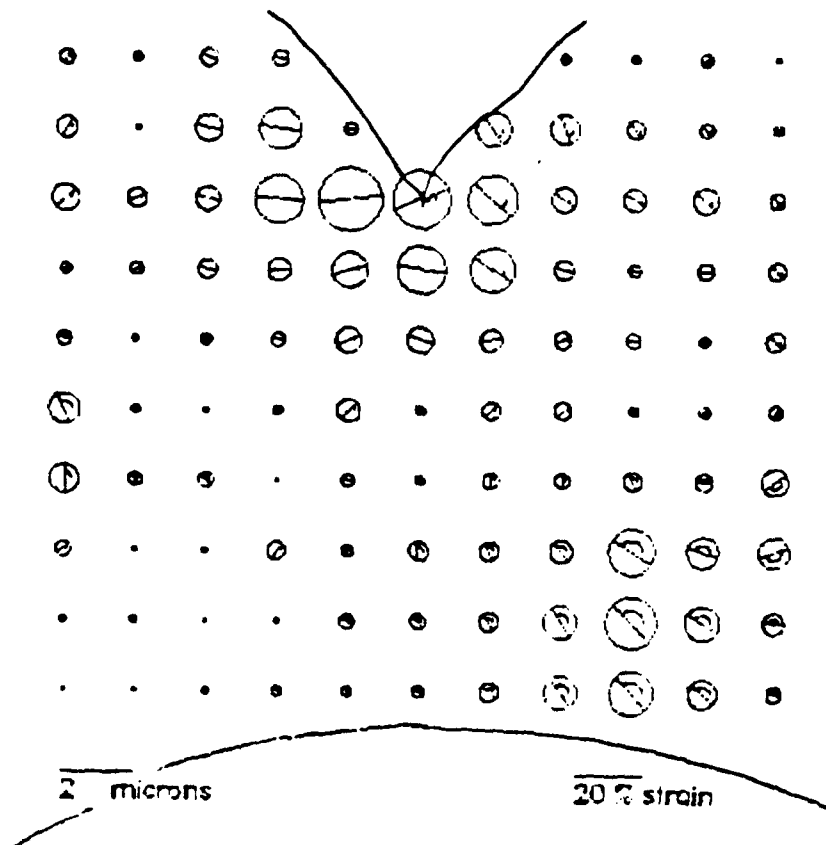
Figure 3-25. Crack Opening Displacement and Mohrs Circles
of Strain in the Bond Wire

Another useful estimate of crack driving force can be made at the point of crack initiation, assuming that the crack is being driven at just above the threshold for fatigue crack growth. This estimate is derived from a recognition that fatigue cracks do not grow unless the cyclic stress intensity is sufficient to generate cyclic plasticity. An estimate of the threshold driving force, ΔK_{th}, can be made using the following relationship:

$$\Delta K_{th} = (1-R) \, \sigma_y \, \sqrt{2\pi r_s} \qquad (3-9)$$

where r_s = the slip distance in the material. For these wires with their extremely small microstructural unit (grain size), the slip distance is only 1 or 2 grain diameters, giving $0.31 < \Delta K_{th} < 0.51 \text{ksi in}^{1/2}$ for R = 0 or $0.15 < \Delta K_{th} < 0.18 \text{ksi in}^{1/2}$ for R ≈ 0.6. These values compare well with the calculated estimates of ΔK at the notch root. Thus, it was assumed that the crack initiated with a value of $\Delta K \approx 0.36 \text{ksi in}^{1/2}$ at the notch tip. The crack growth rate for this condition was estimated to be 2×10^{-12} m/cyc.

To supplement information at the upper end of the curve, the observed fatigue striations can be used. Striations under the conditions existing in the wire at that crack length were forming on each cycle, so that in the striation forming region the average crack growth rate was about 3.6×10^{-7} m/cyc. The approximate driving force for this growth rate was $\Delta K \approx 15 \text{ ksi in}^{1/2}$ from observations of crack growth in the powder metallurgy aluminum alloy 7091, which also has a fine grain size. Final fracture was estimated to occur at $K_c \approx 23 \text{ ksi in}^{1/2}$ while growing at a cyclic rate of $\approx 10 \times 10^{-7}$ m/cyc.

3.2.5.4 Correlation of Crack Growth Rate vs. Crack Driving Force

Measured and estimated crack growth rates are correlated with estimates of the driving force in Figure 3-26. The 3 data points were the results of the calculations described above. Recall that for established fracture mechanics techniques to be applicable, the rate of growth of an identifiable crack-like defect must be uniquely related to a parameter which characterizes the crack tip deformation (Ref. 3-2). Thus, the correlation between the measured and estimated crack growth rates and the estimates of the driving forces shown in Figure 3-26 is significant in that it demonstrates the feasibility of applying fracture mechanics techniques to the microscale of electronic components.

The initial cycling conditions for the wire resulted in an R ratio of approximately 0.67. As the crack grew, a plastic hinge formed in the wire. Within the region of the plastic hinge, reverse loading occurs and the R ratio is shifted to approximately -1.

Comparison between Predicted and Deduced
Fatigue Crack Growth Rates for Bond Wire
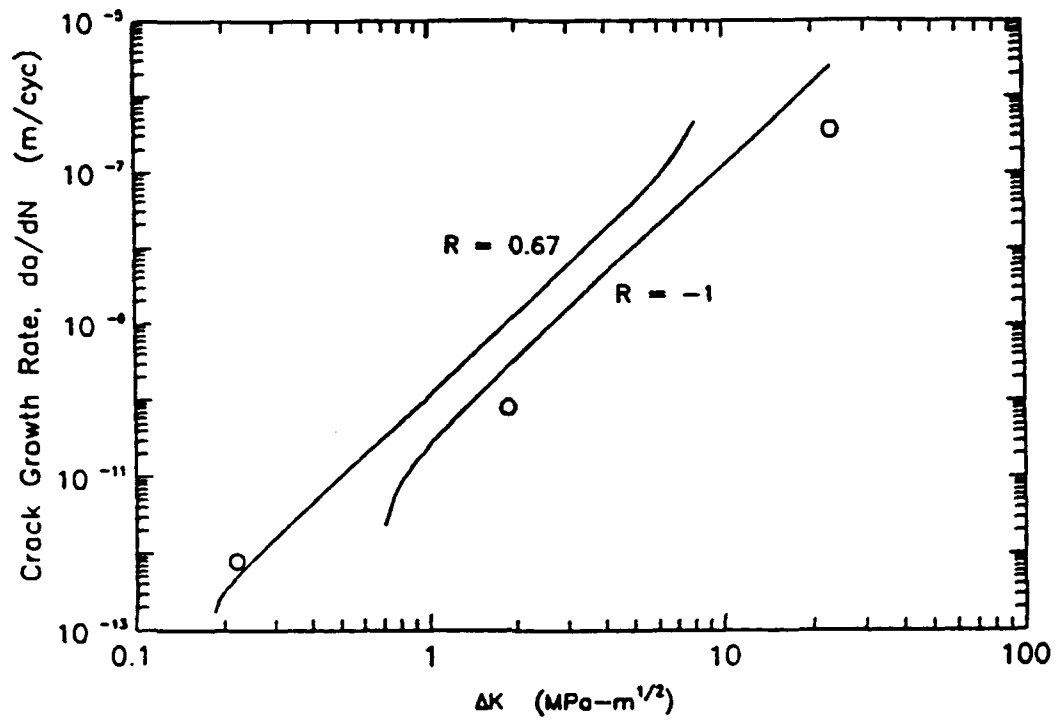
Figure 3-26. Correlation Between the Estimates of Crack Growth Rate and
Crack Driving Force. The three data points are measured and estimated crack
growth rates correlated with estimates of the driving force. The two curves are for
2024 aluminum alloy (Ref. 3-10) at the two R ratios thought to bracket the bond
wire fatigue tests.

Also shown for comparison are two curves, which are the crack growth rates for 2024 aluminum alloy (Ref. 3-10) at these two R ratios thought to bracket the bond wire fatigue tests. Note that the low end of the experimental data agrees well with the 2024 R = 0.67 prediction and the data at the upper end agree reasonably well with the R = -1 prediction. While not essential for the establishment of the applicability of fracture mechanics for microscale structural elements, it is encouraging and convenient to find that the fatigue crack growth behavior is very similar to that for 2024 aluminum alloy.

3.2.6 Discussion of Loop Vibration Fatigue Testing Results

This experimental and computational study was aimed at illuminating a crucial issue in the development of a well-founded methodology. This is to determine if it is possible to quantify the relative contribution to the lifetime of microscale avionics elements that is consumed by processes characterizable by fracture mechanics procedures. In an initial attempt to assess the viability in an efficient way, 0.001-inch diameter Al-1% Si wires, typical of those used in avionics components, were subjected to tension-tension fatigue testing. In order to perform the fatigue testing, pristine wires were cycled in the form of loops; the smaller diameter loops giving rise to higher stress values. Even though some loop diameters were sized to give near yield stress values, no failures were experienced. Indeed, no indications of crack initiation were observed even after a large number of load cycles.

To examine the potential for crack initiation with a stress concentration, artificial defects were introduced at the apex of the loop with an electrical discharge technique used to damage the wire. However, fatigue testing of these wires was also unable to produce any fatigue failures or signs of damage, even after a large number of load cycles. To be certain that this finding was not due to an artifact of the experimental procedure, a large deformation finite element model was used to determine the states of stress that were achieved. These were found to be at near yield stress levels. However, inherent to the wire drawing process is the reduction of the mean flaw size. Thus, coupled with the very small grain size in these wires, the difficulty in obtaining crack initiation and propagation in fatiguing pristine and blunt notched wires is consistent with crack behavior in larger size specimens.

Judging from the results presented in Ref. 3-9, which would indicate that the microstructure of these wires is highly fatigue resistant, fatigue testing of the pristine wires would be expectedly difficult. Nevertheless, calculations performed by Harris and Sire (Ref. 3-11) indicate that fatigue crack initiation and propagation might be possible with a sufficiently sharp, deep starter notch. Thus, a notching technique was undertaken to induce sharp cracks at the apex of the wire loops with a razor blade. This technique has proved to yield consistently sharp notches to reasonably controllable depths. Cycling under these conditions has produced fatigue crack initiation and

growth data that can be correlated with a fracture mechanics approach, thus demonstrating the feasibility of such an approach. While limited in number and with noted material differences, the measured fatigue growth rates compare sufficiently well with predictions made from bulk aluminum fatigue crack growth relations to suggest that, with limited modifications, existing fracture mechanics type of analyses could be used for such small specimens.

4.0 WIRE THERMAL (POWER) CYCLING

This research is summarized in Ref. 4-1.

4.1 INTRODUCTION

Interconnect bond wires provide electrical continuity between the integrated circuit (IC) chip and the chip carrier. These wires are typically 0.001 or 0.005 inch in diameter. Each wire is arched-shaped and ultrasonically bonded at each end, as shown in Figure 4-1. As a result of the bonding process, the ends of the wire are flattened and become areas of high stress concentration, as shown in Figure 4-2. This stress concentration is accentuated on the first bond due to the high angle of attack between the wire and the pad, as shown on the right-hand bond in Figure 4-1. The partially flattened portion of wire that transitions between the undeformed round wire and the heavily deformed bonded end of the wire is referred to as the bond heel. The bond heel material adjacent to the first-made bond often experiences severe tensile plastic deformation as the bonding tool moves up and away from the first-made bond toward the second bond pad. As the wire is drawn upward and then bent downward to form the interconnect arch, the tensile and bending forces on the first bond heel can cause transverse tears to open on the top surface of the bond heel, as shown at the left end of the bonded zone in Figure 4-2. This surface damage introduced during production can significantly reduce the fatigue life of the bond heel. The stress concentration is somewhat less severe on the second bond, as the wire approaches the pad more gradually.

Under typical operating conditions, failure of interconnect bond wires is likely to occur at the heel of the first bond as a result of thermally-induced fatigue. During operation, current on the order of tenths of amps passes through the wires, producing resistive heating of the wire. While the span of the wire becomes hot, the ends of the wires remain relatively cool because the relatively large pads act as heat sinks. Thus, the thermal gradient acts to bend the wire about the wire bond. This action, coupled with the previously noted stress concentration, can give rise to fatigue failures at the wire bonds.

Past studies (Refs. 4-2 through 4-5) have shown that the repeated on-off cycling of current can eventually lead to flexural fatigue failures of the aluminum wires. This section describes an experimental and analytical investigation of the application of fracture mechanics to this microscale failure mechanism.

4.2 APPROACH

This research used the same approach used successfully in the wire mechanical cycling research descr'hed in Section 3.0. The approach was as follows:

- Fabricated test specimens, described in Section 4.3.

- Established the test setup, described in Section 4.4. It produced a square-wave voltage pulse.

- Performed preliminary tests, described in Section 4.5 and Appendix H, to establish:
  - the relation between current density and the wire temperature
  - the failure points of the wires.

- Fabricated a test setup that produced a square-wave current pulse.

- Performed testing (Section 4.6) to quantify crack growth parameters.

- Performed finite element analyses and fracture mechanics analyses, described in Section 4.7.

4.3 TEST SPECIMENS

The test specimens were in situ wire bonds in open microcircuit packages. These tests simulated the physical conditions that wire bonds experience in real packages. In the empty packages, the wires are bonded to the leadframe at one end and the package substrate at the other end.

The test specimens for the initial Hughes tests were eight pieces of aluminum bond wire (0.170 – 0.200 inch in length), which had been ultrasonically bonded to the metallized lands of a dual inline package (DIP). Subsequent test specimens had shorter wires, more representative of actual devices.

4.4 FATIGUE TEST FIXTURE

The description of this fixture is summarized in Ref. 4-6.

An automated test for current cycling 1-mil aluminum bond wires was developed. The test fixture is capable of cycling 500 mA of current at rates of up to 5 Hz through 12 aluminum bond wire samples connected in series and monitoring continuity, recording the total count of cycles, and stopping when continuity is lost.

The construction of this device employed an external power supply for a 500mA current source. This was switched on and off with a power transistor triggered from a TTL (transistor-transistor logic) annunciator game port output of an Apple II+ computer. Continuity was monitored by sensing voltage between wires under test and a current limiting resistor. This voltage
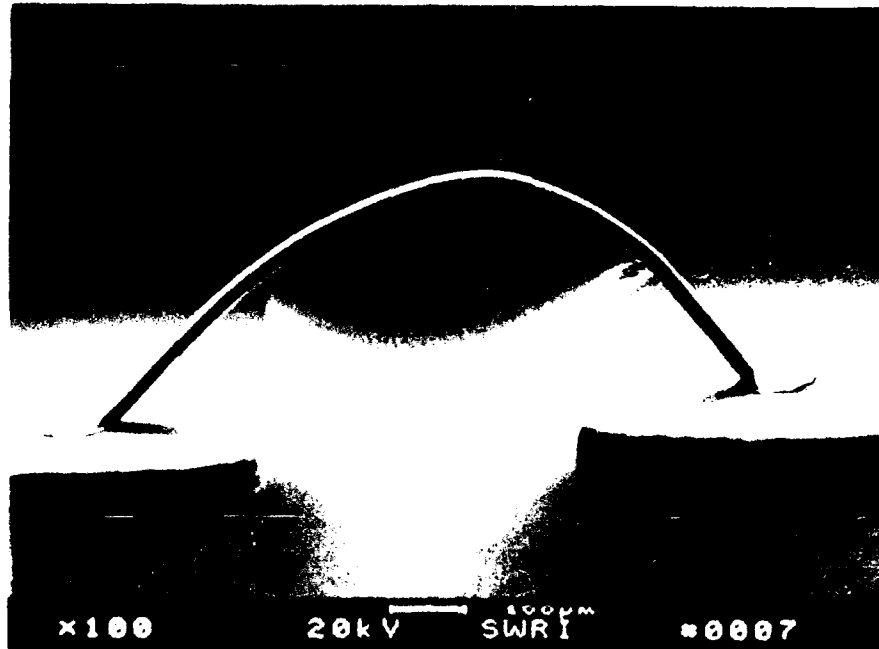
Figure 4-1. Photograph of an Interconnect Wire
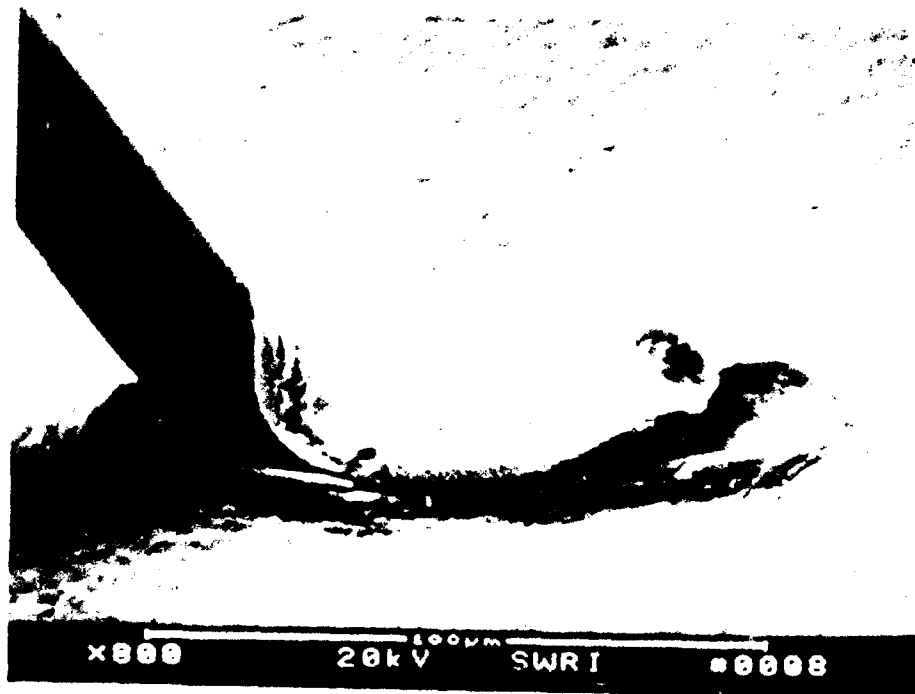
Figure 4-2. Photograph of a Typical Wire Bond Showing
Bond-induced Damage

was used to drive a TTL push button input in the same Apple II+ game port. Refer to Figures 4-3 through 4-5. The pulse rate generation, the continuity monitoring, and recording of the total number of cycles to failure were obtained by an Applesoft program. The final count was recorded on disk. Although a pulse generator and counter have been used instead, the Apple II+ computer was readily available and served both functions.
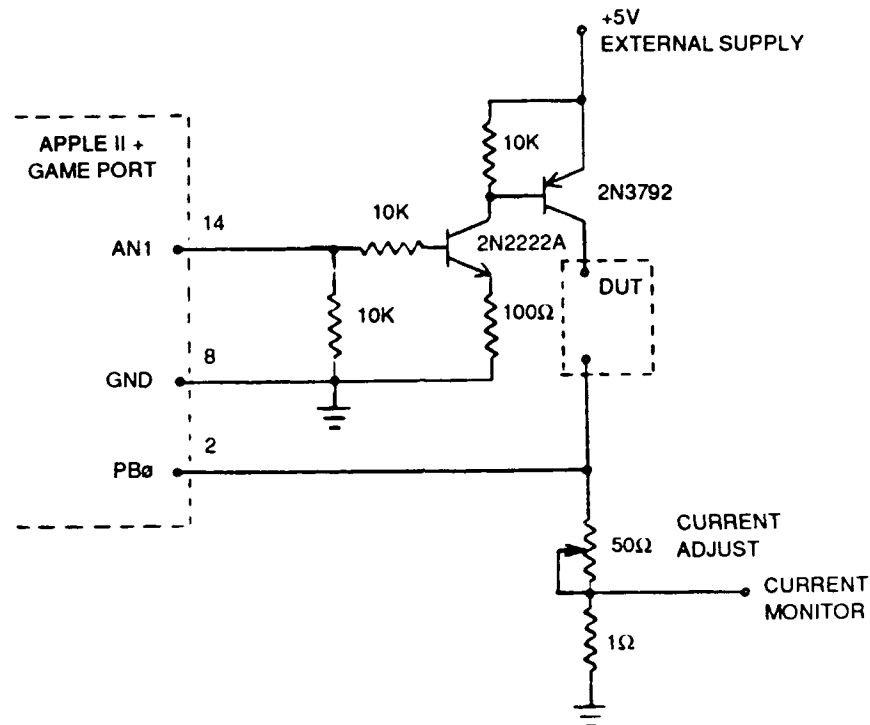
Figure 4-3. Schematic Diagram of Test Fixture for Current Cycling and
Monitoring of Aluminum Bond Wires

Figure 4-4. View Showing Test Setup with Test in Progress. The Test
Fixture is in the Center of the Photo

Figure 4-5. View Showing Detail of Test Fixture

4.5 FATIGUE TESTS WITH CONSTANT-VOLTAGE PULSE

4.5.1 Thermal Measurements

Hughes fabricated test specimens, and used an infrared microscope to measure the emissivity of the wire and the thermal characteristics of the test specimen. This activity is described in Appendix C.

4.5.2 Initial Fatigue Tests

Thermal cycling fatigue tests were performed. It was determined previously that approximately 570 mA will fuze a 1-mil-diameter Al-1% Si wire 0.170 - 0.200 inch in length. In order to determine an upper limit for the power cycling experiments, samples were tested at current levels ranging from 430 to 550 mA.

Six opened DIP packages with four aluminum wires each bonded to the lands were received. Three of these were installed in the fixture (S/Ns 1, 2, and 3). (The terms S/N and sample are used interchangeably here. The numbers are the same, whether they are called S/N or sample.) The wires were connected in series using jumpers.

Cycling was begun, and the current was monitored by means of an oscilloscope across a 1-ohm resistor in series (see Figure 4-3). The waveform of the current, shown in Figure 4-6, indicated an initial inrush current that decayed to a stable value in about 20 milliseconds as the wires became warm.
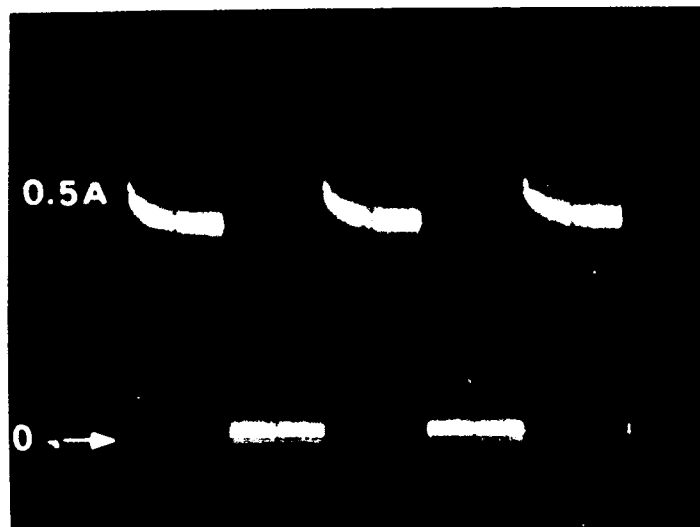
Figure 4-6. Oscilloscope Trace Showing Current Waveform
at Wires Under Test. Vertical: 100ma/div.
Horizontal: 50ms/div.

4-6

The current was on half the time, and the period between the beginning of successive "on" portions of the cycle was 0.2 second. This period was sufficient for the wire to reach thermal equilibrium during each portion of the cycle.

The current level was adjusted so that the in-rush current was approximately 500mA (see Figure 4-6). The wires were visibly flexing when examined with a microscope during current cycling. The top of the wire arch appeared to flex approximately one wire diameter. Cycling was continued on DIP S/Ns 1, 2, and 3 until 1,743,536 cycles accumulated with no failures. The first three DIP packages were removed from the fixture.

Next DIP S/N 4 was installed in the fixture. This time the current was increased until the stabilized level was 550 mA. This resulted in an in-rush current of about 650mA. Cycling continued on DIP S/N 4 until failure occurred at 380,322 cycles.

The failure was an open near the middle of one of the wires. Just prior to the failure (375,000 cycles), the stabilized current had dropped to approximately 500mA and the wires were beginning to sag in the middle. Surfaces of all the wires also appeared to be rough textured near the middle. An analysis of this failure mechanism is presented in Ref. 4-6.

This failure mechanism is interesting. However, it is not observed in deployed devices. It is different than a single-event electrical overstress failure, in which the wire fuses open at its midspan. It also is different than the main focus of this research study – fatigue failure of the wire at its heel.

DIP S/N 5 was then installed in the fixture and the stabilized current was set to 500mA. Cycling continued on DIP 5 until failure occurred at 520,052 cycles. This failure was similar to the failure on S/N 4.

S/Ns 1, 2, and 3 were then reinstalled and cycling continued at 450mA stabilized current. Accumulated cycles totaled 2,037,500 when it was noted that stabilized current had dropped to approximately 400mA. Visual examination of wires disclosed only slight roughening of the surface. Cycling was then continued from that point after readjusting the current to 450mA. From this count it was noted that indications of failure would occur, but continuity was not lost because the cycling could be restarted. The cause of this was isolated to the increase in resistance of the 12 wires in series (S/Ns 1, 2, and 3). The result was a lower logic 1 voltage to the PB0 input to the computer. By increasing the external power supply voltage to approximately 5.8VDC and readjusting the current to the wires, the increased resistance of the wires was compensated and correct operation was restored (refer to Figure 4-3).

DISCUSSION OF INITIAL THERMAL POWER CYCLING EXPERIMENTS

Current cycling at 550A stabilized current resulted in an open at the center of one wire after 380,322 cycles.

Current cycling at 500mA stabilized current resulted in an open at the center of one wire after 520,052 cycles.

Current cycling at 450mA stabilized current indicated no failures after more than 3 million cycles.

At 500 mA and above, the test specimens failed at the center of the wire arch (midway between the endpoints) from what appears to be electromigration (Ref. 4-6). No failures occurred at the heels of the bonds. Thus, in attempting to accelerate the fatigue failure of the heel of the wire by testing at currents several times higher than that in normal operation, a different failure mechanism at a different location in the wire resulted. The electromigration failure at the midspan of the wire is not observed in normal field operation; wires fuze open only when subjected to overstress.

To explain these results and help determine how to change the test to achieve the objective of fatigue failures at the heel, an analysis of the physical phenomena was performed. Hughes derived the equations governing the response to an electric pulse of a length of wire having a positive temperature coefficient of resistance. This analysis is described in Appendix C. The analysis predicts that the midspan temperature becomes infinite at a finite value of the current, so that there is a "thermal runaway."

4.5.3 Subsequent Fatigue Tests

The subsequent fatigue tests to establish the failure points of the wires are described in Appendix B.

The tests to measure fatigue crack growth parameters are described in Section 4.6.

4.6 FATIGUE TESTS WITH CONSTANT-CURRENT PULSE

4.6.1 Specimen Design and Test Configuration

A specially-designed specimen containing six interconnect wires was subjected to current pulses. Higher current levels than normal were used to expedite fatigue failures. The wires were connected in a daisy-chain manner and subjected to a square wave current pulse. Cycles to failure were obtained as a function of peak current level.

This section describes the details of the experimental setup, the fatigue test results and information gathered on the fatigue crack growth rate. Such information is useful in comparing these experimental results to computational and analytical analyses.

As was found in the wire mechanical cycling tests (Section 3.2), the fatigue life of the bond wire material was found to be very sensitive to the degree of stress concentration, with fatigue failures only being produced when sharp, notch-like defects were present in the bond wires. Because the defects resulting from the bonding procedure are uncontrollable and vary from bond to bond, it was anticipated that the fatigue lives would also vary from bond to bond. Thus, it was desirable to test several wires under identical conditions in order to achieve a meaningful range of fatigue lives. The daisy-chain wiring sequence was particularly advantageous to meet these test requirements.

A test specimen was designed so that up to six wires could be tested on a single chip carrier. Interconnect wires were bonded from lead to lead in a "daisy-chain" sequence on a 14-pin leaded chip carrier using the manufacturing technique normally used to bond a wire from a lead to the IC chip. This wiring sequence in shown schematically in Figure 4-7.

Daisy-chaining allowed any number of wires to be connected in series and subjected to current cycling. Because the wires were connected in series, each wire in the loop is subjected to the identical current history. When a wire failed, resulting in an electrical open, the failed wire was simply bridged resulting in a closed loop, and cycling was continued.

As the resistivity of the wires would change as the wire temperature increased and as cracking near the bonds developed, a method was needed to ensure that the current history remained constant. In order to achieve this, a controller was developed to generate a current history identical to any input signal, such as that from a signal generator. Because a current history is generated instead of a voltage history, a constant current history is maintained regardless of changes in resistivity (within bonds).

To expedite the testing, 12 current monitoring controllers were fabricated. Each controller has an adjustable potentiometer which allows the amplitude of the incoming signal, and hence the magnitude of the current history, to be independently set. The complete assembly allows up to 12 different current histories to be generated from a single input pulse. In this way up to 12 different current cycles could be performed at any one time.

A standard signal generator was used for the input history. A square wave with a 50 percent duty cycle, shown in Figure 4-8, was chosen for the cycling. With a frequency of 5 Hz, this cycle was shown to produce local heating in the span of the wire while the ends remained relatively cool (Appendix C). Such a cycle was imposed in all testing described in Section 4.6.
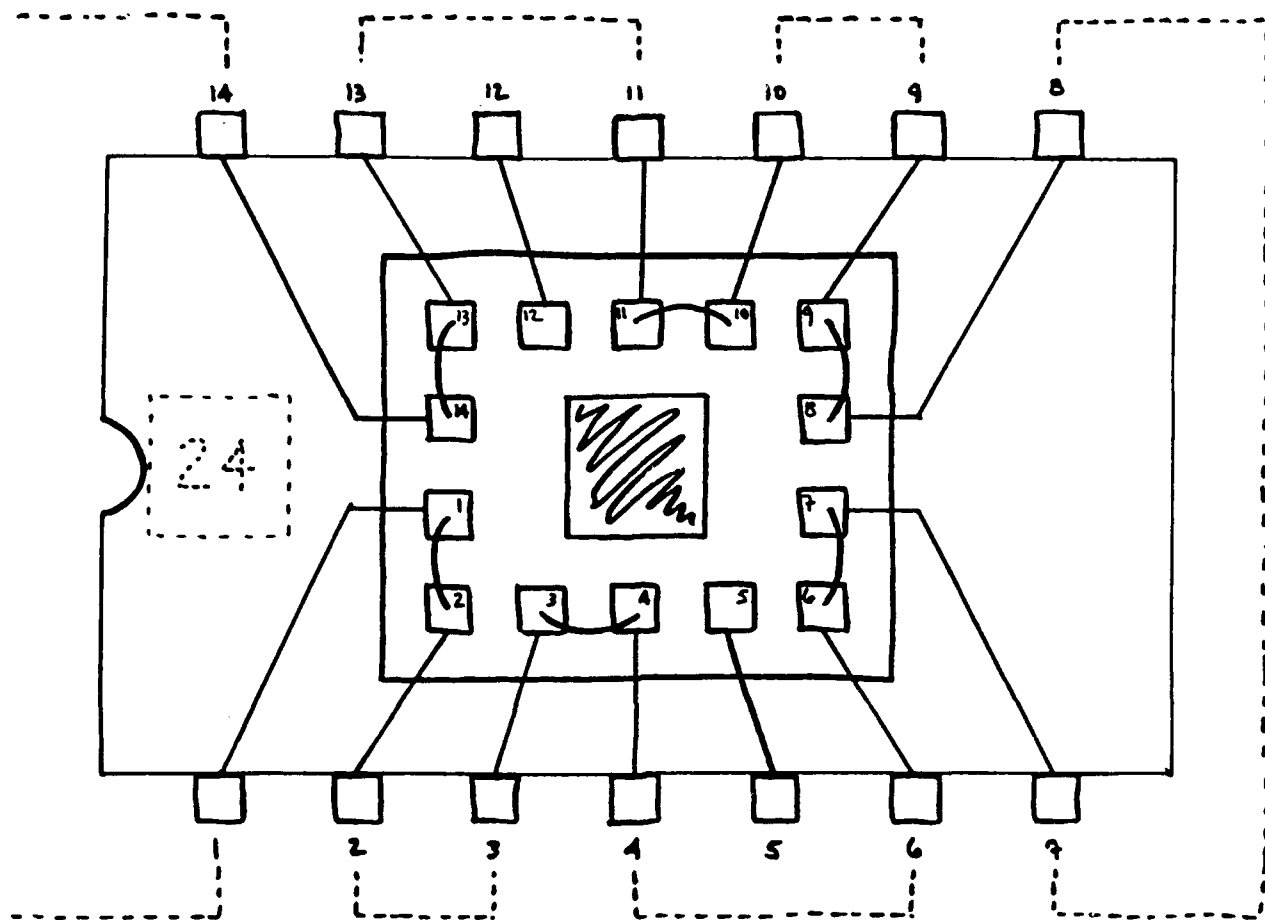
Figure 4-7. Schematic of Daisy Chaining Circuitry

4-10
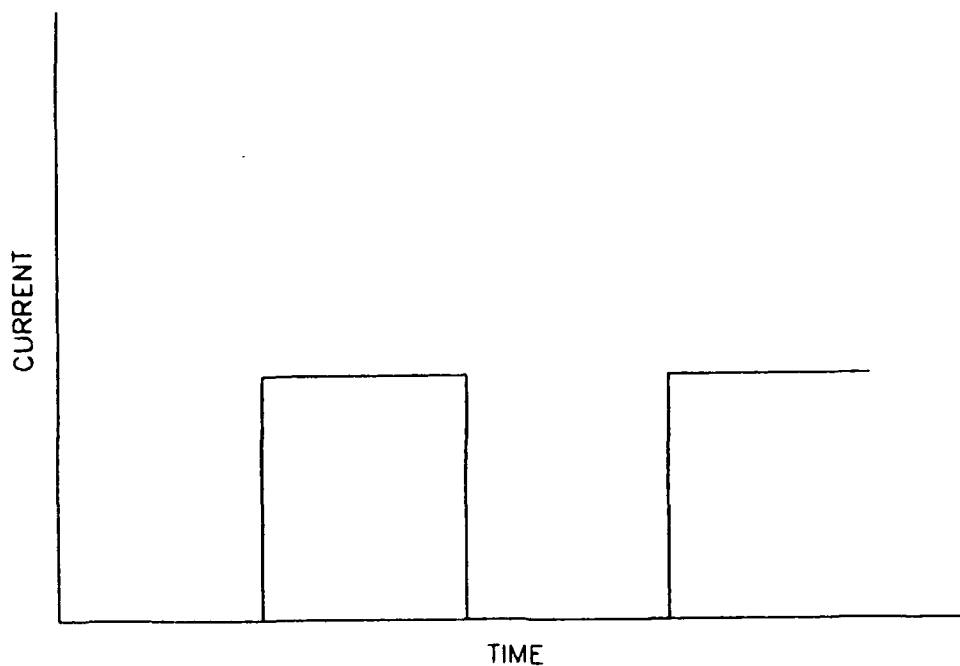
Figure 4-8. Schematic of Current Pulse History

While this test setup prescribed the current history, the experimentation described in Sections 4.4 and 4.5 prescribed the voltage history. A transient thermal analysis of each history (Appendix C) shows that the constant voltage results in a stable system and a steady-state temperature is always reached. For the constant current history, the thermal history depends on a dimensionless current density parameter, Q, which governs the steady-state solution. For values of Q less than π^2, the system is bounded and a steady-state solution temperature is obtained. However, for values of Q greater than π^2, the solution is unbounded and the temperature becomes infinite.

With the constant-current setup, fusing failure occurred at high currents after a relatively small number of cycles. At the same steady-state current, this unwanted fusing failure did not occur with the constant-voltage setup. Fatigue failures at the bond heel were achieved using the constant-voltage setup at steady-state currents more than 20% higher than the highest currents at which fatigue failures were achieved with the constant-current setup.

4.6.2 Experimental Procedure

Each of the 12 circuits was short-circuited using a small wire shunt. The signal generator was adjusted to produce a square wave with a 50 percent duty cycle at a frequency of 5 Hz. Using an oscilloscope as a monitor, the peak current from each controller was adjusted to a desired level

4-11

using the potentiometer. Typically, the peak current ranged from 1.0 to 1.5 amps. Currents greater than 1.5 amps resulted in the bond wires fusing open; currents less than 1.0 amp produced no failures after millions of cycles. While these current levels are roughly an order of magnitude greater than those experienced in service conditions, the relatively high currents used in this testing were used only to accelerate wire failure.

After each controller was adjusted to the desired level, the shunts were replaced with a particular daisy-chain to be tested. The leaded chip carrier was placed into a zero-force socket, wired to a piece of circuit board. The zero-force socket wiring completed the daisy-chain to include up to six wires. Typically, three or six wires were included in a single loop. The test time and the known frequency were used to determine the number of current cycles.

When an electrical open was detected, testing was momentarily interrupted while the failed wire was located and short-circuited. The peak current and number of cycles to failure were noted as a wire failed. When a sufficient number of wires in a circuit had failed, the entire leaded chip carrier was examined under a light reflecting microscope or with a SEM to locate the failure(s).

4.6.3 Power Cycling Fatigue Testing

The goal of this testing was to produce failures at the highly stressed wire bonds. While several failures occurred along the span of the wire as the result of the wire fusing (melting) open, these failures were attributed to the severe testing conditions and were not regarded as typical failures. Thus, only the failures at the wire bonds were noted as failures. All other failures were not addressed in this study.

Series of wires were cycled at peak current levels ranging from 1.0 to 1.5 amps. Cycling above 1.5 amps resulted in fusing of the wire almost immediately upon cycle initiation. In these cases, the entire span of the wire had melted back to the wire bonds. Thus, it was not feasible to cycle above 1.5 amps.

The number of cycles to failure and the peak current level were recorded for each failure occurring at a wire bond. In every instance, failure occurred at the first wire bond. Occasionally, cracking was noted at the second bond. Table 4-1 provides the fatigue life as a function of the peak current. Figure 4-9 shows the variation and dependence of these data.

Cycling at below 1 amp did not result in a fatigue failure. After cycling more than 10^8 cycles, no signs of damage were detected at the wire bonds. As shown in Table 4-1 and in ;ure 4-9, constant voltage pulse testing (Section 4.5 and Appendix H) was able to produce bond failures at current levels above 1.5 amps. These data are reported in this section for completeness.

TABLE 4-1. CYCLES TO FAILURE TEST RESULTS

Current (amps)	Cycles to Failure	Pulse
1.0	1.149×10^7	Constant Current (Section 4.6)
	7.094×10^7	
	1.123×10^8	
1.2	3.241×10^6	
	1.001×10^7	
	8.214×10^7	
1.3	1.141×10^5	
	1.201×10^6	
1.4	9.180×10^5	
	8.925×10^6	
1.5	9.109×10^5	
	1.974×10^6	
1.6	1.487×10^5	Constant Voltage (Section 4.5 and Appendix H)
	5.122×10^5	
1.85	2.780×10^5	

As is seen in Figure 4-9 and in the tabulated data given in Table 4-1, the scatter in the cycles to failure for a given current level is approximately 1 decade. This variation is likely due to the variable amounts of damage produced from the bonding procedure. Such a finding is consistent with the findings of the wire mechanical cycling tests (Section 3.2), which showed the fatigue life of the bond wire to be very sensitive to "sharpness" of a defect.

Peak Current Level versus Cycles to Failure
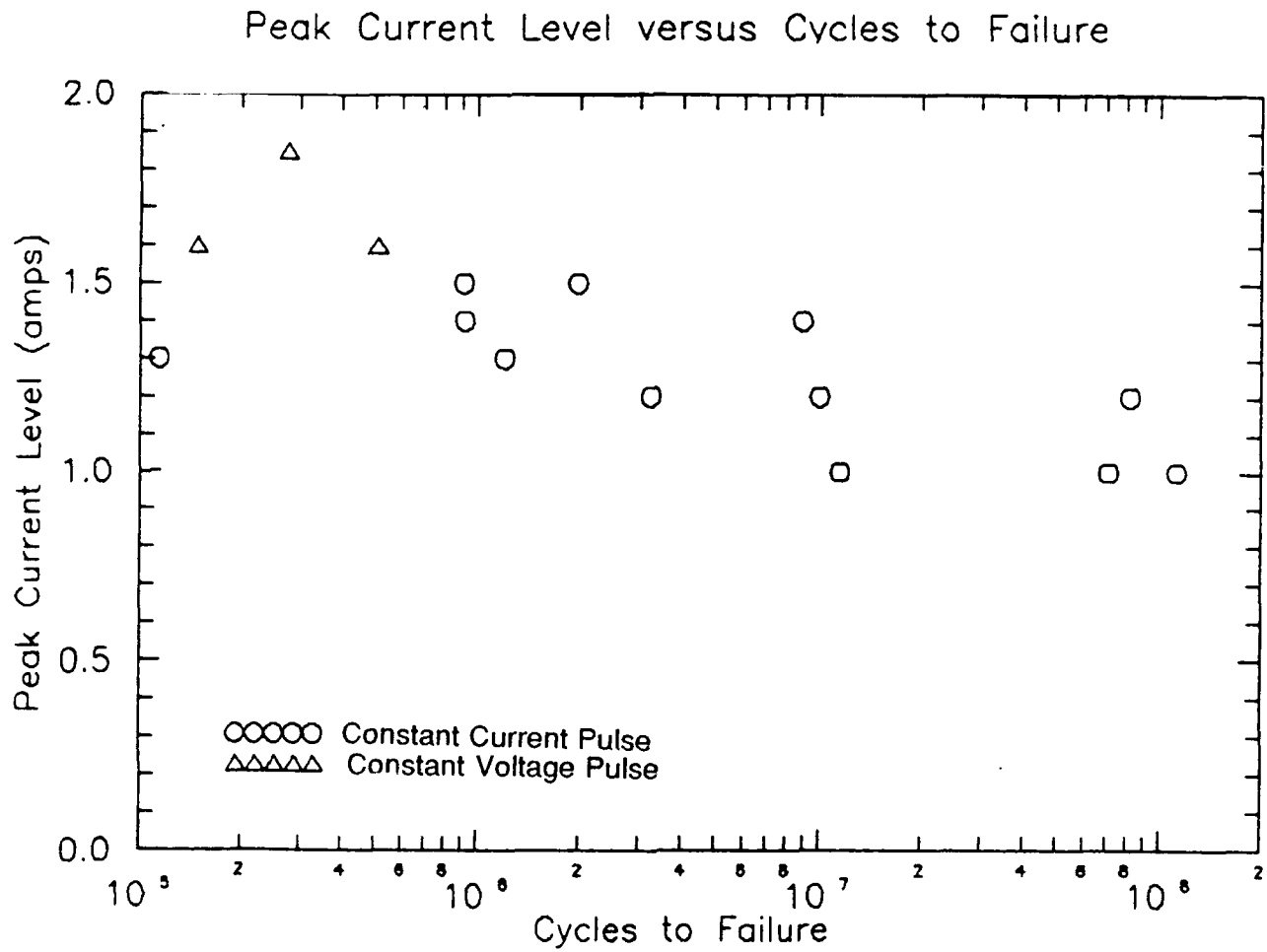
Figure 4-9. Fatigue Life as a Function of Peak Current Level
for Interconnect Wire Bonds

4.6.4 Fatigue Crack Growth Rate Studies

During the power cycling, several wire bonds showed initiation of a fatigue crack in the "heel" of the wire bond. While the growth of these cracks could be monitored as cycling continued, this task proved to be difficult. Albeit for relatively small crack growth rates, the fatigue cracks need only grow a very short distance (on the order of 0.0003 inch) to result in an electrical open. Thus, monitoring the progression of a fatigue crack through the wire bond becomes a tedious task.

As was seen in Figure 4-2, the initial defects resulting from the bonding process are sufficiently sharp to initiate a fatigue crack. Two samples, each containing three wires with initial damage equivalent to that shown in Figure 4-2, were cycled at 1.4 amps. The overall history of this testing is given in Table 4-2 and is described below.

TABLE 4-2. POWER CYCLING CRACK GROWTH
RATE DATA

Average Crack		
Cycles (in)	Crack Depth	Growth Rate (in/cyc)
72,000	None	N/A
270,000	< 0.00003	$< 1.52 \times 10^{-10}$
702,000	~ 0.00003	$\sim 6.94 \times 10^{-11}$
918,000	0.0003	1.25×10^{-9}

After 72,000 cycles one of the two samples was removed from testing for SEM evaluation. No signs of damage above that resulting from the bonding process were detected. Because the sample was gold-coated for careful SEM evaluation, it was not possible to continue cycling on this sample. It was assumed that this sample was representative of the other (unexamined) sample.

Cycling of the previously unexamined sample continued until 270,000 cycles had accumulated at 1.4 amps. Testing was interrupted to examine the wires for signs of additional cracking. Figure 4-10 shows a typical wire bond. The cracking appears to be only slightly more severe than the initial bonding-induced damage. While it is difficult to determine the exact depth, cracking was estimated to be less than 0.1 of the bond thickness, or less than 0.0003 inch.

As the sample was not coated prior to SEM evaluation, cycling of this sample was continued. The sample was inspected using the SEM after 702,000 cycles had accumulated. Figure 4-11 shows damage at the wire bond typical of the three wires on the sample. The cracking was estimated to extend approximately 0.1 of the bond thickness, or 0.0003 inch. This damage is notably more severe than that shown in Figure 4-2 after 270,000 cycles.

Figure 4-10. Typical Wire Bond Showing Fatigue Crack Initiation After
270,000 Cycles at 1.4 Amps
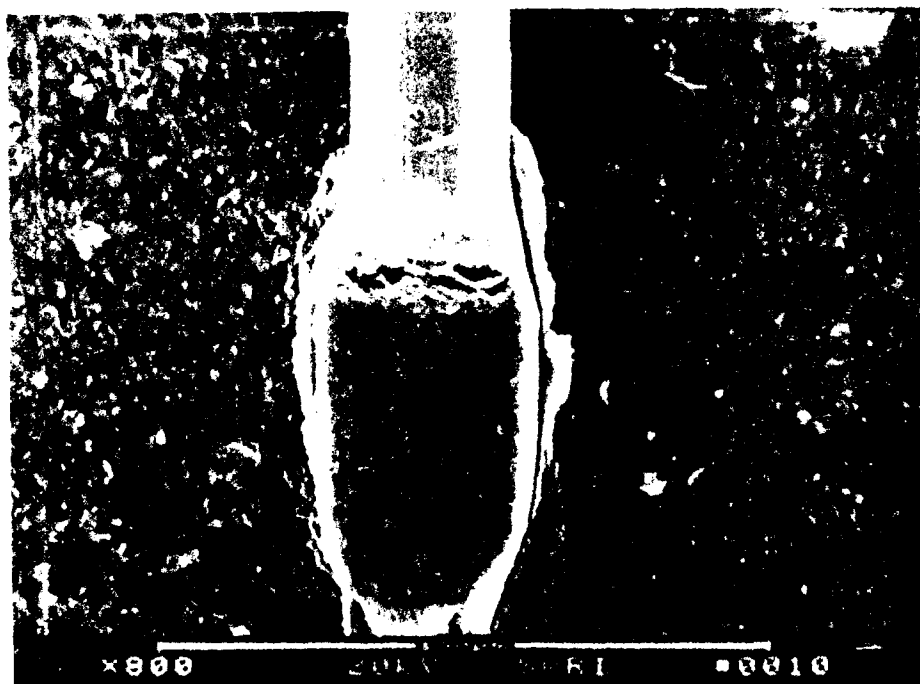
Figure 4-11 Typical Wire Bond Showing Continued Crack Growth
After 702,000 Cycles at 1.4 Amps

Again, cycling was continued after the examination. At 918,000 cycles one of the three wires had failed at the wire bond. This wire is shown in Figure 4-12. To permit examination of the fracture surface, the wire arch was carefully moved away from the bond, as shown in Figure 4-13. An overall view of the fracture surface is shown in Figure 4-14. While a detailed examination of the surface did not reveal any fatigue striations, the fracture surface clearly shows an intergranular failure consistent with those observed in the tests described in Appendix H and in the mechanical vibration testing (Section 3.2).

Cycling of the two unfailed wires was continued with periodic examinations until the remaining wire failed after 8,925,000 cycles. As with the first wire that failed, cracking was never observed to extend more than approximately 0.1 of the bond thickness until complete failure occurred. This large difference in failure times may be attributed to small differences in the initial damage induced by the bonding process. Minor differences in artificially-induced notches in the bond wires resulted in decades of variation in the observed cycles to failure.

4.6.5 Discussion and Conclusions

Due to the large amount of damage and presence of crack-like defects in the heel of wire bonds, wire power cycling experiments were able to produce fatigue failures at the bonds by pulsing current through the bond wires. The fracture surfaces of the fatigue failures at the bonds were intergranular and consistent with those found from mechanical fatigue testing. Although the peak current levels were well above those experienced under nominal service conditions, these high levels were used only to accelerate the test results. The fatigue life of typical wire bonds was determined as a function of the peak current for current levels between 1.0 and 1.85 amps. Attempted cycling above 1.85 amps would result in almost immediate melting of the wire as the current level neared the fusing current.

Attempts to quantify the rate of the fatigue crack growth proved to be difficult. While initiation of fatigue cracks from the bonding-induced defects were readily detected, subsequent fatigue crack growth measurements are only approximate. Difficulties in resolving crack depths and uncertainties in the driving forces and corresponding crack growth rates coupled with the extremely short distances the crack needed to grow to produce a failure made observation of fatigue crack growth nearly impossible.
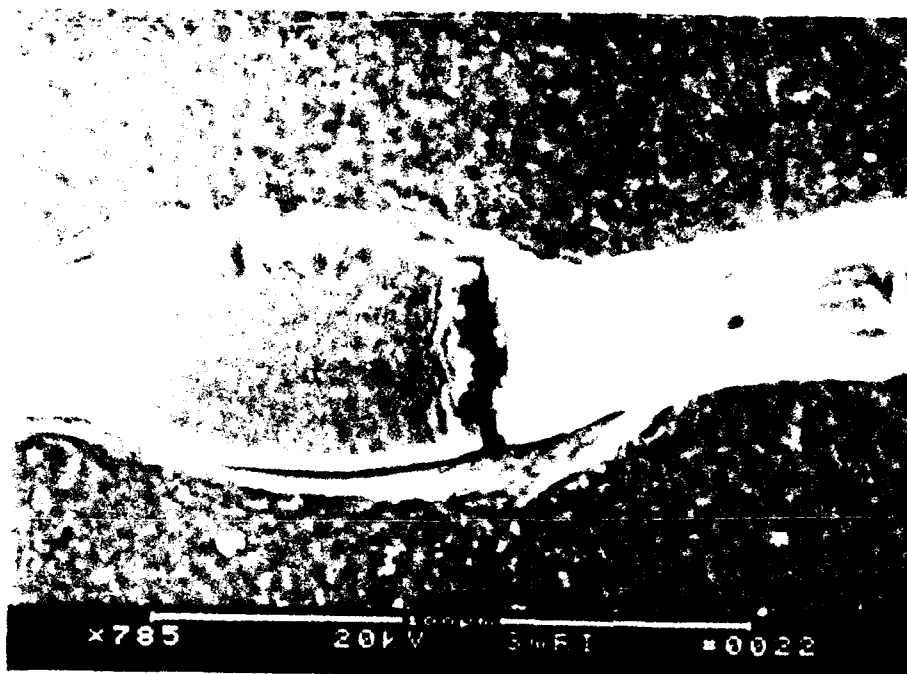
Figure 4-12. Failed Wire Bond After 918,000 Cycles at 1.4 Amps
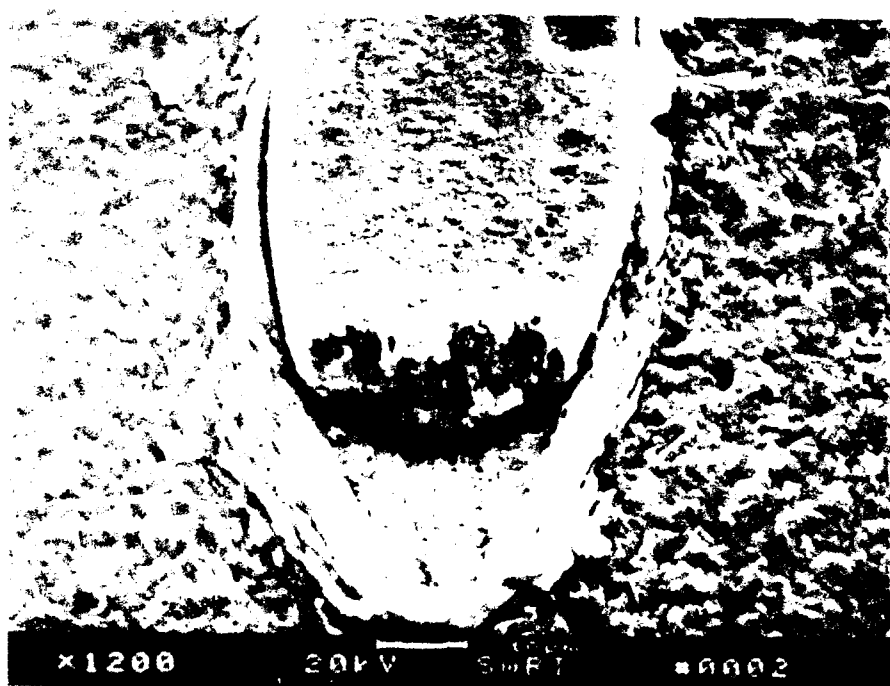
Figure 4-13. Failed Wire Bond Shown in Figure 4-12
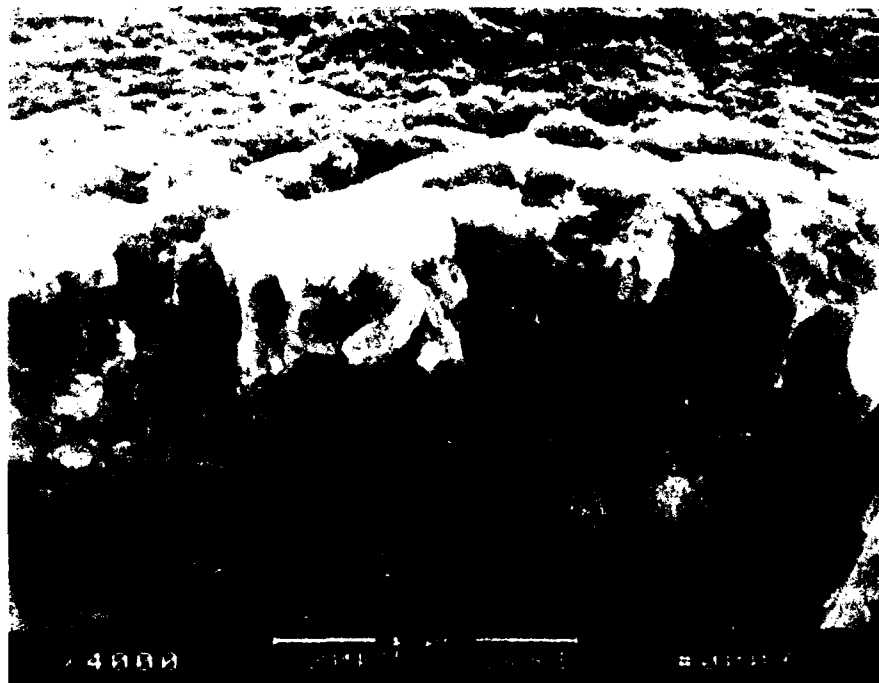
Figure 4-14. Fractured Surface of Wire Bond Shown in Figure 4-13

4.7 ANALYSIS

4.7.1 Introduction

This section describes the model for predicting crack growth for low cycle fatigue of bond wires. It was coded, and the software was delivered to the AF.

The following describes analytical modelling of the bond wire thermally-induced bending displacements and fatigue crack growth through the bond heel. Analytical modelling results are compared with experimental results, and implications of the experimental results concerning the statistical nature of as-fabricated defects are discussed.

4.7.2 Convective Heat Transfer Coefficient

The heat transfer coefficient for free convection, h, is a necessary input to the wire thermal analysis described in Appendix C. The convective heat transfer coefficient can be calculated using the expression:

$$h = N_{NU} \, k_f / D \qquad (4-1)$$

where N_{NU} is the Nusselt number, k_f is the thermal conductivity of the convective fluid (air in this case), and D is the wire diameter. The Nusselt number for free convection is a function of the

4-19

product of the Grashof number, N_{GR}, and Prandtl number, N_{PR}, and is obtainable from empirical data in the literature. Figure 4-15, which is drawn from Ref. 4-7, presents such data. For small diameter wires, $N_{GR} \, N_{PR}$ will be very small. Figure 4-15 shows $\log_{10} N_{NU}$ asymptotically approaching -0.4 for small $N_{GR} \, N_{PR}$, which corresponds to $N_{NU} = 10^{-0.4} \approx$ 0.4. The value of h can then be estimated once k_f is known. The fluid conductivity, k_f, is temperature dependent and is evaluated at the average of the surface and far field temperatures.

Figure 4-16 shows a plot of the heat transfer coefficient for a 1 mil diameter wire in air as a function of the average film temperature. The plot shows that h is not strongly dependent on film temperature in the range of 150 - 550°C. The wire power cycling experiments at SwRI were conducted with currents just below the fusing current and, therefore, wire temperatures close to the melting temperature of Al-1Si, which is approximately 660°C. Assuming an ambient air temperature of 21°C, the average film temperature for a wire at the melting temperature is 340°C, and the corresponding value of h is approximately 0.55 Watts/in^2-°C.

4.7.3 Wire Thermal Displacements

The wire temperature given in Appendix C, with material properties for Al-1% Si alloy in Appendix D, was used to compute the temperature distribution for the wire shown in Figure 4-1. The particular wire analyzed has a length of 0.045 inch. An enlargement of a wire bond and heel region is shown in Figure 4-2. The bonding operation has reduced the thickness of the wire in the heel region to approximately one-third of the original wire diameter, or 0.00033 inch, and the final shape of the wire cross section in the heel of the bond is more rectangular than circular.

A two-dimensional finite element (FE) model of the wire was developed to compute thermal displacements due to current in the wire. The FE model consists of 25 three-noded beam elements, with the elements on either end of the wire having tapered cross sections to account for the bond heels. The end nodes of the wire loop are constrained against translational and rotational displacements to simulate the bonds. Temperatures were computed at the element integration point locations using the temperature equations discussed above and were input to the FE analysis. A plot of the applied temperature distribution for a 1.5-amp current is shown in Figure 4-17. The analysis was performed using the MARC finite element program (Ref. 4-8) with pre- and post-processing performed using the PATRAN program (Ref. 4-9). An elastic modulus of 10,400 ksi was assumed with a Poisson's ratio of 0.33.

4-20

Symbol	Source	Fluid	Diameter cm.	Press Atms.	Fluid Temp.	Cylinder Temp.
+	Kennelly	Air	0.01-0.07	1-22	20 C.	185 C.
ε	Langmuir	Air	0.004-0.05	1	27 C.	1027 C.
δ	Aryton and Kilgour	Air	0.003-0.035	1	10-14	300
•	Rice	Air	4.3-11.3	0.11-1	12-103	82-150
⊙	Petaval	Air	0.11	0.97-168	16	916
●	Petaval	Hydrogen	0.11	0.97-114	16	916
⊶	Petaval	CO₂	0.11	1-35	16	916
△	Davis	Aniline	0.015	1	14	19-64
□	Davis	CCL₄	0.015	1	13	18-63
◇	Davis	Glycerine	0.015	1	19	24-69
▽	Davis	Toluene	0.015	1	15.5	20-65
∧	Eberle	Air	7.6-16	1	20	140-180
■	Ackerman	Water	5	1	30-50	34-92
▼	Koch	Air	1.4-10	1	20	30-190
▪	Wamsler	Air	2.05-8.9	1	15-30	55-240

✳ Saunders Nitrogen 0.11 250 1000
○ Curve Recommended by Davis, A. H.
✱ Curve Recommended by King, W. J.

Coordinates of Recommended Curve

N_{NU}	$N_{GR} \cdot N_{PR}$
+0.490	10^{-4}
+0.550	10^{-3}
+0.661	10^{-2}
+0.841	10^{-1}
1.08	0
1.51	10
2.11	10^{2}
3.16	10^{3}
5.37	10^{4}
9.33	10^{5}
16.2	10^{6}
28.8	10^{7}
51.3	10^{8}
93.3	10^{9}

Rice Approximate (1924)

Recommended Curve

Nusselt (1929)

Y-axis: $\text{Log}_{10}\ (N_{NU_D})$ values: -0.4, 0, 0.4, 0.8, 1.2, 1.6, 2.0

X-axis: $\text{Log}_{10}\ (N_{GR_D} \cdot N_{PR})$ values: -4, -2, 0, 2, 4, 6, 8
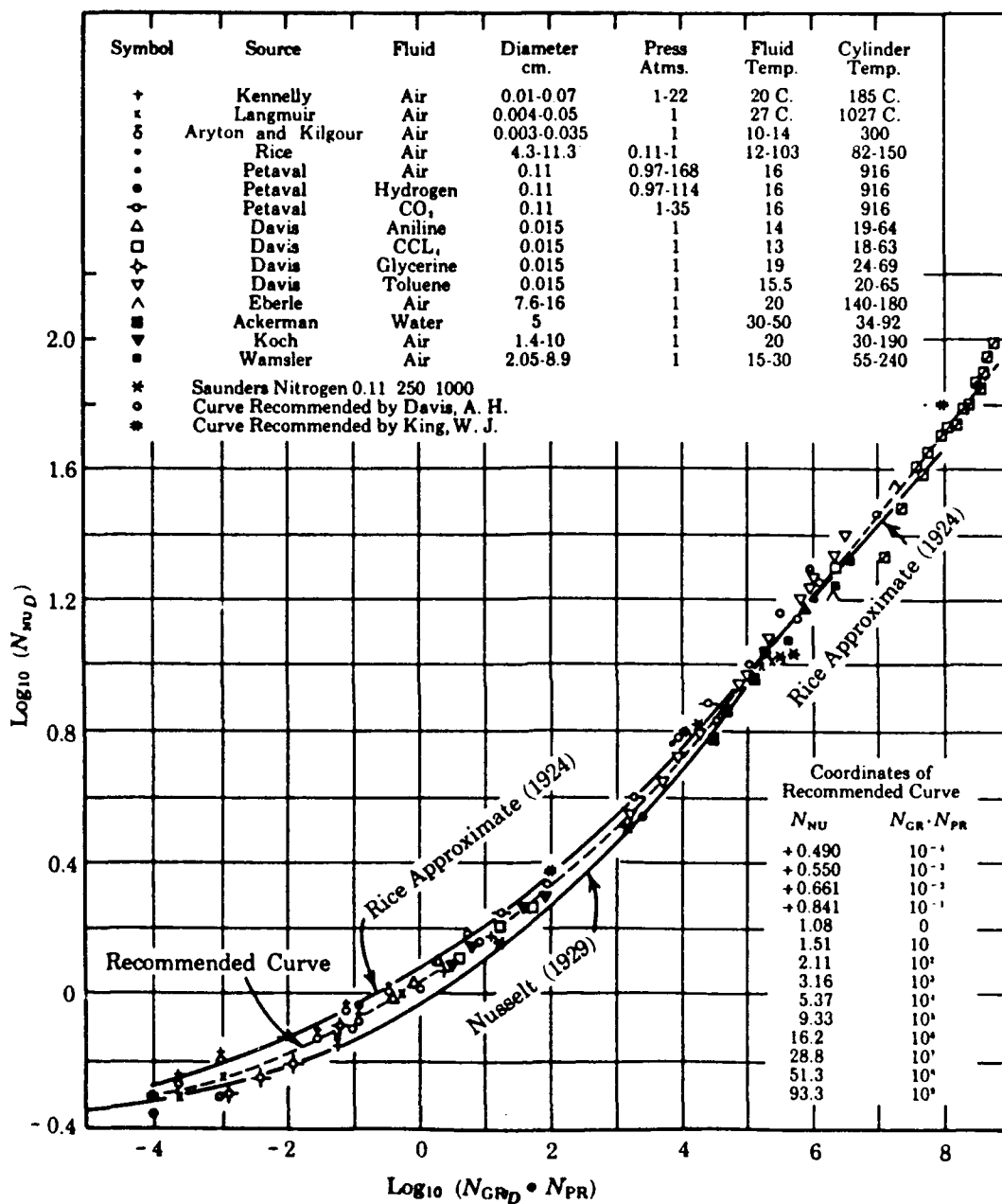
Figure 4-15. Correlation for Free Convection Around Horizontal Cylinders (Ref. 4-7)
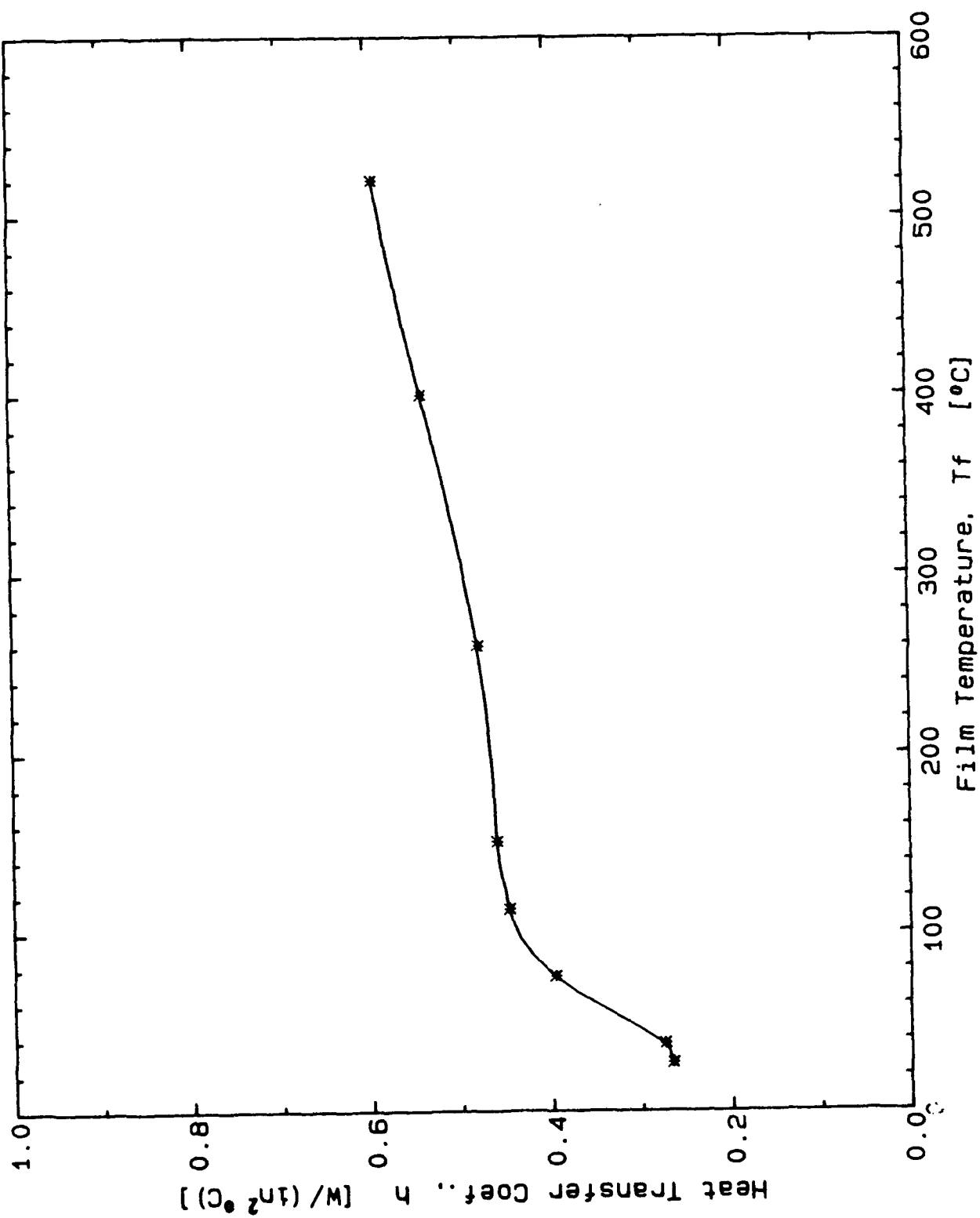
4-21

Figure 4-16. Heat Transfer Coefficient for Free Convection from a 1 Mil Diameter Horizontal Cylinder in Air
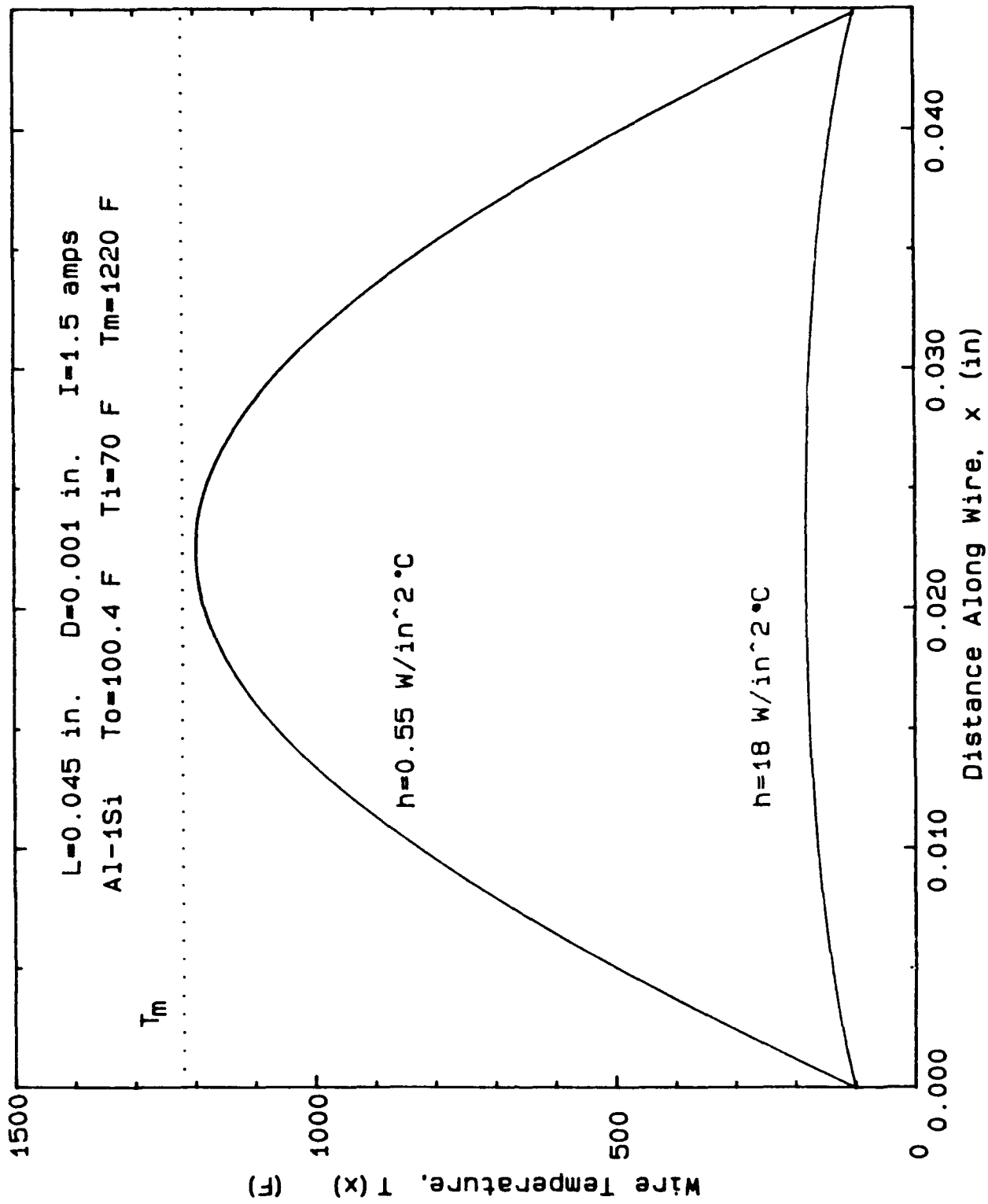
Figure 4-17. Analytical Prediction of Wire Temperature as a Function of Position for Two Different Convective Heat Transfer Coefficients

The displaced shape of the wire loop due to thermal expansion for a current of 1.5 amps and a value of h of 0.55 W/in^2-°C is shown in Figure 4-18 relative to the undeformed wire. The maximum vertical displacement at the center of the wire is 3.3×10^{-4} inch. The thermal expansion produces compressive stress on the top side of the wire in the bond heel.

The value of the bend angle of the beam model at the heel is needed for an input to the detailed stress analysis of the bond heel region which is discussed in the next section. In order to make comparisons with experiments performed with different current levels, the bend angle at various currents was evaluated by use of the finite element beam model. The variation of the convective heat transfer coefficient with film temperature, as shown in Figure 4-16, was accounted for. The results are summarized in Table 4-3, and the bend angle as a function of current is shown in Figure 4-19.

4.7.4 Detailed Analysis of Bond Heel Stresses

A detailed two-dimensional solid model of the wire bond heel region was constructed to obtain accurate stresses across the heel of the bond. The local model was necessary to account for the geometric stress concentration effects of the details of the heel region. The FE solid model, shown in Figure 4-20, was constructed of four-noded quadrilateral plane stress isotropic elements. Translational displacements of the nodes along the bottom of the bond at the bond line were fixed and a linear traction gradient corresponding to a unit moment was applied to the free end of the wire above the heel. The moment was applied so as to produce tension at the top of the wire. The model was analyzed elastically using the finite element program in the J-Integral Module (JIM) of the NASCRAC software (Ref. 4-10).

Displacement results from the detailed bond heel analysis were scaled to match the rotation of the bond heel obtained from the wire loop thermal displacement analysis described above. The resulting deformed shape of the wire bond heel model for a 1.5-amp current is shown in Figure 4-21 relative to the undeformed shape. The rotation of the free end of the wire is 0.58 degrees. Figure 4-22 shows the distribution of meridional stress across the minimum section of the bond heel. Also shown in Figure 4-22 is a linearized stress gradient that corresponds closely to the calculated (slightly nonlinear) gradient. The linear bending stress magnitude of 25 ksi corresponds to a bending moment per unit thickness of $M/B = \sigma W^2/6 = 4.5 \times 10^{-4}$ pounds. This bending moment will be assumed to remain constant as the crack extends across the heel. The other extreme of behavior is a fixed bend angle, but finite element calculations using the beam model with no rotational constraint at the heel (which corresponds to a crack nearly acros· .e heel) revealed that the rotation angle changed considerably. Hence, the situation is far from a fixed bend angle, and a fixed bending moment will be assumed in fracture mechanics calculations for simplicity and conservatism.
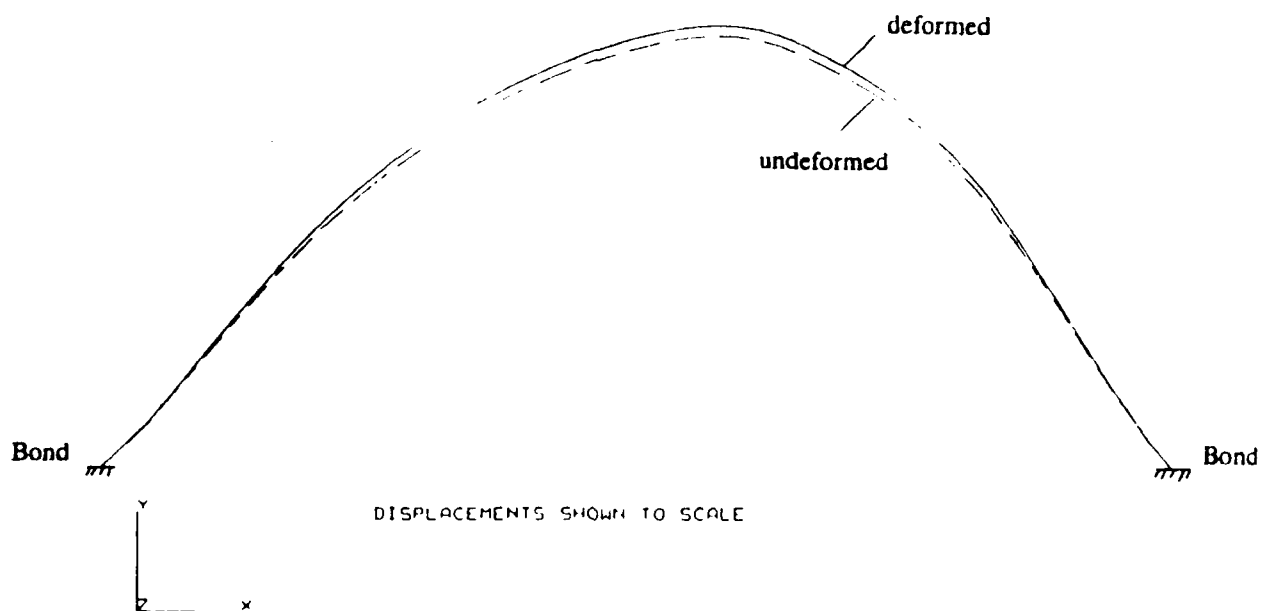
Figure 4-18. Calculated Thermal Deformation of Wire Bond with 1.5-Amp Current

TABLE 4-3. VARIATION OF CONVECTIVE HEAT TRANSFER
COEFFICIENT, BEND ANGLE, AND MAXIMUM WIRE
TEMPERATURE WITH CURRENT

I, amps	h, $W/in^2 \cdot °C$	T_{max}, °C	Heel Rotation, radius
1.0	0.42	319	2.58×10^{-3}
1.2	0.46	493	4.54×10^{-3}
1.4	0.48	858	8.23×10^{-3}
1.5	0.55	1213	1.06×10^{-2}
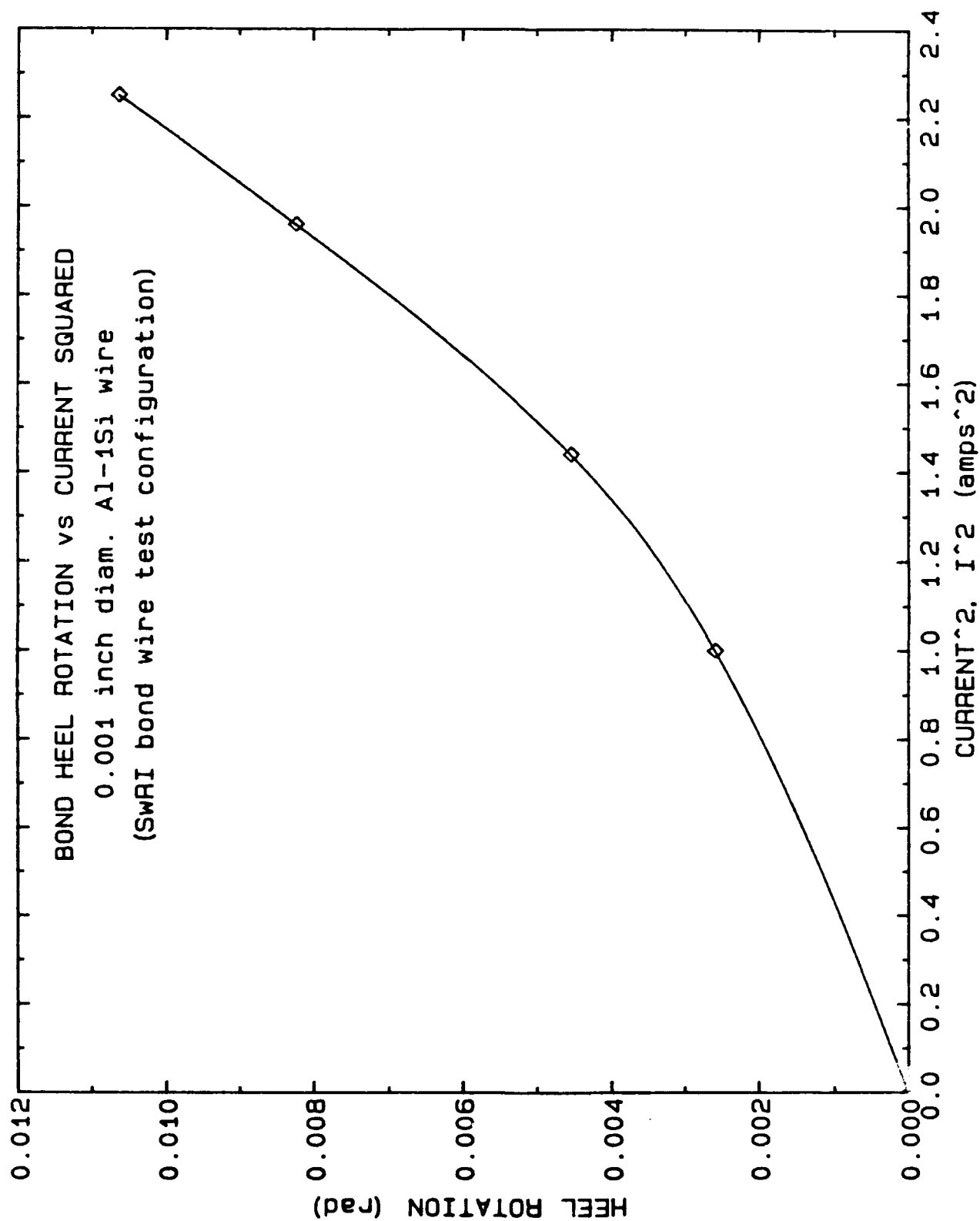
Figure 4-19. Bond Heel Rotation in a 1-Mil-Diameter A1-1Si Wire Bond as a Function of Current Squared
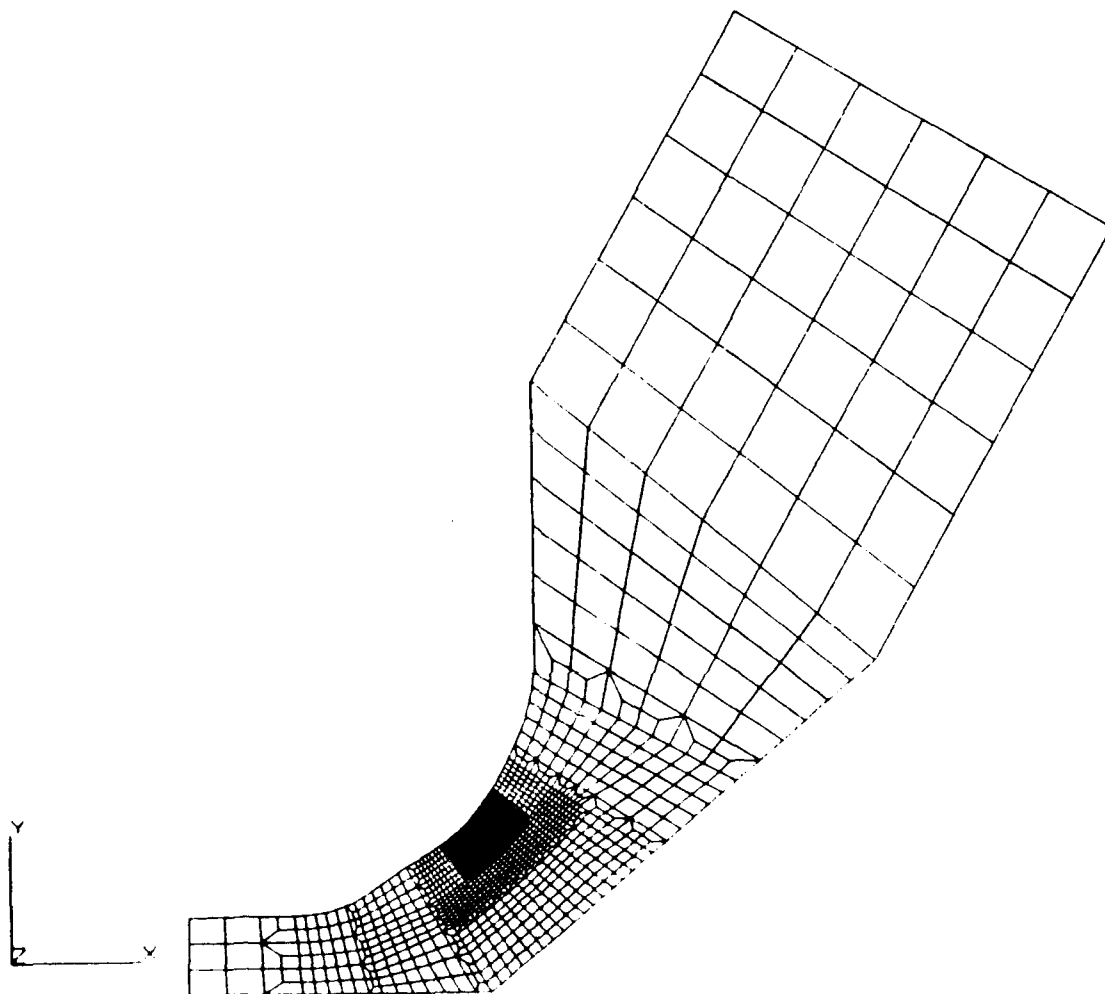
Figure 4-20. Finite Element Model of Wire Bond Heel Area

HUGHES ERFM 1-MIL BOND WIRE WITHOUT CRACK
THERMAL CYCLE ANALYSIS
PURE BENDING   1.5 AMP CURRENT

DISPLACEMENTS SCALED BY 10×
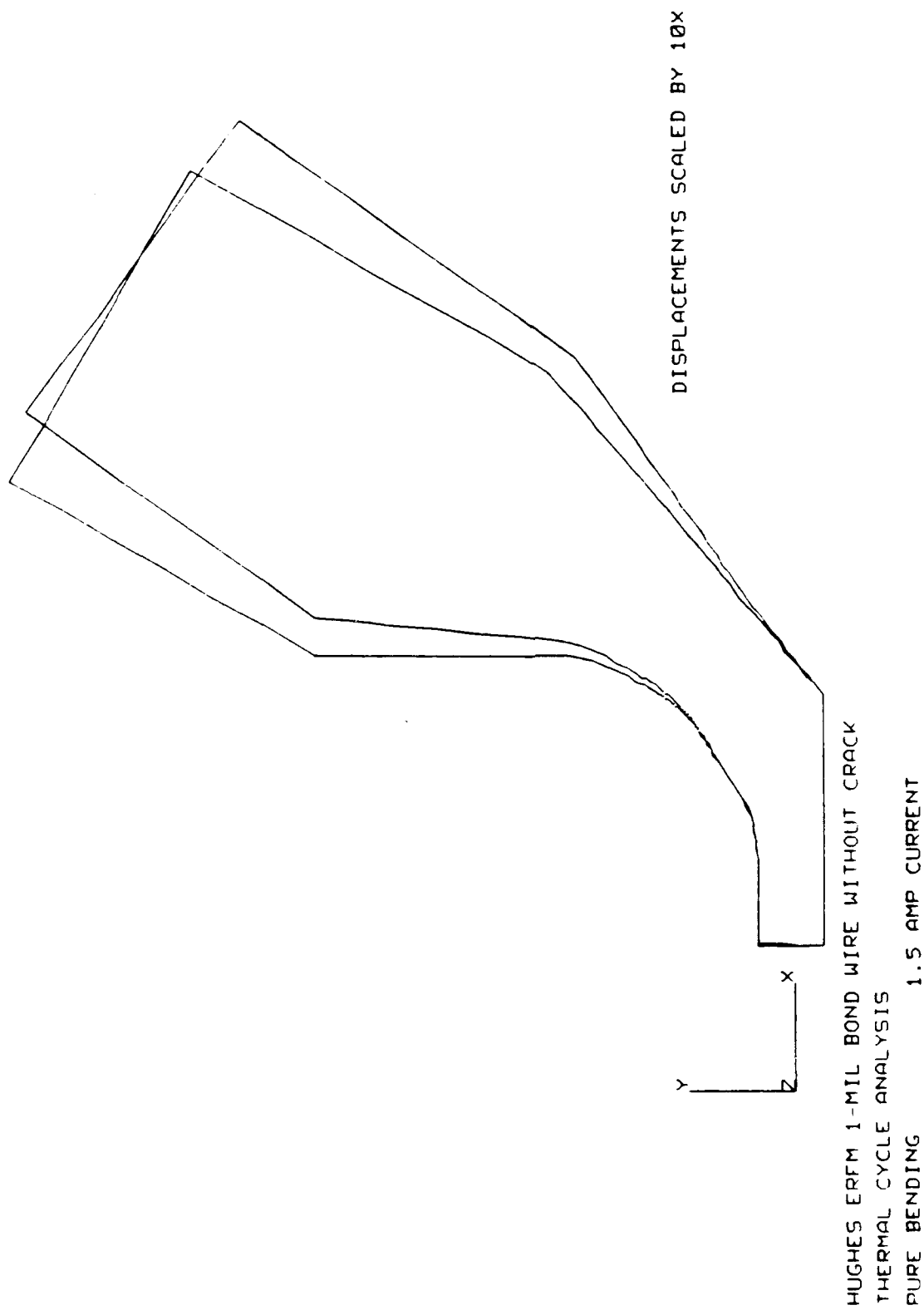
Figure 4-21. Deformed and Undeformed Finite Element Model of Wire Bond Heel Area
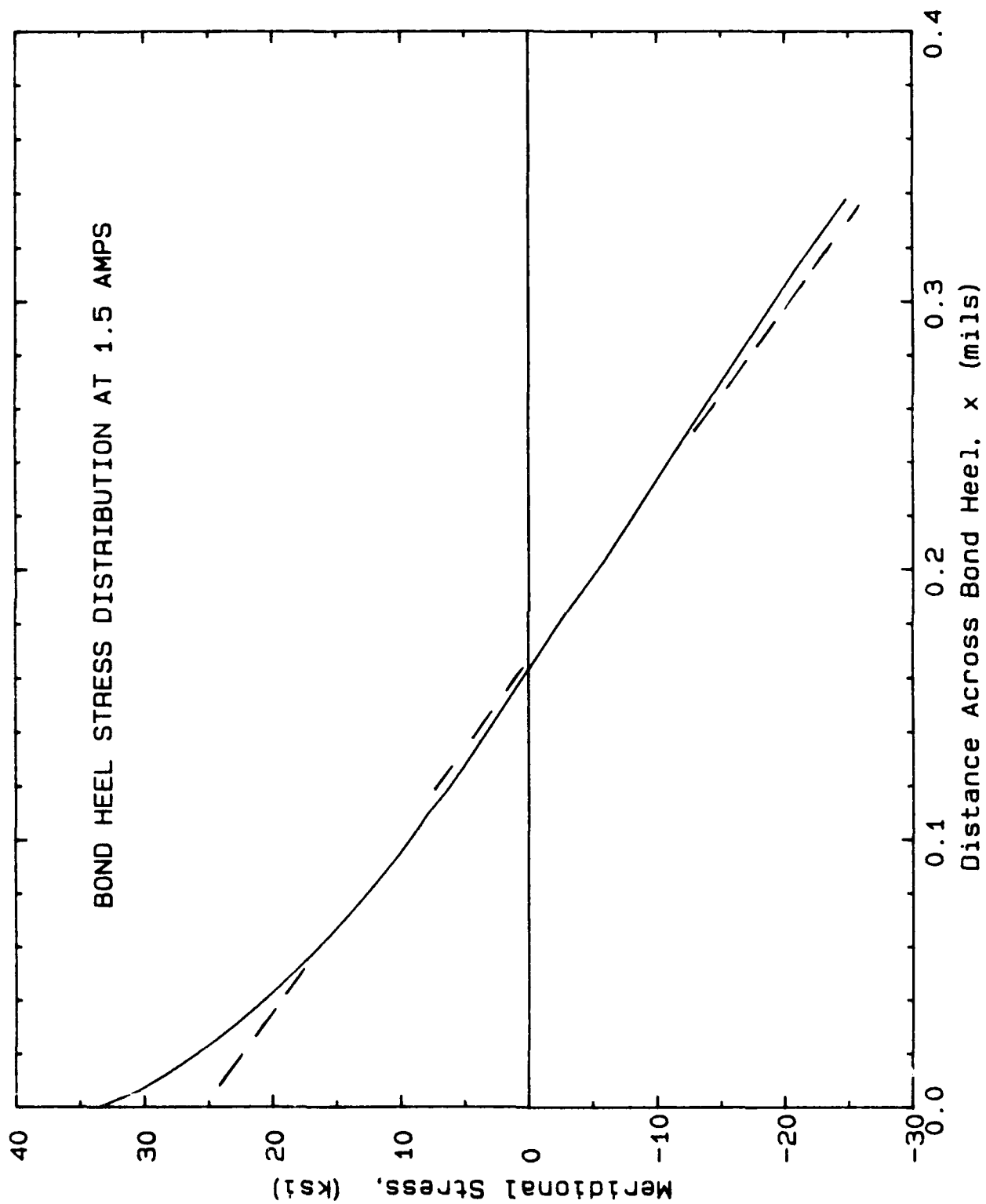
Figure 4-22. Stress Distribution Across the Wire Bond Heel at the Location of Maximum Stress

4.7.5 Fatigue Crack Growth in the Bond Heel

Fatigue crack growth calculations were performed on the bond heel for various initial defect sizes and currents using the NASCRAC code (Ref. 4-11). Fatigue crack growth properties for 2024- T3 aluminum alloy from the FLAGRO compilation (Ref. 4-11) were used, which provides the following fatigue crack growth relation:

$$\frac{da}{dN} = C \frac{\Delta K^n [\Delta K - (1-R)\Delta K_o]^p}{[(1-R)K_c - \Delta K]^q}$$

(4-3)

where $K = K_{max} - K_{min}$, $R = K_{min}/K_{max}$, da/dN is the crack growth rate per cycle, and the following constants apply:

C = 1.8×10^{-8}

n = 2.873

p = q = $1/2$

K_c = 73.4 ksi-in$^{1/2}$

A value of ΔK_o of zero was used. The above constants give da/dN in inches-per-cycle for ΔK in ksi-in$^{1/2}$.

The stress-strain relation for the aluminum wire material is taken as:

$$\epsilon = \frac{\sigma}{E} + \left(\frac{\sigma}{D}\right)^n$$

(4-2)

with $E = 10^4$ ksi, $D = 57.6$ ksi, and $n = 20$. These results are from Ref. 4-12 and are for a commercial aluminum - 1 percent silicon alloy (6082). These properties correspond to a 0.2 percent offset yield strength of 42 ksi. This stress-strain relation is used in conjunction with fully plastic J-solutions for beams in bending to calculate the value of the J-integral that accounts for plasticity in this material. In the results presented above for 1.5 amps, the maximum stresses are just below the yield strength, so plasticity effects will not be large. However, it is desired to include plasticity for generality.

A set of calculations of crack length as a function of 1.5-amp current cycles was made for an initial crack depth of 0.1 the heel thickness (a = 0.033 mils, W = 0.33 mils). The following sets of crack driving force solutions were considered:

4-30

Elastic	Plastic
Three-Point Bending	None
Linearized Stress with Influence Function (LSIF)	None
Pure Bending (Fixed Rotation)	None
LSIF	Plane Strain Pure Bending
Three-Point Bending	Plane Stress Three-Point Bending
Nonlinear Stress Gradient with Influence Function	Plane Strain Pure Bending

All results are for fixed-bending moment, except as noted in the above table. The plane strain fully plastic pure bending solution from Ref. 4-13 was used, because the corresponding three-point bend solution from Ref. 4-14 is of questionable accuracy. The plane strain pure bending solution is not available, but the plane stress three-point bend solution from Ref. 4-14 is probably accurate.

In spite of the small scale of the item being tested, the plane strain crack driving solution is applicable for the following reason: In fracture mechanics, the component dimensions are important only in a relative manner. Specifically, the "plane strain" condition can be met provided the size of the crack tip plastic zone is smaller than the specimen thickness. The former quantity is generally proportional to $(K_c/\sigma_y)^2$ which, in this work, is also a very small number. Thus, it was not inappropriate to assume that the simplicity of a plane strain condition could be used.

Figure 4-23 provides a versus N for each of these six sets of crack driving force solutions. Although there is considerable variation of calculated lifetime using the different crack driving force solutions, they agree with about a factor of 2. This is a relatively narrow band when compared to the order of magnitude of scatter in the experimental results. It is seen that the calculations are not strongly influenced by plasticity or plane strain/plane stress. The fixed rotation result is considerably different than the fixed moment results, and linearization of the stress gradient also has an effect. The results using the nonlinear stress distribution with an influence function for the elastic part and pure bending plane strain for the plastic part are probably the most realistic (for a fixed bending moment), and were used in further calculations for other current levels. Calculations of lifetime were performed for various initial crack sizes and current levels, with the results summarized in Figure 4-24. The experimental results of Table 4-1 are also plotted on this figure. It is seen that there is considerable scatter in the experimental results, but that the results correspond closely to the fracture mechanics predictions based on initial crack depths (a_0) covering a range from 0.002 to 0.16 mil ($a_0/W = 0.006 - 0.48$). This is a wide range of initial crack sizes, but is reasonable, considering the large scatter in the experimental results. The slope of the I-N curve for a given a_0 corresponds closely to what would be attributed to the raw data. This suggests, considering the large amount of scatter, that the fracture mechanics predictions are a reasonable representation of the experimental results. This further suggests that crack initiation is not an important aspect of the problem and that the macroscopic fracture mechanics predictions are

4-31
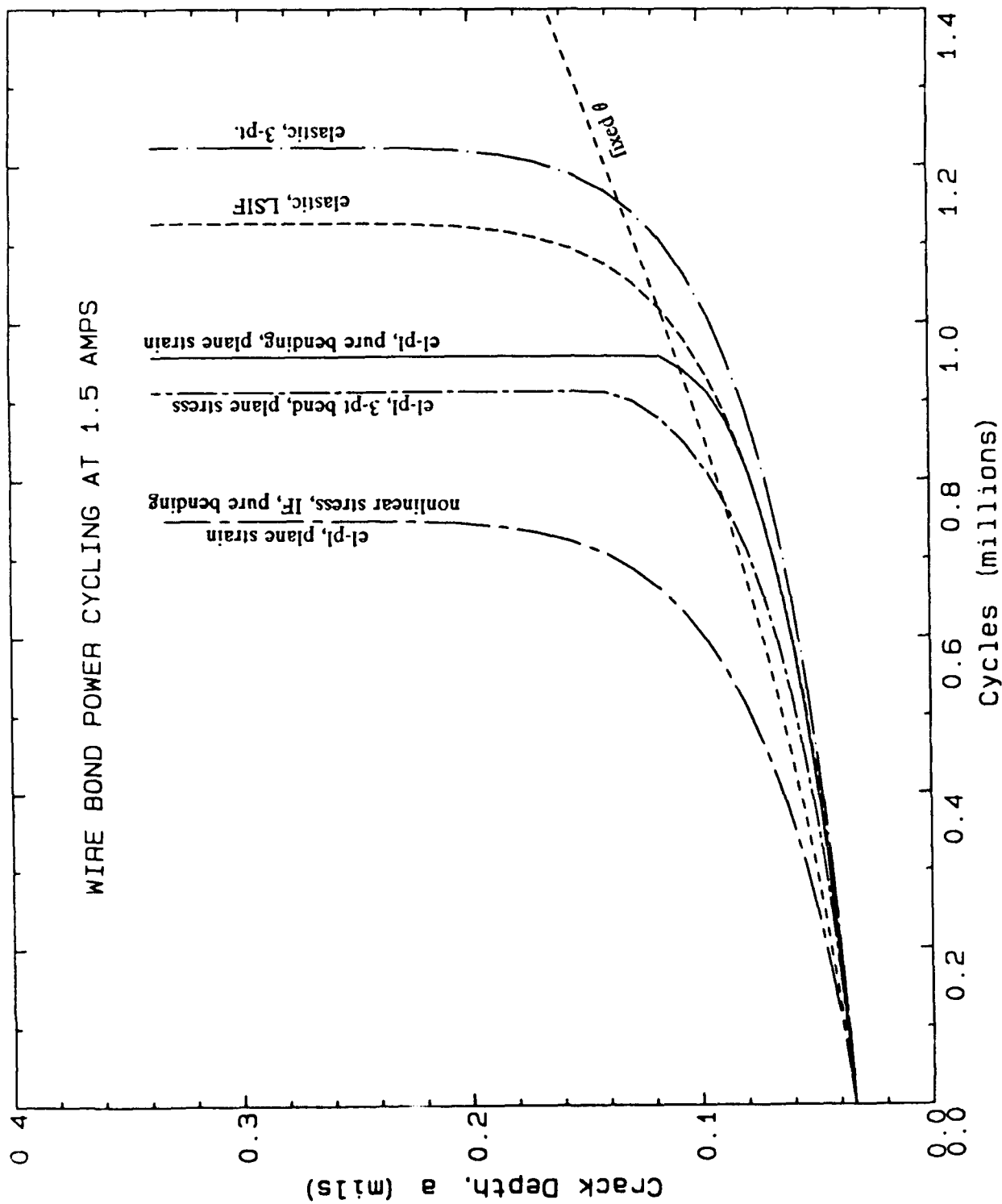
Figure 4-23. Crack Depth Versus 1.5-Amp Current Cycles for an Initial Crack Depth of 0.033 Mil with Different Sets of Crack Driving Force Solutions
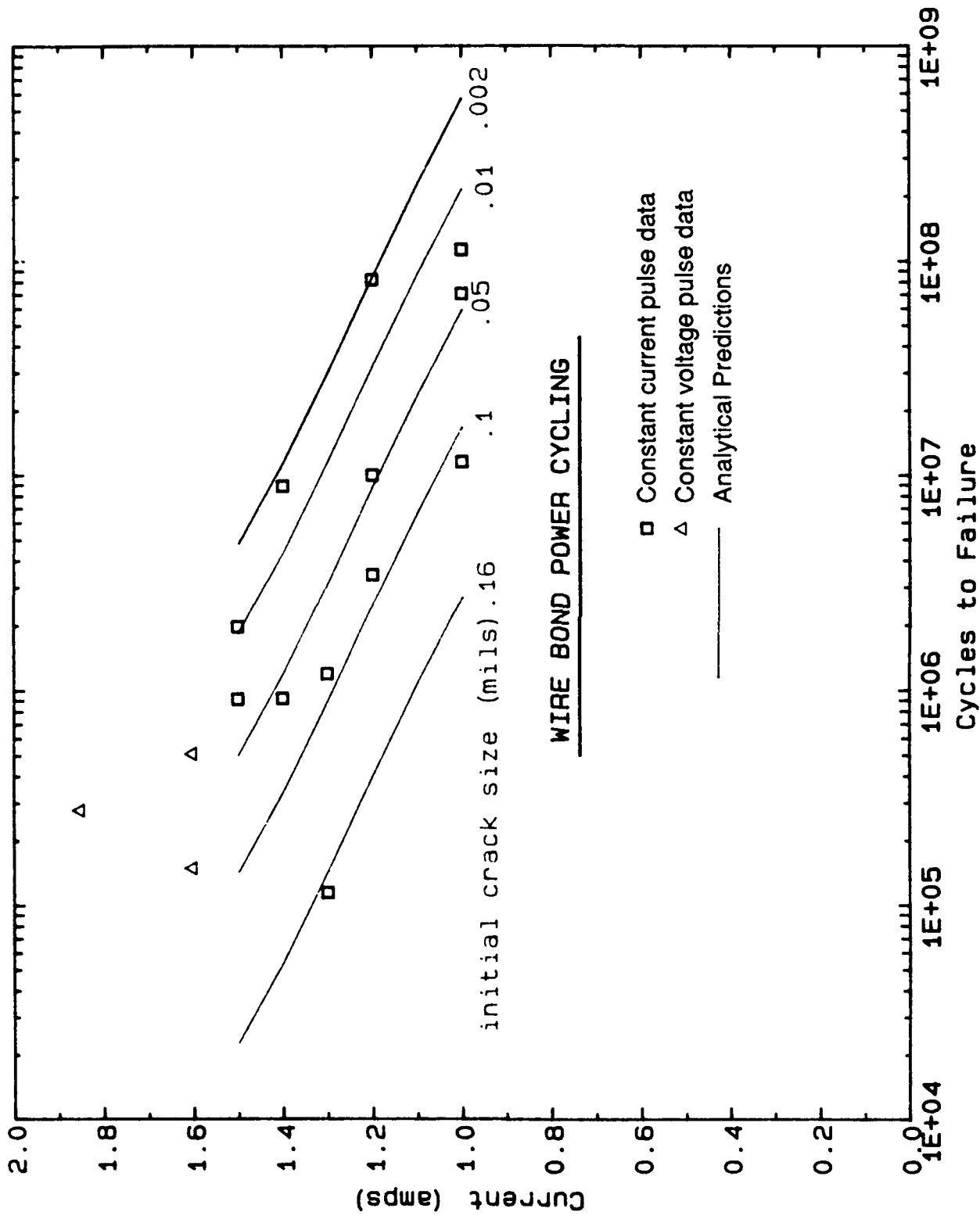
Figure 4-24. Cycles to Failure for Different Current Levels and Initial Crack Depths Along with Experimental Results from Table 4-1

not at variance with the experimental observations. Comparisons of initial defect depths from fractography of the failed wire samples with results shown on Figure 4-24 would be very informative — if such results are observable on the failed samples.

The comparison shown in Figure 4-24 of fracture mechanics predictions and experimental results suggests that the scatter in results is due to variations in the initial defect size. The initial crack size for each constant current pulse test in Figure 4-24 can be estimated from results in that figure. This provides 12 values of initial crack size. These 12 values can then be used as samples from the statistical distribution of initial crack sizes in such wire bonds. Table 4-4, which is an expansion of Table 4-1, summarizes the estimated initial crack size for each constant current pulse test. (The constant voltage pulse tests in Table 4-1 are omitted from consideration, because they are at higher current levels, which are predicted to result in peak temperature close to the melting point of aluminum.)

TABLE 4-4. CYCLES TO FAILURE TEST RESULTS ALONG
WITH ESTIMATED INITIAL DEFECT DEPTH

Current (amps)	Cycles to Failure	Estimated Initial Defect Depth (mils)
1.0	1.123×10^8	0.028
	1.149×10^7	0.12
	7.094×10^7	0.043
1.2	3.241×10^6	0.090
	1.001×10^7	0.041
	8.214×10^7	0.002
1.3	1.141×10^5	0.166
	1.201×10^6	0.091
1.4	8.925×10^6	0.004
	9.180×10^5	0.060
1.5	9.109×10^5	0.036
	1.974×10^6	0.01

The initial crack size distribution for the wire bond can be estimated by listing the estimated initial crack sizes in Table 4-4 in ascending order and estimating the percentile of each of the 12 samples [m/(N+1), where m is the rank (1-12), and N is the sample size (12)]. Such results are included in Table 4-5, which also gives the mean and standard deviation of the data. Figure 4-25 provides a plot on normal probability paper. Also shown in Figure 4-25 is the line corresponding to a normal distribution corresponding to the mean and standard deviation of the

TABLE 4-5. RANKED ORDER TABLE OF ESTIMATED INITIAL DEFECT DEPTHS SHOWING ESTIMATED PERCENTILES OF THE VALUES

m	a, mils	P(a)
1	0.002	0.0769
2	0.004	0.154
3	0.01	0.231
4	0.028	0.308
5	0.036	0.385
6	0.041	0.462
7	0.043	0.538
8	0.060	0.615
9	0.090	0.692
10	0.031	0.769
11	0.116	0.846
12	0.12	0.923

P = m/(N+1) = m/13

Average a = 0.0534 mil

Std. Dev. = 0.0419 mil

data. A fairly good fit to the data is observed. Lognormal and Weibull distributions were also considered, but the normal provided the best fit.

The mean and standard deviation of the data, as given in Table 4-5, along with assuming a normal distribution, result in a probability of negative crack size of 0.13. This physical impossibility can be removed by considering a modified normal distribution as follows:

$$p(a) = \begin{cases} \dfrac{C}{\sigma\sqrt{2\pi}} \ e^{-(a-a^1)^2/2\sigma^2} & a > 0 \\ 0 & a \leq 0 \end{cases} \qquad (4\text{-}4)$$

where C is the value required to give

$$\int_0^\infty p(a)\,da = 1. \qquad (4\text{-}5)$$
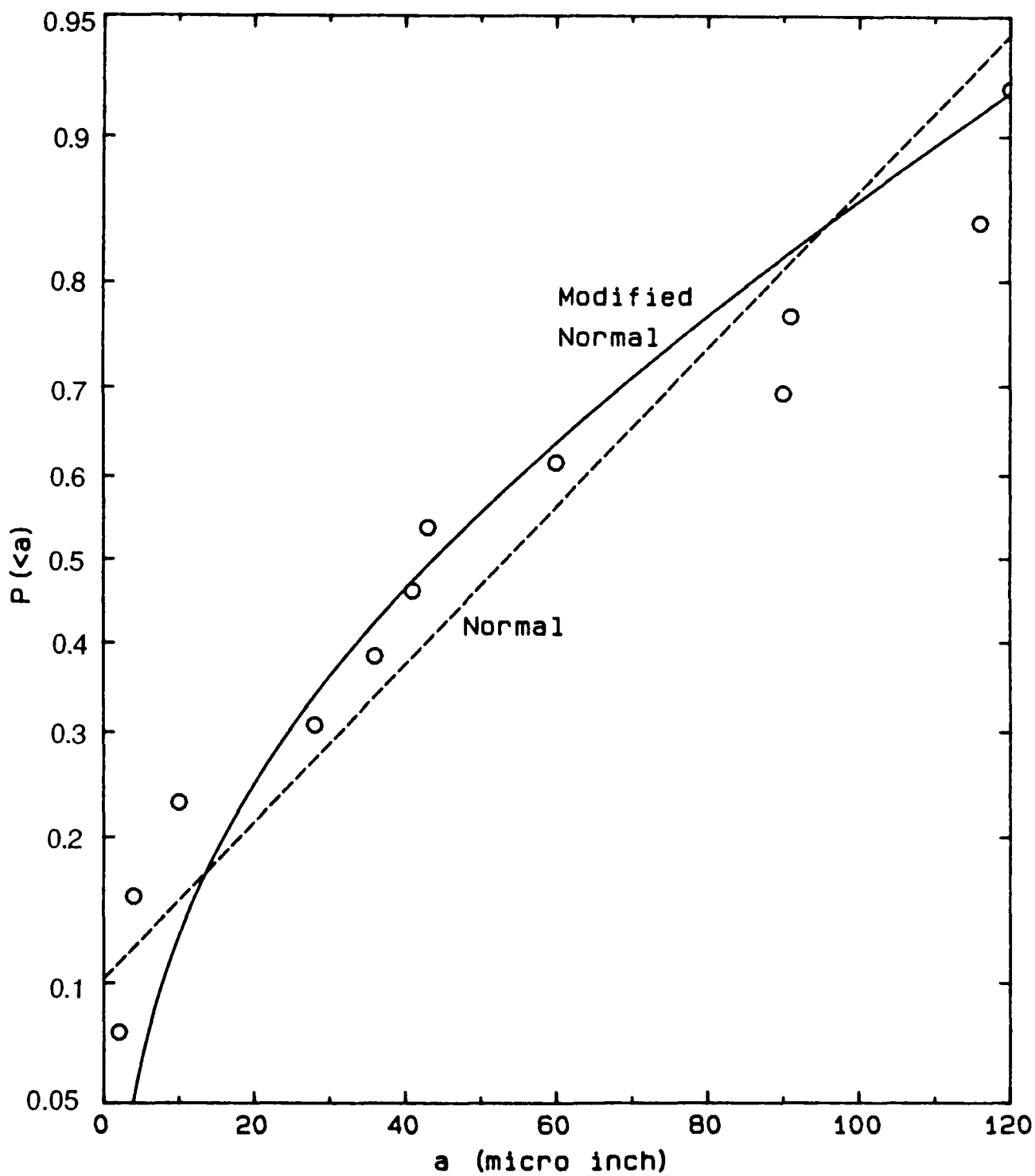
Figure 4-25. Estimated Cumulative Initial Crack Depth Distribution Data of Table 4-5 Along with
Cumulative Distributions Corresponding to the Mean and Standard Deviation of the Data

This density function results in:

$$C = \left[1 - \frac{1}{2} \operatorname{erfc} \frac{a_1}{\sigma\sqrt{2}} \right]^{-1}$$

(4-6)

$$\text{ave } a = \bar{a} = a_1 + C\sigma \, e^{-a_1^2/2\sigma^2}$$

$$(\text{s.d. of } a)^2 = \sigma^2 \left[1 - \left(\frac{C}{\sqrt{2\pi}} e^{-a_1/2\sigma^2} \right)^2 \right] - \sigma a_1 \frac{C}{\sqrt{2\pi}} e^{-a_1/2\sigma^2}$$

The complementary error function, erfc x, is discussed in Ref. 4-15.

Values of the parameters a_1 and σ were evaluated that give the same mean and standard deviation as the data. This resulted in $a_1 = -0.02$ mil and $\sigma = 0.0534$ mil. A negative a_1 is not troublesome, since it is merely a parameter in the distribution of a -- the distribution being a modified normal. The cumulative distribution corresponding to this modified normal with the above values of a_1 and σ is also shown in Figure 4-25. An improved fit to the data is observed, and the possibility of negative crack sizes is eliminated.

Estimates of the initial crack size distribution are very important to probabilistic fracture mechanics analyses of reliability, and the results of Figure 4-25 should be very useful in development of probabilistic models of wire bond reliability.

4.7.6 Concluding Remarks

A procedure for making life prediction of the heel area of wire bonds subject to on-off current cycling was described. Temperature fields are estimated analytically and applied to a finite element model of the wire to calculate thermal displacements and resulting bending moments on the heel. These are used with handbook elastic-plastic crack driving force solutions and fatigue crack growth relations to calculate defect depth as a function of on-off cycles. The bending moment in the cracked section is assumed to remain constant as the crack extends. This is conservative and greatly simplifies the analysis. Crack initiation is not considered, because microscopic examination of bond areas reveals much tearing and deformation of the wire. Such damaged areas readily serve as initial cracks. Lifetime predictions are compared with experimental results produced in this program.

Considerable scatter in the test results was observed, but could be accounted for by considering a realistic range of initial defect sizes. The fracture mechanics predictions made using macroscopic material properties are not inconsistent with the experimental results. In fact, the experimental results can be considered to provide information on the initial crack sizes presented in the

specimens, and these sizes are used to estimate the statistical distribution of initial defect sizes. A normal distribution, modified to eliminate the possibility of negative crack sizes, provided a good representation of the data.

4.8 CONCLUSIONS

The following conclusions are drawn from the wire bond experiments, analysis, and their comparisons:

- Failure of the heel area of the bond occurred due to progressive growth of a crack-like defect from the area initially damaged during the fabrication of the bond.

- Fracture mechanics predictions made using macroscopic material properties and a fatigue crack threshold of zero are not inconsistent with experimental measurements.

- Considerable scatter in the test results was observed, but could be accounted for by considering a realistic range of initial defects sizes.

- A normal distribution, modified to eliminate the possibility of negative crack sizes, provided a good representation of the distribution of initial defect sizes.

- Thermal runaway of the wire bond is predicted and observed under high current conditions.

These results indicate the following regarding the applicability of fracture mechanics to microscale components:

- Fracture mechanics is valid for damage tolerance analysis on the microscale.

- Macroscopic material properties are appropriate in such efforts.

- Additional work remains to be done to define stress levels and material properties relevant to the environments encountered in specific microelectronic components.

5.0 PLATED THROUGH HOLE THERMAL CYCLING

This research is summarized in Ref. 5-1.

5.1 INTRODUCTION

Plated through holes (PTH) provide electrical connections between layers of electronic circuits in printed wire boards (PWB). A typical PTH, shown in Figure 5-1, is formed by drilling a 0.025-inch-diameter hole through the thickness of a multilayer PWB such that it passes through the printed copper circuit path, or trace, of each of the circuit layers to be electrically interconnected. The inside surface of the hole is then plated with a 0.0015-inch-thick layer of copper using electro-depositing techniques. The copper plating extends radially outward from the edges of the hole on the faces of the PWB for a distance of approximately 0.020 inch. Typical PWB material consists of woven glass fiber reinforced epoxy. The particular PWB analyzed is 0.071 inch thick with 12 circuit layers of 0.001-inch-thick copper traces.
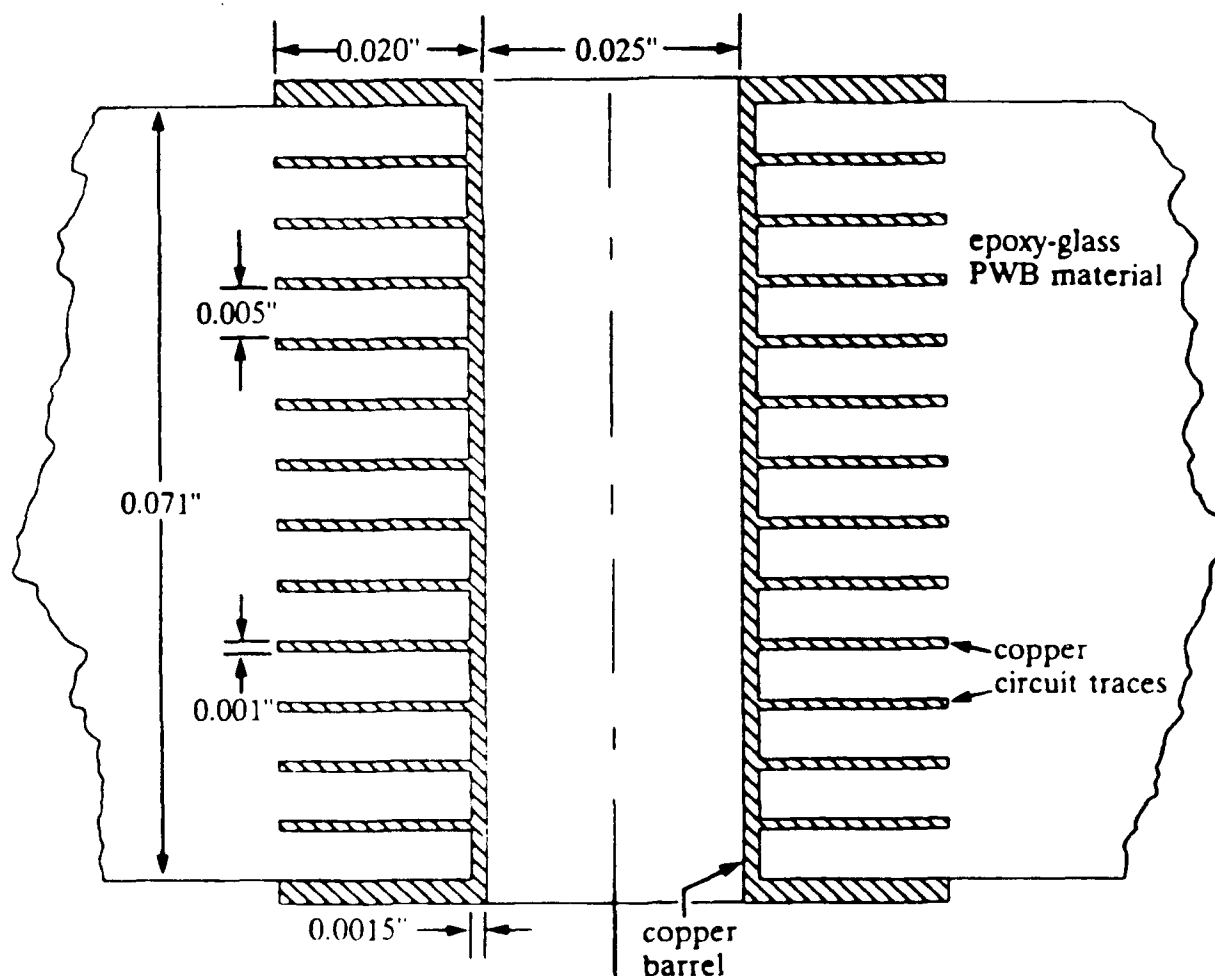
Figure 5-1. Section Through Center of Typical Plated Through Hole

During normal operation, PWBs experience temperature fluctuations associated with the on/off cycles of the electronics and ambient conditions. Failures have been observed in PTHs due to complete circumferential cracking of the copper barrel. The cracks result from large cyclic strains in the copper due to differential thermal expansion between the copper and the epoxy matrix of the PWB. The coefficient of thermal expansion (CTE) of the epoxy-glass PWB material is greater than that of the electro-deposited copper. Exposure to large temperature fluctuations can produce cyclic strains well above yield in the copper barrel of the PTH. Results of an IPC [Institute for Interconnecting and Packaging Electronic Circuits (formerly Institute of Printed Circuits)] round robin evaluation of PTH reliability (Ref. 5-2) showed a large number of PTH failures in less than 400 cycles of a MIL-T-CYCLE thermal test between –65°C and 125°C. In most of the round robin failures, the cracks occurred near the center of the PTH and between copper traces.

Tests by the IPC included neither failure analysis of the PTHs nor studies aimed at determining the mechanisms of failure. Thermal fatigue induced failures of PTHs may be appropriate for analysis using the techniques of experimental micromechanics and fracture mechanics, and it was the purpose of the research reported here to explore the use of these techniques for damage tolerance assessment of PTHs.

Study of the data reported by the IPC led to formulation of a number of questions:

1. How many cycles are spent in crack initiation and how many are required for crack growth?

2. What is the magnitude of the thermally induced strains?

3. Where do cracks initiate?

4. Should these cracks be considered as small fatigue cracks (which generally grow faster than large fatigue cracks) or can the fracture mechanics correlations used for large cracks also be used for PTHs?

5. How quickly do cracks grow through the wall of the PTH?

6. What is the driving force for propagating cracks?

These questions were addressed by this research. The answers obtained are discussed in Section 5.3 and are summarized in Sections 5.3.5 and 5.3.6.

5.2 APPROACH

The investigation included experimentation and analysis. Experiments were performed to measure the crack growth behavior of 150-μm-thick electrodeposited copper foil as used in PTHs. In addition, fatigue cracks were initiated and grown in flat copper foil/PWB laminates and in actual PTHs in PWBs. Crack growth was observed and quantified by means of the stereoimaging technique. Coefficients of thermal expansion over the temperature range of –65°C to +125°C were also measured. Prior to the laboratory experiments, finite element analysis (FEA) was performed to predict strains in the PTHs using available handbook material property data. The predicted strains were used as input to fatigue life analyses to estimate the number of thermal cycles required to initiate a crack in the PTH and to grow the crack to complete fracture of the copper barrel.

5.3 EXPERIMENTS

5.3.1 Crack Growth Rates In Isothermal Tensile Cycling

5.3.1.1 Large Cracks

Fatigue of PTHs requires an understanding of the properties of the material plating the holes. Accordingly, tensile tests and fatigue crack growth rate experiments, using large cracks, were performed on copper plating material removed from PWBs. The results were compared to published crack growth rates for ingot derived wrought copper of comparable purity.

Fatigue crack growth rates through PWB copper were determined by forming specimens from plating removed from a PWB. Tensile tests on this material were performed using standard methods. Thickness of the foils tested was 150 μm. Single edge notched fatigue specimens having a gauge section width w = 13 mm were used. Cracks were initiated and grown to approximately 3.3 mm from notches cut with metal scissors and sharpened with a scalpel blade. Specimens were cycled under load control a with minimum to maximum load (R ratio) of 0.1, at 20 Hz in air. Tests were conducted at two load levels, giving maximum gross section stresses of 111 and 225 MPa. These stresses were chosen to minimize the size of the crack tip plastic zone. No bucking problems of were encountered. Crack length (a) was measured optically, and stress intensity factor was computed from the relation:

$$K = s\sqrt{\pi a}[1.12-0.23(a/w)+10.5(a/w)^2-21.7(a/w)^3+30.4(a/w)^4] \qquad (5-1)$$

5.3.1.2 Small Cracks

Determining the growth rates for small fatigue cracks was accomplished using a novel approach. Fatigue cracks were initiated and grown from a small starting flaw placed in the copper plating still adhering to the PWB by focused ion milling. The resulting initiation flaw

somewhat resembled pores found in other materials from which fatigue cracks were initiated. The flaw used, Figure 5-2, was approximately 10 μm square by 5 to 10 μm deep, with the diagonal of the square oriented to be perpendicular to the loading axis. The specimen was loaded in three-point bending which put the flawed surface under tension stress. The stress intensity factor for the small crack was computed using equivalent beam theory for the composite specimen. The analysis used is summarized in Appendix E.
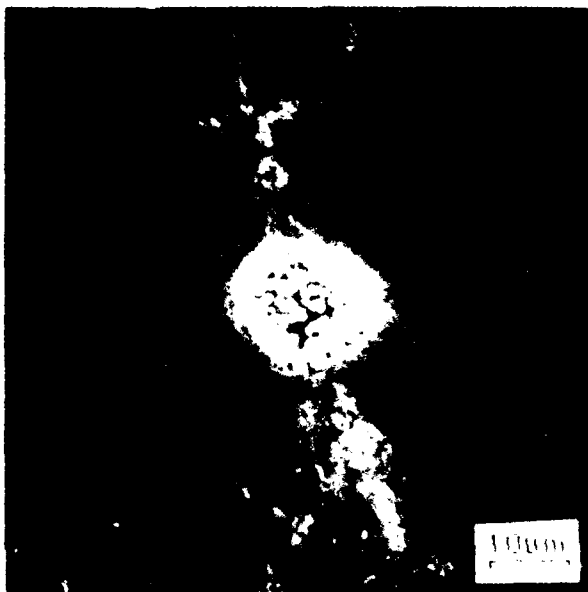
Figure 5-2. Flaw From Which a Small Crack Was
Initiated in the Copper Plating of the PWB. This Flaw,
Approximately 10 μm Square by 6 μm Deep, Was
Formed by Focused Ion Milling.

5.3.1.3 Results

Stress-strain behavior of the electro-deposited copper removed from the PWB is shown in Figure 5-3. Also shown is the fit using the Ramberg-Osgood approximation for a work hardening material. Yield stress was found to be approximately 288 MPa.

An analytical representation is much more convenient to work with than are discrete data. That the well-known Ramberg-Osgood relation was found to provide a good representation of the behavior of the material used in this research was not necessary on physical grounds, but significantly simplified the work. Other types of relations could have been used if they had been found to fit the data equally as well.

5-4
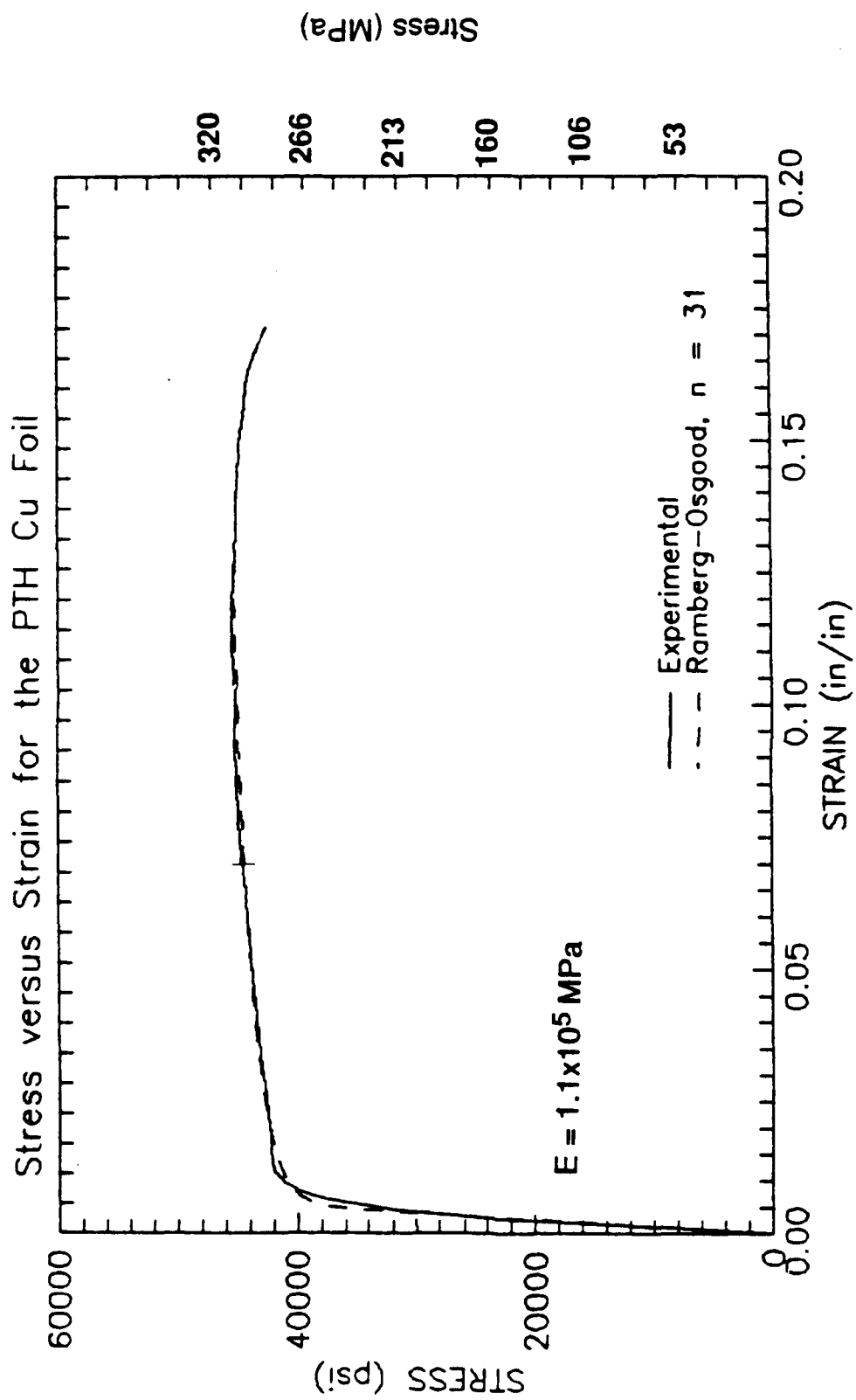
Figure. 5-3. Stress-Strain Curve for the Copper Plating Removed From a Printed Wiring Board

Fatigue crack growth rates for large and small fatigue cracks are shown in Figure 5-4. The triangle symbols denote small crack data, most of which pertain to cracks growing through the plating thickness, while the open circles are large crack data which were added only for reference purposes. Data for the large crack were obtained from a single edge notched specimen of detached copper plating under tension-tension loading, while data for the small crack were obtained for a crack in copper still adhered to the PWB . The correlation between da/dN and ΔK (dashed line) is:

$$da/dN = 1.14 \times 10^{-11} \, \Delta K^{3.59} \quad (m/cy) \qquad (5\text{-}2)$$

which is about the same as measured for ingot produced wrought copper.

The solid line in the figure marks the surface length of the crack (300 μm) at which the crack should have penetrated the thickness of the copper, assuming it was of semicircular shape. Thus, most of the data were obtained before the crack completely penetrated the plating thickness.

The results shown in Figure 5-4 indicate that cracks which are physically small are growing at rates comparable to what would be expected from large cracks even though the applied stresses are 2 or 3 times larger than was used to grow the large cracks. This might seem surprising considering the large body of data that indicates that cracks of this size grow faster than anticipated from large crack growth results (Ref. 5-3). Typical of these data are results from aluminum alloys which show crack growth rates of $\approx 10^{-9}$ m/cy at ΔK values below the threshold stress intensity required for large crack growth, ΔK_{th}. Contrasting these results are data obtained from the fine grained (≈ 5 μm) powder metallurgy derived aluminum alloy 7091, which showed crack growth rates equivalent to those for large cracks down to cracks 32 μm long. This work on aluminum alloys, taken together with a large compilation of other small crack growth rate results, indicates that small cracks grow unexpectedly faster when the crack is able to emulate crack growth in a single crystal. Conversely, if the crack front of either a large or small crack encounters many grain boundaries, then the rates of crack growth would be expected to be similar (Ref. 5-3).

The grain structure of the plated copper used on PWBs is columnar, with the height of the column often being about the plating thickness (≈ 150 μm) while the dimension in the plane of the plating is much smaller (≈ 10 μm). By analogy with crack growth rate results from aluminum alloys, small cracks in copper plating would be expected to grow at comparable rates to large cracks once they were longer than ≈ 30 μm. Since the smallest crack for which we obtained growth rate information was ≈ 40 μm, the crack growth rates measured are about what should be expected.

Crack Growth Rate (m/cyc)

10^{-5} 10^{-6} 10^{-7} 10^{-8} 10^{-9} 10^{-10}

100

ΔK (MPa m$^{1/2}$)

10

ΔK (ksi in$^{1/2}$)

da/dN = 1.14x10^{-11}$\Delta K^{3.59}$ (m/cy)

OOOOO SwRI Fail Data
△△△△△ SwRI Small Crack Data
– – Best Fit Line

10^{-3} 10^{-4} 10^{-5} 10^{-6} 10^{-7} 10^{-8} 10^{-9}

Crack Growth Rate (in/cyc)
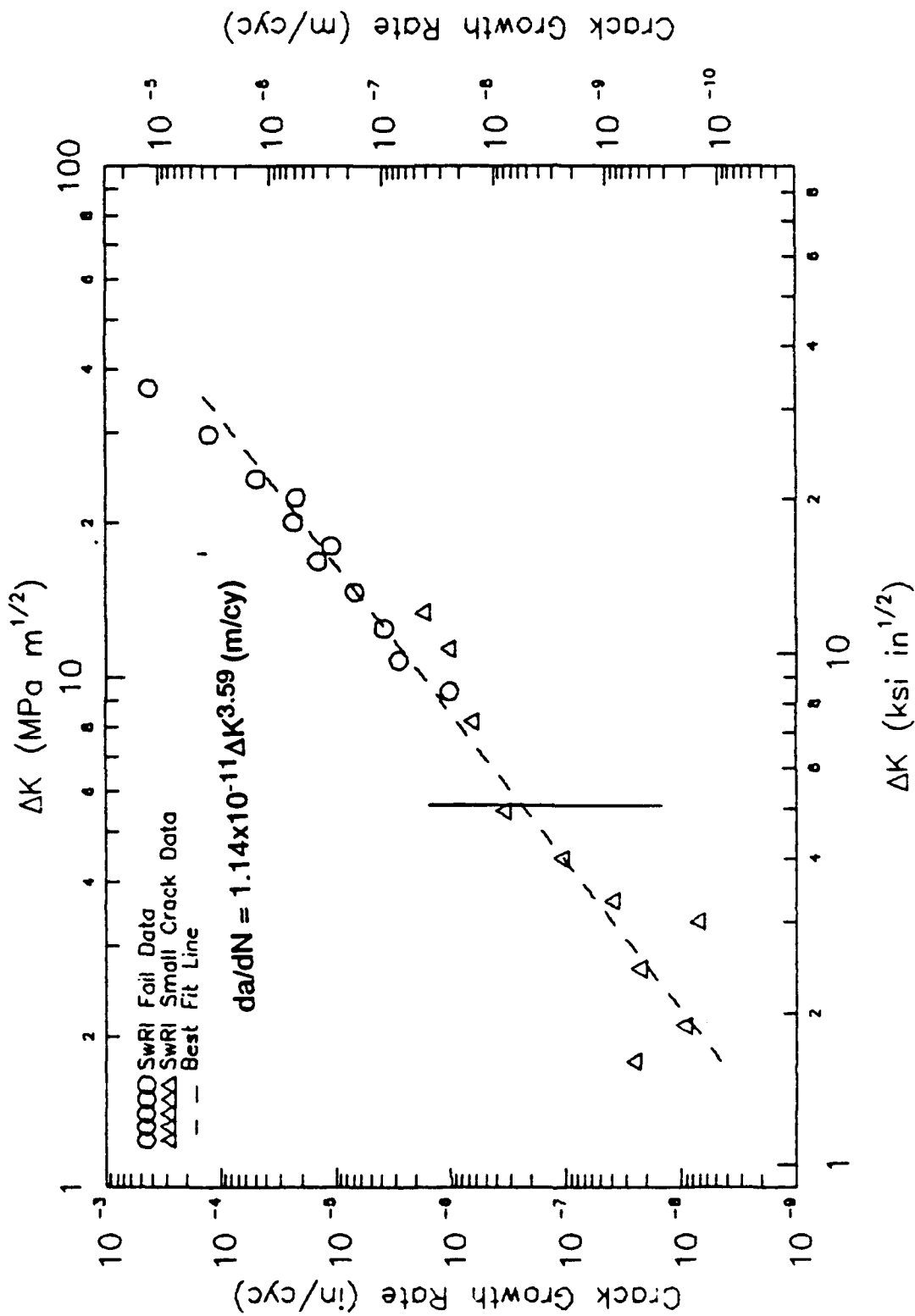
Figure 5-4. Cyclic Mechanical Loading Fatigue Crack Growth Curve for the Copper Plating Material. Crack Growth Data for the Large Crack (O) Were Taken From an Unbacked Foil Removed From the PWB, But the Small Crack Data (△) Were Taken From an Unbacked Foil Removed From the PWB. Crack Length for Complete Penetration of the Crack Through the Plating is Indicated By the Line.

5.3.2 PTH Thermal Cycling Fatigue

5.3.2.1 Approach

Thermal fatigue tests were performed on a specimen having 10 PTHs in a line. This specimen was cut from a test coupon taken from PWBs being fabricated for military electronics use. The specimen was sectioned so that half of each hole was removed, leaving the other half of the hole still embedded in the PWB, similar to the configuration shown in Figure 5-5. This allowed the entire length of the hole and the plating to be viewed.
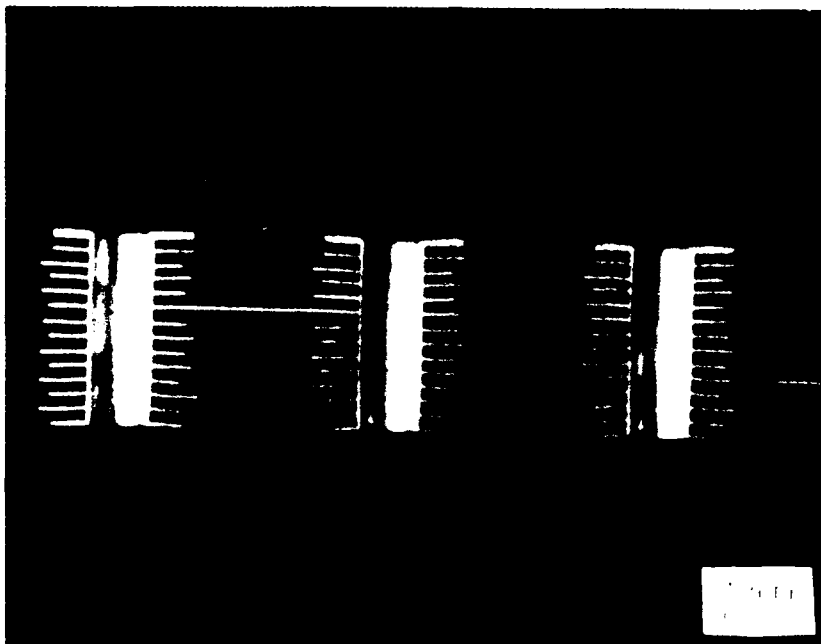
Figure 5-5. Cross Sectional Views of Three of the Plated Through Holes
(PTH) Analyzed Showing the Number and Dimension of the Internal
Interconnects Through Which the PTHs Traverse

Eight holes were selected for detailed examination by scanning electron microscopy (SEM). Initial photographs were made at 400 and 1000X of the center portion of the hole and of region where the hole intersects the outer surface, and at 20X of the entire hole.

Measurements of the displacements caused by thermal cycling were made using the stereoimaging technique (Ref. 5-4). An automated image processing system was used to measure the displacements resulting from changes in temperature. Initially, the measurement focus was on copper within the PTH, but later, measurements were also made from the PWB material.

Thermal cycles were applied in a programmable thermal cycling environmental chamber. Duration of each cycle from ambient to −65 to 125°C and back to ambient was approximately 2 hours.

Plated through hole thermal cycling experiments were performed both in a programmable environmental chamber and within the SEM. Thermal cycling was periodically interrupted so that each hole could be examined for cracks in the SEM. The presence and extent of cracking were determined by stereoimaging the initial photographs against those made after N thermal cycles. A heating-cooling stage which fit within the specimen chamber of the SEM also was used to apply thermal cycles to obtain photographs for analysis of displacements.

5.3.2.2 Initial Experiment

The initial experiment was performed within the SEM over only part of the actual thermal cycle. Hole 1 of the multihole specimen was photographed at 25°C and periodically as temperature was raised to 125°C. Measurements were made of the displacements in the center of the hole from 1000X photographs. Strains computed from measured displacements were 4.9 to 6.2×10^{-3}. Strains were relatively uniform over a 100-μm-gauge length. Assuming this strain change can be linearly extrapolated to the total temperature range experienced by the PTH during MIL-T cycling, the total strain experienced would be approximately 1.1×10^{-2}.

5.3.2.3 Crack Initiation and Growth

The results of the PTHs thermal cycled in the environmental chamber from −65 to 125°C are given in Table 5-1. Cracks were detected in approximately half the holes after 81 cycles. Initiation was determined from examining 1000X photographs. The strain needed for failure in 81 cycles may be estimated from the low cycle fatigue equation for annealed, wrought, ingot copper, which is (Ref. 5-5):

$$\Delta\epsilon_p \Delta N_f^{0.672} = 0.423 \qquad (5\text{-}3)$$

For $\Delta N_f = 81$ cycles, $\Delta\epsilon_p = 0.022$ which is about twice the total strain experimentally determined in the PTH copper. Of course, 81 is the number of cycles for crack initiation, not failure.

Multiple small cracks were initiated within the centerline region of the PTHs, but no cracks were found in the region where the cross section of the copper plating intersects either the outer surface of the PWB or in the central portion of the PWB. Subsequent cycling caused many of the small cracks in the center of the PTH to coalesce to form larger cracks. The PWB was observed to debond from the copper in the central portion of the PTH, as will subsequently be

TABLE 5-1. PTH THERMAL FATIGUE EXPERIMENT
CRACK LENGTH (μm) VS. CYCLES

Hole	Cycle Number				
	21	81	131	180	211
1	no crack	15 (3 cks)	50 (5 cks)	49 2 cks)	1000 (2 cks)
2	no crack	20 (4 cks)	40 (4 cks)	700 (5 cks)	1100 (2 cks)
3	—	No	30 (3 cks)	265 (3 cks)	840 (3 cks)
4	—	—	40 (4 cks)	530 (3 cks)	1100 (2 cks)
5	—	5 (1 ck)	20 (2 cks)	600 (1 ck)	1100 (2 cks)
6	—	No	20 (2 cks)	55 (2 cks)	510 (3 cks)
7	—	No	No	450 (3 cks)	1000 (2 cks)
8	no crack	15 (3 cks)	30 (3 cks)	320 (1 ck)	600 (1 ck)
Avg. crack length (μm)	0	20	65	480	910
Fraction of holes cracked	0/3	4/7	7/8	8/8	8/8
Avg. da/dN (m/cy)		3×10^{-7}	9×10^{-7}	9×10^{-6}	1.4×10^{-5}

NOTES: Only 3 holes inspected at 21 cycles

    Hole No. 4 not inspected at 81 cycles

shown, but the number of cycles required for debonding was not determined. Most likely, the extent of debonding paralleled crack growth, i.e., debonding probably began after some number of cycles and increased with subsequent cycles. By the end of the experiment, debonding was significant all along the PTH, except at the ends.

After 131 cycles, there were cracks in 87% of the holes, and each hole had 2-5 cracks 20-30 μm long. After 180 thermal cycles, 1-3 cracks were found in each hole for a total average crack length of 480 μm. The test was terminated after 211 cycles because 5 of the 8 holes had cracks equal in length to the circumference of half the interior of a PTH. The average number of cracks

was 2 per hole. If the number of cycles to failure is considered to be 200, then using Equation (5-3) gives $\Delta\epsilon_p = 0.012$. For a yield stress of 288 MPa, the elastic strain is $\epsilon_e \approx 0.0026$. Adding $2\epsilon_e$ to $\Delta\epsilon_p$ gives $\Delta\epsilon_{total} = 0.0172$, as compared to 0.011 determined by extrapolation of the measured value, a difference of $\approx 35\%$. Conversely, if ϵ_e is subtracted from the extrapolated value of 0.011, then $\epsilon_p = 0.0058$, and $N_f = 591$ cycles. It is not completely clear how the number of cycles to failure should be defined, because the end result of thermal cycling is not two pieces, as it is in a mechanical test for which eq. (5-3) was defined.

The most obvious reasons for the discrepancy between the number of cycles to failure and strain are (1) the very small grain sized copper in the PTH has a different low cycle fatigue curve than given by eq. (3), which is unlikely, (2) differences in definitions of failure, or (3) a nonlinearity in the strain-temperature relation somewhere in the temperature cycle which increases the plastic strain range on each thermal cycle.

Crack growth rates caused by thermal cycling may be determined from the data in Table 5-1 by 2 methods. The first method uses the average crack length for all the holes (2a), as a function of cycles, and the second considers the crack length data for each hole independently. A log-log plot of average crack length (2a) vs. number of cycles (N) is approximately linear, giving the relationship:

$$2a = 2.16 \times 10^{-7} N^{0.64} \quad \text{(meters)} \tag{5-4}$$

Differentiating gives:

$$da/dN = 3.45 \times 10^{-8} N^{-0.36} \quad \text{(m/cy)} \tag{5-5}$$

Deriving crack growth rates from the data on crack length in each hole gives a rather different view. Both linear and log-log plots of the data in the table are shown in Figure 5-6. Three interpretations have been made, as indicated by the lines in Figure 5-6b. The derived values for crack length (2a) and crack growth rate are given in Table 5- 2.

The average value is given by the least squares fit as:

$$2a = 1.16 \times 10^{-12} N^{3.77} \quad \text{(meters)} \tag{5-6}$$

Differentiating gives:

$$da/dN = 4.37 \times 10^{-12} N^{2.77} \quad \text{(m/cy)} \tag{5-7}$$

and substituting (5-6) into (5-7) gives:

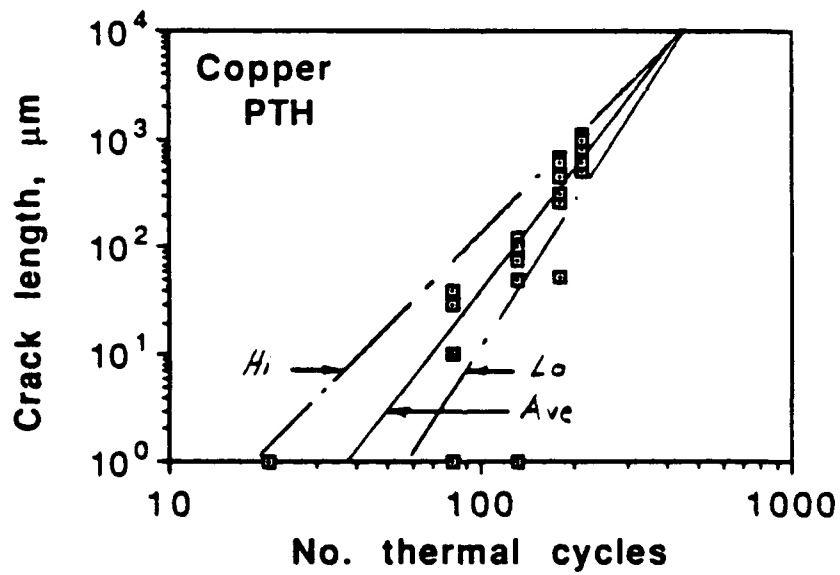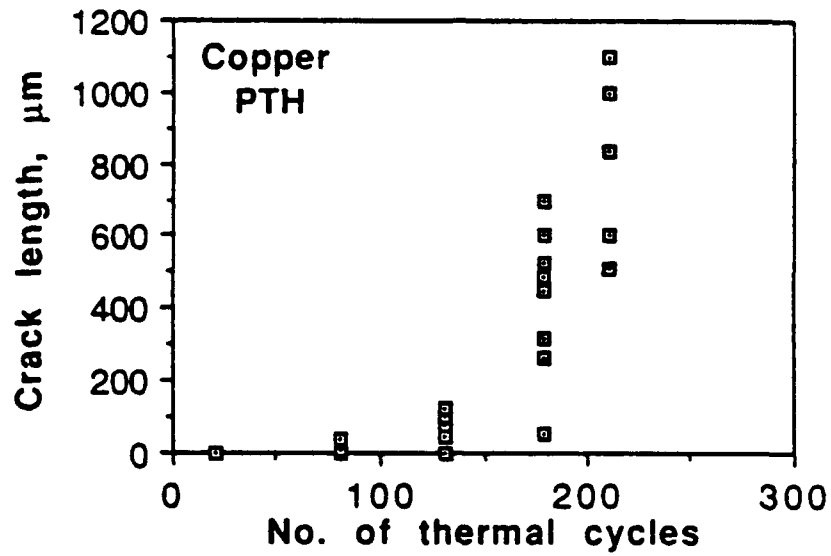$$da/dN = 4.27 \times 10^{-3} a^{0.734} \quad \text{(m/cy)} \tag{5-8}$$

Figure 5-6. Lengths of Cracks Measured in the PTHs as a Function
of the Number of Thermal Cycles. Data From Each Crack
is Shown Separately. (a) A Linear Plot, and (b) a Log-log
Representation of the Same Data.

TABLE 5-2. ESTIMATES OF CRACK GROWTH RATE

	Low	Average	High
$2a = A_0 N^m$ (m)	$A_0 = 1.25 \times 10^{-10}$ $m = 3.0$	1.16×10^{-12} 3.77	1.7×10^{-14} 4.47
$da/dN = B_0 N^n$ (m/cy)	$B_0 = 3.75 \times 10^{-10}$ $n = .0$	4.37×10^{-10} 2.77	7.60×10^{-10} 3.47
$da/dN = C_0 a^p$ (m/cy)	$C_0 = 2.38 \times 10^{-3}$ $p = 0.666$	4.27×10^{-3} 0.734	6.36×10^{-3} 0.777
$2a$ = crack length a = half crack length			

From fracture mechanics, $\Delta K \propto \sqrt{a}$, and from eq. (5-2), $da/dN \propto \Delta K^{3.59}$; therefore, $da/dN \propto a^{1.8}$, but this is about twice the value obtained experimentally. Of course, other interpretations of this data can be made. But, as will be shown, it is difficult to reconcile the growth rates of cracks in the PTH, especially if the data of Figure 5-6 are used, with those derived from the growth of large and small cracks in the PWB (Figure 5-4).

5.3.3 Deformation Measurements

Three series of analyses were performed:

(1) deformation within the PTH as a function of the number of thermal cycles and temperature for a partial thermal cycle (25 to 125°C).

(2) deformation within the PTH and the adjacent PWB for a full thermal cycle (25 to –65 to 125 to 25°C).

(3) around cracks in the PTH at cycle 211 (end of the test) to determine the driving force for the cracks (measurements made between 25 and 125°C).

5.3.3.1 Partial Thermal Cycle

The first analyses were performed on photographs made during the application of a partial thermal cycle within the SEM, during which the temperature was raised from 25 to 125°C. The result of this analysis was determination of the CTE within the copper of the PTH. The value determined was 5.5×10^{-5} /°C. Two values are given for CTE of the PWB in the IPC report (Ref. 5-2): below the glass transition temperature (which can vary between 110 to 137°C), $3.8 < CTE < 9.7 \times 10^{-5}$/°C, and above the transition temperature $21 < CTE < 36.5 \times 10^{-5}$/°C. Thus, measured CTE was about that expected.

The next analysis was of the deformation accumulated during application of thermal cycles. The photograph made initially was compared to that made after 21 full thermal cycles (–65 to 125°C). This analysis gave the surprising result that thermal cycling was causing a cumulative net compressive strain; i.e., strain ratcheting was occurring. Between 0 and 21 cycles, the average cumulative axial strain in the center of the PTH was approximately –0.02.

This unexpected result indicated the need for a more complete analysis of the accumulation of deformation resulting from all the applied thermal cycles. The following additional analyses made were: initial vs. 81 cycles, 81 vs. 131, 131 vs. 180, and 180 vs. 211 cycles. The net strain accumulation along the axis of the PTH with thermal cycles is given in Figure 5-7, which shows that strain accumulates rapidly as thermal cycling is begun and then becomes approximately uniform with additional cycles. Cumulative strain was determined by adding strains in each increment, which can lead to cumulative errors. So a check on the net value was made by measuring the initial vs. final photographs. The value thus derived is compared with that derived from the individual measurements in Table 5-3. There is reasonable agreement between the cumulative strain determined by summing the incremental values (– 0.0618) and that measured between initial and final conditions (– 0.0648). The cumulative strain measured in several other PTHs is included to give an indication of the variation in this parameter between holes. There is quite a bit of variation between individual PTHs, as might be expected.

The experimental partial thermal cycle results obtained to this point were compared to results from a finite element model of this experiment and significant differences were found, raising a number of questions about behavior of copper in the PTH and the PWB material. Thus, it was decided that there was a need to perform a full thermal cycle with incremental measurements of deformation in both the PWB and PTH.

5.3.3.2 Full Thermal Cycle

One of the circuit board specimens with numerous plated through holes was used for this experiment. This specimen had been thermally cycled in the environmental chamber 80 times; therefore, it had experienced thermal "shake down." The specimen was sectioned and mounted in a stage which had been configured to allow the extremes of this thermal cycle to be attained within the SEM. The thermocouple used to measure temperature was mounted in an unsectioned PTH approximately 2 mm away from the PTH from which the observations were made.
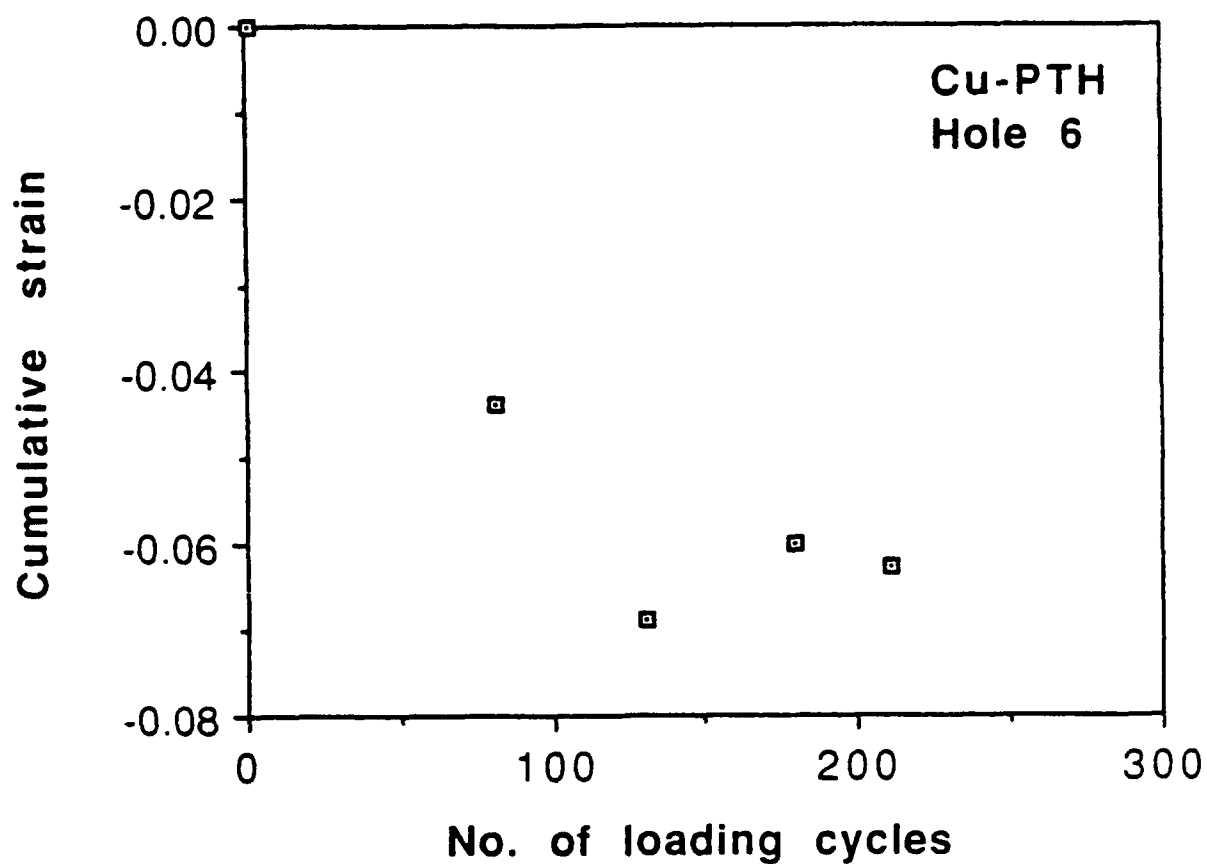
Figure 5-7. Cumulative Strain Within the PTH as a Function of the Number of Thermal Cycles

TABLE 5-3. CUMULATIVE STRAINS CAUSED BY THERMAL CYCLING

Analysis	Axial Strain	Cumulative Strain
PTH No. 6		
initial vs. 21 cycles	− 0.020	− 0.020
initial vs. 81 cycles	− 0.0437	− 0.0437
81 vs. 131 cycles	− 0.0251	− 0.0688
131 vs. 180 cycles	0.009	− 0.0598
180 vs. 211 cycles	− 0.003	− 0.0611
initial vs. 211 cycles	—	−0.0648
PTH No. 3	—	−0.0183
PTH No. 7	—	−0.0532

The experiment, illustrated in Figure 5-8, was begun at 25°C. Measurements were first made during cooling to –65°C. The specimen was then heated to +125°C, and subsequently cooled to 25°C. Photographs were made initially at 25°C and during the cooling portion of the cycle at –5, –35, and –65°C. On the heating portion of the cycle, photographs were made at –35, –5, 25, 55, 90, and 125°C. On the last cooling increment of the thermal cycle, photographs were made at 90, 55, and 25°C. At each point in the thermal cycle, photographs were made at 20, 400 and 1000X. Only the 20X photographs were analyzed.

The thermal cycle used in this experiment approximated that applied in the environmental chamber, resulting in PTH failures after cycling 211 times through the same temperature range. Thermal equilibrium in this experiment was not assured at each temperature for which photographs were made, but there was probably sufficient dwell time at –65 and 125°C to approach thermal equilibrium. The entire thermal cycle lasted 150 minutes in this experiment versus about 130 minutes for the thermal cycle test in the environmental chamber.

Two sets of measurements were made from photographs taken during the thermal cycling experiment, both from 20X photographs. First, measurements of the overall thickness of the PWB and PTH were made at the ends of the hole along its centerline (designated location B) and at two similar locations 800 μm to either side of the PTH in the adjacent PWB (designated as locations A and C). The other set of measurements, covering the entire field, was made between temperature extremes.

Displacements from point measurements at locations A,B and C are shown in Figure 5-9, with the direction of the temperature change superimposed on the measured points, and the initial (i) and final (f) points designated. Note the shrinkage in specimen thickness from the initial to the final point in the cycle, in agreement with earlier measurements (Figure 5-7). At this number of thermal cycles, however, the shrinkage is small, approximately 10 μm.

This figure shows several unexpected results; at two locations, there is actually an expansion shown as temperature is decreased to –35°C. The data have been carefully checked and verified, so this result is thought not to be due to measurement inaccuracies. Overall, however, the material behaves more-or-less as anticipated, so the odd points may be due to a lack of thermal equilibrium. To determine an overall coefficient of thermal expansion (CTE), a line was drawn through all the data using a least squares fit, giving the CTE values in Table 5-4.
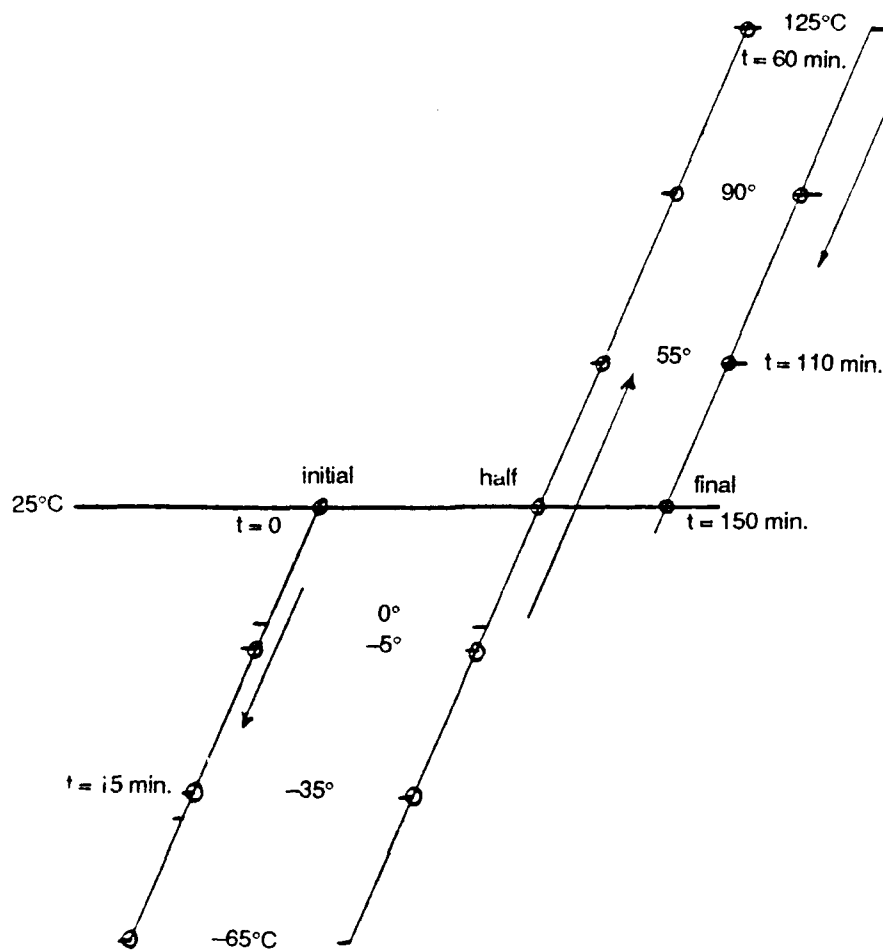
Figure 5-8. Schematic of the Complete Thermal Cycle Performed
Within the SEM Showing the Temperatures at Which Photographs
were Taken for Analysis and the Approximate Lapsed Times at
Each Temperature During the Test
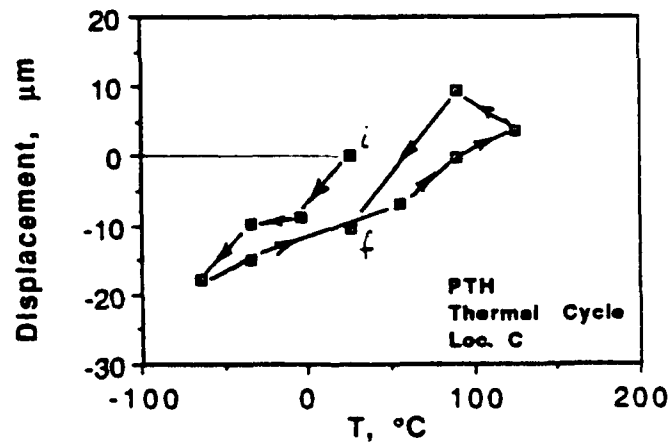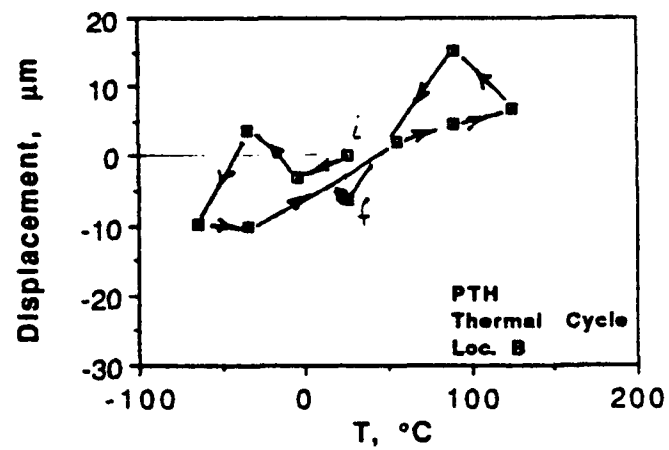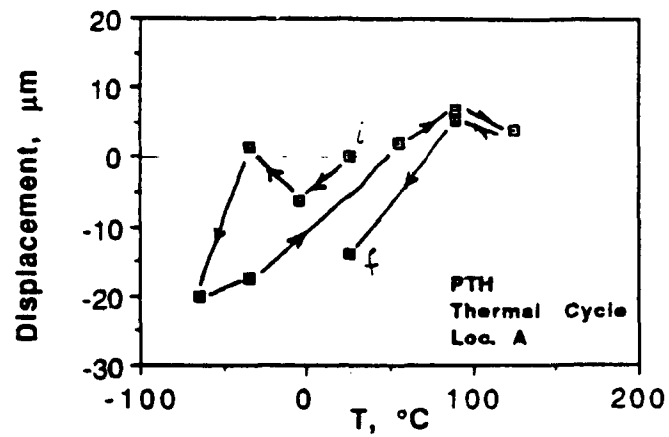
Figure 5-9. Displacement in the PTH (Location B) and Along
Two Lines 800 μm to Either Side of the PTH Showing the Path
of the Displacements as Temperature was Changed. The
Initial and Final Displacement at 25°C are Indicated. Note that
the Specimen has Shrunk in Thickness by About 10 μm During
this thermal Cycle.

TABLE 5-4. ALL DATA - POINT MEASUREMENTS –65 TO 125°C

Location	Material	CTE (x10^{-5}/°C)
A	PCB	5.8
B	PTH	4.6
C	PCB	5.8

These CTE results are similar to those determined in the experiment between 25 and 125°C. However, in looking at these data, it was determined that points only 800 μm from the centerline of the PTH were still under the influence of the hole, so further analyses of photographs made at the temperature extremes were undertaken.

The additional analyses were performed between the end points of the thermal cycle: (1) 25 vs. –65°C, (2) –65 vs. 125°C, and (3) 125 vs. 25°C. These results are shown in Figs. 5-10, 5-11, and 5-12, respectively, and described in the following paragraphs. Actual data are given in Appendix F.

Displacements resulting from the initial cooling part of the cycle (25 to –65°C) are not symmetrical about the centerline of the PTH, Figure 5-10. The reason for the asymmetry is not known. The CTE at either extreme of the region shown in the PWB (designated locations X and Y), was calculated from displacements, and the CTE was determined along the centerline of the PTH (location B). The results are given in Table 5-5.

Similarly, CTE was determined during the heating part of the cycle (–65 to 125°C) from the displacements shown in Figure 5-10; results are given in Table 5-6. Thermal expansion is more uniform in the thickness direction and on each end, but still is not symmetric along the centerline of the PWB; there is in-plane contraction along the centerline of the board. Note how much larger these values are than those which occurred on the cooling part of the cycle.

The displacements resulting from the cooling part of the cycle, 125 to 25°C, are shown in Figure 5-12. Shrinkage is relatively symmetrical, but the PWB is actually expanding in-plane in the center. Computed CTE values are given in Table 5-7.

Values of the CTE measured in the copper are lower than for the PWB alone due to the smaller CTE of copper. But when considered on the individual cooling and heating parts of the cycle, CTE is lower on cooling from 25 to –65° than on heating from –65 to 125°C, and higher yet on cooling from 125 to 25°C. The other interesting result is the overall shrinkage of the PWB of 5 to 10 μm due to the thermal cycling experiment. This agrees qualitatively with previous measurements of contraction caused by numerous thermal cycles.

250 microns   20 microns displacement
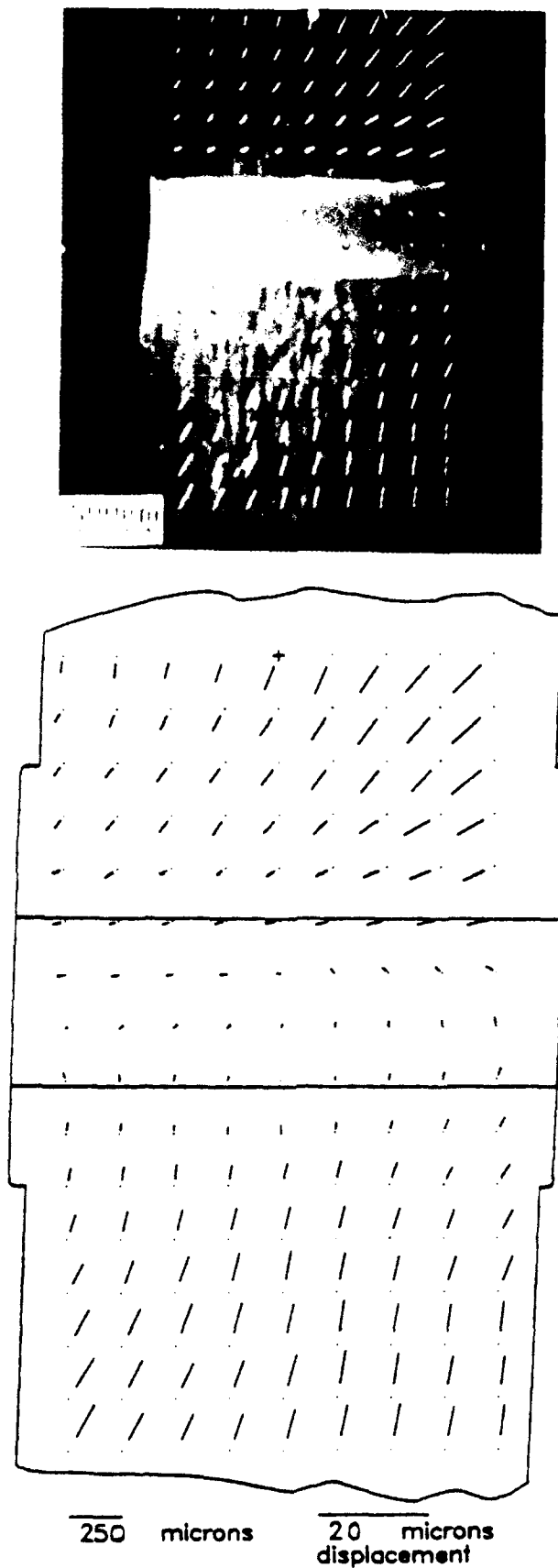
Figure 5-10. Displacements Over the Whole Region
Surrounding the PTH for Cooling From 25 to –65°C

Figure 5-11. Displacements Over the Whole Region
Surrounding the PTH for Heating from –65 to 125°C.
Location of the PTH is Shown. Compared to the
Cooling Part of the Cycle, There is Much More
Symmetry in Displacement.

250 microns   40 microns
displacement

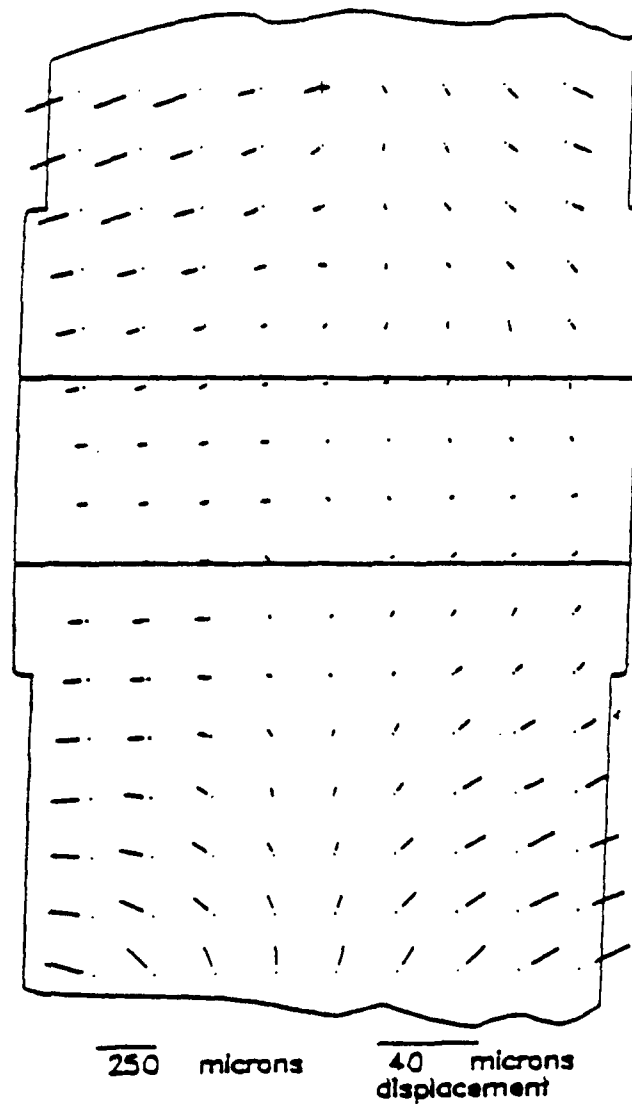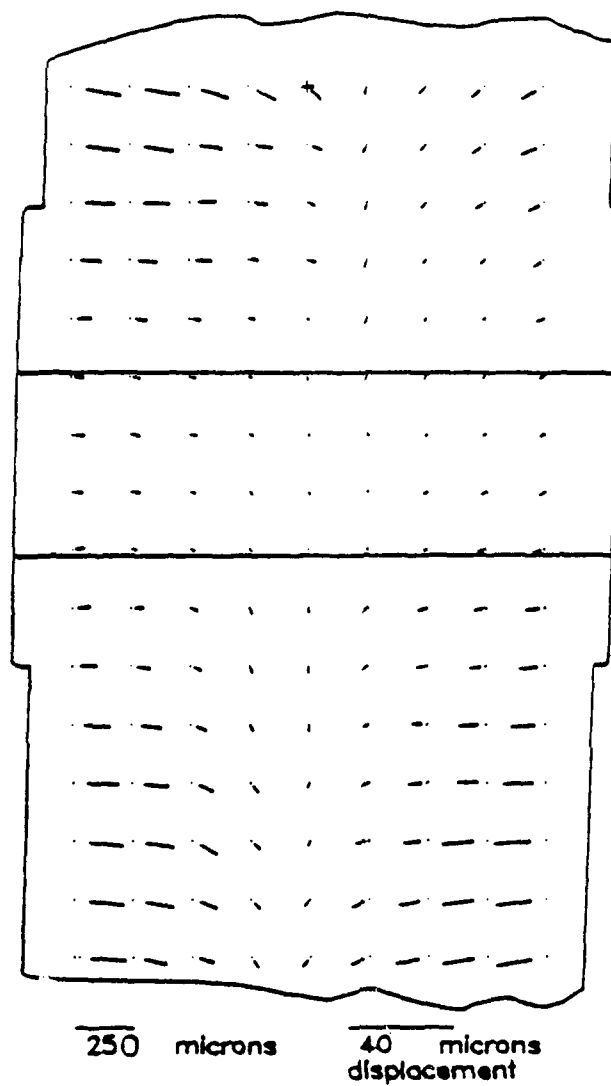Figure 5-12. Displacements Over the Whole Region
Surrounding the PTH for Cooling from 125 to 25°C.
Location of the PTH is Shown.

TABLE 5-5. 25 TO –65°C

Location	Material	CTE (x10^{-5}/°C)
X	PCB	–3.6
B	PTH	–0.23
Y	PCB	–2.2

TABLE 5-6. –65 TO 125°C

Location	Material	CTE (x10^{-5}/°C)
X	PCB	8.0
B	PTH	1.2
Y	PCB	9.0

TABLE 5-7. 125 TO 25°C

Location	Material	CTE (x10^{-5}/°C)
X	PCB	–15
B	PTH	–3.3
Y	PCB	–18

So far as has been determined, the experiment and the measurements are accurate descriptions of the thermal cycles applied previously in the experiment that resulted in cracked PTHs. If temperature had been stabilized at each temperature, then CTE on the initial cooling part of the cycle might have been somewhat larger, but to have equaled the CTE on heating, the cooling CTE would have to be a factor of 3 larger. Similarly, the CTE on cooling from 125 to 25°C is a factor of 5 larger than that on cooling from 25 to –65°C. Thus, the effects of departure from thermal equilibrium would have to be very large to affect CTE to this degree. A more likely explanation is that the CTE increases by a factor of 2 to 3 above the glass transition temperature of the epoxy-fiberglass PWB. For this particular PWB, the glass transition is unknown but the IPC report (Ref. 5-2) gives values for this parameter which range from 100 to 130°C.

A representation of the path dependence of the CTE in the PWB and the PTH is given in Figure 5-13. This figure shows the change of strain with temperature; so the slopes of the lines are the CTE.
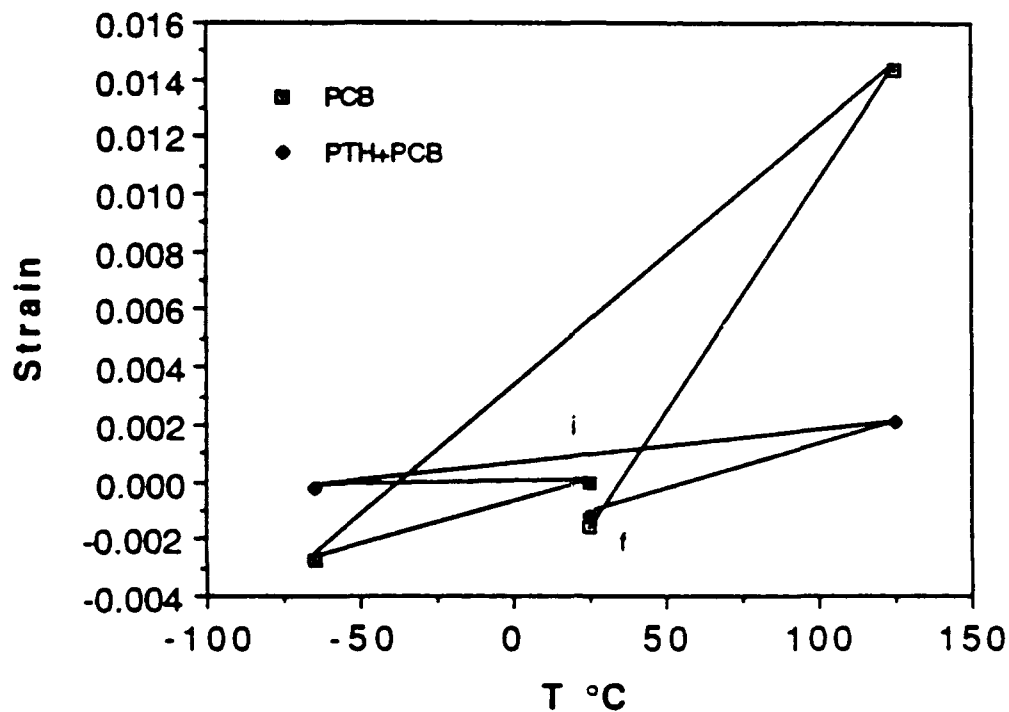
Figure 5-13. Strain as a Function of Temperature as Derived From the Analyses of the End Points in the Temperature Cycle. The Slope of These Lines is the CTE. This Figure Illustrates the Differences in CTE Between Various Parts of the Thermal Cycle and Between the PWB and the Copper PTH.

5.3.3.3 After Thermal Cycling

The appearance of PTH No. 6 after 211 thermal cycles is shown in Figure 5-14. In addition to the cracks, there is ample evidence of a nonuniform distribution of strain. Surface topography of the copper plating is much rougher in the regions between the copper interconnect circuit strips. In effect, the PTH appears to be acting as a shell stiffened by these interconnect strips, and thermal cycling is deforming the shell nonuniformly in between the stiffeners. The resulting deformation pattern is that of a ring stiffened shell buckled in compression, which coincides with the observation that the net compressive strains are accumulating with thermal cycling. The mechanical effect of thermal cycling on the PTH is similar to the phenomenon defined as "thermal ratcheting" (Ref. 5-6), except that the shrinkage of the PWB is an additional driving force for damage accumulation.
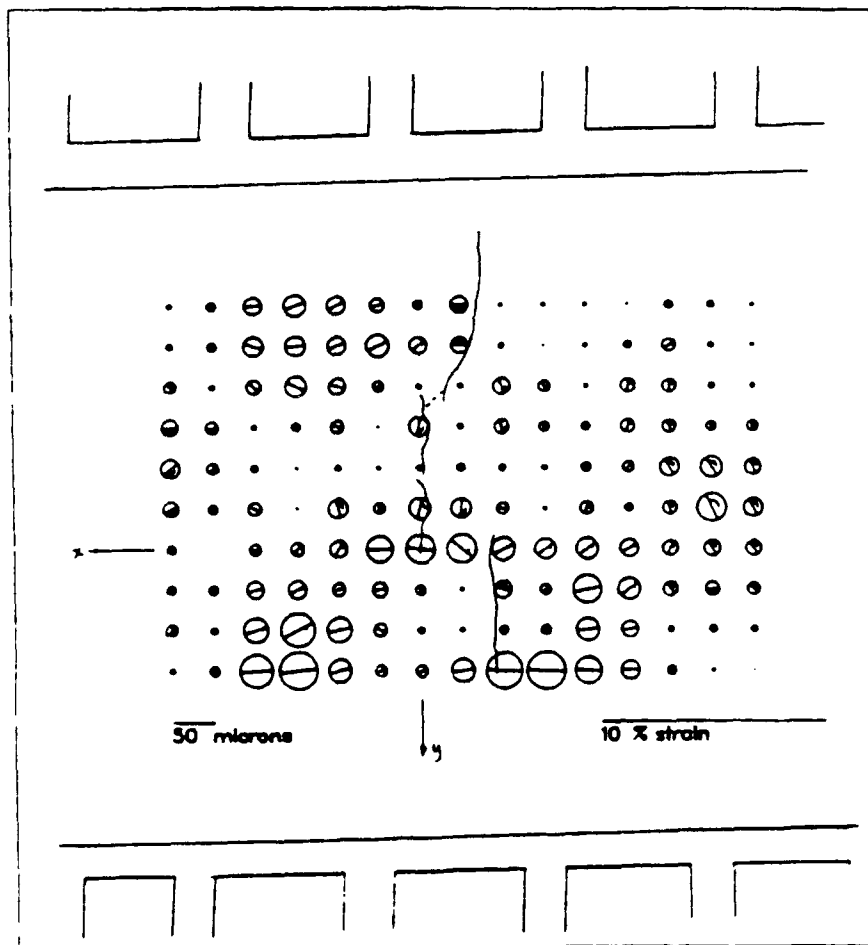
Figure 5-14. (a) Appearance of PTH No. 6 After 211 Thermal Cycles
(–65 to 125°C) Showing Surface Deformation and Cracks.
(b) Mohrs Circles of Strain for the Central Portion of the PTH
Showing the Relationship Between the Strain Levels and
Locations of the Interconnect Plates.

5-25

The lower part of this figure shows the Mohr's circles of strain determined for a temperature change of 25 to 125°. Strains are the largest in the region between the interconnect strip stiffeners, just as indicated by surface topography. Strains are high near crack tips also, but this analysis does not have enough resolution for the magnitude of these strains to be determined with any degree of accuracy.

The displacements caused by increasing temperature from 25 to 125°C around the 120-μm crack seen in Figure 5-14, designated Crack 1, are shown in Figure 5-15. A similar analysis of the crack tip region was also performed at intermediate temperatures on both the increasing and decreasing part of the thermal cycle. The resulting change in Mode I crack opening displacements (ΔCOD) are shown in Figure 5-16. The relative uniformity of the COD in the middle of the crack should be noted. Photographs of this crack at 25°C show that the middle part of the crack was already open about 2 μm. For the temperature change 25–55°C, ΔCOD ≈ 0.35 μm. For 25–125°C, ΔCOD ≈ 1.40 μm. On decreasing temperature from 125 to 75°C, ΔCOD decreased 0.20 μm.

Crack opening displacement for Crack 2 due to a change in temperature from 25 to 125°C has about the same characteristics as Crack 1, with a maximum opening of about 1 μm. The ΔCOD of Crack 3, the large crack seen in Figure 5-14, has essentially the same characteristics as Cracks 1 and 2, with a maximum opening of ≈ 1.5 μm. But this crack is partly bridged (not completely broken) at a distance ≈ 200 μm from the tip.

Fatigue cracks grown under cyclic mechanical stress conditions approaching the assumptions of linear elastic fracture mechanics (small plastic zone compared to the crack length and elastic net section) exhibit a COD which varies as the square root of the distance from the crack tip. Thus, CODs for these cracks were plotted to determine if a similar dependence applied. As may be seen in Figure 5-17, for Crack 2, COD α √y, but Crack 1 does not show this behavior.

To determine the effect of the full temperature cycle (–65 to 125°C), it is necessary to extrapolate the measured ΔCOD values. This has only been done for Crack 1 because it is the only crack for which ΔCOD was measured as a function of temperature. To make this extrapolation, the approximately 2 μm the crack is open at 25 °C was added to the measured values, giving the COD values shown in Figure 5-18. This extrapolation indicates that the crack was open ≈ 0.74 to 1.2 μm at –65°C and 3.4 μm at 125°C, giving a ΔCOD between 2.64 and 2.2 μm. Assuming the crack is closed at –65°C would give a maximum value for ΔCOD of 3.4 μm.
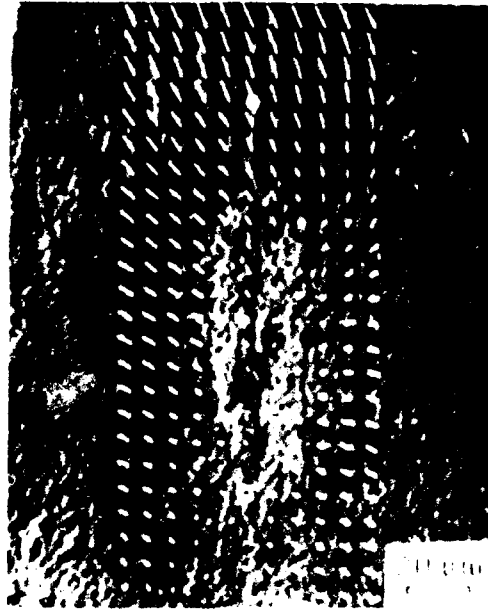
Figure 5-15. Displacements in Crack 1
Caused by Increasing Temperature from
25 to 125°C Superimposed Over the
Crack as Seen at 125°C
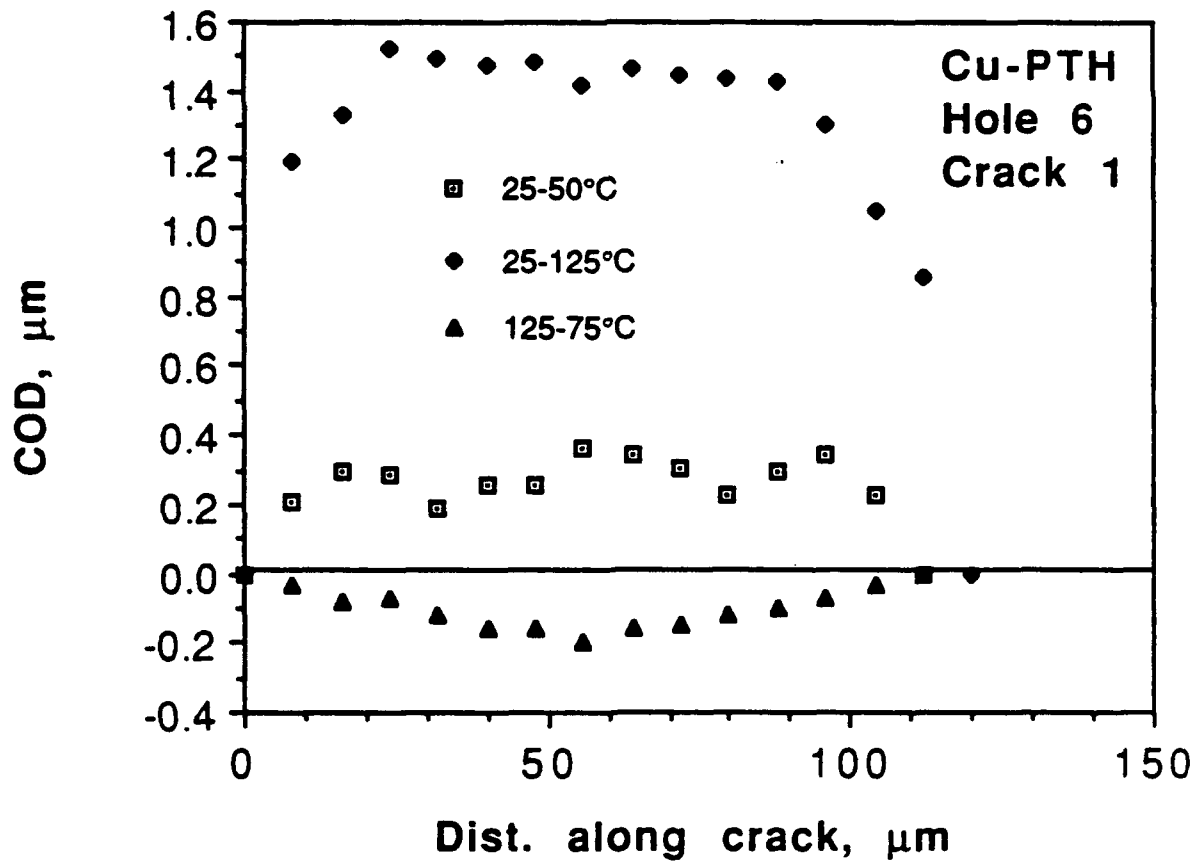
Figure 5-16. Mode I Crack Opening Displacements of the 120-μm-Long Crack
in PTH No. 6 as a Function of the Temperature Range Measured
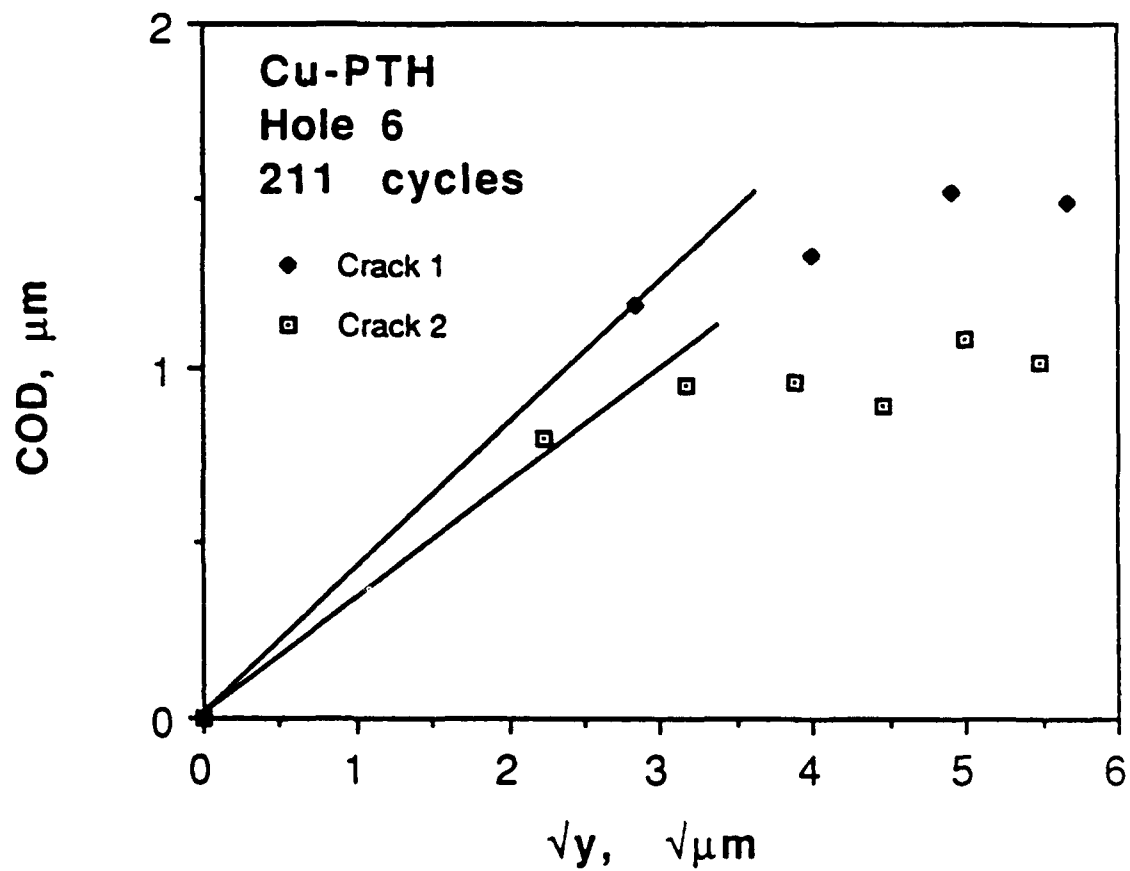
Figure 5-17. Crack Opening Displacement Vs. Square Root of the Distance Behind
the Tip Showing that COD Probably Does Not Depend on $\sqrt{y}$, as Would Be
Expected From Other Fatigue Crack Studies
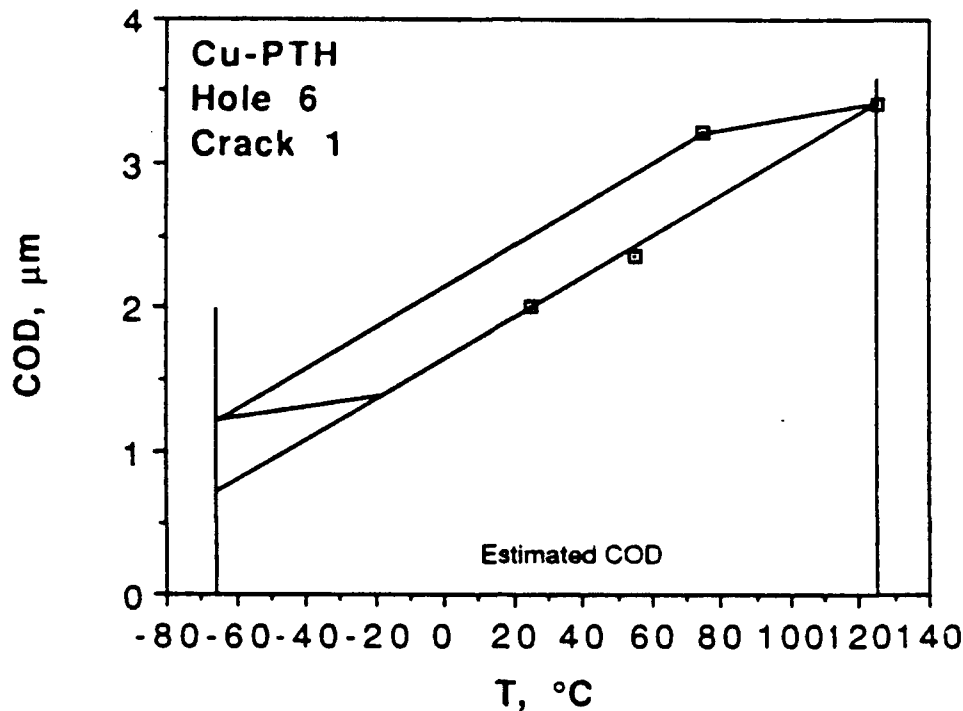
Figure 5-18. Extrapolation of COD Values Measured Over Part
of the Temperature Cycle (25 to 125°C) to the Full
Temperature Cycle (–65 to 125°C)

5.3.4 Estimation of Crack Driving Force

Measured COD values have been used to estimate crack driving force by use of the relation (Ref. 5-7):

$$\Delta K = (E\delta\Delta\sigma)^{1/2} \tag{5-9}$$

where δ = CTOD (the crack tip opening displacement) and $\Delta\sigma$ = range of stress experienced by the crack tip, and E = tensile modulus of the Cu (1.1×10^5 MPa). For the estimates given below $\Delta\sigma \approx$ twice the tensile yield stress (566 MPa), and δ = the maximum change in COD with temperature (2.2 to 3.3 μm). Use of this relationship assumes that the crack is in an elastic body to which a remote stress has been applied. The crack in the PTH is in a fully plastic section under displacement control; thus, the analysis used in deriving eq. (5-9) is not strictly applicable.

Using the above values in eq. (5-9) gives:

$$12 < \Delta K < 14 \text{ MPa}\sqrt{m}$$

and putting these values into eq (5-2) gives a crack growth rate of 7×10^{-8} to 1.5×10^{-7} m/cy, which is about a factor of about 100 less than the crack growth rate as determined from eq. (5-7) at 211 cycles. If eq. (5-2) is used to derive ΔK from the crack growth rate at 211 cycles (1.2×10^{-5} m/cy), then $\Delta K = 47.6$ MPa$\sqrt{m}$. Thus, a simple estimate of driving force, as used for remotely loaded cracks in an elastic section, does not appear to be adequate for conditions found in the PTH.

5.3.5 Additional Results

The PTH specimen was carefully examined in the SEM after termination of the thermal cycling experiment at 211 cycles, particularly to determine if debonding had occurred between the copper plating and circuit board material. Debonding between the PCB material and the Cu of the PTH was found to be the most obvious in the center region of the PCB, as illustrated in Figure 5-19, but there was also evidence that debonding had occurred over most parts of the PTH, except on the outer surfaces.

The large cracks in the PTH were found to extend completely through the thickness of the Cu plating. Although these cracks probably initiated on the exposed surfaces of the copper in the PTH, they quickly grew through the thickness of the plating and then grew around the hole circumference as through cracks. Cracks up to ≈ 130 cycles were probably partially through the plating, but with further cycling, cracks were probably completely through the plating. At the end of the experiment, there is clear evidence that cracks are fully through the plating thickness, as shown in Figure 5-20.

5.3.6 Summary and Conclusions

For cracks with lengths between 30 μm and 6 mm, cyclically loaded by remotely applied stresses, growth rates in plated copper foil were found to be essentially the same as for wrought, ingot-derived copper.

A specimen containing 10 sectioned PTHs was thermally cycled −65 to 125°C (MIL-T). Cracks initiated in half the PTHs after ≈ 90 cycles, and by 211 cycles most of the PTHs had several cracks with a total length equaling approximately their circumference. Had these PTHs been barrel specimens loaded in tension at the ends, each PTH would probably been in two pieces by 200 cycles. The PTHs tested were not electrically separated after 200 cycles.

Crack growth rates in the PTHs were determined by periodic measurement to average between 10^{-7} and 10^{-5} m/cy.

Coefficient of thermal expansion was found to be path dependent in both the PWB and PTH, with large differences in magnitude (up to 5 times) between heating and cooling. The thicknesses of the PWB and PTH were found to decrease with thermal cycles, resulting in a cumulative compressive strain. This behavior is a form of the phenomenon known as "thermal ratcheting," but the mechanistic details were not determined.

Driving forces for thermally cycled cracks in the PTHs were estimated from measured crack opening displacements on the basis of a J-integral analysis. These estimates could not be reconciled with the growth rates measured from cracks in specimens of copper plated foil driven under remotely applied cyclic loading.

Figure 5-19. An Example of Debonding Between
Copper in the PTH and the PWB

Figure 5-20. Edge View of a Crack in PTH Copper,
Illustrating That These Cracks are Fully Through
the Thickness of the Plating

5-31

5.4 ANALYSIS

This section presents preliminary analytical stress and fracture mechanics evaluations of the failure of a PTH subjected to thermal cycling. A nonlinear axisymmetric finite element analysis of a PTH was performed to obtain stress and strain ranges in the copper barrel of a PTH subjected to thermal cycling between –65°C and 125°C. Peak strain range was used in conjunction with available literature data on low cycle fatigue of copper to estimate fatigue crack initiation life. Elastic-plastic J-integral solutions were utilized to perform fatigue crack propagation life calculations for the PTH. Except for the fatigue crack growth data, this analysis was not based upon the results of the experiments described in Section 5.3.

5.4.1 Strain

The geometry of a PTH is axisymmetric; however, the woven glass fiber and epoxy make the PWB material anisotropic, which can result in nonaxisymmetric displacements under loading. Since the copper barrel of the PTH was known to yield, a multiple-load-step nonlinear analysis was required to obtain stresses as a function of temperature through the MIL-T-CYCLE thermal load cycle from –65°C to 125°C. To help minimize the cost of analysis, it was desirable to use an axisymmetric finite element (FE) model rather than a much larger 3-dimensional model.

A small quarter-symmetry 3-dimensional (3-D) FE model of a single layer of PWB was developed and analyzed to determine the extent to which the in-plane anisotropy of the epoxy-glass caused circumferential variations in stresses and displacements. The model consisted of one layer of copper trace sandwiched between two layers of epoxy-glass with a copper layer representing the PTH barrel covering the ID surface of the model. Figure 5-21 shows the FE model which was constructed of 8-noded solid elements. Symmetric displacement boundary conditions were applied to the X-Y and X-Z faces, as well as the top (+X) and bottom (–X) surfaces. The use of symmetric boundary conditions on the top and bottom surfaces effectively models a PTH with infinite length in the X-coordinate directions. This idealization was chosen to best represent a layer at the midthickness of a PWB. A homogeneous anisotropic material model was used to represent the epoxy-glass PWB material. For the 3-D scoping analysis, the copper was assumed to remain elastic. Table 5-8 lists the elastic constants used in the analysis.

The 3-D slice model was thermally loaded using a uniform temperature change of 50°C in a one-step linear analysis using the MARC finite element program (Ref 5-8). Comparisons were made between stress results in the copper barrel at circumferential positions of $\theta = 0°, 45°$, and $90°$. Maximum variations of 3 percent in peak axial stress, and 2.5 percent in peak effective stress were observed. These variations due to the anisotropy of the epoxy-glass were deemed negligible. Therefore, the full nonlinear MIL-T-CYCLE analysis of the PTH was performed using an axisymmetric model.

A half-symmetry axisymmetric FE model of a PTH was developed using 4-noded axisymmetric solid elements as shown in Figure 5-22. Using symmetry conditions, it was only necessary to model the PTH over half of the PWB thickness. It was assumed that modelling the PWB board material out to a radius equivalent to three hole radii would be sufficient for analysis of the response of the copper barrel of the PTH. Figure 5-23 is an exploded view of the model showing the copper and epoxy-glass portions separately. The model was given higher mesh refinement near the center of the PTH barrel in the region of previously observed cracking in the IPC round robin testing.

Material properties for the epoxy-glass were the same as those given in Table 5-8 for the 3-D analysis.

Figure 5-21. Three-Dimensional Finite Element Model of a Single Circuit Layer in a Printed Wiring Board Containing a Plated Through Hole.

TABLE 5-8. PLATED THROUGH HOLE MATERIAL PROPERTIES

Glass/Epoxy Printed Wiring Board (orthotropic)

Orthotropic Material Orientations:
   1 - through thickness direction (X)
   2 - warp direction (Y)
   3 - fill direction (Z)

Tensile Moduli:
$$E_{11} = 0.5 \times 10^3 \text{ ksi}$$
$$E_{22} = 2.5 \times 10^3 \text{ ksi}$$
$$E_{33} = 2.0 \times 10^3 \text{ ksi}$$

Shear Moduli:
$$G_{12} = 0.31 \times 10^3 \text{ ksi}$$
$$G_{23} = 0.31 \times 10^3 \text{ ksi}$$
$$G_{31} = 0.31 \times 10^3 \text{ ksi}$$

Poisson's Ratios:
$$\nu_{12} = 0.07$$
$$\nu_{23} = 0.15$$
$$\nu_{31} = 0.30$$

Coefficients of Thermal Expansion:
$$\alpha_{11} = 4.5 \times 10^{-5} \text{ °C}^{-1}$$
$$\alpha_{22} = 1.0 \times 10^{-5} \text{ °C}^{-1}$$
$$\alpha_{33} = 1.3 \times 10^{-5} \text{ °C}^{-1}$$

Copper Plating (isotropic)

Tensile Modulus:
$$E = 16.0 \times 10^3 \text{ ksi}$$

Poisson's Ratio:
$$\nu = 0.34$$

Coefficient of Thermal Expansion:
$$\alpha = 17.6 \times 10^{-6} \text{ °C}^{-1}$$

Figure 5-22. Axisymmetric Finite Element Model of Plated Through Hole

EPOXY/GLASS
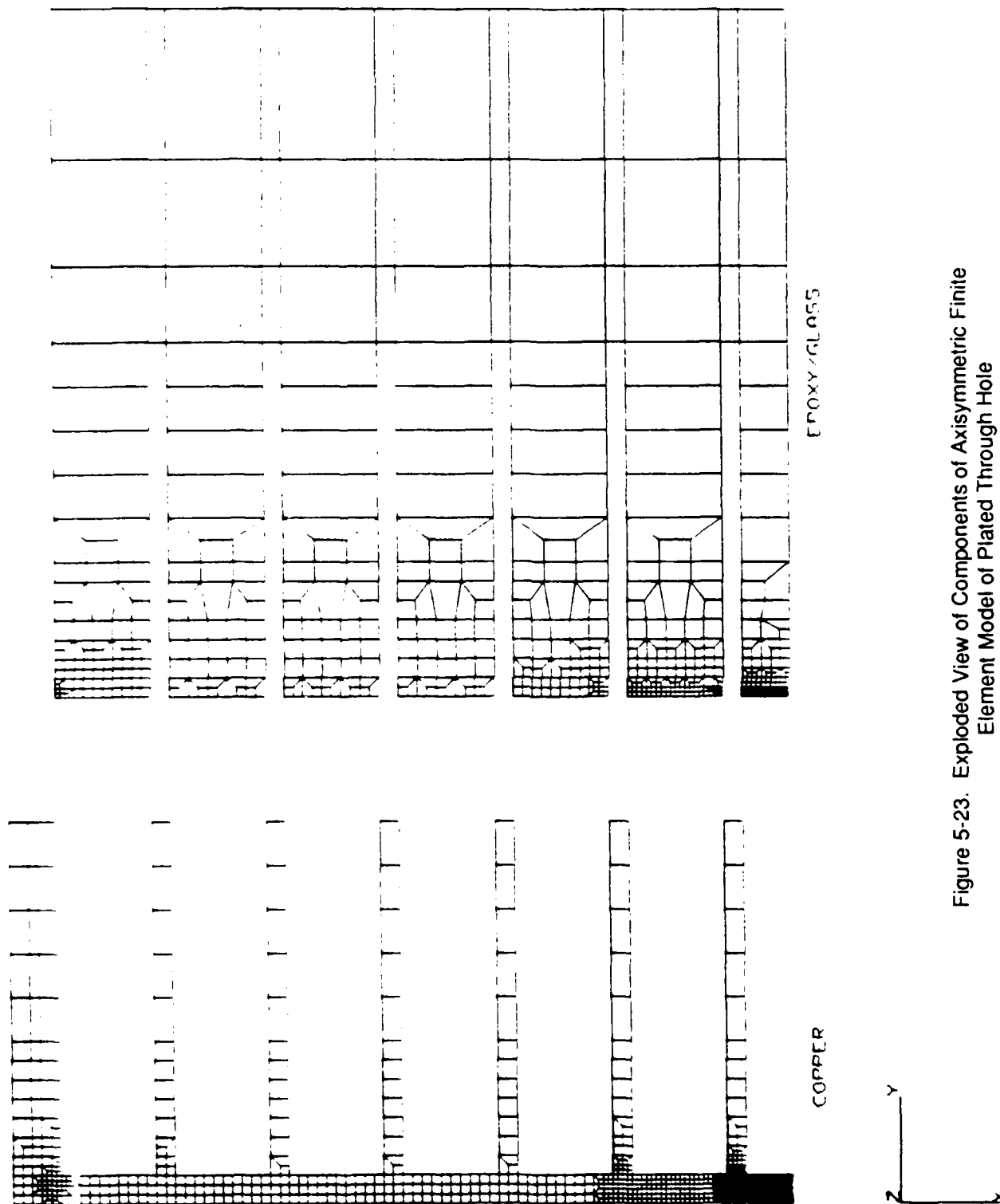
COPPER

Figure 5-23. Exploded View of Components of Axisymmetric Finite
Element Model of Plated Through Hole

In order to account for postyielding behavior in the copper, a power law hardening constitutive model was used as given by:

$$\varepsilon = \frac{\sigma}{E} + \left(\frac{\sigma}{D}\right)^n$$

(5-10)

where E is the elastic modulus for copper given in Table 5-8. Values of D = 194.7 ksi and n = 3.2 were obtained by curve fitting to room temperature data on cyclic stress versus cyclic plastic strain for bulk copper (Ref. 5-9). Although the values of D and n are temperature dependent, no real data were available to quantify the temperature effects. Therefore, the room temperature data were used for this analysis. Fi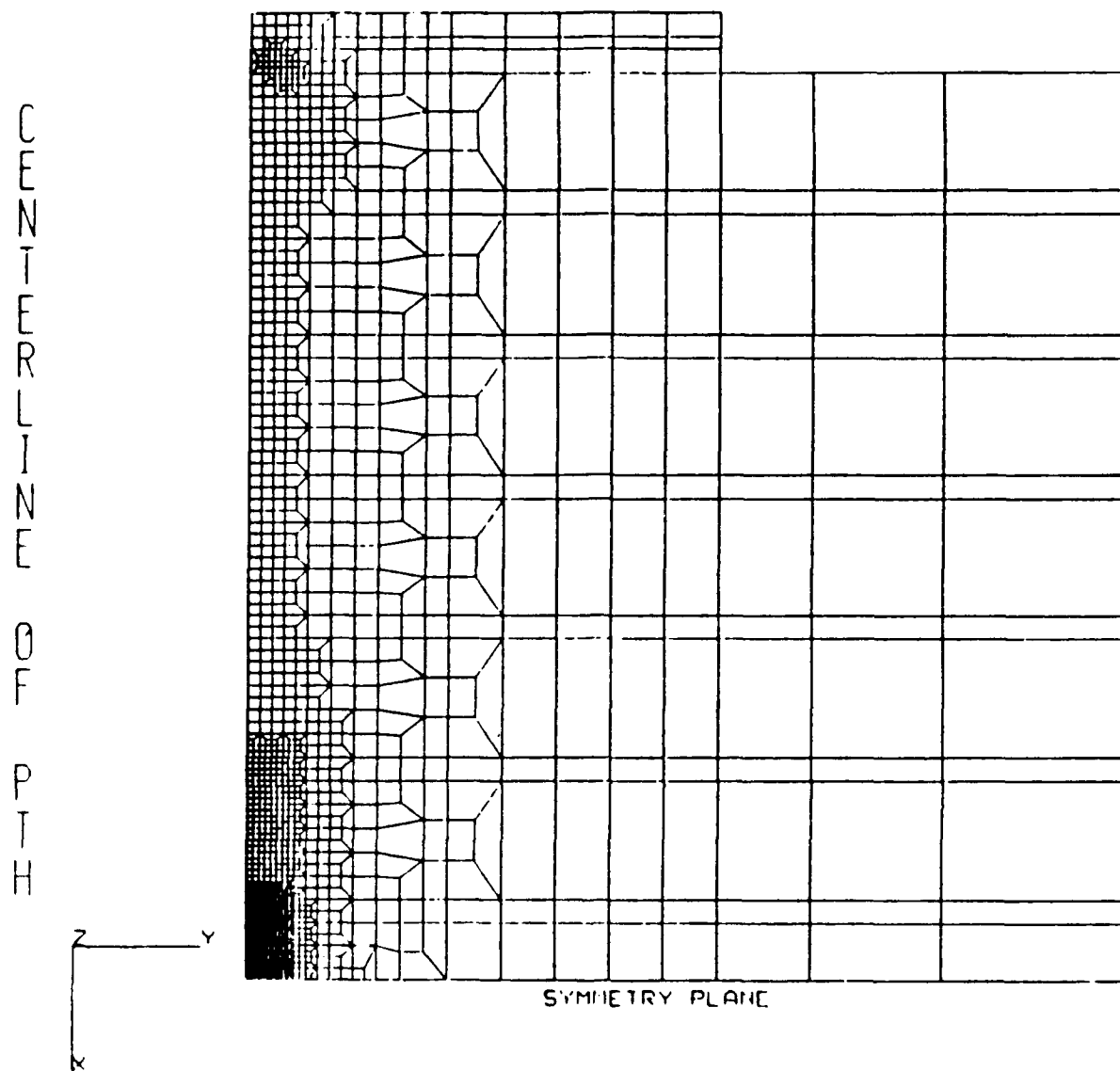gure 5-24 shows a comparison between stress-strain curves for bulk copper from Ref. 5-9 and a monotonic stress-strain curve for electro-deposited copper from testing at SwRI. The SwRI test data were not available in time for use in the current FE analysis. Furthermore, tests could not performed to obtain cyclic stress-strain data for electro-deposited copper due to the difficulty in cycling the thin foil samples with compressive loads to obtain reversed yielding.

The FE model was thermally loaded through the MIL-T-CYCLE using increments of uniform temperature from an initial temperature of 21°C up to a maximum of 125°C. Figure 5-25 shows a plot of the deformed shape of the model boundary at 125°C relative to the undeformed shape at 21°C. It is evident from the deformed shape that the copper barrel of the PTH, with its lower CTE, constrains the thermal expansion of the PWB in the vicinity of the PTH. In subsequent increments, temperature was decreased to a minimum of –65°C. This incremental thermal loading was continued for one and a half more cycles between –65°C and 125°C until a relatively stable stress-strain hysteresis loop was obtained for one of the most highly strained elements in the copper barrel. Figure 5-26 shows a plot of the stress versus plastic strain history for this highly-strained element. Contours of cyclic axial strain range in the copper portions of the model confirm the previous assumption that the peak strain range occurs near the center of the PTH barrel. The maximum strain range occurs at the inner surface of the copper barrel opposite the circuit trace adjacent to the symmetry plane.

5.4.2 Fatigue Crack Initiation

In a nominally defect-free copper barrel of a PTH, a fatigue crack would be expected to form at the location of the maximum cyclic plastic strain. As described above, the current analysis predicts the maximum cyclic plastic strain to occur on the surface of the copper barrel directly opposite a copper trace layer. The magnitude of the maximum effective cyclic plastic strain, from Figure 5-26, is 0.004.
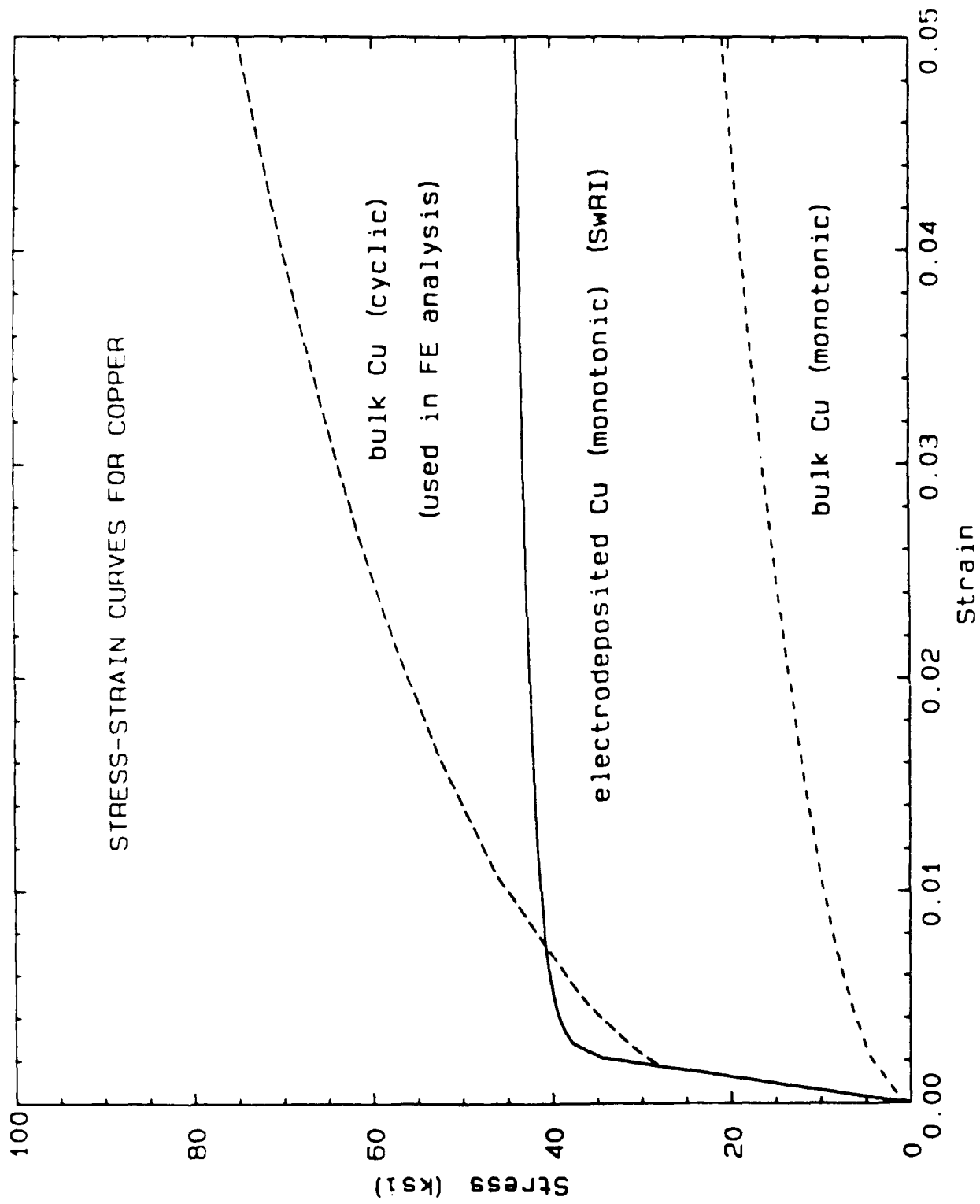
Figure 5-24. Comparison Between Stress-Strain Curves for Bulk and Electro-Deposited Copper

STRESS-STRAIN CURVES FOR COPPER

bulk Cu (cyclic)

(used in FE analysis)

electrodeposited Cu (monotonic) (SwRI)

bulk Cu (monotonic)

Strain

Stress (ksi)

DEFORMED (T=125C)

UNDEFORMED (T=21C)

(DISPLACEMENTS SCALED BY 20x)
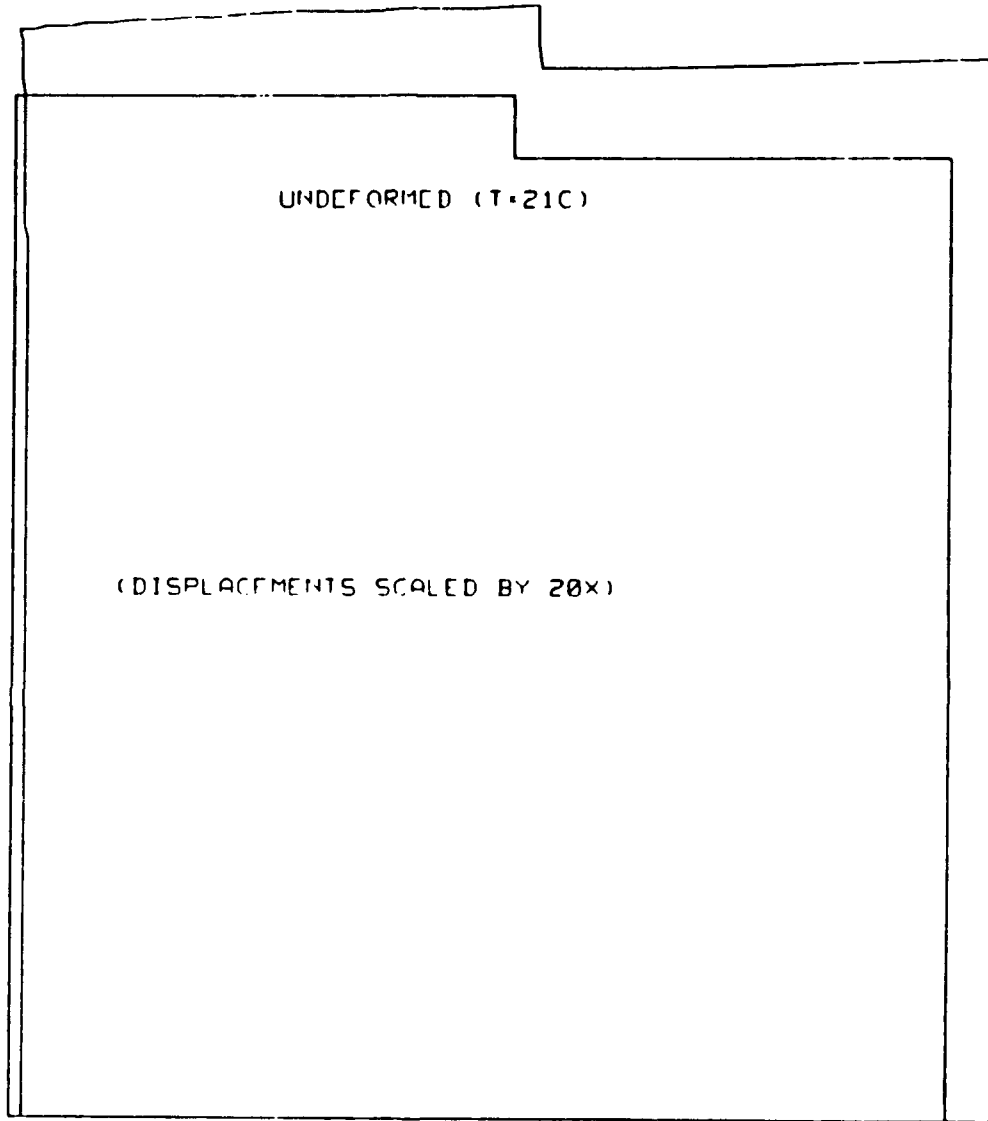
Z———Y

HUGHES ERFM PLATED THROUGH HOLE ANALYSIS (PRELIMINARY)
NO TEMPERATURE DEPENDENT MATERIAL PROPTERIES
FIRST CYCLE, LOAD STEP 6, TEMPERATURE = 125 C

Figure 5-25. Deformed Shape of Plated Through Hole at 125°C Relative to
Undeformed Room Temperature Conditions
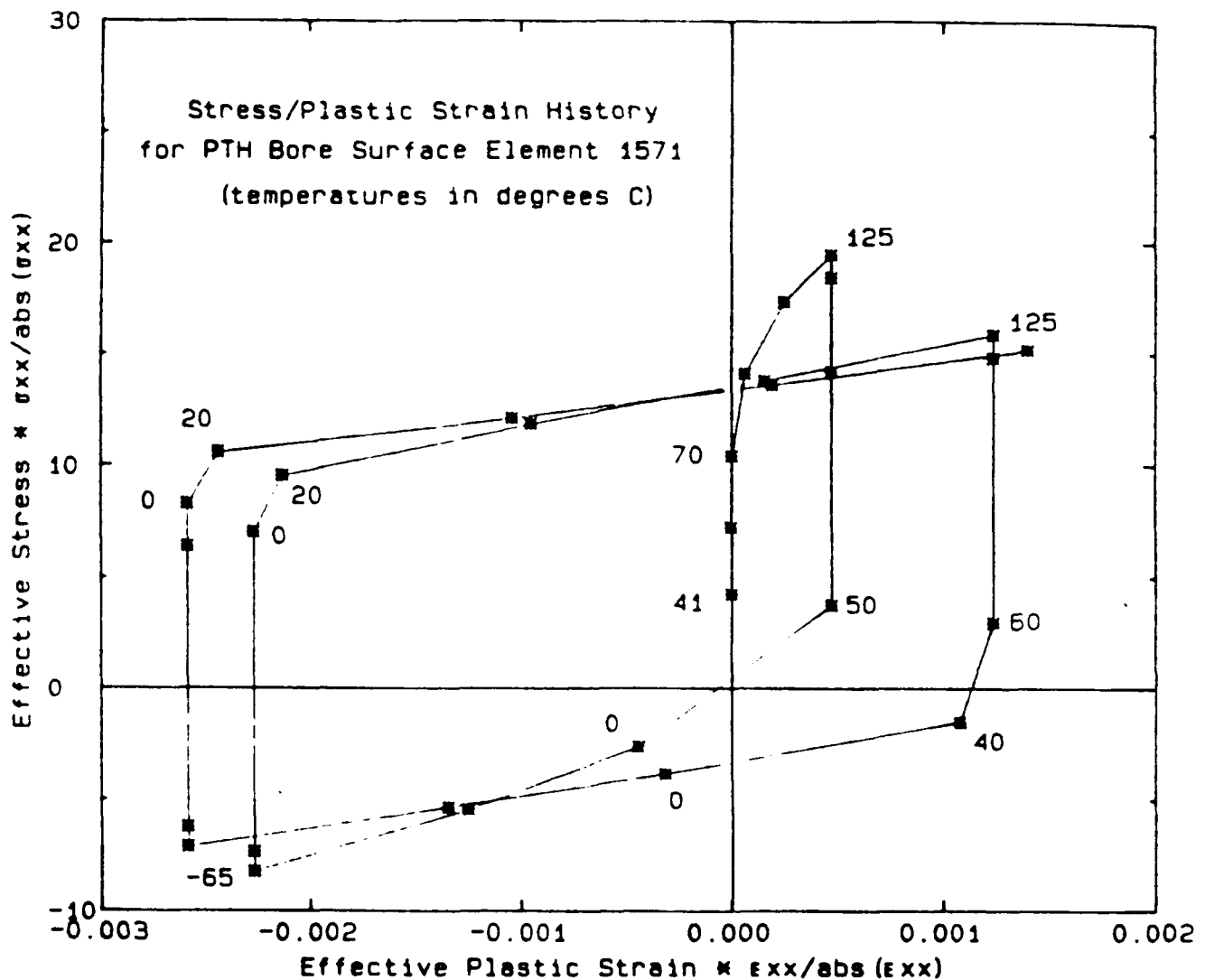
Figure 5-26. Stress-Strain History for Plated Through Hole Bore Surface
Element Near Center of Plated Through Hole

The effective plastic strain range is used to assess fatigue damage by comparison with data from uniaxial tests. Based on the uniaxial low cycle fatigue data for bulk copper shown in Figure 5-27 (reprinted from Ref. 5-9), a plastic strain range of 0.004 would cause failure in approximately 5000 cycles.

Due to the gradients in strain in the PTH, the maximum strain range occurs in a relatively small volume of material. Therefore, failure of a uniformly strained test specimen in 5000 cycles
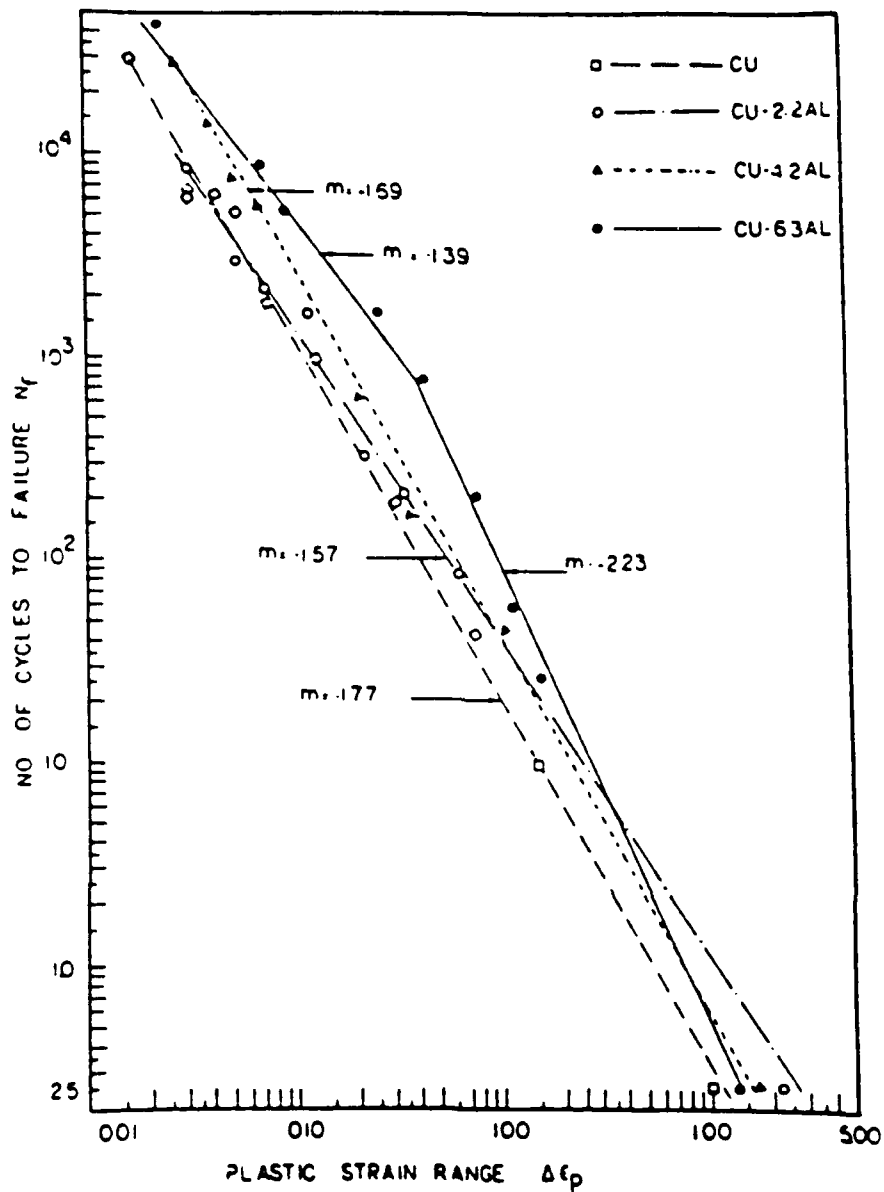
Figure 5-27. Low Cycle Fatigue Behavior of Copper Alloys [Ref 5-9]

at 0.4 percent cyclic strain may be considered equivalent to failure of the small volume of PTH copper experiencing that strain range, and hence crack initiation in the PTH.

This predicted fatigue crack initiation life, however, is more than a factor of 10 greater than that observed in both the IPC tests (Ref. 5-2) and tests at SwRI. The location of predicted initiation also differs from that observed in tests. Cracks in test specimens occur most often between trace layers as opposed to opposite a trace as predicted by the current analysis.

5.4.3 Fatigue Crack Propagation

A fatigue crack propagation analysis was performed on the copper barrel of the PTH using the NASCRAC code (Ref. 5-10). Fatigue crack growth rate data were obtained from testing in this study of electro-deposited copper foil samples at SwRI. Figure 5-28 shows a comparison between the large crack SwRI data from Figure 5-4 and curve fits to bulk copper data from Ref. 5-9 and 5-11. The following Paris relationship was curve fit to the SwRI data and used for the current fatigue crack growth calculations:

$$da/dN = 2.1 \times 10^{-11} \, (\Delta K)^4 \qquad (5\text{-}11)$$

where da/dN is in inches/cycle and ΔK is in ksi-in$^{1/2}$. A fracture toughness, K_{Ic}, of 30 ksi-in$^{1/2}$ was estimated for the analysis based on data from Ref. 5-11.
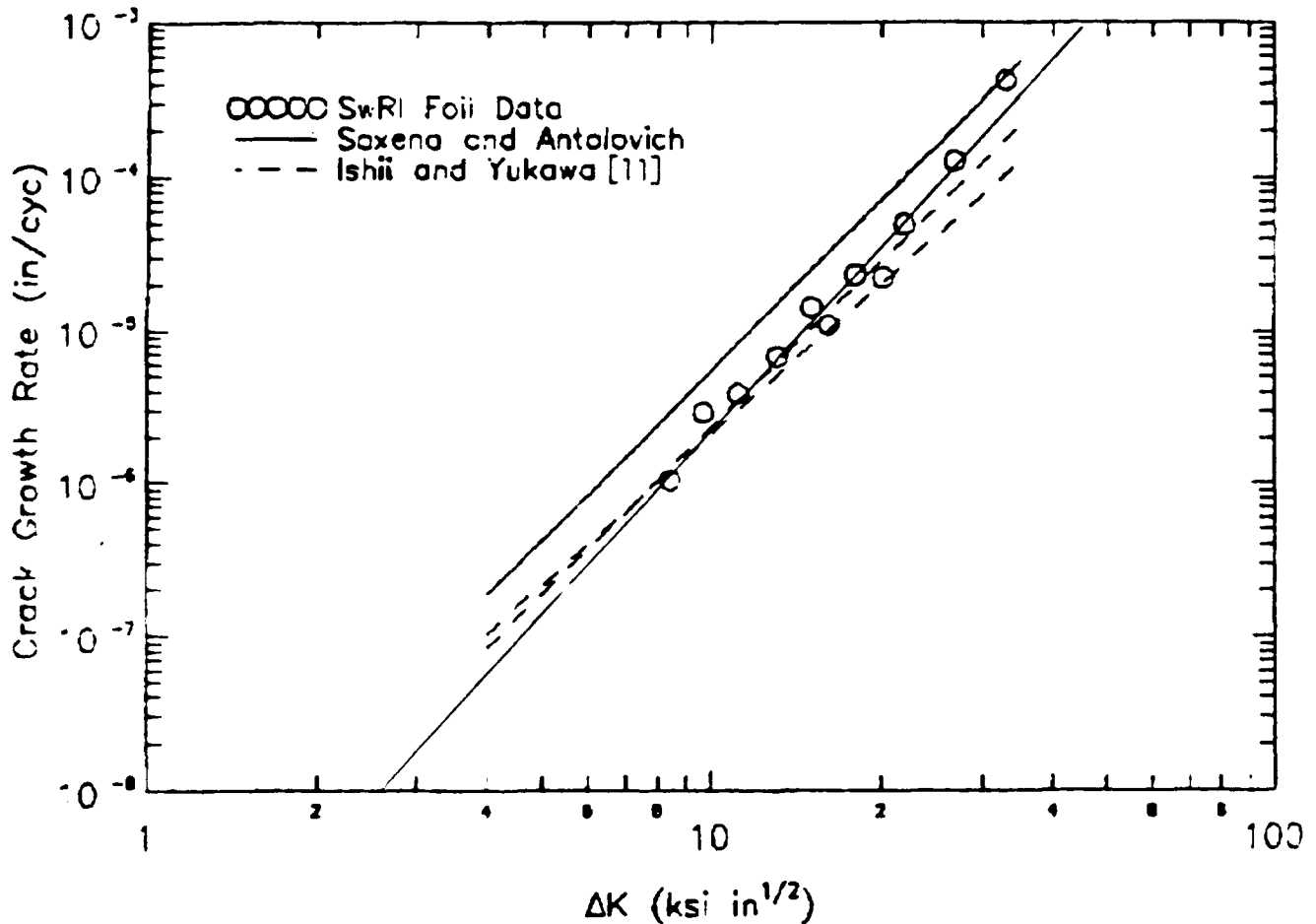
Figure 5-28. Fatigue Crack Growth Rates for Copper Foil and Bulk Copper.

Fatigue crack growth calculations were performed using two different assumed crack geometries — a complete circumferential part-through-wall crack on the ID of a cylinder (Figure 5-29), and a through-wall part-circumferential crack in a cylinder (Figure 5-30). Test observations indicate that, in many cases, several small circumferentially-oriented cracks initiate on the inside surface of the PTH copper barrel and then coalesce into a larger dominant crack. That eventually propagates the full circumference of the barrel and causes failure of the connection. The complete circumferential part-through-wall crack model is an approximation to the case of many surface cracks growing together to form a larger crack prior to growing completely through the thickness of the copper barrel. The through thickness crack model is an approximation to the other extreme in which a crack grows through the barrel wall early in life and then propagates circumferentially as a through-wall crack.

Due to the cyclic plasticity in the copper barrel of the PTH, the fatigue crack growth calculations were performed using the range of the J-integral (ΔJ) as a crack driving force parameter. Solutions for the J-integral for the two crack geometries described above are available in the NASCRAC program. Crack growth calculations are performed by computing ΔJ at each increment of crack growth, converting ΔJ to ΔK, and calculating crack growth rate (da/dN) using Equation 2. The following relationship is used to convert J to K:

$$J = K^2(1-v^2)/E \qquad (5-12)$$

Since the available J-solutions are only for uniform stress, an equivalent uniform stress was computed by averaging through the thickness the axial stress distribution in the copper barrel of the PTH from the FE analysis. A uniform maximum stress of 23.6 ksi was computed using the total stress range for the thermal cycle, and the minimum stress was taken to be zero. This method of computing the effective stress cycle results in a zero R-ratio. However, since R-ratio effects were not accounted for in the fatigue crack growth rate relation (Equation 5-11) due to a lack of data, the arbitrary assignment of R = 0 has no effect on the life calculations.

In the case of the complete circumferential crack, an initial crack depth equal to 10 percent of the copper barrel thickness ($a_i = 0.00015$ inch) was assumed. From this 0.15-mil initial crack depth, the analysis predicted slightly more than 7×10^5 cycles of crack propagation to cause failure. Figure 5-31 is a plot of crack depth as a function of the number of MIL-T-CYCLE thermal cycles. A longer initial crack length could be assumed and the resulting fatigue crack propagation life could be interpolated in Figure 5-31. However, even if the initial crack size were assumed to be as large as 0.5 mil, the predicted propagation life of 2×10^4 cycles is far greater than observed experimentally.

Analysis of a through-wall crack was begun assuming an initial half-crack length, a, of 0.003 inch. Fatigue crack propagation life to failure was predicted to be approximately 1.3×10^4 thermal cycles. Figure 5-32 shows a plot of crack length as a function of fatigue cycles for the through-wall crack.

$\alpha = a/b$

$\gamma = R_i / b$
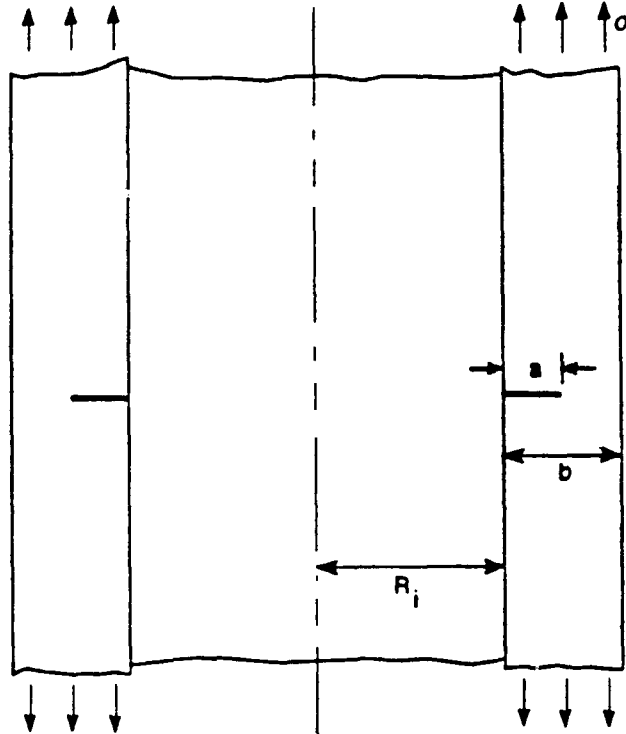
Expression:

$$J = \frac{\sigma^{n+1}}{D^n}\, a\, \frac{h_1(\alpha,n,\gamma)}{(1-\alpha)^n} \left[\frac{3^{1/2}}{2}\; \frac{1}{1+\dfrac{\alpha}{2\gamma+1}}\right]^{n+1}$$

$$\sigma_g = \frac{2}{3^{1/2}}\,(1-\alpha)\left[1+\frac{\alpha}{2\gamma+1}\right]\sigma_0 \qquad \textit{(general yield stress)}$$

$\sigma_0 = $ *uniaxial yield strength*

Limits: $\gamma = 5, 10, 20$ $0 \le \alpha \le 3/4$ $1 \le n \le 10$
           $(\alpha \to 0$ from He 83)

Accuracy: better than 4% for $n = 1$, unknown $n \ne 1$

Figure 5-29. Circumferential Crack (Inside) a Hollow Cylinder (Ref. 5-10)

$$\alpha = (a/\pi R)$$

$$R = \text{Mean Radius}$$

$$\gamma = R/b$$
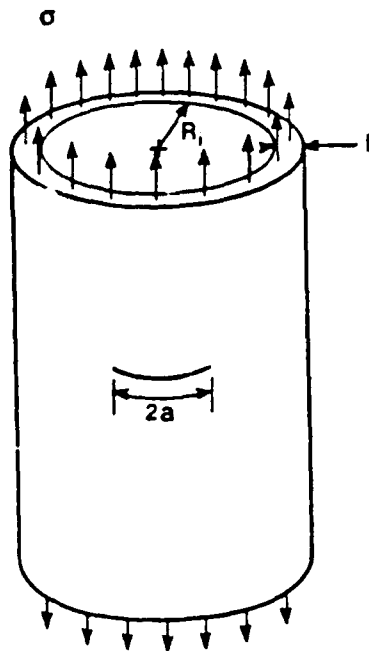
Expression:

$$J = \frac{\sigma^{n+1}}{D^n} a(1-\alpha)\, h_1(\alpha, n, \gamma) \; \frac{1}{\left[1 - \alpha - \dfrac{2}{\pi} \sin^{-1}\left[\dfrac{1}{2}\sin\pi\alpha\right]\right]^{n+1}}$$

$$\sigma_g = \frac{\sigma_0}{\left[1 - \alpha - \dfrac{2}{\pi}\sin^{-1}\left[\dfrac{1}{2}\sin\pi\alpha\right]\right]^{n+1}} \qquad (general\ yield\ stress)$$

σ_0 = *uniaxial yield strength*

Limits: $\gamma = 5, 10, 20$ $1/16 \leq (\alpha/\pi R) \leq 1/2$ $1 \leq n \leq 7$

Accuracy: about 10% for $n = 1$, unknown $n \neq 1$

Figure 5-30. Through Crack in a Cylinder — Circumferential (Ref 5-10)
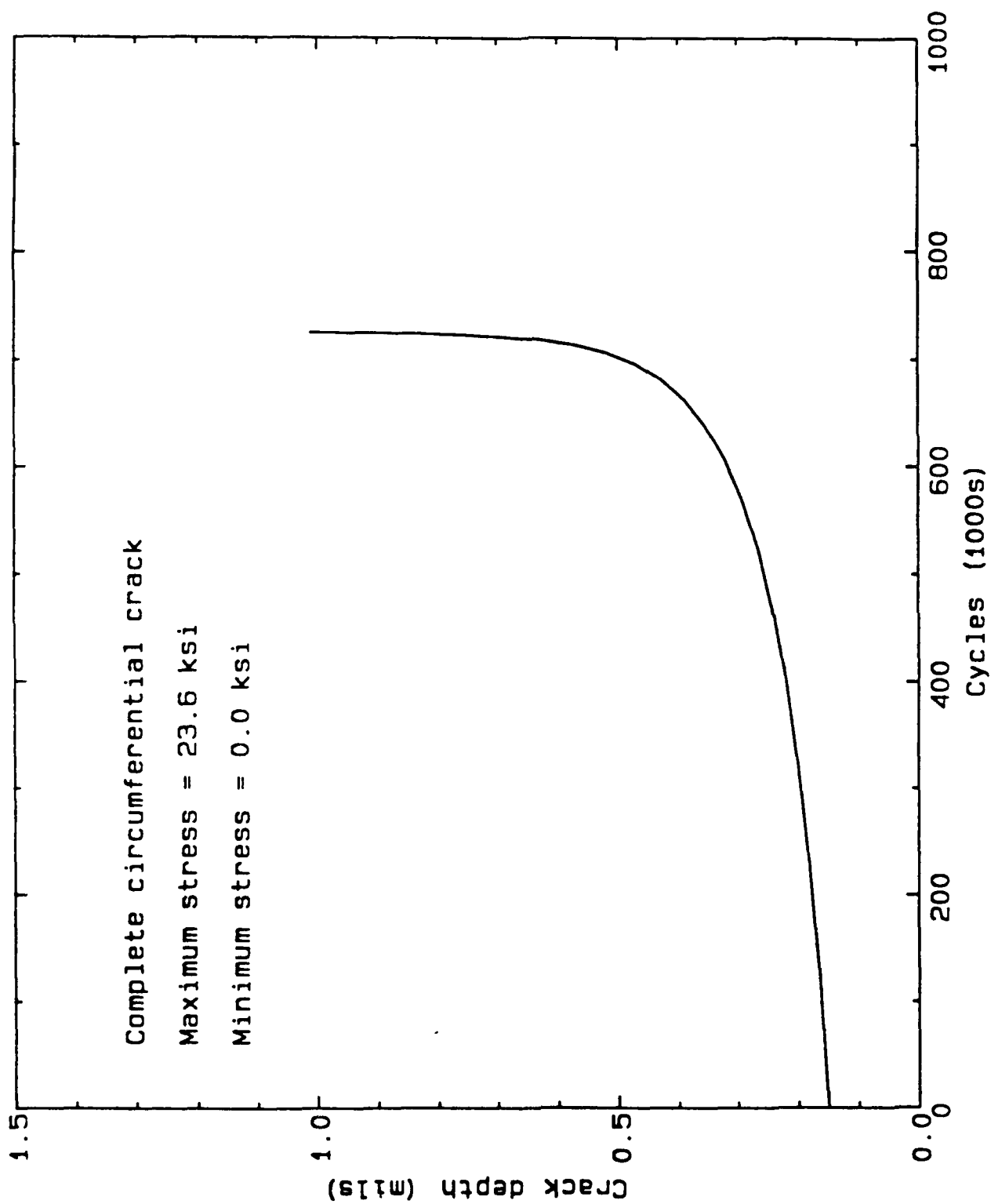
Figure 5-31. Fatigue Crack Depth as a Function of Number of Thermal Cycles for Complete Circumferential Crack

Complete circumferential crack

Maximum stress = 23.6 ksi

Minimum stress = 0.0 ksi
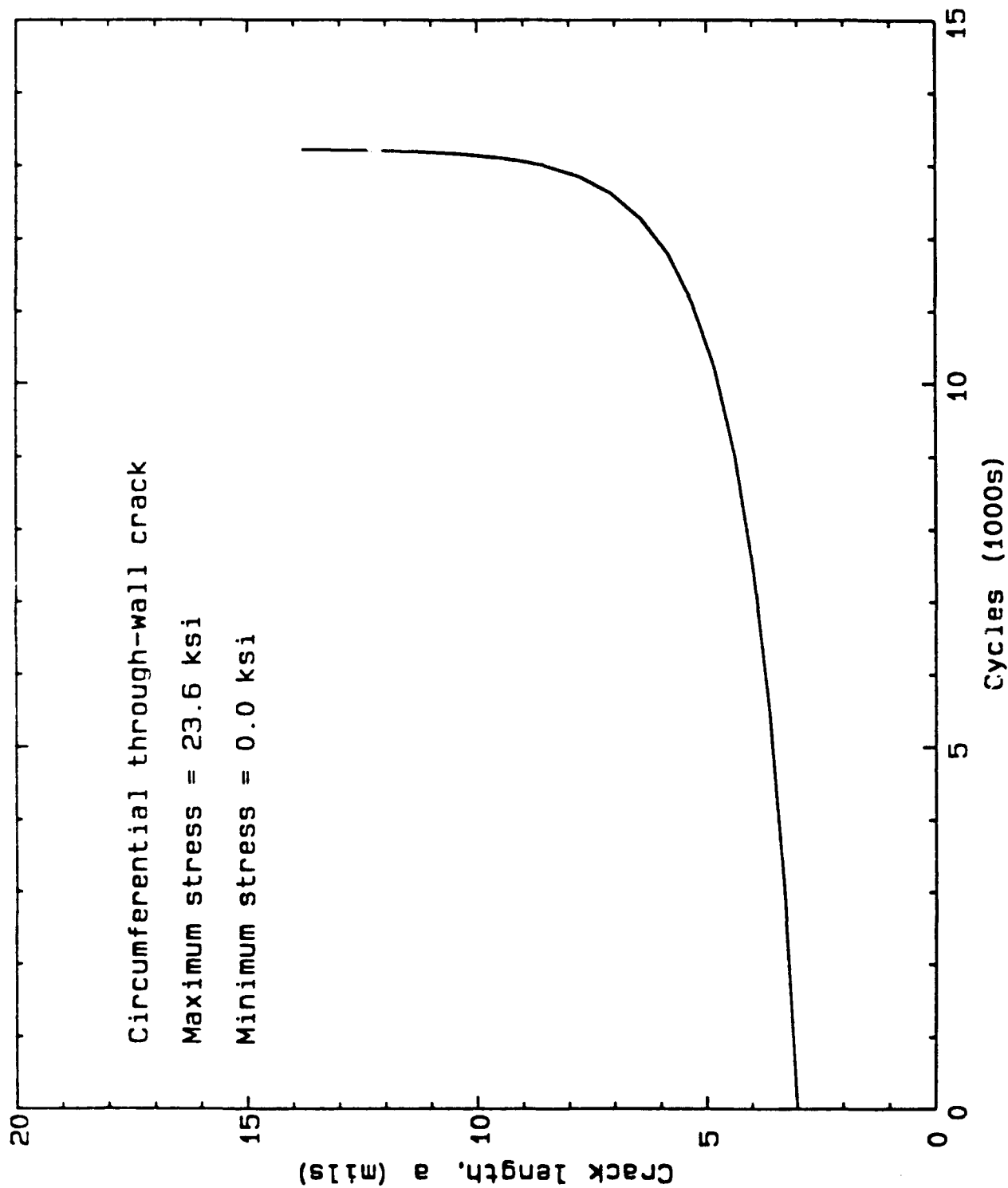
Figure 5-32. Fatigue Crack Depth as a Function of Number of Thermal Cycles for Through-Wall Crack

The computed fatigue crack propagation lives for both crack geometries analyzed are 2 to 3 orders of magnitude longer than observed in testing. Possible reasons for this overprediction of life are discussed below.

5.4.4 Discussion of Fatigue Life Predictions

Fatigue crack initiation and propagation lives computed in this evaluation greatly exceed observed lives for PTHs tested under laboratory conditions. The predicted location of fatigue cracking also differed from observed failures. The possible reasons for this lack of correlation with experimental observations are discussed below.

One potential reason for the lack of correlation with experimental results is the lack of a clear understanding of the behavior of the epoxy-glass PWB material throughout the extreme temperature range of the thermal cycle. The maximum temperature of the thermal cycle is within the range of the glass transition temperature of the epoxy. Strains measured by SwRI indicate a ratcheting-type reduction in the thickness of the PWB that may indicate inelastic deformation in the epoxy matrix at the high temperature end of the cycle. A detailed experimental evaluation of displacements and strains in the copper, epoxy, and glass fibers throughout the MIL-T-CYCLE temperature range could provide valuable information toward understanding the mechanisms involved in failure of plated through holes, and is therefore recommended.

Other significant unknowns are when and to what extent debonding occurs between the electro-deposited copper on the inside of a PTH and the epoxy-glass board material. Debonding has been observed in the vicinity of through-wall cracks in the copper barrel; however, it is not clear when debonding begins and how it may affect the stress and strain distributions in the adjacent copper. Greater damage has been observed in the copper barrel between copper trace layers rather than opposite the trace layers. Early debonding of the copper between traces could be a cause for the difference between observed and predicted cracking locations. The detailed experimental program, recommended above, could answer these questions.

Results of micro-sectioning of failed PTHs reported in Ref. 5-2 indicate that cracks often form adjacent to "resin-rich" zones in the epoxy-glass material. This indicates that the epoxy-glass material is not only anisotropic, but that the inhomogeneity of the composite may play an important role in the formation of fatigue cracks due to thermal cycling. The FE analysis modelled the epoxy-glass as a homogeneous anisotropic material, which would not account for localized zones of potentially high CTE. The effects of inhomogeneity could be accounted for in a more detailed FE analysis of the plated through hole.

Improved characterization of material properties could significantly improve the analytical predictions of fatigue crack initiation and propagation lives. The use of bulk copper cyclic stress-strain data, for example, may be adding to the underprediction of cyclic plastic strains.

Figure 5-24 shows a wide range of monotonic stress-strain behavior, and analogous differences in cyclic stress-strain properties could be present. Certain citations in the bibliography of Ref. 5-2 may provide new data for electro-deposited copper. These sources were not identified in time to be incorporated into the current analyses. Detailed characterization of the behavior of the PWB material at and near the glass transition temperature could help with the evaluation of the observed "ratcheting" of PWB thickness.

The crack driving force solutions used in the fatigue crack growth analysis cannot account for the nonuniformity of stresses on the (prospective) crack plane. This leads to errors in the crack growth results, especially for the part-through crack. Additional disagreement could be due to the fact that experimental observations often showed that several cracks initiate and grow together to coalesce, rather than a single crack growing to failure — as considered in the fracture mechanics analysis.

Although the results of this analytical evaluation of PTH cracking have not shown good agreement with experimental observations, they are significant in identifying the most important areas for further investigation. The potential for improved reliability in fatigue performance of plated through holes through accurate analytical modelling and supporting experimentation certainly warrants further investigation.

5.5 CONCLUSIONS

Techniques have been developed to measure:

- crack growth rate in specimens having the same material and manufacturing processes as PTHs.

- cycles to crack initiation, coalescence, and crack growth rates to fracture in actual PTHs.

- strains as a function of temperature and loading history in PTHs.

Mechanisms have been identified that appear to have significant impact on the fatigue life of PTHs. Although preliminary analytical modelling of PTH thermal cycling did not correlate well with observations, it has helped to identify the analytical aspects that need improvement.

The lack of agreement between observed and predicted fatigue lives of the thermally cycled PTHs is believed to be primarily due to oversimplification of the FEA and lack of adequate material property data. Observed complexities such as thermal racheting of the laminate and debonding of the barrel from the laminate must be accounted for if accurate strain and subsequent fatigue life predictions are to be obtained.

6.0 CONCLUSIONS

6.1 OVERALL SUMMARY AND CONCLUSIONS

This study examined the feasibility of applying traditional fracture mechanics used to analyze large structural systems to microscale elements typical of modern electronics. To accomplish this study a series of related experiments and analysis efforts was conducted on selected microscale elements, including wires having a diameter of 1 mil (25 μm). This is the smallest structure for which a combined experimental and analytical program has been performed successfully.

The key results relevant to the applicability of fracture mechanics to microscale phenomena in electronic assemblies were as follows:

- Crack initiation and propagation under cyclic loading occur in a wire having a sharp artificial initial defect.

- Power cycling through as-manufactured bond wires produces fatigue failures at the bonds under the action of thermal stresses through the progressive growth of a fatigue crack from the installation-induced damage.

Therefore, fracture mechanics is valid for damage tolerance analysis on the microscale.

Sections 6.2, 6.3, and 6.4 describe the conclusions regarding life prediction methods, material/configuration properties and characteristics, and experimental techniques.

6.2 LIFE PREDICTION METHODS

Fracture mechanics based life prediction methods for bond wires and plated through holes were developed and compared with the results of the fatigue tests performed in this program. The results were as follows.

6.2.1 Bond Wire Fatigue

Fracture mechanics predictions are not inconsistent with the fatigue test results reported here. Therefore, fracture mechanics based methods are applicable for predicting the failure free operating period (FFOP) of microelectronic bond wires under cyclic loading.

6.2.2 Plated Through Hole Fatigue

Fatigue crack initiation and propagation lives computed in this evaluation greatly exceed observed lives for PTHs tested under laboratory conditions. Therefore, fracture mechanics based PTH life models need further development.

To make FFOP predictions, the approach described in Ref. 5-2 is the best available. The approach utilizes strength of materials models to predict PTH strain as a function of PTH and

laminate geometry and material properties. The predicted copper strain range is input to a modified Manson universal slopes strain-life equation to calculate cycles to failure. In this approach, crack initiation and crack propagation are not treated explicitly. Rather, it is assumed that overall failure (fracture) of the PTH barrel occurs at the predicted number of cycles.

6.3 MATERIAL/CONFIGURATION PROPERTIES AND CHARACTERISTICS

Bond wire was selected at the beginning of this work to be used for many of the experiments. This selection was done on the bases of ease of analysis and test setup. As the research progressed, it was found that the selected aluminum 1% silicon wire was extremely fatigue resistant because of small grain structure and lack of inclusions. This made the generation of failure data more difficult for the wire loop tests. To generate data, an initial defect had to be seeded into the test specimens, while the wire bond experiments with the wire bonded at both ends did not require seeding of any initial defects. The analysis of the generated data indicated that the threshold cyclic stress intensity factor is nearly 10 times smaller than for bulk 2024-T3 aluminum, a result consistent with the behavior of short cracks in other size specimens. Additionally, it was found that the dependency of the crack growth rate on the crack driving force is very similar to that for bulk 2024-T3 aluminum. Macroscopic fracture mechanics predicts that a small diameter wire is more resistant to fatigue growth than a larger diameter wire. For a given cyclic stress, the threshold crack size is a larger fraction of the wire diameter than for the smaller wire. What this suggests is that, for a given stress cycle and an initial crack depth as a given fraction of the wire diameter, the finer wire will withstand more cycles before failure. An analytical life prediction model was developed for wire bonds using macroscopic fracture mechanics models with bulk material properties, except that a fatigue crack threshold of zero was used, resulting in a prediction not inconsistent with the fatigue test results. A zero value for fatigue crack threshold is commonly observed for short cracks.

The testing done on copper foils and plated through holes showed that a fracture mechanics approach to the analysis of failure mechanism is possible. Unfortunately, the analysis approach selected for use in these experiments was not sufficiently detailed to predict the behavior observed. Specifically, the thickness decreased with thermal cycles, resulting in compressive strain, forming a "thermal ratcheting" effect. Additionally, the copper plating debond from the epoxy-glass laminate was not sufficiently accounted for in the analytical modelling.

A detailed analysis of the problem of bond wire melting under current pulses was accomplished. It was found that a thermal runaway phenomenon was observed in the wire bond testing. At a critical combination of wire size, length, and current density the temperature of the midspan of the wire can theoretically increase without bounds. Calculations shown in Appendix C gave the relationship among the various controlling parameters.

6.4 EXPERIMENTAL TECHNIQUES

6.4.1 Fatigue Testing

The loop configuration is an effective device for mechanical bending cycling fatigue testing of fine wires.

The automated test fixture is effective for power cycling fatigue testing of wire bonds.

The constant-voltage pulse setup and the constant-current pulse setup each has advantages. However, the constant-current setup cannot achieve fatigue failures at as high a current as can the constant-voltage setup, because of the thermal runaway phenomenon.

6.4.2 Production of Initial Defects

A razor blade can place a controllable sharp initial defect into a fine wire for fatigue testing.

Focused ion milling can place a controllable starting flaw in copper plating.

6.4.3 Evaluation/Measurement

Transmission electron microscopy is an effective technique for evaluating the microstructure of fine wires.

Infrared thermography is an effective technique for measuring the temperature of fine wires.

Stereoimaging is an effective technique for measuring displacements and deformations of microscale structures such as fine wires and PTHs/PWBs.

7.0 RECOMMENDATIONS

With these extremely encouraging beginnings, a vigorous follow-up to realize the full potential for ERFM is recommended.

Additional work needs to be done to provide additional credibility to the use of traditional fracture mechanics analysis techniques for microscale structures typical of modern electronics. This work consists of experiments, development of improved analytical techniques for plated through hole/printed wiring board thermal cycling strain and fatigue crack growth, and application of these techniques in fracture control. Specific recommendations are presented below.

7.1 MATERIAL/CONFIGURATION PROPERTIES AND CHARACTERISTICS

Additional work remains to be done to define stress levels and material properties relevant to the environment encountered in specific microelectronic components. To verify the Al - 1% Si wire results indicated in this research and to establish a database for other materials/configurations, tests with large sample sizes are recommended to establish:

- initial defect size distribution
- strain-life (S-N) data for use in crack initiation prediction
- threshold crack driving force
- fatigue crack growth behavior
- electrical and thermal properties.

7.2 PLATED THROUGH HOLE/PRINTED WIRING BOARD THERMAL CYCLING

A detailed experimental evaluation of displacements and strains in the copper, epoxy, and glass fibers throughout the MIL-T-CYCLE temperature range is recommended to answer the following questions:

- when and to what extent debonding occurs between the electro-deposited copper on the inside of a PTH and the epoxy-glass board material. Debonding has been observed in the vicinity of through-wall cracks in the copper barrel; however, it is not clear whe·˙ debonding begins and how it may affect the stress and strain distributions in the adjacent copper. Greater damage has been observed in the copper barrel between copper trace layers rather than opposite the trace layers. Early debonding of the copper between traces could be a cause for the difference between observed and predicted cracking locations.

  Improved characterization of material properties to significantly improve the analytical predictions of fatigue crack initiation and propagation lives is recommended:

- cyclic stress-strain data for electro-deposited copper

- detailed characterization of the behavior of the PWB material at and near the glass transition temperature to help with the evaluation of the observed "racheting" of PWB thickness.

The development of a more detailed finite element model, accounting for the inhomogeneity of the composite, is recommended.

The development of a more complex fatigue growth analysis is recommended to include:

- crack driving force solutions that account for the nonuniformity of stresses on the (prospective) crack plane

- consideration that several cracks initiate and grow together to coalesce, rather than a single crack growing to failure.

7.3 FRACTURE CONTROL

Application of the results of this research to the improvement of fracture control techniques is recommended, specifically to achieve:

- more physically based, and thereby more effective, environmental stress screening regimens

- higher resolution nondestructive examination techniques.

8.0 REFERENCES

1-1   A. H. Burkhard, J. M. Kallis, L. B. Duncan, M. F. Kanninen, and D. O. Harris, "Application of Fracture Mechanics to Microscale Phenomena in Electronic Assemblies," in Advances in Fracture Research, Vol. 2, Proceedings of the Seventh International Conference on Fracture, Houston, Texas, March 1989, Pergamon Press, pp. 977-988.

1-2   A. H. Burkhard and C. E. Leak, "Durability Analysis Using Fracture Mechanics for Avionics Integrity," Institute of Environmental Sciences, 1991 Proceedings of the 37th Annual Technical Meeting, San Diego, California, May 6-10, 1991, pp. 335-342.

1-3   J. Kallis, K. Wong, I. Quart, L. Duncan, K. Hill, B. Rothschild, D. Buechler, and D. Evensen, "Latent Defect Life Model and Data," AFWAL-TR-86-3012, March 1986.

1-4   W. W. Bhagat and B. A. Tagg, "Design-for-Reliability Through Durability Analysis," 1991 Proc. Annual Reliability and Maintainability Symp., January 1991, pp. 516-520.

3-1   C.F. Popelar, M.F. Kanninen, D.L. Davidson, D.O. Harris, R.A. Sire, L.B. Duncan, J.M. Kallis, D.W. Buechler, and D.C. Sandkulla, "Experimentation and Analysis of Fatigue Crack Growth in Microscale Components," 23rd National Symposium on Fracture Mechanics, ASTM Committee E-24 on Fracture Mechanics, College Station, Texas, June 18-20, 1991.

3-2   M.F. Kanninen and C.H. Popelar, Advanced Fracture Mechanics, Oxford University Press, New York, 1985.

3-3   S.P. Timoshenko and J.M. Gere, Theory of Elastic Stability, McGraw-Hill, New York, pp. 76 - 82, 1961; see also: A.E.H.Love, A Treatise on the Mathematical Theory of Elasticity, 4th ed., Dover Publications, New York, pp. 399 - 413, 1905.

3-4   V. Geminov and I. Kopyev, "Fatigue in Thin Wires," Fatigue of Engineering Materials and Structures, Vol. 1, pp 329-331.

3-5   D.C. Sandkulla, "Compilation of Information Related to the Structural Behavior of Al-1% Si Wire Bond Interconnections in Microelectronics," Ref. No. 722630/1007, Interdepartmental Correspondence, Structural Mechanics Department, Hughes Aircraft Company, April 6, 1989. (Appendix A of this report)

3-6   ABAQUS, Example Problems Manual, Version 4.7, Hibbitt, Karlsson and Sorenson, Inc., 1988, pp. 3.2.4-1 - 3.2.4-8.

3-7   D.O. Harris, "Compliance of Edge-Cracked Wires in Bending," Failure Analysis Associates, FaAA-SF-R-90-05-01, May, 1988. (Updated version is Appendix B of this report)

3-8   L.A. James and W.J. Mills, "Review and Synthesis of Stress Intensity Factor Solutions Applicable to Cracks in Bolts," Engineering Fracture Mechanics, 30 (5), 1988.

3-9   North Texas State University Report to SwRI, January 1990.

3-10   D.O. Harris and D.D. Dedhia, "Calculations of Fatigue Crack Growth in Small Aluminum Wires," Failure Analysis Associates, FaAA-SF-R-90-04 11, April, 1990. (Appendix G of this report).

3-11   D.O. Harris , R.A. Sire, and D.D. Dedhia, "Predictions of Initiation and Growth of Fatigue Crack in Notched Wires," Failure Analysis Associates, FaAA-SF-R-90-02-09, February, 1990. (Appendix G of this report).

4-1   D.O. Harris, R.A. Sire, C.F. Popelar, M.F. Kanninen, D.L. Davidson, L.B. Duncan, J.M. Kallis, D.W. Buechler, P.G. Backes, and F. Reizman, "Fracture Mechanics Life Prediction for Microscale Components — with Application to Wire Bonding," Proc. 29th Annual International Reliability Physics Symposium, pp. 35-43, IEEE Catalog No. 91CH2974-4, April 1991.

4-2   F. Villella and M.F. Nowakowski, "Investigation of Fatigue Problem in 1-Mil-Diameter Thermocompression and Ultrasonic Bonding of Aluminum Wire," NASA Technical Memorandum, p. 2, 1970.

4-3   E.D. Metz, "Frequency Power Dependence of Mechanical Failures in Transistor Bonding Wires," Applied Science Report – Motorola Inc., pp. 1-2, 1966.

4-4   W. Day, J. Partridge, "Lead Failure Study for the Motorola 1-Mil Wedge-Bonded 1006323 Transistor," MIT Instrumental Laboratory, p. 5, 1967.

4-5   K.V. Ravi and E.M. Philofsky, "Reliability Improvement of Wire Bonds Subjected to Fatigue Stresses," Central Research Laboratories – Semiconductor Products Division, p. 143, 1972.

4-6   P.G. Backes, "Electromigration in Aluminum Bond Wires Subjected to Current Pulsing," ISTFA/91 Microelectronics Symposium, November 1991.

4-7   Chapman, A.J., Heat Transfer, Third Edition, Macmillan, New York, 1974.

4-8   MARC Finite Element Program, Version K3.3, MARC Analysis Research Corporation, Palo Alto, California, May 1989.

4-9   PATRAN Plus, Version 2.3a, PDA Engineering, Santa Ana, California, July 1988.

4-10   NASCRAC , NASA Crack Analysis Code, Version 2.01, Failure Analysis Associates®, Inc., Palo Alto, California, March 1989.

4-11   Fatigue Crack Growth Computer Program NASA/FLAGRO, JSC-22267, NASA Lyndon B. Johnson Space Center, Houston, Texas, 1988.

4-12   C. Boller and T. Seeger, Materials Data for Cyclic Loading, Part D: Aluminum and Titanium Alloys, Elsevier, Amsterdam, 1987.

4-13   C.F. Shih and A. Needleman, "Fully Plastic Crack Problems, Part 1: Solutions by a Penalty Method," Journal of Applied Mechanics, Vol. 51, March 1984, pp. 48-56.

4-14   V. Kumar, M.D. German, and F. Shih, "An Engineering Approach for Elastic- Plastic Fracture Analysis," Electric Power Research Institute Report EPRI-NP-1931, Palo Alto, California, 1981.

4-15 M. Abramowitz and S.A. Stegun, Handbook of Mathematical Functions, National Bureau of Standards Applied Mathematics Series 55, 1964.

5-1 D.L. Davidson, C.F. Popelar, M.F. Kanninen, D.O. Harris, R.A. Sire, L.B. Duncan, J.M. Kallis D.W. Buechler, and I.C. Chen, "Application of Fracture Mechanics to Plated-Through-Hole Thermal Cycling Fatigue," Symposium on Electronic Packaging in Harsh Environments, 1991 ASME (American Society of Mechanical Engineers) Winter Annual Meeting, Atlanta, GA, December 1-6, 1991.

The strain measurements also are described in the following papers:

D.L. Davidson, "Stereoimaging Determination of Strains in Surface Mounted Components and Plated Through Holes Resulting from Thermal Cycling," Spring Meeting, Materials Research Society, Anaheim, CA, 29 April - 4 May 1991.

D.L. Davidson, "Strains in Plated Through Holes and Surface Mounted Component Solder Joints Resulting from Thermal Cycling," ASM International's 4th Electronic Materials and Processing Conf., Montreal, 19-23 August 1991.

5-2 "Round Robin Reliability Evaluation of Small Diameter Plated Through Holes in Printed Wiring Boards," IPC-TR-579 Technical Report of the IPC, Lincolnwood, IL 60646, September 1988.

5-3 J. Lankford and D.L. Davidson, "The Role of Metallurgical Factors in Controlling the Growth of Small Fatigue Cracks" in **Small Fatigue Cracks**, TMS-AIME, Warrendale, PA (1986), pp. 51-71.

5-4 D.L. Davidson, "The Observation and Measurement of Displacements and Strain by Stereoimaging," **Scanning Electron Microscopy/1979/II**, SEM Inc., AMF O'Hare, IL (1979), pp. 79-86.

5-5 H.E. Boyer, "Atlas of Fatigue Curves," Am. Soc. for Metals, Metals Park, OH, 44073, 1986, p. 397.

5-6 D. Burgreen, "Review of Thermal Cycling" in **Fatigue at Elevated Temperatures**, ASTM STP 520, Am. Soc. Testing Mat., Philadelphia, PA, 1973, pp. 535-550.

5-7 S.J. Hudak and K.S. Chan, "In Search of a Driving Force to Characterize the Kinetics of Small Crack Growth" in **Small Fatigue Cracks**, TMS-AIME, Warrendale, PA (1986), pp. 379-405.

5-8 *MARC Finite Element Program, Version K.4*, MARC Analysis Research Corporation, Palo Alto, California, January 1990.

5-9 A. Saxena and S.D. Antolovich, "Low Cycle Fatigue, Fatigue Crack Propagation and Substructures in a Series of Polycrystalline Cu-Al Alloys," Met. Trans. A, Vol. 6A, September 1975, pp. 1809-1828.

5-10 *NASCRAC, NASA Crack Analysis Code, Version 2.23*, Failure Analysis Associates®, Inc., Menlo Park, California, 1990.

5-11 H. Ishii and K. Yukawa, "The Role of Dislocation Substructures in Fatigue Crack Propagation in Copper and Alpha Brass," Met. Trans. A, Vol. 10A, December 1979, pp. 1881-1887.

APPENDIX A

COMPILATION OF INFORMATION

INTERDEPARTMENTAL CORRESPONDENCE

To:	J. M. Kallis	**c:**	Distribution	**Date:**	06 April 1989	
Org:	72-26-10			**Ref:**	722630/1007	

Subject: Compilation of Information Related to the Structural Behavior of Al-1%Si Wire Bond Interconnections in Microelectronics

From: D. C. Sandkulla
Org: 72-26-33

Bldg: E1   **MS:** D102
Loc: EO **Phone:** 616-1365

The attached report summarizes information obtained on the structural behavior of Al-1% Si wire bonds in microelectronics. The work was performed as part of the Task III wire vibration studies for the Hughes/WRDC Electronics Reliability Fracture Mechanics (ERFM) contract. The report covers the following topics:

- o   Reliability deficiency

- o   Reliability enhancements

- o   Bonding fine Al-1%Si wire

- o   Al-1%Si wire and the influence of silicon dispersion

- o   Wire tensile fatigue and strength investigations

- o   Wire bending fatigue investigations

- o   In situ Al-1%Si wire bond fatigue investigations

The information contained in this report and the cited references will aid the development of wire life models.

Prepared by: _____
D. C. Sandkulla, Staff Engineer
Structural Mechanics Department

Approved by: _____
L. B. Duncan, Project Manager
Structural Mechanics Department
Product Analysis Laboratory

TABLE OF CONTENTS

Compilation of Information Related to The Structural Behavior of Al-1%Si Wire Bond Interconnections In Microelectronics.

I. Reliability deficiency.

A. Causes of integrated circuit failures. The average mix of the cause of failures of military-screened integrated circuits during the four years preceding a study published in May 1988 is shown in Figure 1. <u>Wire bonds are the largest single cause of field failures</u> for any integrated circuit part in both commercial and military applications. These failure percentages are typical for devices in non-plastic packages [14].

B. Dominant Al-1%Si ultrasonic wedge bond failure location and mode. A great problem in the use of Al wires is the fatigue cracking at the transition point between bond and wire loop as shown in Figure 2. This is termed the <u>heel area</u> and represents an extreme weak point in service, particularly when vibration stressed during mission exposures. The wire loop is also subjected to fatigue stressing in the <u>bonding process</u> itself, which is also shown in Figure 2 [3].

Wire bond failures can be caused by <u>high-cycle vibration or low-cycle fatigue</u> thermal cycling. Thermal cycling failure is caused by mismatch of coefficients of thermal expansion of the wires and the materials to which they are bonded. Maximum <u>flexure loading</u> generally occurs at the heels of the bonds [15].

The effects of <u>humidity</u> and <u>direct current</u> on the fatigue behavior of aluminum bonded wire were also found significant [6].

II. Reliability enhancements.

Ultrasonic bonding with aluminum-alloy wire is generally the chosen method in <u>non-plastic packages</u> when maximum bond reliability is required [1].

A. Influence of alloyed aluminum. Ultrasonic bonding using aluminum-alloy wire was developed in the late 1950's as a means of <u>avoiding the "purple plague"</u> obtained when Au wire was bonded to Al chip metallization [1].

Aluminum alloy wire is less likely to sag than Au wire when both are exposed to elevated temperatures and, because Al is a less dense metal than Au, there is less wire flexing in hermetic packages subjected to vibration or g-loading [1].

Higher strength than Au wire and practically unlimited ageing resista ` ɘ [3].

<div align="center">1</div>

B.   Motivation for using silicon. Very pure Al is too soft to be easily drawn to a fine diameter. Therefore, aluminum is alloyed with silicon or magnesium to supply the necessary toughness for drawing [1].

Silicon provides a barrier against the danger of semiconductor poisoning [1].

III.   Bonding fine Al-1% Si wire

Wedge shaped ultrasonic (U/S) bonding of Al-1%Si wire dominates current electronics industry practice [1]. Investigations directed toward the more economical ball bonding process are ongoing [1,16]. The following highlights the U/S bonding of Al-1%Si wire and its influence.

A.   Ultrasonic bonding. In ultrasonic (U/S) bonding, the wire is guided to the bonding site, then pressed onto the surface by a stylus ("bonding wedge") to make the first bond. While the wire is firmly clamped between the bonding tool and the bond pad, a burst of ultrasonic vibration is applied to the wedge. The combination of the pressure and the vibration accomplishes a metallurgical cold weld between the wire and the pad metallization. The function of the ultrasonic energy is to enhance wire deformation and break up the surface oxides at the bonding site. These massive plastic deformations expose atomically clean fresh metal which cold welds very readily. The second bond (stitch bond) site is then laid down parallel to the bond pad plane. The wire is constrained to follow the general direction of the first bond footprint axis in moving to the second bond site as shown in Figure 3. In contrast, the ball bond (first bond) symmetry provided during thermocompression (T/C) and thermosonic (T/S) bonding processes allow the stitch bond (second bond) to be made anywhere within a 360 degree surrounding arc [1].

The acoustic energy frees the dislocations from their pinned positions which then allow the metal to flow under the low compressive force of the bonder. Thus heat at the bond is a by-product of the bonding process and not necessary to cause the bond [2].

B.   Influence of bonding stages [3].   The individual stages of the bonding process can be seen in the electron microscope photographs in Figure 2 as described in the following:

a. After U/S bonding (bond phase 1), the bond area is in a heavily deformed condition. Pronounced surface structuring and high internal defect density induced by U/S stressing, gives numerous crack nuclei or propagation points for the next bond phase. Critical parameters here are sonic intensity (also amplitude and duration), sonic transducer form and, most important, wire condition.

b.   During the next stage of the low frequency bending cycle a fold is developed in the heel zone on bending up (bond phase 2), which results in a crack widening and opening on bending down (bond phase 3).

C. **Contaminants induced.** Contaminants on the surface of the substrate or post that are not swept away by the ultrasonic action can importantly affect bond quality [2].

D. **U/S bonding parameters for best bonds.** A considerable amount of experimental work has been carried out on U/S to thin films using ball and wedge bonding techniques which show low failure rates. But of these failures, examination has shown that approximately 30% were due to defective bonds. Subsequent investigative work looked into the mechanism of welding and went on to define the parameters to obtain good bonds. Ravi [21] presents an investigation directed at such an evaluation. After determining these parameters and the specifications of the wire needed to give strong bonds, there are two significant variables that should be observed and controlled. One of these is the importance of the relationship between bond pull strength and bond deformation (measured in wire diameters) as shown in Figure 4. The second variable is the loop height. Studies performed on U/S bonded 1mil Al-1%Si wire exposed to power or thermal cycling-induced wire-flexure fatigue indicate that optimal practical protection is provided when the loop height to bond length ratio is on the order of 25% [2].

E. **Influence of U/S vibrations.** Vibrations detected when a work table is touched correspond to motions of the order of 1 mil. Vibrations of this magnitude can seriously affect the quality of U/S bonds made with small wire of the order of 1 mil diameter [2].

U/S bonding (e.g., on the semi-conductor crystal) subjects the wires to a high frequency fatigue stressing at 30 to 70 kHz. During loop forming for the second contact, there is a further, now low frequency, alternating bending stressing, resulting from bending-up after U/S bonding, and subsequent bending-down for loop forming [3].

IV. **Al-1%Si wire and the influence of silicon dispersion.**

The tensile properties and fracture characteristics of Al-1%Si wires can be related to the nature of the silicon dispersion in the aluminum matrix [4].

A. **Silicon solubility in aluminum.** Since the solubility of silicon in aluminum is negligible below 250 C as shown in Figure 5 [5], the silicon in the wire would be present as a second phase [4].

B. **Vendor.** The tensile mechanical behavior of wires received from a vendor were found to vary greatly depending on the size and distribution of the silicon and on the strain rate of deformation. Wires were categorized into three types according to their ductility. Type I wire had elongations less than 3% with nonuniform silicon dispersion and particles as large as 2 microns embedded in the aluminum. Type II had elongations from 3 to 7% with a finer silicon dispersion and occasional large particles with an average of .2 microns and particle density of 1E12 per cu cm. The Type III wire had elongations greater

3

than 7% with a fine uniform silicon particle distribution density of 1E15 per cu cm and an average particle size of 200 angstroms. Tensile failures of Type I, II, and III wires were characterized as brittle non-plastic, brittle with some plastic, and ductile fracture in cup and cone, respectively [4].

Another comparative study [24] determined the elastic, tensile and load relaxation properties for bonding wires obtained from three manufacturers (A, B, and C). The nominal diameter and composition of the wire surveyed are 32 micrometers (just larger than 1 mil) and Al-1%Si. The actual chemical composition of these wires are shown in Table 1. Wires A and C were prepared by a drawing process while wires B were processed by extrusion. The nominal breaking load and elongation ranges indicated by the manufacturers are listed in Table 2. The vendor tests were performed in accordance with ASTM standard F 219 [23]. The tensile properties of the wires, as measured in this study, were measured under a constant displacement rate of 0.01 mm/sec using the apparatus shown in Figure 22 and documented in Reference 22. The specimen length was 15 mm resulting in a nominal strain rate of 7E-4 per second. The results of tensile tests are summarizes in Table 3. Each result is based on at least three measurements. In the same table breaking load and elongation values determined by the manufacturers are shown in parentheses. The stiffness (modulus), as shown in Figure 23, of the wires was found to depend on the method of fabrication as well as on thermal and mechanical history. Although the specified breaking load and elongation values of the wires were essentially the same, load relaxation tests revealed substantial differences in the time dependent flow properties of the wires as shown in Figures 24 and 25. As measured from the tensile curves, two of the wires (wires A and B) showed hardening , while wire C showed softening as shown in Figure 26 [24].

Still another in-depth investigation [25] into the ultrasonic bonding , annealing and low temperature aging characteristics of aluminum alloy microelectronic interconnect wire was performed to determine the characteristics of Al-1%Si, Al-1%Mg, and Al-0.5%Mg bonding wires from different vendors. To determine annealing characteristics, a different spool of each wire was placed in an air atmosphere for one hour at a temperature ranging from 125 to 250 C. All spools of a particular wire came from the same bar with the vendor producing the wire being varied as shown in Table 2 of Figure 27. The mechanical properties of each spool were ascertained before and after annealing by using an Instron 1130 tensile test machine with a ten inch gage length and a strain rate of one inch per minute. Five tensile tests per spool determined average properties. Figure 27 illustrates that the ultimate tensile strength of the wires tested all tend to decrease in a similar manner with increasing anneal temperature. This figure also indicates a range of elongation values resulting from vendor processing. These results indicate that the tensile properties of dispersion strengthened Al-1%Si wires are sensitive to silicon particle size and silicon particle distribution, while those of solid solution strengthened Al-Mg wire are dependent upon magnesium concentration [25].

Wire from one wire manufacturer is not necessarily interchangeable with that from another, even when both products are produced to meet the same purchase specification [1]. See the influence of strain rate and the lack of

4

sensitivity to silicon dispersion at the vendor test rate in part F and see part V.D for the impact of defect density and test specimen length.

C.   **Ductility.** The most striking effect of silicon particle size and distribution was upon the ductility of the wires. When a uniform particle distribution with particle sizes of several hundred angstroms was present, a large ductility maximum at strain rates around 1E-4 per sec was observed. This ductility maximum disappeared with increasing particle size, while the strength was maintained. A loss of strength is observed when the silicon particle size increases above 2 microns. Load-elongation curves for the different types of wires described in part B above are shown in Figure 11 [4]. The test configuration was similar to that shown in Figure 12 obtained from Reference 17.

A ductility maximum is accomplished by serrated yielding related to dislocation-dispersed phase interaction. A fine dispersion of silicon causes dislocation locking and unlocking thereby extending the region of wire undergoing deformation. The deformation is not confined to a few slip planes but a number of slip sources which become activated because of the impeding of dislocations by the dispersed silicon [4].

The influence of temperature is also presented in Figure 27 [25] with still more data in Table 3 [24]. True stress-strain curves are shown in Figure 26 [24].

D.   **Elevated temperature aging.** Aging the wires at elevated temperature results in a loss in strength and ductility because of silicon particle growth as seen in Figure 6. These data points were based on 15 minute exposures at each temperature. Aging of Type III wires above 200 C for longer than 30 sec results in loss of ductility maximum and serrated yielding [4]. Aging influences shown in Figure 27 for various aluminum alloys and vendor sources indicate a universal trend in ultimate strength decrease with increasing temperature with elongations being quite variable for Al-1%Si wire types. Silicon particle coarsening in the Al-1%Si wires caused embrittlement at annealing temperatures as low as 150 C [25] (also, see vendor discussion above).

E.   **Shelf aging.** Slip bands are not observed in unaged wires. Growth of particles by aging wires results in a loss in strength and ductility [4]. This aging is caused by the relaxation of cold working stresses induced during drawing. The ultimate tensile strength always falls, perhaps as much as several grams in hard-temper 1 mil Al-1%Si wire, but the elongation may either rise or fall [1].

Low temperature annealing, which was performed to simulate prolonged storage of the wires, resulted in changes in the properties of the wires [24].

F.   **Strain rate.** As would be expected for fcc metals, the yield and tensile strengths are not greatly affected by the change in the strain rate. The large ductility in the intermediate strain rate range is accomplished by serrated yielding of the wire. Figure 7 is a plot of ductility as a function of strain rate for Type II and III wire. Type III wire displays a ductility maximum and serrated yielding over a strain rate range around 1E-4 per sec., whereas no serrated yielding or ductility maximum was observed for Type II wire [4]. Notice that

5

vendor performed tests near 1.7E-3 per sec. are insensitive to silicon dispersions of at least that in Type II wire.

G. **Tensile strength.** The ultimate tensile strength of the as-received Al-1%Si wire (based on the original area of the 0.001 inch diameter wire) was approximately 38 ksi. This is the tensile strength one would expect of the cold-worked aluminum alloy. The <9 ksi strength levels found in the integrated circuit wire and the heat-treated wire are values expected for the alloy in the annealed condition. The tensile test fixture and load train used to obtain this data is shown in Figure 12 [17]. Also, see Tables 1, 2, and 3 as well as the various figures depicting the influences of temperature aging, strain rate, vendor, and tensile test type (sample length and defect density) on ultimate and yield load/stress levels.

H. **Stiffness [24].** Stiffness of the Young's modulus is a material property, which can be determined from the stress-strain curves in the elastic region (as in Figure 26 [24]). In wires that have the same composition, the stiffness can still be different because of different grain texture. Figure 23 indicates the differences in effective modulus as a function of yield stress for different wires. As discussed in part B above, vendor variability in texture is significant for the moduli evaluated in the Al-1%Si wires. Room temperature annealing does not appear significant for the Al-1%Si wire tested (type C). These stiffness results include the effect of anelasticity.

I. **Load relaxation [24].** It has been suggested that the load relaxation properties of bonding wires can be used to distinguish subtle differences in the microstructure of the wires. The instrument shown in Figure 22 was used to perform a relaxation study (see part B above for additional information on this study). A summary of the results of the load relaxation tests conducted in this work is shown in Figure 24. The plots in Figure 25 exhibit a concave downward shape which indicates that the rate of deformation is controlled by diffusion processes. Although the specified breaking load and elongation values of the wires were essentially the same, load relaxation tests revealed substantial differences in the time dependent flow properties of the wires.

V. **Wire tensile fatigue and strength investigations.**

A. **Fatigue of very thin copper and gold wires show a different failure mode for 1 and 4 mil diameters [8].** In tension testing of gold wires, "thick" (about 4 mils) wire fails by a transcrystalline fracture without large-scale deformation (necking) while the thin (1 mil) wires were regularly observed to neck down, yielding a chisel-edge rupture. A distinct difference in surface topology of the "thick" and "thin" wires corresponds to a difference in fracture mode. Tension-tension stress cycle amplitudes between yield and ultimate are supported by thick wires only up to 100 to 1000 cycles, whereas the thin wires sustained approximately 100000 cycles before rupture. These results were rationalized by arguments based on the absence of extrusion-like features on thin wire surfaces up to 100000 cycles which may be interpreted as the absence of persistent slip bands of the type observed in macroscopic specimens. This stands in contrast to the thick wires, which resembled typical surface structure of fatigued copper single crystals (another fcc metal). A

6

schematic arrangement of the fatigue test apparatus and the test results obtained are shown in Figure 8.

B.   **Fracture and fatigue of high strength filaments [13].** Work in the area of composites has required the evaluation of the failure characteristics of the thin fibers which strengthen matrix materials. Graphite and S-glass filaments and tungsten wire on the order of 1 mil in diameter were evaluated. The details of the high frequency fatigue testing machine are included in Reference 13 with a schematic shown in Figure 9. Monotonic strength evaluations were performed using the test set up shown in Figure 10.

C.   **Hughes strength and fatigue tests of Al-1%Si wire.** Tests were performed at room temperature on as-received 1 mil diameter Al-1%Si wire obtained from the Sigmund Cohn Corporation (see label, Figure 13). This wire complies with Hughes standard HMS 20-1603 and falls under the product designation Type II Class 2 [9]. An Instron 35052 equipped with a 500 gram load cell was used with the test set up shown in Figure 14. The 1 mil wire with a 1 inch gage length was epoxied to relatively stiff wires designed to eliminated load eccentricities. The test configuration was similar to that shown in Figure 12.

1.   **Monotonic tensile test.** Survey tests using a small sample size were performed on 1 and 2 inch gage length specimens. These samples were run at a cross head speed of 0.05 in/min. This small sample size suggests that the wire's elastic modulus, tensile strength (based on a 1 mil diameter), and elongation were near 9 msi, 43 ksi, and 2% respectively. A load deflection plot for a 1 inch gage length sample is shown in Figure 15. Photos of scanning electron microscope (SEM) views of the failures indicate extreme necking to a ductile rupture as shown in Figure 16.

2.   **Fatigue tensile test.** A tension-tension fatigue test cycled from approximately 1 to 9 grams (about 5 to 50% of ultimate capacity) at 5 Hz was attempted. The test can not be classified as constant displacement or load. Initially, a constant displacement was applied because the apparatus would not accommodate a constant load experiment without costly alteration. The progressive elongation of the wire with cycling tended to lower the mean tensile load with a resulting slack lower load condition. To avoid this undesirable situation, the mean load level was increased every 10000 cycles to achieve about a 1 to 9 gram cyclic load range. This did not provide a control for the fatigue inducing parameter and the test was terminated after 343500 cycles without failure. It was concluded that future tension-tension fatigue tests should be performed under constant load conditions because of wire ductility. Furthermore, this test was thought to exemplify (more closely) the constant load rather than displacement fatigue evaluation. This would imply that support of a similar constant load range could continue for test durations exceeding 343500 cycles.

D.   **The influence of sample length [24].** The differences between two tests performed using different gage lengths and strain rates are discussed in Reference 24. In the standard method (ASTM F 219 [23]) of testing the sample length is 245 mm and the normal strain rate in the sample during testing is about 1.7E-3 per sec, while their work was performed using 15 mm

7

A-11

and 7E-4 per sec, correspondingly. Generally, the effect of increasing strain rate is to increase the breaking load and to decrease elongation. However, the difference in strain rates was considered negligible in this respect, thus leaving the different gauge lengths to be responsible for the differences in the results (This contention appears true for gold wires but differs for fine well distibuted silicon particle Al-1%Si wires which are sensitive to strain rates near 7E-4 as shown in Figure 7 [4].). Reference 24 contends that the most likely explanation is that the <u>results are controlled by the inhomogeneities and defects in the wires</u>. The distribution of defects seems to be such that in a long sample the probability of finding a particular type of defect is high and the results are consistent from sample to sample. <u>In a short specimen</u>, however, <u>the probability of finding a particular type of defect seems to be much less, thus yielding better results on the average, but with much more scatter.</u> Consequently, it is anticipated that results from short specimens under these conditions are more descriptive of both structural differences and defect densities of the wires. The results of the reference 24 study for gold wire are shown in Figure 28 on a plot of breaking load versus elongation. The figure compares the standard test method results to that of their study. It was suggested that a similar trend could be expected for Al-1%Si wire with significant variability in the short specimen test being expected.

VI. Wire bending fatigue investigations.

A.   Near-bond test simulation for Al-1%Si and other fine wire. Fatigue testing in conjunction with metallurgical examination has been found useful for the selection of superfine wires with favorable fatigue properties. Figure 17 shows the principle of such a fatigue tester schematically. A defined test notch is impressed in the wire samples by the grips. The bending angle, predetermined by the crank setting of the drive, is taken as a measure of stress. The low frequency alternating bending test is made at constant bending angle. By testing to failure point by variation of the bending angle, Wohler curves are obtained which provide a good estimation of fatigue behavior. Such curves for superfine wires of a heterogeneous and a homogeneous AlSi and AlCu4 alloy are given in Figure 18. The good fatigue behavior of the AlCu4 alloy, the less good behavior of the homogeneous AlSi alloy and the poor properties of the heterogeneous AlSi alloy with low Fe, Zn and Cu additions (<0.4%) are evident. The reason for the poor fatigue properties is to be found in the precipitation particles which are relatively large compared with the cross section area. Longitudinal microsections of the AlSi wires in homogeneous and heterogeneous conditions indicate that the boundaries between precipitates and matrix are points of weakness which promote crack formation and propagation under fatigue loading. Corresponding fatigue tests on bonded wires show comparable fatigue trends, but the number of load cycles to failure are significantly lower than for unbonded wires. Clear improvements in the bond behavior of Al wires can thus be obtained by the control of grain structure [3].

B.   Hughes fine-wire-cantilever vibrated sinusoidally. This test consists of a fine wire (about 1 mil) cantilever fixtured to a shaker table capable of fatiguing the wire using sinusoidal vibration. The response stress level at the base is determined from the deformed shape caused by the constant frequency base acceleration input. The number of cycles to crack initiation and various

propagation points to cantilever detachment are obtained by the product of the test frequency and the accumulated time to these occurances. Accordingly, performing this test for different specimen stress levels to obtain corresponding cycles to crack initiation and various crack propagation stages to detachment failure will produce data in support of a life prediction model development. This could take on the form of S-N curves or fracture mechanics relations. The following is a list of considerations related to a test of this type:

1. **Measuring peak deformation.** This could be accomplished through the use of slow exposure photography or high speed video taping. High speed videos with optical aides at 6000 Hz are available. The identification of the complete deformed shape could effectively nullify concerns related to damping, atmospheric resistance and large deflections of the cantilever. Deformations must be large enough to measure accurately.

2. **Ease of viewing and measuring crack data.** To obtain crack initiation and propagation data (if they occur), the test must be stopped periodically to inspect the specimens. Given that failures are expected at the base of the cantilever, this location could be viewed while the cantilever is in a deformed configuration similar to, but not in excess of, the vibration response deformed shape. The orientation of the specimen must be considered along with the inspection of both high stress surfaces where cracks could occur in reversed bending. It has been suggested that viewing in a scanning electron microscope (SEM) would reveal the best results because of this instruments large depth of field. SEMs capable of holding 14 by 14 inch fixturing are available.

3. **Cycle counting estimates.** As previously described, performing each test at a constant frequency will facilitate cycle counting by time measurement to a desired occurrence (e.g., crack initiation). It is suggested that a trial run be performed to obtain the detachment failure time. The actual test can the be run to some fraction of this time (e.g., 60% of the detachment failure time) wereupon the test would be stopped for crack inspection. Subsequent inspections could then be performed at a fraction of the remaining life (e.g., 10% of the detachment failure time).

4. **Wire cantilever length.** This is a function of the desired deformed shape measurement limitation in part 2 above. For a given base input, the response deformation can be estimated using fundamental beam theory. This estimate is applicable for tip deflections smaller than 30% of the length in a vacuum. The extreme surface to volume influences of fine wire (e.g., 4000 for 1 mil wire) render the test sensitive to atmospheric resistance in air. A rough calculation for a half inch cantilever tested at resonance indicates that atmospheric resistance in air is approximately nine times the wires inertial loading. These factors should be considered to insure that measurable deflection responses will occur for available base acceleration input capabilities. The capability of the cantilever to support itself must also be addressed. A 1 mil wire cantilevered a half inch was found capable of self support with a length to width aspect ratio of 500.

5. Wire end weight. Preliminary studies suggest that the mass of the wire is adequate to achieve stress levels necessary to induce timely wire failures. However, the use of an end weight could facilitate tuning natural frequencies and reducing required input accelerations found necessary to reduce test time or accommodate existing test equipment. If possible, the use of end weights should be avoided because the difficulties associated with end weight attachment are likely to damage small wires and introduce concerns with respect to test repeatability (e.g., symmetry of the weight).

6. Test frequency. The test could be performed at or off resonance. Tests performed at resonance will require a pre-test vibration survey at varied frequency to determine the resonance frequency. The frequency corresponding to the largest response deformation at a constant acceleration input is the resonant frequency. Tests performed at this frequency will provide the largest response deformations for any level of input. If degradation of the wire material produces a shift in the natural frequency because of increased base flexibility, tests initially performed at resonance may require constant monitoring of deformed shapes (i.e., stress levels) as responses shift off resonance. The sensitivities with respect to induced base flexibility and off resonance shifts are academic without being proven through test. If this phenomena is significant, testing at resonance could be used to detect the degradation of wire material seen as a decrease in response. Such an approach could conceivably be used to induce cracks at resonance with arrest occurring on off resonance shifts. In an attempt to perform a constant stress experiment, test frequencies off resonance could provide the least variation in responses resulting from specimen natural frequency shifts. An analytical evaluation of peak base stress response for a 1 mil half inch long cantilever (see Figure 19) indicates that linear responses in a vacuum are insensitive to input frequencies less than half its natural frequency. Consequently, it is recommended that below resonance tests be performed.

7. Base input acceleration. The base input is influenced by the shaker limitations, the specimen natural frequency, the desired test frequency, and the desired response stress level. When determining the specimen size and the test frequency for various desired response stress levels, the shaker selected for the test must be capable of the task.

8. Damping. The system damping can be measured during the vibration survey of an uncracked wire. The system estimate for design could be a Q equal to the square root of the wire natural frequency. The significance of damping as influenced by cracks is unknown. Possible components are material damping, acoustic radiation and friction on the crack if nucleated. The use of a video measurement of the deformed shape before and during crack growth would provide continuous stress level data and alleviate concerns related to damping.

9. Surface to volume ratio and air resistance. The extreme surface to volume influences of fine wire (e.g., 4000 for 1 mil wire) render the test sensitive to atmospheric resistance in air. A rough calculation for a half inch cantilever tested at resonance indicates that atmospheric resistance in air is approximately nine times the wires inertial loading.

10

10. Fixture. A test fixture should consider the following:

   a.   The direction of vibration to reduce gravitational influences (i.e., a vertical cantilever).

   b.   Repeatability in wire attachment and care.

   c.   The number of specimens tested at one time.

   d.   Dynamically it must act as a rigid body.

   e.   Possible adaption for deformed shape crack viewing and SEM viewing limitations.

   f.   Ease of specimen removal for viewing cracks in wires and changing specimens. Consideration must be given to consistent orientation of specimens during test.

   g.   The support must be conductive for SEM viewing (e.g., the epoxy used to bond the wire base must be conductive).

C.   **Other bending test configurations.** The literature on bending fatigue testing of fine wire is limited. Aside from the aforementioned, this work is summarized in Figures 20 [18] and 21 [12,19] and References 12, 18, 19, and 20.

VII.   **In situ Al-1%Si wire bond fatigue investigations.**

A.   **In situ bond pull tests [17].** To investigate the strength of the wire in the packaged integrated circuit device, a technique was developed to stress the wire loops in situ until failure. The loads applied, nature of the fracture, and its location were recorded. The test set up and a load path diagram are shown in Figure 29. As an example of this approach, the Al-1%Si flying leads on several circuits of a given design were tested in two conditions: (1) devices were tested in the "as-received" condition, and (2) after a storage period at elevated temperature. In the as-received devices, the percentage of total bond failures was 12% and the average failure load of the wire was 3.7 g. The percentage of bond failures in the devices stored at elevated temperature was 52% and the average failure load of the wire was 3.5 g. The bond failure loads varied randomly from 1.0 to 4.0 g. It can be seen, therefore, that the elevated temperature storage did not markedly affect wire strength but did weaken the wire bonds. In this particular test program, all the wire-bond failures occurring in the devices stored at elevated temperature were in the heel of the package lead bond.

B.   **In situ on-off mode fatigue investigation [11, 21].** The fatigue of wire bonds due to repeated flexure when semiconductor devices are operated in an on-off mode (see Figure 30) has been investigated. Upon the application of power to a semiconductor device, there are two causes of flexure in wire bonds: (1) an immediate jerk due to I2R heating of the individual wires and (2) a more gradual flex due to package heating. An accelerated fatigue testing

11

apparatus (see Figure 31) was constructed and the major fatigue variables, aluminum alloy composition and bonding mechanism, were tested. The data showed Al-1%Mg wires to exhibit superior fatigue characteristics (by about a factor of five as seen in Figure 32) compared to Al-1%Cu or Al-1%Si and ultrasonic bonding to be better than thermosocompression bonding (by a factor of two as seen in Figure 33) for fatigue resistance. Reference 21 also discusses the influence of bonding at the heel (see Figure 34) and proposes an idealized mechanism of crack propagation in dispersion hardened and solid solution hardened alloys (see Figure 35). Based on these results highly reliable devices were fabricated using Al-1%Mg wire with ultrasonic bonding which withstood 1.2E5 power cycles with no failures.

C.   **In situ testing of the effect of humidity and electric current on the fatigue behavior of aluminum bond wire [6].** The high strain, low cycle fatigue behavior of Al-1%Si wire bonds used in microcircuits were evaluated at cyclic strain amplitudes giving less than 1000 cycles to failure.   In particular, the effects of (i) cyclic plastic strain amplitude, (ii) humidity and (iii) direct current were investigated (the apparatus used was similar to that in Figure 2). Cyclic stress-strain curves indicate that life under strain controlled fatigue decreases with increasing plastic strain amplitude. Regardless of humidity and electric current, the wire bond progressively softened to failure. At equivalent plastic strain amplitudes, the presence of a humid environment causes significant degradation in fatigue life of the wire bond. At constant total strain amplitude, fatigue life was also found to decrease with increasing values of direct current. The fatigue curves generated by this study are presented in Figure 36. The kinetics of the fatigue process and the mechanisms responsible for the degradation in fatigue life and durability of the bond wire in humid environments and at increasing currents is discussed.

REFERENCES

1.   B. L. Gehman, "Bonding Wire Microelectronic Interconnections", IEEE Transactions on Components, Hybrids, and Manufacturing Technology, Vol. CHMT-3, No. 3, p. 375-83, September 1980.

2.   J. Kleis, "A Guide to Improved Bonding Wire Selection and Utilization", Cooper Division of the Sterndent Corporation, Mt. Vernon, New York,

3.   A. Biachoff and H. Theide, "Metallurgical Aspects of Processing and Use of Superfine Wires In Semi-conductor Technology", Wire 5, p. 202-05, 1981.

4.   K. V. Ravi and E. Philofsky, "The Structure and Mechanical Properties of Fine Diameter Al-1%Si Wire", Metallurgical Transactions, Vol. 2, p. 711-17, March 1971.

5.   "American Society for Metals Handbook", Eighth Edition, Vol. 8, p. 263.

6.   D. Maguire, B. R. Livesay, and T. S. Srivatsan, "The Effect of Humidity and Electric Current On The Fatigue Behavior of Aluminum Bonded Wire", Electromagnetics Laboratory, Georgia Institute of Technology.

12

7.   G. Abowitz, "Variation of Properties of Fine Wires With Diameter", WPAFB Doc No. ASC-TDR-63-641, Aug. 1963.

8   R. Hofbeck, K. Hausmann, and B. Ilschner, "Fatigue of Very Thin Copper And Gold Wires", Scripta Metallurgica, Vol. 20, pp. 1601-05, 1986.

9.   HAC Standard, "Wire, Aluminum for Microelectronic Circuits", HMS 20-1603, Sep. 1970.

10.   M. A. Adams, "An Investigation of the Strength of Aluminum Wire Used In Integrated Circuits", NASA Tech Brief 70-10275 (NPO-11219)/JPL, Aug. 1970.

11.   K. V. Ravi and E. M. Philofsky, "Reliability Improvement of Wire Bonds Subjected To Fatigue Stresses", 10th Ann. Proc. IEEE Reli. Phy. Sym., pp. 143-49, 1972.

12.   V. N. Geminov, "Fatigue of Ductile and Brittle Wires At A Constant Strain Amplitude", AIAA TIS 3/26, In Fatigue and Fracture of Metals, Moscow, pp.239-44, A75-12749, 1974.

13.   N. L. Holt and I. Finnie, "Fracture and Fatigue of High Strength Filaments", Final Report on a Research Project at U. C. Berkeley, 9/25/74 to 8/30/75.

14.   "Semiconductor Economics Report", Vol. 2, No. 9, p. 13, D M Data Inc., May 1988.

15.   A. H. Burkhard, J. M. Kallis, L. B. Duncan, M. F. Kanninen, and D. O. Harris, "Application of Fracture Mechanics to Microscale Phenomena In Electronic Assemblies".

16.   A. J. Otto, "Aluminum Wire For Ball Bonding", IEEE Electronic Component Conference Proceedings, p. 550-56, 1987.

17.   "JPL Space Programs Summary 37-56", Vol. III, NPO-11219/1902, p. 149-53, August 1970.

18.   S. Tanaka, M. Ichikawa, and S. Akita, "Statistical Aspects of the Fatigue Life of Nickel-Silver Wire Under Two-Level Loading", International Journal of Fatigue, Vol. 2, No. 4, p. 159-63, October 1980.

19.   V. Geminov and I. Kopyev, "Fatigue of Thin Wire", Fatigue of Engineering Materials and Structures, Vol. 1, p. 329-31, March 1979.

20.   N. de N. Donaldson, "A Noble Spring-Clip: Fatigue-Resistant Electrical Connection For Implant Use", J. Biomed. Eng., Vol. 6, p. 237-41, July 1984.

21.   K. V. Ravi and R. White, "Reliability Improvement of 1 Mil Aluminum Wire Bonds for Semiconductors", Final Report (NASA-CR-129779), December 1971.

22.   S.-P. Hannula, J. Wanagel and C.-Y. Li, "Evaluation of Mechanical Properties of Thin Wires for Electrical Interconnections", IEEE Transactions, Vol. CHMT-6, No. 4, p. 494-502, December 1983.

13

23. "Standard Methods of Testing Fine Round and Flat Wire for Electron Devices and Lamps", ASTM Designation: F219-79 (Reapproved 1984).

24. S.-P. Hannula, J. Wanagel, and C.-Y. Li, "A Comparative Study of The Mechanical Properties of Bonding Wire", Semiconductor Processing, ASTM STP 850, p. 485-99, Dinesh C. Gupta, Ed., American Society for Testing and Materials, 1984.

25. D. F. Herbert, "The Annealing and Low Temperature Aging Characteristics of Fine Diameter Wire Produced from Dilute Aluminum Alloys", Semiconductor Processing, ASTM STP 850, p. 458-71, Dinesh C. Gupta, Ed., American Society for Testing and Materials, 1984.

14

TABLE 1—Chemical composition of the wires in ppm wt-%.

Type of Wire	Manufacturer	Au	Al	Si	Mg	Cu	Ag	Fe	Be	Pt	Ca	Pb
Au	A	Bal		5-10	1-3	1-3	10-30	5-10	7±1		≤2	
	B	Bal				1	25		1			
	C	Bal		0.1	20	0.7	20	0.6	5	16	0.1	
Al-1Si	A		Bal	1.00[a]	2-4	≤1	<1	5-10			<2	
	B		Bal	1.0[a]		<10						
	C		Bal	0.95[a]	0.3	0.7	2	1.			0.1	0.7

[a] wt-%.

TABLE 2—Mechanical properties of the bonding wire test samples according to the manufacturers.

Type of Wire	Specified Property	Manufacturer		
		A	B	C
Au	Breaking load (g)	>8	>8	9.4
	Elongation (%)	3-6	4-8	4.7
Al-1Si	Breaking load (g)	19-21	17-22	14.6
	Elongation (%)	1-4	1-4	2.3

TABLE 3--Tensile properties of the bonding wires.

Wire		Yield Strength (0.2% Offset) (YS) (MPa)	Tensile Strength (UTS) (MPa)	Breaking load (g)	Elongation (%)	YS/UTS
Au	A	156 ± 12	194 ± 19	10.0 ± 1.0[b]	5.5 ± 1.7	0.79 ± 0.10
				(8.8 ± 0.1)[b]	(4.1 ± 0.7)[b]	
		160 ± 16[a]	186 ± 4[a]	9.5 ± 0.3[a]	5.6 ± 0.6[a]	0.86 ± 0.07[a]
	B	158 ± 11	190 ± 8	10.2 ± 0.4	6.5 ± 0.6	0.80 ± 0.06
				(9.7 ± 0.3)	(4.2 ± 0.1)	
		151 ± 5[a]	183 ± 2[a]	9.8 ± 0.1[a]	7.1 ± 0.6[a]	0.82 ± 0.02[a]
	C	162 ± 12	199 ± 9	10.2 ± 0.5	6.5 ± 1.1	0.79 ± 0.03
				(9.4 ± ?)	(4.7 ± ?)	
		152 ± 6[a]	182 ± 4[a]	9.4 ± 0.2[a]	5.4 ± 0.5[a]	0.83 ± 0.05[a]
Al-1Si	A	235 ± 7	256 ± 21	21.1 ± 1.7	2.9 ± 1.3	0.93 ± 0.05
				(19.8 ± 0.1)	(2.1 ± 0.2)	
	B	206 ± 4	224 ± 6	19.4 ± 0.5	4.3 ± 0.7	0.88 ± 0.04
				(18.5 ± 0.0)	(3.2 ± 0.3)	
	C	232 ± 11	260 ± 12	15.3 ± 0.7	2.4 ± 0.9	0.89 ± 0.04
				(14.6 ± ?)	(2.3 ± ?)	
		214 ± 4[a]	239 ± 4[a]	14.1 ± 0.2[a]	3.9 ± 0.6[a]	0.90 ± 0.01[a]

[a] After low temperature annealing.
[b] ( ) Calculated from manufacturer's test results.

VENDOR RELATED FAILURES
SCREENED PARTS

WIRE BONDS 26%

DIE ATTACH 6%

CRACKED DIE 2%

PACKAGE 5%

DIFFUSION/OXIDE 13%

OTHER 4%

METALIZATION 9%

TEST ERRORS 19%

CONTAMINATION 15%

4 YEAR AVERAGE
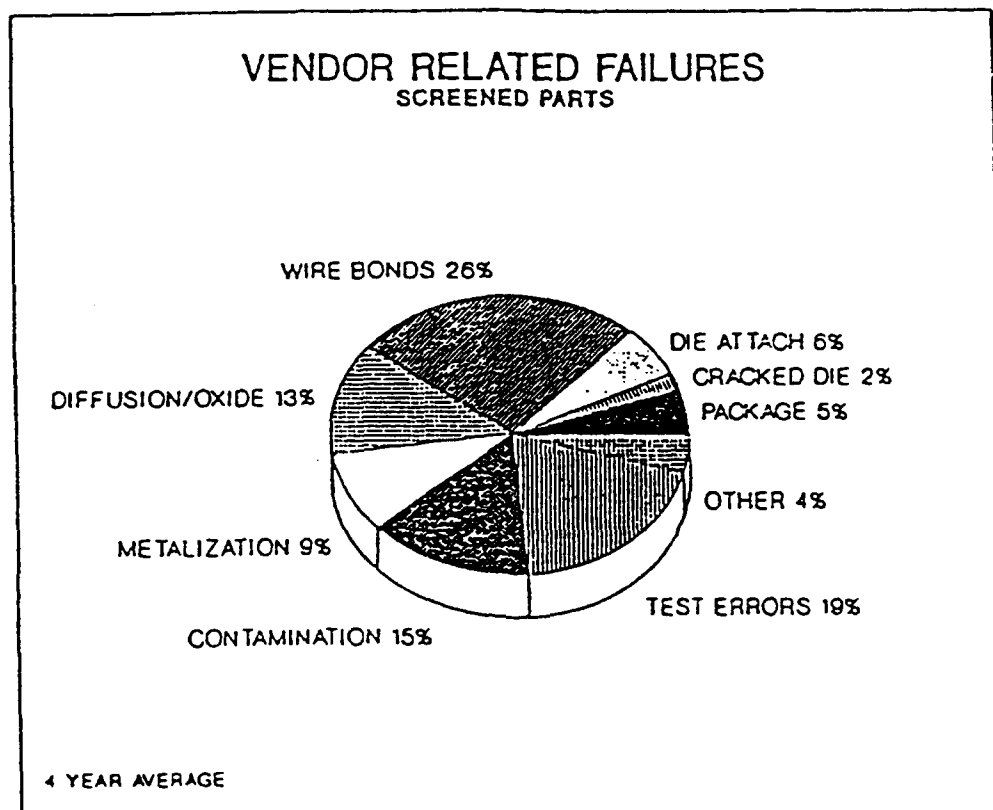
FIGURE 1

FIGURE 2

Fig. 6   Ultrasonic bonding process
(schematic)

Halbleiterkristall = semi-conductor chip. Systemträger = substrate
Draht = wire. Sonotrode = ultrasonic transducer. Druck und Ultra-
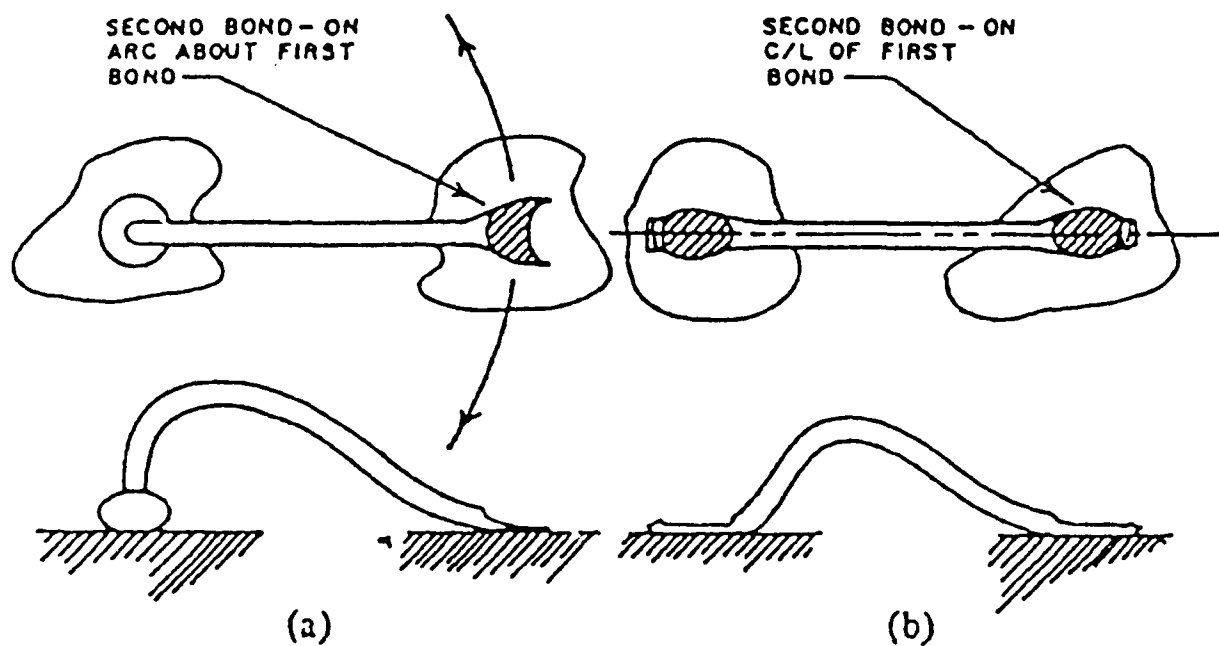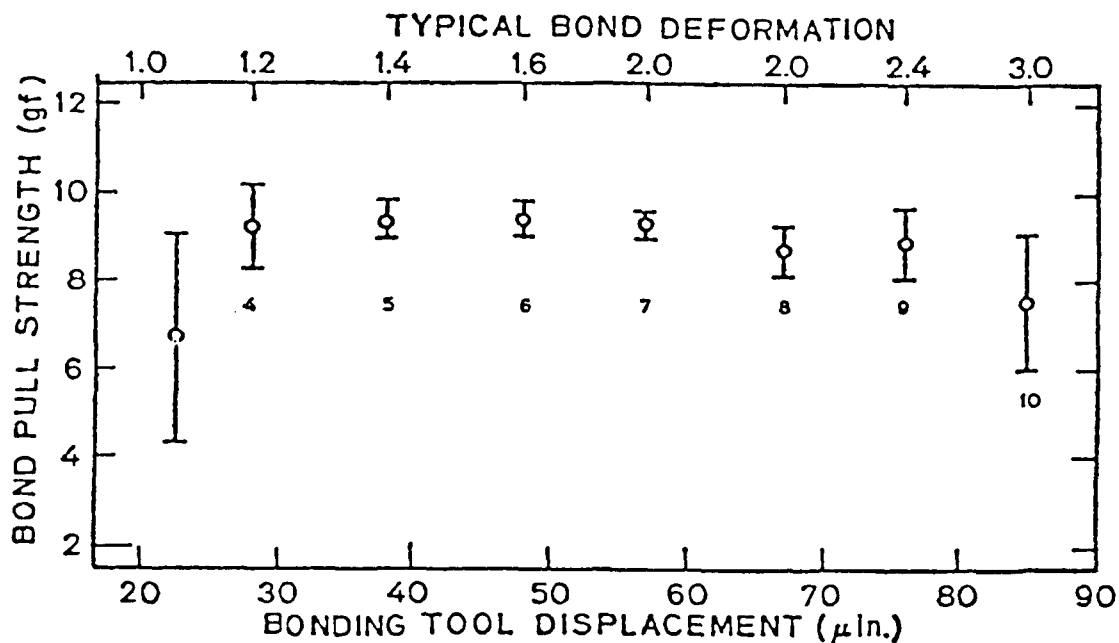schall-Energie = pressure and ultrasonic energy.

10 μm

Fig. 5   AlSi wire; bond area (heel)
(Electron microscope)

Fig. 7
Crack formation in heel area
of Al-alloy wire during
ultrasonic bonding
(Electron microscope)

Bond phase 1   Bond phase 2   Bond phase 3

Fig. 1. Wire bond configurations. (a) Ball-and-stitch T/C and T/S bonds. (b) Ultrasonic bonds.

FIGURE 3

TYPICAL BOND DEFORMATION

Bond pull strength vs. bonding tool displacement amplitude (ultrasonic power) and bond deformation for 1 mil diameter gold wire bonded to thin-film (0.8mm) aluminum on silicon. The error bars represent ± one standard deviation of the mean, and the small numbers under the error bars are the ultrasonic power supply power-dial settings. The bonding force was 30 gf. The bonding time was 45 ms, and the bonding tool foot-length was 4.5 mils (0.11mm).[11]

TYPICAL BOND DEFORMATION (wire diameters)
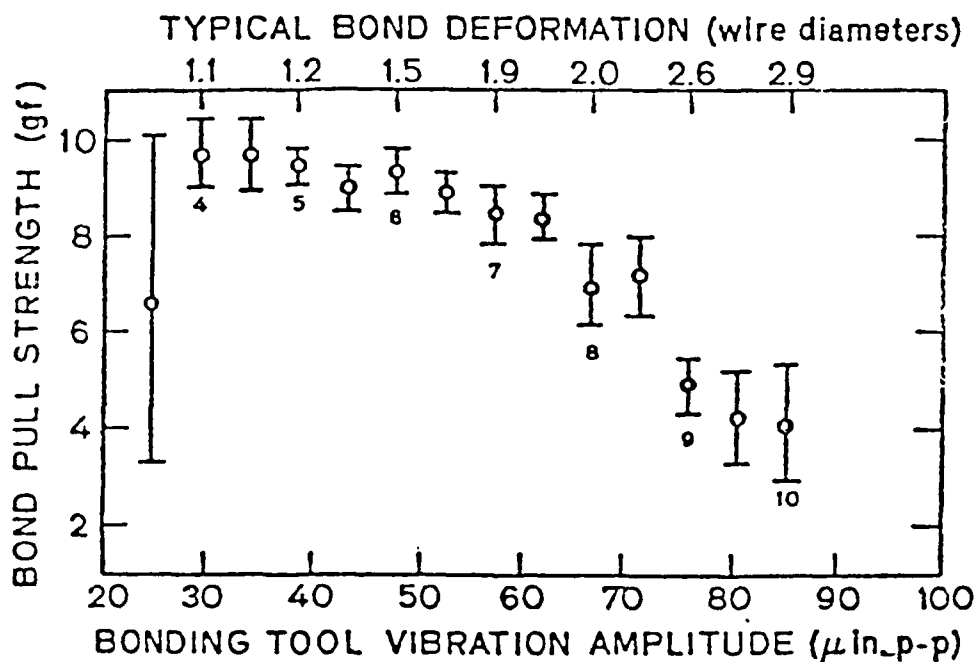
Bond pull strength vs. bonding tool displacement amplitude for one mil diameter 1% silicon aluminum wire. The bonding parameters are the same as for Figure 2 except that the bonding force was 25 gf.[11]

FIGURE 4

Al-Si   Aluminum-Silicon

°C — Atomic Percentage Silicon
Weight Percentage Silicon
L.A.W.

°C — Atomic Percentage Silicon
Weight Percentage Silicon
L.A.W.
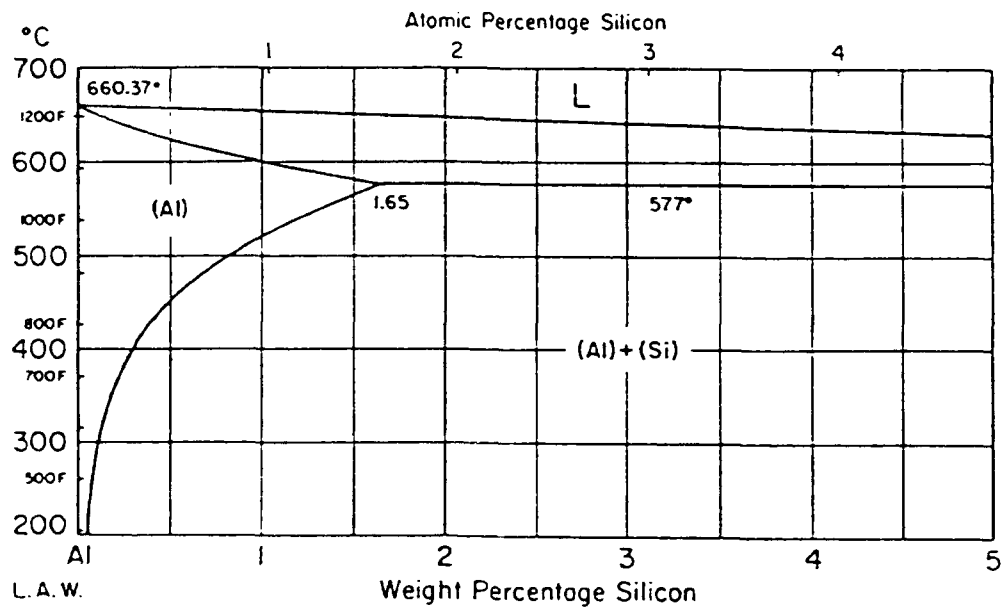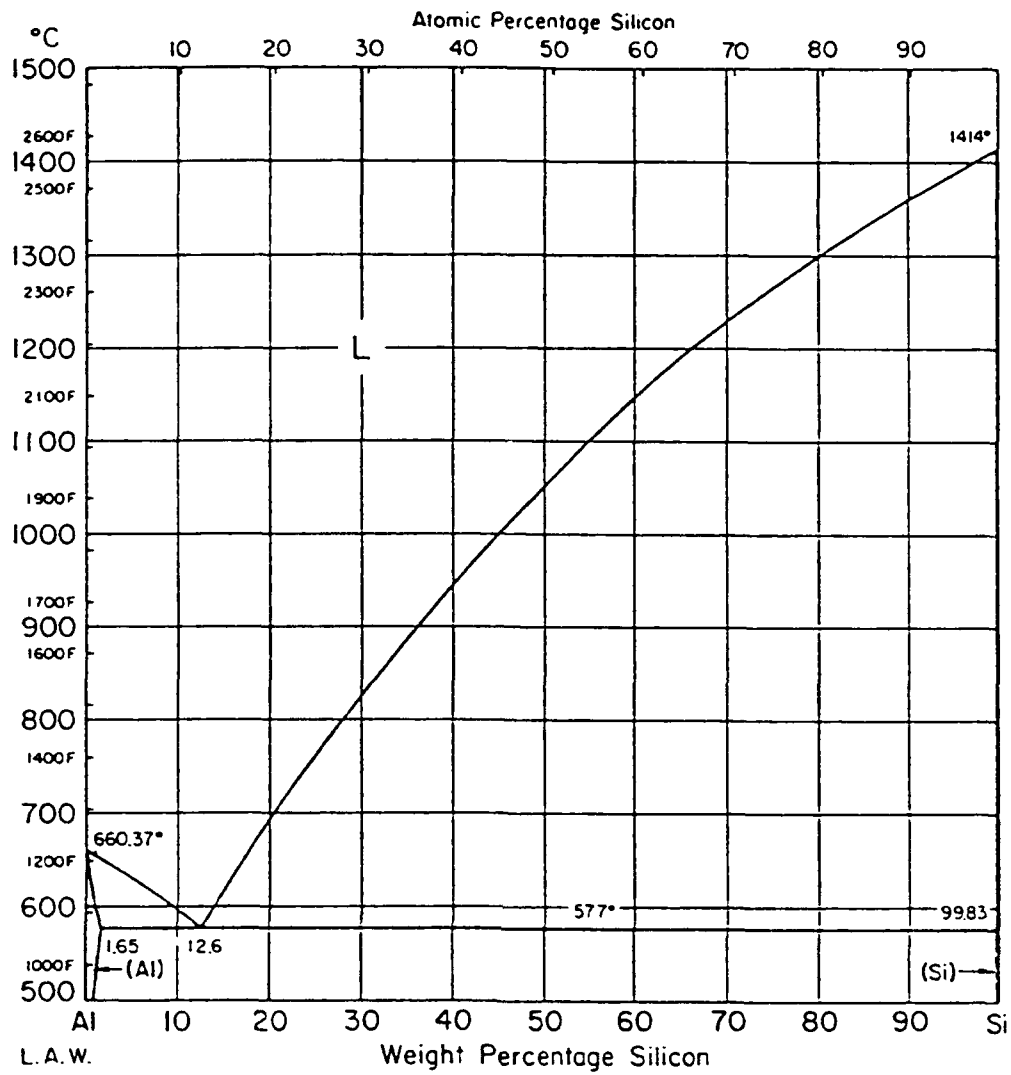
FIGURE 5

A-25
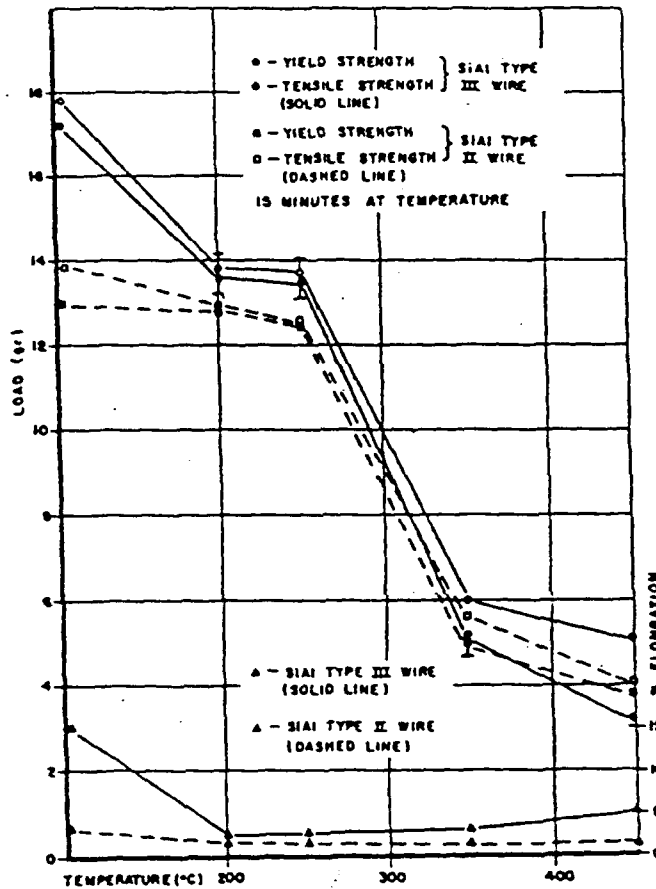
Fig. 5–A plot of the yield strength and the tensile strength as a function of aging temperature for two types of wires. At the bottom of the figure the percent elongation is plotted as a function of aging temperature. Strain rate $= 8.3 \times 10^{-4}$ (sec)$^{-1}$. (Each data point represents an average of at least five tests.)

FIGURE 6
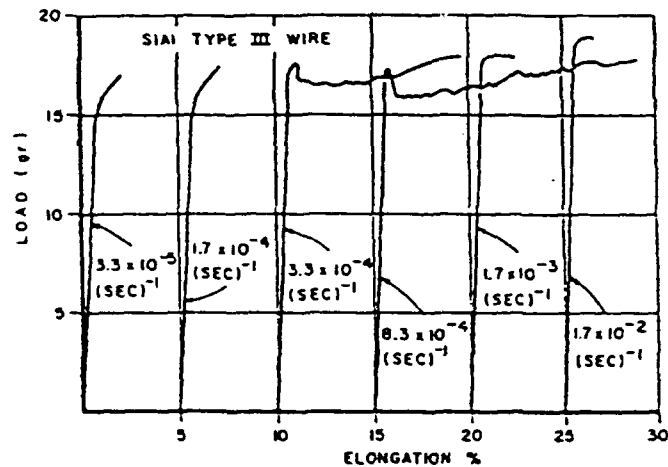
Fig. 4(a)—Load-elongation curves as a function of strain rate for a Type III wire.
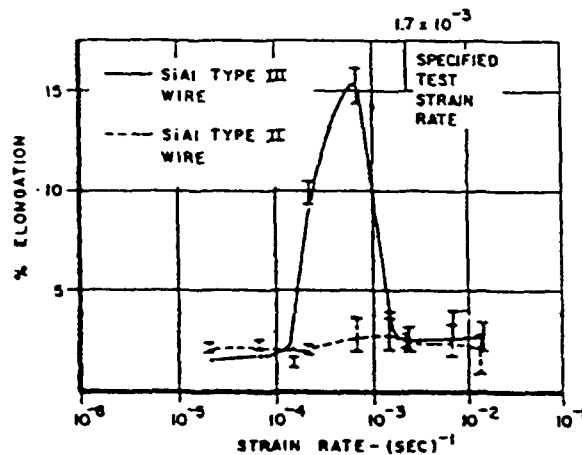
Fig. 4(b)—Percent elongation as a function of strain rate for Type II and Type III wires. The manufacturers' specified test rate is indicated. (Each data point represents an average of at least five tests.)

FIGURE 7

A-27
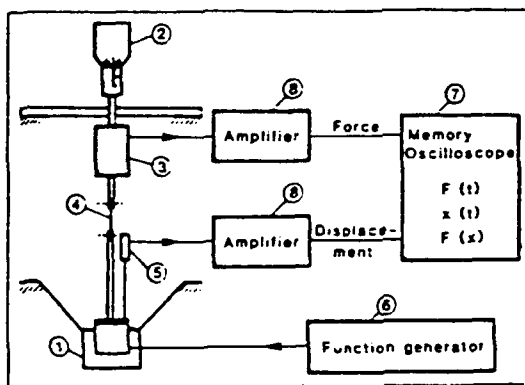
FIG. 1
Schematic arrangement of the fatigue test apparatus
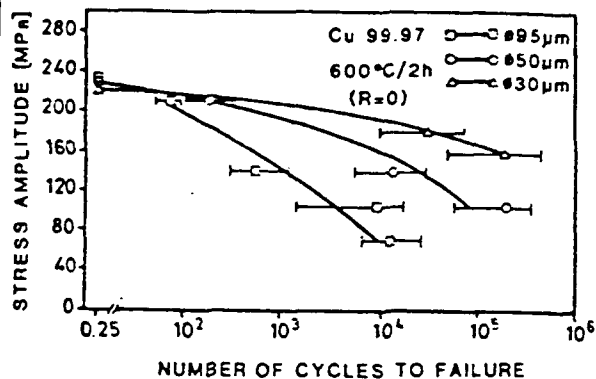
FIG. 2
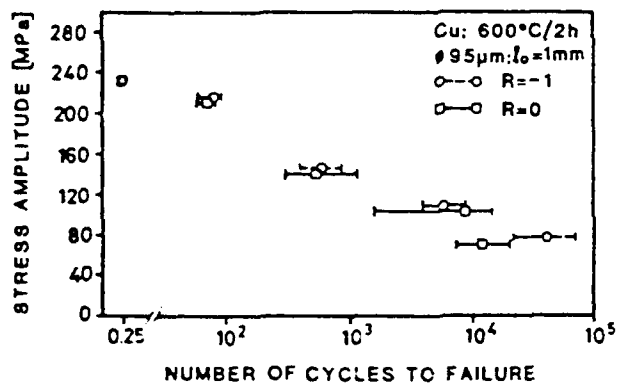Fatigue curves of thin copper wires of different diameter fatigues in alternate tension.

FIG. 3
Fatigue curves at alternate tension and tension-compression of thin copper wires
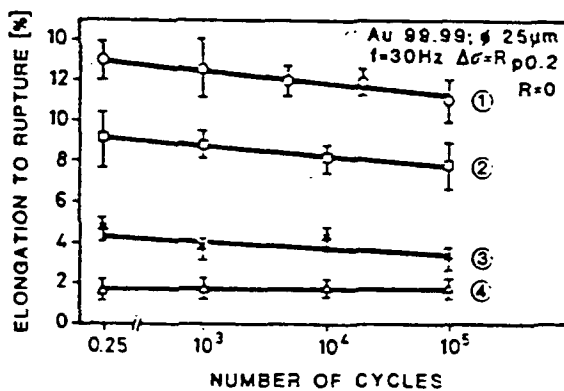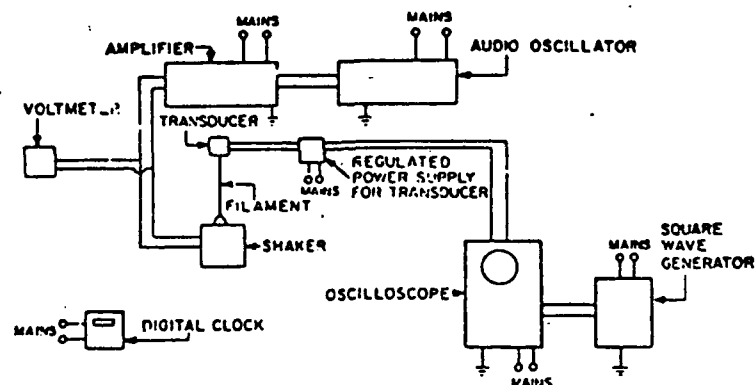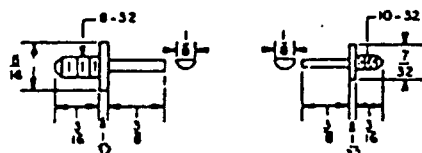(∅ 95 μm)

FIG. 4
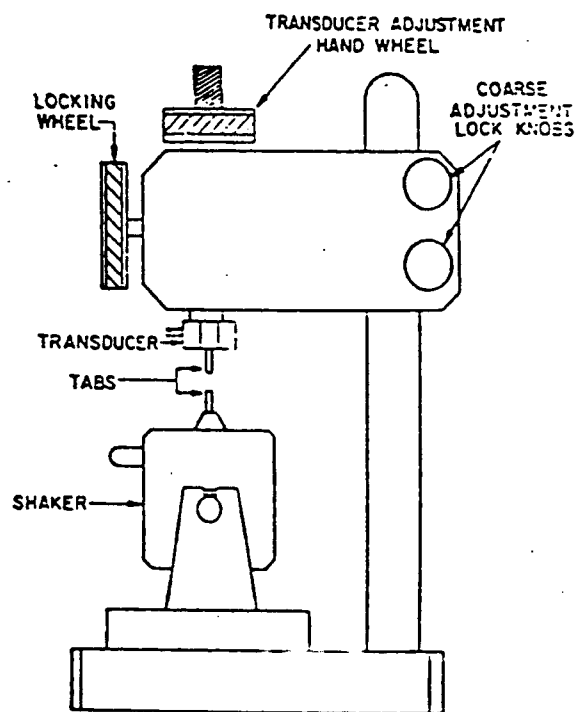Elongation to rupture of fatigued gold wires
(∅ 25 μm).

FIGURE 8

A-28

EQUIPMENT DIAGRAM FOR FILAMENT FATIGUE TESTING
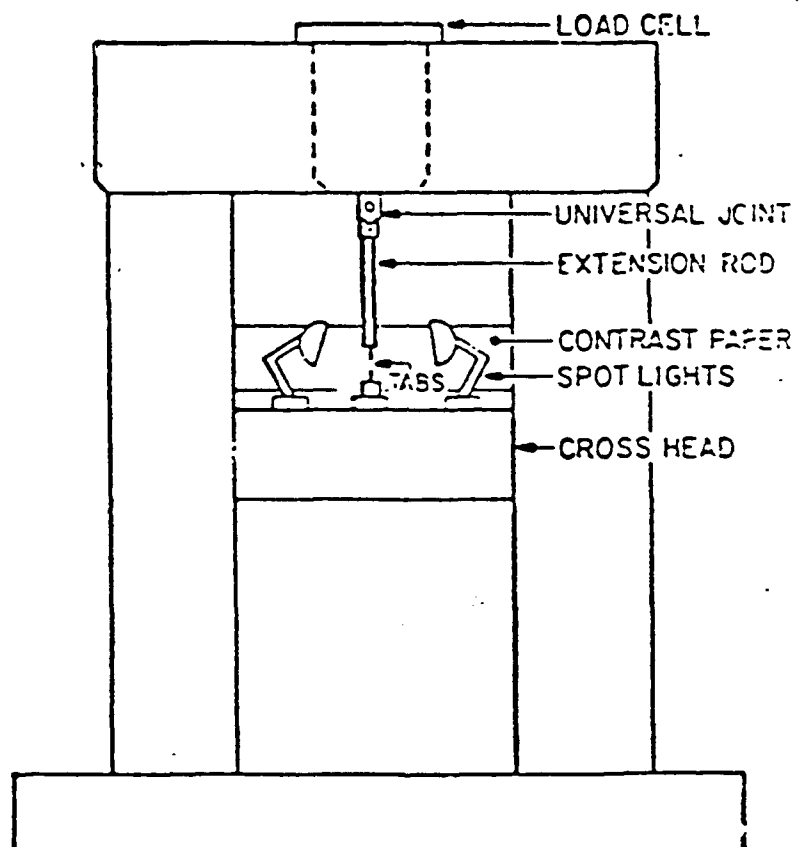

FATIGUE MOUNTING TABS

FILAMENT FATIGUE TESTING MACHINE

FIGURE 9

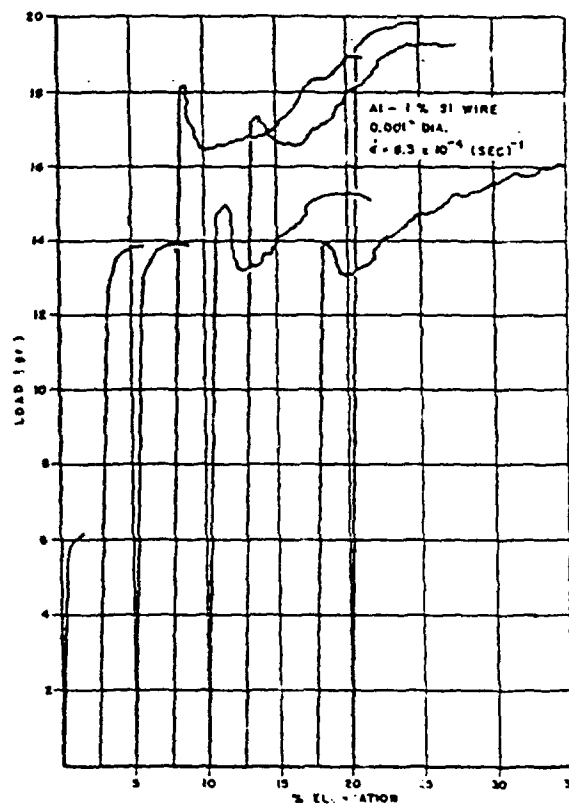TEST SET UP FOR STATIC TESTING FILAMENTS

FIGURE 5

FIGURE 10

Fig. 1—Load-elongation curves for different Al-1 pct Si alloy wires. The curves have been offset along the strain axis for the sake of clarity.
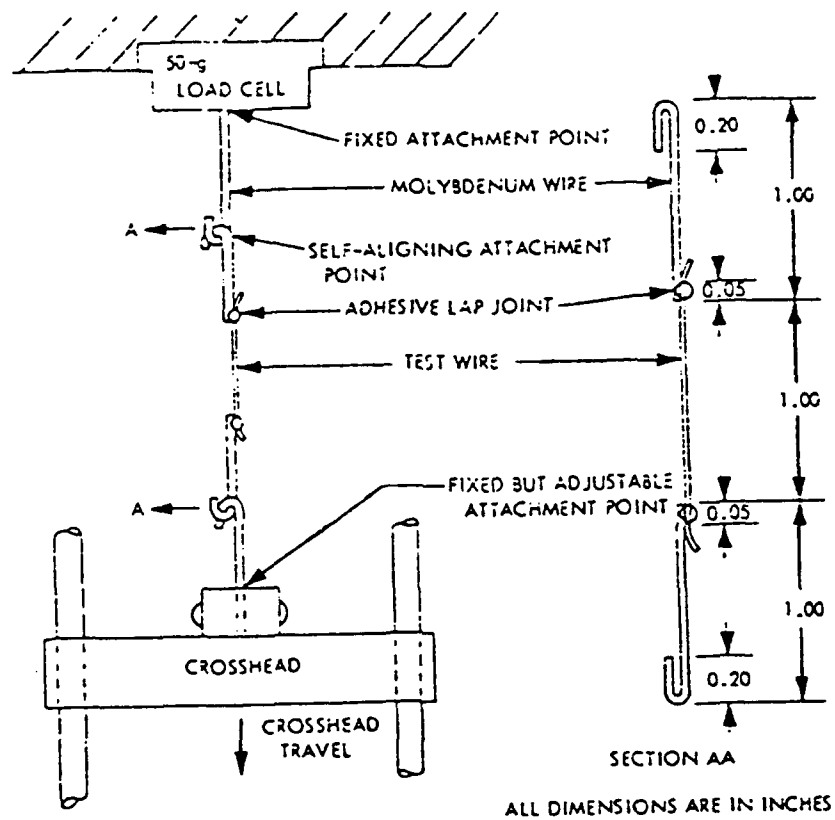
FIGURE 11

Fig. 6. Tensile test fixture and load train

FIGURE 12

FIGURE 13

FIGURE 14

FIGURE 15

FIGURE 16

Fig. 8 Fatigue testing of superfine wires
(schematic)

Einspannung = wire grips; Biegewinkel = bending angle; Stößel = pusher; Draht = wire; Führung = guide; Gewicht = weight; Zählwerk = counter; Antrieb = drive

FIGURE 17
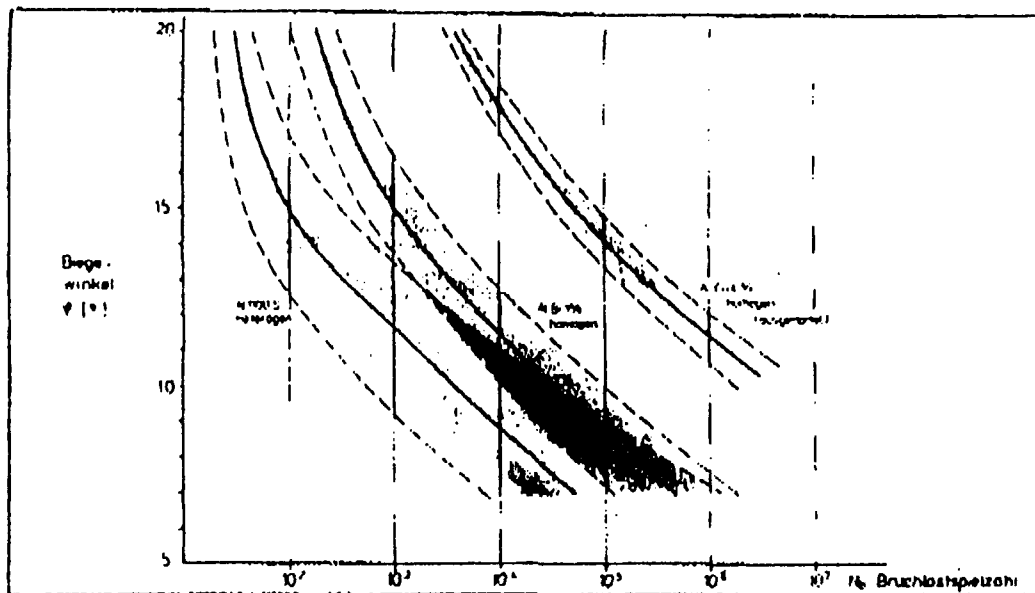
Fig. 9
Alternating fatigue strength
of Al-alloy superfine wires

Biegewinkel = bending angle; Bruchlast-
spielzahl = no. of load cycles to failure;
heterogen = heterogeneous; homogen
(ausgehärtet) = homogeneous (harden-
ed)

FIGURE 18

A-38

S

1/ 6/89

S
T
R
E
S
S

T
R
A
N
S

P
S
i
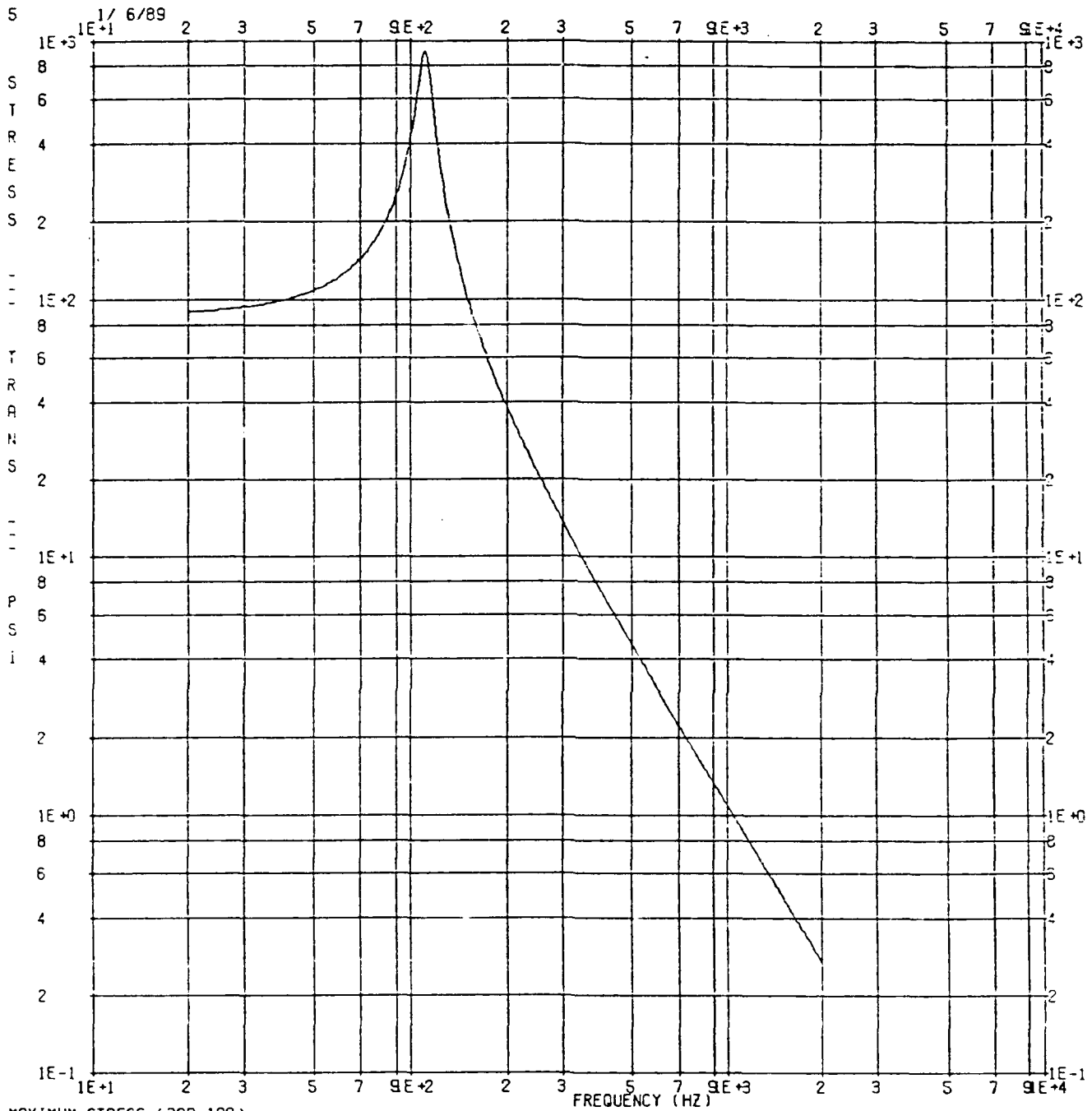
FREQUENCY (HZ)

MAXIMUM STRESS (BAR 100)
1 MIL WIRE BOND ANALYSIS. 1/6/89. WIRE.RCF
20 TO 1000 HZ 1G FREQUENCY RESPONSE. MODES BELOW 300 HZ. Q = $1^{0.5}$
X BASE 1 G SINE SWEEP EXCITATION AND ABSOLUTE RESPONSE

SUBCASE 1

FIGURE 19
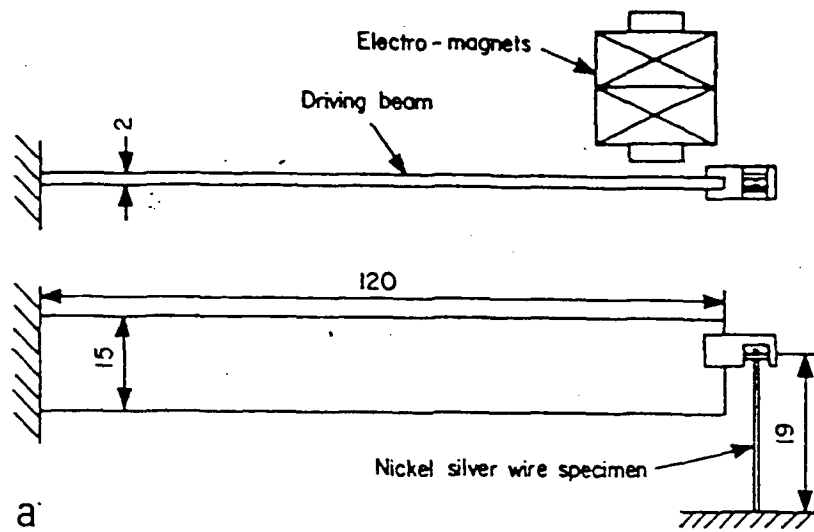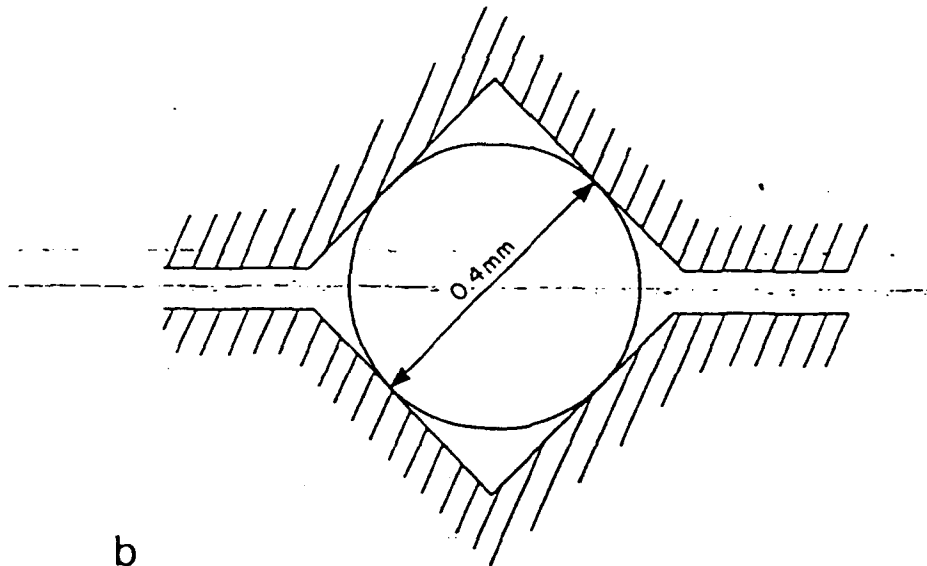
Fig. 1   Fatigue testing machine (a) and method of clamping the wire (b): dimensions in mm

FIGURE 20
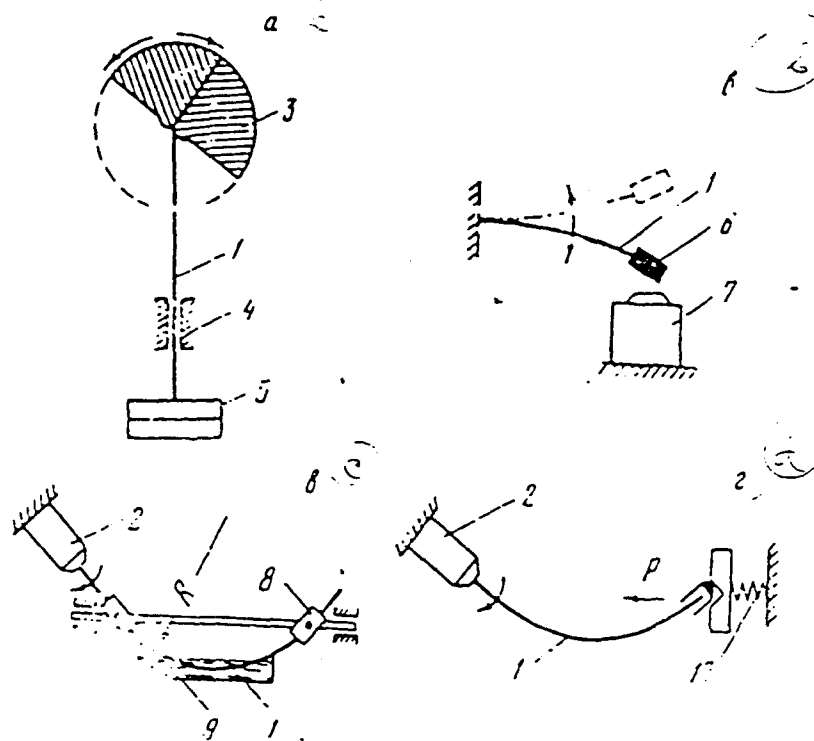
Рис. 1. Схемы испытания проволок на усталость

а — изгиб по радиусу; б — консольный изгиб; в — круговой изгиб; г — продольный изгиб;
1 — образец; 2 — двигатель; 3 — сектор; 4 — направляющая; 5 — груз; 6 — башмачок;
7 — электромагнит; 8 — подшипник; 9 — жидкость; 10 — пружина
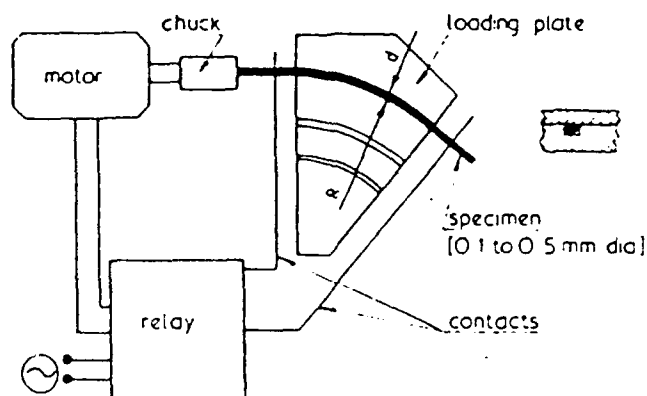
Fig. 1. Device for fatigue testing of thin wires.

FIGURE 21
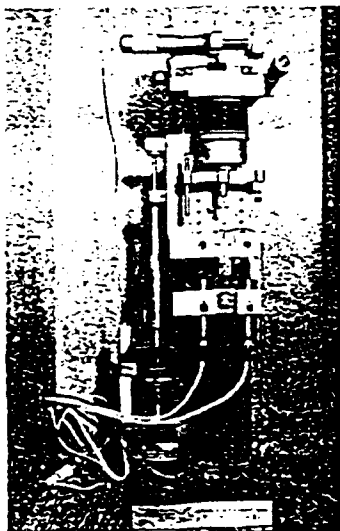
Fig. 1. Testing machine.

Testing Machine

In order to measure the mechanical properties of small specimens such as thin wires and films. a miniaturized mechanical testing system has been developed. A detailed description of the apparatus is given elsewhere [3]. For the purpose of this paper a short description of the testing system is given next.

A photograph of the testing machine is shown in Fig. 1. The machine contains two separate load trains, one for large displacements (load train 1; up to 5 cm displacement) and the other one for small displacements (load train 2; up to 12 μm displacement). The load train for large displacements consists of a synchronous instrument motor, a precision speed reducer, a slide joint, a micrometer head, and a translation stage with a dual roller bearing system. The specimen and the specimen holder system is placed between a fixed solid plate and a moving crosshead.

The small displacements of load train 2 are made possible by using a piezoelectric translator. Extensions up to 12 μm can be obtained with the translator. An applied voltage of 0 ··· −1600 V is required to achieve the full range of extension. The specimen is placed between the piezoelectric translator and the moving crosshead, the movement of which is needed for specimen mounting. During the test the crosshead is, however, locked. The specimen is aligned by using an x-y stage, while viewing it directly with a microscope.

A small load cell can be placed on either side of the crosshead depending on which load train is used. Miniature precision load cells with a high spring constant were employed having either a maximum range of ±25 g or ±1000 g.

The wire specimen is gripped from both ends between two small metal plates, which are tightened against each other with screws. This mechanical gripping system was found to produce slip-free performance for tensile and load relaxation tests. For fatigue tests a short wire specimen is first inserted into a hypodermic tubing having an outer diameter of 0.2 mm and inner diameter of 0.1 mm. The tube is crimped near the ends of the gauge section for mechanical gripping. A small specimen length to diameter ratio can be achieved through this arrangement to facilitate low cycle fatigue testing.

The strain of the specimen is measured by two capacitance probes. Two probes, 180° apart, were used simultaneously to minimize the error due to misalignment of the specimen holding system.

Because of the requirements of good temperature stability in the testing system, the machine was enclosed in a styrofoam insulated box. The temperature of the surrounding room was controlled to 20± 0.5°C by an air conditioner and auxiliary heaters. Large air fans were used in the room. With these precautions the temperature fluctuations inside the box were <0.1°C. The insulating box also served the function of preventing vibrations in the strain measuring assembly caused by air circulation.

The output from the load cell and the capacitance probes were simultaneously recorded by using a programmable multichannel digital data acquisition system [4]. The maximum acquisition rate of this system is 10 points/second.

FIGURE 22
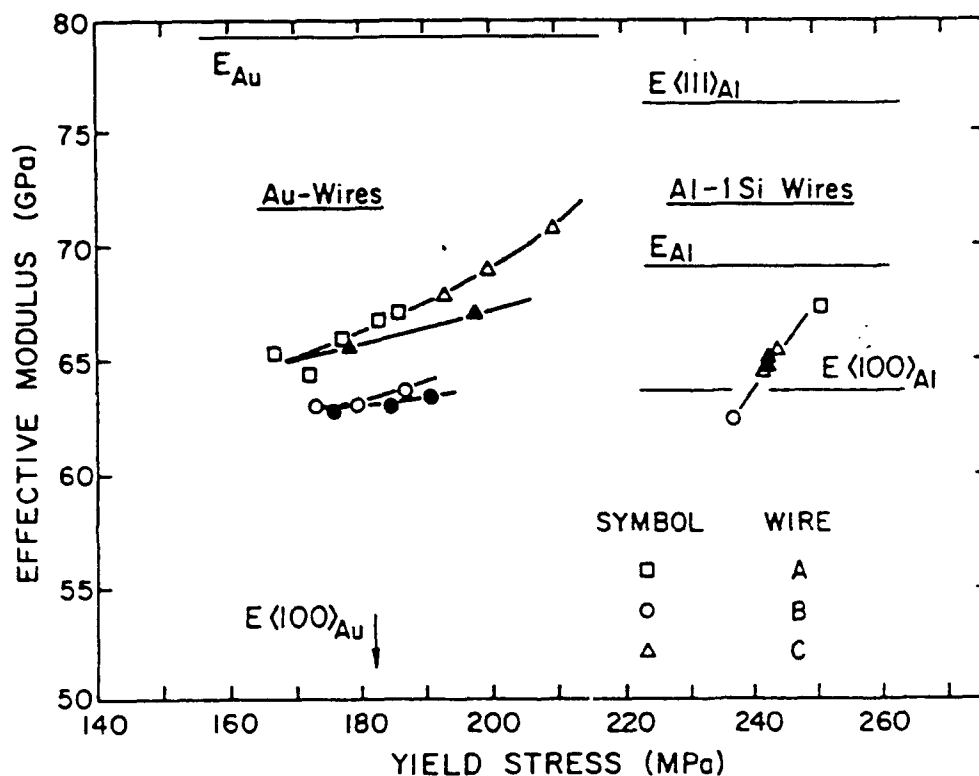
FIG. 2--Effective modulus as a function of yield stress for different wires. Open symbols are for as received wires and closed symbols are for annealed wires.

FIGURE 23
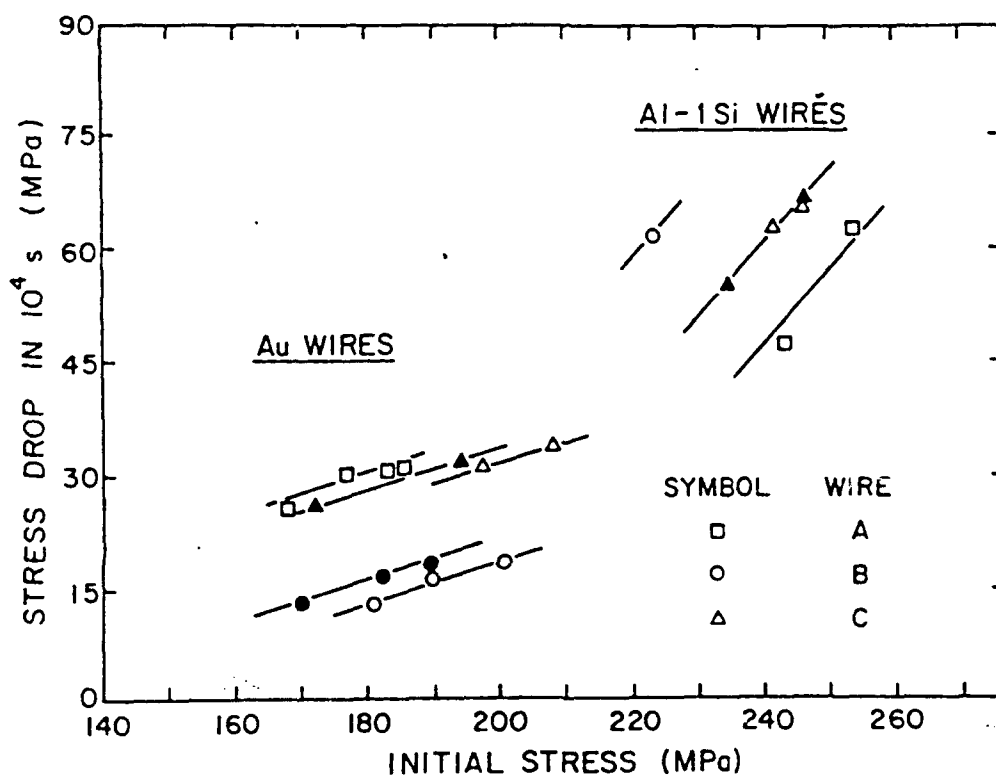
FIG. 3—A summary of load relaxation test results. The stress drop during the first 10^4 seconds of relaxation is plotted as a function of the initial stress of the relaxation. Open symbols are for as received wires and closed symbols are for annealed wires.

These results show substantial differences in the behavior of both the gold and the aluminum 1-percent silicon wires. In general, when the two groups of wires are considered, the Al-1Si alloy wires exhibit twice the stress drop in a fixed period of time as compared to the gold wires. This shows that the aluminum wires are much more unstable under stress than the gold wires.

FIGURE 24
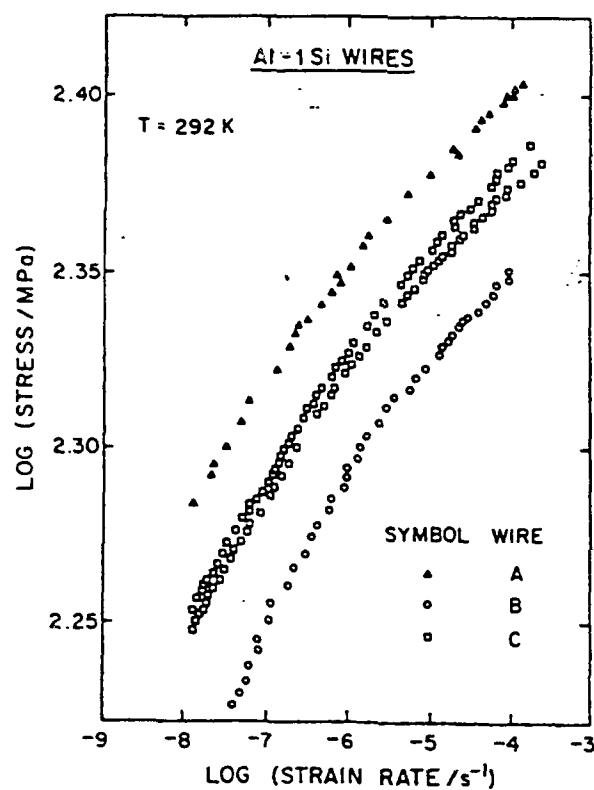
FIG. 4—Logarithmic stress versus logarithmic strain rate curves as obtained from successive load relaxation tests.

FIGURE 25
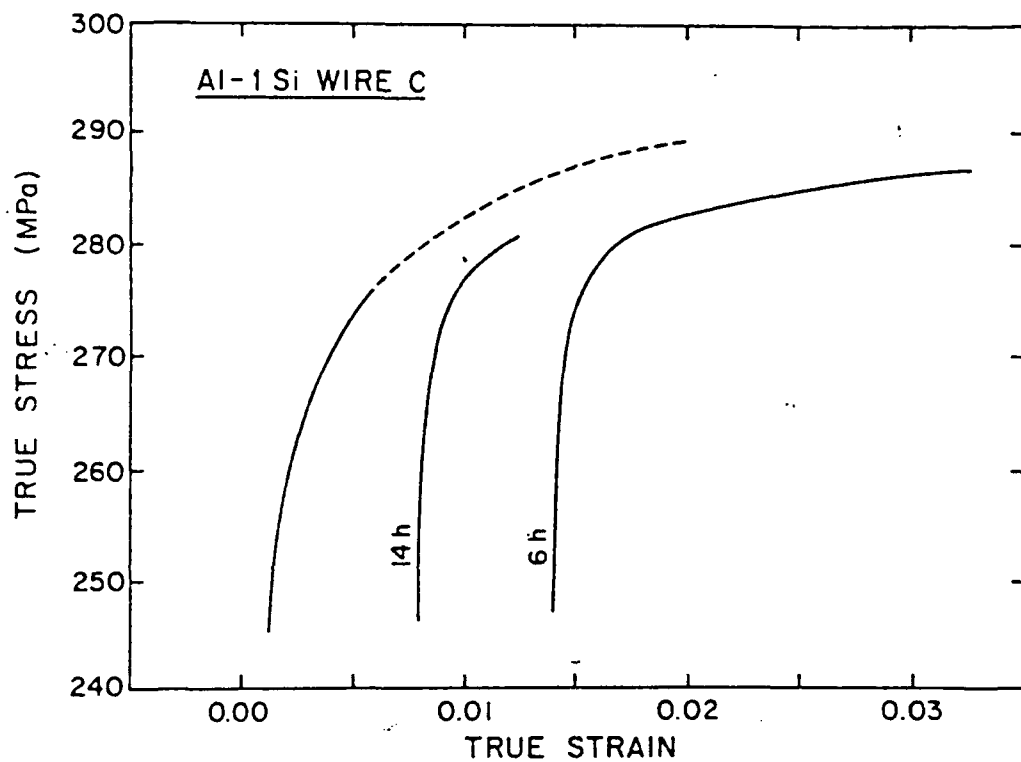
FIG. 7--True stress versus true strain curves for aluminum 1-percent silicon wire C. The interruptions in the solid lines are due to successive load relaxation tests. The times for interruptions are indicated in the diagram. The dashed line is a result from a continuous tensile test.

FIGURE 26

TABLE 2 -- Wire Identification

Wire #	Alloy	Vendor	Bar
1	Al-1Si	1	1
2	Al-1Si	2	1
3	Al-1Si	3	1
4	Al-1Si	4	1
5*	Al-1Si	3	2
6	Al-1Mg	2	1
7	Al-1Mg	3	1
8	Al-1Mg	3	1
9	Al-1Mg	5	1
10	Al-½Mg	2	2

* 1.25 mil diameter wire. All other wires are 1.00 mil diameter wires.
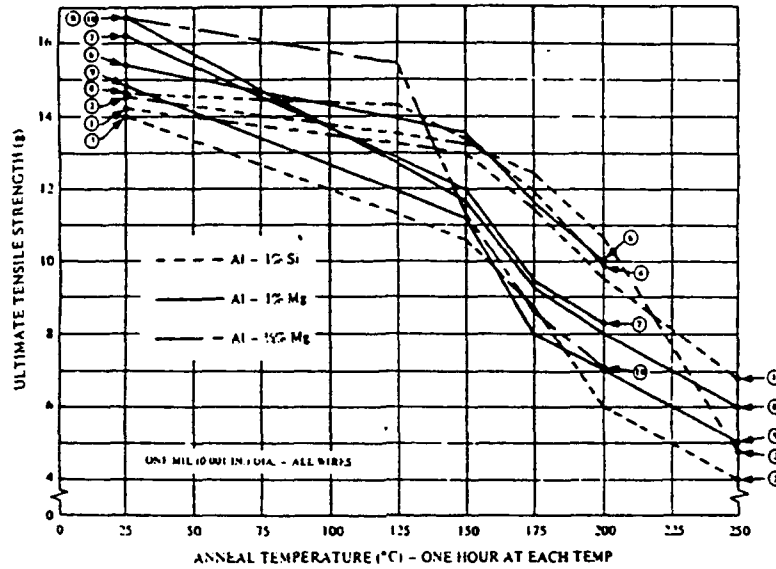
FIGURE 5-- Ultimate Tensile Strength vs Anneal Temperature
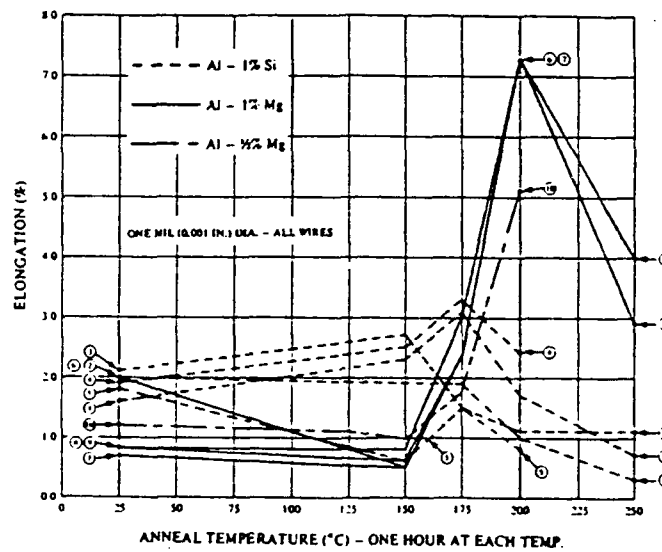
FIGURE 6-- Elongation vs Anneal Temperature

FIGURE 27

A-47
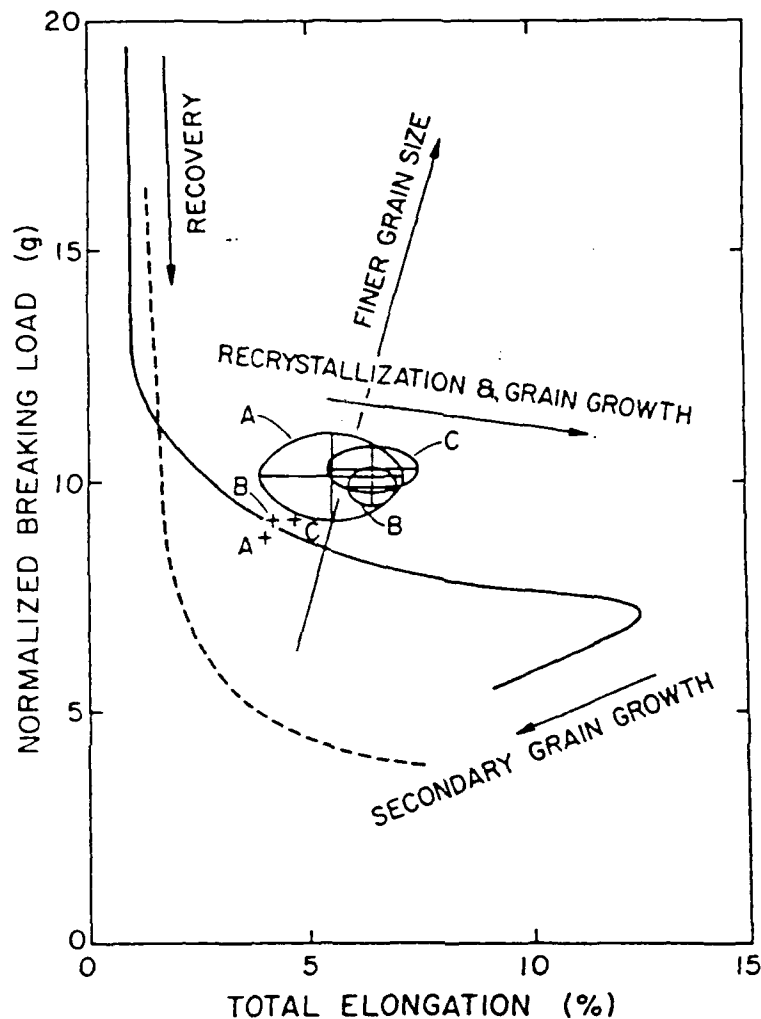
FIG. 1--Breaking load versus elongation data for the gold wires.
Breaking load values are normalized to correspond to a 25 μm wire
diameter. Crosses represent the manufacturers values obtained with
the standard method of testing (ASTM F 219) while the circles show the
standard deviation range of the results obtained in this work with
subsized specimens. The curves are included for reference. The solid
line curve is indicative for a wire that has been processed "properly"
and the dashed line curve is for poorly processed wire.

FIGURE 28
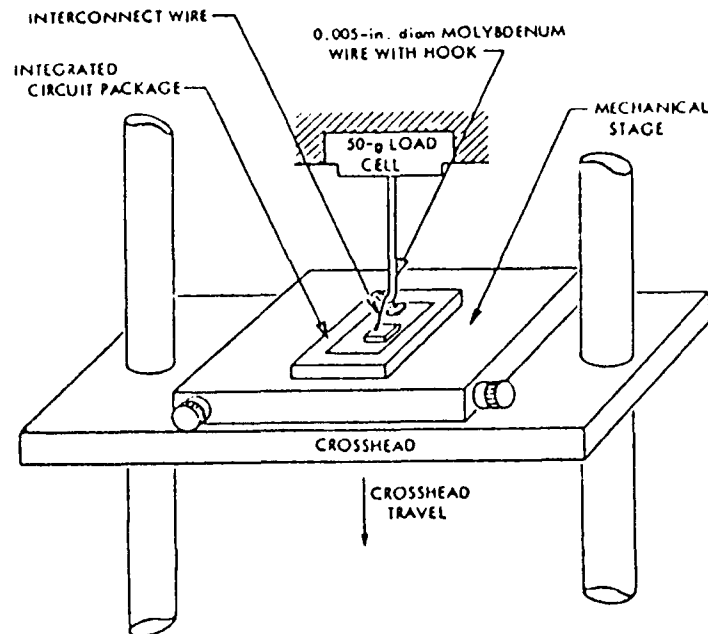
Fig. 2. Integrated circuit interconnect wire test
configuration
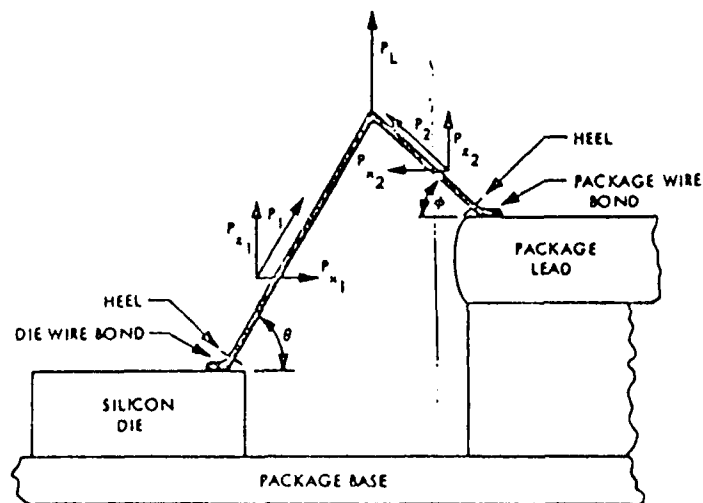
Fig. 3. Microloop pull test loading conditions

FIGURE 29

WIRE (ALUMINUM)

POWER ON CONDITION

HEEL

POST (KOVAR)

PACKAGE (KOVAR)

POWER OFF CONDITION
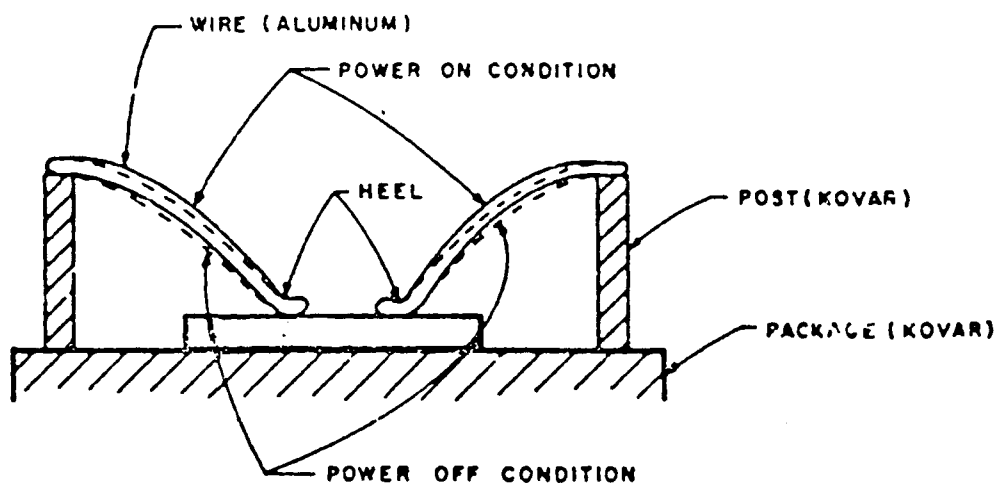
Failure occurs at the heel of the bond.

FIGURE 30

CANTILEVERED BEAM

DEVICE HOLDERS

DIRECTION OF MOTION
OF NEEDLE

NEEDLE

WIRE BOND

DIE

TO-18 PACKAGE
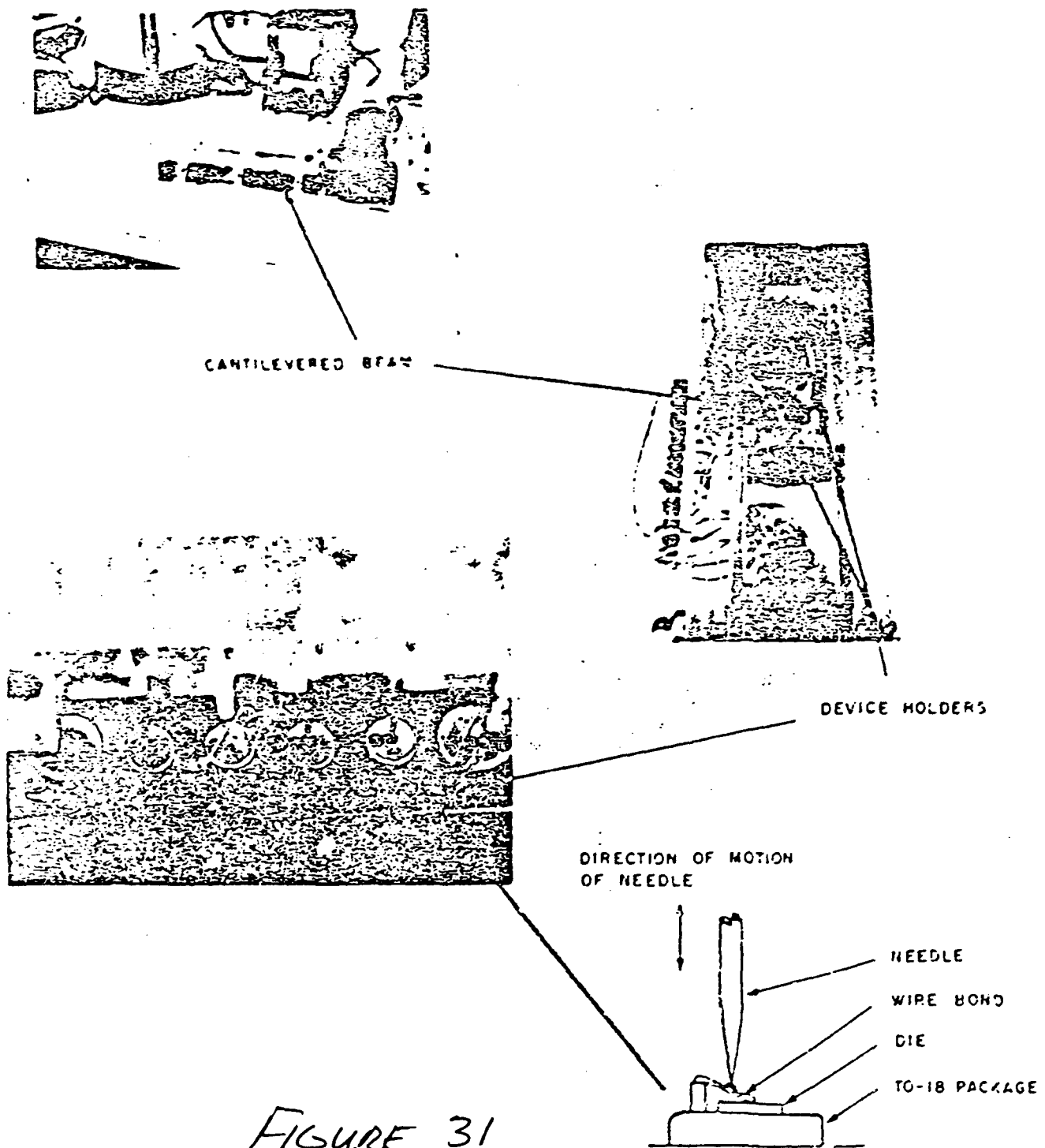
FIGURE 31

The accelerated Fatigue Testing Apparatus

Figure 23. Fatigue Curves for Different Al Alloy Wires obtained by the Accelerated Fatigue Testing of Wire Bonds

Al-Mg (ULTRASONIC)

Al-Cu (ULTRASONIC)

Al-Si (ULTRASONIC)

Al-Si (TC)

> 10^5

MEASURED WIRE DEFLECTION IN A 2N2222 TRANSISTOR OPERATING IN A ONE MINUTE ON - ONE MINUTE OFF MODE AND DISSAPATING 500 mW (SEE FIGURES 24 & 25)

$\times 10^3$ CYCLES TO FAILURE

DEFLECTION X 10^{-4} IN

9825-11-1

FIGURE 32

54
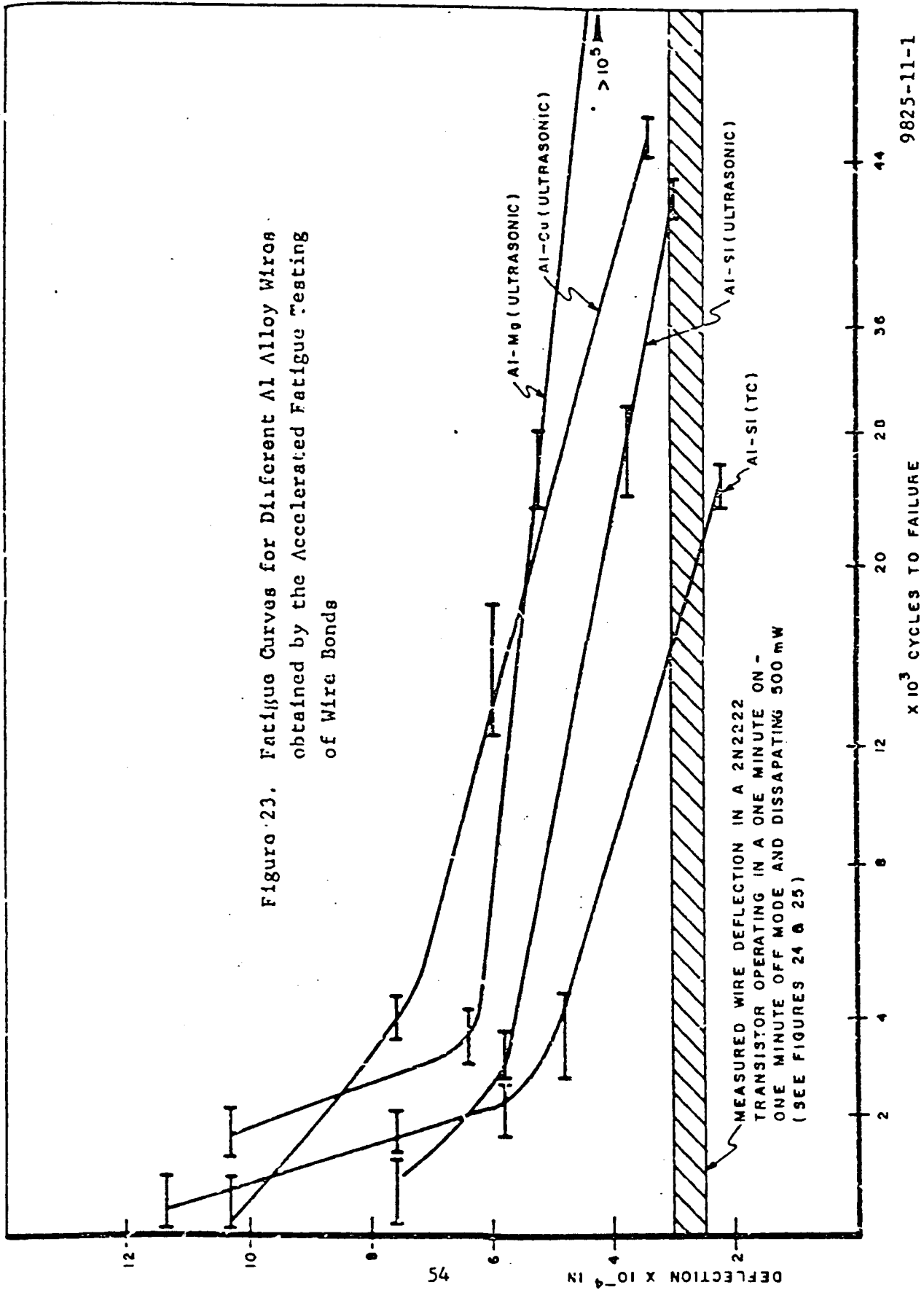
A-52

Figure 26. Fatigue Curves for Thermocompression
and Ultrasonic Bonded Al-1% Si Wire Bonds

FIGURE 33

9828-11-1

A-53

POSITION OF WIRE AFTER
POST BOND USING SMALL LOOP
HEIGHT

POSITION OF WIRE FOLLOWING
INITIAL BOND TO DIE

NOTCH AT HEEL ENLARGED
DUE TO WIRE FLEX DURING
BONDING

FINAL POSITION OF WIRE
WITH LARGE LOOP HEIGHT

INITIAL POSITION OF WIRE

DAMAGE AT HEEL
MINIMIZED

FINAL POSITION OF WIRE
WITH EXTRA LARGE LOOP
HEIGHT

INITIAL POSITION
OF WIRE

HEEL EXPERIENCES
FLEXURE DURING BONDING

PARTIAL BOND
LIFT
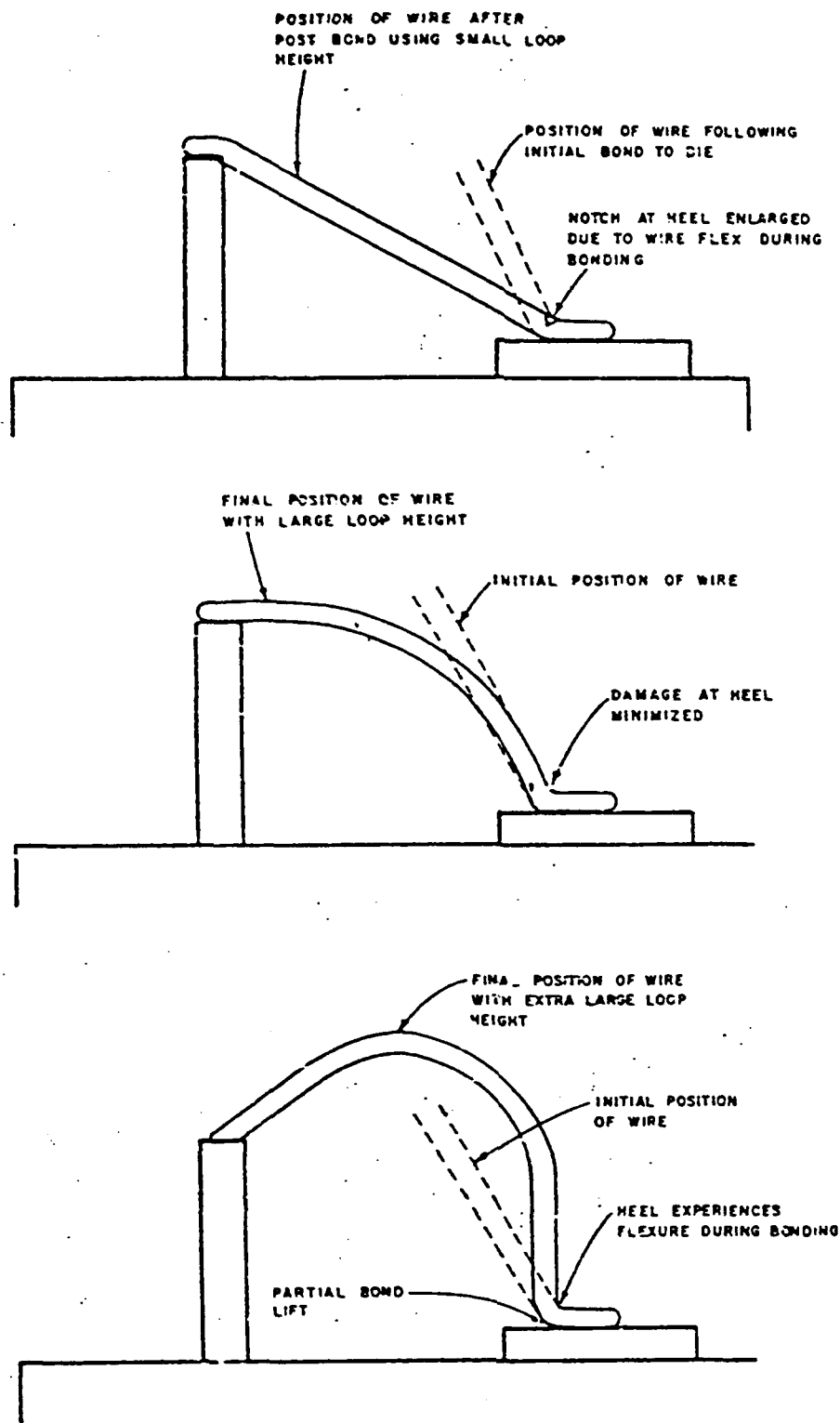
Figure 28.   Effect of Wire Loop Height on Damage at the
Heel of the Bond During Manufacture

FIGURE 34

9830-11-1

A-54
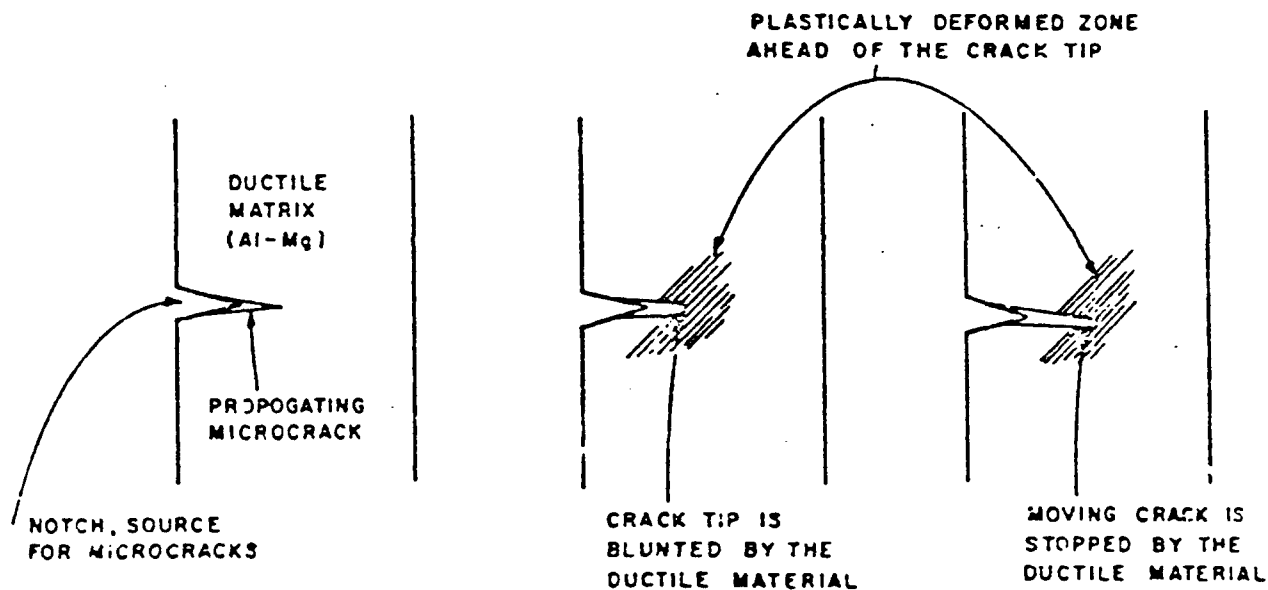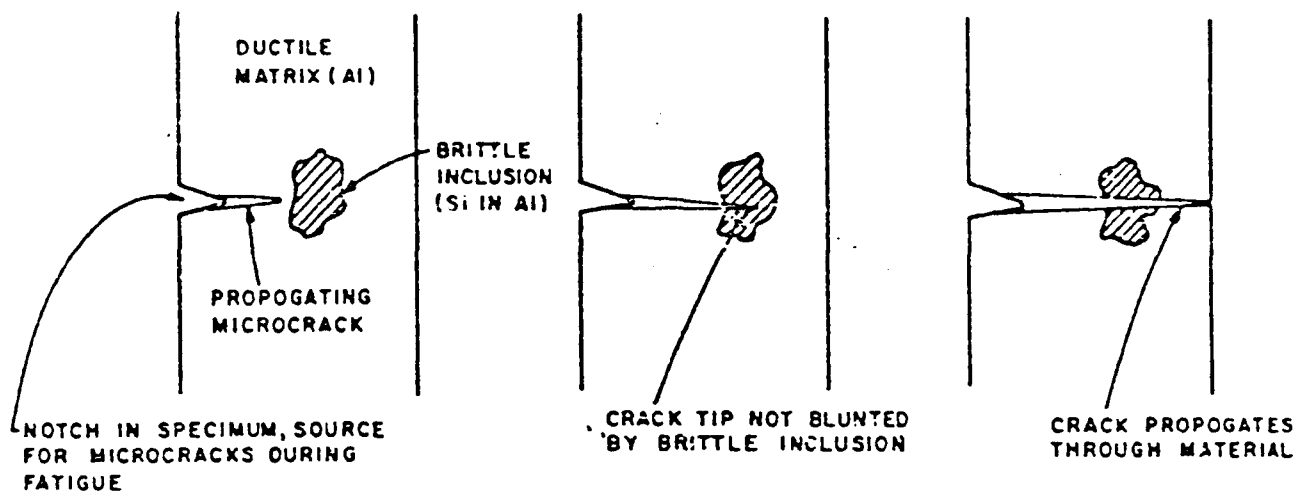
Figure I-1   Idealised Sketches of the Mechanism of Crack
Propogation in Dispersion Hardened and Solid
Solution Hardened Alloys.

FIGURE 35
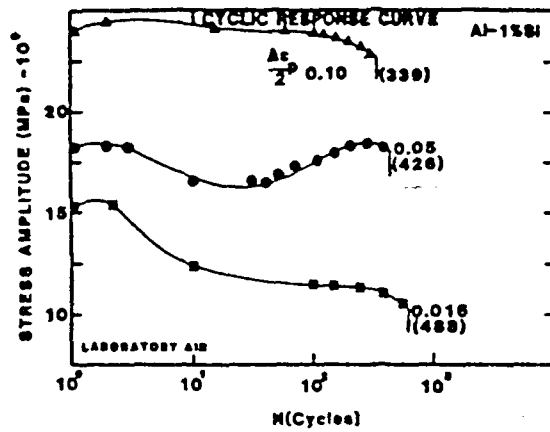
Figure 3   Cyclic response curve for the
Al-1%Si bond wire fatigued in
laboratory air at different
plastic strain amplitudes.
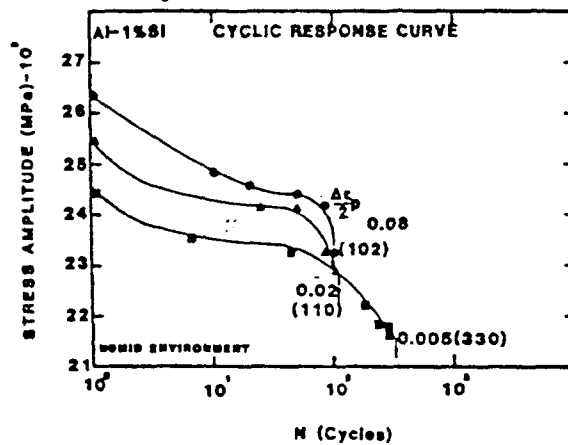
Figure 4   Cyclic response curve of the
Al-1%Si bond wire showing
softening to failure at all
plastic strain amplitudes in
the humid environment.
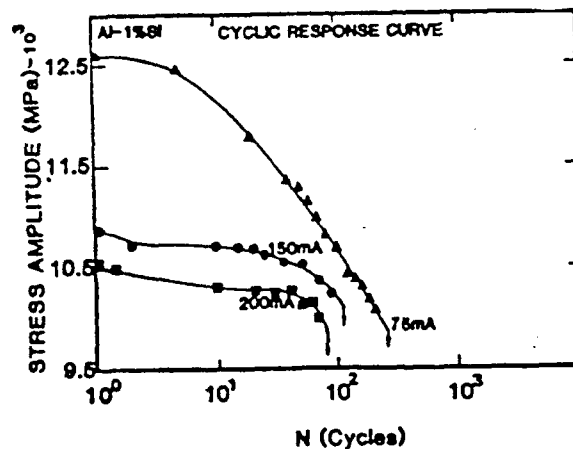
Figure 5   Cyclic response curve for the
Al-1%Si bond wire showing
softening to failure for the
different values of electric
current through the bond.

FIGURE 36

A-56

APPENDIX B

COMPLIANCE OF EDGE-CRACKED WIRES IN BENDING

D.O. Harris
Failure Analysis Associates®, Inc
Menlo Park, California

May 7, 1990

INTRODUCTION

The purpose of this document is to report the results for the compliance of edge-cracked wires as a function of the size of the crack. The compliance is obtained by use of the corresponding stress intensity factor (K) solution, beam theory, and basic principles of linear elastic fracture mechanics.

DEVELOPMENT OF EQUATIONS

Figure 1 shows the geometry of the edge-cracked wire (circular beam) in bending along with the cracked cross-section. The geometry of the crack is that considered by Forman [1], who states that it is closely representative of the configuration of cracks growing in cyclic bending. The K-solution for bending is [1]

$$K = \sigma\sqrt{\pi a}\ F(\beta)$$
$$F(\beta) = 0.541\left[\frac{\tan\beta}{\beta}\right]^{1/2}\frac{1 + 0.216(1 - \sin\beta)^4}{\cos\beta} \tag{1}$$

$$\beta = \frac{\pi a}{2D}$$

The stress σ is the bending stress, which is related to the bending moment, M

$$\sigma = \frac{M\frac{D}{2}}{I} = \frac{32}{\pi}\frac{M}{D^3} \tag{2}$$

Page 1

B-1
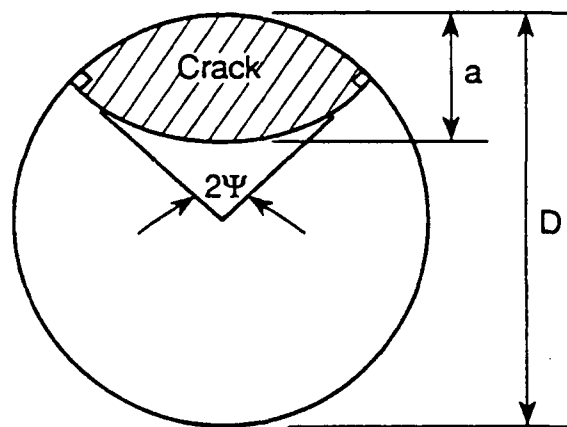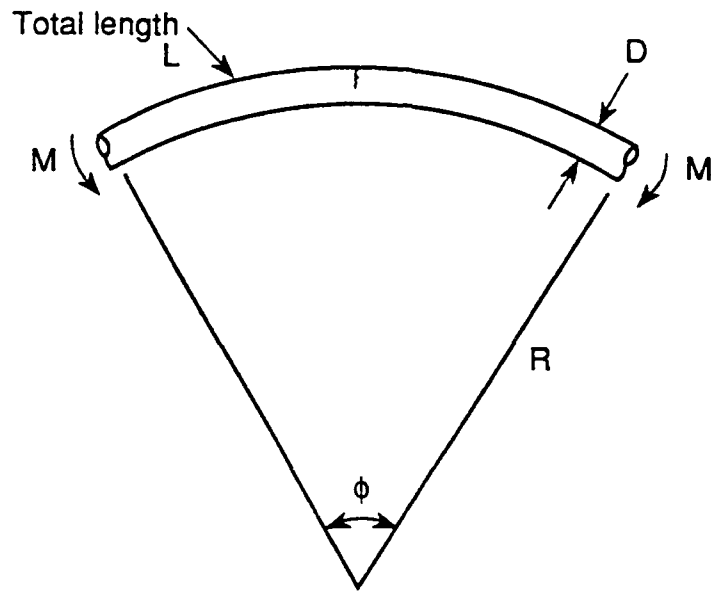
Figure 1.   A cracked circular beam in bending showing configuration of cracked cross-
section.

The use of this expression for σ and the above definition for β provides the following expression for K

$$K = 7.793 \; \frac{M}{D^{5/2}} \; \frac{\tan^{1/2}\beta \left[1 + 0.216(1 - \sin\beta)^4\right]}{\cos\beta} \tag{3}$$

The crack area will be needed in the following calculation. Figure 1 shows the assumed geometry of the cracked cross-section and the definition of the angle ψ. The crack depth, a, and area, A, in terms of ψ can be obtained from geometry

$$\frac{A}{R^2} = \psi - \frac{1}{2}\sin 2\psi + \tan^2\psi \left(\frac{\pi}{2} - \psi - \frac{1}{2}\sin 2\psi\right) \tag{4a}$$

$$\frac{a}{R} = 1 - \cos\psi + \tan\psi \left(1 - \sin\psi\right) \tag{4b}$$

$$\beta = \frac{\pi a}{4R} = \frac{\pi}{4}\left[1 - \cos\psi + \tan\psi \left(1 - \sin\psi\right)\right] \tag{4c}$$

$$r = \frac{a(D - a)}{D - 2a}$$

$$R = \frac{1}{2} D$$

The value of the radius of the crack area, r, is also given above.

The compliance of the beam, λ, is the proportionality constant between the bending moment, M, and angle, ψ

$$\varphi = M \; \lambda \tag{5}$$

This relationship holds for cracked or uncracked sections, and the variation of λ with a/D is the desired end result. The value of λ for the uncracked section is obtainable from beam theory. Denoting this as λ_0

$$\phi = M \lambda_0 = \frac{L}{EI} M = \frac{64}{\pi} \frac{L}{ED^4} M$$

$$\lambda_0 = \frac{64L}{\pi ED^4} \tag{6}$$

The stored energy in the beam, U, is

$$U = \frac{1}{2} M \phi = \frac{1}{2} M^2 \lambda \tag{7}$$

The strain energy release rate, G, is defined as

$$G = \frac{\partial U}{\partial A} \tag{8}$$

where A is crack area [2]. G is also related to the stress intensity factor, K [2]. For plane stress this relation is

$$G = \frac{K^2}{E} \tag{9}$$

SOLUTION AND RESULTS

Combining Equations 8 and 9, and using the other equations given above provides the following result

$$\frac{\partial U}{\partial A} = \frac{\partial U}{\partial \psi} \frac{\partial \psi}{\partial A} = \frac{K^2}{E}$$

$$\frac{\partial U}{\partial \psi} = \frac{\partial A}{\partial \psi} \frac{K^2}{E}$$

Evaluating $\partial A/\partial \psi$ from Equation 4a, using the K-solution in Equation 3 and using Equation 7 (holding M constant and replacing partial derivatives with ordinary derivatives) yields the following differential equation

$$\frac{dU}{d\psi} - \frac{d}{d\psi}\left(\frac{1}{2}M^2\lambda\right) - \frac{1}{2}M^2\frac{d\lambda}{d\psi}$$

$$- \frac{D^2}{4}\frac{\tan\psi}{\cos^2\psi}(\pi-2\psi-\sin2\psi)\,60.731\,\frac{M^2}{D^5}\frac{\tan\beta[1+0.216(1-\sin\beta)^4]^2}{\cos^2\beta}$$

(β is given in terms of ψ in Equation 4c)

This provides a differential equation for λ as a function of ψ that can be solved by separating variables and integrating

$$\int_{\lambda_0}^{\lambda} d\lambda - \lambda - \lambda_0 - \frac{30.367}{ED^3}\int_0^{\psi}\frac{\tan\beta(x)\{1+0.216[1-\sin\beta(x)]^4\}^2}{\cos^2\beta(x)}\frac{(\pi-2x-\sin2x)\tan x}{\cos^2 x}dx$$

Defining the integral as $I(\psi)$ and using the value of λ_0 provides the following expression

$$\frac{\pi}{64}\frac{ED^4}{L}\lambda(\psi) - 1 + 1.491\frac{D}{L}I(\psi) \tag{10}$$

The value of the integral $I(\psi)$ is easily obtained by numerical integration. Table 1 summarizes the results, which were obtained on an HP15C hand calculator. Corresponding results are plotted in Figure 2.

As an example, for a wire of length 4 times its diameter, with a crack 30% of the diameter, Table 1 gives $I \approx 0.24$

$$\frac{\pi}{64}\frac{ED^4}{L}\lambda(0.3) - 1 + 1.491\left(\frac{1}{4}\right)(0.24) - 1.089$$

This is only approximately 9% higher than the compliance of the uncracked wire. Thus, it appears that cracks of depths of 30% of the diameter do not have an appreciable influence on the wire compliance. This small effect is probably due to the curvature of the crack front. If the crack front was straight at its maximum depth, then it would have a larger effect on the compliance. Figure 2 shows that the compliance begins to increase much more rapidly with crack depth as a/D increases beyond 0.3.

Table 1
Summary of Crack Sizes and Compliances

ψ radians	a/D	$I(\psi)$
0	0	0
0.1	0.048	0.0010
0.2	0.091	0.0068
0.3	0.131	0.0198
0.4	0.169	0.0417
0.5	0.203	0.0735
0.6	0.236	0.1164
0.7	0.267	0.171
0.8	0.297	0.240
0.9	0.326	0.323
1.0	0.353	0.423
1.1	0.380	0.541
1.2	0.406	0.680
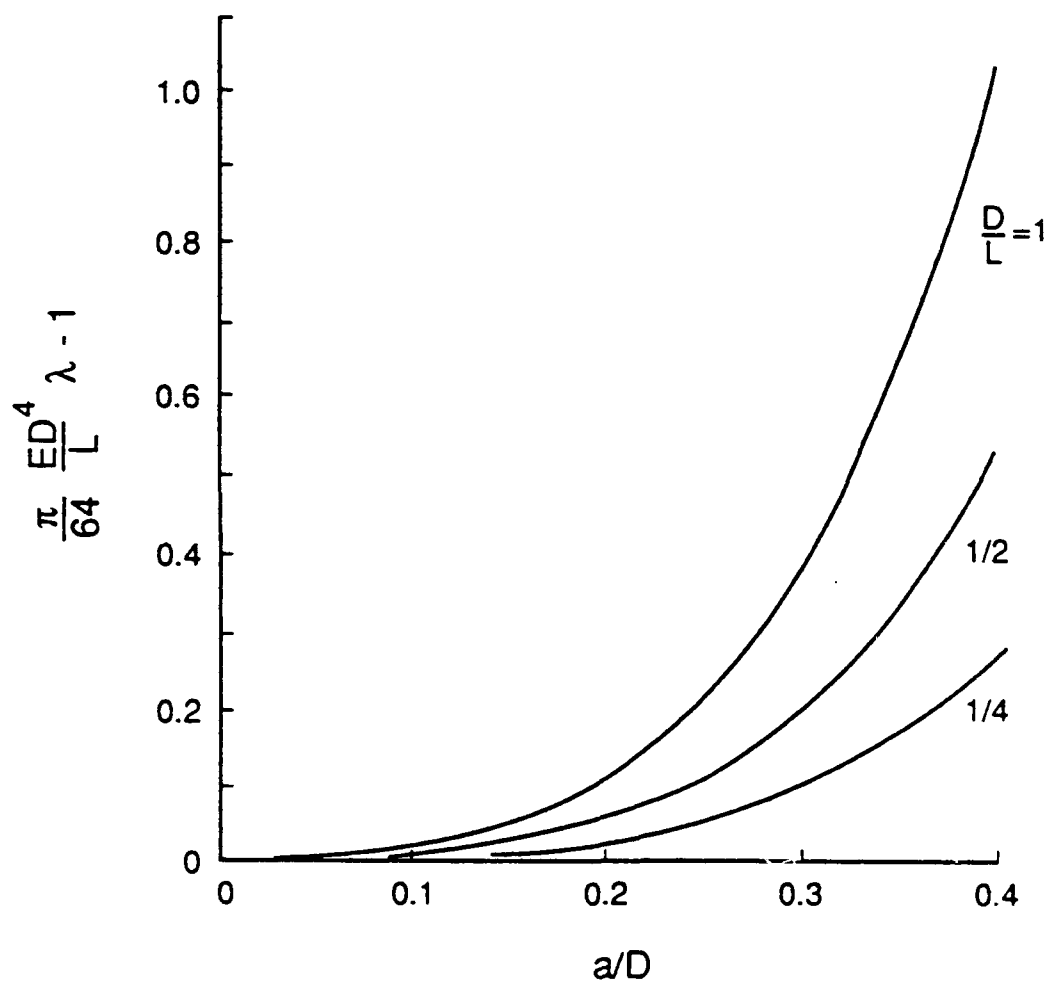
Figure 2.   Compliance as a function of crack depth for various diameter to length ratios.

01274 b

REFERENCES

1. R.G. Forman and V. Shivakumar, "Growth Behavior of Surface Cracks in the Circumferential Plane of Solid and Hollow Cylinders," *Fracture Mechanics: Seventeenth Symposium*, ASTM STP 905, Philadelphia, Pennsylvania, 1986, pp. 59-74.

2. P.C. Paris and G.C. Sih, "Stress Analysis of Cracks," *Fracture Toughness Testing and its Applications*, ASTM STP 381, Philadelphia, Pennsylvania, 1965, pp. 30-81.

Page 8

B-8

APPENDIX C

THERMAL RESPONSE OF WIRES TO AN ELECTRIC PULSE

James M. Kallis and Fremont Reizman

Abstract - An analytical and experimental investigation was performed of the thermal response to an electric pulse of a length of wire. A closed-form solution for the steady-state temperature distribution was derived, accounting for ohmic heat generation with temperature dependent resistivity, conduction heat losses out the ends of the wire, and radial heat losses from the surface of the wire. For a wire having a positive temperature coefficient of resistance, the steady-state solution has the following significant characteristics: 1) The temperature becomes infinite at a finite value of the current density, that is, a thermal "runaway" occurs; 2) The runaway current density increases with increasing radial heat transfer coefficient; 3) The temperature increases very slowly with increasing current density until the runaway value is approached and then increases very rapidly with further increases in the current density. The inhomogeneous initial-boundary value problem representing the transient thermal response was analyzed for constant voltage and constant current pulses. The transient analysis results were as follows: 1) Constant voltage - The asymptotic solution is bounded, that is, the system is stable and a steady-state solution always is reached. 2) Constant current - An infinite-series solution was derived. The system is stable (bounded asymptotic solution) only for low current densities; for current densities greater than or equal to the steady-state runaway value, the temperature becomes infinite when the pulse is turned on and steady state is not achieved. Temperatures of 25×10^{-6}m (1 mil) diameter Al - 1% Si wires were measured with an infrared microscope. The measurements agree qualitatively with the analytical predictions. The predictions of the transient analysis also are consistent with, and could explain the results of, power cycling fatigue tests of microelectronic device bond wires conducted in the program of which this investigation was a part.

INTRODUCTION

Background

This investigation was part of the Electronics Reliability Fracture Mechanics program (Contract No. F33615-87-C-3403) [1]. It was motivated by the results of thermal (power) cycling fatigue tests of 25×10^{-6}m (1 mil) diameter Al-1% Si microelectronic device bond wires [2] - [3]. The objective of these tests was to achieve fracture of the wire at the bond heel - the partially flattened portion of wire between the undeformed round wire and the heavily deformed bonded end of the wire (see Fig. 1).

In the initial tests, the outcome was very sensitive to the steady-state current. With a current 79% as high as the fusing current, no failures occurred after more than 3 million cycles. When the current was increased 11% (1.11 times as high as the aforementioned value), failure occurred after 0.5 million cycles at the midspan of the wire arch from what appeared to be electromigration [3]. No failures occurred at the heels of the bonds. Thus, in attempting to accelerate the fatigue failure of the heel of the wire by testing at higher currents, a different failure mechanism at a different location in the wire resulted. Eventually, fatigue failures at the bond heel were achieved [2].

Results of tests using a square-wave voltage pulse differed from those using a square-wave current pulse. With the constant-voltage setup, an inrush current was observed, that is, the current was high at turn-on and decayed to its steady-state value. With the constant-current setup, fusing failure occurred at high currents after a relatively small number of cycles. At the same steady-state current, this unwanted fusing failure did not occur with the constant-voltage setup. Fatigue failures at the bond heel were achieved using the constant-voltage setup at steady-state currents more than 20% higher than the highest currents at which fatigue failures were achieved with the constant-current setup [2].

Previous Work

A literature search revealed work performed for application to fuses and to microelectronic bond wires. Resistance measurements and infrared radiometer temperature measurements of 25×10^{-6}m (1 mil) diameter Al wires indicated a "thermal runaway" phenomenon [4]. The wire resistance and temperature "... remained relatively constant..." for currents between 0.2 and 0.5A. For higher currents, "...the resistance increased very rapidly indicating a dramatic temperature increase...". This behavior is consistent with the aforementioned results of the initial power cycling fatigue tests.

Solutions for the steady-state temperature distribution in a wire, neglecting radial heat losses, have been published [5] – [6]. No transient analysis was found in the literature for a wire having a nonzero temperature coefficient of resistance. However, after this work was completed, the authors discovered that Ref. 12 presents the steady-state solution, including radial heat losses, and the transient solution for a constant-current pulse for a wire having a positive temperature coefficient of resistance.

Ref. 7 documents the transient solution for a constant-current pulse for a wire having a temperature coefficient of resistance of zero. However, the phenomenon of interest here - thermal runaway - occurs only for a positive temperature coefficient of resistance.

The initial-boundary value problem solved in this paper is listed as an exercise in Ref. 8 (p. 166, Exercise 2), but the solution is not presented. The book by Carslaw & Jaeger [9] presents solutions of the partial differential equation solved in this paper with different boundary conditions.

Present Investigation

The scope of the research described here was as follows:
- Analysis
    - steady-state thermal response as function of
        - current density

- radial heat losses

- transient thermal response for

  - constant current pulse

  - constant voltage pulse

- Measurements

  - temperature distribution and history of a typical microelectronic device bond wire

  - comparison of analysis and test results

    - thermal

    - electrical

    - fatigue life.

ANALYSIS

Statement of the Problem

The configuration analyzed is a length of initially isothermal wire subjected to a square-wave electric pulse. The ends of the wire are held at a constant temperature, which may be different than the ambient temperature.

Assumptions

The following simplifying assumptions are made:

1) The temperature and current are uniform over the wire cross section. In other words, the average temperature and current over the cross section are considered.

2) Inductive and capacitive effects are neglected. That is, the rate of change of current is not limited by these effects. This appears to be a good assumption for a nearly straight length of wire.

3) Except for the resistivity, the material properties of the wire are independent of temperature. Specifically, the temperature dependence of thermal conductivity, density, and specific heat is neglected. This is a good assumption for Al-1% Si for temperatures at least as high as 100°C. (If thermal runaway occurs and the wire temperature approaches its melting temperature, the material properties would not be expected to remain independent of temperature. However, this effect is not expected to change the basic conclusions from this analysis.)

4) Radial heat losses are accounted for by a heat transfer coefficient that is constant along the wire length. Actually the heat transfer coefficients for free convection and radiation vary with temperature. However, as is shown below, the simplified analysis predicts the qualitative results of tests.

Definitions

The following terms, illustrated in Fig. 2, are defined:

L = wire length

x = distance from end of wire

t = time after pulse is turned on

V = voltage across wire

I = current

$T(x,t)$ = temperature

T_0 = temperature of ends of wire [$T(0,t) = T(L,t) = T_0$ for $t > 0$]

h = radial heat transfer coefficient (assumed uniform along length of wire)

T_∞ = temperature of medium into which radial heat transfer is occurring

ρ = resistivity

ρ_0 = resistivity at temperature T_0

α = temperature coefficient of resistance

k = thermal conductivity

ρ_D = mass density

C_p = specific heat

E = energy input

A = cross-sectional area

D = wire diameter.

Initial-Boundary Value Problem

1. Derivation of Partial Differential Equation

The governing equations are obtained from the energy balance for an elemental

volume of area A and length dx:

$$E(x, t) = (\rho_D A \, dx) C_p \frac{\partial T}{\partial t}.$$

(1)

The energy input is the sum of the electrical dissipation and the net inward heat flow:

$$E(x,t) = I^2 \rho(x, t) \frac{dx}{A} - [T(x,t) - T_\infty] \pi h D \, dx$$

$$+ kA \left(\frac{\partial T}{\partial x}(x+dx, t) - \frac{\partial T}{\partial x}(x, t) \right)$$

$$= I^2 \rho(x, t) \frac{dx}{A} - [T(x,t) - T_\infty] \pi h D \, dx + kA \frac{\partial^2 T}{dx^2}(x, t) \, dx.$$

(2)

Substituting (2) into (1) yields:

$$\rho_D A C_p \frac{\partial T}{\partial t}(x, t) = \frac{1}{A}(I(t))^2 \rho(x, t) - [T(x,t) - T_\infty] \pi h D + kA \frac{\partial^2 T(x, t)}{\partial x^2}.$$

(3)

For a metal, the resistivity is a linear function of the temperature in the temperature range of interest:

$$\rho(x, t) = (\rho_0) \left\{ 1 + \alpha [T(x,t) - T_0] \right\}.$$

(4)

The current and resistance are related to each other by Ohm's law. However the voltage across an element is a function of x and t and is not known a priori.

Substituting (4) into (3) and putting the equation in standard form yields the following partial differential equation:

$$\frac{\rho_D\, A\, C_P}{\rho_o\, \alpha}\frac{\partial \rho}{\partial t} - \frac{kA}{\rho_o\, \alpha}\frac{\partial^2 \rho}{\partial x^2} =$$

$$\left(\frac{I^2}{A} - \frac{\pi\, h\, D}{\alpha \rho_o}\right)\rho + \frac{\pi\, h\, D\rho_\infty}{\alpha\, \rho_o}\,. \tag{5}$$

The boundary conditions are:

$$\rho\,(0, t) = \rho_0. \tag{6}$$

$$\rho\,(L, t) = \rho_0. \tag{7}$$

The initial condition is:

$$\rho\,(x, 0) = \rho_0. \tag{8}$$

This is an inhomogeneous initial-boundary value problem [8]. The differential equation and both the boundary conditions are inhomogeneous.

2. Dimensionless Form

Define the following dimensionless quantities:

$$P \equiv \rho/\rho_0 = 1 + \alpha\,(T - T_o)\,. \tag{9}$$

$$\lambda \equiv Q - H, \tag{10}$$

C-8

where:

$$Q \equiv \frac{\rho_0 \, \alpha \, L^2 \, I^2}{kA^2} \, .$$

(11)

and:

$$H \equiv \frac{\pi \, hDL^2}{kA} .$$

(12)

Q is a dimensionless current density parameter. It is proportional to the square of the current density I/A. The parameter H is a dimensionless radial heat loss parameter. Thus λ is a dimensionless net heat input parameter:

$$\chi \equiv x/L.$$

(13)

$$\tau \equiv \frac{t}{\left(\frac{\rho_D C_p L^2}{k} \right)} = \frac{a}{L^2} \, t.$$

(14)

τ is a dimensionless time called the Fourier modulus, and a is the combination of physical properties called the thermal diffusivity [10]:

$$a \equiv \frac{k}{\rho_D \, C_p} .$$

(15)

Substituting (9) through (15) into (5) through (8) yields the following inhomogeneous initial-boundary value problem:

DE: $\qquad \dfrac{\partial P}{\partial \tau} - \dfrac{\partial^2 P}{\partial \chi^2} = \lambda \, P + HP_\infty .$

(16)

C-9

$$P(0, t) = 1. \tag{17}$$

BC:
$$P(1, \tau) = 1. \tag{18}$$

IC: $\qquad P(\chi, 0) = 1.$ (19)

Thermal Response

1. Steady State

This is the same as the analysis in [2], with different notation and with all the parameters in dimensionless form.

At steady state, (16) - (18) reduce to the following inhomogeneous boundary value problem:

DE:
$$\frac{d^2 P(\chi)}{d\chi^2} + \lambda P(\chi) = -HP_\infty. \tag{20}$$

$$P(0) = 1. \tag{21}$$

BC:

$$P(1) = 1. \tag{22}$$

The solution depends on the sign of λ, the net heat input parameter defined in (10) as Q-H. The sign of the current density parameter Q, defined in (11), is the same as the sign of the wire temperature coefficient of resistance. The sign of the radial heat loss parameter H, defined in (12), is always positive :

$\lambda < 0$: This occurs if $\alpha < 0$ or if $|Q| < H$. The solution is:

$$\frac{P_\chi - \frac{H}{\lambda} P_\infty}{1 - \frac{H}{\lambda} P_\infty} = \cosh S\chi + \frac{1 - \cosh}{\sinh S} \sinh S\chi, \tag{23}$$

where:

$$S \equiv |\lambda|^{1/2}.$$

(24)

The resistivity is finite for all finite values of the current:

$\lambda = 0$: This occurs if $\alpha > 0$ and $Q = H$. The solution is:

$$P(\chi) = 1 + \frac{H}{2} P_\infty \chi (1 - \chi).$$

(25)

This also can occur if $\alpha = 0$ and $H = 0$. In this case, the resistivity has the trivial solution $\rho(\chi) = \rho_0$. The solution for the temperature distribution is obtained from (3):

$$\frac{T(\chi)}{T_0} = 1 + (1/2) q\chi (1 - \chi),$$

(26)

where:

$$q \equiv \frac{\rho_0 L^2 I^2}{T_0 k A^2}.$$

(27)

The temperature rise is proportional to the square of the current density. Thus, as for $\lambda < 0$, the temperature is finite for all finite values of the current:

$\lambda > 0$: This occurs if $\alpha > 0$ and $Q > H$. The solution is:

$$\frac{P(\chi) + \frac{H}{\lambda} P_\infty}{1 + \frac{H}{\lambda} P_\infty} = \cos S\chi + \frac{1 - \cos S}{\sin S} \sin S\chi.$$

(28)

This solution has been published previously in Ref. 12. The solution for zero radial heat losses (H=0) has been published twice [5] – [6].

The key feature of the solution is that, in contrast to the solution for $\lambda < 0$ and the solution for $\lambda = 0$, the temperature becomes infinite at a finite value of the current. That is, a thermal "runaway"

occurs. From (28), $P \rightarrow \infty$ when sin $S = 0$, which occurs when $S = \pi$. Thus, thermal runaway occurs when:

$$\lambda \equiv Q - H = \pi^2.$$

(29)

From (29), the following are seen:

o   Thermal runaway can occur with finite radial heat losses $(H > 0)$.

o   The runaway value of the current density increases with increasing radial heat losses.

To show the temperature dependence on the current, (28) is solved for the midspan resistivity for the case of zero radial heat losses:

$$P(1/2) = \cos (1/2)S + \frac{1 - \cos S}{\sin S} \sin (1/2)S.$$

(30)

In this case, S is proportional to the current density:

$$S = \left(\frac{\rho_0 \alpha L^2}{k}\right)^{1/2} \frac{I}{A}.$$

(31)

(30) is plotted in Fig. 3. The resistivity, and hence the temperature, is a very sensitive function of the dimensionless current density S. It increases very slowly with increasing S until S approaches π and then increases very rapidly (runs away) with further increases in S. This is in contrast with the relation for a material having zero temperature coefficient of resistance, for which the temperature increases as the square of the current density (Eqs. 26 and 27).

2. Transient

The thermal responses for the two types of electric pulse – constant current and constant voltage – are analyzed here. To simplify so that the differences between the two pulse types are shown clearly, the analysis is carried out for zero radial heat losses ($H = 0$). The inhomogeneous initial-boundary value problem (Eqs. 16-19) becomes:

DE:
$$\frac{\partial P}{\partial \tau} - \frac{\partial^2 P}{\partial \chi^2} = QP. \tag{32}$$

$$P(0,\tau) = 1. \tag{33}$$

BC:

$$P(1,\tau) = 1. \tag{34}$$

IC: $P(\chi,0) = 1.$ (35)

2.1 Constant Current

In this case, Q is constant, and the partial differential equation is linear.

The problem is solved by the method of variation of parameters [8]. The solution is expanded in a series of eigenfunctions associated with the related homogeneous problem.

In terms of the variable:
$$u(\chi,\tau) \equiv P(\chi,\tau) - 1, \tag{36}$$

the solution is:

$$u(\chi,\tau) = 4Q \sum_{n=1,3,5,\dots}^{\infty} \left(\frac{1 - \exp\left\{-[(n\pi)^2 - Q]\tau\right\}}{[(n\pi)^2 - Q]\, n\pi} \sin n\pi\chi \right). \tag{37}$$

As stated in the Previous Work section, this solution has been published previously in Ref. 12.

The asymptotic solution depends on the sign of the factor $\pi^2 - Q$ in the first term of the series.

$\underline{Q < \pi^2}$: In this low-current-density case, the coefficient of τ is negative. The exponential term decays and goes to zero as $\tau \to \infty$. The asymptotic solution is bounded, and the steady-state solution is the Fourier sine series representation of (28).

$\underline{Q = \pi^2}$: The solution can be obtained directly from the initial-value problem for the time-dependent coefficients $T_n(\tau)$ of the eigenfunctions:

$$\text{DE:} \quad \frac{dT_n}{d\tau} - \left[(n\pi)^2 - Q\right] T_n = \left\{ \begin{array}{l} 0 \ (n \text{ even}) \\ \frac{4Q}{n\pi} \ (n \text{ odd}) \end{array} \right\} \tag{38}$$

$$\text{IC:} \quad T_n(0) = 0. \tag{39}$$

For $Q = \pi^2$, the solution for $T_1(\tau)$ is

$$T_1(\tau) = \frac{4}{\pi} Q\tau. \tag{40}$$

The coefficient $T_1(\tau)$ grows linearly with increasing τ, and therefore, the asymptotic solution is unbounded.

$\underline{Q > \pi^2}$: Examination of (37), or (38) and (39), shows that the coefficient $T_1(\tau)$ grows exponentially and that the asymptotic solution is unbounded.

Thus, the system described by the initial-boundary value problem is:

- stable for $Q < \pi^2$
- unstable for $Q \geq \pi^2$.

2.2 Constant Voltage

In this case, Q is a function of τ and depends on the unknown P:

$$\frac{\partial P(\chi, \tau)}{\partial \tau} - \frac{\partial^2 P(\chi, \tau)}{\partial \chi^2} - Q(\tau) P(\chi, \tau) = 0.$$

$$(41)$$

It does not appear possible to solve (41) analytically. Instead the approach is to show that the asymptotic solution is always bounded.

To do this, define the instantaneous average value of $P(\chi, \tau)$ by integrating over the wire length:

$$P_{avg}(\tau) \equiv \int_0^1 P(\chi, \tau) \, d\chi.$$

$$(42)$$

Integrating each term in (41) yields:

1st term:

$$\int_0^1 \frac{\partial P}{\partial \tau}(\chi, \tau) \, d\chi = \frac{dP_{avg}(\tau)}{d\tau} .$$

$$(43)$$

2nd term:

$$\int_0^1 \frac{\partial^2 P}{\partial \chi^2}(\chi,\tau)\, d\chi = \frac{\partial P}{\partial \chi}(\chi,\tau)\ \Big|_0^1$$

$$= \frac{\partial P}{\partial \chi}(1,\tau) - \frac{\partial P}{\partial \chi}(0,\tau). \tag{44}$$

By symmetry, we have:

$$\frac{\partial P}{\partial \chi}(1,\tau) = -\frac{\partial P}{\partial \chi}(0,\tau). \tag{45}$$

Substituting (45) into (44) yields:

$$\int_0^1 \frac{\partial^2 P}{\partial \chi^2}(\chi,\tau)\, d\chi = -2\frac{\partial P}{\partial \chi}(0,\tau). \tag{46}$$

3rd term:

$$\int_0^1 Q(\tau)\, P(\chi,\tau)\, d\chi = Q(\tau)\, P_{avg}(\tau). \tag{47}$$

From Ohm's law:

$$I = V/R. \tag{48}$$

From the definition of resistivity:

$$R = L\rho_{avg}/A. \tag{49}$$

Substituting (48) and (49) into (11) yields:

$$Q = \frac{\alpha V^2}{k\rho_o}\frac{1}{P_{avg}^2}. \tag{50}$$

Substituting (50) into (47) yields:

$$\int_0^1 Q(\tau)\, P(\chi,t)\, d\chi = \frac{\alpha V^2}{k\rho_o}\frac{1}{P_{avg}(\tau)}. \tag{51}$$

Combining (43), (46), and (51), the integral of (41) can be written as:

$$\frac{dP_{avg}}{d\tau}(\tau) = \frac{\alpha V^2}{k\rho_o}\frac{1}{P_{avg}(\tau)} - 2\frac{\partial P}{\partial \chi}(0,\tau).$$

(52)

Differentiating both sides of (52) with respect to τ yields:

$$\frac{d}{d\tau}\left[\frac{dP_{avg}(\tau)}{d\tau}\right] = \frac{\alpha V^2}{k\rho_o}\frac{d}{d\tau}\left[\frac{1}{P_{avg}(\tau)}\right]$$

$$-2\frac{d}{d\tau}\left[\frac{\partial P}{\partial \chi}(0,\tau)\right].$$

(53)

Now determine the sign of each of the terms on the right-hand side of (53) in the warm-up period, when $P_{avg}(\tau)$ is increasing.

1st term: Since:

$$\frac{dP_{avg}(\tau)}{d\tau} > 0,$$

we have:

$$\frac{d}{d\tau}\left[\frac{1}{P_{avg}(\tau)}\right] < 0.$$

(54)

Therefore, the first term is negative.

2nd term: assuming that $P(\chi,\tau)$ is a well-behaved function, its slope at $\chi = 0$ must increase as P_{avg} increases: (55)

$$\frac{d}{d\tau}\left[\frac{\partial P}{\partial \chi}(0,\tau)\right] > 0.$$

(56)

Therefore the second term is negative.

Since each of the terms on the right-hand side of (35) is negative, the left-hand side is negative:

$$\frac{d}{d\tau}\left[\frac{dP_{avg}}{d\tau}\right] < 0. \tag{57}$$

Thus, the rate of change $dP_{avg}/d\tau$ decreases with increasing time.

As the wire heats up, the first term on the right-hand side of (52) decreases monotonically from its finite initial value:

$$\frac{\alpha V^2}{k\rho_o}$$

and the second term increases monotonically from zero. Thus, the difference between these terms decreases, and:

$$\frac{dP_{avg}}{d\tau} \rightarrow 0 \text{ as } \tau \rightarrow \infty.$$

Therefore, P_{avg} asymptotically approaches the steady state solution.

2.3   Comparison of Constant-Current and Constant-Voltage Pulse

The predicted transient thermal response of wires to each type of pulse is shown in Fig. 4.

MEASUREMENTS

Approach and Apparatus

Direct measurements were undertaken on 25×10^{-6}m (1 mil) diameter Al-1%Si bond wires using an infrared imaging apparatus, Barnes CompuTherm (EDO Corp., Barnes Engineering; Shelton, CT 06484). This instrument can operate at high magnification, with a spatial resolution of about 10 micrometers. Although 2 seconds are required to scan out a complete image, the scan motions can be stopped and the evolution of temperature at a single point can be followed with a time resolution of about 100 microseconds.

The CompuTherm uses a cooled InSb detector operating in the 3 to 5-micrometer wavelength range. By combining data from two isothermal images at known temperature, the proprietary software calculates the emissivity for each pixel separately. Thereafter, a pixel-by-pixel emissivity correction can be made. It is, therefore, unnecessary to coat or paint metallic objects to get a known high emissivity. Although some initial experiments were done with carbon-flashed wires, all the data reported here were taken on uncoated wires. The emissivities were generally measured in the vicinity of $60°$C and were always approximately 0.3. This is a surprisingly high value for "bare" aluminum, but could have resulted from pitting or oxide coating, especially after the wire had been conditioned by repeated experiments. It also could have resulted from the draw marks produced in the fabrication process of drawing down the wire from larger diameter wire stock.

Three types of measurements were performed. In the steady state (dc current), the temperature profile along the wire was plotted for several values of current. Also, the peak temperature was plotted as a function of the current. In the transient mode, the time-dependence of temperature at midspan was measured when the current was turned abruptly on and off, producing a square-wave voltage pulse. (These measurements were not made with the aforementioned constant-current setup.)

Temperature Profile

Two wires (shown in Fig. 1) were imaged, with special care to keep the whole wire in good focus. The steady-state temperature was measured at a number of points along the length, and plotted as a function of distance along the curved wire.

The results are plotted in Fig. 5, at several values of current. The temperature is generally higher in the center than at the ends as expected, but the profiles also show some complex features not easily accounted for. The "shoulders" may be due to radial heat losses from the lands to which the wires are bonded.

The temperature profiles of the two wires all show the expected general shape, with a maximum in the center. However, the details of the profiles are different for the two wires and may indicate differing patterns of pitting or oxidation.

Current Dependence of Steady-State Midspan Temperature

In these studies, wires were thermally imaged at a point near the center of the wire span. The emissivity of the wire was measured using the CompuTherm algorithm. The software then produced images corrected to true temperature.

The center temperatures were measured at many values of current for several different wires, having lengths of 29, 34, and 172 wire diameters. Most measurments were made with the temperature of the package into which the wires were bonded controlled at a value above room temperature.

The results are presented in Fig. 6. The measurements are plotted in the dimensionless variables defined in the Analysis section. To show the increase in the importance of radial heat losses from free convection as the length-to-diameter ratio L/D increases, the radial heat loss term is omitted from the abscissa.

Thermal Time Constant

Using the CompuTherm in its "stare" mode, several thermal images were recorded from a point near the center of the wire as it was excited by a square-wave voltage source. Figures 7a and 7b are derived from these images at two different time scales. They show that about half the total temperature change is achieved in a few milliseconds, followed by a much slower drift to a steady state. This drift can last 100 ms. Heating is slightly slower than cooling, perhaps because the increase in resistivity delays the attainment of steady conditions.

The shorter time constant of about 5 ms agrees in order of magnitude with the time constant calculated from the length and thermal diffusivity of the wires. The longer time constant may be associated with the temperature rise of the wire supports.

COMPARISONS OF PREDICTIONS WITH TEST RESULTS

Steady State

The measurements shown in Fig. 6 enable comparison with the predictions of the steady-state analysis. In particular, the test data show the occurrence of thermal runaway and the effect of radial heat losses.

For the conditions of these tests, radial heat losses were significant. This is seen by comparing the test data with the prediction for zero radial heat losses.

In general, radial heat losses (accounted for by h) consist of radiation and convection. Order-of-magnitude calculations [2] showed that radiation is negligible compared with convection for the wire dimensions and temperatures in these tests. This conclusion agrees with the results of previous research on heat transfer from long, fine wires [11].

The radial free convection heat loss becomes larger relative to the axial conduction heat loss as:

o   the wire length-to-diameter ratio L/D increases and

o   for a given L/D value, as the temperature T_0 of the ends of the wires increases relative to the laboratory ambient temperature.

In these tests, data were measured for:

o   L/D = 29, 34 and 172

o   for L/D = 172, T_0 = 38°C and 59-69°C.

Fig. 6 shows the following significant results:

o   Except for the three data points for L/D = 34, the shape of each curve is as predicted – a very

      slow increase in temperature with increasing current until a critical value is approached and a

      very rapid temperature increase with further increases in current.

o   The current at which a given temperature rise occurs increases as convective losses become

      more important - as the wire length-to-diamenter ratio L/D increases and, for a given L/D, as

      the temperature T_0 of the ends of the wire increases.

These results agree with the predictions of the steady-state analysis:

o   Thermal runaway can occur with radial heat losses from the wire.

o   The runaway curent density increases with increasing radial heat losses.

As mentioned in the Introduction section of this paper, the predicted thermal runaway phenomenon

also was observed in previous tests [4]. Thus, in spite of the simplified treatment of convection,

the analysis correctly predicts the occurrence of thermal runaway and the qualitative effect of radial

heat losses.

To obtain quantitative agreement with measurements such as those in Fig. 6, convection would

have to be treated more accurately. This complexity was not warranted for the purposes of this

paper. For other wire materials and configurations, the temperature vs. current curve can be

measured using the technique described in the Measurements section of this paper.

Transient

The predictions (Fig. 4) of the transient analysis, of the difference in stability between the constant-current and the constant-voltage pulse, are consistent with and could explain the fatigue test results described in the Background section of this paper. To achieve a sufficiently large temperature rise to produce fracture at the heel of the wire in a reasonable number of cycles, the current was set very close to the value at which the midspan temperature becomes infinite.

In the constant-current case, a slight increase in the quantity Q can make the system unstable and result in a fusing failure. This could result from:

o   an increased current.

o   a reduction in cross-sectional area due to crack growth.

o   a change in material properties due to thermal cycling.

In the constant-voltage case, the current always decays from its inrush value to the steady-state value, and the temperature increases gradually to the steady-state value. This qualitative behavior was observed in the constant-voltage tests (see Ref. 3 and Fig. 7 of this appendix).

In hindsight, it seem obvious that the constant-voltage case is stable, because the current decreases as the wire heats up. It also is plausible that the constant-current case is subject to instability, because the voltage across the wire increases as the wire heats up. However, no relevant analytical or experimental work on the difference in stability of the constant-voltage and constant-current pulse appears to have been published prior to this appendix.

CONCLUSIONS

The following conclusions are drawn from these analyses and test results:

- Thermal runaway can occur for a wire having a positive temperature coefficient of resistance.

- The steady-state midspan temperature in a wire bond is a very sensitive function of the current density. The temperature increases very slowly with increasing current density until the runaway value is approached and then increases very rapidly with further increases in the current density.

- Thermal runaway can occur with radial heat losses from the wire. The runaway current density increases with increasing radial heat transfer coefficient.

- The transient thermal response to a square-wave electric pulse of a length of wire having a positive temperature coefficient of resistance depends on the setup:

  Constant voltage. The system always is stable, and a steady-state solution is reached.

  Constant current. The system is stable only for small values of the current density. At high current densities, the temperature increases without bound. The runaway current density is the same as the value at which the steady-state midspan temperature becomes infinite.

REFERENCES

[1] A. H. Burkhard and C. E. Leak, "Durability Analysis Using Fracture Mechanics for Avionics Integrity," Proc. Institute of Environmental Sciences 37th Annual Technical Meeting, May 1991.

[2] D. O. Harris, R. A. Sire, C. F. Popelar, M. F. Kanninen, D. L. Davidson, L. B. Duncan, J. M. Kallis, D. W. Buechler, P. G. Backes, and F. Reizman, "Fracture Mechanics Life Prediction for Microscale Components -- With Application to Wire Bonding," Proc. 29th Annual International Reliability Physics Symposium, pp. 35-43, IEEE Catalog No. 91CH2974-4, April 1991.

[3] P. G. Backes, "Electromigration in Aluminum Bond Wires Subjected to Current Pulsing," accepted for presentation at International Symposium for Testing and Failure Analysis (ISTFA)/91 Microelectronics Symposium, November 1991.

[4] W. Day and J. Partridge, "Lead Failure Study for the Motorola 1-Mil Wedge-Bonded 1006323 Transistor," Massachusetts Institue of Technology Instrumentation Laboratory Report E-2218, December 1967.

[5] L. D. Yurk, "A New Approach to the Rating of Fuses for Electronic Circuits," IEEE Trans. on Industrial Electronics & Control Instrumentation, Vol. IECI-24, pp. 317-321, November 1977.

[6] J. T. May, M. L. Gordon, W. M. Piwnica, and S. B. Bray, "The DC Fusing Current & Safe Operating Current of Microelectric Bonding Wires," Proc. International Symp. for Testing & Failure Analysis, pp. 121-131, November 1989.

[7] V. A. Nieberlein, "The Heating & Failure of Microelectronic Wires from an Electric Pulse," AD-A134 592, September 1982.

[8] P. W. Berg & J. L. McGregor, Elementary Partial Differential Equations, Preliminary Edition, Chapter 5, Holden-Day, Inc., San Francisco, 1964.

[9] H. S. Carslaw & J. C. Jaeger, Conduction of Heat in Solids, Second Edition, pp. 404-405, Oxford U. Press, 1959.

[10] F. Kreith, Principles of Heat Transfer, Third Edition, 1976 Impression, p. 144, Intext Press, Inc., New York, 1973.

[11] E. Loh, "Physical Analysis of Data on Fused-Open Bond Wires," IEEE Trans. on Components, Hybrids, & Manufacturing Technology, Vol. CHMT-6, pp. 209-217, June 1983.

[12] M. Coxon, C. Kershner, & D.M. McEligot, "Transient Current Capacities of Bond Wires in Hybrid Microcircuits," IEEE Trans. on Components, Hybrids, & Manufacturing Technology, Vol. CHMT-9, pp. 279-285, September 1986.

FIGURE CAPTIONS

1. Laboratory test specimens of 25×10^{-6}m (1 mil) diameter A1-1% Si microelectronic device bond wires.

    a) Wire length = 0.86×10^{-3}m = 34 wire diameters.
    b) Wire length = 0.74×10^{-3}m = 29 wire diameters.

2. Analytical model configuration.

3. Predicted steady-state temperature dependence on net heat input for wire having a positive temperature coefficient of resistance.

4. Predicted transient thermal response of wires to an electric pulse.

5. Measured steady-state temperature profile.

    a) Wire shown in Fig. 1a.
    b) Wire shown in Fig. 1b.

6. Measured current dependence of steady-state midspan temperature.

7. Measured transient thermal response of wire to square-wave voltage pulse.

    a) Scale in sec.
    b) Scale in ms.
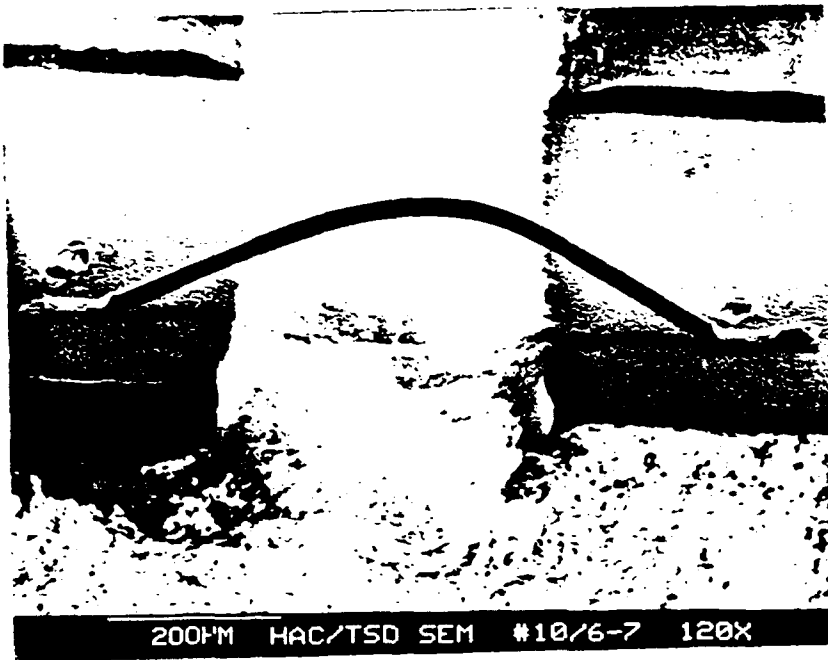
Fig. 1a
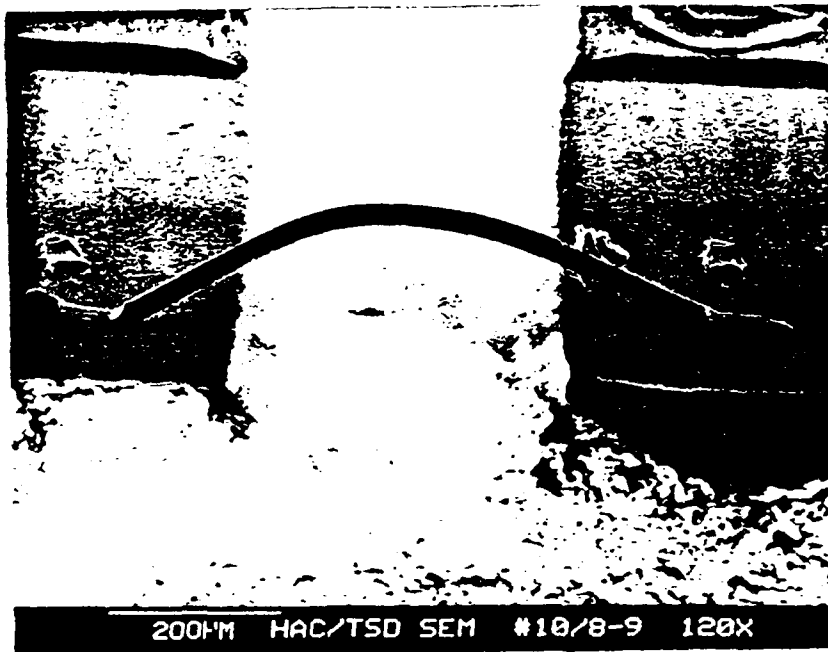
Fig. 1b

Fig. 1. Laboratory test specimens of 25×10^{-6} m (1 mil) diameter A1-1% Si microelectronic device bond wires.

    a) Wire length=0.86×10^{-3}m=34 wire diameters.

    b) Wire length=0.74×10^{-3}m=29 wire diameters.

$T=T_\infty$

$T=T_0$ $T=T_0$

$T=T(x,t)$

current $I(t) \longrightarrow$ D

$\longrightarrow$ X

0   voltage   L

$V(t)$

Fig. 2. Analytical model configuration

DIMENSIONLESS CURRENT DENSITY
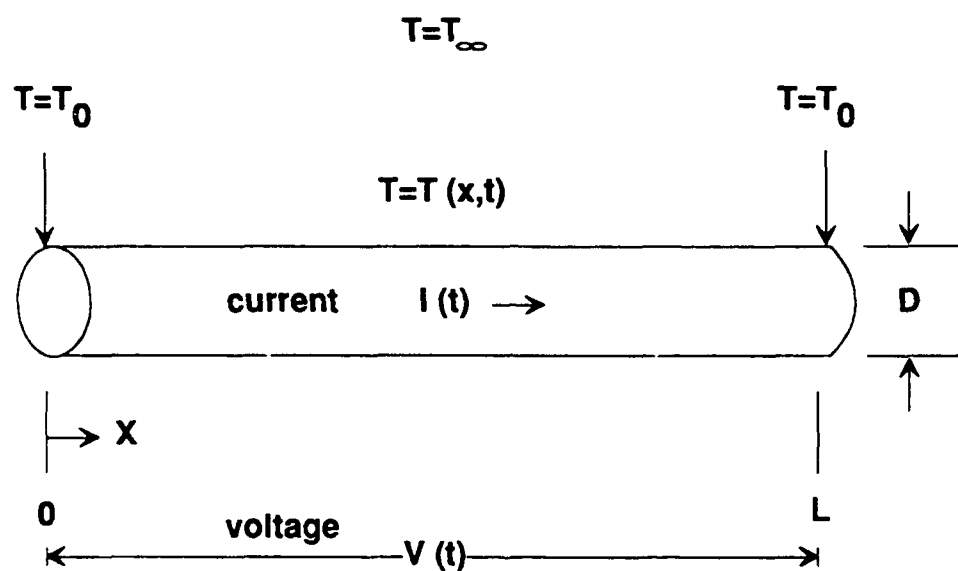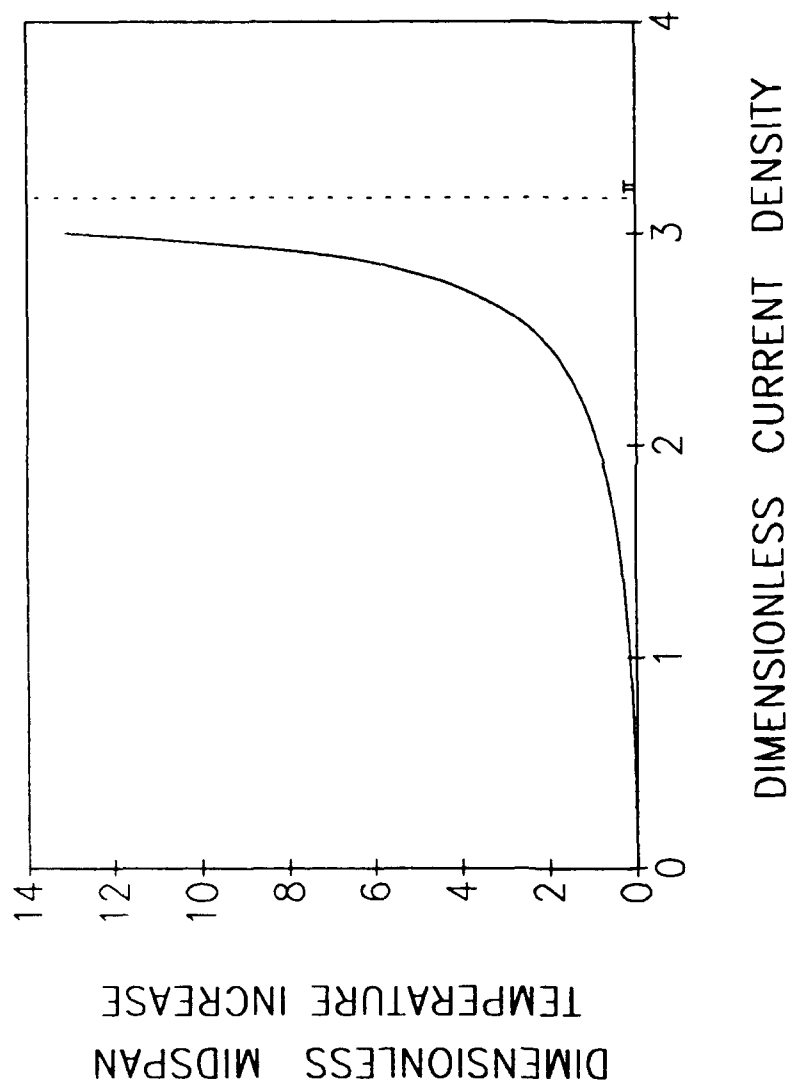
FIGURE 3.   Predicted steady state temperature dependence on net heat input for wire having a positive temperature coefficient of resistance.

CONSTANT VOLTAGE
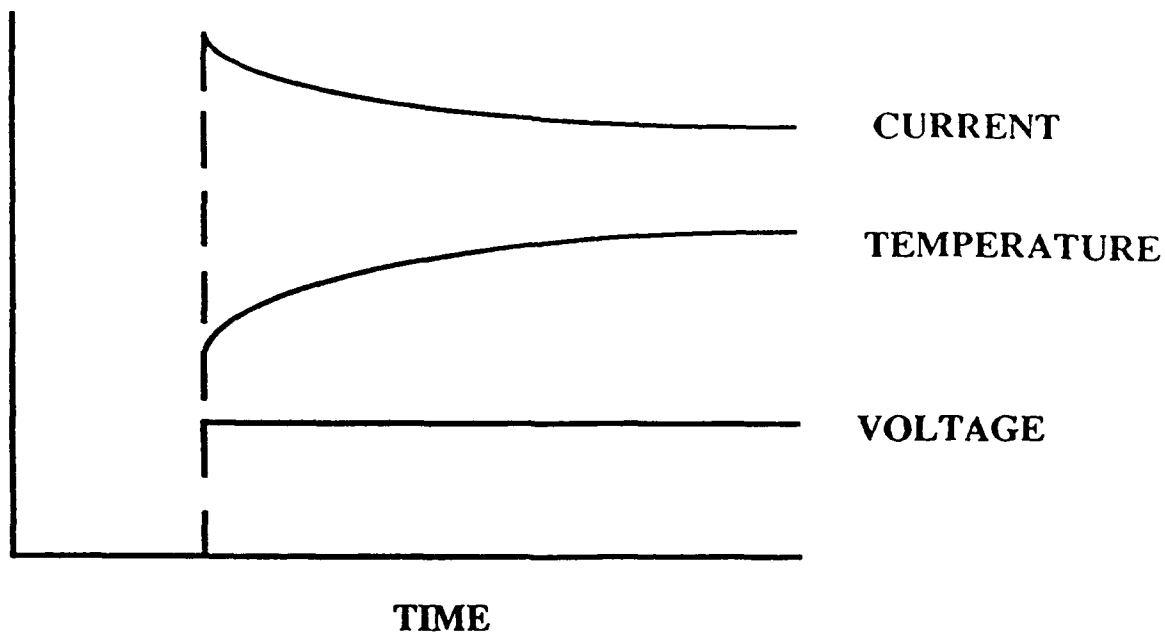
CONSTANT CURRENT
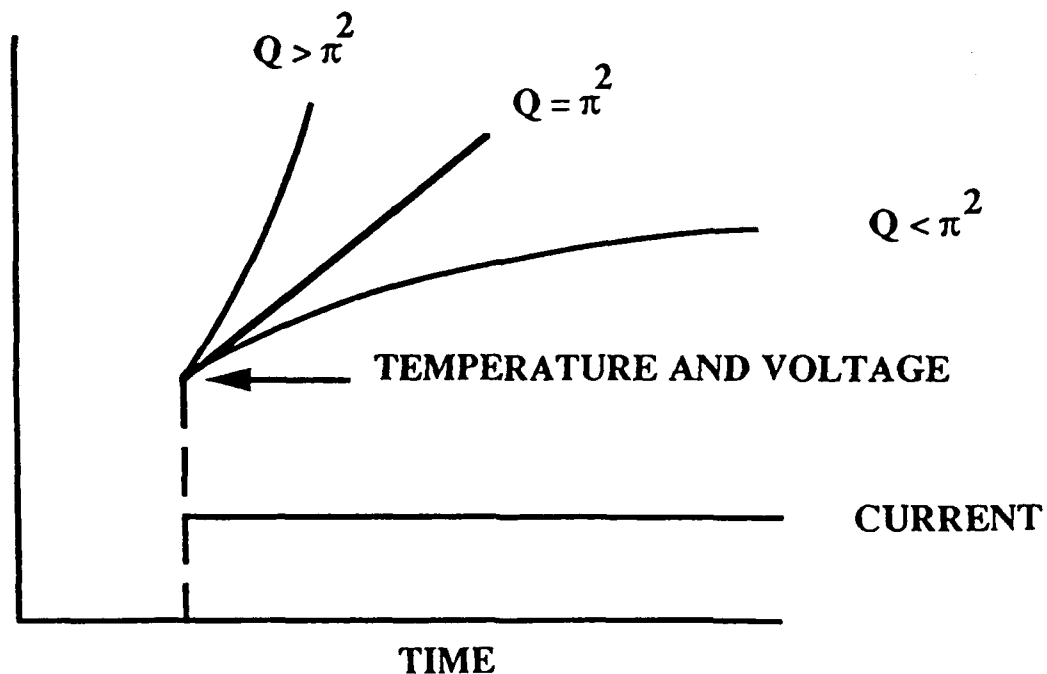
Figure 4. Predicted Transient Thermal Response of Wires to an Electric Pulse.
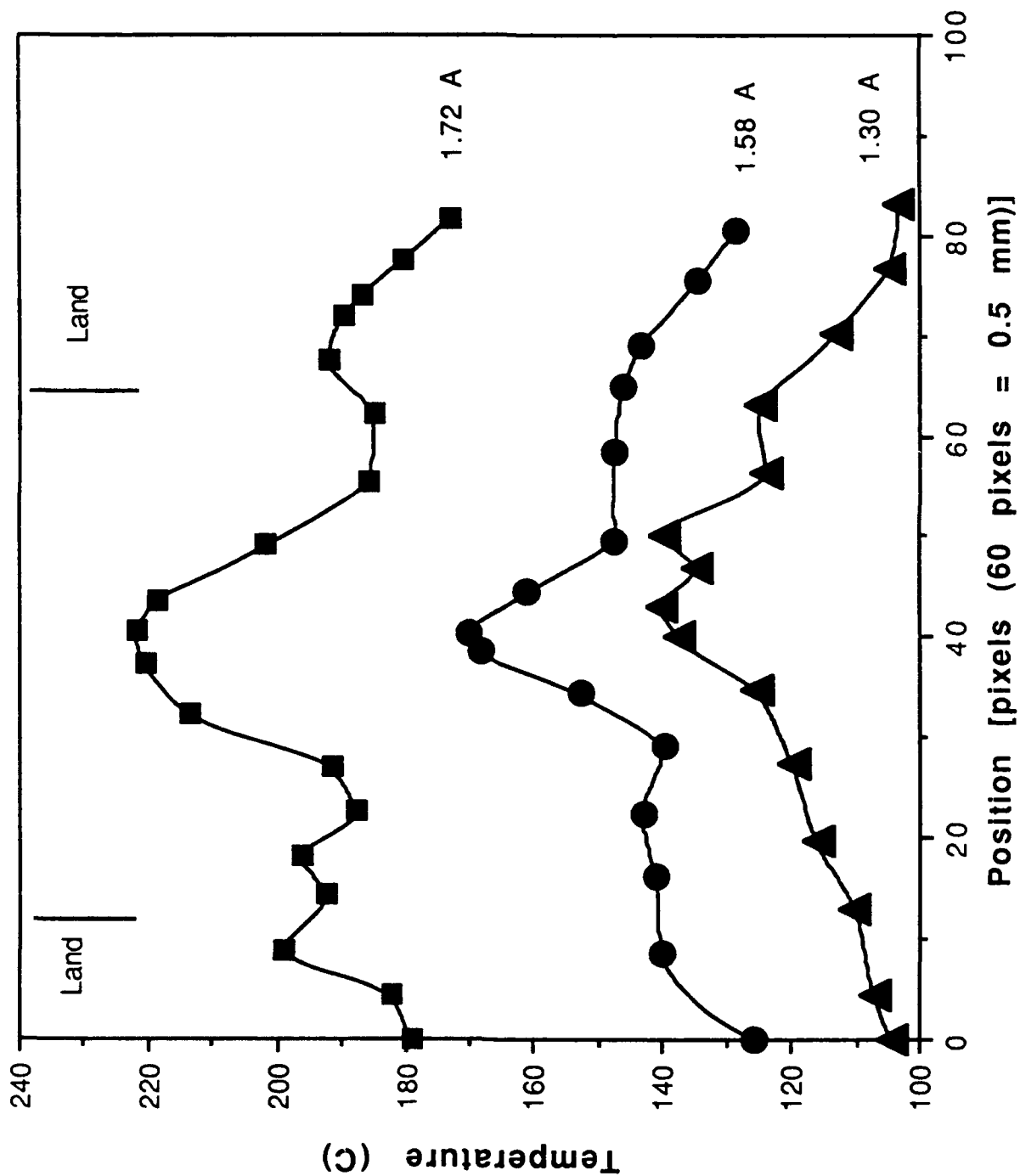
Fig. 5a. Measured steady-state temperature profile for wire shown in Fig. 1a.
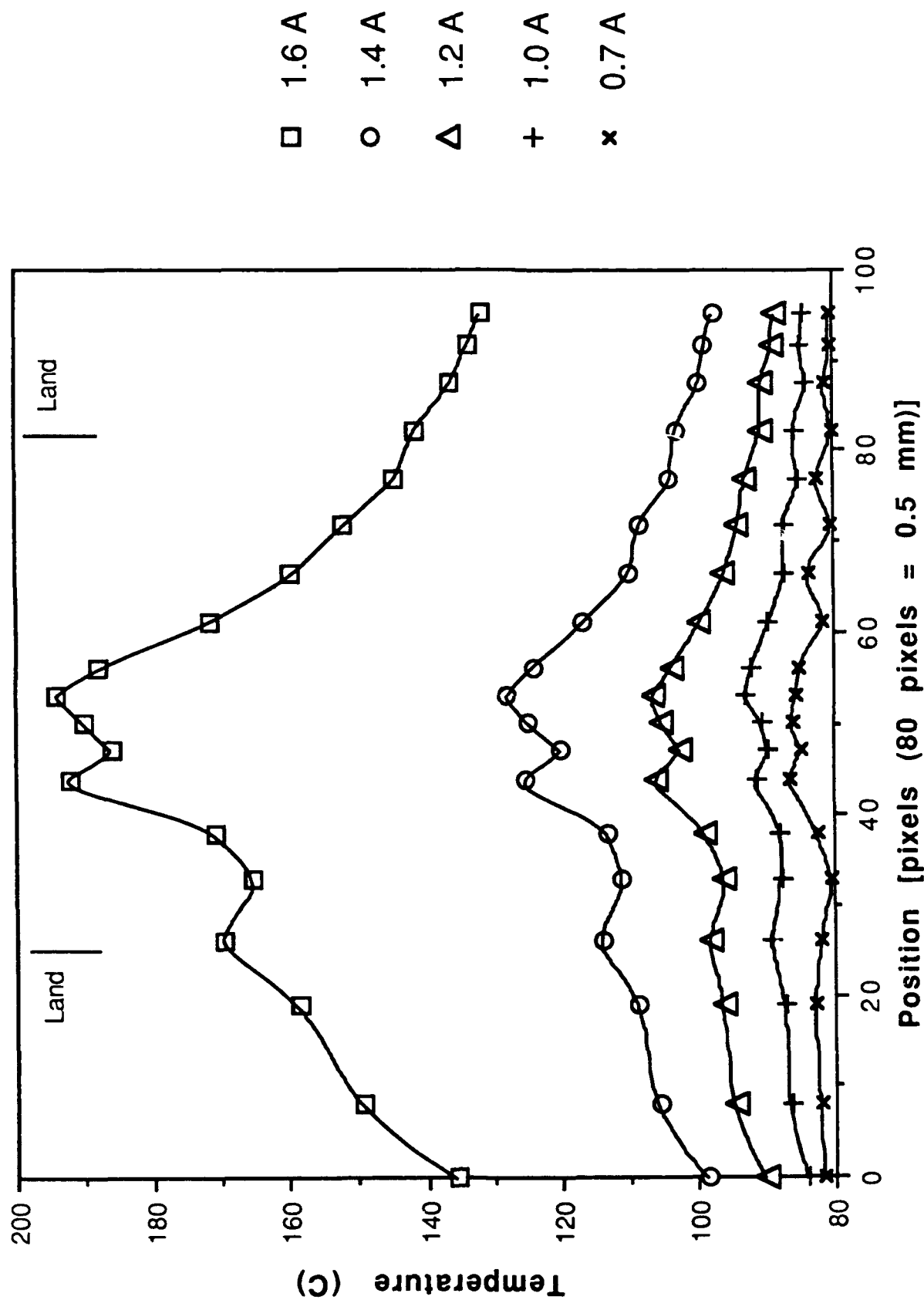
Fig. 5b. Measured steady-state temperature profile for wire shown in Fig. 1b.
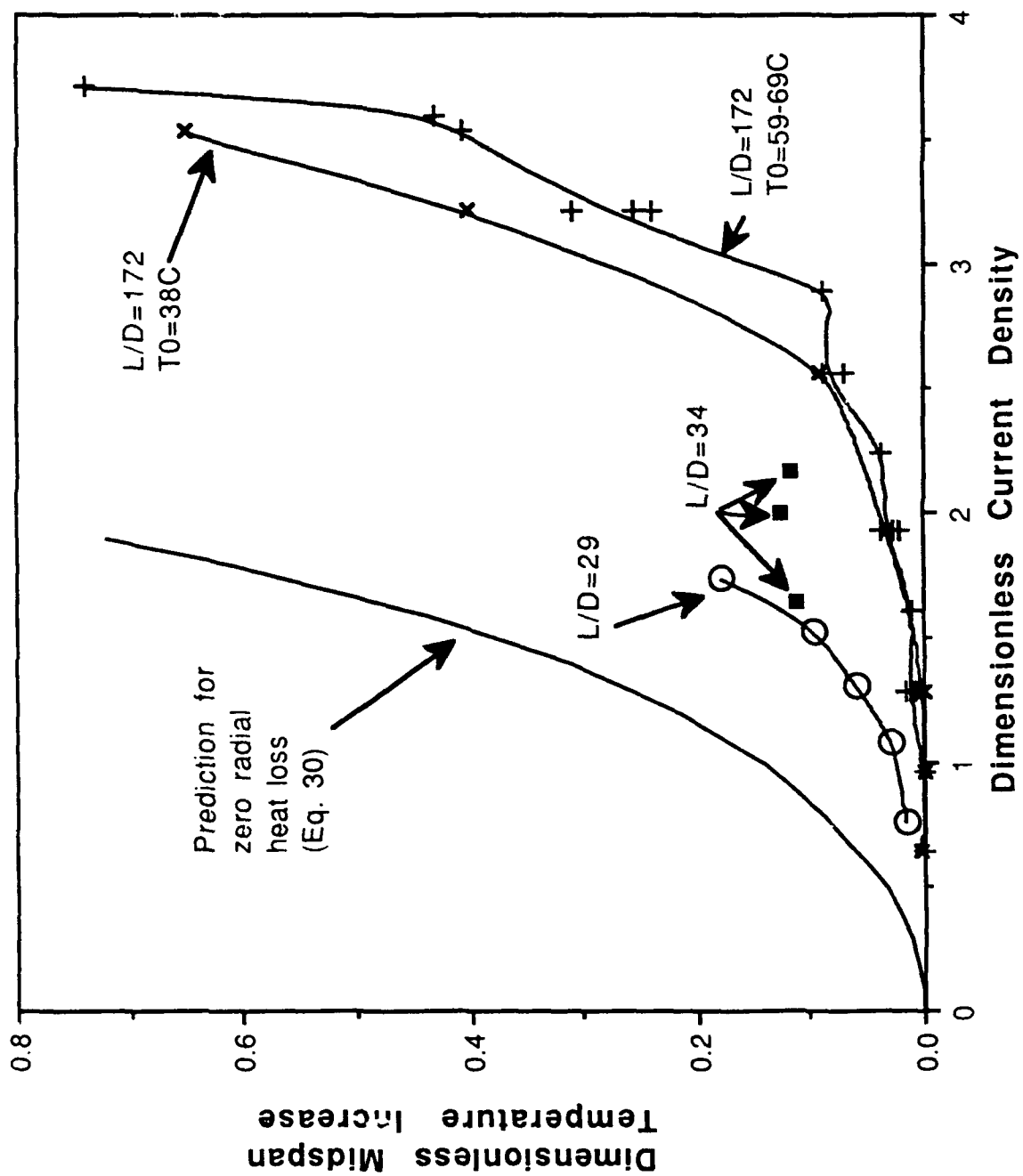
Fig. 6. Measured current dependence of steady-state midspan temperature.
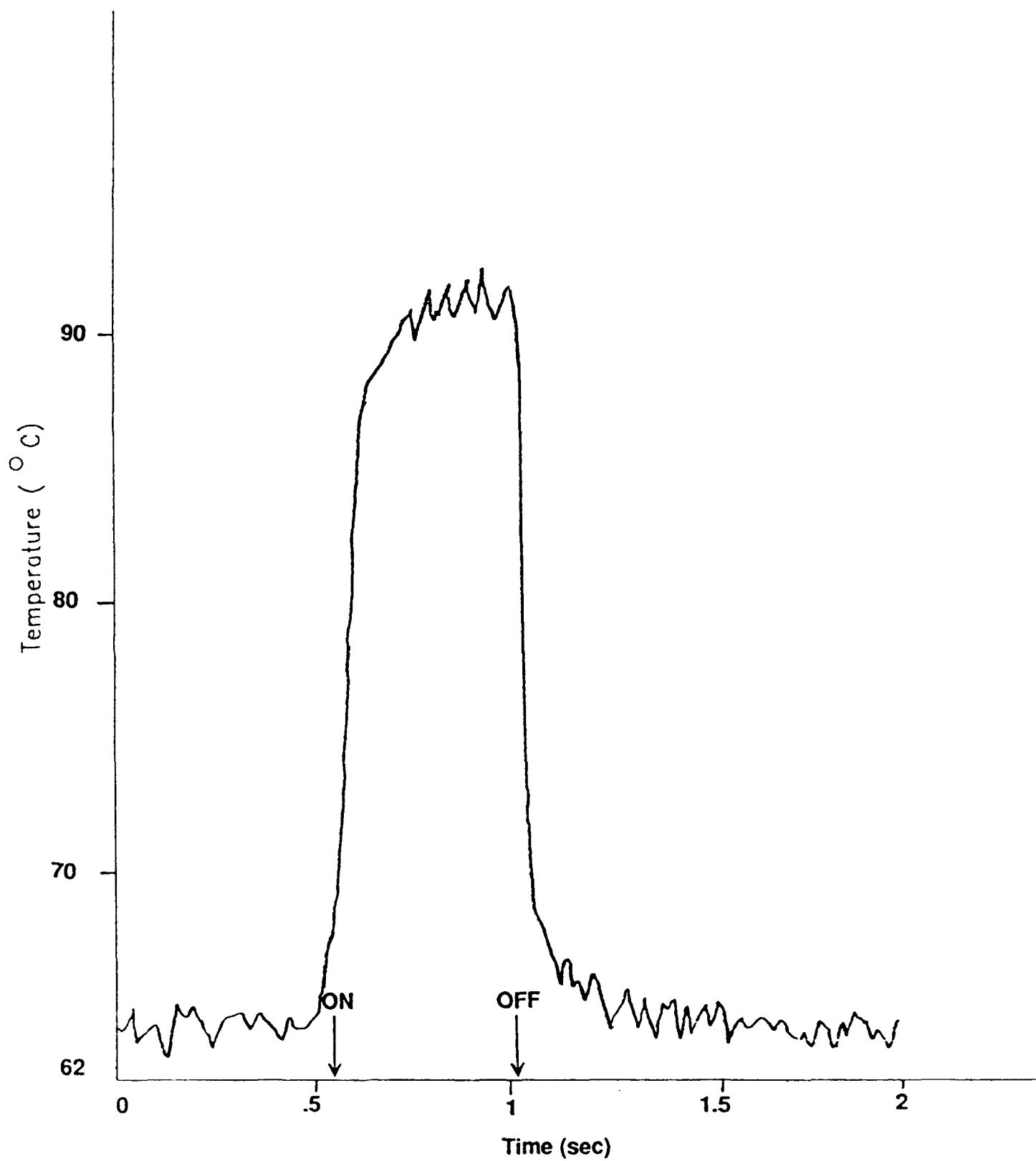
Fig. 7a. Measured transient thermal response of wire to square-wave voltage pulse (scale in sec).
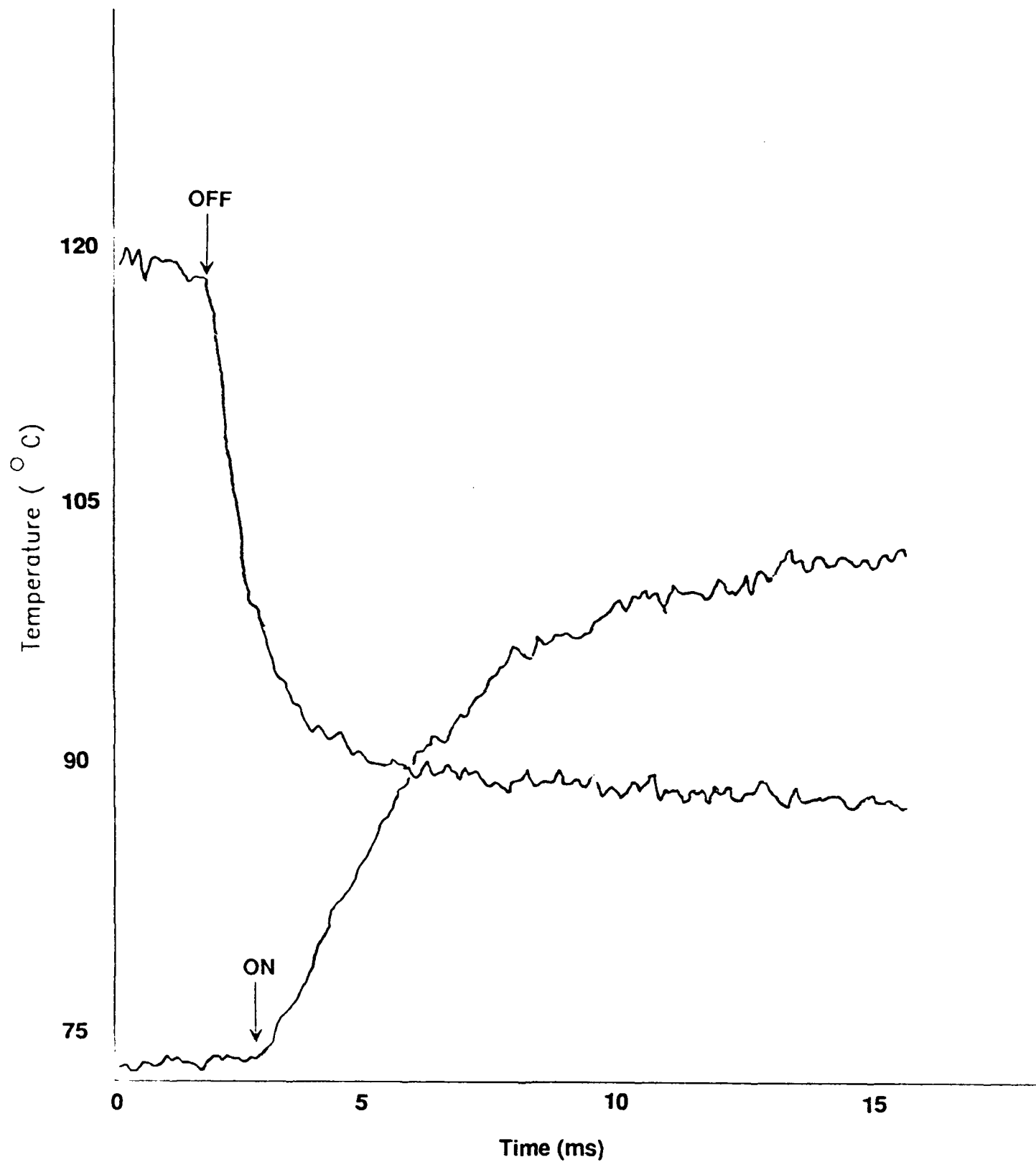
Fig. 7b. Measured transient thermal response of wire to square-wave voltage pulse (scale in ms).

APPENDIX D

PROPERTIES OF AI-1% SI ALLOY

INTERDEPARTMENTAL CORRESPONDENCE

To: Distribution

Subj: Properties of
    Al-1% Si Alloy

Date: 27 April 1990
Ref: 722610/0060JMK

From: J.M.Kallis
Org: 72-26-10

Bldg: E1 M/S: B105
Loc: EO Phone: 66540

The electrical and thermal properties of Al-1% Si alloy, used in the form of 1 mil diameter wires in microelectronic devices, have been compiled. The recommended values are as follows:

Property	Value	Comparison with pure Al
Electrical resistivity (at 0°C)	2.53 micro-ohm-cm	5% higher
Temperature coefficient of resistance (0-100°C)	0.0046/°C	6% lower
Thermal conductivity (at approximately 73-100°C)	2.1 W/(cm-°K)	14% lower
Density	2.70 g/cm³	Same to within 0.2%
Specific heat (at approximately 27°C)	0.214 cal/(g-°C)	Same to within 0.5%

The sources of these data are described in the attachment to this IDC.

J. M. Kallis

J.M.Kallis, Chief Scientist
Product Analysis Laboratory

JMK/amc

ATTACHMENT

1.0 ELECTRICAL RESISTIVITY & TEMPERATURE COEFFICIENT OF RESISTANCE

These values were measured by Sigmund Cohn Corp., a supplier of wire for Hughes microelectronic devices, and are listed in a data sheet (Ref. 1). The resistivity was measured per ASTM Spec. F487-88 with a bridge and a digital ohmmeter, using 1 ft of 10-mil-diameter wire (Ref. 2).

The data sheet lists values for hard and for annealed. The wire is sold only heat treated - either fully annealed or stress relieved (partly annealed). The annealed values should be used for either fully or partly annealed wire (Ref. 2).

At ambient temperature (21°C), the resistivity is 2.77 micro-ohm-cm. This is within 9% of the values measured at 21°C by Hughes for 1-mil-diameter wire (Ref. 3): 2.91 - 3.01 micro-ohm-cm.

It appears unlikely that the 1-mil-diameter wire has a higher resistivity than the 10-mil-diameter wire. Therefore the Hughes and Sigmund Cohn Corp. data are comparable. The Sigmund Cohn Corp. value is more credible, because their experimental parameters (temperature, wire length, etc.) appear to be more closely controlled.

2.0 THERMAL CONDUCTIVITY

This value was deduced from values for Al-Si alloys having various weight percentages of Si.

Thermal conductivity is difficult to determine for Al. It is generally calculated from electrical resistivity measurements (Ref. 4, p. 173). The thermal conductivity of Al-1% Si has not been measured directly (Refs. 2 & 5).

The value for Al-1% Si was interpolated from values listed for other Al-Si alloys:

Weight Percent Si	Thermal Conductivity W/(Cm-$^{\circ}$K)	Temperature, $^{\circ}$K	Source
0	2.40	350-400	Ref. 6, p.9
0.2	2.305	349.6	Ref. 6, pp. 481-482
11.0 - 14.0	1.703	346.2	Ref. 6, pp. 481-482
13.0	1.715	353.0	Ref. 6, pp. 481-482
13.0	1.757	373.0	Ref. 6, pp. 481-482
20.0	1.686	373.0	Ref. 6, pp. 481-482

It was assumed that the thermal conductivity is a continuous, monotonically decreasing value of the weight percent Si. It was also assumed that the thermal conductivity is relatively insensitive to temperature in the range 346-373°K. Both these assumptions appear plausible.

The data taken from Ref. 6 are from five sources. The specimen preparation techniques were not the same for all sources. The effects on thermal conductivity of the specimen preparation techniques are neglected here.

Accordingly, a single curve was drawn through these data with a French curve (Fig. 1). In this figure, the values for temperatures in the range 346-353°K are plotted with diamonds, and those for 373°K are plotted with squares. To obtain two independent curves, the inverse of the thermal conductivity was plotted and the thermal conductivity was plotted. Fig. 1 shows that a plausible curve can be drawn with a French curve for each of the two plots. The interpolated value for 1% Si is 2.12 W/(cm-°K) for the upper curve and 2.15 W/(cm-°K) for the lower curve. Since this interpolation is not rigorous, the best estimate is obtained by rounding to 2 decimal places: 2.1 W/(cm-°K).

Dr. R. Bogaard of CINDAS has deduced thermal conductivities of Al alloys from electrical resistivity data (Ref. 5). He was unaware of the electrical resistivity measurements in Ref. 1. He estimated that the Sigmund Cohn Corp. electrical resistivity data are consistent with a thermal conductivity of 2.1 W/(cm-°K). He expects that the value is between 2.0 and 2.2 W/(cm-°K).

3.0 DENSITY

Per Ref. 4, pp. 167-168, this is calculated as the "...sum of density contributions of each element". The elemental densities at 20°C are (Ref. 7, pp. 98 and 102):

   Al: 2.702 g/cm^3
   Si: 2.4 g/cm^3

The calculated value agrees closely with that in Fig. 2, p. 168, of Ref. 4.

4.0 SPECIFIC HEAT

Per Ref. 4, p. 180, "...the specific heat of the alloy in the annealed condition is assumed to vary with composition in a linear manner." The elemental specific heats are (Ref. 8, pp. 2-64 and 2-65):

   Al: 0.215 cal/(g-°C)
   Si: 0.162 cal/(g-°C).

REFERENCES

1) "Properties of Metals & Alloys", Sigmund Cohn Corp.,
    121 South Columbus Ave., Mount Vernon, NY 10553.

2) Private communcation with Frank Fitzpatrick, Sigmund Cohn
    Corp., (914) 664-5300, 22 Jan 90.

3) J.F.Alvarez, "Resistivity Measurements of 0.001 Inch Dia-
    meter Al-1% Si Bond Wire (LSR N530)", Hughes Aircraft Co.
    Interdepartmental Correspondence 7641.20/1790, 27 Feb 90.

4) K.R.Van Horn (ed.), Aluminum, Vol. I, American Society for
    Metals, Metals Park, OH, 1967.

5) Private communication with Dr. Ron Bogaard, CINDAS (Center
    for Information and Numerical Data Analysis), Purdue U.,
    (317) 494-9393, 20 April 90.

6) Y.S.Touloukian, et al., Thermal Conductivity - Metallic
    Elements and Alloys, IFI/Plenum, New York-Washington, 1970.

7) N.A.Lange (ed.), Handbook of Chemistry, Handbook Publishers
    Inc., Sandusky, OH, 1946.

8) W.M.Rohsenow and J.P.Hartnett (eds.), Handbook of Heat Trans-
    fer, McGraw-Hill Book Co., New York, 1973.

FIG. 1. THERMAL CONDUCTIVITY OF Al-Si ALLOYS

K+E 10 X 10 TO THE CENTIMETER 18 X 25 CM
KEUFFEL & ESSER CO. MADE IN U.S.A.
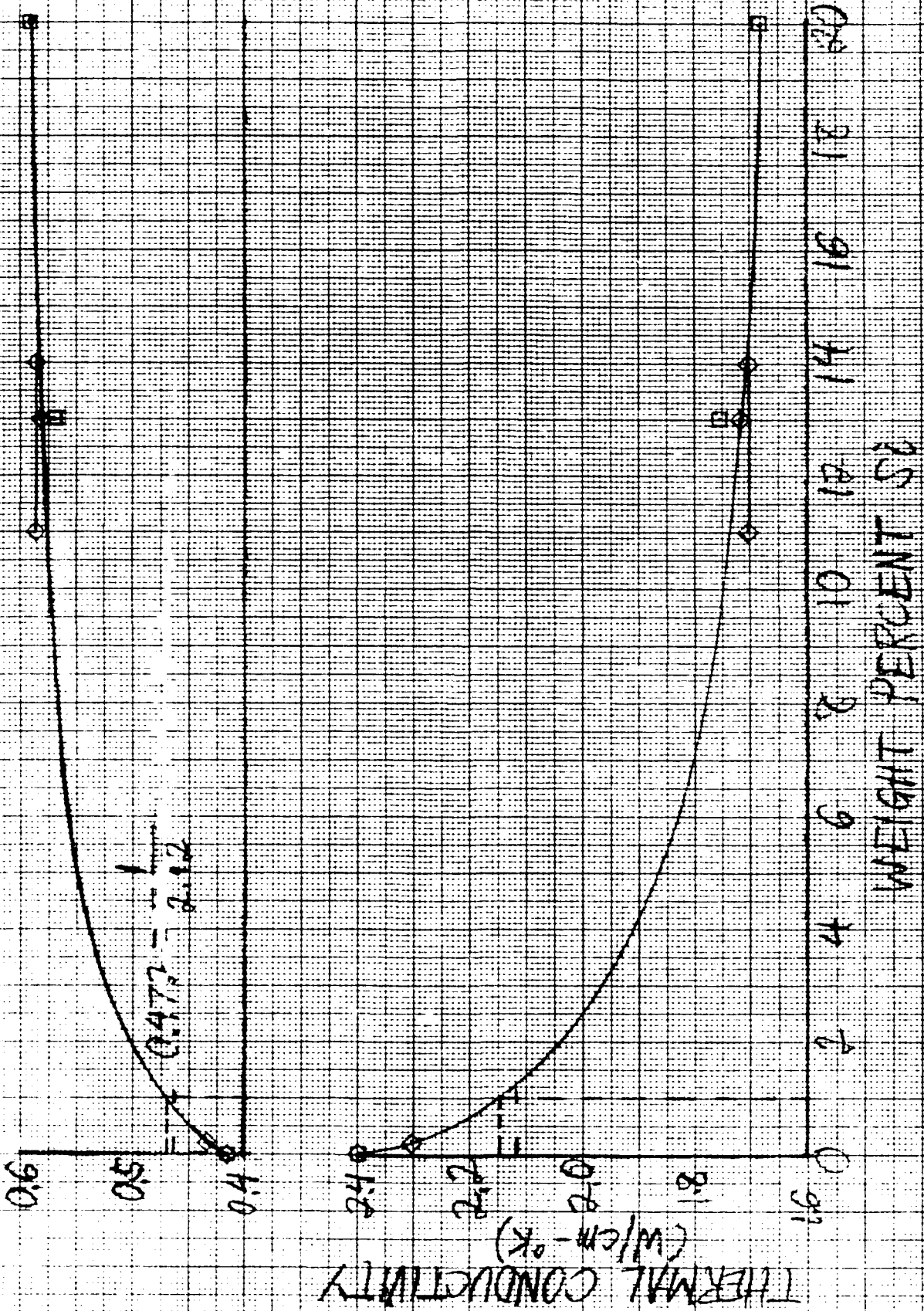
FIG. 1a. THERMAL CONDUCTIVITY OF Aℓ-Si ALLOYS

(0-100 WEIGHT PERCENT Si)

THERMAL CONDUCTIVITY OF Si:

(5 W/cm-°K AT 27°C

REF: A.S. GROVE PHYSICS +
TECHNOLOGY OF
SEMICONDUCTOR DEVICES, p. 103
WILEY, N.Y., 1967

THERMAL CONDUCTIVITY (W/cm-°K)

WEIGHT PERCENT Si
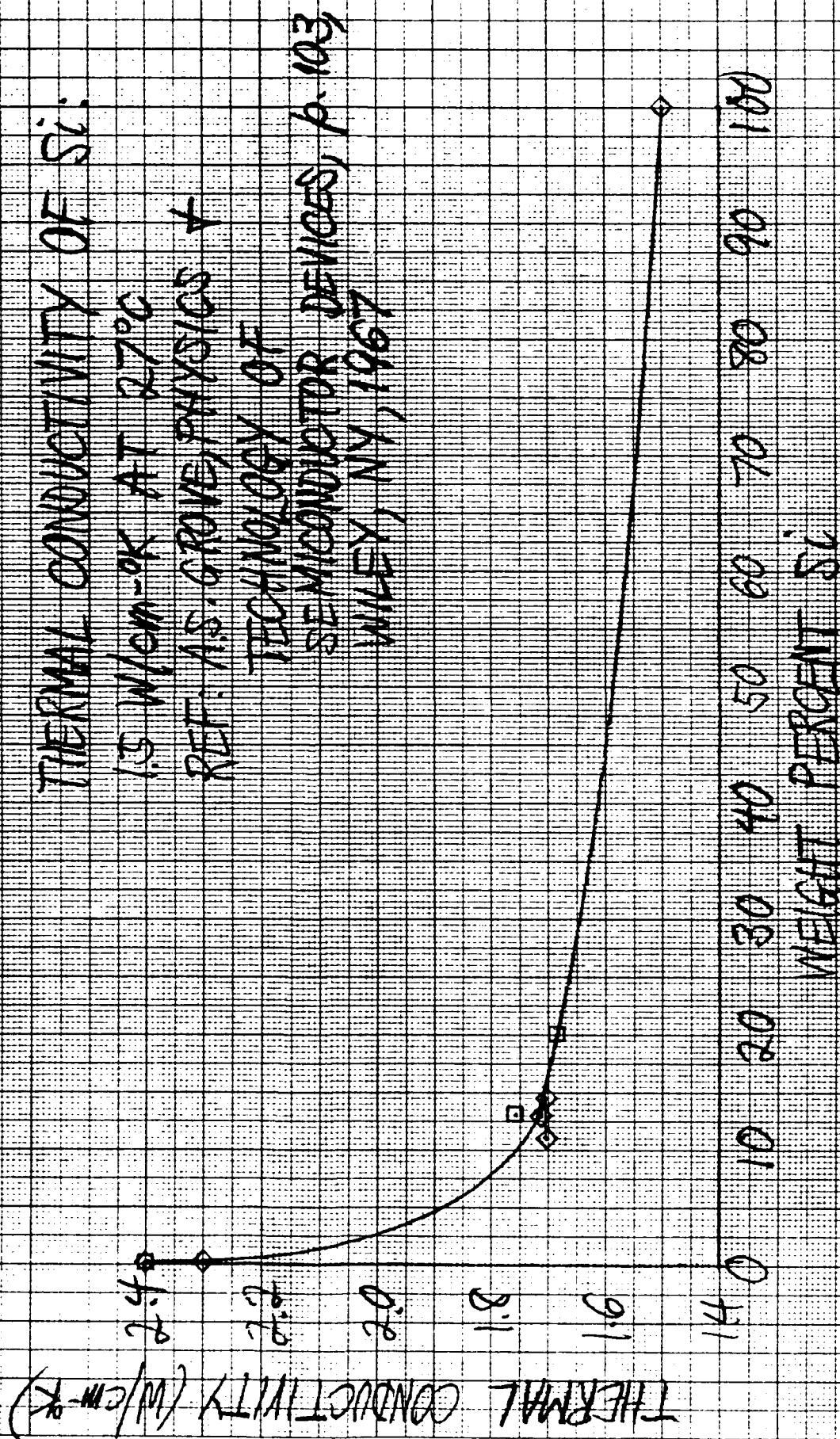
APPENDIX E

COPPER PLATING STRESS/CRACK GROWTH

Derivation of the equations used to compute surface stress in a composite beam of copper plating on printed circuit board. The resulting stress was used to compute ΔK for the small cracks initiated in an artificial flaw.

Measured crack growth data and computed ΔK for
small cracks in Cu plating on PCB

CONSIDER THE FOLLOWING BI-MATERIAL BEAM SUBJECTED TO PURE BENDING
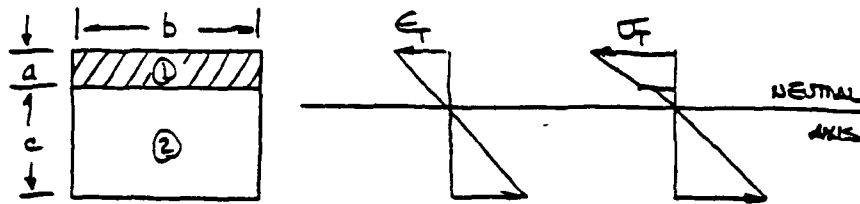
CONSTRUCT AN "EQUIVALENT" BEAM OF MATERIAL 1 TO DETERMINE σ_1 BY
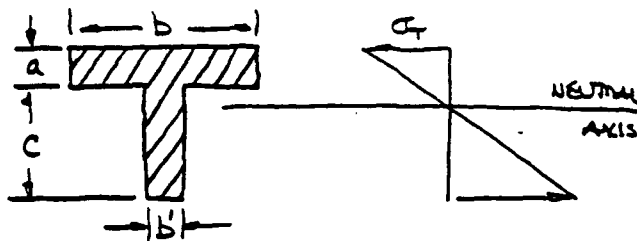
$$b' = \left(\frac{E_2}{E_1}\right) b$$

THE LOCATION OF THE NEUTRAL AXIS, $\bar{y}$, COINCIDES WITH THE CENTROIDAL AXIS
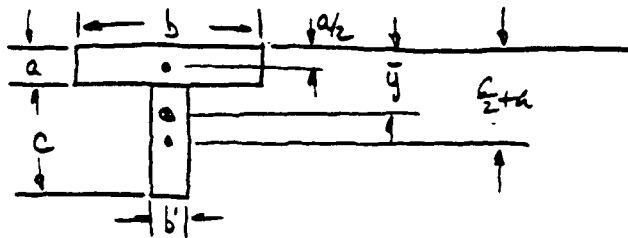
$$\bar{y} = \frac{ab(a/2) + b'c(c/2 + a)}{ab + b'c}$$

$$= \frac{\frac{1}{2}a^2 b + \frac{1}{2}b'c^2 + ab'c}{ab + b'c}$$

E-3

THE MOMENT OF INERTIA ABOUT THE NEUTRAL AXIS IS GIVEN BY

$$I = \frac{1}{12} b'c^3 + b'c\left[\left(\frac{c}{2}+a\right) - \bar{y}\right]^2$$

$$+ \frac{1}{12} ba^3 + ab\left(\bar{y} - \frac{a}{2}\right)^2$$

THE OUTER FIBER STRESS, σ_F, IS CALCULATED BY

$$\sigma_F = \frac{M\bar{y}}{I}$$

FATIGUE CRACK GROWTH RATE CALCULATIONS
FOR Cu FOIL/PWB BEAM IN BENDING

ELASTIC MODULUS OF Cu FOIL = 16×10^6 psi = 1.1×10^5 MPa
ELASTIC MODULUS OF PWB = 2.5×10^6 psi = 1.7×10^4 MPa
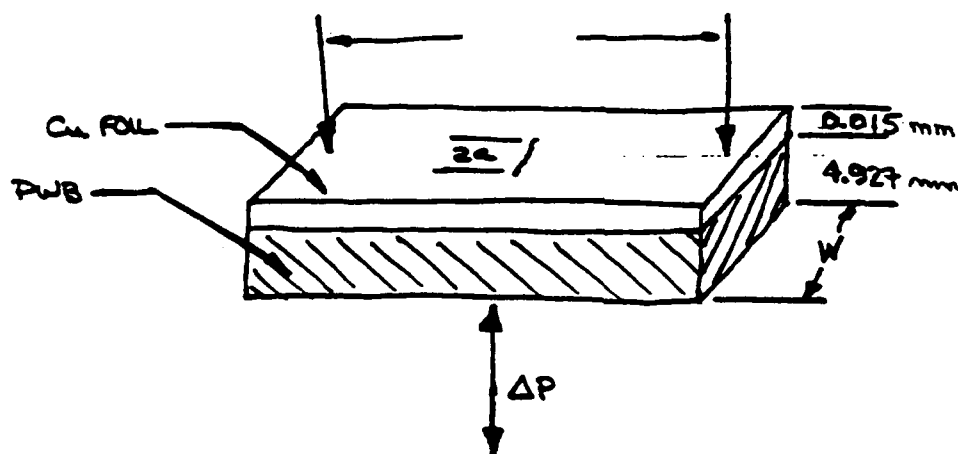
ΔP [1] (N)	W [1] (mm)	a [1] (mm)	$\Delta\sigma$ [2] (MPa)	ΔK [3] (MPa$\sqrt{m}$)	da/dN [1] (m/cyc)
20	12.7	0.0198	321	1.77	6.60×10^{-10}
20	12.7	0.0272	321	2.08	2.46×10^{-10}
20	12.7	0.0453	321	2.68	3.62×10^{-10}
14	7.62	0.0508	374	3.31	1.86×10^{-10}
14	7.62	0.0610	374	3.63	1.02×10^{-9}
14	7.62	0.0889	374	4.38	2.79×10^{-9}
14	7.62	0.1366	374	5.43	4.77×10^{-9}
14	7.62	0.3048	374	8.11	1.68×10^{-8}
14	7.62	0.5791	374	11.2	2.74×10^{-8}
14	7.82	0.8000	374	13.2	4.41×10^{-8}

(1) FROM D.L. DAVIDSON TEST MEASUREMENTS

(2) FROM BEAM BENDING (EQUIVALENT BEAM) BENDING THEORY = Cu FOIL MIDPLANE STRESS

(3) $\Delta K = 1.24 \Delta\sigma \sqrt{a}$ FROM D.O. HARRIS (FLAW) NASCRAC

APPENDIX F

PTH DISPLACEMENT STRAIN DATA

Data from the analysis of displacements and strains of the PTH
temperature cycle between:

25 down to -65°C

-65 up to 125°C

125 down to 25°C

Displacements and strains for

25 to -65°C

Column headers: **X Y DX DY EXX EYY EM QYY QMAX EA EB EC EEFF**

(handwritten annotation, center of page: 25°C λ~65°C)

(handwritten annotations in upper-left and lower-left margins are illegible)

X	Y	DX	DY	EXX	EYY	EM	QYY	QMAX	EA	EB	EC	EEFF
-100.0	375.0	-0.1004	-0.8247	-0.0003	-0.0004	-0.0003	0.0001	0.0001	-0.0003	-0.0004	0.0007	0.0007
-75.0	375.0	-0.1618	-0.7904	-0.0005	-0.0005	-0.0005	-0.0007	0.0007	-0.0002	-0.0008	0.0010	0.0011
-50.0	375.0	-0.1597	-0.8479	-0.0007	-0.0006	-0.0007	-0.0003	0.0003	-0.0002	-0.0008	0.0013	0.0013
-25.0	375.0	-0.1831	-0.8279	-0.0007	-0.0003	-0.0005	-0.0013	0.0014	0.0002	-0.0012	0.0010	0.0013
0	375.0	-0.2060	-0.7535	-0.0011	-0.0009	-0.0005	-0.0027	0.0029	0.0009	-0.0020	0.0011	0.0020
25.0	375.0	-0.2425	-0.6912	-0.0021	0.0074	-0.0014	-0.0018	0.0035	0.0004	-0.0031	0.0027	0.0025
50.0	375.0	-0.3125	-0.6792	-0.0030	0.0033	-0.0011	-0.0013	0.0027	0.0003	-0.0025	0.0022	0.0034
75.0	375.0	-0.3761	-0.6940	-0.0020	-0.0012	-0.0010	-0.0021	0.0014	-0.0003	-0.0017	0.0020	0.0027
100.0	375.0	-0.4806	-0.8636	-0.0009	-0.0011	-0.0004	-0.0004	0.0007	0.0021	-0.0008	0.0017	0.0021
-100.0	350.0	-0.1018	-0.7516	-0.0001	-0.0007	-0.0005	-0.0012	0.0014	0.0000	-0.0012	0.0008	0.0009
-75.0	350.0	-0.1431	-0.7533	-0.0000	-0.0008	-0.0010	-0.0017	0.0019	0.0002	-0.0019	0.0009	0.0012
-50.0	350.0	-0.1298	-0.8136	-0.0016	-0.0013	-0.0011	-0.0019	0.0010	0.0000	-0.0019	0.0019	0.0022
-25.0	350.0	-0.1448	-0.8727	-0.0018	-0.0006	-0.0007	-0.0001	0.0036	-0.0006	-0.0016	0.0022	0.0022
0	350.0	-0.2366	-0.7823	-0.0012	0.0004	-0.0005	0.0028	0.0040	0.0011	-0.0025	0.0014	0.0023
25.0	350.0	-0.2563	-0.7059	-0.0021	-0.0012	-0.0009	-0.0007	0.0035	0.0015	-0.0025	0.0009	0.0025
50.0	350.0	-0.3211	-0.6534	-0.0026	-0.0009	-0.0017	-0.0017	0.0023	0.0009	-0.0026	0.0017	0.0025
75.0	350.0	-0.3735	-0.7247	-0.0017	-0.0004	-0.0008	-0.0006	0.0043	0.0001	-0.0022	0.0022	0.0038
100.0	350.0	-0.4695	-0.7575	-0.0008	-0.0027	-0.0014	-0.0035	0.0024	0.0007	-0.0030	0.0028	0.0037
-100.0	325.0	-0.1002	-0.7742	-0.0001	-0.0026	-0.0020	-0.0013	0.0021	0.0001	-0.0035	0.0026	0.0029
-75.0	325.0	-0.1153	-0.7173	-0.0003	-0.0023	-0.0006	0.0006	0.0023	-0.0001	-0.0025	0.0039	0.0042
-50.0	325.0	-0.1403	-0.7587	-0.0006	-0.0033	-0.0011	0.0005	0.0030	-0.0001	-0.0033	0.0042	0.0044
-25.0	325.0	-0.1328	-0.8124	-0.0011	-0.0031	-0.0021	-0.0014	0.0020	-0.0010	-0.0032	0.0028	0.0029
0	325.0	-0.1955	-0.7618	-0.0016	0.0002	-0.0007	-0.0003	0.0021	0.0004	-0.0019	0.0014	0.0019
25.0	325.0	-0.2318	-0.7731	-0.0024	-0.0003	-0.0009	-0.0004	0.0051	0.0007	-0.0024	0.0017	0.0024
50.0	325.0	-0.3037	-0.7606	-0.0023	-0.0003	-0.0013	-0.0018	0.0062	-0.0003	-0.0028	0.0034	0.0036
75.0	325.0	-0.3471	-0.6880	-0.0012	-0.0023	-0.0017	-0.0027	0.0060	0.0006	-0.0052	0.0052	0.0061
100.0	325.0	-0.3895	-0.6576	-0.0005	-0.0048	-0.0023	-0.0009	0.0057	0.0008	-0.0054	0.0046	0.0058
-100.0	300.0	-0.2592	-0.6339	-0.0012	-0.0051	-0.0018	-0.0015	0.0051	0.0012	-0.0048	0.0036	0.0049
-75.0	300.0	-0.2113	-0.6257	0.0012	-0.0047	-0.0038	0.0031	0.0030	0.0014	-0.0042	0.0028	0.0043
-50.0	300.0	-0.1554	-0.6418	-0.0014	-0.0042	-0.0028	-0.0022	0.0023	0.0004	-0.0047	0.0043	0.0052
-25.0	300.0	-0.1524	-0.6908	0.0003	-0.0006	-0.0022	0.0038	0.0024	0.0007	-0.0037	0.0044	0.0047
0	300.0	-0.1490	-0.7541	0.0002	-0.0031	-0.0026	0.0038	0.0039	-0.0014	-0.0037	0.0051	0.0053
25.0	300.0	-0.1899	-0.7251	-0.0010	-0.0037	-0.0022	-0.0030	0.0054	-0.0010	-0.0034	0.0045	0.0047
50.0	300.0	-0.2468	-0.6554	-0.0014	-0.0031	-0.0017	-0.0013	0.0061	0.0001	-0.0040	0.0041	0.0047
75.0	300.0	-0.2180	-0.5926	-0.0010	-0.0036	-0.0021	-0.0015	0.0073	0.0006	-0.0049	0.0045	0.0053
100.0	300.0	-0.2875	-0.5261	-0.0005	-0.0041	-0.0022	-0.0023	0.0061	0.0005	-0.0051	0.0041	0.0062
-100.0	275.0	-0.2702	-0.4981	-0.0002	-0.0056	-0.0026	-0.0015	0.0062	0.0010	-0.0060	0.0051	0.0067
-75.0	275.0	-0.1863	-0.4987	0.0005	-0.0061	-0.0026	-0.0031	0.0077	0.0012	-0.0062	0.0052	0.0051
-50.0	275.0	-0.1771	-0.5382	0.0009	-0.0054	-0.0019	-0.0022	0.0069	0.0006	-0.0049	0.0037	0.0051
-25.0	275.0	-0.1563	-0.5779	0.0011	-0.0077	-0.0039	-0.0024	0.0050	0.0003	-0.0056	0.0050	0.0062
0	275.0	-0.1422	-0.5896	0.0004	-0.0079	-0.0038	-0.0033	0.0059	0.0007	-0.0077	0.0078	0.0090
25.0	275.0	-0.1500	-0.5642	0.0001	-0.0058	-0.0035	-0.0026	0.0074	0.0002	-0.0084	0.0076	0.0090
50.0	275.0	-0.1447	-0.5443	-0.0001	-0.0045	-0.0028	-0.0016	0.0086	0.0007	-0.0062	0.0055	0.0068
75.0	275.0	-0.1217	-0.5256	0.0003	-0.0042	-0.0017	-0.0011	0.0092	0.0002	-0.0048	0.0045	0.0054
100.0	275.0	-0.1592	-0.4617	0.0000	-0.0030	-0.0021	-0.0002	0.0100	0.0008	-0.0051	0.0034	0.0044
-100.0	250.0	-0.2359	-0.3589	-0.0001	-0.0037	-0.0013	0.0000	0.0092	0.0014	-0.0060	0.0042	0.0054
-75.0	250.0	-0.1742	-0.3123	-0.0003	-0.0056	-0.0018	-0.0019	0.0074	0.0017	-0.0069	0.0047	0.0063
-50.0	250.0	-0.1571	-0.4124	0.0000	-0.0065	-0.0026	-0.0015	0.0086	0.0011	-0.0081	0.0052	0.0072
-25.0	250.0	-0.1078	-0.4397	0.0005	-0.0078	-0.0035	-0.0021	0.0092	0.0007	-0.0092	0.0070	0.0088
0	250.0	-0.1195	-0.4164	0.0010	-0.0092	-0.0042	-0.0006	0.0100	0.0008	-0.0084	0.0085	0.0103
25.0	250.0	-0.0863	-0.3838	0.0013	-0.0084	-0.0035	-0.0015	0.0074	0.0003	-0.0072	0.0076	0.0093
50.0	250.0	-0.0629	-0.3984	0.0008	-0.0070	-0.0030	-0.0031	0.0056	0.0002	-0.0058	0.0069	0.0081
75.0	250.0	-0.0834	-0.3619	0.0007	-0.0057	-0.0021	-0.0022	0.0049	0.0003	-0.0048	0.0060	0.0068
100.0	250.0	-0.0954	-0.3493	0.0001	-0.0042	-0.0017	-0.0038	0.0043	0.0003	-0.0042	0.0043	0.0054
-100.0	225.0	-0.1506	-0.2682	-0.0001	-0.0030	-0.0013	-0.0024	0.0051	0.0009	-0.0034	0.0034	0.0035
-75.0	225.0	-0.1033	-0.2266	0.0005	-0.0037	-0.0018	-0.0011	0.0073	0.0012	-0.0038	0.0026	0.0039
-50.0	225.0	-0.0655	-0.2171	0.0011	-0.0054	-0.0027	-0.0002	0.0073	0.0018	-0.0055	0.0037	0.0056
-25.0	225.0	-0.0179	-0.1895	0.0013	-0.0066	-0.0027	-0.0002	0.0079	0.0013	-0.0066	0.0053	0.0070
0	225.0	-0.0053	-0.1648	0.0002	-0.0072	-0.0035	0.0000	0.0073	0.0002	-0.0072	0.0070	0.0082

F-5

C1	C2	C3	C4	C5	C6	C7	C8	C9	C10	C11	C12	C13
0.0095	0.0094	-0.0056	-0.0038	0.0018	-0.0011	-0.0047	-0.0034	-0.0040	0.5869	0.4690	0 0 50	0 0 -50
0.0075	0.0073	-0.0052	-0.0021	0.0032	-0.0023	-0.0037	-0.0047	-0.0026	0.5333	0.3884	0 0 50	0 0 -25
0.0063	0.0058	-0.0049	-0.0009	0.0040	-0.0032	-0.0029	-0.0041	-0.0017	0.4226	0.3199	0 0 50	0 0 0
0.0038	0.0036	-0.0029	-0.0008	0.0021	-0.0019	-0.0018	-0.0023	-0.0014	0.3779	0.2890	0 0 50	0 0 25
0.0036	0.0036	-0.0023	-0.0013	0.0011	-0.0006	-0.0018	-0.0022	-0.0014	0.3546	0.2687	0 0 50	0 0 50
0.0031	0.0030	-0.0021	-0.0009	0.0011	0.0007	-0.0015	-0.0019	-0.0011	0.2635	0.2183	0 0 50	0 0 75
0.0020	0.0019	-0.0015	-0.0004	0.0005	-0.0006	-0.0009	-0.0014	-0.0005	0.2318	0.1694	0 0 50	0 0 -100
0.0032	0.0032	-0.0018	-0.0014	0.0010	-0.0002	-0.0016	-0.0018	-0.0014	0.6627	0.7698	0 0 25	0 0 -100
0.0050	0.0049	-0.0030	-0.0020	0.0025	-0.0012	-0.0025	-0.0020	-0.0029	0.6514	0.6063	0 0 25	0 0 -75
0.0067	0.0066	-0.0045	-0.0015	0.0032	-0.0029	-0.0033	-0.0022	-0.0044	0.6736	0.5205	0 0 25	0 0 -50
0.0064	0.0061	-0.0047	-0.0008	0.0026	-0.0039	-0.0031	-0.0023	-0.0038	0.5915	0.3843	0 0 25	0 0 -25
0.0063	0.0058	-0.0050	-0.0005	0.0007	-0.0016	-0.0029	-0.0008	-0.0028	0.5028	0.3471	0 0 25	0 0 0
0.0039	0.0036	-0.0031	-0.0005	0.0008	-0.0001	-0.0018	-0.0005	-0.0012	0.4061	0.2304	0 0 25	0 0 25
0.0018	0.0018	-0.0012	-0.0002	0.0004	-0.0005	-0.0009	-0.0012	-0.0005	0.3826	0.1975	0 0 0	0 0 50
0.0017	0.0016	-0.0012	-0.0008	0.0007	-0.0002	-0.0008	-0.0005	-0.0003	0.3181	0.1432	0 0 0	0 0 75
0.0008	0.0008	-0.0006	-0.0008	0.0026	-0.0003	-0.0004	-0.0008	-0.0015	0.2354	0.1534	0 0 0	0 0 100
0.0023	0.0023	-0.0015	-0.0009	0.0047	-0.0001	-0.0011	-0.0008	-0.0034	0.7197	0.7393	0 0 0	0 0 -100
0.0045	0.0043	-0.0034	-0.0004	0.0039	-0.0004	-0.0021	-0.0010	-0.0056	0.6967	0.6207	0 0 0	0 0 -75
0.0070	0.0064	-0.0056	0.0006	0.0052	-0.0014	-0.0032	-0.0011	-0.0047	0.7051	0.4720	0 0 0	0 0 -50
0.0062	0.0058	-0.0049	-0.0001	0.0045	-0.0047	-0.0029	-0.0005	-0.0032	0.7311	0.3182	0 0 0	0 0 -25
0.0052	0.0043	-0.0047	-0.0006	0.0022	-0.0038	-0.0021	-0.0003	-0.0028	0.6377	0.2543	0 0 0	0 0 0
0.0042	0.0033	-0.0039	-0.0003	0.0004	-0.0011	-0.0016	-0.0007	-0.0022	0.4878	0.1672	0 0 0	0 0 25
0.0027	0.0024	-0.0023	-0.0006	0.0001	-0.0003	-0.0012	-0.0003	-0.0009	0.4156	0.1076	0 0 0	0 0 50
0.0016	0.0015	-0.0009	-0.0006	0.0004	0.0000	-0.0008		-0.0004	0.3976	0.0420	0 0 0	0 0 75
0.0007	0.0007	-0.0004	-0.0003	0.0001		-0.0004	-0.0003		0.3077	0.0419	0 0 0	0 0 100

Displacements and strains for

-65 to 125°C

Handwritten annotation (top): −65°C / 125°C

X	Y	DX	DY	EXX	EYY	EM	QXY	QMAX	EA	EB	EC	EEFF
-100.0	375.0	-1.9682	-0.9694	0.0047	-0.0016	0.0015	-0.0025	0.0069	0.0050	-0.0019	-0.0031	0.0050
-75.0	375.0	-1.5690	-0.8708	0.0109	-0.0007	0.0051	-0.0021	0.0118	0.0110	-0.0008	-0.0102	0.0123
-50.0	375.0	-1.0798	-1.0233	0.0181	-0.0017	0.0082	-0.0018	0.0198	0.0181	-0.0017	-0.0164	0.0200
-25.0	375.0	-0.6519	-1.0143	0.0162	-0.0022	0.0070	-0.0021	0.0186	0.0163	-0.0023	-0.0140	0.0176
0.0	375.0	-0.2994	-1.0667	0.0121	-0.0030	0.0046	-0.0021	0.0153	0.0122	-0.0031	-0.0092	0.0127
25.0	375.0	-0.0018	-1.0936	0.0156	-0.0031	0.0062	-0.0030	0.0189	0.0157	-0.0032	-0.0125	0.0166
50.0	375.0	0.4230	-1.1213	0.0234	-0.0029	0.0103	-0.0016	0.0263	0.0234	-0.0029	-0.0206	0.0256
75.0	375.0	1.0575	-1.0695	0.0170	-0.0040	0.0065	-0.0047	0.0215	0.0172	-0.0043	-0.0129	0.0179
100.0	375.0	1.9305	-0.5339	0.0076	-0.0023	0.0027	-0.0043	0.0108	0.0081	-0.0028	-0.0053	0.0082
-100.0	350.0	-1.7791	-0.7407	0.0036	-0.0030	0.0003	-0.0051	0.0083	0.0045	-0.0039	-0.0006	0.0049
-75.0	350.0	-1.5689	-0.7180	0.0081	-0.0019	0.0031	-0.0033	0.0105	0.0083	-0.0022	-0.0061	0.0086
-50.0	350.0	-1.1094	-0.7945	0.0152	-0.0032	0.0060	-0.0001	0.0184	0.0152	-0.0032	-0.0120	0.0161
-25.0	350.0	-0.7707	-0.8353	0.0189	-0.0051	0.0069	-0.0013	0.0240	0.0189	-0.0051	-0.0138	0.0196
0.0	350.0	-0.2394	-0.7322	0.0206	-0.0066	0.0070	-0.0016	0.0272	0.0206	-0.0066	-0.0140	0.0210
25.0	350.0	0.2836	-0.7765	0.0226	-0.0069	0.0078	-0.0003	0.0295	0.0226	-0.0069	-0.0156	0.0231
50.0	350.0	0.8236	-0.7088	0.0208	-0.0060	0.0074	0.0023	0.0268	0.0208	-0.0060	-0.0148	0.0214
75.0	350.0	1.3307	-0.6193	0.0115	-0.0088	0.0013	0.0036	0.0206	0.0116	-0.0089	-0.0027	0.0122
100.0	350.0	1.7654	-0.2207	0.0052	-0.0056	-0.0002	0.0052	0.0120	0.0058	-0.0062	-0.0004	0.0069
-100.0	325.0	-1.6008	-0.6118	0.0027	-0.0024	-0.0002	0.0118	0.0128	0.0066	-0.0063	-0.0003	0.0074
-75.0	325.0	-1.4553	-0.7728	0.0062	-0.0057	0.0003	0.0086	0.0147	0.0076	-0.0071	-0.0005	0.0085
-50.0	325.0	-1.1486	-0.6759	0.0146	-0.0032	0.0057	0.0019	0.0179	0.0146	-0.0033	-0.0113	0.0153
-25.0	325.0	-0.6875	-0.6036	0.0196	-0.0081	0.0058	0.0036	0.0279	0.0197	-0.0082	-0.0115	0.0198
0.0	325.0	-0.1290	-0.4794	0.0178	-0.0092	0.0043	-0.0009	0.0270	0.0178	-0.0092	-0.0086	0.0178
25.0	325.0	0.2398	-0.4910	0.0208	-0.0099	0.0054	0.0045	0.0311	0.0210	-0.0101	-0.0109	0.0210
50.0	325.0	0.8260	-0.5290	0.0212	-0.0076	0.0068	0.0067	0.0296	0.0215	-0.0080	-0.0135	0.0218
75.0	325.0	1.3104	-0.2511	0.0105	-0.0111	-0.0003	0.0084	0.0231	0.0113	-0.0118	-0.0005	0.0134
100.0	325.0	1.6007	-0.0913	0.0045	-0.0090	-0.0022	0.0060	0.0148	0.0052	-0.0096	0.0045	0.0096
-100.0	300.0	-1.1845	-0.6279	0.0018	-0.0030	-0.0006	0.0167	0.0173	0.0081	-0.0092	0.0012	0.0101
-75.0	300.0	-1.0872	-0.5053	0.0044	-0.0051	-0.0003	0.0145	0.0173	0.0083	-0.0090	0.0007	0.0100
-50.0	300.0	-0.0292	-0.6404	0.0125	-0.0042	0.0042	0.0081	0.0186	0.0135	-0.0051	-0.0083	0.0136
-25.0	300.0	-0.3475	-0.4304	0.0158	-0.0061	0.0049	-0.0047	0.0224	0.0161	-0.0063	-0.0098	0.0162
0.0	300.0	-0.0825	-0.3055	0.0087	-0.0064	0.0011	-0.0001	0.0151	0.0087	-0.0064	-0.0023	0.0090
25.0	300.0	0.0619	-0.3017	0.0141	-0.0068	0.0037	0.0024	0.0211	0.0142	-0.0069	-0.0074	0.0142
50.0	300.0	0.6234	-0.3721	0.0220	-0.0077	0.0072	0.0095	0.0312	0.0228	-0.0085	-0.0143	0.0230
75.0	300.0	0.0688	-0.1019	0.0123	-0.0065	0.0029	0.0130	0.0229	0.0143	-0.0086	-0.0058	0.0144
100.0	300.0	1.5454	-0.1435	0.0051	-0.0037	0.0007	0.0090	0.0125	0.0070	-0.0056	-0.0014	0.0074
-100.0	275.0	0.7741	-0.4644	0.0015	-0.0049	-0.0017	0.0161	0.0173	0.0089	-0.0104	-0.0034	0.0106
-75.0	275.0	-0.7784	-0.4683	0.0038	-0.0022	0.0008	-0.0151	0.0162	0.0114	-0.0073	-0.0016	0.0095
-50.0	275.0	-0.6033	-0.5108	0.0089	-0.0033	0.0011	-0.0135	0.0206	0.0107	-0.0092	-0.0022	0.0121
-25.0	275.0	-0.2103	-0.4007	0.0107	-0.0041	0.0033	-0.0004	0.0148	0.0081	-0.0041	-0.0066	0.0108
0.0	275.0	-0.0579	-0.1981	0.0081	-0.0042	0.0020	0.0006	0.0123	0.0116	-0.0042	-0.0039	0.0081
25.0	275.0	0.1630	-0.2314	0.0116	-0.0033	0.0041	0.0010	0.0149	0.0164	-0.0033	-0.0083	0.0120
50.0	275.0	0.5410	-0.1297	0.0159	-0.0071	0.0044	0.0093	0.0240	0.0111	-0.0076	-0.0089	0.0165
75.0	275.0	0.8966	-0.0461	0.0096	-0.0032	0.0032	0.0126	0.0158	0.0094	-0.0047	-0.0065	0.0112
100.0	275.0	1.3287	0.1071	0.0042	-0.0018	0.0030	0.0096	0.0128	0.0036	-0.0034	-0.0060	0.0095
-100.0	250.0	0.3843	-0.4080	0.0005	-0.0039	-0.0017	-0.0096	0.0106	0.0043	-0.0070	-0.0033	0.0070
-75.0	250.0	-0.3249	-0.3494	0.0012	-0.0030	-0.0009	-0.0093	0.0102	0.0052	-0.0060	-0.0017	0.0062
-50.0	250.0	-0.3422	-0.2995	0.0045	-0.0052	-0.0004	-0.0054	0.0111	0.0069	-0.0059	-0.0007	0.0065
-25.0	250.0	0.0849	0.1214	0.0067	-0.0029	0.0019	0.0029	0.0100	0.0046	-0.0031	-0.0038	0.0069
0.0	250.0	0.0937	0.0612	0.0045	-0.0023	0.0011	0.0014	0.0069	0.0087	-0.0023	-0.0022	0.0046
25.0	250.0	0.1592	0.0649	0.0086	-0.0012	0.0037	0.0021	0.0100	0.0127	-0.0013	-0.0074	0.0094
50.0	250.0	0.4995	0.0433	0.0126	-0.0031	0.0047	0.0030	0.0160	0.0085	-0.0032	-0.0095	0.0132
75.0	250.0	0.7463	0.0477	0.0067	-0.0009	0.0029	0.0083	0.0113	0.0088	-0.0027	-0.0058	0.0087
100.0	250.0	0.9820	-0.1028	0.0028	-0.0013	0.0021	0.0135	0.0136	0.0011	-0.0047	-0.0041	0.0089
-100.0	225.0	0.2442	-0.3427	0.0005	-0.0039	0.0017	-0.0036	0.0056	0.0016	-0.0045	-0.0034	0.0047
-75.0	225.0	0.1512	-0.2964	0.0012	-0.0043	0.0016	-0.0032	0.0063	0.0013	-0.0047	-0.0031	0.0048
-50.0	225.0	-0.1478	-0.2335	0.0013	-0.0034	-0.0010	-0.0009	0.0048	0.0004	-0.0034	-0.0021	0.0035
-25.0	225.0	-0.0940	-0.2266	0.0001	-0.0020	-0.0009	0.0017	0.0027	0.0004	-0.0023	-0.0019	0.0024
0.0	225.0	-0.0671	-0.0937	0.0002	-0.0009	-0.0004	0.0010	0.0015	0.0004	-0.0011	-0.0007	0.0011

Col1	Col2	Col3	Col4	Col5	Col6	Col7	Col8	Col9	Col10	Col11		X		Y
0.0123	-0.0104	-0.0005	0.0109	0.0113	0.0022	0.0052	-0.0004	0.0107	-0.1228	0.0181	0.0	225.0	0.0	25.0
0.0166	-0.0137	-0.0013	0.0150	0.0164	0.0068	0.0068	-0.0006	0.0143	-0.0002	0.5418	0.0	225.0	0.0	50.0
0.0079	-0.0053	-0.0024	0.0077	0.0102	0.0092	0.0026	0.0005	0.0048	0.0820	0.6150	0.0	225.0	0.0	75.0
0.0076	-0.0024	-0.0050	0.0074	0.0124	0.0124	0.0012	0.0008	0.0016	0.0766	0.7334	0.0	225.0	0.0	100.0
0.0064	0.0055	-0.0056	-0.0001	0.0058	-0.0016	-0.0028	-0.0055	0.0000	-0.1534	-0.1843	0.0	200.0	0.0	-100.0
0.0057	0.0051	-0.0048	0.0003	0.0045	-0.0004	-0.0026	-0.0048	-0.0003	-0.1369	0.1700	0.0	200.0	0.0	-75.0
0.0039	-0.0030	-0.0037	0.0007	0.0044	-0.0004	0.0015	-0.0037	0.0007	-0.1630	0.1952	0.0	200.0	0.0	-50.0
0.0036	-0.0018	-0.0018	0.0036	0.0054	0.0011	0.0009	-0.0017	0.0036	-0.0927	0.1443	0.0	200.0	0.0	-25.0
0.0073	-0.0058	-0.0009	0.0067	0.0076	0.0040	0.0029	-0.0003	0.0061	0.0000	0.0000	0.0	200.0	0.0	25.0
0.0072	-0.0047	-0.0024	0.0071	0.0095	0.0039	0.0023	-0.0020	0.0066	0.1451	0.1562	0.0	200.0	0.0	50.0
0.0064	-0.0032	-0.0032	0.0064	0.0095	0.0082	0.0016	-0.0008	0.0040	0.0141	0.3567	0.0	200.0	0.0	75.0
0.0048	-0.0016	-0.0032	0.0048	0.0079	0.0079	0.0008	-0.0005	0.0011	0.0485	0.3402	0.0	200.0	0.0	100.0
0.0051	-0.0011	-0.0037	0.0048	0.0086	0.0086	0.0005	-0.0006	0.0005	0.0729	0.4150	0.0	200.0	0.0	-100.0
0.0084	0.0068	-0.0077	0.0009	0.0087	0.0027	0.0034	-0.0075	0.0007	-0.0845	-0.1903	0.0	175.0	0.0	-75.0
0.0061	0.0044	-0.0058	0.0015	0.0073	0.0019	0.0022	-0.0057	0.0014	-0.0461	0.1218	0.0	175.0	0.0	-50.0
0.0044	0.0022	-0.0059	0.0037	0.0096	0.0035	0.0011	-0.0056	0.0034	-0.0619	0.1161	0.0	175.0	0.0	-25.0
0.0059	-0.0025	-0.0031	0.0056	0.0086	0.0037	0.0012	-0.0027	0.0051	-0.0852	0.0896	0.0	175.0	0.0	25.0
0.0056	-0.0038	-0.0017	0.0055	0.0071	0.0009	0.0019	-0.0016	0.0054	-0.0805	0.1299	0.0	175.0	0.0	50.0
0.0056	0.0002	-0.0030	0.0028	0.0058	-0.0002	0.0001	-0.0030	0.0028	0.0418	0.2892	0.0	175.0	0.0	75.0
0.0033	0.0013	-0.0022	0.0009	0.0032	0.0027	0.0007	-0.0014	0.0001	0.0626	0.2970	0.0	175.0	0.0	100.0
0.0023	0.0005	-0.0010	0.0005	0.0014	0.0012	0.0003	-0.0007	0.0002	0.0578	0.3089	0.0	175.0	0.0	-100.0
0.0010	0.0004	-0.0006	0.0002	0.0009	0.0002	0.0002	-0.0006	0.0003	0.0538	0.3476	0.0	150.0	0.0	-75.0
0.0007	0.0076	-0.0082	0.0005	0.0087	0.0028	0.0038	-0.0079	0.0004	0.1625	-0.0516	0.0	150.0	0.0	-50.0
0.0091	0.0057	-0.0065	0.0008	0.0074	0.0033	0.0029	-0.0061	0.0011	0.1198	0.0771	0.0	150.0	0.0	-25.0
0.0071	0.0038	-0.0057	0.0019	0.0076	0.0045	0.0019	-0.0050	0.0031	0.1384	-0.0316	0.0	150.0	0.0	0.0
0.0058	0.0005	-0.0043	0.0038	0.0081	0.0046	0.0003	-0.0036	0.0061	0.0412	0.0363	0.0	150.0	0.0	25.0
0.0047	0.0035	-0.0027	0.0062	0.0088	0.0020	0.0018	-0.0025	0.0042	0.0628	0.0563	0.0	150.0	0.0	50.0
0.0062	-0.0028	-0.0016	0.0044	0.0061	0.0024	0.0014	-0.0014	0.0006	0.0247	0.2758	0.0	150.0	0.0	75.0
0.0045	0.0009	-0.0019	0.0010	0.0029	0.0020	0.0005	-0.0015	0.0004	0.0577	0.3023	0.0	150.0	0.0	100.0
0.0019	0.0015	-0.0023	0.0008	0.0032	0.0021	0.0007	-0.0019	0.0015	0.0778	0.3239	0.0	150.0	0.0	-100.0
0.0023	-0.0020	-0.0052	0.0031	0.0083	0.0078	0.0010	-0.0025	0.0061	0.0796	0.3872	0.0	150.0	0.0	-75.0
0.0052	-0.0042	-0.0047	0.0005	0.0052	0.0005	0.0021	-0.0047	0.0050	0.3960	0.0132	0.0	125.0	0.0	-50.0
0.0051	0.0031	-0.0047	0.0015	0.0062	0.0025	0.0016	-0.0036	0.0022	0.2551	0.0476	0.0	125.0	0.0	-25.0
0.0048	-0.0008	-0.0027	0.0035	0.0062	0.0044	0.0004	-0.0025	0.0011	0.1868	0.0648	0.0	125.0	0.0	0.0
0.0037	-0.0017	-0.0037	0.0021	0.0058	0.0022	0.0008	-0.0014	0.0025	0.0553	0.2174	0.0	125.0	0.0	25.0
0.0013	0.0010	-0.0012	0.0002	0.0014	0.0013	0.0005	-0.0006	0.0034	0.0622	0.1811	0.0	125.0	0.0	50.0
0.0025	-0.0013	-0.0012	0.0025	0.0037	0.0033	0.0007	-0.0001	0.0021	0.0648	0.1822	0.0	125.0	0.0	75.0
0.0064	-0.0043	-0.0020	0.0063	0.0082	0.0025	0.0022	-0.0018	0.0011	0.1396	0.2701	0.0	125.0	0.0	100.0
0.0061	0.0023	-0.0037	0.0060	0.0098	0.0061	0.0012	-0.0027	0.0023	0.1624	0.4222	0.0	125.0	0.0	-100.0
0.0076	0.0008	-0.0060	0.0062	0.0132	0.0121	0.0004	-0.0030	0.0051	0.1925	0.7181	0.0	125.0	0.0	-75.0
0.0035	0.0007	-0.0062	0.0034	0.0060	0.0058	0.0008	-0.0003	0.0062	0.3882	0.2075	0.0	100.0	0.0	-50.0
0.0030	-0.0016	-0.0034	0.0030	0.0044	0.0004	0.0019	-0.0009	0.0119	0.2297	-0.0860	0.0	100.0	0.0	-25.0
0.0042	0.0038	-0.0030	0.0035	0.0031	0.0004	0.0000	-0.0004	0.0080	0.2401	-0.0036	0.0	100.0	0.0	0.0
0.0024	0.0000	-0.0035	0.0021	0.0041	0.0066	0.0007	-0.0020	0.0035	0.1437	0.0827	0.0	100.0	0.0	25.0
0.0040	0.0014	-0.0021	0.0040	0.0066	0.0051	0.0021	-0.0003	0.0011	0.1554	0.1222	0.0	100.0	0.0	50.0
0.0069	0.0042	-0.0026	0.0069	0.0096	0.0068	0.0011	-0.0020	0.0023	0.1916	0.1728	0.0	100.0	0.0	75.0
0.0133	0.0099	-0.0027	0.0127	0.0155	0.0048	0.0062	-0.0038	0.0051	0.2370	0.4268	0.0	100.0	0.0	100.0
0.0103	-0.0042	-0.0028	0.0103	0.0164	0.0114	0.0119	-0.0034	0.0069	0.0108	0.6883	0.0	100.0	0.0	-100.0
0.0080	0.0000	-0.0061	0.0069	0.0139	0.0120	0.0080	-0.0006	0.0080	0.1086	1.0838	0.0	100.0	0.0	-75.0
0.0055	-0.0017	-0.0028	0.0054	0.0091	0.0091	0.0035	0.0021	0.0035	0.2385	0.3128	0.0	75.0	0.0	-50.0
0.0038	-0.0030	-0.0049	0.0035	0.0040	0.0037	0.0011	-0.0042	0.0011	0.2978	-0.2024	0.0	75.0	0.0	-25.0
0.0055	-0.0043	-0.0028	0.0051	0.0059	0.0005	0.0023	-0.0031	0.0023	0.3126	0.1074	0.0	75.0	0.0	25.0
0.0079	-0.0099	-0.0042	0.0069	0.0070	0.0021	0.0051	-0.0058	0.0051	0.3359	0.0211	0.0	75.0	0.0	50.0
0.0076	-0.0048	-0.0061	0.0001	0.0103	0.0034	0.0069	-0.0054	0.0069	0.3610	0.2979	0.0	75.0	0.0	75.0
0.0120	-0.0071	-0.0049	0.0021	0.0169	0.0024	0.0080	-0.0019	0.0080		0.4282	0.0	75.0	0.0	100.0
0.0142	-0.0096	-0.0042	0.0042	0.0180	0.0035	0.0113	-0.0018	0.0113		0.8554	0.0	75.0	0.0	-100.0
0.0118	-0.0002	-0.0101	0.0051	0.0204	0.0048	0.0127		0.0127		0.9977	0.0	75.0	0.0	-75.0
0.0091	0.0030	-0.0089	0.0060	0.0149	0.0001	0.0060		0.0060		1.2541	0.0	50.0	0.0	100.0
0.0065	-0.0004	-0.0054	0.0058	0.0112	0.0015	0.0025		0.0025		-0.6127	0.0	50.0	0.0	-100.0
0.0048	-0.0026	-0.0022	0.0048	0.0070	0.0032	0.0013		0.0044		-0.3425	0.0	50.0	0.0	-75.0

-50.0	50.0	-0.1514	0.2627	0.0083	-0.0031	0.0026	-0.0011	0.0114	0.0083	-0.0031	-0.0052	0.0084
-25.0	50.0	-0.0223	0.1793	0.0114	-0.0007	0.0054	0.0002	0.0121	0.0114	-0.0007	-0.0108	0.0128
0	50.0	0.4390	0.1899	0.0140	-0.0038	0.0051	-0.0023	0.0179	0.0141	-0.0038	-0.0102	0.0145
25.0	50.0	0.7563	0.3089	0.0170	-0.0024	0.0073	-0.0040	0.0198	0.0172	-0.0026	-0.0145	0.0185
50.0	50.0	1.1399	0.3144	0.0155	-0.0046	0.0054	-0.0086	0.0218	0.0163	-0.0055	-0.0109	0.0166
75.0	50.0	1.6116	0.5330	0.0078	-0.0054	0.0012	-0.0111	0.0172	0.0098	-0.0074	-0.0024	0.0102
100.0	50.0	1.7064	0.5211	0.0034	-0.0063	-0.0014	-0.0108	0.0145	0.0058	-0.0087	0.0029	0.0089
-100.0	25.0	-0.9383	0.4562	0.0038	-0.0024	0.0007	0.0054	0.0082	0.0048	-0.0034	-0.0014	0.0050
-75.0	25.0	-0.4616	0.3482	0.0078	-0.0021	0.0029	0.0006	0.0099	0.0078	-0.0021	-0.0057	0.0081
-50.0	25.0	0.1625	0.3458	0.0122	-0.0022	0.0050	-0.0009	0.0145	0.0122	-0.0022	-0.0100	0.0130
-25.0	25.0	0.0282	0.2478	0.0126	-0.0009	0.0059	-0.0003	0.0134	0.0126	-0.0009	-0.0117	0.0140
0	25.0	0.4718	0.3533	0.0139	-0.0016	0.0062	-0.0033	0.0158	0.0141	-0.0018	-0.0123	0.0153
25.0	25.0	0.8143	0.3107	0.0183	-0.0001	0.0091	0.0002	0.0185	0.0183	-0.0001	-0.0182	0.0211
50.0	25.0	1.2354	0.4162	0.0183	-0.0034	0.0074	-0.0008	0.0217	0.0183	-0.0034	-0.0149	0.0194
75.0	25.0	1.8136	0.6358	0.0096	-0.0024	0.0036	-0.0010	0.0121	0.0096	-0.0025	-0.0072	0.0100
100.0	25.0	1.9651	0.8991	0.0042	-0.0035	0.0003	-0.0047	0.0091	0.0049	-0.0042	-0.0007	0.0053
-100.0	0.0	-1.0442	0.5970	0.0035	-0.0009	0.0013	0.0016	0.0047	0.0036	-0.0011	-0.0025	0.0037
-75.0	0.0	-0.5056	0.5575	0.0072	-0.0012	0.0030	-0.0015	0.0085	0.0073	-0.0012	-0.0060	0.0078
-50.0	0.0	-0.2410	0.4174	0.0129	-0.0009	0.0060	-0.0050	0.0147	0.0133	-0.0014	-0.0119	0.0146
-25.0	0.0	-0.1572	0.2733	0.0157	-0.0006	0.0076	-0.0050	0.0170	0.0161	-0.0009	-0.0152	0.0181
0.0	0.0	0.7281	0.1720	0.0167	-0.0004	0.0082	-0.0032	0.0174	0.0169	-0.0006	-0.0163	0.0192
25.0	0.0	0.9321	0.2220	0.0241	-0.0001	0.0121	0.0068	0.0249	0.0245	-0.0003	-0.0242	0.0281
50.0	0.0	1.8959	0.6420	0.0208	0.0001	0.0097	0.0064	0.0233	0.0213	-0.0020	-0.0193	0.0235
75.0	0.0	1.8448	0.6592	0.0063	-0.0015	0.0027	0.0011	0.0073	0.0063	-0.0010	-0.0054	0.0068
100.0	0.0	2.1373	0.7475	0.0023	-0.0014	0.0005	-0.0018	0.0041	0.0025	-0.0016	-0.0009	0.0026

Displacements and strains for

125 to 25°C

X	Y	DX	DY	EXX	EYY	EM	GXY	GMAX	EA	EB	EC	EEFF
-100.0	375.0	1.9541	0.3652	-0.0041	0.0011	-0.0015	-0.0004	0.0052	0.0011	-0.0041	0.0029	0.0042
-75.0	375.0	1.7587	0.2772	-0.0093	0.0008	-0.0042	-0.0005	0.0101	0.0008	-0.0093	0.0085	0.0103
-50.0	375.0	1.2708	0.2707	-0.0176	0.0008	-0.0084	0.0016	0.0185	0.0009	-0.0176	0.0167	0.0199
-25.0	375.0	0.7273	0.2766	-0.0206	0.0009	-0.0098	0.0037	0.0218	0.0011	-0.0207	0.0196	0.0233
0.0	375.0	0.3203	0.3772	-0.0205	0.0008	-0.0104	0.0036	0.0216	0.0010	-0.0206	0.0197	0.0233
25.0	375.0	-0.2571	0.3933	-0.0211	-0.0002	-0.0111	-0.0015	0.0213	-0.0002	-0.0211	0.0209	0.0242
50.0	375.0	-0.7901	0.1868	-0.0208	0.0015	-0.0064	-0.0032	0.0195	0.0014	-0.0209	0.0223	0.0250
75.0	375.0	-1.2443	0.2632	-0.0130	0.0002	-0.0031	0.0001	0.0132	0.0002	-0.0130	0.0128	0.0149
100.0	375.0	-1.9526	0.1417	-0.0060	0.0002	-0.0010	-0.0009	0.0059	0.0001	-0.0061	0.0062	0.0071
-100.0	350.0	1.9398	0.2474	-0.0045	0.0024	-0.0044	-0.0005	0.0069	0.0025	-0.0045	0.0020	0.0045
-75.0	350.0	1.7588	0.2174	-0.0105	0.0017	-0.0085	0.0014	0.0123	0.0018	-0.0105	0.0088	0.0113
-50.0	350.0	1.1311	0.2428	-0.0186	0.0019	-0.0091	0.0038	0.0207	0.0019	-0.0188	0.0170	0.0207
-25.0	350.0	0.6814	0.3070	-0.0201	0.0017	-0.0090	0.0040	0.0223	0.0021	-0.0203	0.0182	0.0223
0.0	350.0	0.2332	0.2818	-0.0197	0.0017	-0.0117	0.0047	0.0218	0.0019	-0.0199	0.0180	0.0220
25.0	350.0	-0.3280	0.3762	-0.0235	0.0002	-0.0130	0.0017	0.0237	0.0002	-0.0235	0.0234	0.0271
50.0	350.0	-0.9321	0.3190	-0.0227	-0.0033	-0.0057	-0.0003	0.0194	-0.0033	-0.0227	0.0260	0.0203
75.0	350.0	-1.5222	0.3151	-0.0118	0.0004	-0.0028	0.0015	0.0122	0.0004	-0.0118	0.0114	0.0134
100.0	350.0	-1.8644	0.2249	-0.0053	0.0017	-0.0010	-0.0010	0.0050	0.0019	-0.0053	0.0056	0.0063
-100.0	325.0	2.0150	0.1502	-0.0055	0.0034	-0.0046	0.0024	0.0092	0.0035	-0.0056	0.0021	0.0057
-75.0	325.0	1.7588	0.1493	-0.0132	0.0041	-0.0100	0.0080	0.0191	0.0050	-0.0141	0.0092	0.0143
-50.0	325.0	1.9809	0.0976	-0.0219	0.0019	-0.0091	0.0046	0.0242	0.0021	-0.0221	0.0200	0.0244
-25.0	325.0	0.5222	0.0902	-0.0198	0.0016	-0.0072	0.0085	0.0230	0.0025	-0.0206	0.0181	0.0225
0.0	325.0	0.1016	0.2109	-0.0157	0.0014	-0.0113	0.0069	0.0185	0.0021	-0.0164	0.0143	0.0179
25.0	325.0	-0.3327	0.3304	-0.0211	-0.0014	-0.0124	0.0054	0.0204	-0.0011	-0.0215	0.0225	0.0254
50.0	325.0	-0.9310	0.5153	-0.0231	-0.0017	-0.0052	0.0000	0.0215	-0.0017	-0.0231	0.0248	0.0277
75.0	325.0	-1.5347	0.2618	-0.0120	0.0016	-0.0019	-0.0015	0.0136	0.0016	-0.0120	0.0104	0.0131
100.0	325.0	-1.8532	0.2066	-0.0052	0.0014	-0.0025	0.0012	0.0067	0.0014	-0.0053	0.0038	0.0055
-100.0	290.0	1.6447	0.0909	-0.0047	0.0002	-0.0019	0.0157	0.0163	0.0057	-0.0107	0.0050	0.0107
-75.0	290.0	1.1591	0.0185	-0.0107	-0.0003	-0.0025	0.0139	0.0174	0.0032	-0.0142	0.0110	0.0149
-50.0	290.0	0.7685	0.0951	-0.0166	0.0024	-0.0055	0.0103	0.0216	0.0037	-0.0179	0.0142	0.0189
-25.0	290.0	0.2706	0.1681	-0.0138	0.0048	-0.0070	0.0087	0.0162	0.0012	-0.0151	0.0139	0.0168
0.0	290.0	0.0945	0.2348	-0.0113	0.0051	-0.0067	0.0085	0.0126	-0.0004	-0.0130	0.0133	0.0152
25.0	290.0	-0.2926	0.4075	-0.0180	0.0029	-0.0075	0.0042	0.0214	0.0032	-0.0182	0.0151	0.0195
50.0	290.0	-0.8220	0.3563	-0.0212	0.0049	-0.0082	0.0145	0.0299	0.0068	-0.0231	0.0163	0.0237
75.0	290.0	-1.3765	0.1858	-0.0115	0.0026	-0.0044	0.0159	0.0212	0.0062	-0.0150	0.0088	0.0151
100.0	290.0	-1.7210	0.0959	-0.0048	0.0029	-0.0010	0.0156	0.0174	0.0077	-0.0097	0.0020	0.0102
-100.0	275.0	1.3347	0.1256	-0.0038	-0.0010	-0.0024	0.0166	0.0168	0.0060	-0.0108	0.0048	0.0108
-75.0	275.0	1.0766	0.0699	-0.0096	-0.0026	-0.0061	0.0108	0.0129	0.0003	-0.0126	0.0122	0.0143
-50.0	275.0	0.6088	-0.0179	-0.0157	0.0015	-0.0071	0.0102	0.0201	0.0029	-0.0171	0.0142	0.0183
-25.0	275.0	0.2015	0.1474	-0.0119	0.0003	-0.0061	0.0060	0.0131	0.0005	-0.0126	0.0121	0.0143
0.0	275.0	0.0132	0.2784	-0.0051	0.0012	-0.0032	0.0051	0.0065	0.0001	-0.0064	0.0063	0.0074
25.0	275.0	-0.1210	0.2563	-0.0127	0.0048	-0.0039	0.0068	0.0188	0.0055	-0.0133	0.0078	0.0134
50.0	275.0	-0.5797	0.2489	-0.0202	0.0051	-0.0075	0.0139	0.0288	0.0069	-0.0220	0.0151	0.0225
75.0	275.0	-1.1392	0.1439	-0.0111	0.0029	-0.0041	0.0185	0.0232	0.0053	-0.0157	0.0082	0.0147
100.0	275.0	-1.4233	0.0928	-0.0045	0.0028	-0.0008	0.0210	0.0222	0.0082	-0.0119	0.0016	0.0129
-100.0	250.0	-0.9923	0.1270	-0.0029	0.0001	-0.0015	0.0125	0.0128	0.0089	-0.0079	0.0030	0.0080
-75.0	250.0	0.6206	0.1016	-0.0157	0.0013	-0.0039	0.0104	0.0115	0.0041	-0.0076	0.0077	0.0102
-50.0	250.0	0.4104	0.0781	-0.0119	0.0012	-0.0053	0.0076	0.0112	0.0018	-0.0109	0.0106	0.0124
-25.0	250.0	0.2023	0.1773	-0.0051	0.0004	-0.0033	0.0040	0.0085	0.0003	-0.0076	0.0024	0.0082
0.0	250.0	-0.0223	0.2602	-0.0127	0.0025	-0.0012	0.0027	0.0078	0.0009	-0.0051	0.0066	0.0051
25.0	250.0	-0.0795	0.2585	-0.0049	0.0026	-0.0034	0.0037	0.0126	0.0027	-0.0077	0.0024	0.0100
50.0	250.0	-0.4153	0.1775	-0.0094	0.0034	-0.0046	0.0117	0.0198	0.0053	-0.0145	0.0069	0.0147
75.0	250.0	-0.7252	0.0939	-0.0126	0.0031	-0.0019	0.0175	0.0201	0.0082	-0.0120	0.0093	0.0122
100.0	250.0	-0.9486	0.0384	-0.0069	0.0026	-0.0001	0.0171	0.0180	0.0089	-0.0091	0.0038	0.0104
-100.0	225.0	0.7717	0.1032	-0.0028	0.0004	-0.0012	0.0105	0.0106	0.0041	-0.0065	0.0002	0.0066
-75.0	225.0	0.4773	0.1170	-0.0044	-0.0003	-0.0024	0.0072	0.0082	0.0018	-0.0065	0.0047	0.0067
-50.0	225.0	0.3562	0.1073	-0.0069	-0.0006	-0.0037	0.0056	0.0084	0.0004	-0.0079	0.0075	0.0089
-25.0	225.0	0.2038	0.1597	-0.0060	0.0021	-0.0020	0.0044	0.0092	0.0026	-0.0066	0.0040	0.0066
0.0	225.0	0.0096	0.1815	-0.0045	0.0040	-0.0003	0.0026	0.0089	0.0042	-0.0047	0.0005	0.0052

C1	C2	C3	C4	C5	C6	C7	C8	C9	C10	C11	In1	In2
0.0066	0.0040	-0.0065	0.0025	0.0090	-0.0022	-0.0020	0.0024	-0.0064	0.2286	0.0700	225.0	25.0
0.0103	0.0063	-0.0102	0.0039	0.0140	-0.0095	-0.0032	0.0020	-0.0084	0.1148	-0.2703	225.0	50.0
0.0087	0.0037	-0.0067	0.0050	0.0137	-0.0121	-0.0018	0.0014	-0.0051	-0.0204	-0.4697	225.0	75.0
0.0067	0.0015	-0.0064	0.0048	0.0112	-0.0109	-0.0008	0.0006	-0.0022	0.0500	0.4860	225.0	-100.0
0.0059	0.0024	-0.0059	0.0035	0.0094	-0.0093	-0.0012	0.0007	-0.0018	0.1307	0.5007	200.0	-75.0
0.0055	0.0043	-0.0051	0.0007	0.0058	-0.0042	-0.0022	0.0002	-0.0042	0.1039	0.3306	200.0	-50.0
0.0066	0.0054	-0.0059	0.0005	0.0064	-0.0024	-0.0027	0.0002	-0.0057	0.0787	0.1455	200.0	-25.0
0.0037	0.0015	-0.0037	0.0022	0.0059	-0.0022	-0.0007	0.0020	-0.0034	0.0761	0.0441	200.0	0.0
0.0023	0.0064	-0.0022	0.0017	0.0039	-0.0018	-0.0002	0.0015	-0.0019	0.0000	0.0000	200.0	25.0
0.0026	0.0005	-0.0025	0.0019	0.0044	-0.0006	-0.0003	0.0019	-0.0024	0.0792	0.0614	200.0	50.0
0.0046	0.0031	-0.0045	0.0014	0.0059	-0.0033	-0.0015	0.0009	-0.0040	0.0508	0.1578	200.0	75.0
0.0049	0.0037	-0.0046	0.0009	0.0055	-0.0048	-0.0018	0.0005	-0.0032	0.0057	-0.1975	200.0	-100.0
0.0044	0.0029	-0.0044	0.0030	0.0059	-0.0058	-0.0015	0.0005	-0.0015	-0.0707	-0.4674	175.0	-75.0
0.0020	0.0000	-0.0020	0.0011	0.0031	-0.0026	0.0000	0.0004	-0.0013	0.1710	0.2522	175.0	-50.0
0.0033	0.0009	-0.0029	0.0001	0.0031	-0.0010	-0.0014	0.0000	-0.0029	0.1478	0.2142	175.0	-25.0
0.0041	0.0028	-0.0037	0.0003	0.0040	-0.0022	-0.0017	0.0001	-0.0033	0.0944	0.1599	175.0	25.0
0.0037	0.0034	-0.0029	0.0005	0.0023	-0.0004	0.0013	0.0011	-0.0023	0.0422	0.0641	175.0	50.0
0.0055	0.0046	-0.0036	0.0009	0.0045	-0.0018	-0.0013	0.0009	-0.0036	0.1349	0.2281	175.0	75.0
0.0036	0.0035	-0.0049	0.0004	0.0053	0.0000	-0.0023	0.0002	-0.0048	0.1421	0.1830	175.0	-100.0
0.0028	0.0027	-0.0026	0.0009	0.0017	-0.0013	-0.0018	0.0009	-0.0026	0.0759	0.3117	150.0	-75.0
0.0017	0.0007	-0.0020	0.0007	0.0014	-0.0012	-0.0013	0.0016	-0.0011	0.0367	0.3795	150.0	-50.0
0.0024	0.0008	-0.0009	0.0002	0.0026	-0.0029	0.0004	0.0015	-0.0008	0.0142	0.1954	150.0	-25.0
0.0032	0.0028	-0.0024	0.0012	0.0039	-0.0014	-0.0004	0.0009	-0.0017	0.0985	0.1124	150.0	0.0
0.0042	0.0042	-0.0027	0.0009	0.0027	-0.0006	-0.0014	0.0002	-0.0026	0.0857	0.0583	150.0	25.0
0.0030	0.0027	-0.0024	0.0000	0.0006	-0.0014	-0.0021	0.0020	-0.0022	0.0814	0.0295	150.0	50.0
0.0038	0.0027	-0.0024	0.0009	0.0020	-0.0006	-0.0014	0.0005	-0.0023	0.0927	-0.0443	150.0	75.0
0.0050	0.0043	-0.0036	0.0000	0.0046	-0.0008	-0.0013	0.0009	-0.0036	0.0843	0.1332	150.0	-100.0
0.0035	0.0031	-0.0044	0.0000	0.0044	-0.0004	-0.0022	0.0000	-0.0043	0.0640	0.2522	150.0	-75.0
0.0019	0.0009	-0.0030	0.0006	0.0030	-0.0013	-0.0015	0.0005	-0.0026	0.0503	0.3223	125.0	-50.0
0.0014	0.0007	-0.0019	0.0005	0.0025	-0.0022	-0.0002	0.0009	-0.0011	0.0351	0.4698	125.0	-25.0
0.0014	0.0013	-0.0014	0.0007	0.0020	-0.0019	0.0007	0.0000	-0.0006	0.0211	0.2053	125.0	0.0
0.0017	0.0040	-0.0015	0.0002	0.0021	-0.0016	-0.0004	0.0002	-0.0010	0.0905	0.0926	125.0	25.0
0.0041	0.0027	-0.0028	0.0012	0.0018	-0.0014	-0.0007	0.0023	-0.0012	0.0948	0.0749	125.0	50.0
0.0038	0.0036	-0.0036	0.0009	0.0015	-0.0014	-0.0020	0.0009	-0.0016	0.1172	0.0666	125.0	75.0
0.0056	0.0053	-0.0053	0.0011	0.0045	-0.0006	-0.0014	0.0011	-0.0036	0.1625	0.0053	125.0	-100.0
0.0064	0.0060	-0.0060	0.0011	0.0065	-0.0002	-0.0021	0.0002	-0.0053	0.1357	-0.1265	125.0	-75.0
0.0049	0.0030	-0.0048	0.0018	0.0071	-0.0048	-0.0025	0.0009	-0.0051	0.0624	-0.2653	100.0	-50.0
0.0042	0.0005	-0.0038	0.0033	0.0072	-0.0061	-0.0015	0.0013	-0.0028	0.0527	-0.3801	100.0	-25.0
0.0054	0.0046	-0.0048	0.0002	0.0051	-0.0045	-0.0002	0.0013	-0.0012	0.0326	0.4944	100.0	0.0
0.0033	0.0032	-0.0024	0.0008	0.0017	-0.0016	0.0007	0.0002	-0.0011	0.0212	0.3063	100.0	25.0
0.0027	0.0026	-0.0017	0.0012	0.0008	-0.0004	0.0034	0.0007	-0.0018	0.1076	0.0631	100.0	50.0
0.0041	0.0040	-0.0028	0.0008	0.0016	-0.0016	0.0014	0.0003	-0.0016	0.0767	0.0436	100.0	75.0
0.0057	0.0044	-0.0054	0.0012	0.0065	-0.0020	-0.0010	0.0002	-0.0019	0.0944	0.0788	100.0	-100.0
0.0090	0.0067	-0.0086	0.0011	0.0105	-0.0021	-0.0021	0.0018	-0.0052	0.1041	-0.0595	100.0	-75.0
0.0101	0.0063	-0.0100	0.0019	0.0137	-0.0050	-0.0033	0.0014	-0.0080	0.0386	-0.2260	100.0	-50.0
0.0089	0.0046	-0.0089	0.0037	0.0131	-0.0104	-0.0032	0.0006	-0.0076	0.0335	-0.4175	75.0	-25.0
0.0060	0.0019	-0.0074	0.0043	0.0134	-0.0124	-0.0023	0.0019	-0.0044	0.0515	0.6229	75.0	0.0
0.0078	0.0060	-0.0059	0.0058	0.0008	-0.0133	-0.0009	0.0011	-0.0019	0.0632	0.7850	75.0	25.0
0.0064	0.0056	-0.0059	0.0014	0.0062	-0.0080	-0.0030	0.0048	-0.0011	0.0309	0.4085	75.0	50.0
0.0072	0.0049	-0.0056	0.0003	0.0034	-0.0061	-0.0028	0.0033	-0.0023	0.2637	0.1711	75.0	75.0
0.0087	0.0082	-0.0064	0.0017	0.0049	-0.0024	-0.0035	0.0022	-0.0047	0.1659	0.1191	75.0	-100.0
0.0084	0.0079	-0.0065	0.0016	0.0051	-0.0019	-0.0041	0.0018	-0.0064	0.1263	0.0802	75.0	-75.0
0.0146	0.0123	-0.0130	0.0006	0.0136	-0.0010	-0.0039	0.0014	-0.0065	0.2608	-0.3243	75.0	-50.0
0.0168	0.0124	-0.0160	0.0035	0.0195	-0.0079	-0.0062	0.0006	-0.0117	0.0902	-0.3821	75.0	-25.0
0.0132	0.0065	-0.0122	0.0057	0.0172	-0.0142	-0.0062	0.0005	-0.0129	0.0085	-0.8501	50.0	-100.0
0.0108	0.0044	-0.0108	0.0064	0.0084	-0.0172	-0.0033	0.0014	-0.0052	0.0349	-1.1465	50.0	-75.0

-50.0	0.0	50.0	0.1832	0.2440	-0.0068	-0.0020	-0.0044	-0.0026	0.0055	-0.0016	-0.0071	0.0087	0.0093
-25.0	0.0	50.0	0.0779	0.2919	-0.0098	-0.0008	-0.0053	-0.0018	0.0092	-0.0007	-0.0099	0.0106	0.0118
0.0	0.0	50.0	-0.2644	0.1445	-0.0150	-0.0043	-0.0096	0.0012	0.0108	-0.0042	-0.0150	0.0193	0.0202
25.0	0.0	50.0	-0.7028	0.0866	-0.0167	-0.0047	-0.0107	0.0063	0.0136	-0.0039	-0.0175	0.0214	0.0228
50.0	0.0	50.0	-1.0648	-0.0167	-0.0136	-0.0040	-0.0088	0.0088	0.0130	-0.0023	-0.0153	0.0176	0.0191
75.0	0.0	50.0	-1.4915	0.0633	-0.5075	-0.0038	-0.0057	0.0129	0.0134	0.0011	-0.0124	0.0113	0.0137
100.0	0.0	50.0	-1.6444	0.0698	-0.0035	-0.0046	-0.0041	0.0121	0.0121	0.0020	-0.0101	0.0081	0.0107
-100.0	0.0	25.0	0.8933	0.4112	-0.0030	-0.0015	-0.0023	-0.0047	0.0050	0.0002	-0.0047	0.0045	0.0054
-75.0	0.0	25.0	0.5071	0.3548	-0.0059	-0.0024	-0.0041	-0.0044	0.0056	-0.0013	-0.0070	0.0083	0.0089
-50.0	0.0	25.0	0.2176	0.2332	-0.0108	-0.0007	-0.0057	-0.0025	0.0103	-0.0006	-0.0109	0.0115	0.0129
-25.0	0.0	25.0	0.1431	0.2976	-0.0150	-0.0001	-0.0076	-0.0016	0.0150	-0.0001	-0.0151	0.0151	0.0174
0	0.0	25.0	-0.5480	0.2268	-0.0186	-0.0038	-0.0112	-0.0005	0.0148	-0.0038	-0.0186	0.0223	0.0239
25.0	0.0	25.0	-0.9172	0.1419	-0.0174	-0.0045	-0.0109	0.0039	0.0135	-0.0042	-0.0177	0.0218	0.0232
50.0	0.0	25.0	-1.2510	0.1622	-0.0128	-0.0045	-0.0086	0.0073	0.0111	-0.0031	-0.0142	0.0173	0.0184
75.0	0.0	25.0	-1.6431	0.2772	-0.0070	-0.0032	-0.0051	0.0067	0.0076	-0.0013	-0.0089	0.0102	0.0111
100.0	0.0	25.0	-1.8291	0.2682	-0.0033	-0.0035	-0.0034	0.0046	0.0046	-0.0011	-0.0057	0.0068	0.0073
-100.0	0.0	0.0	0.8867	0.4999	-0.0032	-0.0007	-0.0019	-0.0026	0.0036	-0.0001	-0.0037	0.0038	0.0044
-75.0	0.0	0.0	0.5313	0.4281	-0.0061	-0.0009	-0.0035	-0.0039	0.0064	-0.0003	-0.0067	0.0070	0.0079
-50.0	0.0	0.0	0.2497	0.2742	-0.0109	-0.0003	-0.0056	-0.0020	0.0108	-0.0002	-0.0110	0.0112	0.0128
-25.0	0.0	0.0	0.0748	0.2971	-0.0155	0.0000	-0.0077	0.0035	0.0158	-0.0002	-0.0157	0.0155	0.0180
0	0.0	0.0	-0.4960	0.5087	-0.0207	-0.0016	-0.0112	0.0056	0.0199	-0.0012	-0.0211	0.0224	0.0251
25.0	0.0	0.0	-1.0254	0.5275	-0.0211	-0.0022	-0.0117	0.0016	0.0190	-0.0021	-0.0212	0.0233	0.0258
50.0	0.0	0.0	-1.4577	0.4476	-0.0138	-0.0021	-0.0079	-0.0014	0.0118	-0.0020	-0.0138	0.0159	0.0173
75.0	0.0	0.0	-1.8484	0.3507	-0.0057	-0.0013	-0.0035	0.0008	0.0044	-0.0013	-0.0057	0.0070	0.0074
100.0	0.0	0.0	-1.8644	0.3707	-0.0026	-0.0013	-0.0020	0.0013	0.0019	-0.0011	-0.0029	0.0040	0.0041

APPENDIX G

MODEL FOR HIGH CYCLE FATIGUE OF BOND WIRES

G.1 FATIGUE CRACK INITIATION PREDICTION

G.1.1 Summary

This section describes the model for predicting cycles to crack initiation for high cycle fatigue of bond wires. It was coded and the software was delivered to the AF.

This section provides results of an analysis of initiation and growth of fatigue cracks from the root of a notch in a 1 mil diameter wire of aluminum - 1% silicon alloy. The analysis is based on the principles of linear elastic fracture mechanics and uses macroscopic fatigue and fracture material properties. The results were used to provide guidance in the planning of the tests described in Section 3.2.

G.1.2 Fracture Mechanics Background

The analyses are based on principles of linear elastic fracture mechanics (LEFM), which are based on the observation that classical elasticity predicts that the stresses near the tip of a crack always have the same spatial variation whose magnitude is controlled by a single parameter, K (Refs.G-1 through G-3). This parameter is called the stress intensity factor and is a function of the loading and geometry of the crack body. For instance, the normal stress perpendicular to the plane of the crack is given by the expression

$$\sigma_y = \frac{K}{\sqrt{2\pi r}} \cos\frac{\theta}{2} \left(1 + \sin\frac{\theta}{2}\sin\frac{3\theta}{2}\right) \tag{G-1}$$

This expression is applicable to cases where there is symmetry with respect to the crack plane. This is referred to as Mode I loading, and the stress intensity factor is often denoted as K_I. This discussion is limited to Mode I loading, and the subscript "I" is omitted.

The fact that the stresses near the crack tip are controlled by K suggests that final crack instability is controlled by the applied value of K, and fatigue crack growth is controlled by the cyclic value of K, $\Delta K (= K_{max} - K_{min})$. With restrictions, this is borne out by experimental results.

The K-solution depends on geometry and loading and is available for a wide range of crack geometries from a variety of sources (Refs. G-4 through G-6). The geometry of interest in this discussion is an edge-cracked round bar in pure bending, which is shown in Figure G-1. The K-solution for this geometry is (Refs. G-7 through G-9)
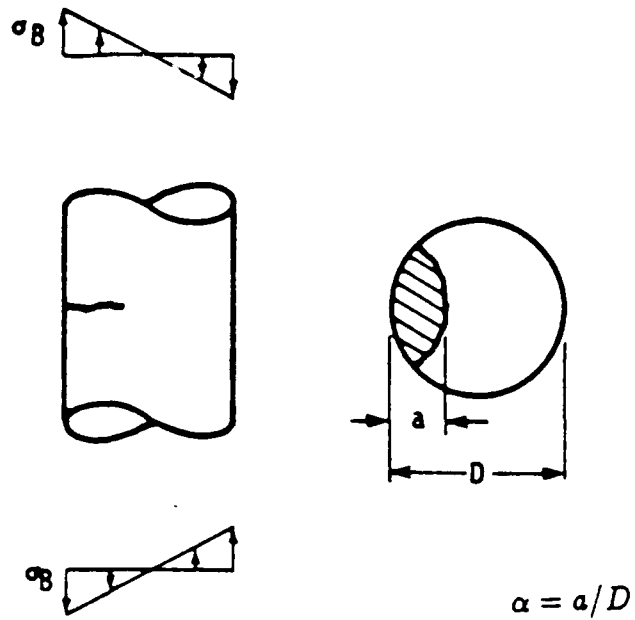
Figure G-1. Geometry of a Cracked Circular Bar in Bending
Considered in Discussion. (Note that a Curved Crack Front is
Considered, Which is Representative of a Growing Crack.
The Initial Notch in the Wire will Probably have a Straight Crack
Front, which will Somewhat Elevate K for a Given a.)

$$K = \sigma^B \sqrt{\pi a F_B} \qquad\qquad (G-2)$$

$$F_B = 0.59 \sec \beta \sqrt{\frac{\tan \beta}{\beta}} \left(0.923 + 0.199\gamma^4\right)$$

$$\beta = \frac{\pi a}{2D}$$

$$\gamma = 1 - \sin \beta$$

Figure G-1 defines the parameters in this equation.

One of the necessary conditions for LEFM to be applicable is that the net section stress not greatly exceed the yield strength of the material. The net section stress is calculated based on the remaining uncracked cross section. In the current case, it is based on bending of a circular cross-section which has had a circular arc piece of material removed. The evaluation of the bending moment of inertia, I, is complicated, so the equations involved are not included here. They are included in the FLAGRO Code (Ref. G-6) and have been incorporated into the NASCRAC Code (Ref. G-7).

G.1.3 Sharp Notches

The elastic stress analysis of cracks can be extended to predict the stress field near the tip of deep slender notches (Refs. G-2, G-8). Using the coordinate system of Figure G-2, the equation for a sharp notch that corresponds to Equation G-1 is

$$\sigma_y = \frac{K}{\sqrt{2\pi r'}} \left\{ \cos \frac{\theta}{2} \left(1 + \sin \frac{\theta}{2} \sin \frac{3\theta}{2} \right) + \frac{\rho}{2r'} \cos \frac{3}{2}\theta \right\} \qquad (G-3)$$

This equation is for small θ and $\rho/2 < r' < \rho$. Note that Equation G-3 reduces to Equation G-1 when $\rho = 0$, i.e., in the limiting case of a sharp notch, which is a crack.

The elastically calculated maximum stress at the notch root occurs when $r' = \rho/2$ and $\theta = 0$, and is equal to

$$\sigma_{y,max} = 2 \frac{K}{\sqrt{\pi \rho}} \qquad\qquad (G-4)$$

Consequently, the maximum stress at a long slender notch can be estimated from the stress intensity factor solution for the corresponding crack problem. This allows the wealth of available crack solutions to be applied to estimation of stresses at notch roots. Such estimates are useful in predictions of crack initiation at stress raisers — as will be demonstrated in a later section of this discussion.
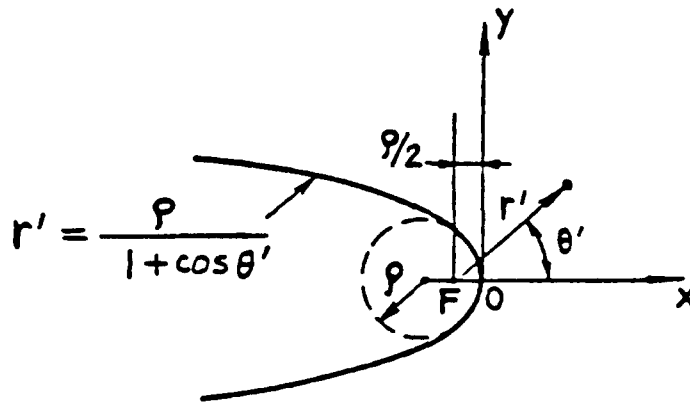
Figure G-2. Coordinate System Near a Sharp Notch Root.

G.1.4 Material Properties

Material properties for prediction of fatigue crack initiation and growth in aluminum - 1% silicon wires were obtained from literature results for macroscopic specimens. The fatigue crack characteristics of 2024-T3 aluminum alloy was used as being representative. No fatigue crack growth data for Al-1%Si were readily found.

Fatigue crack growth properties from the FLAGRO compilation (Ref. G-6) were used, which provides the following fatigue crack growth relation

$$\frac{da}{dN} = C\frac{\Delta K^n[\Delta K - (1-R)\Delta K_0]^p}{[(1-R)K_c - \Delta K]^q} \tag{G-5}$$

where $\Delta K = K_{max} - K_{min}$, $R = K_{min}/K_{max}$, da/dN is the crack growth rate per cycle, and the following constants apply:

$$
\begin{aligned}
C &= 1.8 \times 10^{-8} \\
n &= 2.873 \\
p &= q = 1/2 \\
K_c &= 73.4 \text{ ksi-in}^{1/2}
\end{aligned}
$$

A nominal value of $\Delta K_0 = 2.5$ ksi-in$^{1/2}$ was used, but ΔK_0 was considered to be variable. The above constants give da/dN in inches-per-cycle for ΔK in ksi-in$^{1/2}$.

Strain life (S-N) data for Al-1%Si were obtained from Ref. G-9. The parameter D_a was employed to account for mean stress effects

$$D_a = \left[(\sigma_a + \sigma_m) \in_a E \right]^{1/2} \qquad \text{(G-6)}$$

E = modulus of elasticity

σ_a = stress amplitude (1/2 peak-to-peak)

σ_m = mean stress

$\in_a$ = strain amplitude

The cycles to failure, N, and D_a are related by the expression

$$D_a = \left[\sigma_f' (2N)^{2b} + E\sigma_f' \in_f' (2N)^{b+c} \right]^{1/2} \qquad \text{(G-7)}$$

The parameters σ_f', $\in_f'$, b, c, and E are constants, with the following values from Page 20 of Ref.G-9:

σ_f' = 88.6 ksi

$\in_f'$ = 1.085

b = -0.099

c = -0.857

E = 9,280 ksi

The other material property required is the cyclic stress-strain curve, which is given in Ref. G-9 as:

$$\in_a = \frac{\sigma_a}{E} + \left(\frac{\sigma_a}{D} \right)^m$$

$$m = 19.6$$

$$D = 57.6 \text{ ksi} \qquad \text{(G-8)}$$

This equation provides the relationship between the strain amplitude and stress amplitude at the tip of the hysteresis loops during cyclic plastic deformation (Refs. G-9, G-10).

G.1.5 Procedures and Results for Crack Initiation

The cycles to initiation for a sharp notch of radius ρ under conditions of loading between specified nominal bending stresses $\sigma_{B,max}$ and $\sigma_{B,min}$ will be calculated. This is accomplished by first calculating K_{max} and K_{min} for a notch of depth a by use of the K-solution (Equation G-2). The extreme of the elastically calculated stresses at the notch root are then obtained from

Equation G-4. These stresses will generally be above the yield strength of the material, and the stresses and strains needed for calculation of D_a (Equation G-5) must include the effects of plasticity. Such effects can be estimated by use of Neuber's rule (Ref. G-9)

$$\sigma_e \in_e = \sigma_p \in_p \qquad \text{(G-9)}$$

where the subscript "e" denotes elastic values (as obtained from Equation G-4 and Hooke's law), and the subscript "p" denotes the plastic values (which are to be used in calculation of D_a). Neuber's rule (Equation G-9) and the cyclic stress-strain curve (Equation G-8) are used to determine σ_a, σ_m, and $\in_a$, for use in determination of D_a (Equation G-6). Details of the procedures involve some complexities in evaluation of the conditions at the extremes of the loading cycle, as discussed in Section 10.2 of the NASCRAC User's Manual (Ref. G-7) and in Ref. G-10.

The stress and strain conditions at the extremes of the loading cycles allow D_a in Equation G-6 to be calculated, from which cycles to failure is evaluated by use of Equation G-7. In this discussion, cycles to failure from Equation G-7 is taken as cycles to initiation of a crack at the root of the notch.

The results obtained in terms of $\Delta K/\rho^{1/2}$ for various R-ratios are presented in Figure G-3. This figure shows that R has virtually no effect on the initiation lifetime.

As an example of the use of Figure G-3, consider a 1 mil (10^{-3} in) diameter wire with $\sigma_{B,max} = 60$ ksi, $\sigma_{B,min} = 15$ with a notch of depth 0.3 mil and root radius 0.03 mil. The value F_B for $a/D = 0.3$ is 0.65. Equation G-2 then gives:

$$K_{max} = 60 \, (0.0003\pi)^{1/2} \, 0.64 = 1.19 \text{ ksi-in}^{1/2}$$
$$K_{min} = 1.19/4 = 0.30$$
$$\Delta K = K_{max} - K_{min} = 0.89$$

and:

$$\Delta K/\rho^{1/2} = 0.89/(0.03 \times 10^{-3})^{1/2} = 163 \text{ ksi}$$

From Figure G-3, cycles to initiation is about 80.

G.2 FATIGUE CRACK GROWTH PREDICTION

G.2.1 Summary

This section describes the model for predicting crack growth for high cycle fatigue of bond wires. It was coded and the software was delivered to the AF.
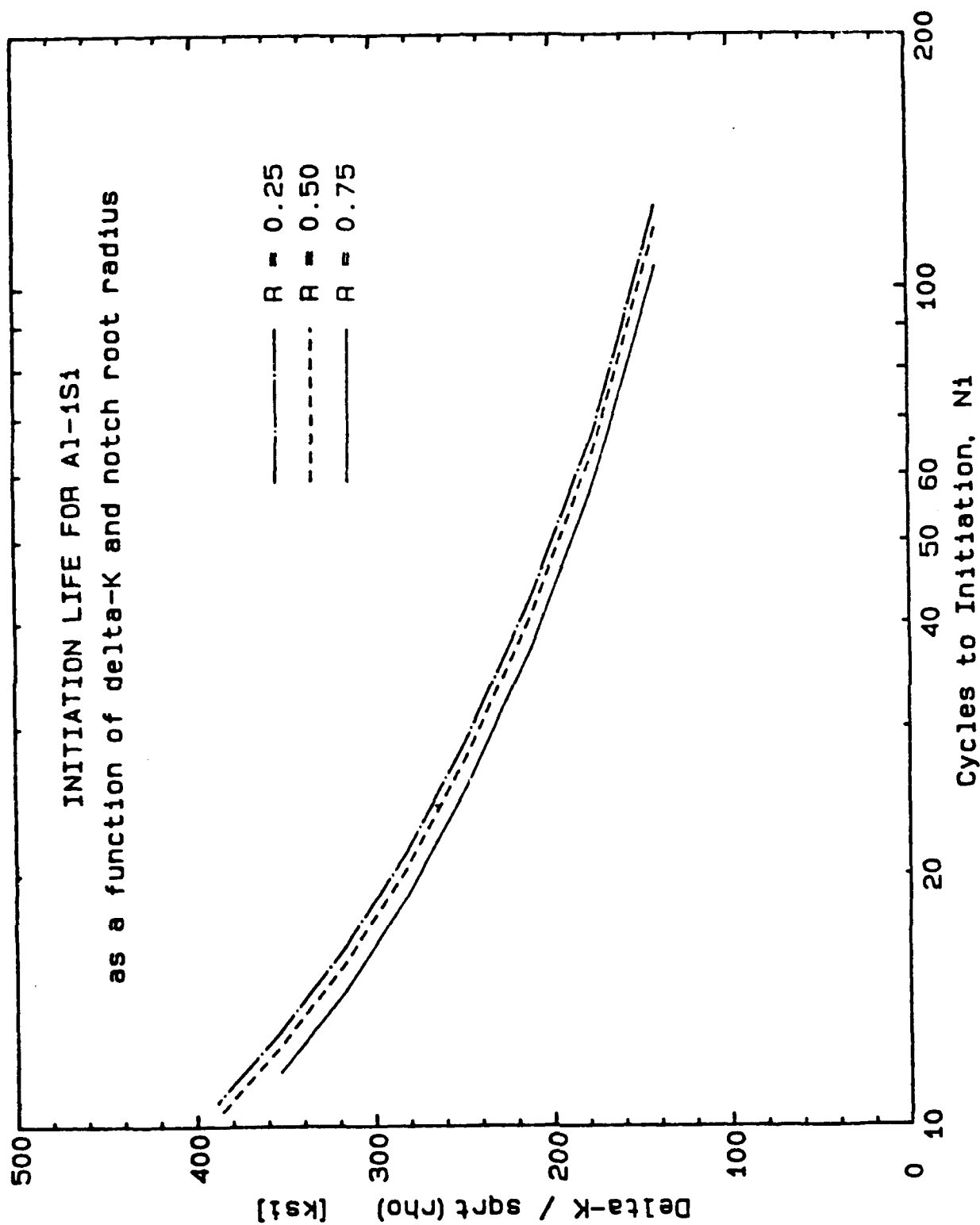
Figure G-3. Cycles to Initiation as a Function of $\Delta K/\rho^{1/2}$ for Various R-Ratios for Aluminum-1% Silicon 1-Mil Wire in Cyclic Bending.

This section describes a model for fatigue crack growth in small diameter wires. Aluminum wires of diameter 1 and 5 mils were considered, which were subjected to two types of cyclic loading, (1) uniform nominal tension loading varying between zero and a specified maximum, σ_t, and (2) pure bending varying between zero and σ_0. The calculations were performed assuming conventional macroscopic fatigue crack growth and fracture toughness properties. The crack geometry considered is an edge-crack in a circular bar.

G.2.2 Fatigue Crack Growth Characteristics

The fatigue crack growth characteristics of metals are not highly dependent on alloy or strength level. Aluminum alloy 2024-T351 was selected as being representative of the aluminum wire, and the fatigue crack growth characteristics for this alloy from the FLAGRO compilation (Ref. G-11) was employed. Figure G-4 shows the data and fit from Ref. G-11, from which the following fatigue crack growth relation is obtained:

where:

$$\frac{da}{dN} = C \, \Delta K^n \, \frac{\left[\Delta K - (1 - C_o R)^d \, \Delta K_{th}\right]^p}{\left[(1 - R) \, K_c - \Delta K\right]^q}$$ (G-10)

$$
\begin{aligned}
C &= 1.8 \times 10^{-8} \\
n &= 2.87 \\
C_0 &= 1 \\
d &= 1 \\
\Delta K_{th} &= 2.5 \text{ (nominal)} \\
K_c &= 73.4 \\
p &= 1/2 \\
q &= 1/2
\end{aligned}
$$

(All units are in kips, inch, cycles, i.e., stress intensity factors in ksi-in$^{1/2}$.) In this equation, $\Delta K = K_{max} - K_{min}$ and $R = K_{min}/K_{max}$. Fatigue life calculations are carried out for a ΔK_{th} of 2.5, as well as for ΔK_{th} of zero.

G.2.3 Fracture Toughness

The fracture toughness is taken to be 33 ksi-in$^{1/2}$. In the current context, failure is considered to occur when $K_{max} = 33$ ksi-in$^{1/2}$. Equation G-10 has a toughness related term in it, which is taken above as 73.4 ksi-in$^{1/2}$. The latter value can be considered as a curve fitting parameter. Figure G-4 shows data for K_{max} above 33 ksi-in$^{1/2}$, so the failure criterion employed will somewhat underestimate life, but not substantially so.
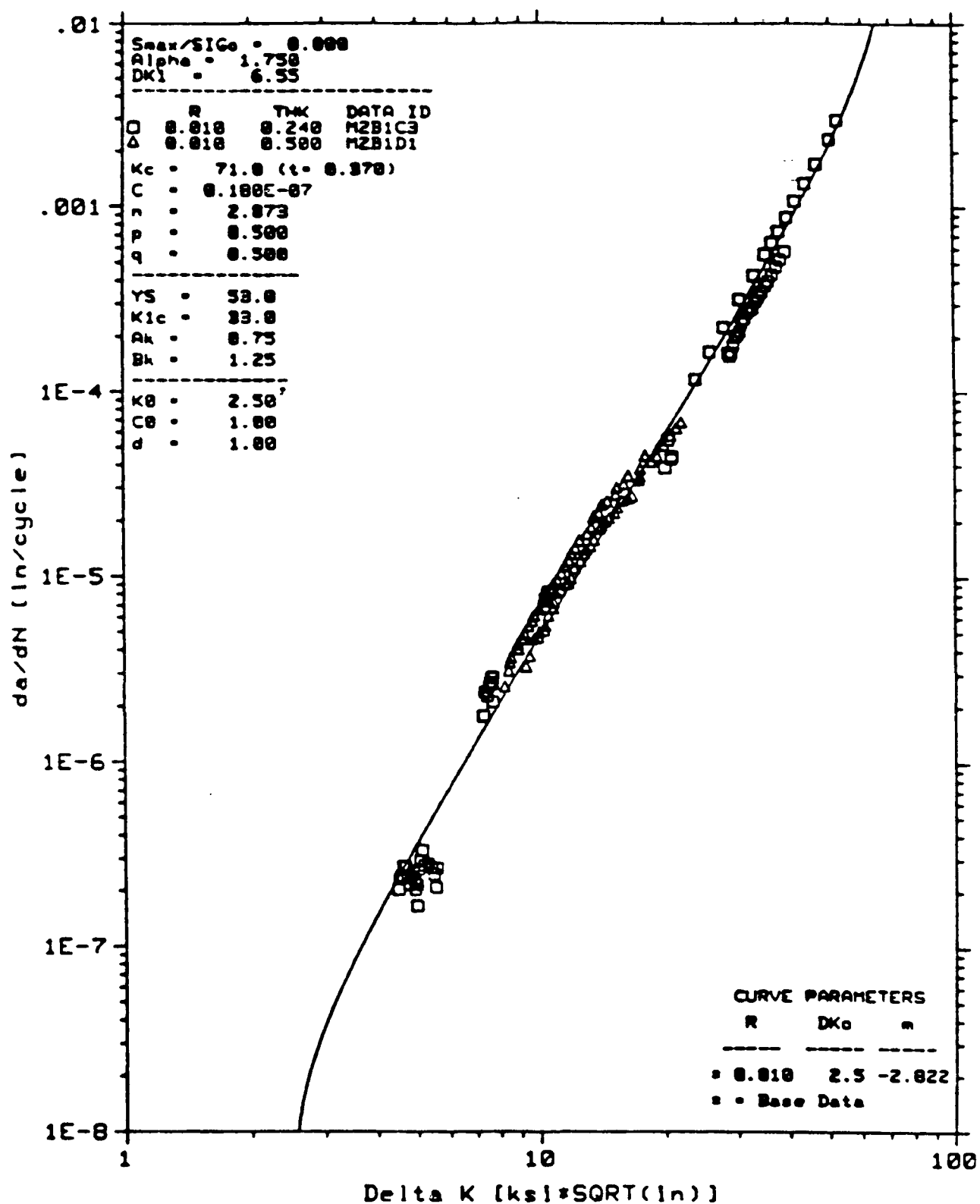
Figure G-4. Da/dN Data Fit, 2024-T351 Al, L-T, 75F (from Ref. G-11)

G.2.4 Stress Intensity Factor Solution

The stress intensity factor for an edge crack with a curved crack front in a circular bar in tension and bending was drawn from Ref. G-12. The curvature of the crack front corresponded closely to those observed in naturally growing edge cracks in circular bars. The expressions for the stress intensity factor for an edge crack of depth a in a bar of diameter D is given as:

$$K = \begin{cases} \sigma_t \sqrt{\pi a}\ F_t & \text{for uniform tension} \\ \sigma_b \sqrt{\pi a}\ F_b & \text{for pure bending} \end{cases} \qquad (G-11)$$

where:

$$F_t = 0.92\left(\frac{2}{\pi}\right)\sec\beta\left[\frac{\tan\beta}{\beta}\right]^{1/2}\left\{0.752 + 2.02\alpha + 0.377\gamma^3\right\}$$

$$F_b = 0.92\left(\frac{2}{\pi}\right)\sec\beta\left[\frac{\tan\beta}{\beta}\right]^{1/2}\left\{0.923 + 0.199\gamma^4\right\}$$

$$\alpha = a/D$$

$$\beta = \frac{\pi\alpha}{2}$$

$$\gamma = 1 - \sin\beta$$

As stated in Ref. G-13, the K-solution "should have good accuracy for $a \ll D$, reasonable accuracy for $a < d/2$, and the proper limiting condition for $a \rightarrow D$."

G.2.5 Fatigue Crack Growth Calculations

When K is expressed in terms of a (Equation G-11) and inserted into the fatigue crack growth relation (Equation G-10), a first-order differential equation for a versus N results. This equation cannot be solved in closed form, so the numerical procedures incorporated in the NASCRAC Computer Code (Refs. G-13, G-14) were employed. The code provides a versus N for a specified initial crack size and cyclic stress level. The critical crack size and threshold crack size can also be obtained. (The threshold crack size is the size crack that just exceeds threshold conditions.)

G.2.6 Results

Figures G-5 through G-7 provide results of cycles to failure (once a crack has initiated) for 1-mil diameter wires in cyclic bending. A cyclic stress of 15 ksi is considered, with different values of R in each figure. Results are presented for various values of ΔK_0, which is the fatigue crack growth threshold for $R = 0$ (see Equation G-5) for macroscopic fatigue cracks.
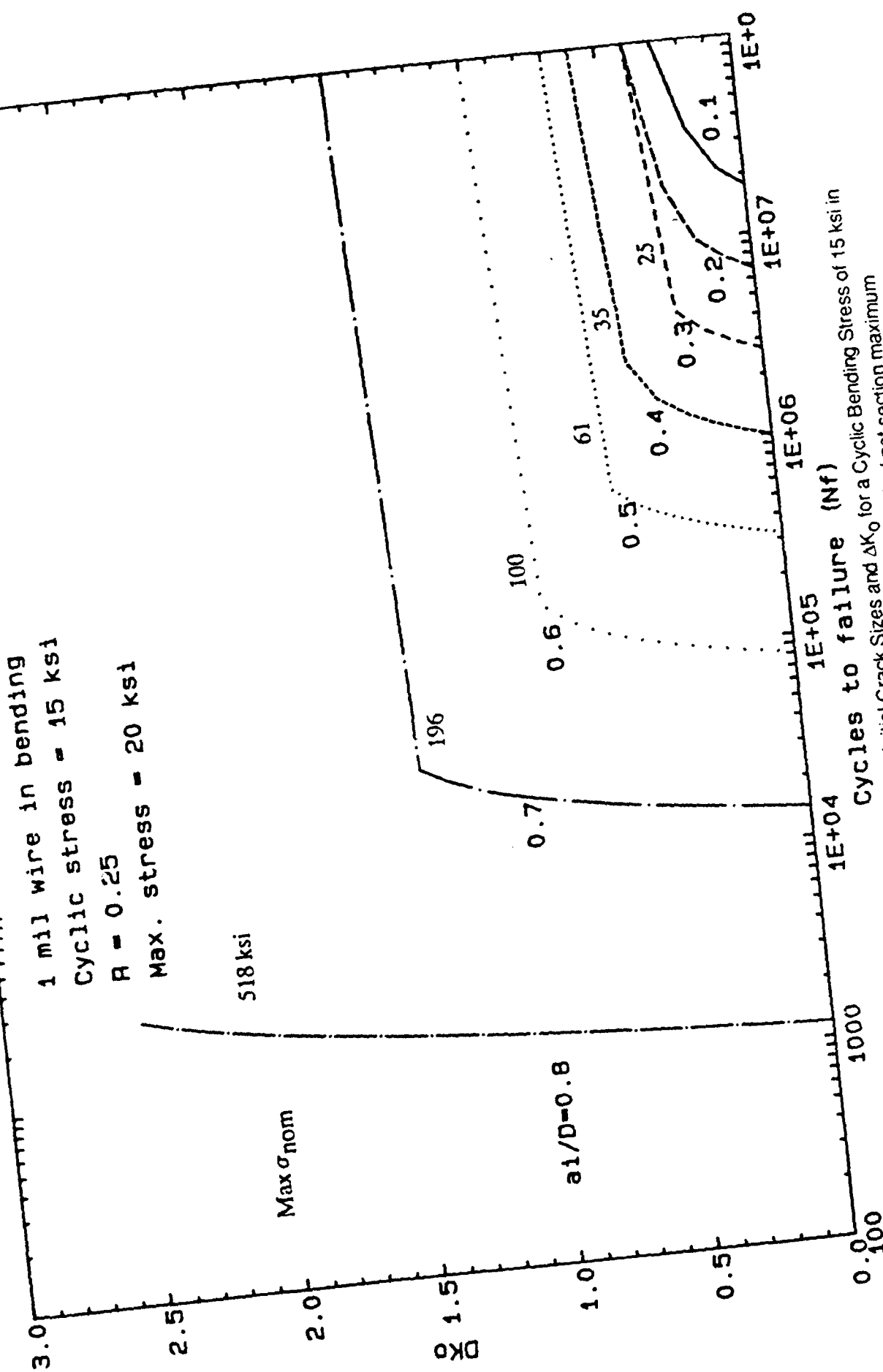
Figure G-5. Cycles to Failure for Various Initial Crack Sizes and ΔK_o for a Cyclic Bending Stress of 15 ksi in a 1-mil Diameter Aluminum Wire with R = 0.25. Nominal net section maximum bending stresses are also shown.
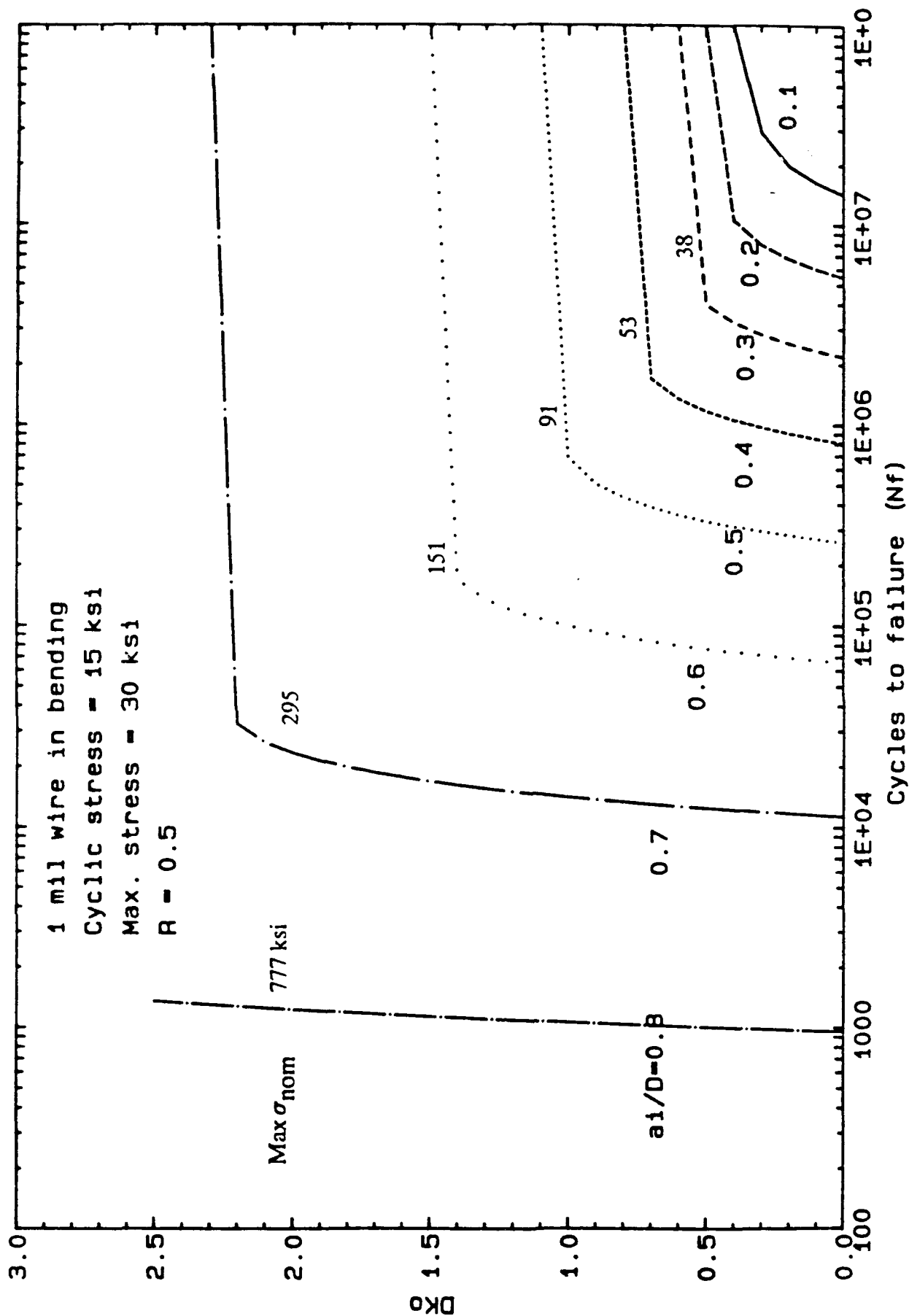
Figure G-6. Cycles to Failure for Various Initial Crack Sizes and ΔK_0 for a Cyclic Bending Stress of 15 ksi in a 1-mil Diameter Aluminum Wire with R = 0.50. Nominal net section maximum bending stresses are also shown.

G-12
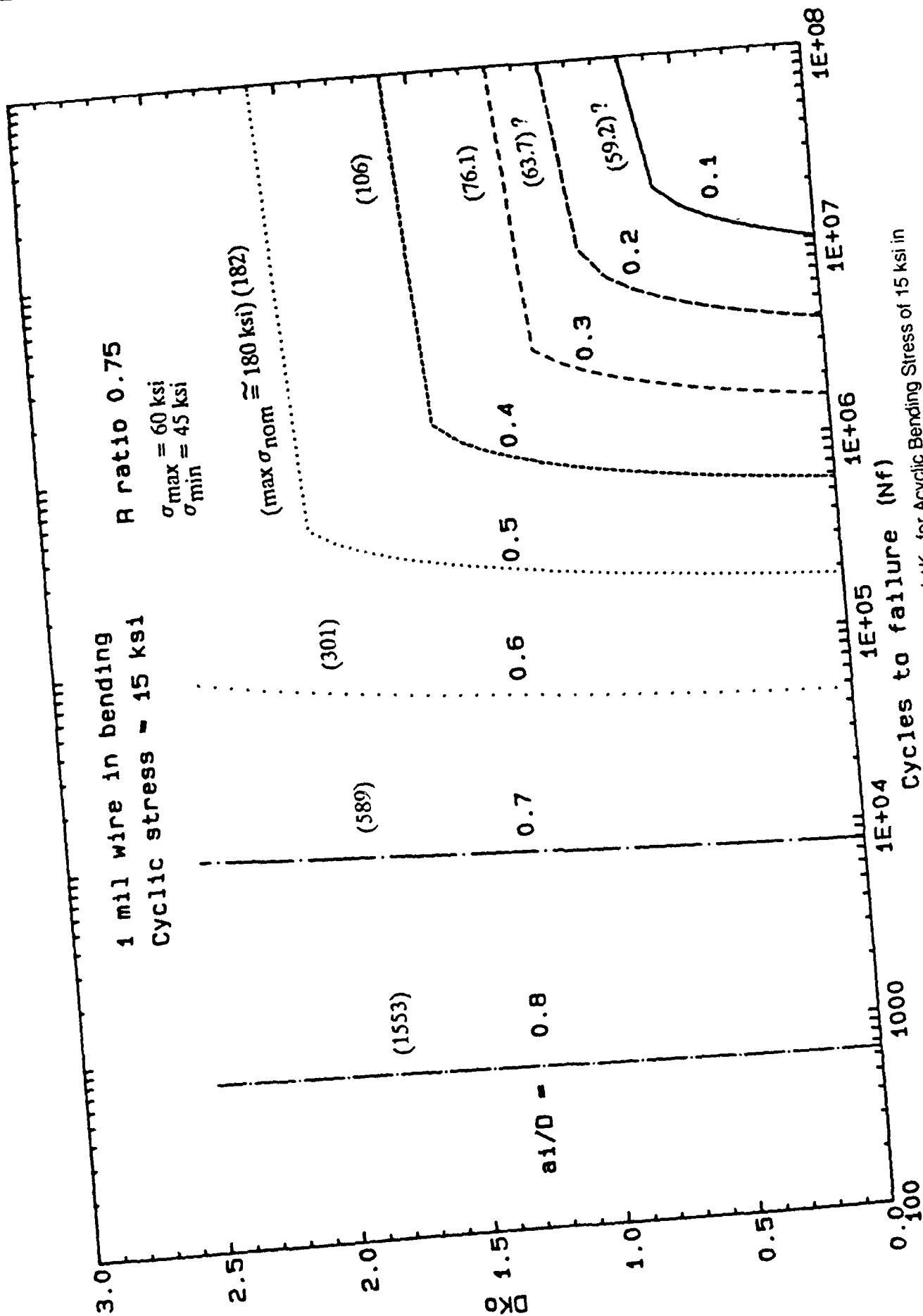
Figure G-7. Cycles to Failure for Various Initial Crack Sizes and ΔK_0 for Acyclic Bending Stress of 15 ksi in a 1-mil Diameter Aluminum Wire with R = 0.75. Nominal net section maximum bending stresses are also shown.

G-13

Results for different values of ΔK_o are presented, because there is question concerning the presence of a threshold for small cracks. The cracks treated here would be considered as small cracks. Values of ΔK_o ranging from 0 (no threshold) to 2.5 ksi-in$^{1/2}$ (macroscopic value) are considered. Curves are shown for various initial crack sizes (a$_i$). Also shown by each curve is the maximum net section nominal bending stress calculated by use of results in the FLAGRO Code, which have been incorporated into the NASCRAC Code.

These results were used in selecting test variables in the fatigue life testing of sharply notched wires in bending described in Section 3.2. Cyclic stresses high enough to produce failure in a reasonable number of cycles without producing nominal stresses well above the yield strength (at least at the initial crack size) were desired.

Figures G-8 and G-9 provide results for the given initial crack depth corresponding to a specified cyclic tension and lifetime. The figures are for 1- and 5-mil-diameter wires, respectively. Results are presented that were obtained using Equation 3-19 with $\Delta K_{th} = 2.5$ ksi-in$^{1/2}$ and 0. The 2.5 value is the nominal threshold ΔK value for macroscopic specimens. However, short cracks often do not exhibit such threshold behavior, and a threshold of zero may be more representative of the behavior of cracks in small wires. Results are presented for stresses as high as 50 ksi, even through the monotonic yield strength is below this. All calculations, including final failure, are based on strictly elastic calculations. Hence, no consideration of large net section stresses is made.

The results of Figures G-8 and G-9 show a narrow range of finite lifetime when a threshold of 2.5 ksi-in$^{1/2}$ is used. For instance, in Figure G-8 for a stress of 20 ksi, failure is predicted to occur in less than 3000 cycles, or not at all. This ignores failure due to anything other than a pre-existing crack that extends as a (macroscopic) fatigue crack. This behavior is predicted because once the crack exceeds threshold conditions, it will grow to failure in a few cycles, because the difference in threshold and critical crack size is not large. Figures G-10 and G-11 present the threshold and critical crack sizes for 1 and 5 mil wires, respectively. When no threshold is used, the calculated life continually increases with decreasing initial crack depth or decreasing stress levels.

Figures G-12 and G-13 provide lifetime versus initial crack depth for the case of cyclic bending stress, for 1 and 5 mil wires, respectively. These results are presented for a threshold of 2.5 and 0. As expected, for a given stress and the initial crack size, slightly higher lifetimes are obtained compared to the wire in tension. The critical and threshold crack sizes for a 1 and 5 mil wires are shown in Figures G-14 and G-15, respectively.
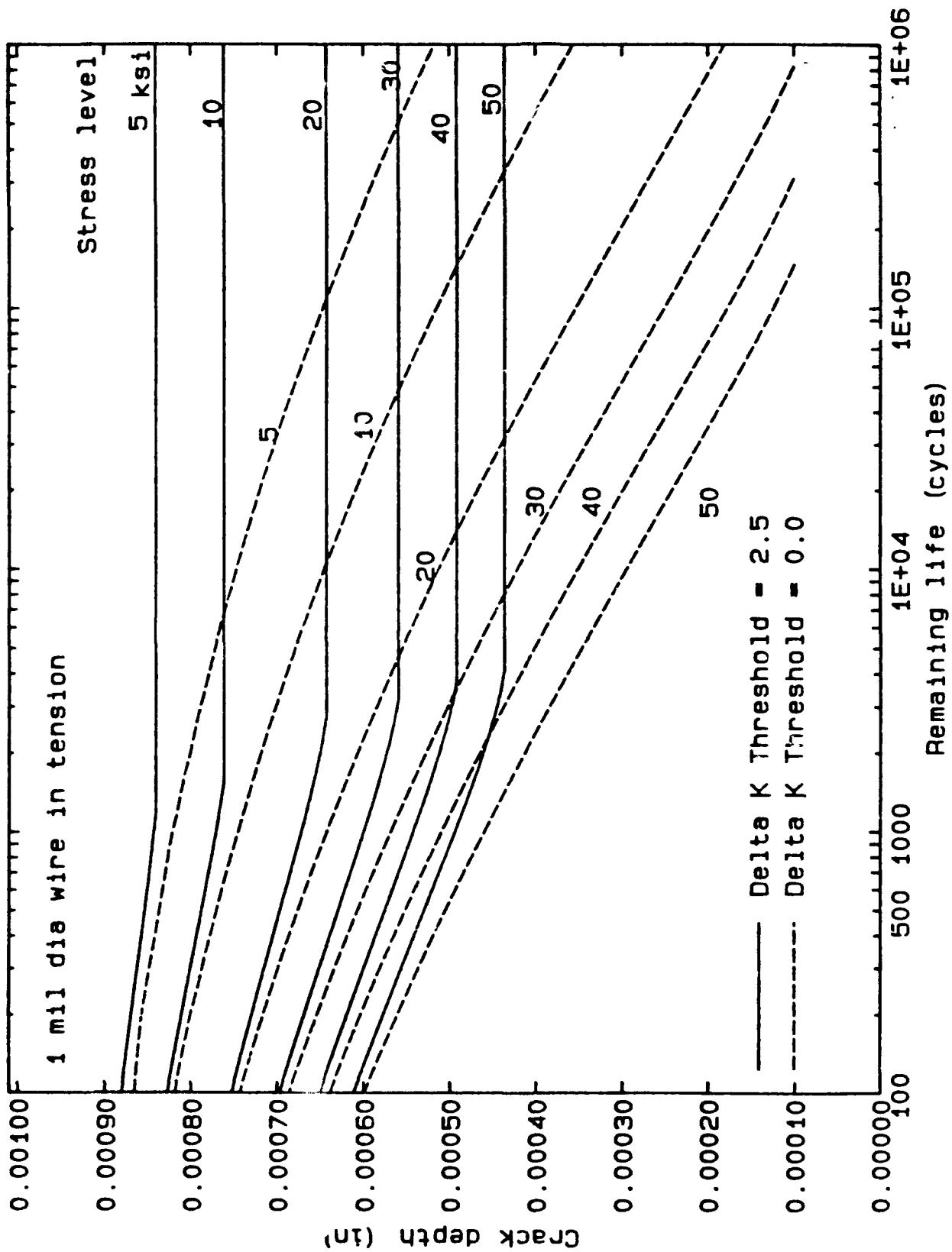
Figure G-8. Predicted Cyclic Lifetime for a Given Initial Crack Subjected to Various Stress Levels for a 1-mil-diameter Wire in Tension
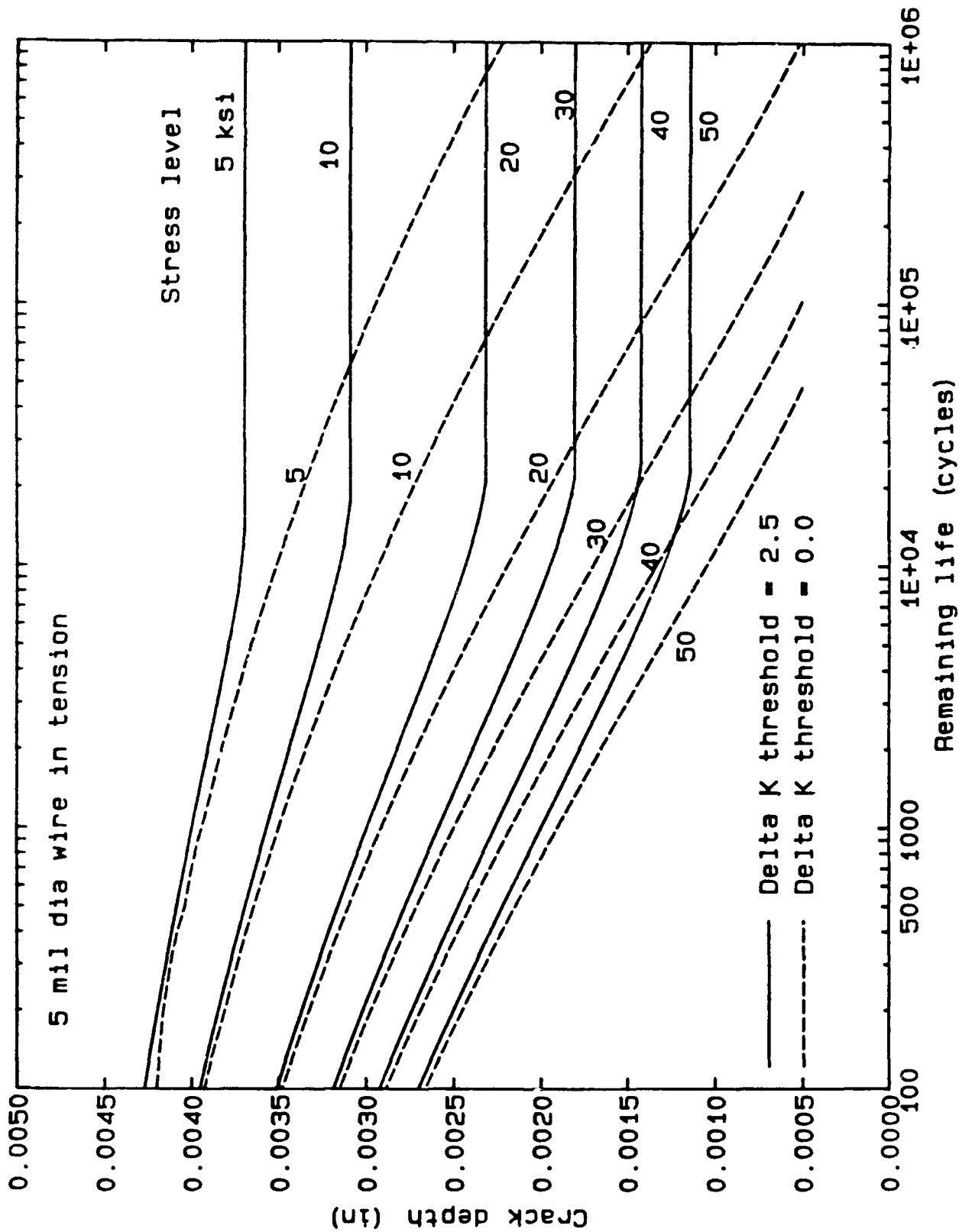
Figure G-9. Predicted Cyclic Lifetime for a Given Initial Crack Subjected to Various Stress Levels for a 5-mil-diameter Wire in Tension
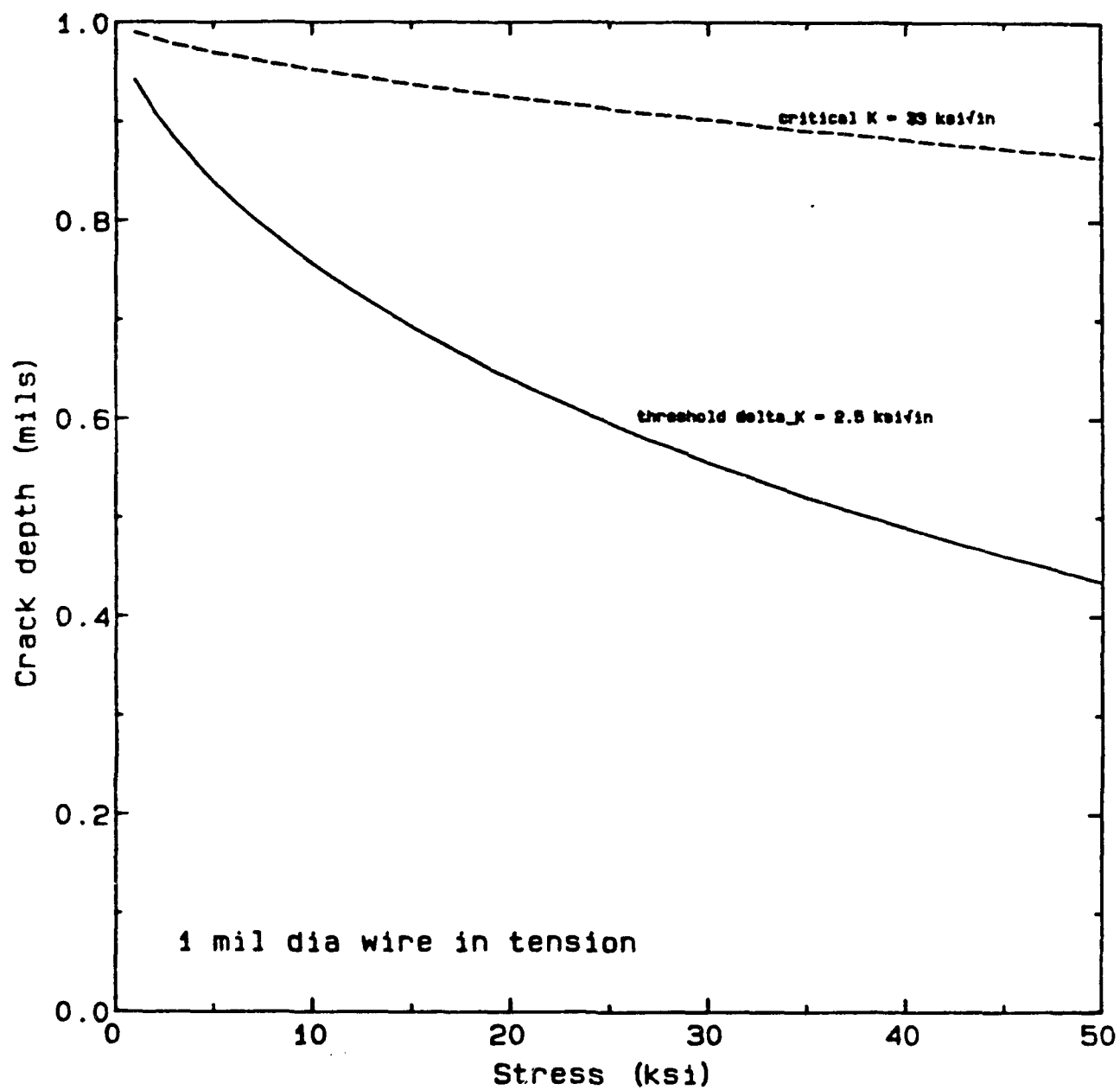
Figure G-10. Critical and Threshold Crack Size as a Function of Cyclic Stress
for a 1-mil-diameter Wire in Tension
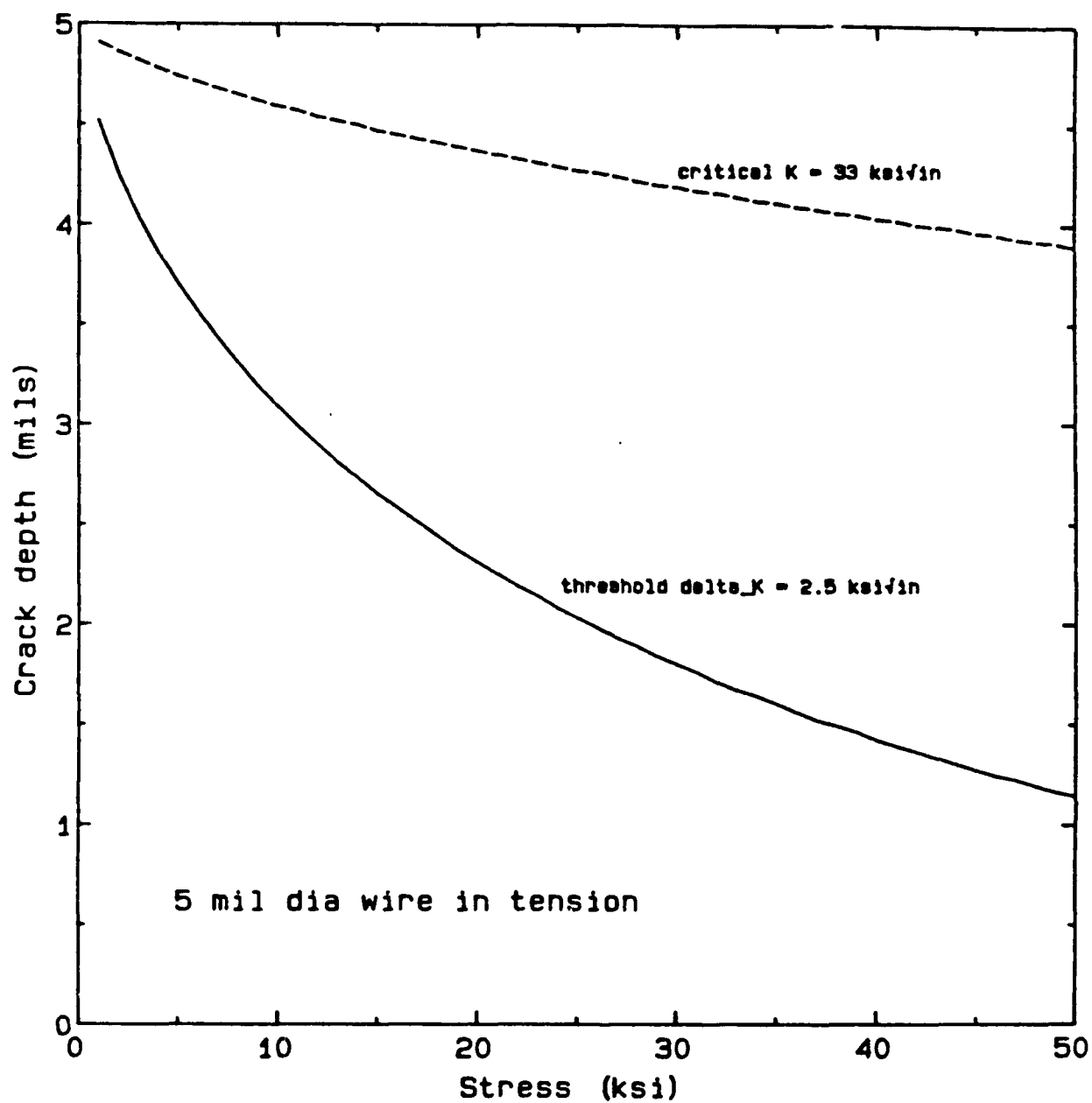
Figure G-11. Critical and Threshold Crack Size as a Function of Cyclic Stress
for a 5-mil-diameter Wire in Tension
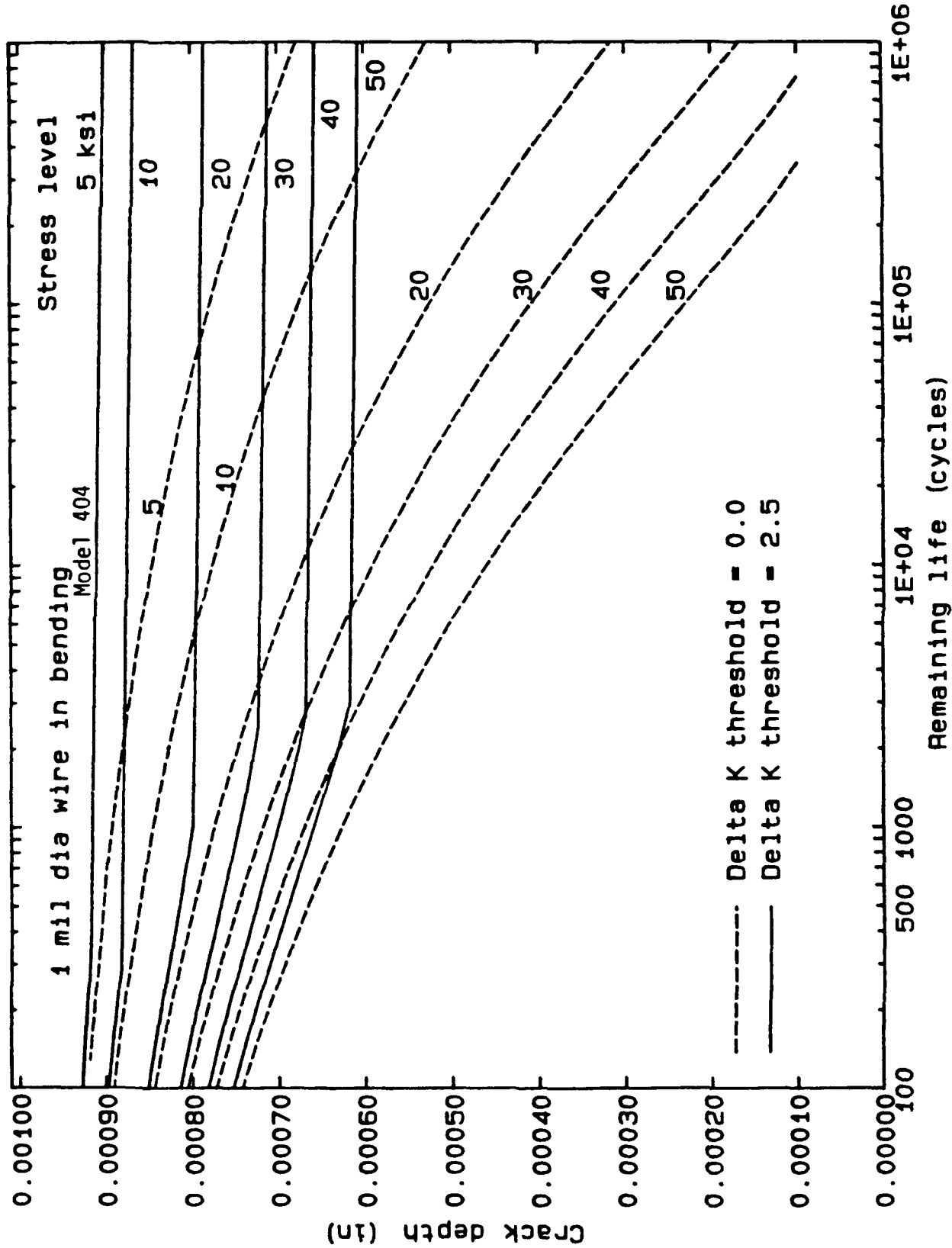
Figure G-12. Predicted Cyclic Lifetime for a Given Initial Crack Subjected to Various Stress Levels for a 1-mil-diameter Wire in Bending
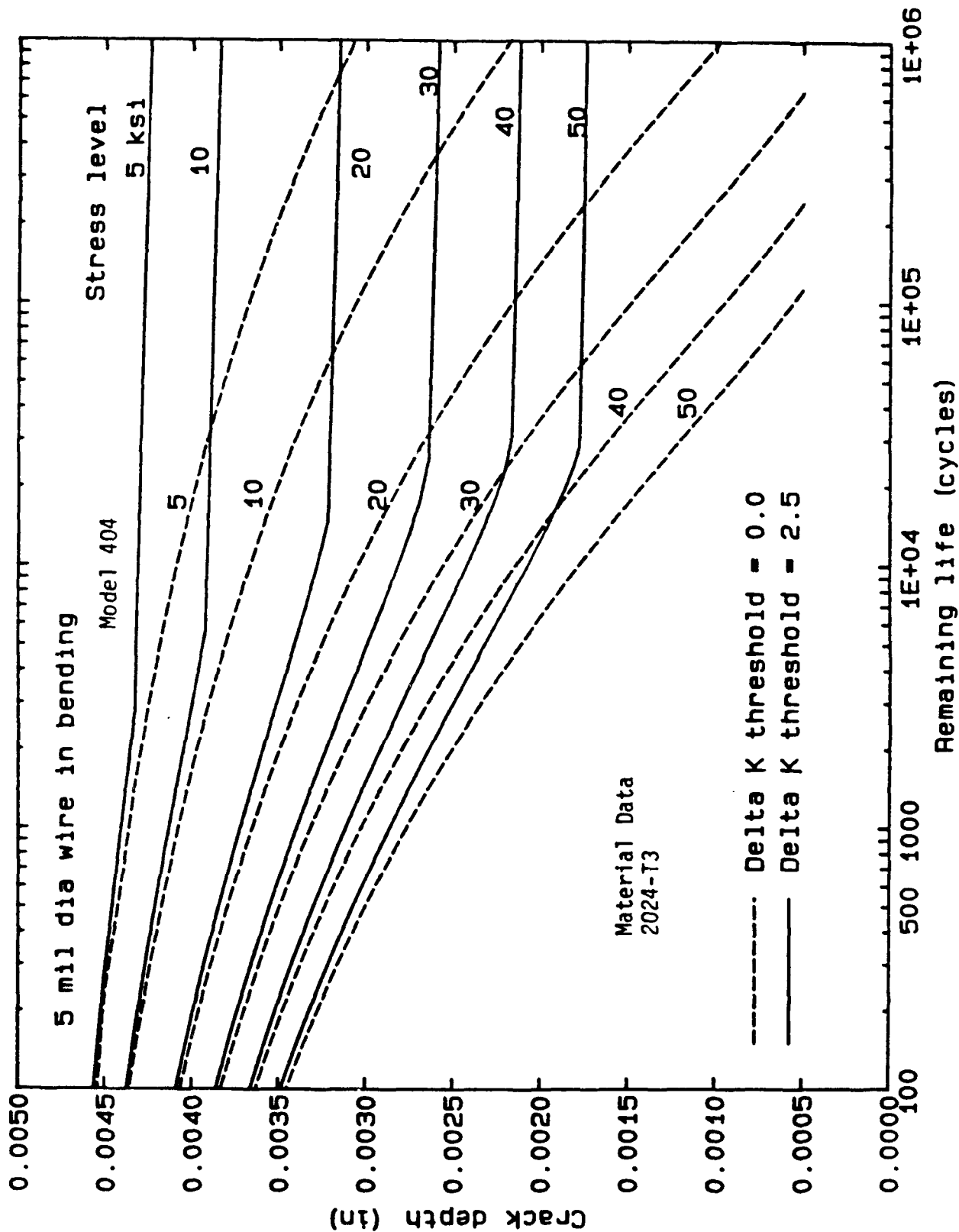
Figure G-13. Predicted Cyclic Lifetime for a Given Initial Crack Subjected to Various Stress Levels for a 5-mil-diameter Wire in Bending
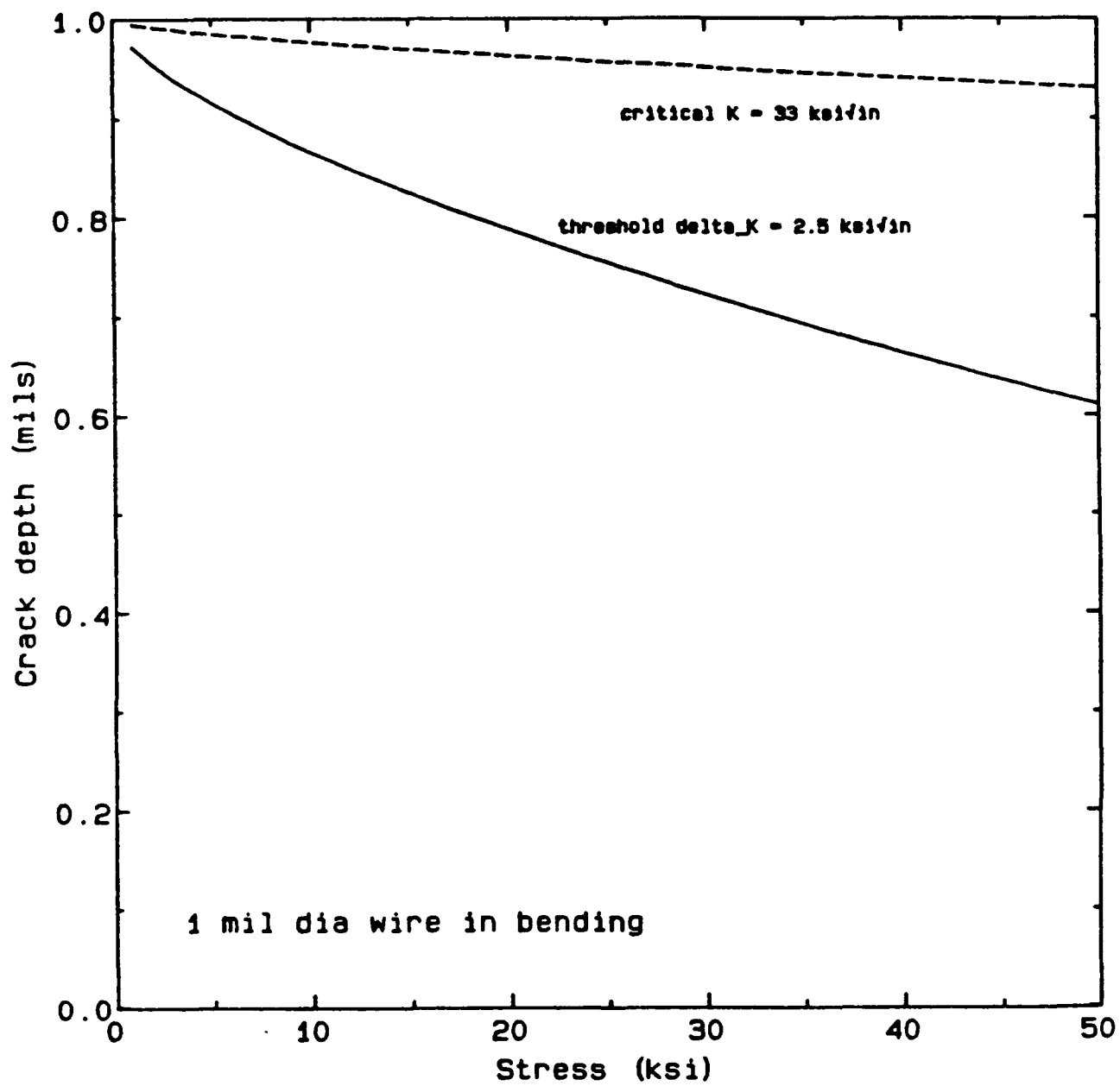
Figure G-14. Critical and Threshold Crack Sizes as a Function of Cyclic Stress
for a 1-mil-diameter Wire in Bending
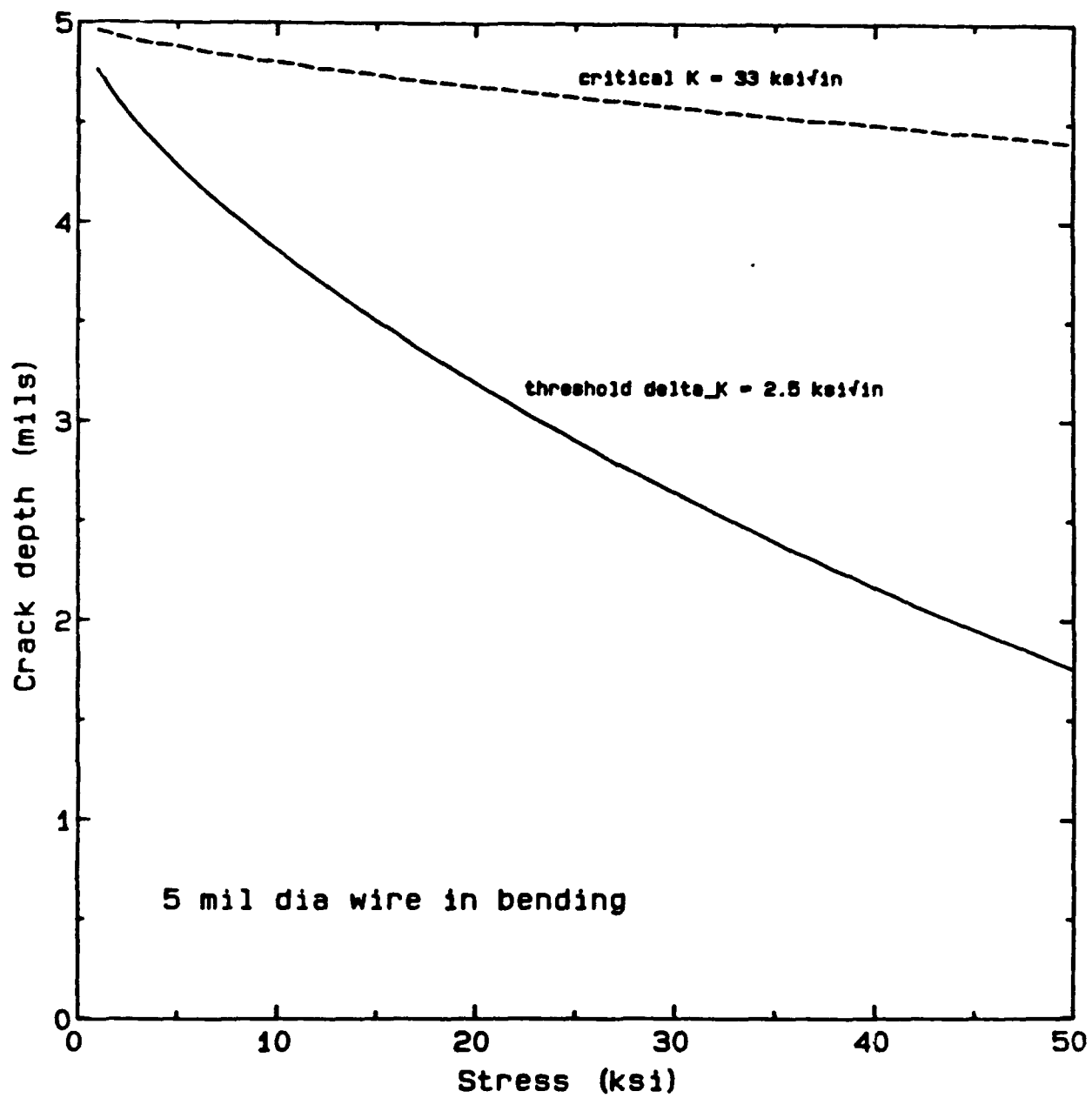
Figure G-15. Critical and Threshold Crack Sizes as a Function of Cyclic Stress
for a 5-mil-diameter Wire in Bending

These results predict that the 1-mil-diameter wire is much more resistant to fatigue crack growth than the 5-mil-diameter wire. For example, for $\Delta K_{th} = 2.5$, with a 50 ksi cyclic bending stress, the threshold crack size is 60% of the wire diameter for the 1-mil-diameter wire and is 30 % of the wire diameter for the 5 mil diameter wire. For $\Delta K_{th} = 0$, with a 50 ksi cyclic bending stress, a 1-mil-diameter wire having an initial crack depth 40% of the wire diameter will fail in 2×10^4 cycles, and a 5-mil-diameter wire having an initial crack depth of 40% of the wire diameter will fail in 7×10^3 cycles. These values scale roughly as the square foot of the ratio of the wire diameters (2.2). This increased resistance to fatigue crack growth with decreasing scale is a well known prediction of macroscopic fracture mechanics. The difficulty of achieving failures of the 1-mil diameter wires in the tests described in Section 3.2 is consistent with this prediction.

REFERENCES

G-1 P.C. Paris and G.C. Sih, "Stress Analysis of Cracks," Fracture Toughness Testing and Its Applications, ASTM STP 381, Philadelphia, Pennsylvania, 1965, pp. 30- 81.

G-2 H. Tada, P.C. Paris, and G.R. Irwin, Stress Analysis of Cracks Handbook, Second Edition, Paris Productions, Inc., St. Louis, Missouri, 1985.

G-3 M.F. Kanninen and C.H. Popelar, Advanced Fracture Mechanics, Oxford University Press, New York, 1985.

G-4 Y. Murakami, et al., Stress Intensity Factors Handbook, Pergamon Press, Oxford, England, 1987.

G-5 R.G. Forman, "Growth Behavior of Surface Cracks in the Circumferential Plane of Solid and Hollow Cylinders," Fracture Mechanics: Seventeenth Volume, ASTM STP 905, Philadelphia, Pennsylvania, 1986, pp. 59-74.

G-6 Fatigue Crack Growth Computer Program NASA/FLAGRO, JSC-22267, NASA Lyndon B. Johnson Space Center, Houston, Texas, 1988.

G-7 NASCRAC, NASA Crack Analysis Code, User's and Theory Manuals, Version 2.0, Failure Analysis Associates, Inc., Palo Alto, California, 1989. NASCRAC is a trademark of the Failure Group, Inc.

G-8 M. Creager and P.C. Paris, "Elastic Field Equations for Blunt Cracks with Reference to Stress Corrosion Cracking," International Journal of Fracture Mechanics, Vol. 3, 1967, pp. 247-252.

G-9 C. Boller and T. Seeger, Materials Data for Cyclic Loading, Part D: Aluminum and Titanium Alloys, Elsevier, Amsterdam, 1987.

G-10 N.E. Dowling, "Stress-Strain Analysis of Cyclic Plastic Bending and Tension," Journal of Engineering Materials and Technology, Vol. 100, No. 2, April 1978, pp. 157-163.

G-11 R.G Forman, "Derivation of Crack Growth Properties of Materials for NASA/FLAGRO," Materials Branch Report 86-ES5-1, Lyndon B. Johnson Space Center, Houston, Texas, June 1986.

G-12 R.G. Forman and V. Shivakumar, "Growth Behavior of Surface Cracks in the Circumferential Plane of Solid and Hollow Cylinders," Fracture Mechanics: Seventeenth Symposium, ASTM STP 905, Philadelphia, Pennsylvania, 1986, pp. 59-74.

G-13 NASCRAC , NASA CRack Analysis Code, User's Manual, Version 2.0, Failure Analysis Associates, Inc., Palo Alto, California, 1989.

G-14 D.O. Harris, C.J. Bianca, E.D. Eason, L.D. Salter, and J.M. Thomas, "NASCRAC – A Computer Code for Fracture Mechanics Analysis of Crack Growth," AIAA Paper 87-0847, 28th Structures, Structural Dynamics and Materials Conference, Part I, 1987, pp. 662-667.

APPENDIX H

WIRE THERMAL (POWER) CYCLING FATIGUE TESTS TO ESTABLISH FAILURE POINTS OF THE WIRES

This appendix documents the tests performed subsequent to the initial tests described in Section 4.5. The test specimens are described in Section 4.3, and the fatigue test fixture is described in Section 4.4. The results of the tests described in this appendix established the test setup, test specimen geometry, and test parameters for the tests (described in Section 4.6) to quantify crack growth parameters.

With the lessons learned from the tests and analysis described in Section 4.5.2, the following activities were started:

- To evaluate when crack initiation occurs during lifetime, power cycling of S/Ns 1, 2, and 3 was continued. The analysis and the previous test results were employed to select the current to avoid failure at the midspan.

- The fabrication of test specimens having shorter (more representative of actual devices) wires than those used in the first set of experiments was started. Shortening the wires enables operation at higher currents without causing failure at the midspan. (The analysis predicts that the runaway current is inversely proportional to the wire length; industry experience on wire failure by fusing is consistent with this prediction.)

- The development of a procedure to produce a defect in a wire bond heel was started.

Fabrication of six new samples with shorter wires was begun. While waiting for these samples to be prepared, the last of the samples with long wires, S/N 6, was modified so that the geometry of the wires would place more stress at the heel of the wire bond during current cycling.

The modifications to S/N 6 were made using an IC probe station to alter the configuration of the wire to mimic that of a wire that had been pull tested, at one end for two wires and at both ends for the other two wires. S/N 6 was then submitted for SEM examination to determine whether any defects had been introduced at the bond heels and to document the bond conditions prior to cycling.

At this point, samples S/Ns 1, 2, and 3 were removed from the fixture after experiencing over 16 million cycles without a failure. S/N 6 was installed in the test fixture after SEM analysis and current cycled at 500mA. After 1.3 million cycles, S/N 6 experienced a failure. SEM examination disclosed that two wires had failed (fractured) at bond heels. Since the test fixture is programmed

to shut off when the circuit opens and since all wires are connected in series, either 1) the failure of these two wires must have been simultaneous or 2) the second wire was very close to failure and failed after the first due to subsequent handling. No significant cracks were noted at the heels of any of the other wires. SEM photos show the condition of these wires both before and after failure. The before images were taken after the wires were pulled, but before current cycling. Refer to Figures H-1 through H-16.

When the six new samples, serialized 7 through 12, with shorter wires and six wires per sample were received, S/N 7 was immediately submitted for SEM analysis. While waiting for results of the SEM analysis on S/N 7, S/N 8 was used to determine the approximate fusing current for the new shorter wires by slowly increasing current through a wire until the wire fused open. Fusing currents varied from 1.7A to 3.2A on the five wires tested. The variation in fusing currents correlated with wire length. Wires bonded to adjacent lands on the sides of the package were longer than those bonded to adjacent lands at the ends of the package. Below approximately 1.6A, little or no in-rush current was observed. This means that very little heating of the wire is occurring at less than 1.6A input current. Accordingly, the test fixture was modified, because in its original configuration, current drive capability was limited to approximately 1.6A with nominal voltages. The modification consisted of adding a 2N5684 power transistor to the output wired in a Darlington configuration to increase the current gain. This modification allows currents approaching 1.8A (now limited by resistor power handling capabilities) to be obtained.

Sample S/N 7 was installed in the test fixture after SEM examination, and current cycling was begun with a steady-state current of 1.65A. This produced an in-rush current of 1.8A. This is the highest current level that the present test fixture is capable of sustaining reliably. Further modifications could be made to the test fixture to allow it to cycle at higher current levels. However, before additional significant changes were made to the present test fixture design, cycling was initiated in order to establish a baseline for the new samples. After approximately 1400 cycles the wire bonded between pins 3 and 4 (side of package) fused open. A jumper was connected across the fused wire in the test fixture to take it out of the circuit and cycling was continued. A second failure occurred after 33,000 cycles. Visual observation indicated a possible crack at the heel of the wire bond at pin 2. Electrical measurements indicated pin 2 was open. SEM examination disclosed that a fracture was present at the pin 2 bond heel. SEM photos of S/N 7, both before and after cycling, showing the fracture at the heel of the wire bonded to pin 2 and cracks at the heels of several other wires are attached. Refer to Figures H-17 through H-27.

Figure H-1. Sample No. 6. SEM Photo Showing the Four Wires in
S/N 6 Before Cycling
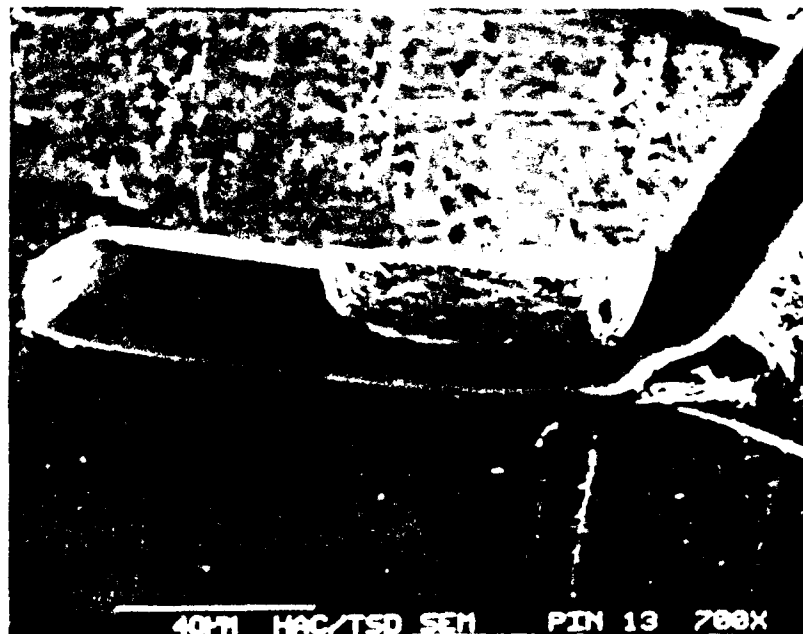
Figure H-2. Sample No. 6. SEM Photo of Wire Bond at Pin 13,
Before Cycling

H-3

Figure H-3. Sample No. 6. SEM Photo of Heel of Wire Bond at
Pin 13, Before Cycling

Figure H-4. Sample No. 6. SEM Photo of Top of Wire Bond at
Pin 13, Before Cycling

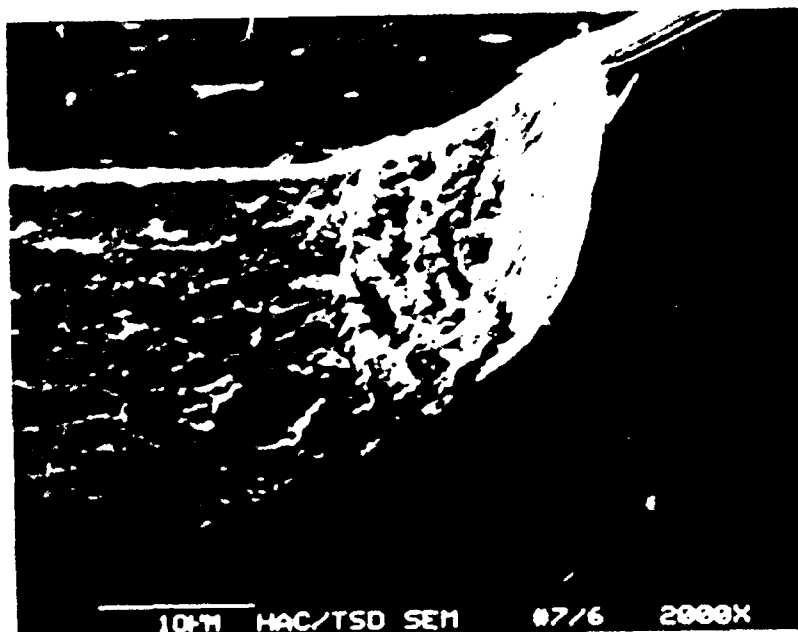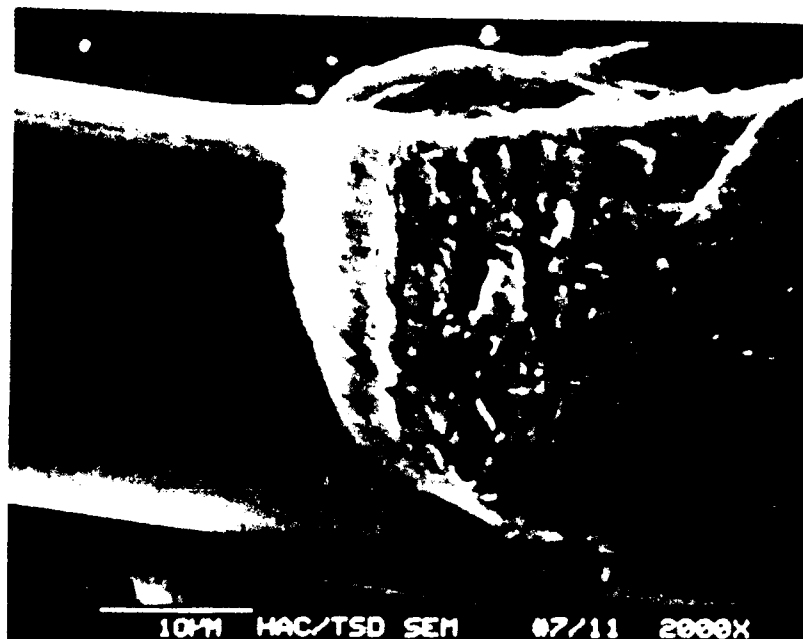Figure H-5. Sample No. 6. SEM Photo of Bond at Pin 13,
After Cycling

Figure H-6. Sample No. 6. SEM Photo of Portion of Wire Bond
Remaining on Bond Pad of Pin 13, After Cycling
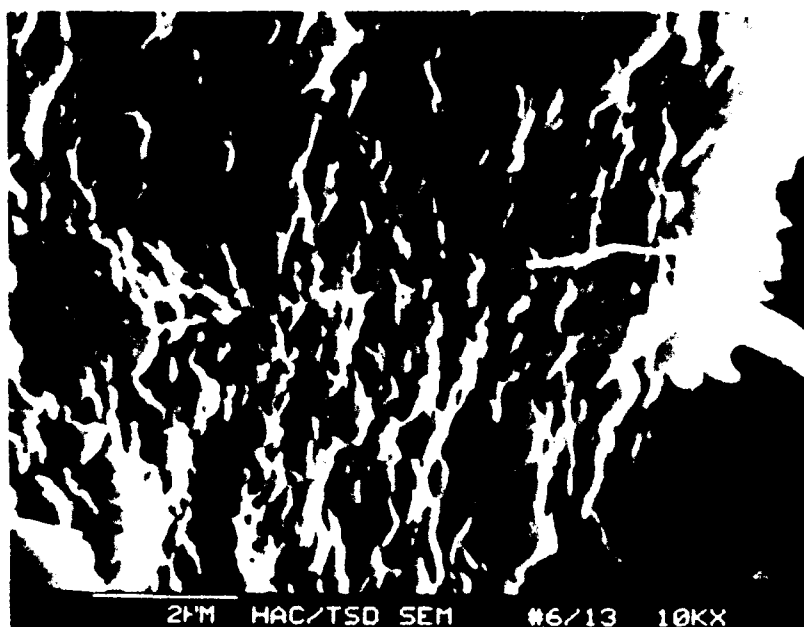
Figure H-7. Sample No. 6. SEM Photo of Detail of Area Shown in
Figure 4-12, After Cycling

Figure H-8. Sample No. 6. SEM Photo of Wire Fractured from Bond
at Pin 13, After Cycling
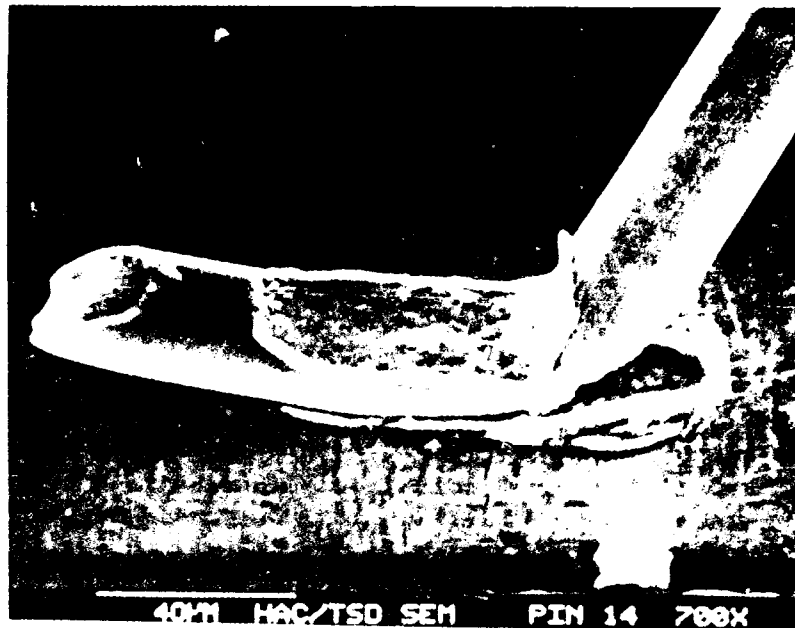
Figure H-9. Sample No. 6. SEM Photo of Wire Bond at Pin 14, Before Cycling

Figure H-10. Sample No. 6. SEM Photo of Heel of Wire Bond at Pin 14, Before Cycling

Figure H-11. Sample No. 6. SEM Photo of Top of Wire Bond at
Pin 14, Before Cycling

Figure H-12. Sample No. 6. SEM Photo of Bond at Pin 14
After Cycling

H-8
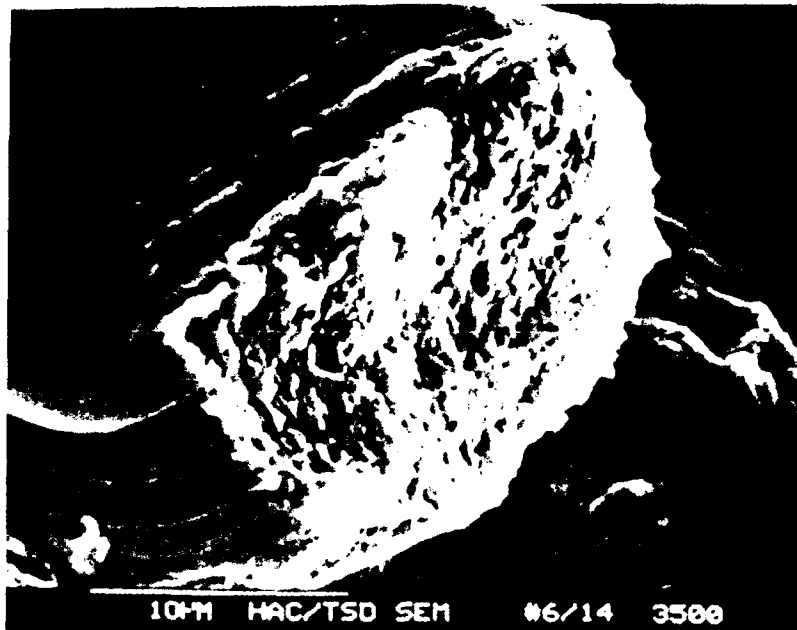
Figure H-13. Sample No. 6. SEM Photo of Portion of Wire Bond
Remaining on Bond Pad of Pin 14, After Cycling
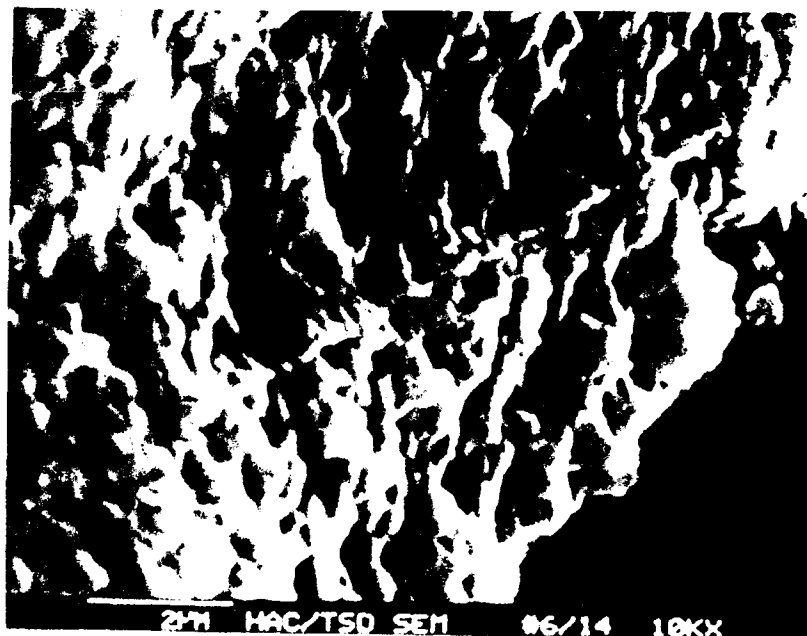
Figure H-14. Sample No. 6. SEM Photo of Detail of Area Shown in
Figure H-13, After Cycling

Figure H-15. Sample No. 6. SEM Photo of Wire Fractured from Bond
at Pin 14, After Cycling

Figure H-16. Sample No. 6. SEM Photo, Reverse Angle View of
Area Shown in Figure H-12, After Cycling
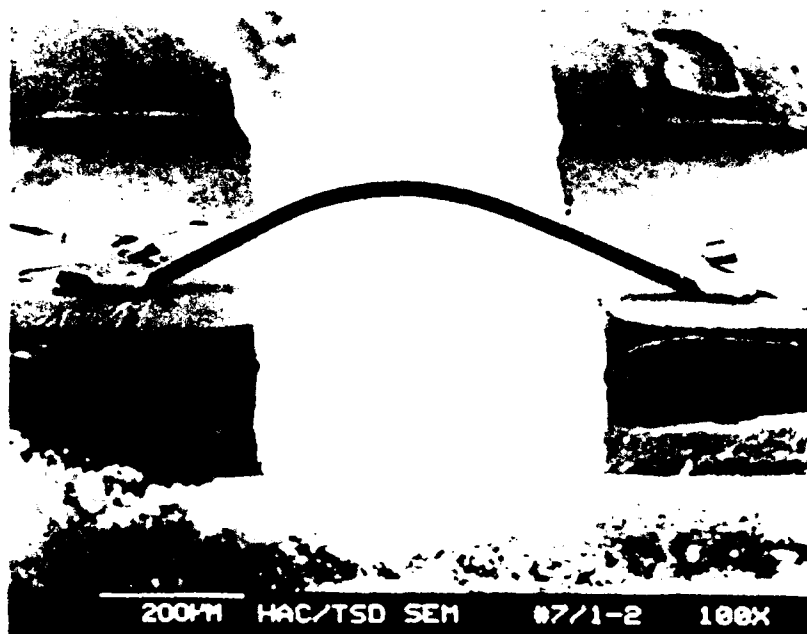
Figure H-17. Sample No. 7. SEM Photo of Wire Bonded Between
Pins 1 and 2, Before Cycling
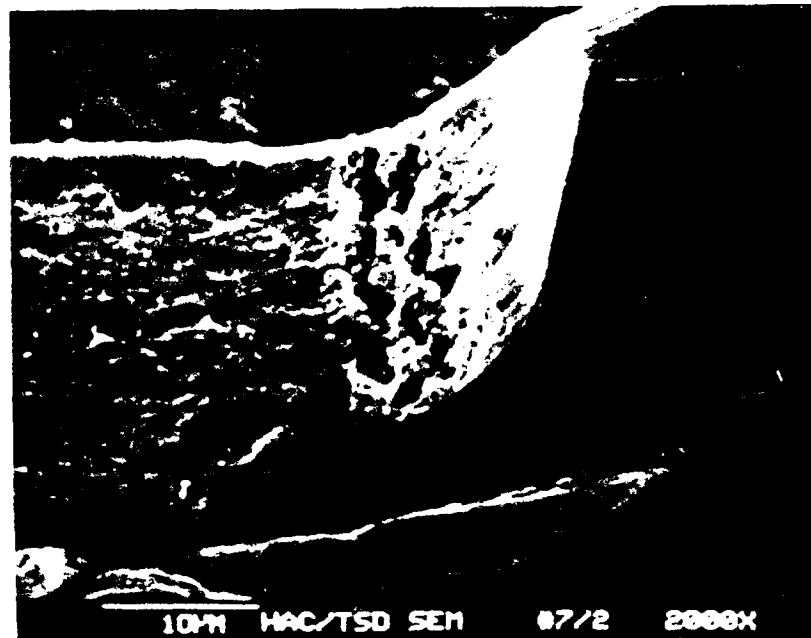
Figure H-18. Sample No. 7. SEM Photo of Bond at Pin 2,
Before Cycling

H-11
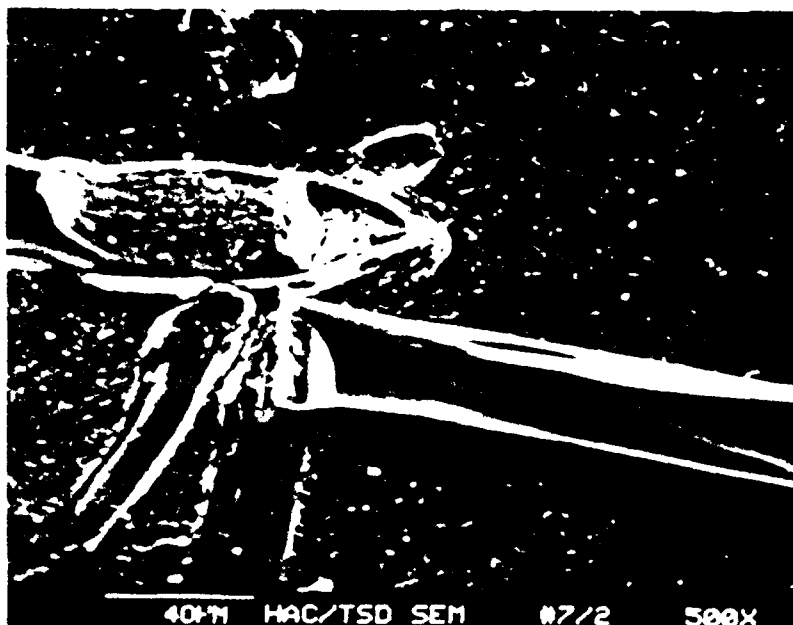
Figure H-19. Sample No. 7. SEM Photo of Bond at Pin 2,
After Cycling
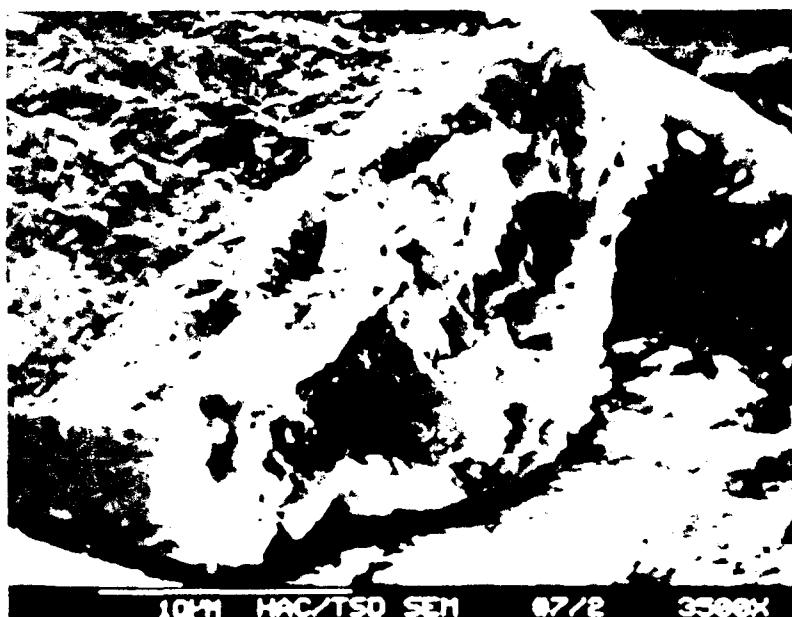
Figure H-20. Sample No. 7. SEM Photo of Portion of Wire Bond
Remaining on Bond Pad of Pin 2, After Cycling
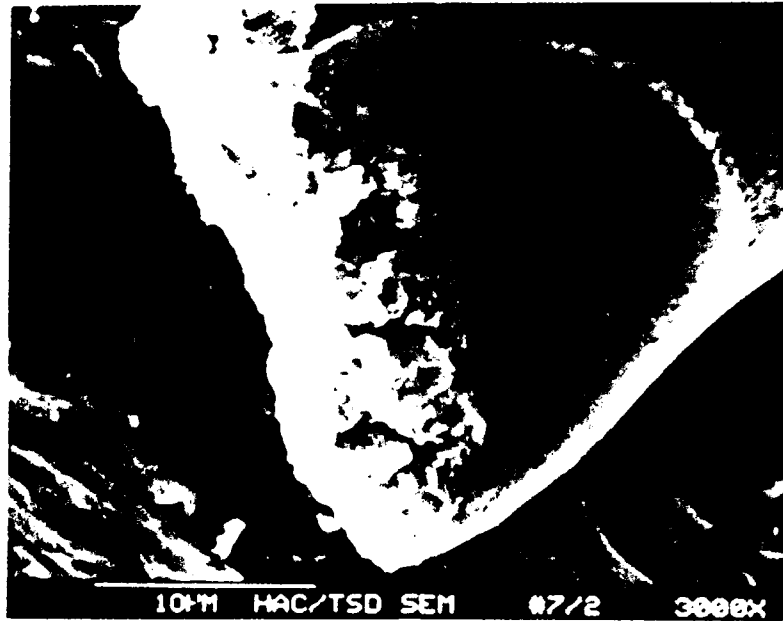
Figure H-21. Sample No. 7. SEM Photo of Wire Fractured from
Bond at Pin 2, After Cycling
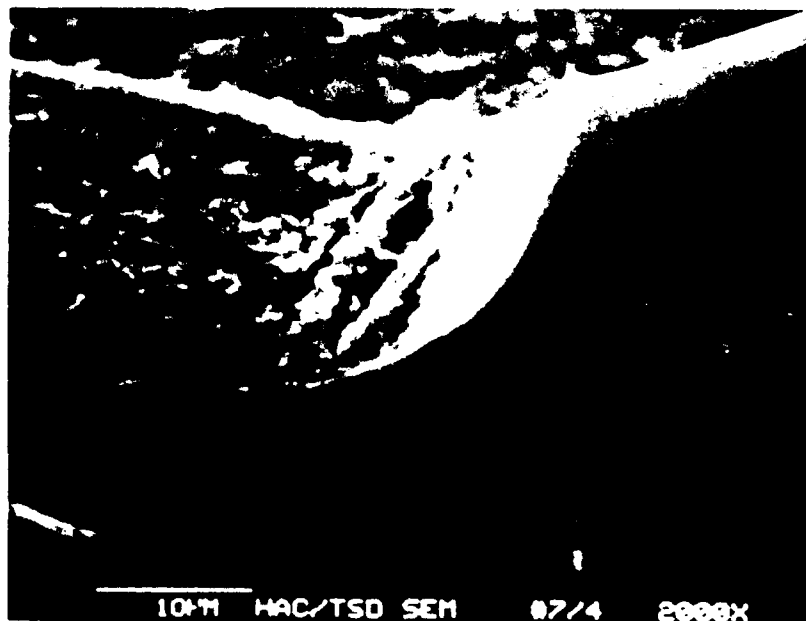
Figure H-22. Sample No. 7. SEM Photo of Bond at Pin 4, Before
Cycling Note: The Wire Bonded Between Pins 3 and 4 Fused
Open After 1400 Cycles.

Figure H-23. Sample No. 7. SEM Photo of Bond at Pin 4, After
Cycling. Note: The Wire Bonded Between Pins 3 and 4 Fused
Open After 1400 Cycles.

Figure H-24. Sample No. 7. SEM Photo of Bond at Pin 6,
Before Cycling
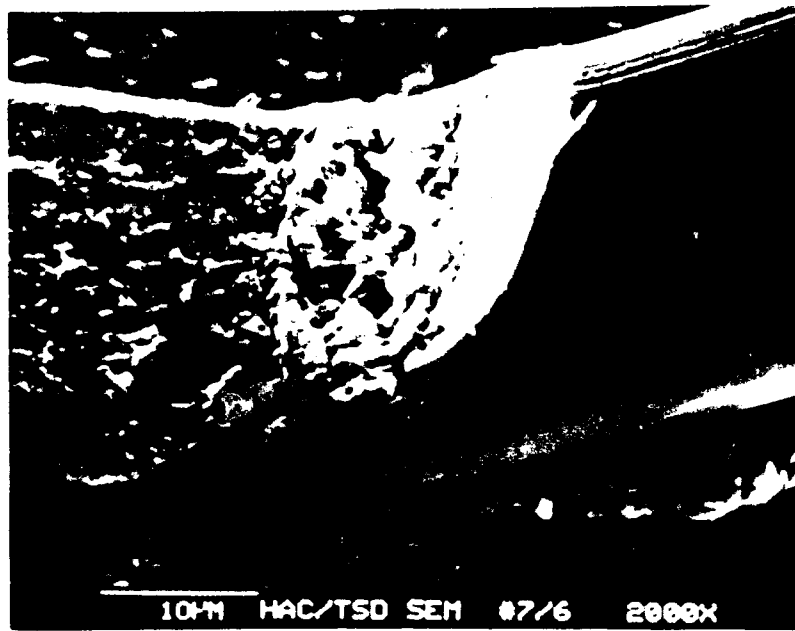
Figure H-25. Sample No. 7. SEM Photo of Bond at Pin 6,
After Cycling

Figure H-26. Sample No. 7. SEM Photo of Bond at Pin 11,
Before Cycling

Figure H-27. Sample No. 7. SEM Photo of Bond at Pin 11,
After Cycling

The remaining four samples, S/N 9 through 12, were photographed with the SEM to document the current bond conditions. Since sample S/N 7 was found to fail due to fatigue fracture after 33,000 cycles, cycling was begun on sample S/N 9, at the same current level as S/N 7, without any additional pulling of the wires.

Therefore, sample S/N 9 was installed in the fixture under the same conditions as sample S/N 7, and cycling was begun. All wires were connected in series. As each wire became open, it was bridged with a jumper and cycling continued, but at a slightly higher current to ensure that there was enough in-rush current to cause wire flexure.

Sample S/N 10 was submitted for infrared thermal imaging using the Barnes infrared microscope to document the thermal profile of samples with the shorter wires. The results are described in Appendix C.

Later, the wire dimensions were measured and the order of bonding was documented and correlated with the failure results.

Current cycling of sample S/N 9 was begun at 1.5A steady-state current and 1.6A in-rush current. The pin 3-4 wire fused open within 244 cycles. Cycling was resumed with higher current and with pins 3-4 bridged with a jumper. This procedures was continued until all six wires were open. The results are summarized below:

WIRE PINS	CUMULATIVE CYCLES	TYPE OF FAILURE	CURRENT (Steady State/In-Rush)	WIRE LENGTH (Approximately)
3-4	244	Fused	1.5A/1.6A	44.2 mils
10-11	5812	Fused	1.55A/1.7A	39.7 mils
6-7	65,929	Fused	1.65A/1.8A	28.7 mils
13-14	75,077	Fused	1,65A/1.8A	29.4 mils
8-9	142,250	Fused	1/8A/1.85A	28.5 mils
1-2	148,698	Fractured (pin 2 bond)	1.85A/1.95A	23.9 mils

Each of the bonds was examined with the SEM after the test, and fracture growth was noted at bonds to pins 2, 6, 11, and 13. Each of these cracked bonds was the first of the two bonds made for the wire. Refer to Figures H-28 through H-54 for SEM photos of wire bonds and crack growth.

Comparison of final current at failure with approximate wire length indicated full correlation between wire length and current handling capability. Therefore, in future tests, the wires were grouped by length to prevent the need for readjusting current after failure. This ensures that all wires are similarly stressed throughout the test.

A review of earlier photos of samples 1 through 7 disclosed that fractures to the pin 13 bond of sample S/N 6 and to the pin 6 and pin 11 bonds of sample S/N 7 were also at the first of the two wire bonds made. In no case was any fracturing found at the second bond of any of the wires. The first of the two bonds also was characteristically rough compared to the second bond in each case.

Because of these results, Hughes decided to conduct a test using samples with the longer wires in which the test conditions are similar to those for samples S/Ns 1, 2, and 3, but with the sample in a heated temperature chamber. It was hypothesized that fatigue fracturing is temperature dependent and that such a test will result in fatigue fractures with relatively few current cycles. Additional test samples both with the shorter wires and with the longer wires were fabricated, and modifications were made to allow current cycling of one sample at a time in a temperature chamber.

SEM photos of each bond were obtained before cycling and after cycling so that minor crack growth could be readily determined. The wire dimensions were measured and the order of bonding was documented and correlated with the failure results.

The wire lengths were measured by using 1) a tool maker's microscope to measure the horizontal distance between the wire bonds and 2) a research microscope with a calibrated focusing knob to measure the height of the wire arch. The approximate wire length was then calculated assuming an isosceles triangular wire arch shape using the Pythagorean theorem.
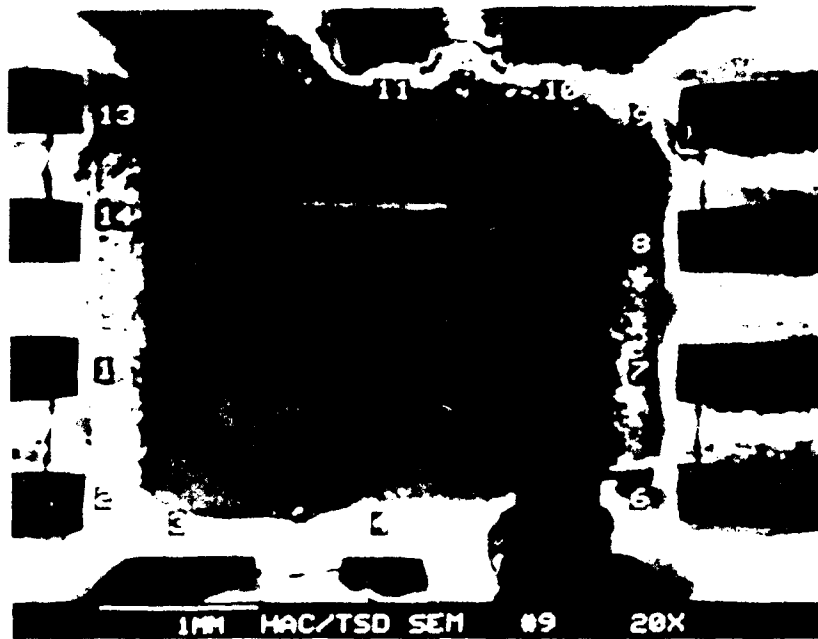
Figure H-28. Overall SEM View of S/N 9 Die Cavity After Current
Cycling. The Layout Configuration for Short Wire Samples
is Shown.

Figure H-29. SEM View of Wire Bonded Between Pins 1 and 2.
Pin 2 (left) Was Bonded First.

Figure H-30. SEM View of Pin 1-2 Wire After Current Cycling.
The Wire Opened at the Pin 2 Bond Heel.
Note the Thermal Damage to the Center of the Wire.
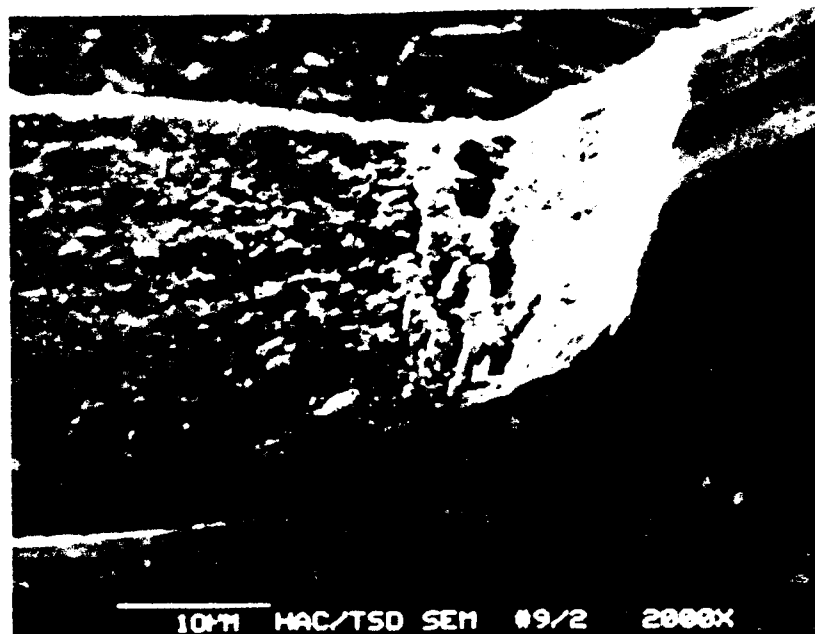
Figure H-31 SEM View of Pin 2 Bond Before Current Cycling.
Note roughness at top of bond. Refer to Figure H-29, left.
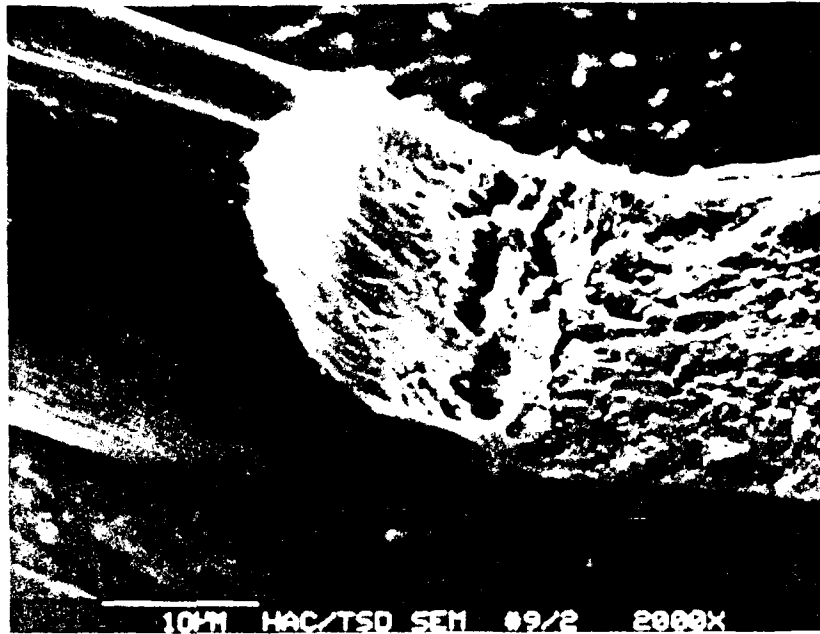
Figure H-32. SEM View of Pin 2 Bond Before Current Cycling
From Other Side
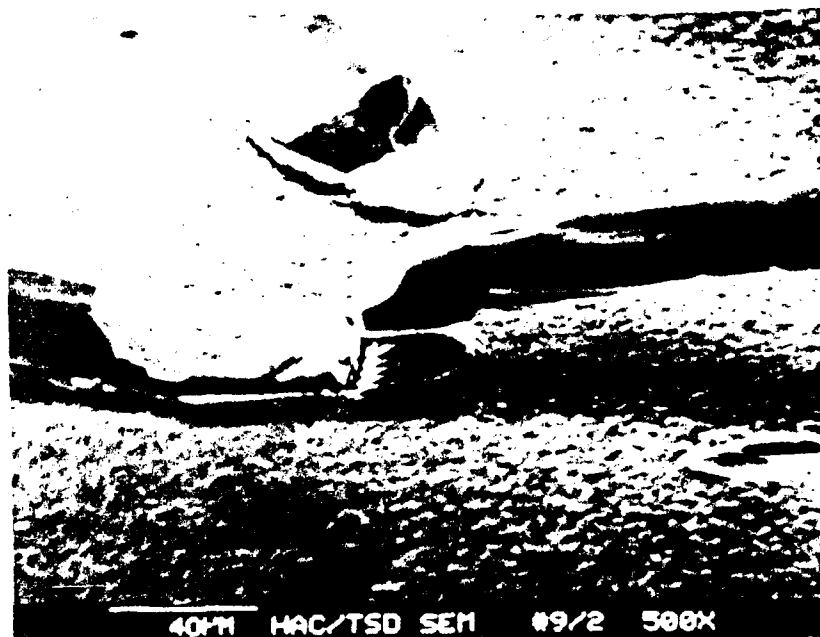
Figure H-33. SEM View of Fractured Pin 2 Bond After Current Cycling.
Refer to Figure H-30, Left
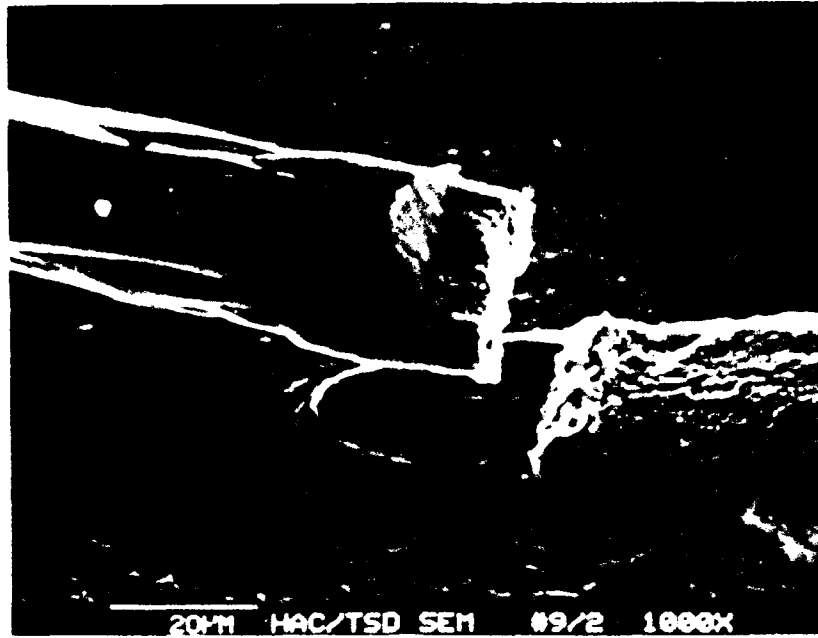
Figure H-34. SEM View of Fractured Pin 2 Bond From Opposite Side.
Note thermal damage near the bond.

Figure H-35. SEM View of Wire End at Pin 2 Bond Showing Detail of
Fracture Face
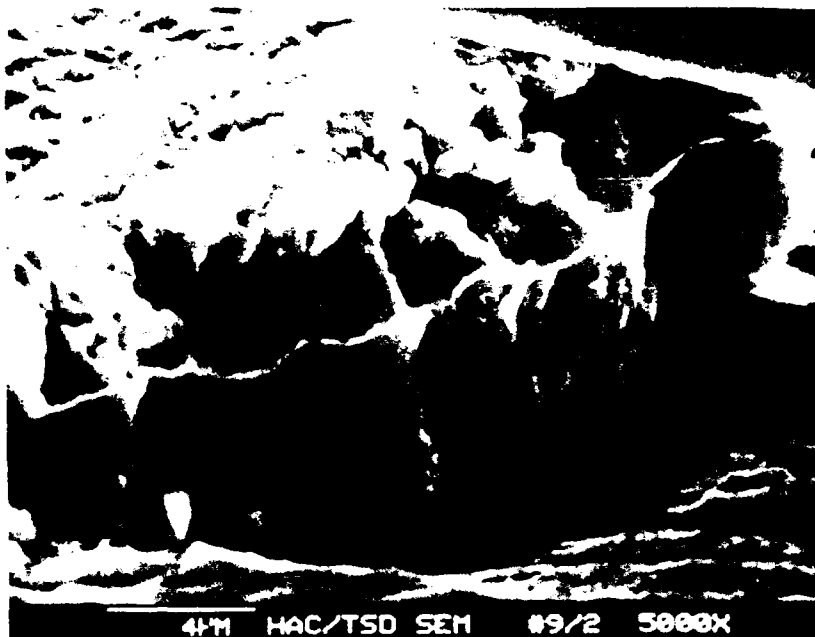
Figure H-36. SEM View of Pin 2 Bond Fracture Face Showing
Detail of Fracture

Figure H-37. SEM View of Pin 1 Bond After Current Cycling.
Note Complete Absence of Any Fracture Growth.

H-22
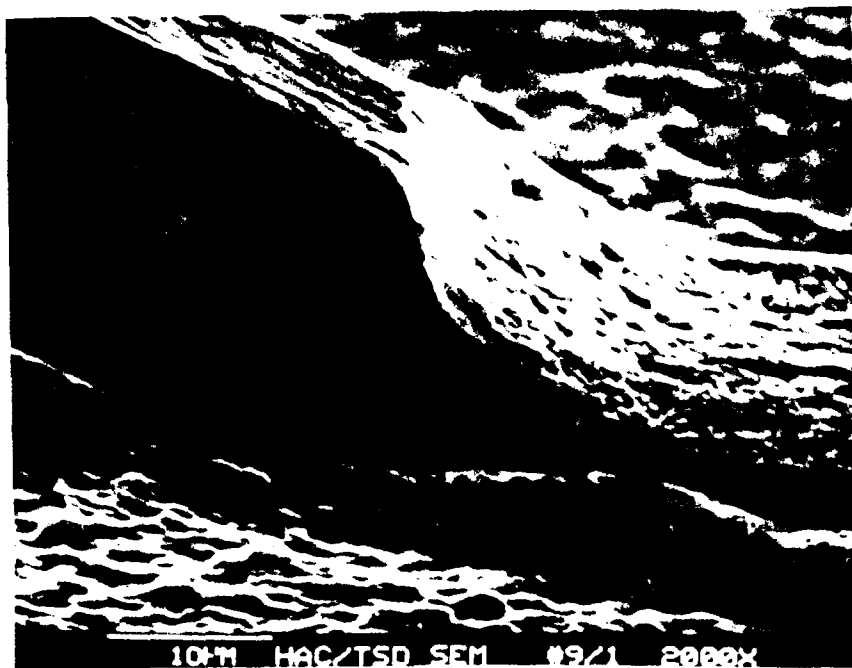
Figure H-38. SEM View of Pin 1 Bond After Current Cycling From
Opposite Side. Compare Smoothness of Bond With that Shown in
Figures H-31 and H-32. This Was Typical of All of the Samples Examined.
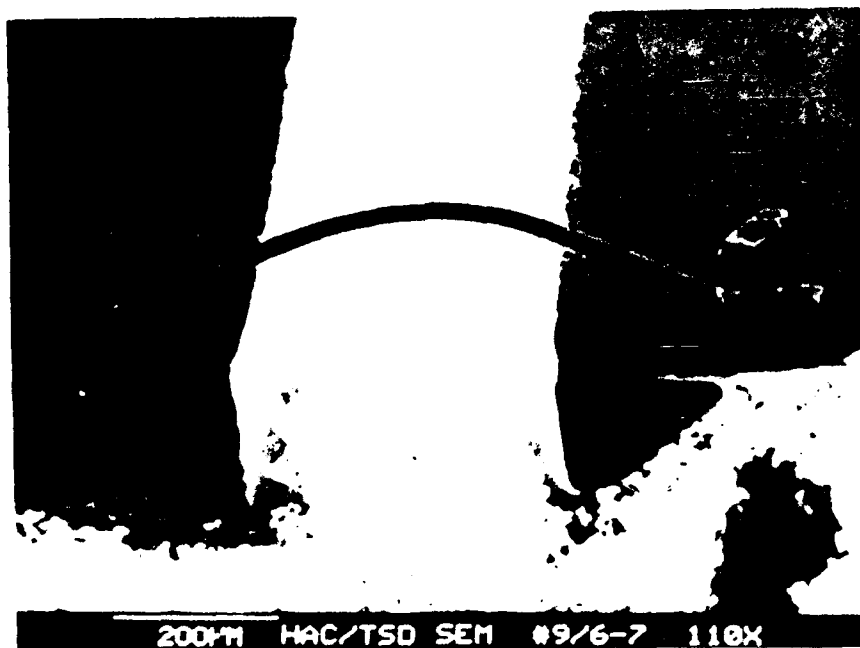
Figure H-39. SEM View of Bond Wire Between Pins 6 and 7 Before
Current Cycling. The Bond on the Right (pin 6) Was Made First.

Figure H-40. SEM View of Bond Wire Between Pins 6 and 7 After
Current Cycling
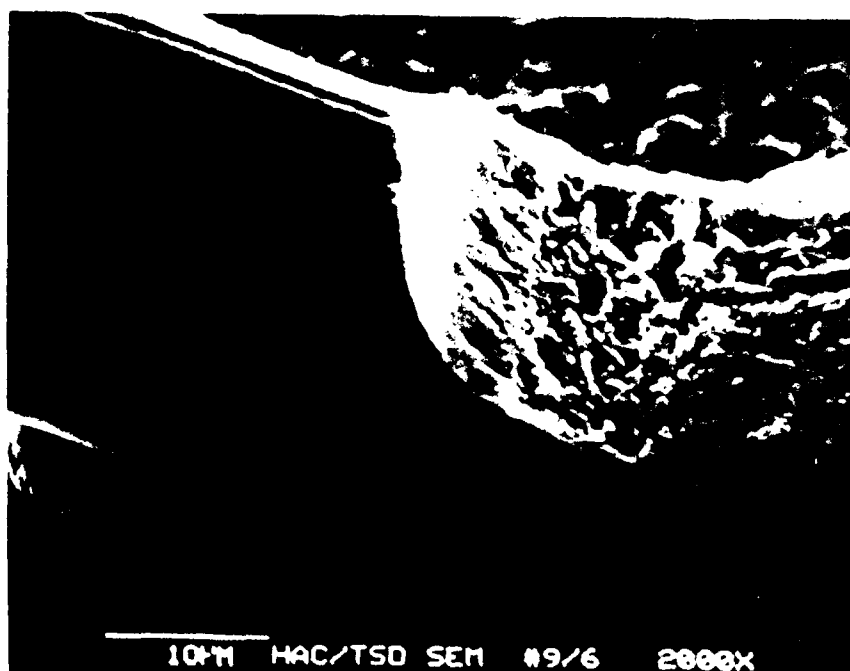
Figure H-41. SEM View Showing Detail of Pin 6 Bond Before
Current Cycling
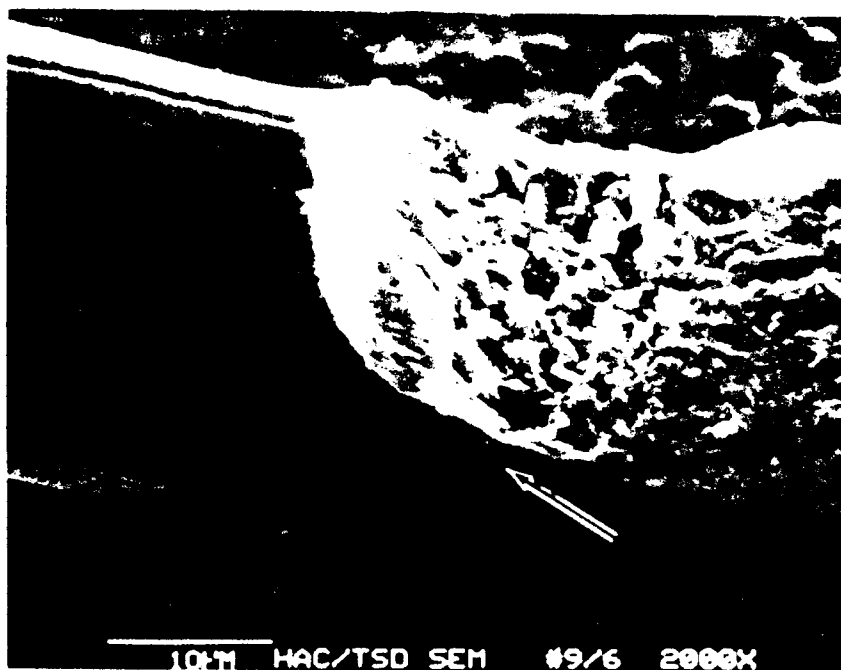
Figure H-42. SEM View Showing Detail of Pin 6 Bond After Current
Cycling. Note Crack Growth Indicated

Figure H-43. SEM View of Bond Wire Between Pins 10 and 11 Before
Current Cycling. The Bond on the Left (pin 11) Was Made First.
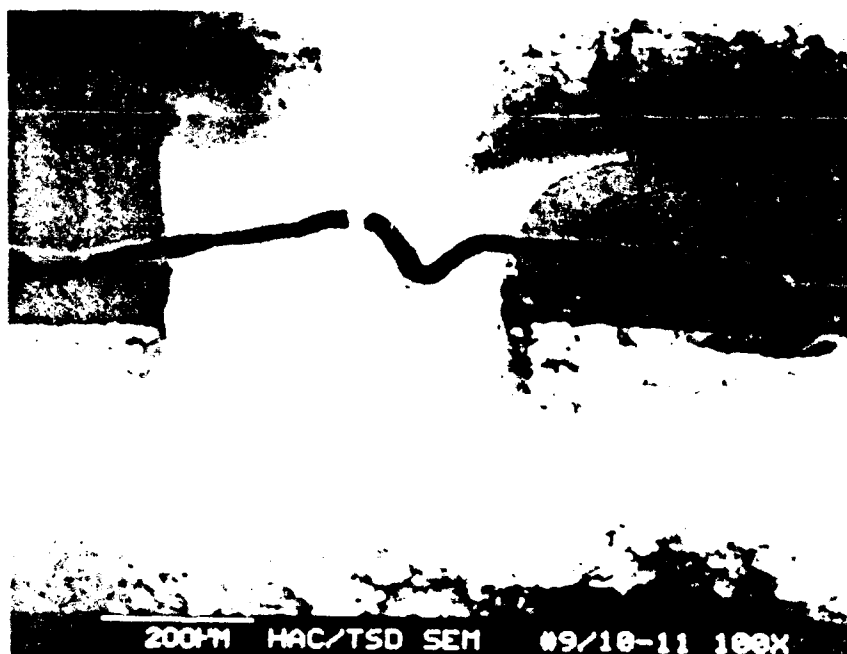
Figure H-44. SEM View of Bond Wire Between Pins 10 and 11
After Current Cycling

Figure H-45 SEM View Showing Detail of Pin 11 Bond Before
Current Cycling

Figure H-46. SEM View of Pin 11 Bond After Current Cycling
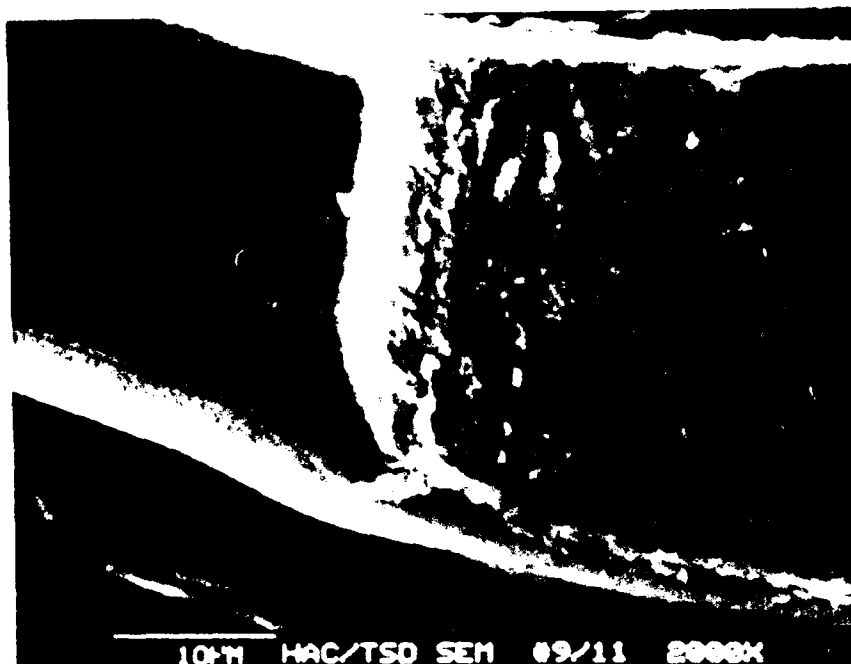
Figure H-47. SEM View From Other Side Showing Detail of Pin 11
Bond Before Current Cycling

H-27

Figure H-48. SEM View From Other Side Showing Detail of Pin 11
Bond After Current Cycling
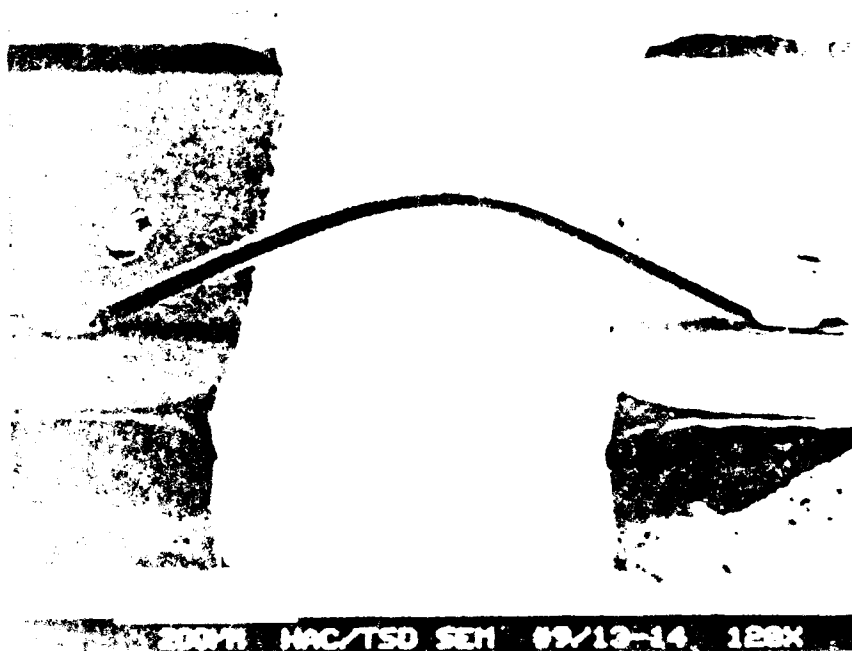
Figure H-49. SEM View of Bond Wire Between Pins 13 and 14 Before
Current Cycling. The Bond on the Right (Pin 13) Was Made First.
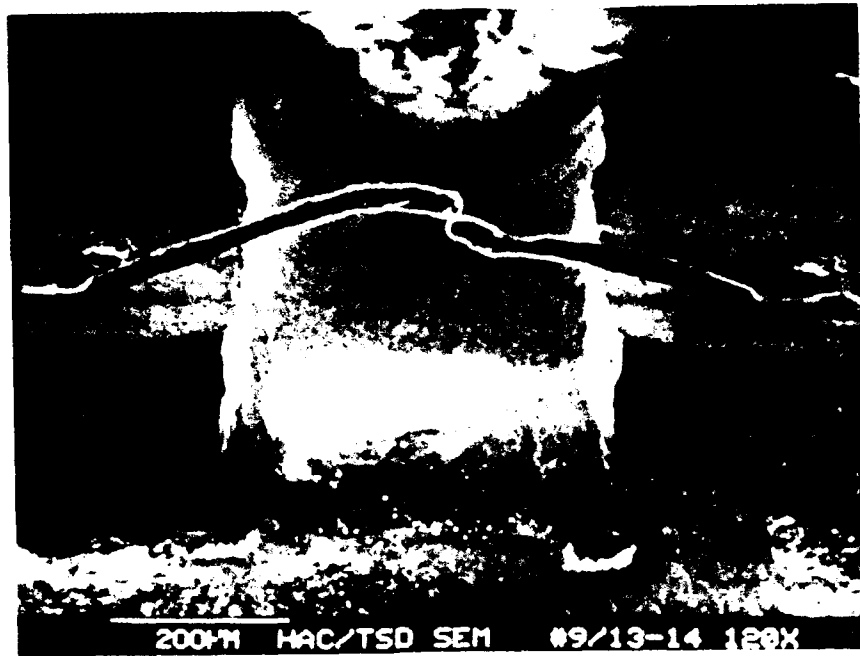
Figure H-50. SEM View of Bond Wire Between Pins 13 and 14 After
Current Cycling
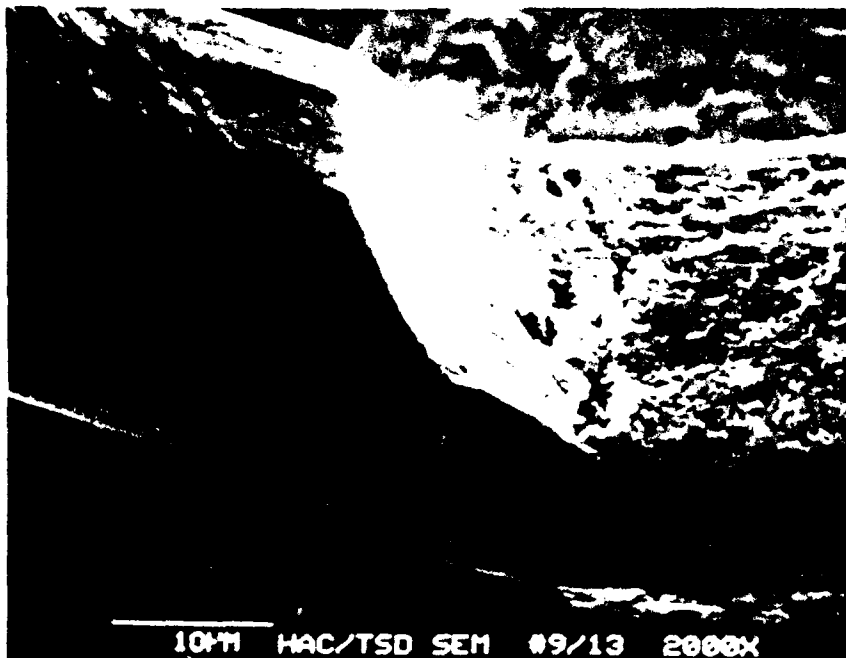
Figure H-51. SEM View of Pin 13 Bond Showing Detail Before
Current Cycling
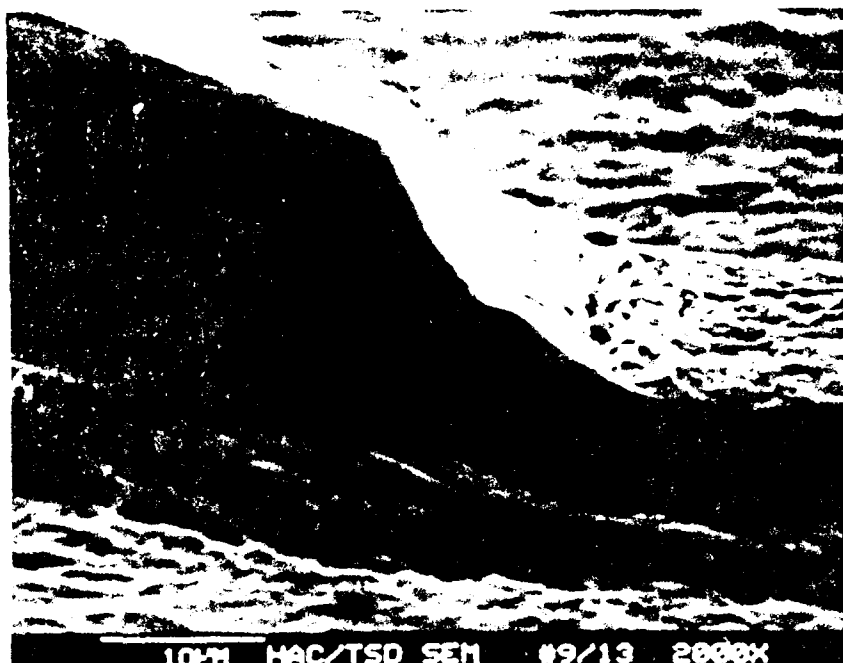
Figure H-52. SEM View Pin 13 Bond Showing Detail of Fracture Growth
After Current Cycling
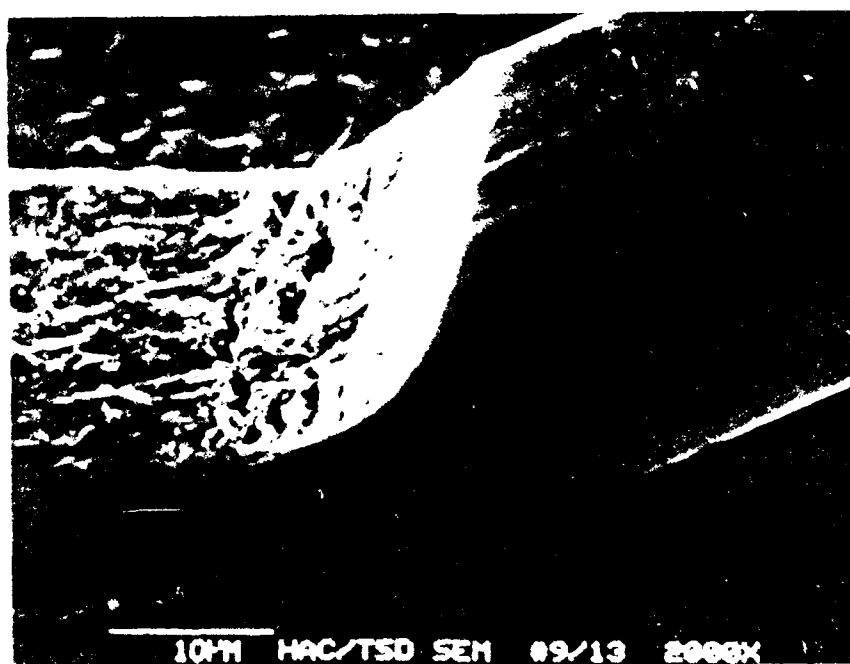
Figure H-53. SEM View of Pin 13 Bond From Other Side Showing Detail
Before Current Cycling
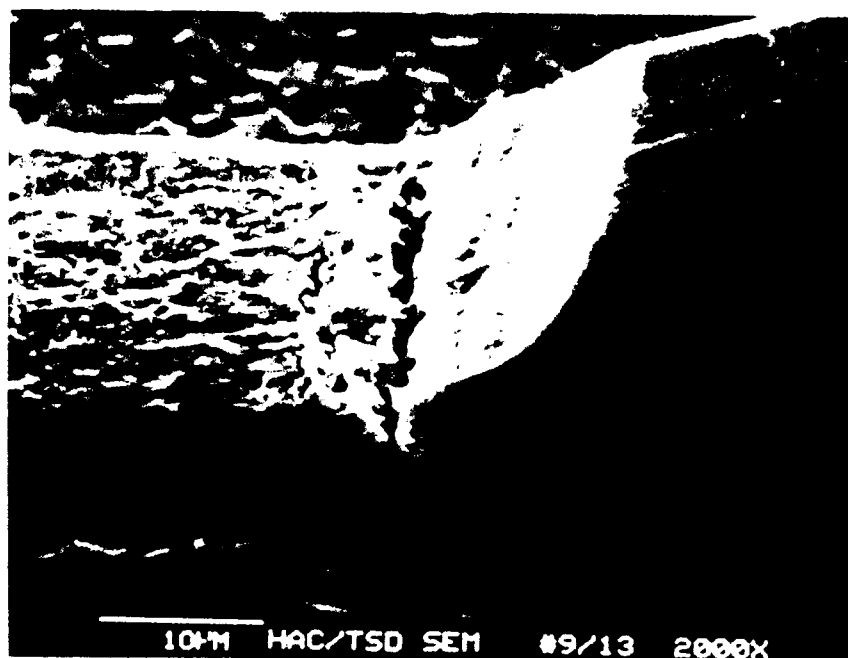
Figure H-54. SEM View of Pin 13 Bond From Other Side Showing
Detail of Fracture Growth After Current Cycling

One of the long wire samples, S/N 13, was current cycled at 150°C until failure occurred in all four wires. Current cycling of sample S/N 13 was begun at 0.45A steady-state current and 0.5A in-rush current at 150°C. This procedure was continued until all four wires were open. The results are summarized below:

WIRE PINS	CUMULATIVE CYCLES	TYPE OF FAILURE	WIRE LENGTH (Approximate)
Sample 13			
8-14	1,085,818	Fused	174 mils
9-13	1,405,076	Fused	171 mils
1-7	1,498,280	Fused	166 mils
2-6	2,096,995	Fused	169 mils

Each of the bonds was examined with the SEM after the test. A comparison of the before and after photos of the wires and bonds in sample 13 indicated that each wire failed due to opening at the midpoint. Typically this began with the wire sagging and then melting open. Damage to the bonds appeared to be mostly a result of the large deformation from sagging wires. Refer to Figures H-55 through H-60 for views of typical damage.

H-31

Ambient temperature current cycling of samples S/Ns 19, 20, and 21 was begun at 1.3A steady-state current and 1.35A in-rush current on a group of nine wires with wire lengths as indicated below:

Sample	Wires	Length
19	6-7	30 mils
	8-9	30 mils
	13-14	30 mils
20	1-2	31 mils
	6-7	31 mils
	13-14	29 mils
21	1-2	30 mils
	10-11	30 mils
	13-14	31 mils

The current cycling was continued until 4,233,000 cycles had accumulated with no failures on the above nine wires.

Current cycling of samples S/Ns 19, 20, and 21 was restarted at 1.6A steady-state current and 1.7A in-rush current on a group of five different wires. This procedure was continued until four of the five wires were open. The results are summarized below:

WIRE PINS	CUMULATIVE CYCLES	TYPE OF FAILURE	\WIRE LENGTH (Approximate)
Sample 19			
1-2	2,124,538	Fused	33 mils
Sample 20			
8-9	512,148	Fused & Fractured	35 mils
10-11	279,811	Fused & Fractured	35 mils
Sample 21			
3-4	82353	Fused	36 mils
6-7	5,516,538	No Failure	26 mils

Current cycling of samples S/N 19 and 20 was restarted at 1.6A steady-state current and 1.7A in-rush current on another group of two different wires. This procedure was continued until both wires were open. The results are summarized below:

WIRE PINS	CUMULATIVE CYCLES	TYPE OF FAILURE	\WIRE LENGTH (Approximate)
Sample 19			
10-11	135	Fused	42 mils
Sample 20			
3-4	8263	Fused	38 mils

Finally current cycling of sample S/N 21 was restarted at 1.76A steady state current and 1.79A in-rush current on the last remaining wire. The results are summarized below:

WIRE PINS	CUMULATIVE CY .ES	TYPE OF FAILURE	\WIRE LENGTH (Approximate)
Sample 21			
8-9	77,124	Fused	32 mils

Each of the bonds was examined with the SEM after the test, and fracture growth was noted at bonds to the following pins:

Sample 19   pin 2

Sample 20   pins 3, 9 and 10

Sample 21   pins 3 and 9

Refer to photos in Figures H-61 through H-85. The other bonds appeared unchanged. In each of the above cases, fracture growth was noted only at the first of the two bonds made to each wire.

The remaining tests, to quantify crack growth parameters, are described in Section 4.6.
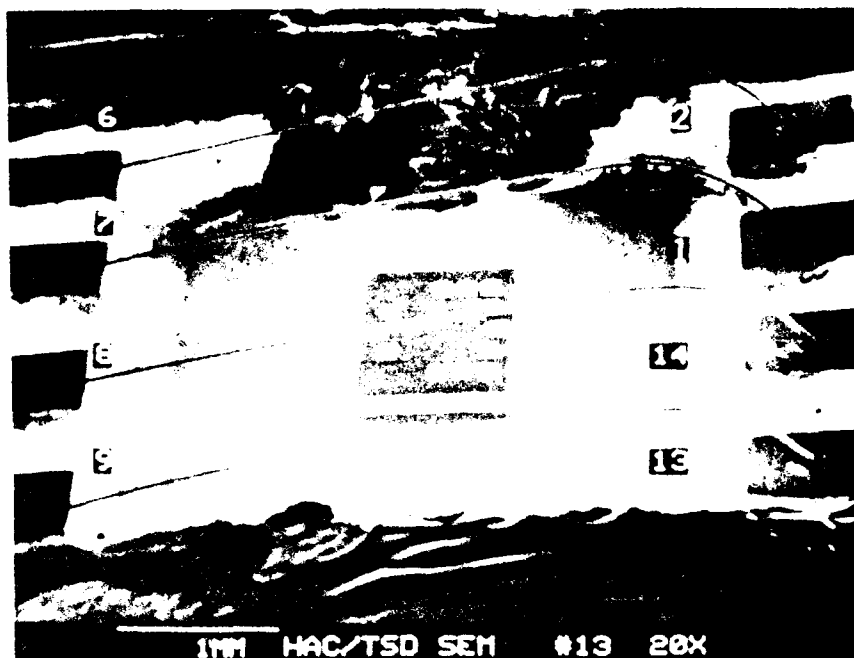
Figure H-55. Overall SEM Vew of Sample #13 Before Current
Cycling at Temperature
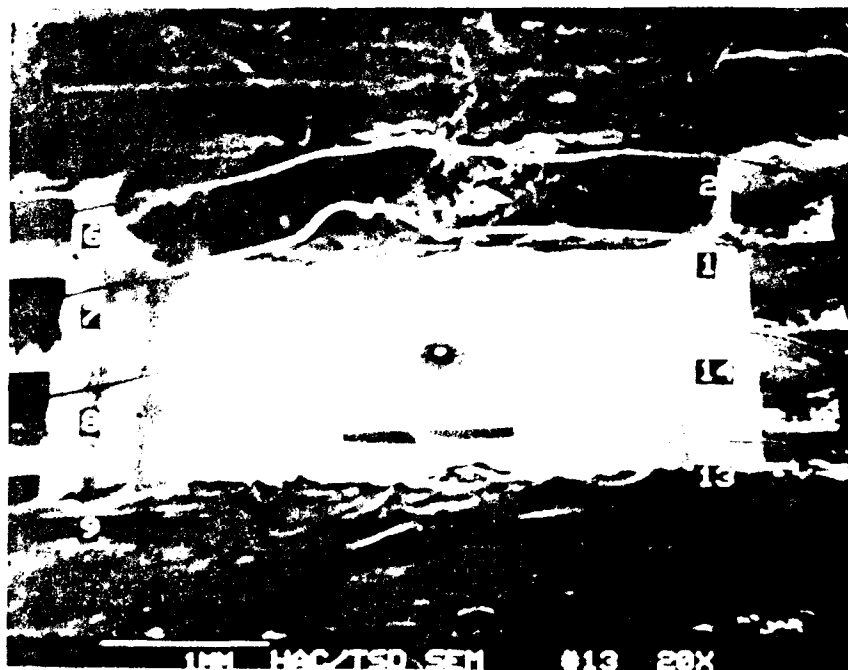
Figure H-56. Overall SEM View of Sample #13 After Current
Cycling at Temperature. Note Especially the Sagging Wires at
Bonds 1, 2, 13 and 14.

H-34

Figure H-57. SEM View of Sample #13 Pin 14 Bond
Before Current Cycling at Temperature
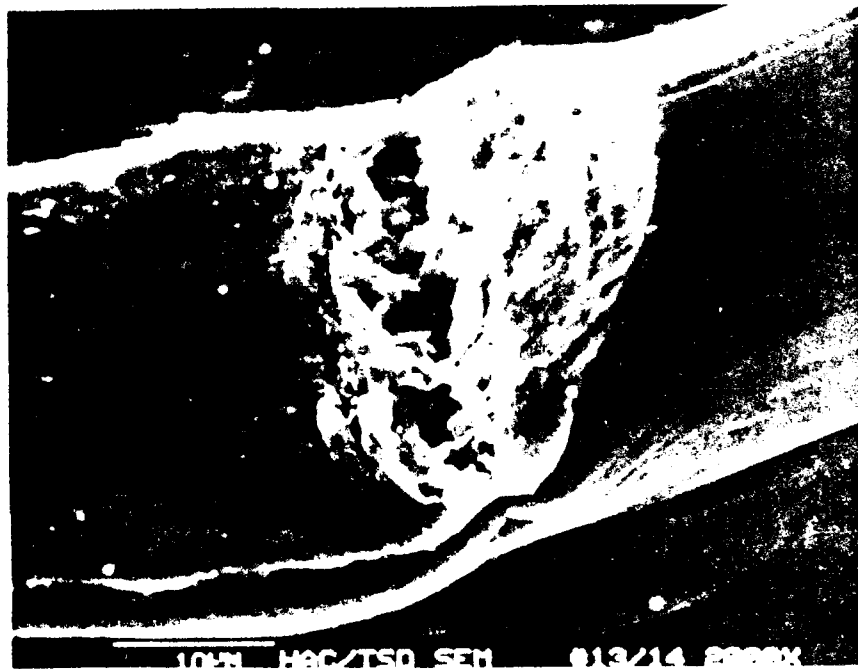
Figure H-58. SEM View of Sample #13 Pin 14 Bond
After Current Cycling at 150°C

H-35
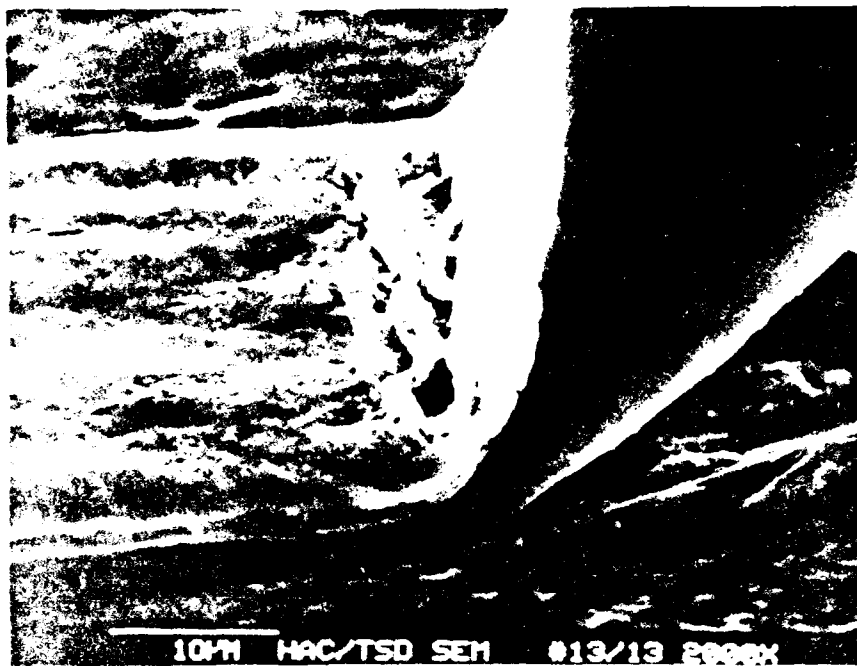
Figure H-59. SEM View of Sample #13, Pin 13 Bond
Before Current Cycling at 150°C
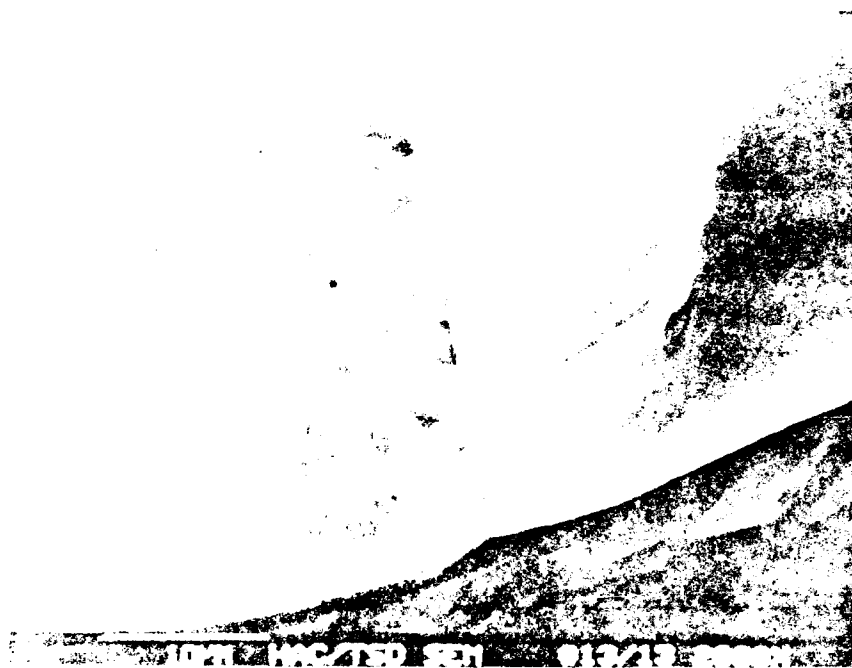
Figure H-60. SEM View of Sample #13 Pin 13
Bond After Current Cycling at 150°C
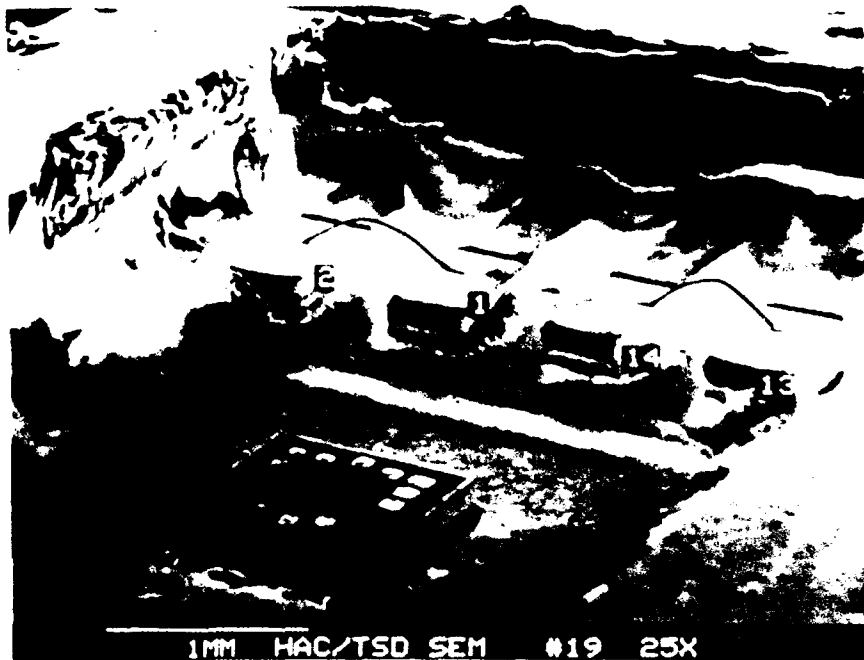
Figure H-61. View of Sample 19 Package Cavity Showing Part
of Bond Wire Configuration for Short Wires.

Figure H-62. View of Other End of Sample 19 Package Cavity
Showing Typical Bond Wire Configuration for Short Wires.
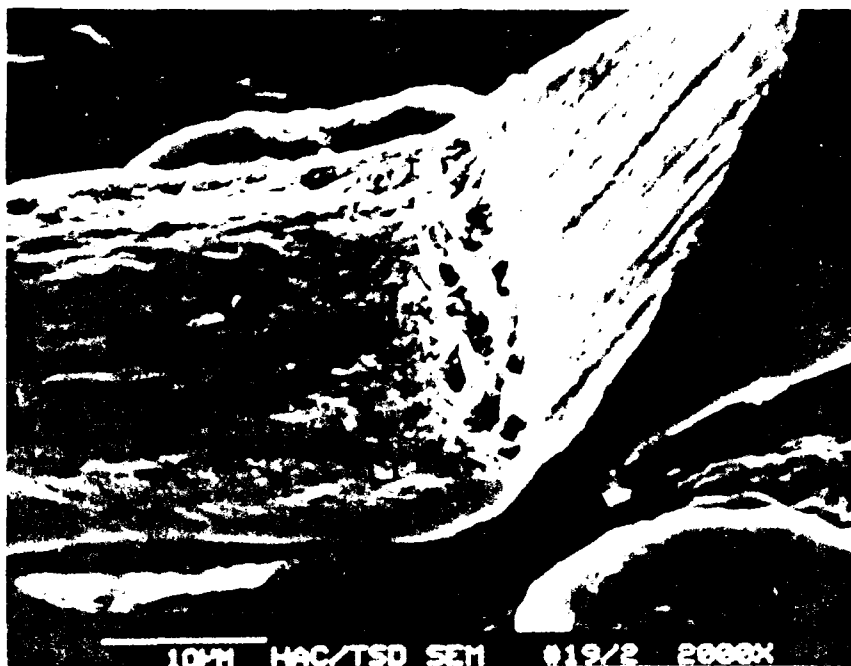
Figure H-63. View of Sample 19 Pin 2 Wire Bond Before
Current Pulsing

Figure H-64. View of Sample 19 Pin 2 Wire Bond After Current
Pulsing 1.6A for 2,124,538 Cycles. Note crack growth.
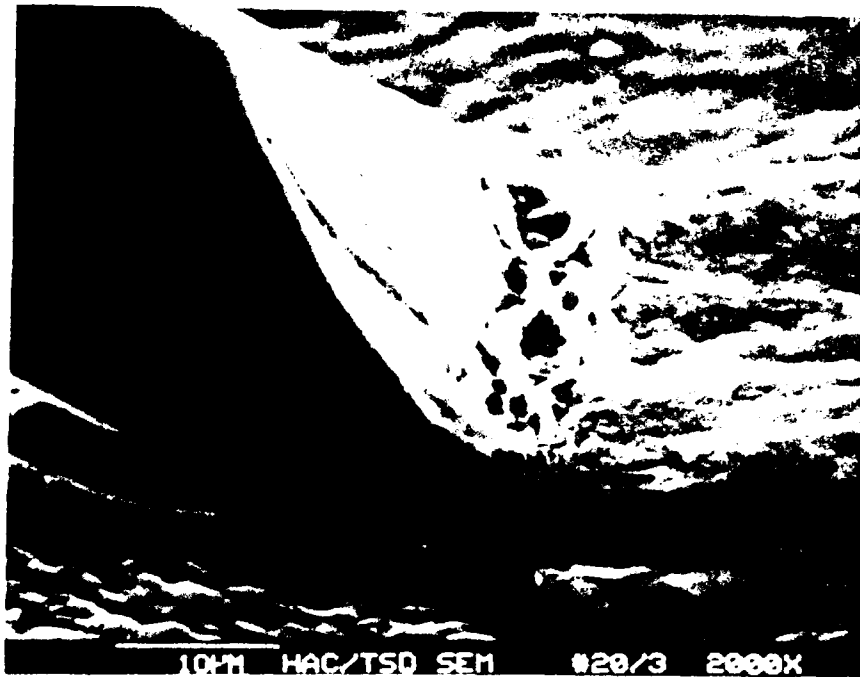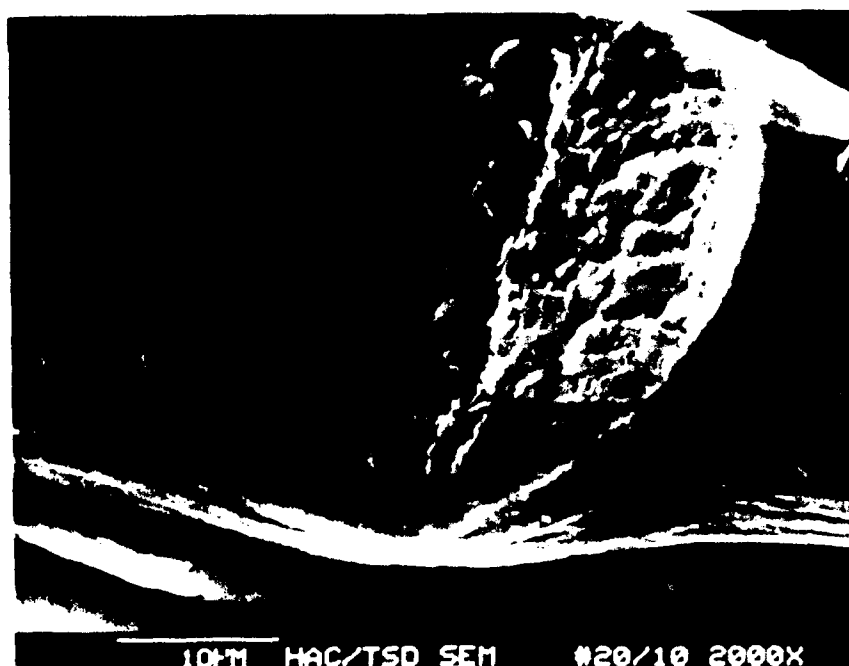
Figure H-65. View of Sample 20 Pin 3 Wire Bond Before
Current Pulsing
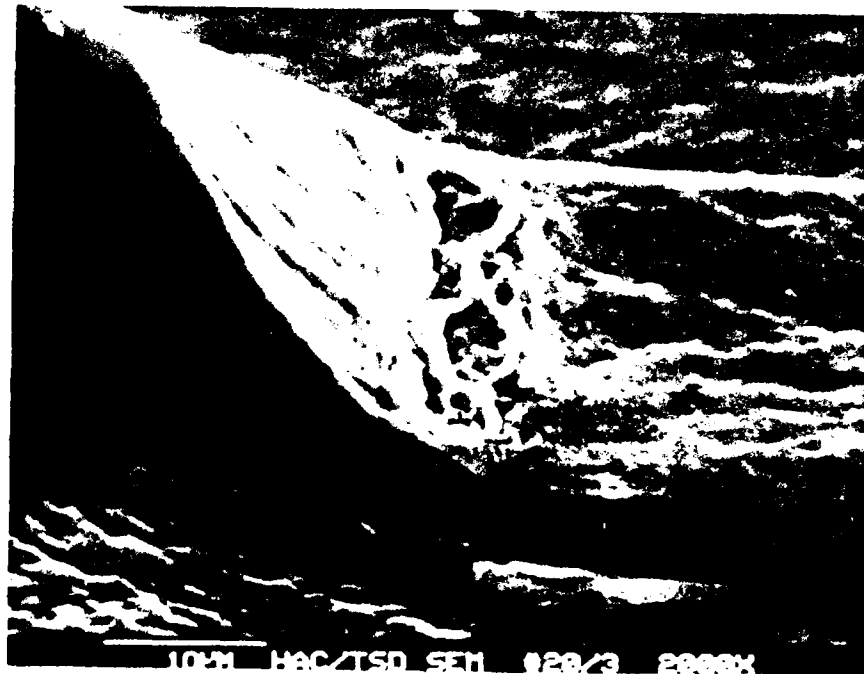
Figure H-66. View of Sample 20 Pin 3 Wire Bond After Current
Pulsing 8264 Cycles at 1.6A. Note Crack Growth.

Figure H-67. Detail View of Sample 20 Pin 3 Wire Bond Before
Current Pulsing

Figure H-68. Detail View of Crack Growth in Sample 20 Pin 3 Wire
Bond After Current Pulsing
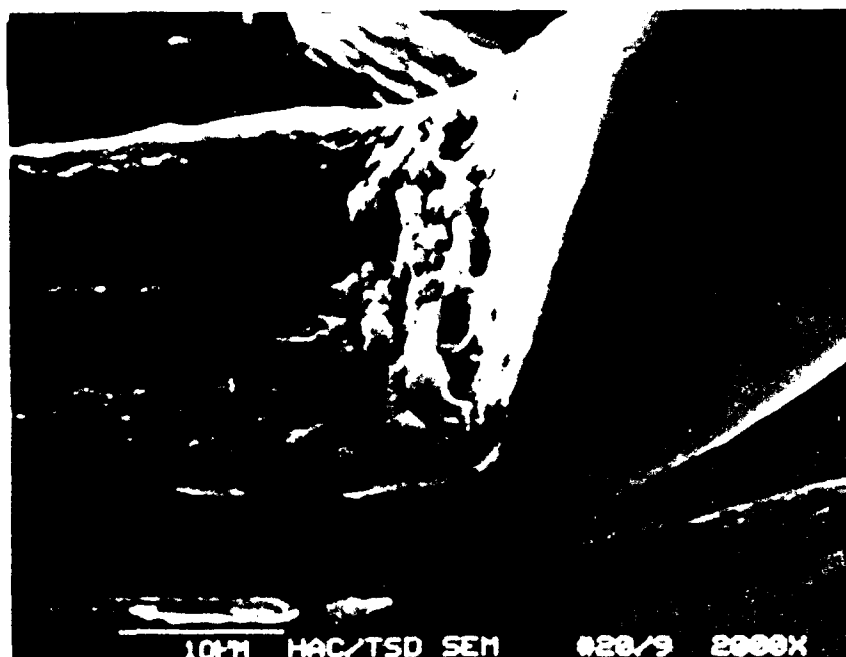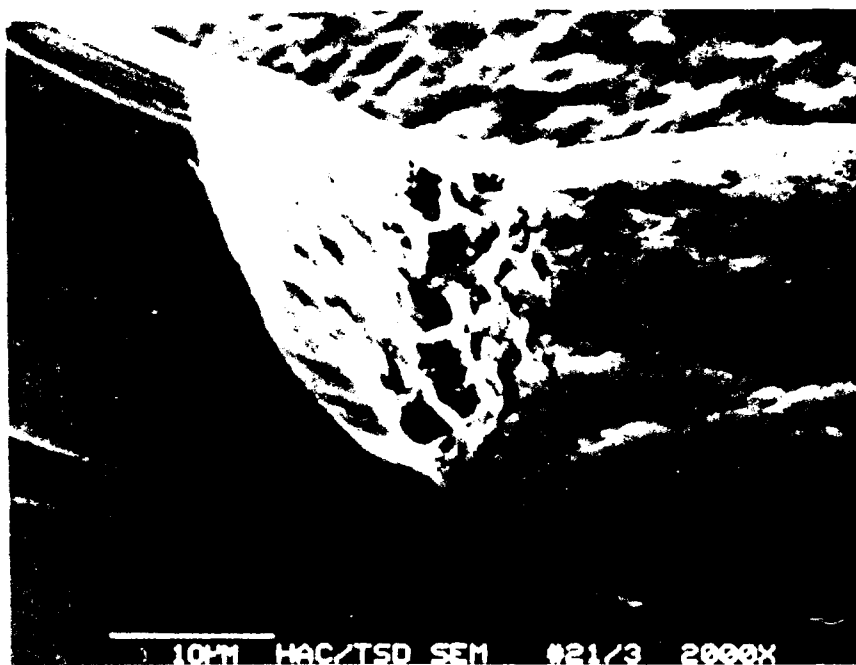
Figure H-69. View of Sample 20 Pin 9 Wire Bond Before
Current Pulsing
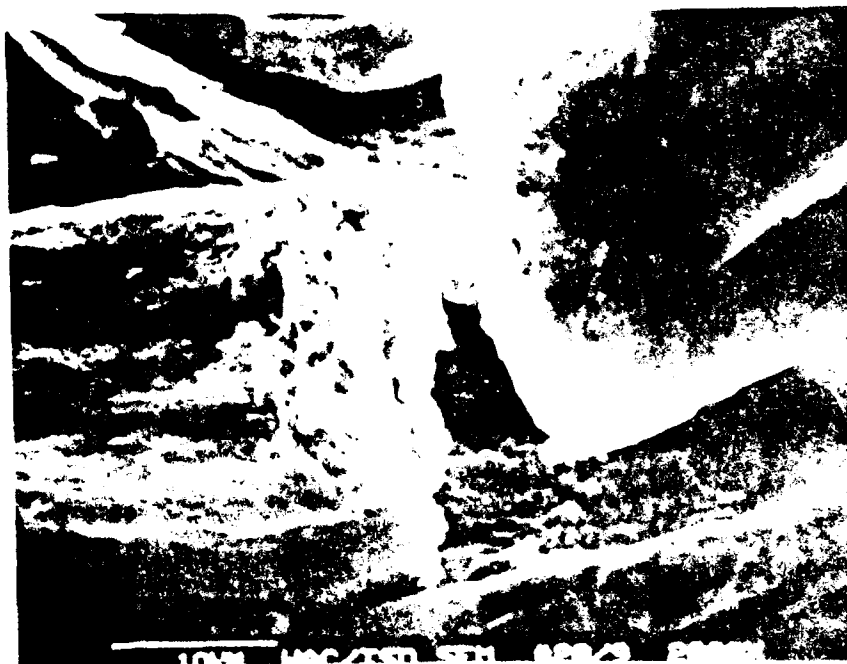
Figure H-70. View of Sample 20 Pin 9 Fractured Wire Bond
After Current Pulsing 512,148 Cycles at 1.6A

H-41

Figure H-71. Another View of Fractured Bond at Pin 9
of Sample 20

Figure H-72. Detail View of Fracture Face of Sample 20 Pin
9 Wire Bond
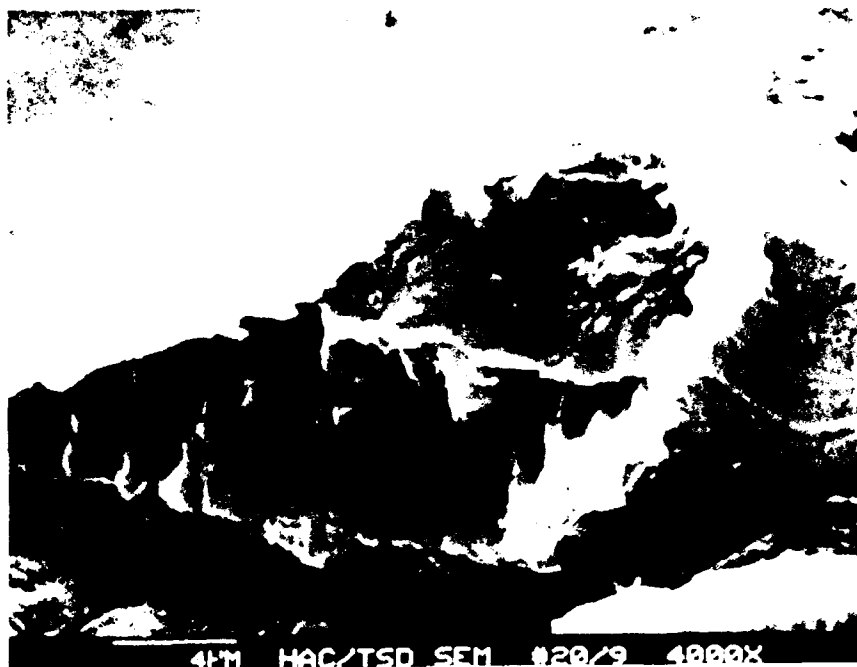
Figure H-73. Another Detail View of Sample 20 Pin 9 Wire
Bond Fracture Face

Figure H-74. View of Sample 20 Pin 10 Wire Bond Before
Current Pulsing

Figure H-75. View of Sample 20 Pins 10-11 Bond Wire After
Current Cycling 279,811 Cycles at 1.6A. Note Fracture at
Pin 10 Wire Bond.
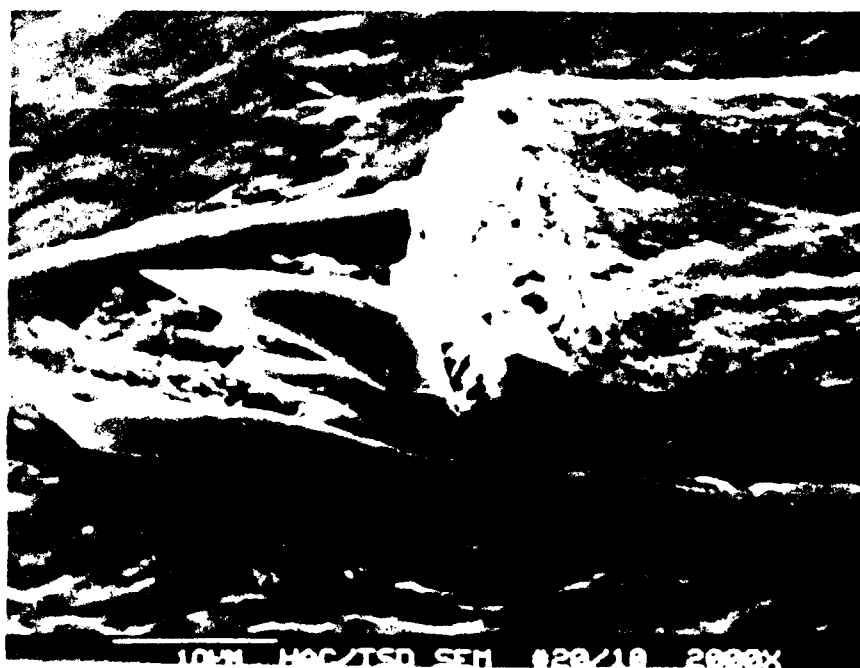
Figure H-76. View of Sample 20 Pin 10 Wire Bond After
Current Pulsing. Note Fracture Face.

Figure H-77. Detail View of Sample 20 Pin 10 Wire Bond
Fracture Face. Note Fused Aluminum at Right Side Adhering to
Parting Line of Fracture Face.

Figure H-78. View of Sample 20 Pin 10 Bond Wire Mating to
Fracture Face. Note That the Wire Fused Up to the Fracture Face.

Figure H-79. View of Sample 21 Pin 3 Wire Bond Before
Current Pulsing

Figure H-80. View of Sample 21 Pin 3 Wire Bond After Current
Pulsing 82,353 Cycles at 1.6A. Note Crack Growth

Figure H-81. Detail View of Crack Growth in Sample 21 Pin 3
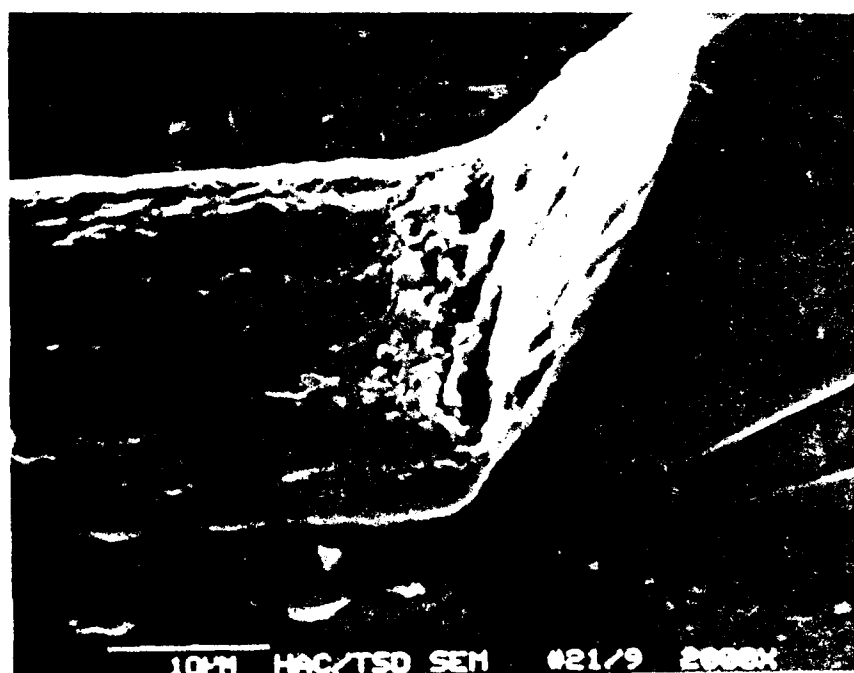Wire Bond After Current Pulsing

Figure H-82. View of Sample 21 Pin 9 Wire Bond Before
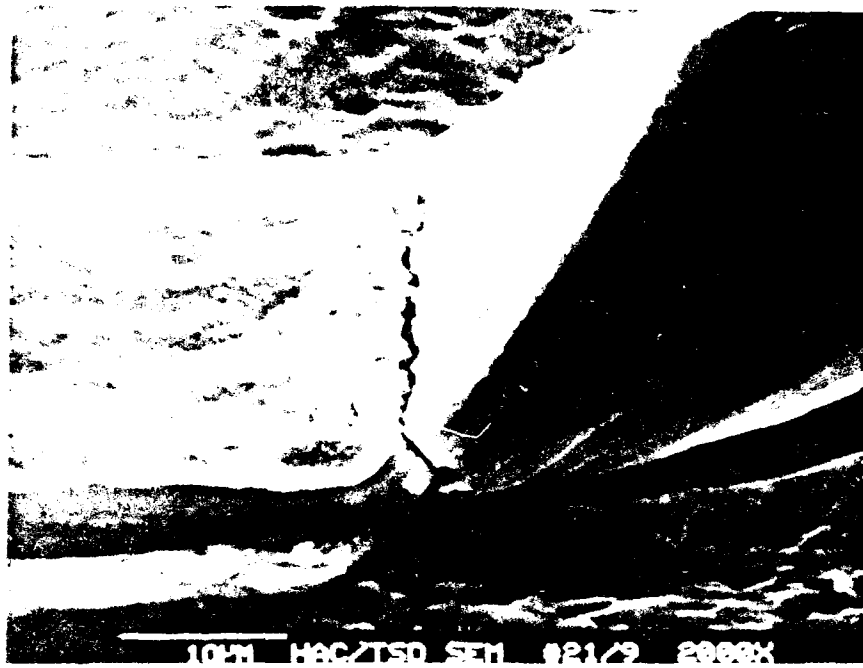Current Pulsing

H-47

Figure H-83. View of Sample 21 Pin 9 Wire Bond After Current
Pulsing 775,124 Cycles at 1.76A. Note Crack Growth.

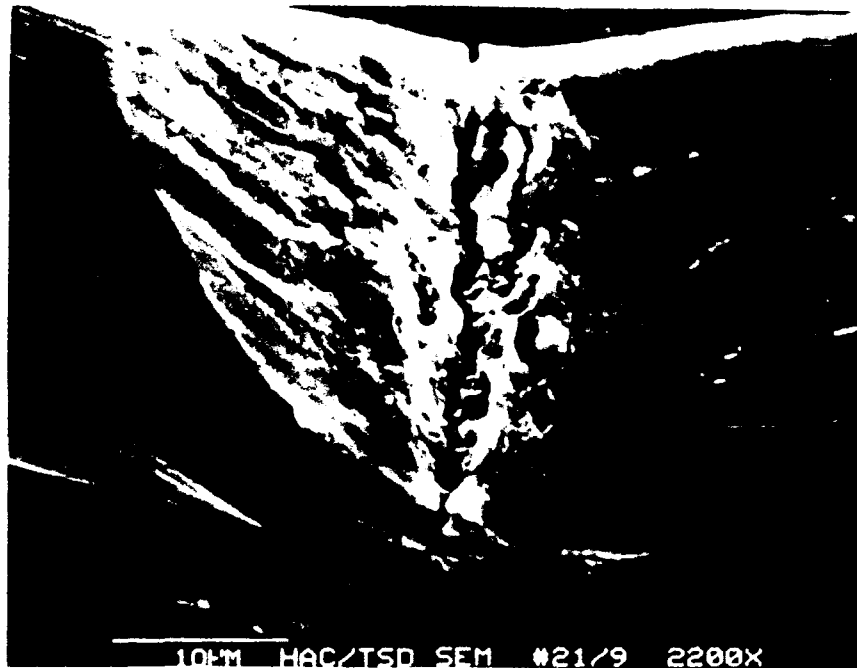Figure H-84. Another View of Sample 21 Pin 9 Wire Bond
Before Current Pulsing

Figure H-85. Another View of the Crack Growth in Sample 21
Pin 9 Wire Bond After Current Pulsing.